CO_2 Capture by Absorption with Potassium Carbonate
Second Quarterly Report 2007

Quarterly Progress Report
Reporting Period Start Date: April 1, 2007
Reporting Period End Date: June 30, 2007

Authors: Gary T. Rochelle,
Andrew Sexton, Jason Davis, Marcus Hilliard, Qing Xu, David Van Wagener, Jorge M. Plaza,
Fred Closmann, Amornvadee Veawab (Univ. of Regina), Manjula Nainar (Univ. of Regina)

July 27, 2007
DOE Award #: DE-FC26-02NT41440
Department of Chemical Engineering
The University of Texas at Austin

Disclaimer

Abstract

The objective of this work is to improve the process for CO_2 capture by alkanolamine absorption/stripping by developing an alternative solvent, aqueous K_2CO_3 promoted by piperazine (PZ). The best K^+/PZ solvent, 4m K^+/4 m PZ, and the best process configuration, double matrix stripper and double intercooled absorber, requires equivalent work of 35 kJ/mole CO_2 to produce CO_2 at 10 MPa. The pilot plant results demonstrate that 5mK^+/2.5mPZ solvent has an absorption rate 1.5 times faster than 7 m MEA and 2 times faster than 6.4mK^+/1.6mPZ. Inhibitor A is effective at reducing oxidative degradation over a wide range of metal concentrations and solvent types. Piperazine and aminomethylpropanol (AMP) are resistant to oxidative degradation catalyzed by dissolved iron. The thermal degradation of MEA becomes significant at 120^{o}C, but piperazine appears to be resistant to thermal degradation. The MEA vapor pressure over 7 m MEA at 40^{o}C is 6.6 Pa. The solubility of potassium sulfate in MEA/PZ solvents is increased at greater CO_2 loading.

Contents

Disclaimer 3
Abstract 4
Contents 5
List of Figures 7
List of Tables 10
Introduction 11
Experimental and Modeling Methods 11
Results and Discussion 11
Subtask 1.2b – Literature Review of Properties 11
Subtask 1.8a – Predict Absorber Flowsheet Options 11
Subtask 1.8b – Predict Stripper Flowsheet Options 11
Task 2 – Pilot Plant 12
Subtask 3.2 – Oxidative Degradation 12
Subtask 3.3 – Thermal Degradation 12
Subtask 3.4 – Amine Volatility 12
Subtask 4.1 – Sulfate Precipitation 12
Conclusions 12
Future Work 13
Subtask 1.2b – Literature Review of Properties 13
Subtask 3.4 – Amine Volatility 14
Task 1 – Modeling Performance of Absorption/Stripping of CO_2 with Aqueous K_2CO_3 Promoted by Piperazine 15
Subtask 1.2b – Literature Review of Properties 15
Subtask 1.8a – Predicted Absorber Performance 24
Introduction 24
Experimental 24
K_2CO_3/Piperazine 24
MEA 31
Solubility analysis for K_2CO_3/PZ loaded solutions 36
Conclusions 37
Future Work 37
Subtask 1.8b – Predicted Stripper Performance with 4m K^+/4m PZ 38
Introduction 38
Experimental 38
AspenPlus Stripper Model Design 38
Absorber/Stripper System Model in AspenPlus 39
Conclusions and Future Work 42
Task 3 – Solvent Losses 43

Subtask 3.2 – Oxidative Degradation 43
Introduction 43
Experimental 43
Results 45
Conclusions and Future Work 51
Subtask 3.3 – Thermal Degradation 52
Introduction 52
Theory 53
Monoethanolamine 53
Piperazine 54
Methods 54
High Temperature MEA Experiment 54
MEA Full Range Temperature Experiments 54
Piperazine Experiment 54
GC Methods 55
HPLC Methods 55
pH Titration Method 55
Results and Discussion 55
MEA High Temperature Experiments 55
MEA Full Temperature Range Experiments 57
Piperazine Experiments 61
Future Work 62
Pure Component Systems: MEA, PZ, and H_2O – Chapter VIII 63
Task 4 – Solvent Reclaiming 64
Subtask 4.1a – Reclaiming by crystallization – potassium sulfate 64
Method 1 64
Method 2 64
Method 3, CO_2 loaded 64
Examples: 65
Task 5 – Corrosion 77
References 86

List of Figures

Figure 1: Absorber modeling conditions for 4.5 m/4.5 m K^+/PZ 25

Figure 2: Change in CO_2 removal due to change in semilean feed position for 4.5m/4.5 m K_2CO_3/PZ. 0.5 kPa CO_2 lean solvent. No intercooling 26

Figure 3: Temperature and CO_2 rate profiles for absorber with semilean feed at 0.30 column height and no intercooling. Solvent 4.5m/4.5 m K_2CO_3/PZ. 0.5 kPa CO_2 lean solvent. 27

Figure 4: Change in CO_2 removal due to change in intercooled semilean feed position for 4.5m/4.5 m K_2CO_3/PZ. 0.5 kPa CO_2 lean solvent. 28

Figure 5: Temperature and CO_2 rate profiles for absorber with semilean feed and intercooling at 0.70 column height. Solvent 4.5m/4.5 m K_2CO_3/ PZ. 0.5 kPa CO_2 lean solvent. 28

Figure 6: Change in CO_2 removal due to change in 2nd intercooling stage with fixed semilean feed position for 4.5m/4.5 m K_2CO_3/PZ. 0.5 kPa CO_2 lean solvent. 29

Figure 7: Temperature and CO_2 rate profiles for absorber with intercooled semilean feed at 0.70 and intercooling at 0.90 column height. Solvent 4.5m/4.5 m K_2CO_3/PZ. 0.5 kPa CO_2 lean solvent. 30

Figure 8: Temperature and CO_2 rate profiles for absorber with intercooled semilean feed at 0.70 and intercooling at 0.90 column height. Solvent 4.5m/4.5 m K_2CO_3/ PZ. 0.7 kPa CO_2 lean solvent 31

Figure 9: Absorber modeling conditions for 11 m MEA 32

Figure 10: Change in CO_2 removal due to change in semilean feed position for 11 m MEA. No intercooling 33

Figure 11: Temperature and CO_2 rate profiles for absorber with semilean feed at 0.30 column height and no intercooling. Solvent 11 m MEA. 33

Figure 12: Change in CO_2 removal due to change in intercooled semilean feed position for 11 m MEA. 34

Figure 13: Temperature and CO_2 rate profiles for absorber with semilean feed and intercooling at 0.70 column height. Solvent 11 m MEA. 34

Figure 14: Change in CO_2 removal due to change in 2nd intercooling stage with fixed semilean feed position for 11 m MEA. 35

Figure 15: Temperature and CO_2 rate profiles for absorber with intercooled semilean feed at 0.70 and intercooling at 0.90 column height. Solvent 11 m MEA. 35

Figure 16: Results of conductivity variations due to water addition for K^+/PZ 37

Figure 17: Double Matrix Stripper Configuration 39

Figure 18: CO_2 Removal Configuration with Double Matrix Stripper 40

Figure 19: Optimum Lean Loading for 4 m K^+/4 m PZ, double matrix stripper (230/160 kPa, 0.185 split), 90% CO_2 removal, 15 m absorber packing. 42

Figure 20: May 2007 MEA experiment (Oxidative degradation of 7m MEA, α = 0.40, 55^{o}C, 1400 RPM, 0.1mM Fe, 5mM Cu, 98%O_2/2%CO_2) 45

Figure 21: May 2007 PZ experiment (Oxidative degradation of aqueous PZ, α = 0.60, 55^{o}C, 1400 RPM, 0.1mM Fe, 98%O_2/2%CO_2) 47

Figure 22: April 2007 PZ experiments (Oxidative degradation of aqueous PZ, α = 0.60, 55^{o}C, 1400 RPM, 0.1mM Fe, 5mM Cu, +/- 100mM "A", 98%O_2/2%CO_2) 47

Figure 23: June 2007 MEA/PZ experiment (Oxidative degradation of 7m MEA/2m PZ, α = 0.40, 55^{o}C, 1400 RPM, 0.1mM Fe, 100mM "A", 98%O_2/2%CO_2) 48

Figure 24: June 2007 MEA/PZ experiment (Oxidative degradation of 7m MEA/2m PZ, α = 0.40, 55^{o}C, 1400 RPM, 0.1mM Fe, 5mM Cu, 100mM "A", 98%O_2/2%CO_2) 49

Figure 25: March 2007 AMP experiment (Oxidative degradation of 3M AMP, α = 0.55, 55^{o}C, 1400 RPM, 1mM Fe, 98%O_2/2%CO_2). 50

Figure 26: AMP Structure 50

Figure 27: MEA degraded at 150^{o}C for 3 weeks on HP-5 GC column 56

Figure 28: MEA losses at 150^{o}C over an 8 week period 57

Figure 29: MEA losses over an 8 week period at 100^{o}C 58

Figure 30: MEA losses at 120^{o}C over an 8-week period 59

Figure 31: MEA losses at 135^{o}C over an 8-week period 60

Figure 32: Piperazine losses in aqueous PZ with 0.8 moles CO_2/ over time at 120^{o}C and 135^{o}C 62

Figure 33: Conductivity dependence on concentration -1 65

Figure 34: Conductivity dependence on concentration -2 66

Figure 35: Conductivity dependence on concentration -3 66

Figure 36: Activity coefficient of K^+ and $SO_4^=$, effect of MEA concentration 71

Figure 37: Activity coefficient of K+ and SO4=, effect of CO2 loading 71

Figure 38: Activity coefficient of K+ and SO4=, effect of T 72

Figure 39: Product of γ, effect of temperature 72

Figure 40: Product of γ, effect of CO_2 loading 73

Figure 41: Product of γ, effect of MEA concentration 73

Figure 42: Relative Saturation, effect of T 74

Figure 43: Relative Saturation, effect of CO_2 loading 74

Figure 44: Relative Saturation, effect of MEA concentration 75

Figure 45: Cyclic polarization curve of an aqueous solution of MEA/PZ (5/1.2 kmol/m^2) containing the oxidative degradation Inhibitor A and 0.20 mol/mol CO_2 loading at 80^{o}C under 10.13 kPa O_2. 79

Figure 46: Effect of concentration of the oxidative degradation Inhibitor A on polarization behavior of carbon steel in aqueous solutions of MEA/PZ (5/1.2 kmol/m^3) containing the oxidative degradation Inhibitor A with the concentrations of 0, 1,000, 10,000 and 30,000 ppm, 0.20 mol/mol CO_2 loading, 1 wt % acetic acid at 80^{o}C under (a) 0.00 kPa O_2 and (b) 10.13 kPa O_2. 79

Figure 47: Effect of concentration of the oxidative degradation Inhibitor A on corrosion rates of carbon steel in aqueous solutions of blended MEA/PZ (5/1.2 kmol/m^3) containing 0.20 mol/mol CO_2 loading, 1 wt % acetic acid, and various concentrations of Inhibitor A at 80°C. 80

Figure 48: Effect of solution temperature on polarization behavior of carbon steel in blended MEA/PZ (5/1.2 kmol/m^3) solution containing 0.20 mol/mol CO_2 loading, 1 wt % acetic acid and 1000ppm Inhibitor A..... 80

Figure 49: Effect of solution temperature on polarization behavior of carbon steel in blended MEA/PZ (5.0/1.2 kmol/m^3) solution containing 0.20 mol/mol CO_2 loading, 1 wt % acetic acid and 1000ppm Inhibitor A. 81

Figure 50: Effect of $CuCO_3$ on polarization behavior of carbon steel in blended MEA/PZ (5/1.2 kmol/m^3) solutions containing 0.20 mol/mol CO_2 loading, 1 wt % acetic acid, the oxidative degradation Inhibitor A with concentrations of 0, 1,000, 10,000 and 30,000 ppm, and $CuCO_3$ with concentrations of 0 and 250 ppm at 80^{o}C under (a) 0.00 kPa O_2 and (b) 10.13 kPa O_2..... 82

Figure 51: Effect of $CuCO_3$ on corrosion rate of carbon steel in blended MEA/PZ (5/1.2 kmol/m^3) solution containing 0.20 mol/mol CO_2 loading, 1 wt % acetic acid and various concentrations of Inhibitor A and $CuCO_3$, at 80°C (a) 0.00 kPa O_2 and (b) 10.13 kPa O_2. 83

Figure 52: Effect of solution temperature on polarization behavior of carbon steel in blended MEA/PZ (5/1.2 kmol/m^3) solutions containing 0.20 mol/mol CO_2 loading, 1 wt % acetic acid, 1000ppm Inhibitor A, and $CuCO_3$ with concentrations of 0 and 250 ppm at 40 and 80^{o}C in the absence of O_2. 84

Figure 53: Comparison of corrosion rates of carbon steel in blended MEA/PZ (5/1.2 kmol/m^3) solution containing 0.20 mol/mol CO_2 loading, 1 wt % acetic acid, 1000ppm Inhibitor A and $CuCO_3$ with concentrations of 0 and 250 ppm, at 40 and 80°C in the absence of O_2. 84

Figure 54: Effect of CO_2 loading on polarization behavior of carbon steel in blended MEA/PZ (5/1.2 kmol/m^3) solutions containing 1 wt % acetic acid, 1000ppm Inhibitor A and $CuCO_3$ with concentrations of 0 and 250 ppm under 10.13 kPa O_2 and CO_2 loadings of 0.20 and 0.40 mol/mol at 80°C. 85

Figure 55: Effect of CO_2 loading on corrosion rate of carbon steel in blended MEA/PZ (5/1.2 kmol/m^3) solutions containing 1 wt % acetic acid, 1000ppm Inhibitor A, $CuCO_3$ with 0 and 250 ppm under 10.13 kPa O_2 at 80°C. 85

List of Tables

Table 1: Summary of Reviewed Literature Documents 16

Table 2: Density and Viscosity of Potassium Carbonate Solutions (Hitchcock & McIlhenny, 1935) 17

Table 3: Specific Gravity and Viscosity of Potassium Carbonate Solution (Bocard & Mayland, 1962) 18

Table 4: Relative Density and Viscosity of Potassium Carbonate Solutions (Gonclaves & Kestin, 1981) 19

Table 5: Density of K^+/PZ Mixtures at 25 and 40°C (Cullinane) 20

Table 6: Viscosity of Aqueous PZ at 25 and 70°C (Cullinane) 22

Table 7: Flue gas conditions used for simulation cases 25

Table 8: Absorber design conditions for all K^+/PZ modeling cases 26

Table 9: CO_2 removal results for K_2CO_3/ PZ absorber configurations 31

Table 10: Absorber design conditions for all MEA modeling cases 32

Table 11: CO_2 removal results for MEA absorber configurations 36

Table 12: Rate Comparison of 7 m MEA Low Gas Flow Degradation Experiments (mM/hr) 46

Table 13: Degradation Product Rate Comparison for aqueous Piperazine (mM/hr) 48

Table 14: Rate Comparison for 7m MEA/2m PZ Low Gas Flow Experiments (mM/hr) 49

Table 15: Rate Comparison of Four Different Amine Systems (mM/hr) 52

Table 16: MEA losses at 100°C as a function of MEA concentration 58

Table 17: MEA losses at 100°C as a function of CO2 loading 59

Table 18: MEA Losses (%) over an 8-week time span at varying MEA concentrations, CO_2 loadings and temperatures 61

Table 19: Solubility of K_2SO_4 in amine solution 67

Table 20: Regression result 69

Table 21: Correlation matrix 69

Table 22: Sum of squares 70

Introduction

The objective of this work is to improve the process for CO_2 capture by alkanolamine absorption/stripping by developing an alternative solvent, aqueous K_2CO_3 promoted by piperazine. This work expands on parallel bench-scale work with system modeling and pilot plant measurements to demonstrate and quantify the solvent process concepts.

Gary Rochelle is supervising the bench-scale and modeling work. Six graduate students (Andrew Sexton, Jason Davis, Jorge Plaza, David Van Wagener, Qing Xu, Eric Chen) have received a portion of their support from this contract during this quarter for direct effort on the scope of this contract. These students and additional students (Marcus Hilliard, Fred Closmann) have also been supported on related activities by the TXU Carbon Management Program. Subcontract work was performed by Manjula Nainar at the University of Regina under the supervision of Amy Veawab.

Experimental and Modeling Methods

Subtask 1.8a describes modeling methods in RateSep™ to predict absorber performance with intercooling.

Subtask 1.8b describes development of a rate model in RateSep^{TM} for the double matrix stripper with 4 m K^+/4 m PZ.

The attachment addressing task 2 provides a detailed description of the pilot plant setup and methods for the three campaigns with K^+/PZ.

Subtask 3.2 presents methods for analyzing amine degradation products by anion and cation chromatography.

Subtask 3.3 describes experimental methods to degrade piperazine and MEA at 100 – 150^{o}C. Analytical methods are presented to determine degradation products by gas chromatography, HPLC, and pH titration.

Subtask 4.1 describes a method for measuring the solubility of potassium sulfate in loaded amine solutions with ion conductivity.

Task 5.3 describes electrochemical methods for measuring corrosion.

Results and Discussion

Progress has been made on nine subtasks in this quarter:

Subtask 1.2b – Literature Review of Properties

Available measurements of viscosity, density, and ionic conductivity in solutions of MEA, K_2CO_3 and PZ have been compiled and reviewed.

Subtask 1.8a – Predict Absorber Flowsheet Options

RateSep™ models of the absorber have been used to optimize the use of intercooling with 4.5 m K^+/ 4.5 m PZ and with 11 m MEA.

Subtask 1.8b – Predict Stripper Flowsheet Options

RateSep^{TM} models of the absorber and stripper with 4 m K^+/ 4 m PZ have been used to optimize lean loading and predict the energy performance of the system.

Task 2 – Pilot Plant

A dissertation is being prepared by Eric Chen to document the pilot plant work with K^+/piperazine. Drafts of Chapters 2 and 3 are attached. Chapter 2 describes the experimental setup, methods, and results. Chapter 3 provides data reconciliation and a simple analysis of mass transfer performance.

Subtask 3.2 – Oxidative Degradation

Analyses of oxidative degradation products have been completed on seven experiments in the low gas flow apparatus (98 O_2, 2% CO_2) with 3 M 2-amino-2-methyl propanol (AMP), aqueous piperazine, 7 m MEA, and 7 m MEA/2 m PZ. These experiments included 0.1 mM Fe^{++}, 5 mM Cu^{++}, and/or 100 mM Inhibitor A.

Subtask 3.3 – Thermal Degradation

Samples of loaded MEA have been degraded at 100, 120, 135, and 150°C. Samples of 5 m loaded piperazine were degraded at 120 and 135°C. These initial samples were analyzed by gas chromatography.

Subtask 3.4 – Amine Volatility

Two chapters are attached of a Ph.D. dissertation on the thermodynamics of K^+/PZ/MEA/CO_2/H_2O. In Chapter VIII the properties of MEA and PZ have been adjusted to match liquid heat capacities and heats of vaporization of the pure components. In Chapter IX the NRTL parameters have been adjusted to accurately represent the heat capacity and MEA volatility in the system MEA-H_2O

Subtask 4.1 – Sulfate Precipitation

Measurements of potassium sulfate solubility in loaded solutions of MEA have been correlated by the electrolyte NRTL model of AspenPlus.

Subtask 5.3 – Corrosion

The corrosion of carbon steel was measured in 5 M MEA/1.2 M PZ containing 0.2 mol CO_2 mole amine and 1 wt% acetic acid with up to 30,000 ppm of oxidation Inhibitor A.

Conclusions

1. Double intercooling to 40°C in the absorber improves CO_2 removal by 12% with 4.5 m K^+/4.5 m PZ and by 8% with 11 m MEA by delaying the approach to a pinch at the bottom of the column.
2. With 4 m K^+/4 m PZ, an optimum lean loading of 0.378 provided a rich loading of 0.500 with 15 m of absorber packing and double intercooling. The double matrix stripper provided an equivalent energy requirement of 35.0 kJ/mol CO_2 with compression to 10 MPa.
3. The pilot plant results demonstrate that 5mK^+/2.5mPZ solvent has an absorption rate 1.5 times faster than 7 m MEA and 2 times faster than 6.4mK^+/1.6mPZ. Flexipac 1Y structured packing performed 1.8 times better than the Flexipac AQ Style 20 structured packing. The mass transfer performance in the pilot plant of 5mK^+/2.5mPZ matched the performance of the wetted wall column at 40°C.
4. The oxidative degradation of 7 m MEA produces more formate (0.66 vs. 0.40 mM/hr) and less nitrate/nitrate (0.24 vs. 0.46 mM/hr) in the presence of 5 mM Cu^{++}, as compared to experiments with only 0.6 mM Fe^{++}.

5. In the low gas flow apparatus, the production rate of formate (2.35 mM/hr) in 7m MEA/2m PZ (0.1 mM Fe^{++}, 5 mM Cu^{++}) was six times faster than 7 m MEA. 100 mM Inhibitor A reduced the formate rate to 0.30 mM/hr.
6. AMP is very resistant to oxidative degradation. With 3 M AMP/1 mM Fe^{++}, formate was produced at less than 0.01 mM/hr.
7. After eight weeks of reaction, MEA losses were less than 1.8% at 100°C, 3 to 45% at 120°C, and 12 to 71% at 135°C. The greatest losses were observed with 0.5 moles CO_2/mole MEA in 11 m MEA.
8. After three weeks of reaction at 120 and 135°C, the apparent losses of piperazine in aqueous PZ with 0.8 moles CO_2/mole PZ were less than 5% when measured by pH titration, cation chromatography, and HPLC. However, the apparent losses determined by gas chromatography were 33 to 40%. It is possible that the high temperature (up to 250°C) of the gas chromatograph resulted in degradation of the sample.
9. The activity coefficient of MEA at infinite dilution in water varies from 0.15 at 25°C to 0.64 at 100°C. The MEA vapor pressure over 7 m MEA at 40°C is 6.6 Pa. The heat capacity of 7 m MEA varies from 3.714 kJ/kg-K at 40°C to 3.998 at 100°C.
10. The solubility of potassium sulfate in MEA/PZ solvents increases significantly with CO_2 loading and decreases with MEA and PZ concentration. It is a weak function of temperature which mirrors the effect of temperature on the solubility in water.
11. In the absence of Cu^{++}, oxidation Inhibitor A increases the corrosion of carbon steel from 4 to 12 mm/yr with or without oxygen.
12. Cu^{++} is an effective corrosion Inhibitor in the presence of oxidation Inhibitor A (up to 30,000 ppm). With 30,000 ppm A in the presence of oxygen, the corrosion rate is reduced from 9.0 to 0.024 mm/yr with the addition of 250 ppm $CuCO_3$.

Future Work

We expect the following accomplishments in the next quarter:

Subtask 1.2b – Literature Review of Properties

Correlations of viscosity, density, ionic conductivity, surface tension, and pH in solutions of MEA, K_2CO_3 and PZ will be reviewed and presented in the final report.

Subtask 1.3b – Stripper Model

The stripper/absorber model in RateSep™ will be used to determine the optimum pressures and split ratio with the double matrix configuration. The model will also be used to determine the energy requirement with a simple stripper.

Subtask 1.7 – Simulate and Optimize Packing Effects

The absorber data from campaigns 1, 2, and 4 will be simulated with the RateSep™ model.

Task 2 – Pilot Plant

Eric Chen will complete his Ph.D. dissertation in August. This document will be submitted as a topical report that will provide a comprehensive description of the pilot plant results with the K^+/PZ solvent.

Subtask 3.2 – Oxidative Degradation

Extended experiments will be conducted on MEA, PZ, and AMP solutions in an effort to collect simultaneous gas-phase and liquid-phase product analysis. An analytical method will be implemented with the ion chromatograph to determine amino acids in degraded solutions.

Subtask 3.3 – Thermal Degradation

The MEA data will be regressed to provide a kinetic model for the degradation at stripper conditions. Analyses by HPLC and cation chromatography will be developed to measure the amount of degradation products in each of the samples.
A full matrix of piperazine experiments with 8 weeks of degradation will be completed. If measurable amounts of PZ losses are detected, then a similar kinetic model regression will be applied to the PZ data.

Subtask 3.4 – Amine Volatility

A dissertation will be completed on the thermodynamics of the system K^+/PZ/MEA/CO_2/H_2O. Amine volatility in loaded MEA and PZ solutions will be represented in AspenPlus with the electrolyte/NRTL model.

Subtask 4.1 – Sulfate Precipitation

AspenPlus will be used to represent potassium sulfate solubility in MEA and MEA/PZ with the electrolyte/NRTL model.

Task 1 – Modeling Performance of Absorption/Stripping of CO_2 with Aqueous K_2CO_3 Promoted by Piperazine

Subtask 1.2b – Literature Review of Properties

by Fred Closmann

(Supported by TXU Carbon Management Program)

Overview of Issue

The research group is interested in developing an understanding of certain physical properties of K^+/PZ systems over various CO_2 loadings to allow monitoring and adjustment of loading of systems for CO_2 removal. Of particular interest is the ability to perform real-time monitoring of one or more of these physical properties to allow pilot-scale or full-scale operational changes of CO_2 loading using on-line measurement instrumentation. Through correlation of the physical property measurements with CO_2 loading over practical temperature and loading ranges, relationships between these properties and loading will be made. The physical properties of interest include solution pH, density, viscosity, ionic conductivity and surface tension.

The primary tasks associated with this effort include the review of available data generated by others, including laboratory studies of unloaded and loaded solutions, and data generated by bench-scale studies of K^+/PZ solvents. The data was generated using a variety of conditions and solvent solutions. For example, the work of Bocard and Mayland (1962) was performed to better understand vapor-liquid equilibrium data for the hot potassium carbonate process and, therefore, utilized solutions of K_2CO_3, whereas more recent work by Cullinane (2005) and Derks (2005) investigated the use of PZ as a solvent. Because of this variety of conditions and aqueous investigation media, several different correlations between these physical parameters and loading are being pursued.

Table 1 summarizes the reviewed literature data, presenting the conditions over which the various studies were conducted to allow comparisons between the data sets to be made. As listed in the table, certain three-parameter relationships could be drawn from the data as presented by some of the authors. For example, five of the studies reported a concentration-temperature-density relationship, but utilized a different basis for calculating concentration (i.e., normality in gm equivalents or concentration in kmol/m^3). In future efforts, we will normalize the data to understand the level of correlation between data sets. Some of that effort is reported here.

The work reviewed and reported did not focus on the viability of making on-line measurements, nor the on-line instrumentation available for this purpose. It is understood that instruments designed and available for these purposes will have inherent error, as well as operational limitations.

Physical Parameters and MEA as a Base Case

Recent pilot-scale work performed by this group (Rochelle) utilized ionic conductivity and density as an on-line measurement tool. Pilot plant work performed at the SRP in 2005 is presented in the M.S.E. Thesis of R. E. Dugas (2006). Pilot plant studies were performed on monoethanolamine (MEA) as a base case solvent for carbon dioxide capture and presented by Dugas. Pilot plant run lean loadings were initially controlled by measurement of ionic conductivity. Of note, equations were developed to predict loading using ionic conductivity, temperature, and MEA concentration. The ionic conductivity meters utilized in the pilot plant

operation failed. Lean loading was then controlled by density, with correlations created using total organic carbon (TOC) measurements made with a Shimadzu TOC-5050A Analyzer. When a loading of 0.3 was attempted in this work, ten or more data points were needed to create good correlation between density and TOC. Dugas notes that loading was accurately linked to solution density once the subject pilot plant campaign was concluded. After applying a temperature-density correction, a linear dependence was observed, and a correlation between CO_2 loading and density was created. The correlation was then used to calculate absorber rich and lean loadings from densities, and the calculated loadings were used in all subsequent calculations. Dugas also notes that, using the density correlation developed during the campaign as a parameter, density did allow the lean loading to be held steady, but the desired loading was not always maintained.

Table 1: Summary of Reviewed Literature Documents

Author(s)	Solvent Type	CO_2 Loaded (Y/N)	Data Type	Temp Range	Parameter Relationships
Hichcock & McIlhenny (1935)	K_2CO_3	N	ρ, μ	20 – 40°C	$T-N-\rho$ $T-N-\mu$
Bocard & Mayland (1962)	K_2CO_3	N	ρ, μ	15.6 –115.6°C	$T-wt\%-SpGr$ $T-wt\%-\mu$
Cook & Lowe (1976)	PZ	N	ρ, μ	25 & 35°C	$T-m-\rho$ $T-m-\eta$
Gonclaves & Kestin (1981)	K_2CO_3	N	ρ, μ	20 – 60°C	$T-m-\rho$ $T-m-\eta$
Derks, Hogendoorn & Versteeg (2005)	PZ	N	ρ, μ	20 – 50°C	$T-C-\rho$ $T-C-\mu$
Cullinane (2005)	K^+/PZ	Y	ρ, μ	20 – 70°C	$T-m-\rho$ $T-m-\mu$
Dugas (2006)	MEA	Y	ρ, μ, T, cond.	~40°C	ρ as func. of CO_2 loading
Alletag & Brown (2006)	MEA/PZ	Y	μ, cond.	25 – 70°C	$T-C_{CO_2}-\mu$ $T-C_{CO_2}-cond$

The pilot plant work reported by Dugas did not utilize the hotpot process or PZ, but the report does represent a fundamental or base case understanding of measurement conditions using MEA, and how to proceed with expanding our understanding. As stated above, the review of data developed by others primarily focused on the use of K^+/PZ as a solvent solution.

Density/Specific Gravity

In laboratory work performed using a range of alkali solution normalities (1 to 8-N), Hitchcock and McIlhenny (1935) studied the effects of loading (alkali normality in gm-eq. NaOH) on fluid density and viscosity at what they considered to be a reasonable range of temperatures and compositions. Their work studied aqueous solutions of sodium hydroxide, sodium carbonate, potassium hydroxide, and potassium carbonate. Using 10 mL laboratory

pycnometer bottles, the authors measured solution density for each of the 1 to 8-N alkali solutions at temperatures of 20, 30 and 40°C. Their data for potassium carbonate solutions are represented in Table 2. The authors studied an additional eight solution series comprised of sodium hydroxide, sodium carbonate and potassium hydroxide, but that data is not presented as we are primarily interested in the behavior of K^+/PZ solutions in this data review.

In general, for a given temperature, density was observed to increase with normality for the potassium carbonate solutions. For a given normality and temperature, the density of the potassium carbonate solution was slightly greater (~ 0.5 %) than the comparable sodium carbonate solution (data not shown). As expected for most aqueous solutions, the density slightly decreased for each solution with increases in temperature.

Table 2: Density and Viscosity of Potassium Carbonate Solutions (Hitchcock & McIlhenny, 1935)

T = 20°C			T = 30°C			T = 40°C		
Normality	Density	Viscosity	Normality	Density	Viscosity	Normality	Density	Viscosity
0.9479	1.0526	1.1459	0.9447	1.049	0.9255	0.9417	1.0453	0.7659
1.82	1.1003	1.3051	1.813	1.0964	1.0594	1.806	1.092	0.8771
2.78	1.1514	1.5184	2.768	1.1468	1.2335	2.757	1.1422	1.0233
3.616	1.1945	1.7638	3.602	1.1899	1.4257	3.587	1.185	1.178
4.421	1.2349	2.0372	4.403	1.2299	1.641	4.385	1.2248	1.3539
5.268	1.2764	2.3677	5.246	1.2717	1.9321	5.225	1.2663	1.5926
6.097	1.3159	2.7925	6.073	1.3108	2.2355	6.049	1.3054	1.8324
7.112	1.3631	3.4422	7.084	1.3578	2.7376	7.057	1.3525	2.218

Density in g/cm^3
Viscosity in cp

Bocard and Mayland (1962) performed a study to better understand mass transport considerations when using the hot potassium carbonate process. Generated data included solubility of CO_2, specific gravity, and viscosity over a range of temperature and CO_2 loading. The study focused on aqueous solutions of K_2CO_3 at various degrees of conversion to $KHCO_3$. The raw data from their study was not presented in the reviewed article, but instead presented as a linear plot of specific gravity and temperature (°F). We utilized this plot to create the data presented in Table 3. As presented by the authors in their paper, a linear relationship between specific gravity and temperature existed for each of the three K_2CO_3 solutions as they experienced a 0, 40, and 60% conversion to $KHCO_3$ when loaded with CO_2. Specific gravity was found to decrease with temperature in a linear relationship. As is also expected with aqueous carbonate solutions, the specific gravity of the 22 wt % $KHCO_3$ solution was less than the specific gravity of the 26 and 30 wt % solutions. The data supported the conclusion that specific gravity increased with conversion of K_2CO_3 to $KHCO_3$ through addition of CO_2.

Table 3: Specific Gravity and Viscosity of Potassium Carbonate Solution (Bocard & Mayland, 1962)

K_2CO_3 %Wt	22		26		30	
Temperature	Sp. Gr.*	Viscosity	Sp. Gr.*	Viscosity	Sp. Gr.*	Viscosity
70	1.206/1.212/1.222	1.26	1.25/1.26/1.271	1.46	1.29/1.308/NA	1.73
100	1.196/1.205/1.213	0.96	1.24/1.25/1.262	1.08	1.281/1.298/NA	1.25
130	1.188/1.195/1.205	0.74	1.231/1.242/1.254	0.85	1.272/1.29/NA	0.99
160	1.18/1.187/1.197	0.6	1.223/1.234/1.245	0.7	1.263/1.28/NA	0.81
190	1.171/1.178/1.188	0.5	1.214/1.228/1.236	0.58	1.255/1.271/NA	0.66
220	1.154/1.17/1.18	0.41	1.206/1.2171.28	0.46	1.247/1.262/NA	0.53

* Sp. Gr. data quoted for 0, 40 and 60% conversion to $KHCO_3$. NA denotes data not available.
Viscosity in abs. cp.; all viscosity data is for 0% conversion to $KHCO_3$.

Derks et al. (2005), investigated the solubility, density and viscosity of aqueous PZ solutions loaded with nitrous oxide (N_2O) utilizing the "N_2O analogy" for estimation of these properties in comparable CO_2 loaded solutions; the premise for the analogy is that N_2O and CO_2 have similar configurations, molecular volumes, and electronic structures, with the beneficial quality that N_2O is a non-reactive gas.

The authors confined their measurements to density and viscosity in aqueous solutions of PZ at four different concentrations (0.623 to 1.686 kmol/m^3) over a temperature range of 293.15 K to 323.15 K, with no loading of N_2O. Measurements of density (not presented here) were made with a commercial density meter at controlled temperature (within +/- 0.05 K). The data were graphed by the authors and found to follow a linear dependence over the PZ concentrations used in the study. The data also demonstrated a decrease in density with temperature. While the authors measured density and viscosity at a range of PZ concentrations and temperatures, these parameters were not measured with N_2O loadings to mimic CO_2 loading.

Gonclaves and Kestin (1981) utilized aqueous solutions of Na_2CO_3 and K_2CO_3 in laboratory studies of density and viscosity at atmospheric pressure and a temperature range of 20 to 60°C. Their density and viscosity data are presented as normalized to pure water solutions (reported as "specific" values), with the greatest K_2CO_3 concentration studied 7.619 mol/kg. The K_2CO_3 solution measurement data has been tabulated and presented here as Table 4. The data exhibited an expected behavior of increasing density with increasing concentrations of K_2CO_3. Density generally decreased with increasing temperature up to 50°C, then increased in samples measured at 60°C.

The authors created a fit to the data as follows:

$$\rho(T, c) = \rho^* \sum_{i=0}^{4} \sum_{j=0}^{3} d_{ij} (c / c^*)^i \left(\frac{t}{T^*} \right)^j$$

where: $\rho^* = 1 kg \cdot m^{-3} \cong 0.06243 lbm \cdot ft^{-3}$

$c^* = 1 mol \cdot kg^{-1} = 10^{-3} lbmol \cdot lb^{-1}$

$T^* = 1K = 1.8R$

Table 4: Relative Density and Viscosity of Potassium Carbonate Solutions (Gonclaves & Kestin, 1981)

Solution No.	Conc. (mol/kg)	Rel. Vis / Rel. Dens.	Temperature °C					
			20	25	30	40	50	60
1	0.057	η	1.0204	1.0216	1.0224	1.0237	1.0248	1.0248
		ρ	1.00705	1.007	1.00695	1.00689	1.00684	1.00687
2	0.115	η	1.0381	1.0395	1.0407	1.043	1.0451	1.046
		ρ	1.01403	1.01393	1.01385	1.01373	1.01366	1.01367
3	0.236	η	1.0732	1.0777	1.0805	1.0842	1.0879	1.0904
		ρ	1.02821	1.028	1.02785	1.02761	1.0275	1.02752
4	0.472	η	1.1489	1.1554	1.1609	1.1693	1.1759	1.1815
		ρ	1.05509	1.05472	1.05443	1.05402	1.05385	1.05387
5	0.608	η	1.1994	1.2038	1.2138	1.2248	1.2328	1.2393
		ρ	1.07006	1.06644	1.06923	1.06872	1.06847	1.06851
6	1.236	η	1.4483	1.4614	1.4728	1.491	1.5049	1.5163
		ρ	1.13536	1.13462	1.13403	1.13327	1.13294	1.13305
7	2.812	η	2.3511	2.3649	2.3772	2.3971	2.4105	2.4239
		ρ	1.27426	1.27325	1.27247	1.27156	1.2714	1.2719
8	3.326	η	2.7536	2.7619	2.7676	2.7779	2.7818	2.7887
		ρ	1.31312	1.31208	1.31129	1.31044	1.31036	1.31101
9	4.701	η	4.2127	4.1807	4.15	4.0937	4.0489	4.012
		ρ	1.4048	1.40376	1.40299	1.40228	1.40324	1.40429
10	5.109	η	4.7718	4.7184	4.6635	4.5755	4.5002	4.4369
		ρ	1.42917	1.42811	1.42735	1.4267	1.42698	1.42813
11	6.253	η	6.7482	6.5851	6.4465	6.1961	5.9996	5.8433
		ρ	1.49026	1.4892	1.48852	1.48796	1.48845	1.4899
12	7.619	η	10.1822	9.7669	9.4111	8.8326	8.3897	8.0411
		ρ	1.55263	1.55163	1.551	1.5507	1.55149	1.55329

All data referenced to values for water at the same temperature.

In dissertation work performed at the University of Texas at Austin, Cullinane (2005) investigated solvent behavior of the K^+/PZ mixture for CO_2 absorption, with particular interest placed on quantifying and modeling thermodynamic properties and the rate of CO_2 absorption. Cullinane measured density and viscosity of loaded and unloaded solutions. The density of the K^+/PZ mixtures was measured with a Mettler/Paar #DMA46 Digital Density Meter. Densities of mixtures were measured at 25 and 40°C. Cullinane reported that amine had little effect on density, and that the main contribution to density (increases) was the salt concentration (K_2CO_3/ $KHCO_3$). Cullinane's data for density of K^+/PZ mixtures at 25 and 40°C are included with this discussion in Table 5.

Table 5: Density of K^+/PZ Mixtures at 25 and 40°C (Cullinane)

Density of K^+/PZ Mixtures at 25 and 40°C					
T °C	K^+ (m)	PZ (m)	Loading	ρ_{meas}	ρ_{pred}
	1	1	0.25	1.053	1.054
	1	1	0.5	1.067	1.057
	1	2.5	0.286	1.065	1.058
	2.5	2.5	0.5	1.138	1.134
	3	0.3	0.455	1.152	1.153
	3	0.3	0.909	1.163	1.157
	3	0.9	0.769	1.165	1.157
25	5	2.5	0.667	1.237	1.247
	1	1	0.25	1.047	1.048
	1	1	0.5	1.059	1.05
	1	2.5	0.143	1.046	1.05
	1	2.5	0.285	1.057	1.051
	2.5	2.5	0.25	1.108	1.125
	2.5	2.5	0.5	1.132	1.127
	5	0.5	0.455	1.228	1.235
	5	0.5	0.909	1.236	1.239
40	5	2.5	0.667	1.227	1.24

M denotes molality.

ρ_{pred} value was predicted using Cullinane's curve fit relationship.

For a given temperature (e.g., 25°C), the density of aqueous PZ solutions exhibited slight increases with increased PZ concentration. At a higher temperature (40°C), the solutions of the same concentrations exhibited lower densities. When solutions of K^+/PZ were loaded with CO_2 from an initial loading of 0.25 to 0.667 mol CO_2/(mol K^+ and mol PZ), the density of solution increased from 1.053 g/cm^3 to 1.237 g/cm^3. Other data generated by Cullinane with no PZ present in solution suggest that increases in density can largely be attributed to K^+ in solution; a set of measurement results wherein K^+ concentration was increased from 1.5 m 12.0 m and CO_2 loading was simultaneously decreased exhibited an increase in density from 1.085 to 1.466 g/cm^3. These measurements prevent the reader from concluding that CO_2 loading lead to increases in density.

A regression of data was performed to provide an empirical representation of density as follows:

$$\rho\left(g/cm^3\right) = 1.130 + 0.0537\left[K^+\right] - 1.204X10^{-3}\left[K^+\right]^{-2} + 1.882X10^{-3}\left[PZ\right] - 0.442X10^{-3}T + 9.010X10^{-3}\alpha$$

As discussed earlier in this section, Dugas (2006) and the SRP team at the University of Texas conducted multiple runs on the close-looped absorption/stripping pilot plant at the Pickle Research Center in 2005 using MEA. At the initiation of the pilot plant runs, CO_2 loading was controlled using ionic conductivity. Two ionic conductivity meters were utilized in the system, with both experiencing failures one week into the pilot plant campaign. The team switched to using density as the controlling parameter for CO_2 loading. CO_2 concentrations were determined using a Shimadzu TOC-5050A Total Organic Carbon (TOC) analyzer, with several measurements recorded and averaged to account for significant scatter in TOC data. Loading was accurately linked to solution density once the subject pilot plant campaign was concluded. After applying a temperature-density correction, a linear dependence was observed, and a correlation between CO_2 loading and density was created. Dugas also notes that, using the

density correlation developed during the campaign as a parameter, density did allow the lean loading to be held steady, but the actual value was not always maintained. A linear relationship between loading (g CO_2/kg soln) and density at 40°C (kg/L) was developed as:

$$y = -898x^2 + 2921x - 2028$$

where: y = CO_2 concentration (g CO_2/kg solution)

x = Density at 40°C (kg/L)

No other parameters were utilized in the estimation of lean loading by Dugas after a conversion to using a density correlation for lean loading was made.

Viscosity

Hitchcock and McIlhenny measured viscosity in potassium carbonate solutions and concluded that the logarithm of viscosity generally followed a linear relationship with temperature over the temperature and concentration ranges studied. As discussed above, the data published by the authors was tabulated in Table 2 and presented with this quarterly report. For the potassium carbonate solutions, viscosity decreased with increasing temperature, and increased with increasing solution normality. When evaluated using the specific viscosity (viscosity of solution/viscosity of water at same temperature, using viscosity of water from the International Critical Tables) as opposed to the absolute viscosity, the authors reported that the potassium carbonate solutions at lower concentrations exhibited a slight increase in specific viscosity, but at higher concentrations, a slight decrease. The authors suggest that the viscosity behavior of the solutions at higher concentrations is possibly the result of non-electrolyte behavior.

Bocard and Mayland reported the viscosity measurements included in this report as Table 3 at solutions of 22 wt %, 26 wt %, and 30 wt % K_2CO_3 over the temperature range of 100 to 250°F. The authors created a plot of absolute viscosity as a function of temperature; the data exhibited a logarithmic dependence. When a regression was performed using the natural log of absolute viscosity versus temperature, a linear dependence was observed as follows:

$$\ln(\mu) = 0.929 - 0.0074(T°F)$$

As seen in data from the other studies reviewed, the viscosity of solutions at a given K_2CO_3 concentration decreased with increasing temperature. As the solution K_2CO_3 concentration was increased from 22 wt % to 30 wt %, the viscosity of solution increased. The authors (Bocard and Mayland) also noted that, as K_2CO_3 was converted to $KHCO_3$, with CO_2 additions, solution viscosity was not appreciably affected.

Gonclaves and Kestin reported relative viscosity (relative to water) data for K_2CO_3 solutions that increased with temperature at a given concentration up to a concentration of 3.33 mol/kg K_2CO_3 in solution, then decreased with temperature thereafter for K_2CO_3 concentration increases. Their data demonstrated a clear increasing effect on viscosity as K_2CO_3 concentration was increased, regardless of temperature. This observation is consistent with that seen by Bocard and Mayland.

Derks et al. reported a pattern of increasing viscosities with increasing PZ concentrations over a range of practical temperatures. The authors' data also supported the understanding that viscosity decreases with temperature for a given PZ concentration. As discussed above, the solutions studied were not loaded with N_2O. The authors plotted viscosity versus PZ concentration. That plot demonstrates a logarithmic relationship between the two parameters.

When the natural log of viscosity was plotted against PZ concentration, a linear dependence was observed.

Cullinane also reported viscosities of unloaded and loaded aqueous PZ solutions (Table 6) generated in the laboratory with a Cannon-Fenske viscometer. The unloaded solutions exhibited an increase in viscosity with increase in PZ concentration, and a decrease in viscosity with increase in temperature. In solutions where K^+ and PZ were held constant, the viscosity of solution did not change.

Cullinane created a regression of the data generated in his work and came up with an expression of viscosity in terms of aqueous salt and PZ concentration as follows:

$$\mu = \left\{\mu_w{}^{A_0+1} \exp\left(B\left[K^+\right] + C\alpha^2\right) + De^{E/T}\left[PZ\right] + Fe^{G/T}\left[PZ\right]^2\right\} \times \left\{1 + H\left[K^+\right]\left[PZ\right] + I\left(\left[K^+\right]\left[PZ\right]/T\right)\right\}$$

where: $A_0 = A_1\left[K^+\right] + A_2\left[K^+\right]^2$ and

A_1 is -0.021, A_2 is 2.79E-03, B is 0.153, C is -0.020, D is 2.00E-05, E is 2943.4, F is 2.43E-08, G is 4076.7, H is -0.082, and I is 35.24.

Other work conducted by students (A. Alletag and A. Brown) at the University of Texas at Austin Department of Chemical Engineering in fulfillment of undergraduate course ChE 264 requirements centered on the measurement of viscosity in aqueous amine solutions with increasing loadings of CO_2 under controlled conditions. The measurements were made for the same solutions at 25, 40, 55 and 70°C. The authors of the study plotted the natural logarithm of the viscosity data against the inverse of the temperature readings and found near-straight line dependence in the data.

Table 6: Viscosity of Aqueous PZ at 25 and 70°C (Cullinane)

Viscosity of Aqueous PZ at 25 to 70°C					
T °C	PZ (m)	V_{exp} (cSt)	ρ_{model} (g/cm^3)	μ_{meas} (cP)	μ_{pred} (cP)
	0.5	1.09	0.999	1.09	1.09
	1	1.29	1	1.28	1.3
	1.5	1.52	1.001	1.52	1.52
25	1.8	1.66	1.01	1.66	1.66
	0.5	0.78	0.992	0.78	0.78
	1	0.91	0.993	0.91	0.91
	1.5	1.04	0.994	1.03	1.04
40	1.8	1.13	0.995	1.13	1.13
	0.5	0.55	0.983	0.54	0.54
	1	0.61	0.984	0.6	0.61
	1.5	0.69	0.985	0.68	0.68
60	1.8	0.74	0.986	0.73	0.73
	0.5	0.46	0.979	0.45	0.46
	1	0.52	0.98	0.51	0.51
	1.5	0.58	0.981	0.57	0.57
70	1.8	0.61	0.981	0.6	0.6

The data also demonstrated an increase in viscosity with loading throughout the measured temperature range, with the authors noting an adherence to the Arrhenius' equation for temperature dependence.

Finally, we reviewed the work performed by Cook and Lowe (1975) on pinacol and PZ to determine densities and viscosities at much lower aqueous concentrations (~0.08 to 0.18

mols/kg) than seen in the other data reviewed for our purposes. Their work was performed at temperatures of 25°C and 35°C. The authors created a polynomial fit for their data and drew conclusions about the behavior of pinacol versus PZ in aqueous solutions that are not relevant to our work. We will use their data in the future to allow a better understanding of low-end concentration behavior of PZ.

Other Parameters of Interest

The group looked at the effects of loading on other parameters in order to create useful correlations. Those parameters included pH, surface tension, and ionic conductivity. The amount of information available for review related to these parameters is limited, but presented herein. As previously discussed, Dugas and the SRP at the University of Texas' Pickle Research Center initially utilized ionic conductivity in pilot plant runs performed in 2005, but resorted to the use of density after repeated failures of the conductivity instrumentation.

In addition to collecting viscosity data, Alletag and Brown measured ionic conductivity using a Mettler Toledo-SevenEasy conductivity meter capable of measuring total conductivity in the range of 0.00 to 1000 mS/cm with an accuracy of +/- 0.5 mS/cm. The authors reported a linear dependence when they plotted the natural log of conductivity versus the inverse of temperature, and reported an Arrhenius relationship in the parameters. They also reported an increase in conductivity with increases in loading which is expected as a result of a greater concentration of ionic species in solution.

Derks et al. made measurements of surface tension (γ) in aqueous solutions of various amines, using water with no amines as a base case. Their studies demonstrated that the addition of small amounts of PZ to water did not affect the surface tension. The authors noted that the addition of small amounts of alkanolamines (i.e., DEA and MDEA) reduced surface tension measurably, but quote data generated by others to come to this conclusion. Errors or inconsistencies in instrument operation and measurement between the data sets could have resulted in these differences between surface tension measurements in water, PZ, and DEA/MDEA solutions.

Conclusions and Future Work

We will continue to review the body of available data to broaden our understanding of the effects of potassium, amine, and CO_2 loading on overall solvent solution physical behavior. The effort will focus on solving the problems associated with the real-time monitoring of CO_2 loading using one or more of these physical parameters (i.e., pH, density, viscosity, surface tension and ionic conductivity).

As we have collected these physical data, we have created the need to normalize the data to a uniform set of conditions, namely solvent concentrations. For example, Bocard and Mayland reported their work in terms of the wt % K_2CO_3, whereas Cullinane presented his work in terms of the molality of potassium in solution. The different concentrations of solvent reported further complicate the analysis of different solvents. In addition to the concentration basis differences, the authors report their physical parameter results as raw data, or data normalized to the properties of water at the stated conditions.

We will attempt to present the literature data using a comparable set of input conditions (i.e., molality), and analyze the physical parameter results on a normalized basis (specific to water at study temperatures) to broaden our understanding of the behavior of these physical parameters with respect to CO_2 loading during system operations.

We will also attempt to explain the behavior of systems in terms of more theoretical considerations such as charge density of ions in solution. For example, a cursory review of the atomic properties of sodium and potassium ions was made. Sodium exhibits a greater ionization potential than potassium (5.1 vs. 4.3 eV/atom) (O'Connor, 1977) and, because of its smaller diameter, a greater charge density than potassium (1.1×10^5 vs. 0.41×10^5). We will explore whether these properties explain the different viscosity behavior of sodium and potassium carbonate salts in solution.

The ultimate goal of this work is to create reliable correlations between the CO_2 loading and these measurable physical parameters so that the on-line monitoring of loading can be measured and maintained during pilot-scale and full-scale operations of CO_2 scrubbing systems.

Subtask 1.8a – Predicted Absorber Performance

by Jorge M. Plaza

(Supported by this contract and the TXU Carbon Management Program)

Introduction

Ongoing research by Chen has developed a rate-based absorber model with RateSep™ for the 5 m/2.5 m K_2CO_3/Piperazine solvent. This model utilizes the equilibrium data by Cullinane (2005) that were translated into Aspen Plus® by Hilliard (2005). Chen developed rate constants to allow the use of activity-based kinetics. This work uses the tools developed by Chen to analyze a system with 4.5 m/4.5 m K_2CO_3/piperazine solvent.

Similarly, extensive work has been conducted to develop a model for MEA as solvent in the absorber. Ziaii (2006), using Aspen Plus® and previous work by Freguia (2002), Hikita (1977), and Aboudheir (2002), developed a rate-based calculation model for the absorber that uses activity-based rate expressions for non-equilibrium reactions. Based on conditions from previous work by Ziaii (2006–2007) an absorber performance analysis was conducted for 11 m MEA.

An absorber optimization to maximize CO_2 removal was set up using a fixed packing height and varying the position of the Semilean feed and an additional intercooling point for both MEA and K/PZ. Results and conclusions are presented as well as an outline for future work.

Finally, observations by Hilliard and Chen have made necessary to determine the maximum possible loading for 4.5 m/4.5 m K_2CO_3/piperazine before the appearance of solid precipitate. An initial approach to a laboratory method to measure solubility based on conductivity has been proposed based on work by Qing. Results and conclusions are presented in this report.

Experimental

K_2CO_3/Piperazine

Flue gas conditions were taken from a study case provided by Trimeric. Table 7 presents the conditions of the flue gas used for the modeling analysis.

Table 7: Flue gas conditions used for simulation cases

Variable	Value
Flow (kmol/s)	5.4879
Temperature (^{o}C)	40.0
Pressure (kPa)	111.33
Mol fraction	
H_2O	0.0670
CO_2	0.1270
N_2	0.7569
O_2	0.0491

Calculations were carried out using Aspen Plus and the rate model developed by Chen. The modeled system is shown in Figure 1.

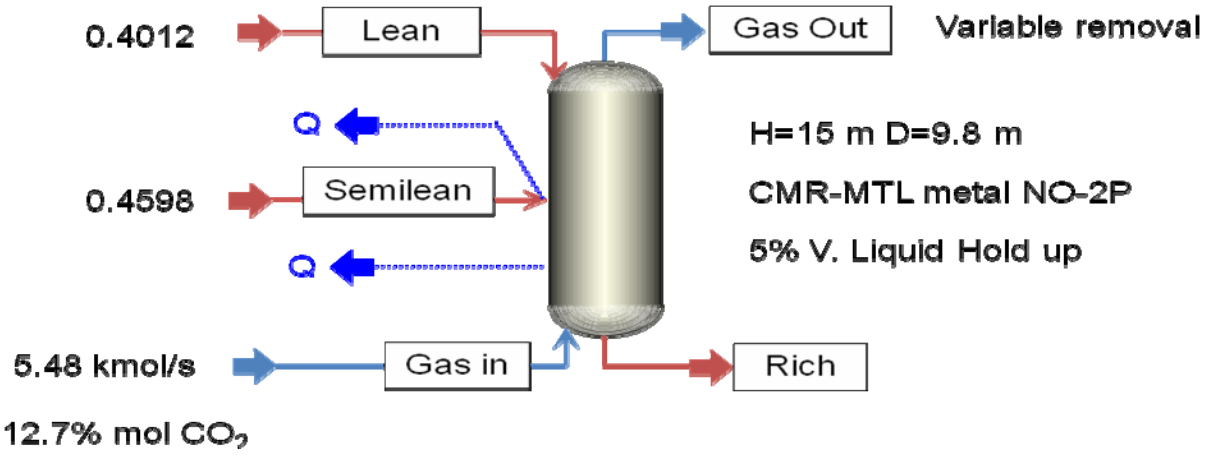

Figure 1: Absorber modeling conditions for 4.5 m/4.5 m K^+/PZ

Results from the stripper analysis provided an optimum loading (moles of CO_2/moles of alkalinity) of 0.4012 for the lean stream and 0.4598 for the semilean stream. The flow split between the streams was 0.1850(mol semilean/mol lean). These values correspond to 0.5 kPa partial pressure of CO_2 in the lean stream at 40°C. Table 8 summarizes the design conditions for the absorber.

Table 8: Absorber design conditions for all K^+/PZ modeling cases

Variable	Value
Diameter (m)	9.8
Height (m)	15.0
Packing Characteristics	
Type	CMR
Vendor	MTL
Material	Metal
Dimension	NO-2P
Liquid hold up (%)	5

Initially, the position of the semilean feed was optimized without any type of cooling (Figures 2 and 3). The optimum position of the semilean feed was found at a third from the top of the column.

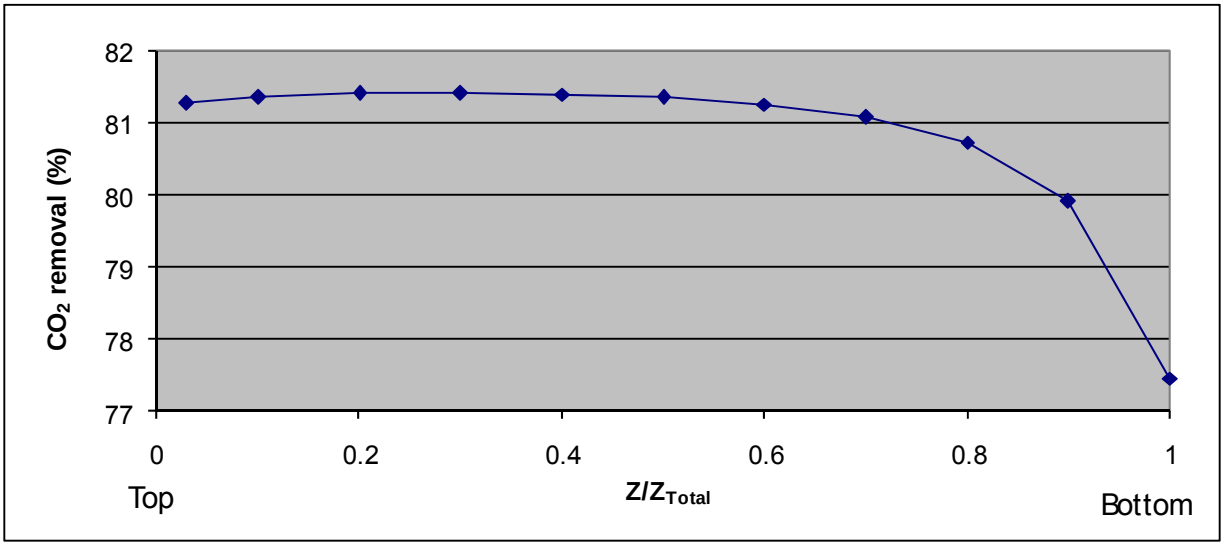

Figure 2: Change in CO_2 removal due to change in semilean feed position for 4.5m/4.5 m K_2CO_3/PZ. 0.5 kPa CO_2 lean solvent. No intercooling

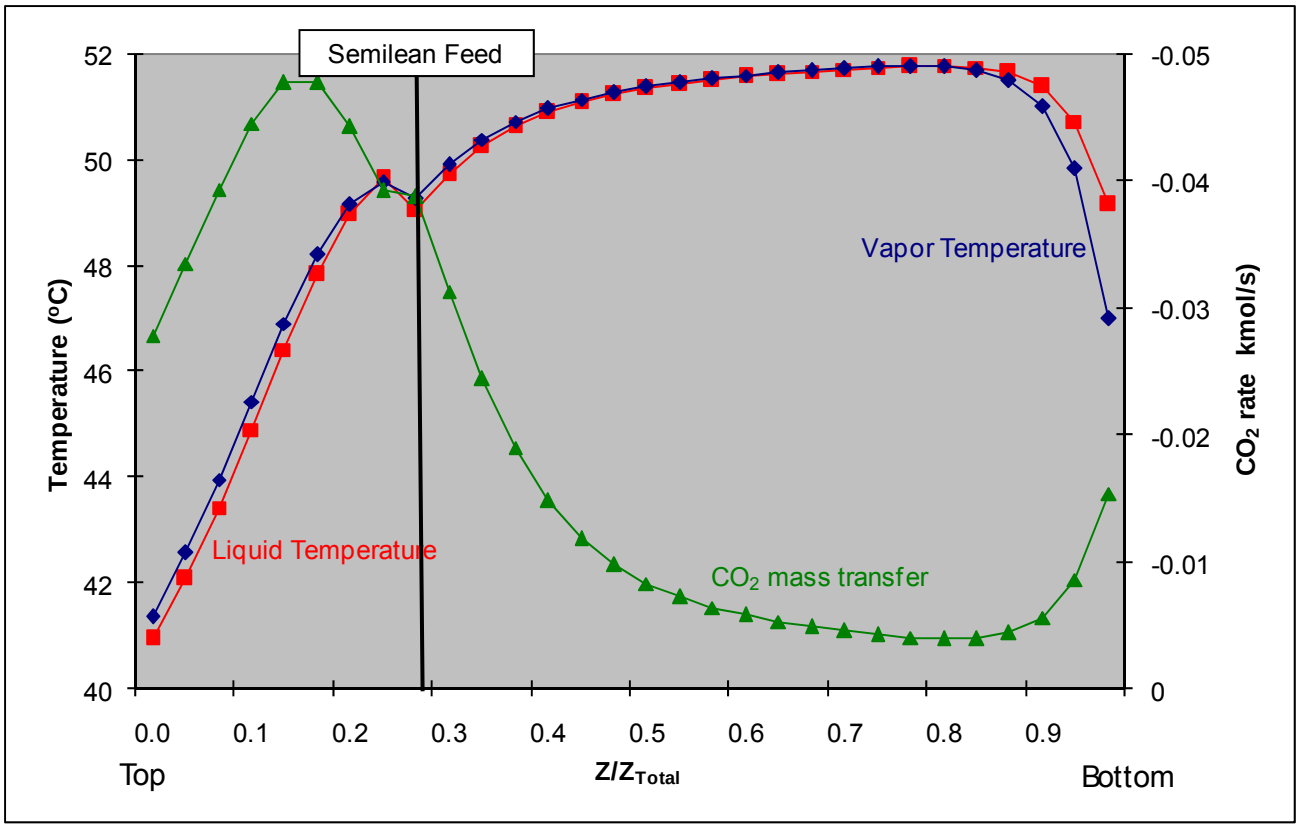

Figure 3: Temperature and CO_2 rate profiles for absorber with semilean feed at 0.30 column height and no intercooling. Solvent 4.5m/4.5 m K_2CO_3/PZ. 0.5 kPa CO_2 lean solvent.

Intercooling was set up so the selected stage would reach 40°C which has been established as a minimum temperature using cooling water. Initially, it was considered for the stage in which the semilean stream was fed into the column. The idea was to reduce the irreversibility generated by the difference in temperature between the semilean feed and the liquid at the point of entry. Figure 4 shows behavior of CO_2 removal with respect to the position of the intercooled semilean feed. The optimum position changed from the upper half of the column to the lower third. Figure 5 shows the temperature and CO_2 rate profiles found in the absorber.

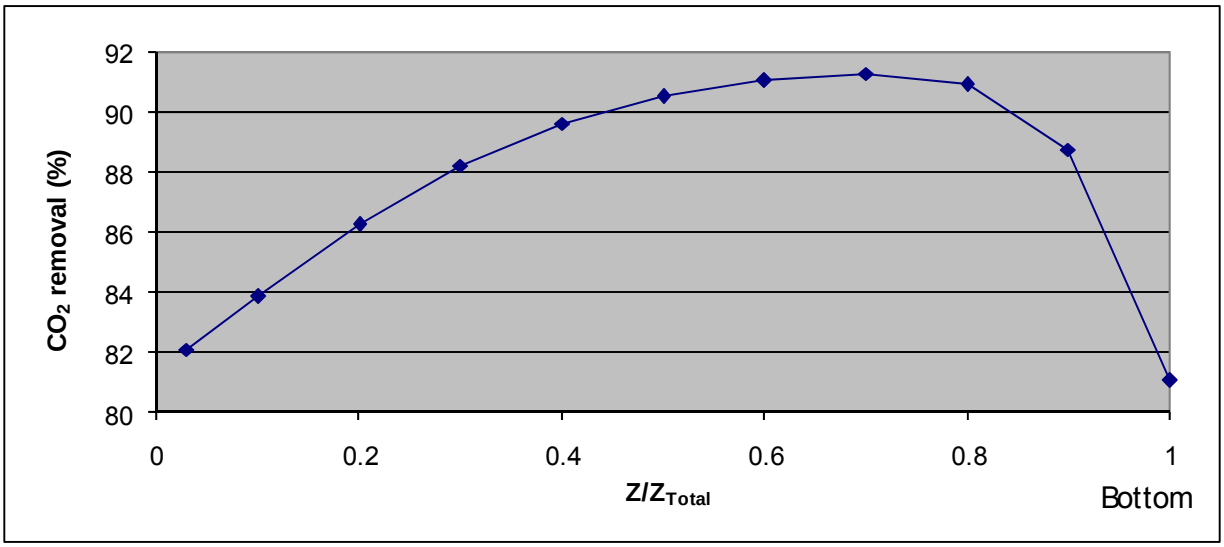

Figure 4: Change in CO_2 removal due to change in intercooled semilean feed position for 4.5m/4.5 m K_2CO_3/PZ. 0.5 kPa CO_2 lean solvent.

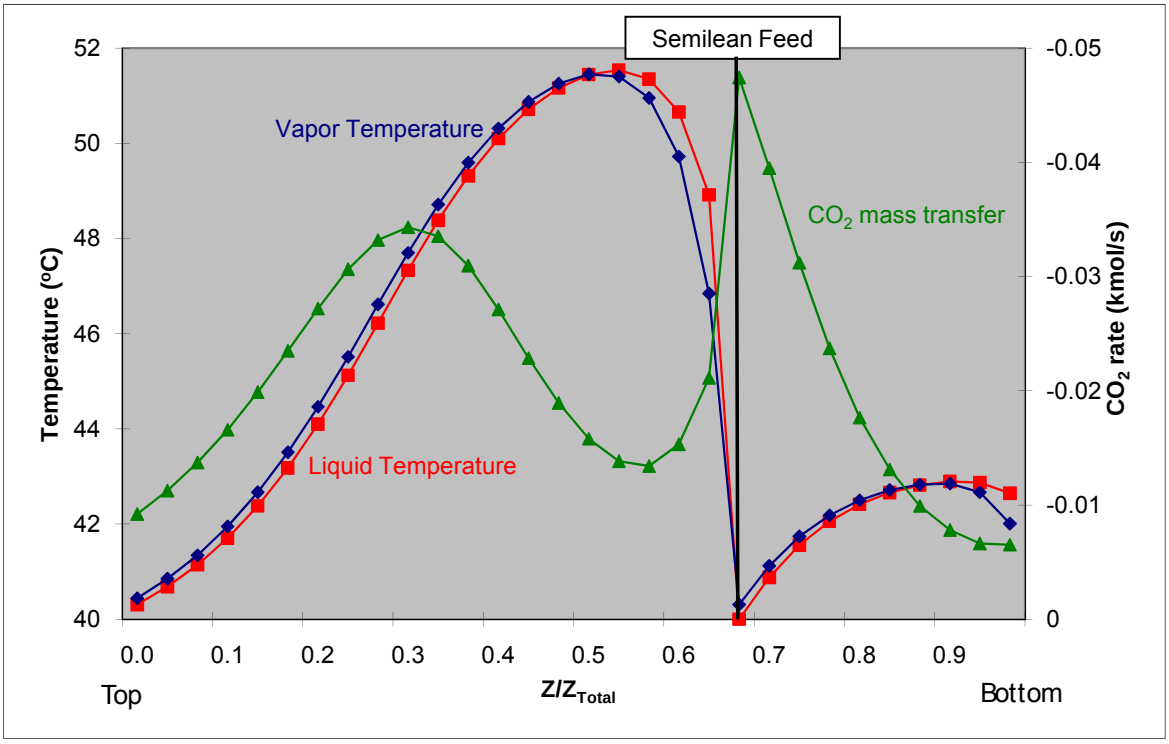

Figure 5: Temperature and CO_2 rate profiles for absorber with semilean feed and intercooling at 0.70 column height. Solvent 4.5m/4.5 m K_2CO_3/ PZ. 0.5 kPa CO_2 lean solvent.

An additional intercooling stage was proposed to increase performance. CO_2 removal vs. position of the 2nd intercooling was plotted to determine the optimum placement. The semilean feed was left fixed as well as the first intercooling. Figures 6 and 7 show the results of this procedure.

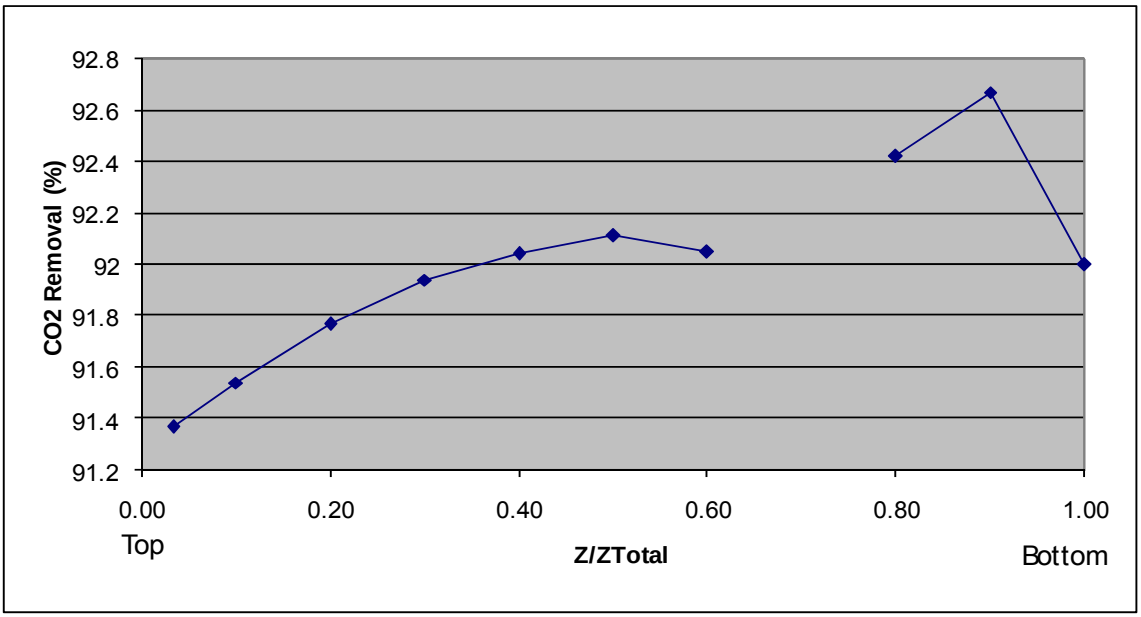

Figure 6: Change in CO_2 removal due to change in 2nd intercooling stage with fixed semilean feed position for 4.5m/4.5 m K_2CO_3/PZ. 0.5 kPa CO_2 lean solvent.

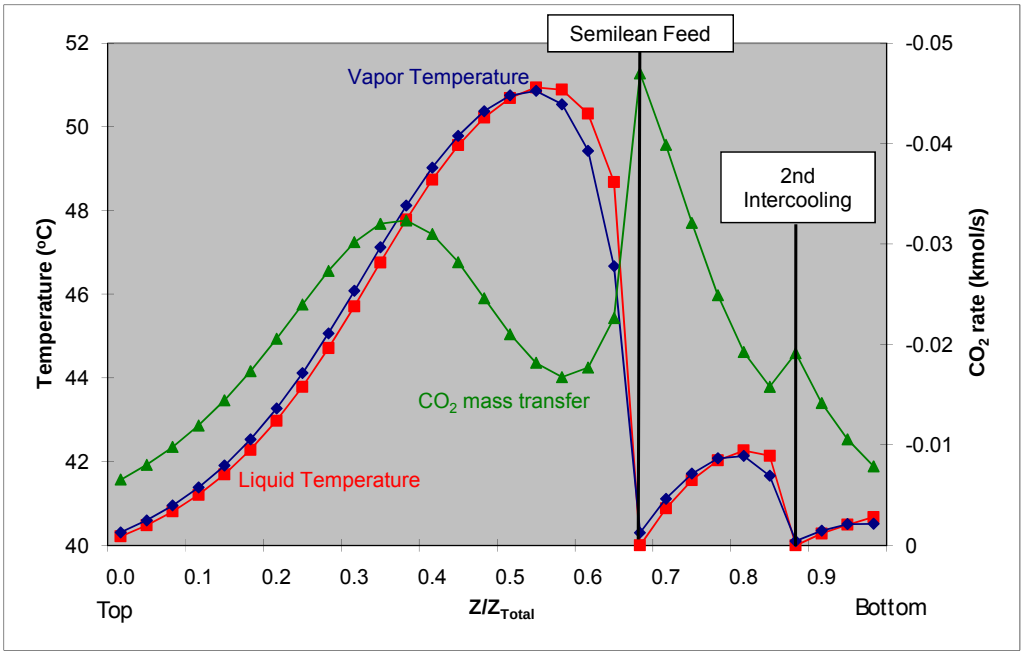

Figure 7: Temperature and CO_2 rate profiles for absorber with intercooled semilean feed at 0.70 and intercooling at 0.90 column height. Solvent 4.5m/4.5 m K_2CO_3/PZ. 0.5 kPa CO_2 lean solvent.

An additional optimum was studied for the stripper. It provides a higher loading lean solvent corresponding to 0.7 kPa CO_2 partial pressure. The lean solvent loading is 0.4208, the semilean is 0.4743 and the split is at 0.1453. Figure 8 shows the resulting profiles obtained following the optimization steps previously mentioned.

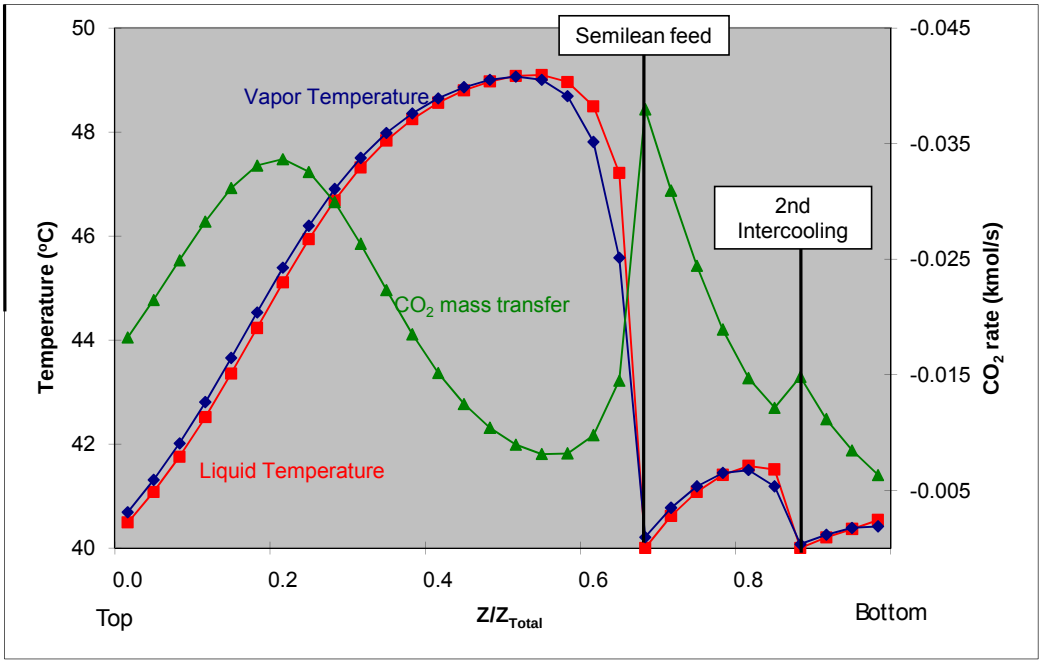

Figure 8: Temperature and CO_2 rate profiles for absorber with intercooled semilean feed at 0.70 and intercooling at 0.90 column height. Solvent 4.5m/4.5 m K_2CO_3/ PZ. 0.7 kPa CO_2 lean solvent

Results for each the various operating conditions modeled are presented in Table 9.

Table 9: CO_2 removal results for K_2CO_3/ PZ absorber configurations

CO_2 Pressure in lean Solvent	0.5 kPa	0.7 kPa
Intercooling	**CO_2 Removal (%)**	
None	81.41	71.62
Single	91.29	82.93
Double	92.67	84.38

MEA

The same procedure as for K^+/PZ was used to maximize CO_2 removal for the absorber using MEA. Flue gas and column design specification are presented in Table 10. Inlet lean and semi-lean solvent conditions were taken from work by Ziaii (2007). Figure 9 summarizes the conditions used for the optimization.

Table 10: Absorber design conditions for all MEA modeling cases

Variable	Value
Diameter (m)	10.6
Height (m)	15.0
Packing Characteristics	
Type	CMR
Vendor	MTL
Material	Metal
Dimension	NO-2P
Liquid hold up (%)	1

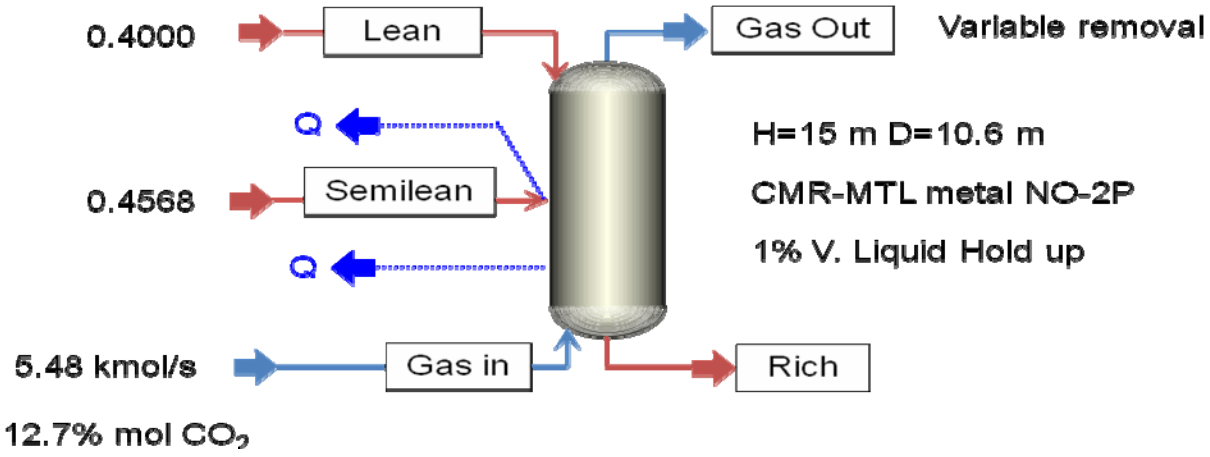

Figure 9: Absorber modeling conditions for 11 m MEA

Figures 10 through 15 show the steps taken to maximize the MEA absorber.

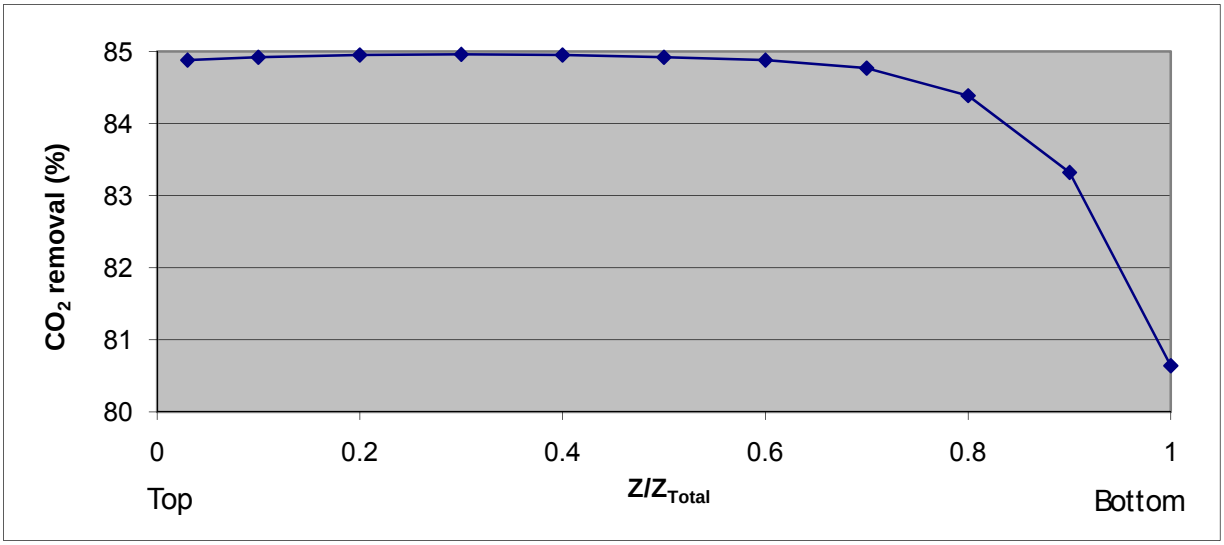

Figure 10: Change in CO_2 removal due to change in semilean feed position for 11 m MEA. No intercooling

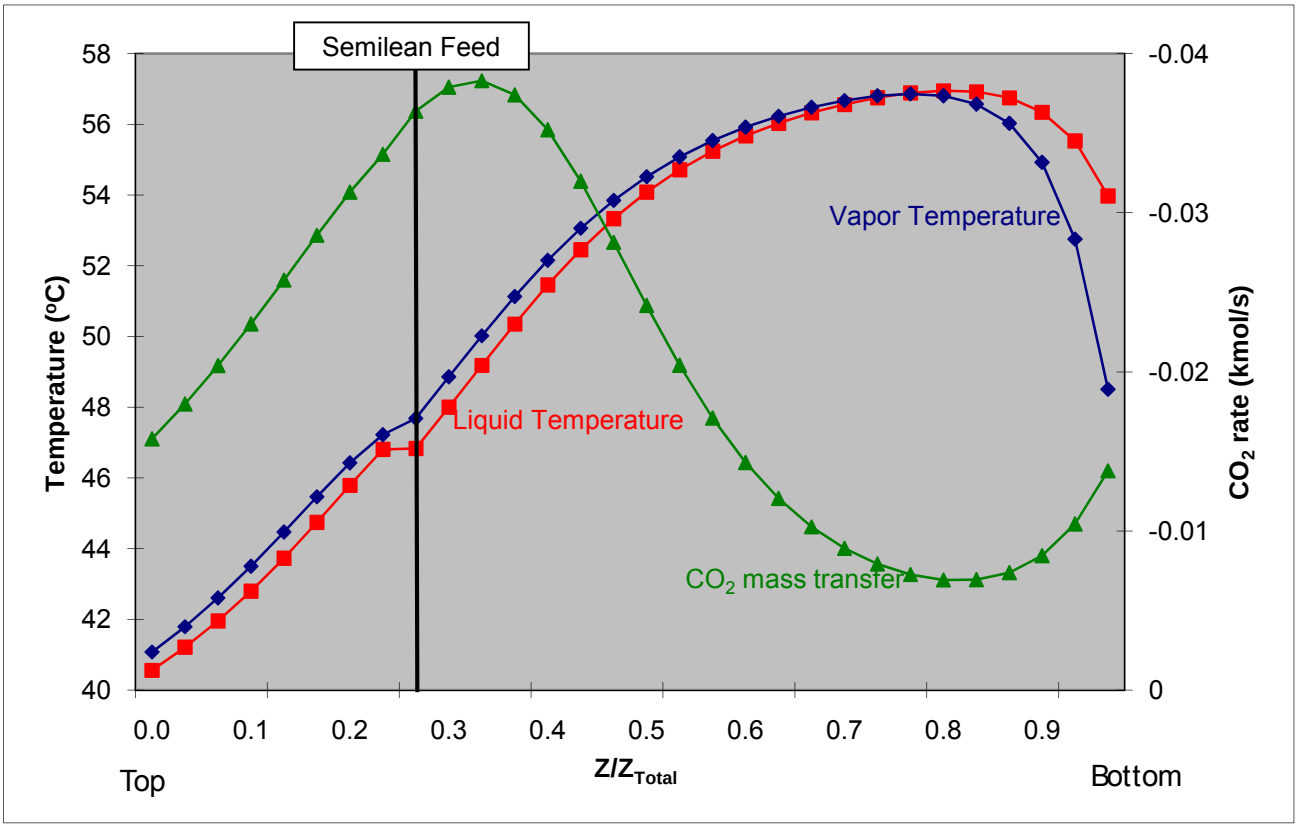

Figure 11: Temperature and CO_2 rate profiles for absorber with semilean feed at 0.30 column height and no intercooling. Solvent 11 m MEA.

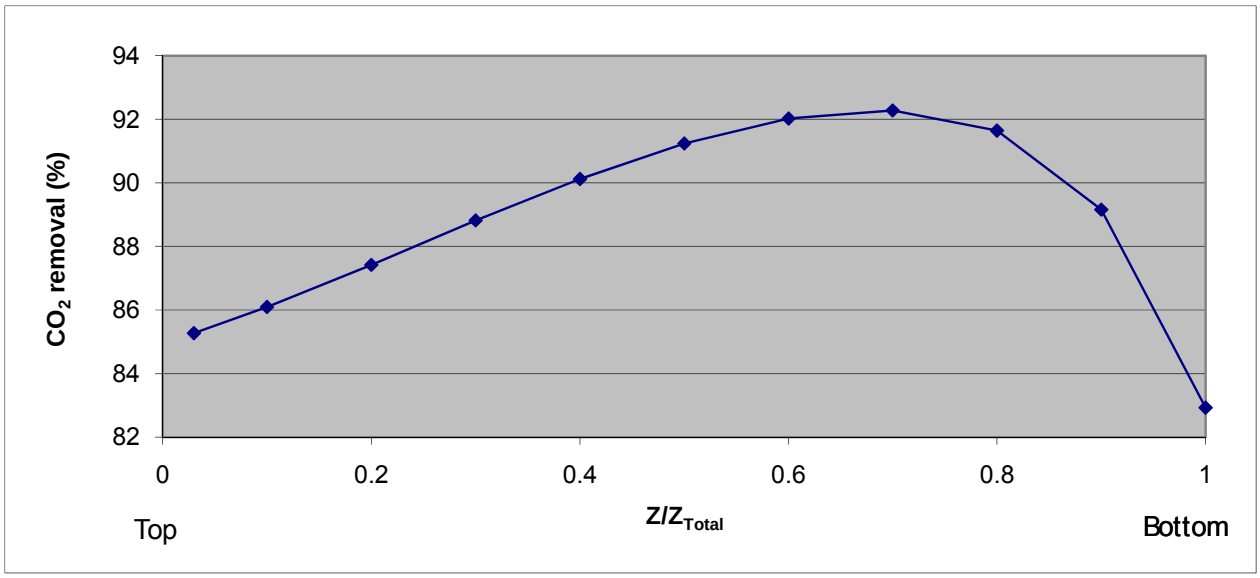

Figure 12: Change in CO_2 removal due to change in intercooled semilean feed position for 11 m MEA.

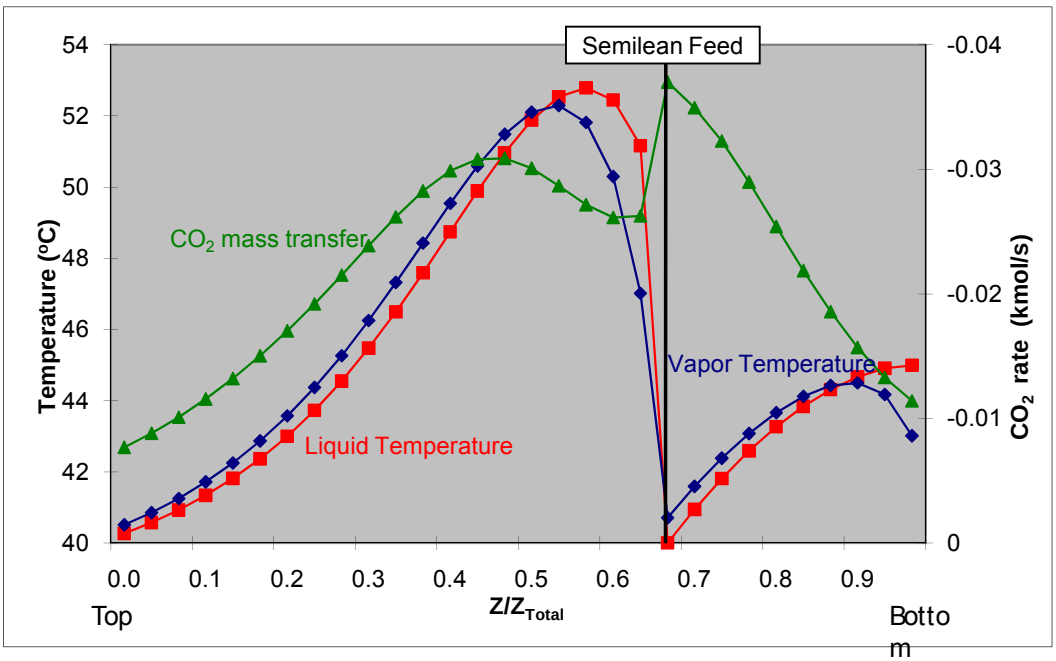

Figure 13: Temperature and CO_2 rate profiles for absorber with semilean feed and intercooling at 0.70 column height. Solvent 11 m MEA.

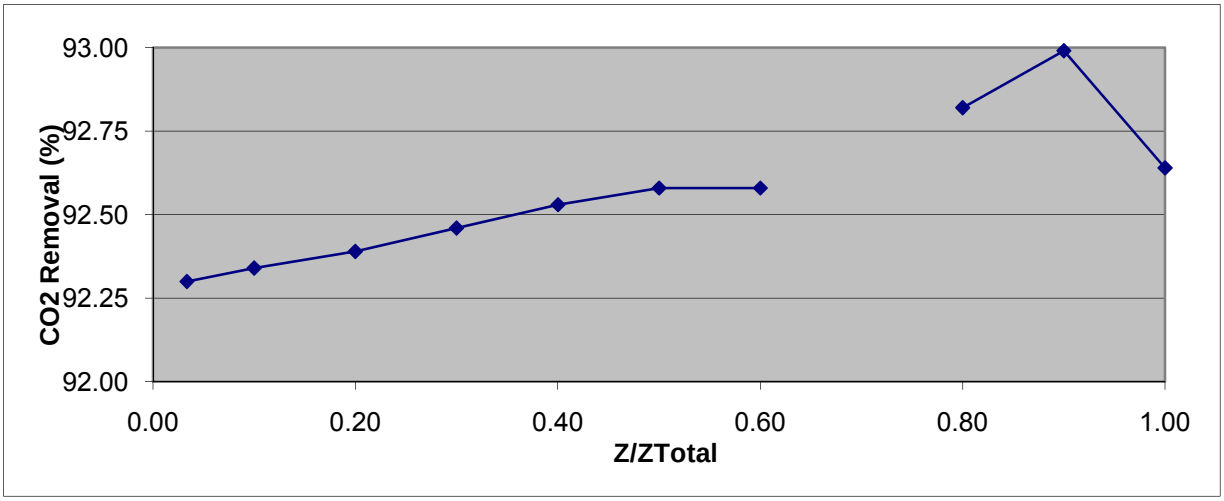

Figure 14: Change in CO_2 removal due to change in 2nd intercooling stage with fixed semilean feed position for 11 m MEA.

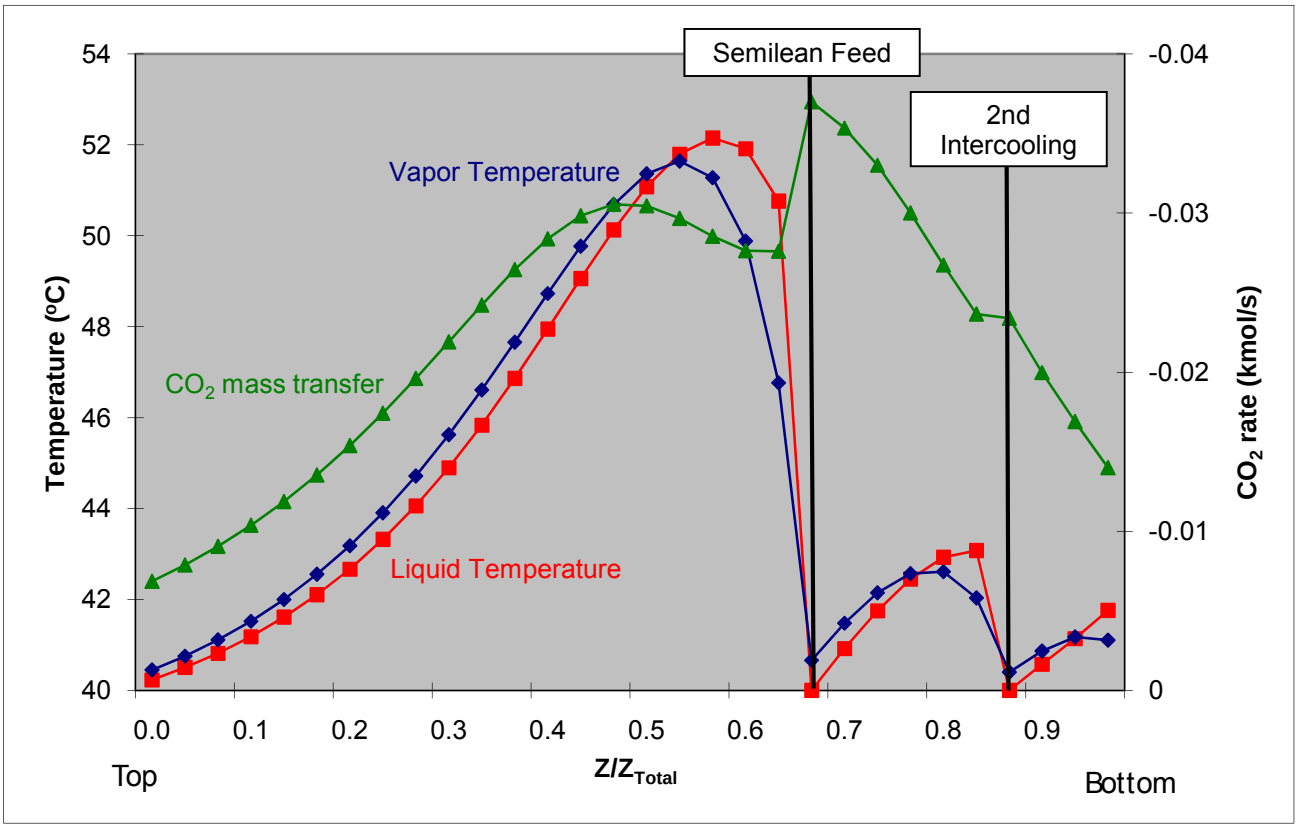

Figure 15: Temperature and CO_2 rate profiles for absorber with intercooled semilean feed at 0.70 and intercooling at 0.90 column height. Solvent 11 m MEA.

Table 11 shows a summary of the results for the MEA optimization modeling runs.

Table 11: CO_2 removal results for MEA absorber configurations

Intercooling	CO_2 Removal (%)
None	84.96
Single	92.28
Double	92.99

Solubility analysis for K_2CO_3/PZ loaded solutions

Observations by Chen and Hilliard while using loaded solutions of K_2CO_3/PZ generated concerns with the formation of crystals at the loading levels used for the simulation of the absorber/stripper system.

Solubility measurements were proposed to determine the maximum concentration of K_2CO_3/PZ at the carbon dioxide loading levels obtained by the modeling conditions.

The implemented method was based on work by Xu and consists on the measurement of changes in conductivity due to the addition of water. For this purpose slurry was prepared with $KHCO_3$ and piperazine and maintained at 40^{o}C which is the minimum temperature in the absorber. Water was then added to dissolve solids present and the conductivity was measured. At the saturation point the curve of conductivity vs. addition of water was expected to present an abrupt change in slope.

Initially, a 5 m /5 m K_2CO_3/PZ, which gives an initial loading of 0.33, was prepared and water was added to observe the change in the slope. The experiment was concluded when a clear solution was observed in the reactor. However, as Figure 16 shows, the change of slope was gradual and there is no way to determine a saturation point. This behavior might be due to the fact that the change in conductivity is caused by a change in concentration of ions forming and disappearing as the concentration of water changes since ionic species have different conductivities. Additionally the appearance of zwitterions ($H^{+}PZCOO^{-}$) might change the conductivity behavior of the solution.

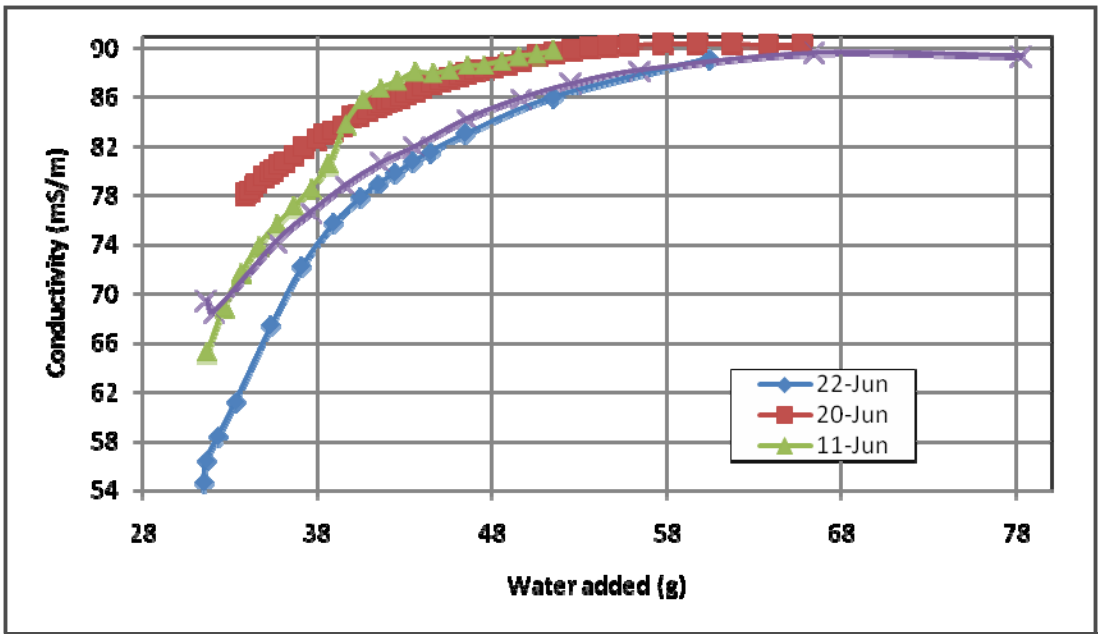

Figure 16: Results of conductivity variations due to water addition for K^+/PZ

Conclusions

Both systems (MEA – K^+/PZ) presented a pinch towards the bottom of the column when no intercooling was used. (Figures 3 and 11). The intercooled semilean feed breaks that pinch allowing the column to reach higher removal (around 9% more). The addition of a second intercooling stage allowed the absorber to increase performance by delaying the approach to a pinch at the bottom of the column. Thus, double intercooling improves removal of carbon dioxide by around 12% for K^+/PZ and 8% for the 11 m MEA.

By using double intercooling it is possible to reach more than 90% removal with the 0.5 kPa CO_2 lean 4.5/ 4.5 m K^+/PZ and the 11m MEA. Results for the 0.7 kPa lean loading case show that supplementary operating schemes are required to reach desirable performance. It might be necessary to consider an additional intercooling stage and/or alternatives that provide higher liquid hold up thus providing higher reaction times.

The results of the solubility analysis (Figure 16) show that the selected approach does not lead to an answer. After four trials it has not been possible to determine if there will be any slurry issues at the conditions modeled in the absorber. A different method needs to be envisioned to determine solubility conditions.

Future Work

Work on intercooling will continue to determine liquid split required for the intercooling stage. Additionally other configurations have been proposed for the 2nd intercooling stage due to its position close to the bottom of the column, such as a reflux between the bottom of the column and the intercooling stage.

A new approach has been planned for the solubility analysis. It consists of a gradual increase in temperature of the loaded solution until total dissolution is reached. Then the solution is cooled until precipitation is observed. Conductivity measurements will be taken

throughout this process. The plot of the logarithm of conductivity vs. the inverse of the temperature should present a change of slope that can be related to the saturation of the solution.

Additionally, slurries with different loadings will be prepared, decanted, and analyzed to determine loading conditions. This implies quantifying total CO_2, PZ and K^+.

Subtask 1.8b – Predicted Stripper Performance with 4m K^+/4m PZ

by David Van Wagener

(Supported by this contract and the TXU Carbon Management Program)

Introduction

During this quarter, work was done to further develop the computer model for CO_2 removal using the potassium carbonate and piperazine solvent. In Quarter 1 of this year, a double matrix stripper equilibrium model was developed in Aspen Custom Modeler (ACM) for the 4.5m K^+/4.5m PZ solvent. This stripper model was used in conjunction with the absorber model developed by Plaza to generate a complete simulation of the solvent. The absorber model, along with the compression and cross exchange sections, was modeled in AspenPlus. Each simulation was run independently with specifications for the conditions for the entering and exiting streams in each section. Two variables in the stripper section were optimized to yield a minimum equivalent work for the section. Additionally, intercooling was optimized in the absorber to keep the temperatures in the stages closer to 40°C and increase absorption rates. The results of these simulations were submitted to Trimeric, who used the data for their SBIR contract.

For more in-depth analysis of the absorption/stripping process, a complete model containing all four sections would be useful. With the entire process in one model, a more comprehensive study on the effect of certain variables in the cost of the system could be completed. In order to integrate the stripper with the absorber section, already modeled using RateSep^{TM}, a stripper model was to be made in AspenPlus. Using this stripper model, a comprehensive system model was put together.

Experimental

AspenPlus Stripper Model Design

The stripper designed in AspenPlus was to have a design identical to the double matrix stripper in the ACM model. The configuration in the previous model was the specified design proposed by Oyenekan. The design incorporated two separate strippers with a split feed. The pressure in the first stripper was higher than the pressure in the second stripper. The majority of the liquid flow entered the first stripper, and it exited as an intermediate lean stream. This stream was fed to the midsection of the second stripper, where it finally exited at the bottom as a lean stream. The minor liquid flow from the split of the feed was fed directly to the top of the second stripper, and it exited from the middle of the stripper as a semilean stream. This configuration was advantageous because it realized the benefits of high pressure stripping. Additionally, "free stripping" was accomplished by feeding the cool, minor feed stream to the top of the low-pressure absorber to contact the rising vapor stream, which had a high water mole fraction. The cool liquid exchanged water in the vapor phase for CO_2 from the liquid phase. Lastly, the overall irreversibility of the process was reduced by utilizing two strippers to decrease the

pressure from stripper operation to absorber operation more gradually (Oyenekan, 2006). This configuration is summarized in Figure 17.

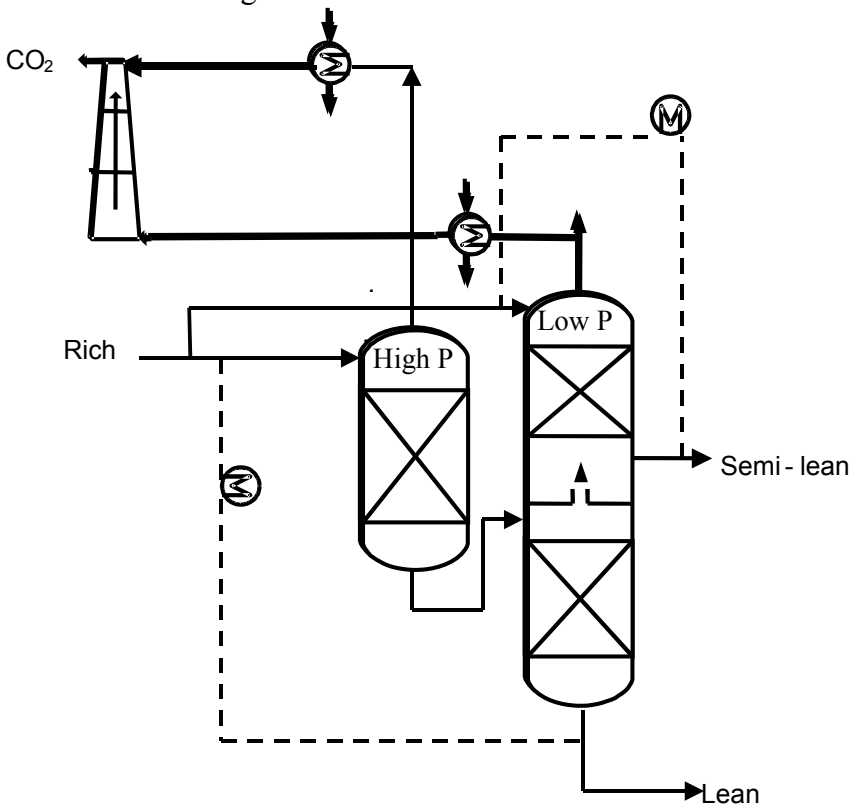

Figure 17: Double Matrix Stripper Configuration

At the time this model was created in AspenPlus, the physical solubility of 4.5m K^+/4.5m PZ was in question. For this reason, the solvent for the AspenPlus stripper model was changed to 4m K^+/4m PZ. Similar to the ACM model, the new model in AspenPlus used equilibrium stages for its calculations. The stripper and compression sections were constructed with several design specifications. The reboiler duties of the strippers were specified in order to achieve the desired lean stream loading and equal reboiler temperatures. Additionally, five degree, cold-side approaches were specified for the two cross heat exchangers. A five degree approach for each liquid flow was accomplished in Aspen by varying the temperature of the respective feed stream to the stripper until the inlet and outlet streams had a five degree differential. Initial guesses of the steam temperatures were drawn from the ACM model results, and the Aspen model was evaluated using flows and loadings equal to those in the ACM model.

Absorber/Stripper System Model in AspenPlus

Once the AspenPlus double matrix stripper model was confirmed to be operational, the stripper and compression sections were imported to the absorber model developed by Plaza in the previous quarterly report. The absorber model also included the cross exchange section. The only alteration to the absorber model was the addition of design specifications which defined stage temperatures of 40°C where intercooling was present. The new complete model was initially sensitive to connecting the appropriate streams in certain orders. After attempting to connect the streams in various orders, the successful method was determined to require

connection of the semilean streams first because their flows were smaller and had less impact on the system. Following the convergence with the two minor flow streams connected, the two major flow streams were connected. The only stream which was not recycled to the absorber was the lean stream. The recycle was essentially balanced by including a design specification to replace the specification in the loading of the lean stream exiting the stripper. The new specification varied the duty of the reboiler in the second stripper so that the total flow of CO_2 in the lean stream returning to the absorber equaled total flow of CO_2 entering the absorber in its lean stream. This specification ensured a close on the CO_2 mass balance, but water and solvent losses were neglected due to their volatility in the stripper. A major change made to the flowsheet was the final compression pressure for the multistage compressor. Initially the compressor was designed to compress to 10 MPa, but this pressure was above the critical pressure for CO_2, and the model often crashed while attempting to perform the flash calculations in this region. The compressor was specified to reach only 1 MPa, a subcritical CO_2 pressure, which enhanced the stability of the simulation. The complete flowsheet is shown in Figure 18.

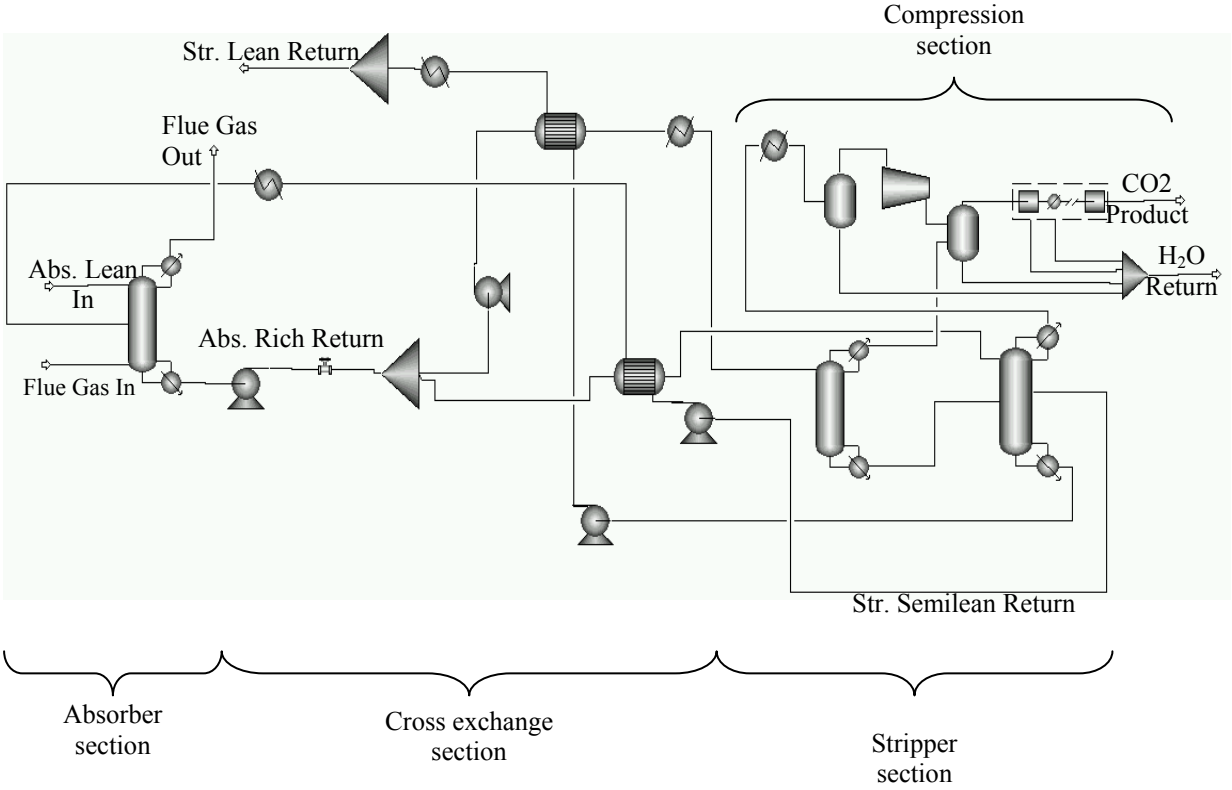

Figure 18: CO_2 Removal Configuration with Double Matrix Stripper

Running simulations with the integrated flowsheet was different than running the independent absorber and stripper simulations. In previous work when the two models were separate, rich and lean loadings were chosen to approximate 90% removal in the absorber. These loadings corresponded to CO_2 equilibrium partial pressures of 5 kPa and 0.5 kPa at 40°C. The specific loadings were then used as specifications for both models. However, since the integrated flowsheet simultaneously calculated the performances of the absorber, cross exchange, and stripper sections, the loadings could be optimized to reduce the energy requirement.

In addition to the configuration with the intercooled absorber and double matrix stripper, an alternate flowsheet was constructed using an absorber with no intercooling and only a simple stripper. This simplified process was to be used as a "worst-case scenario" to compare to the performance of the more advanced configuration.

The lean loading, among several other variables, was an input specification for the flowsheet. For any given lean loading, the solvent flow rate was varied to achieve 90% removal in the absorber with 15 meters of packing. This calculation provided a rich loading, and the reboiler duties in the stripper section were varied to ensure that the lean stream exiting the stripper section at the same CO_2 flow as the lean stream entering the absorber section. Finally, the equivalent work was calculated from the work requirements of the reboilers, pumps, and compressors:

$$W_{stripper} = 0.75 Q_{reb} \left(\frac{T_{reb} + 10°C - T_{cw}}{T_{reb} + 10°C} \right) \quad (1)$$

$$W_{eq} = \frac{W_{stripper1} + W_{stripper2} + W_{LPcomp} + W_{multicomp} + \sum W_{pump}}{n_{CO_2, product}} \quad (2)$$

Using these calculations, the equivalent work of the process was minimized by determining the optimal lean feed loading. The response of the equivalent work to the lean loading had a quadratic pattern in a range near the optimum. The long-term goal is to optimize to operating conditions in addition to the lean loading 1) the operating pressure of the high-pressure stripper, and 2) the split ratio. The split ratio in this work was defined as:

$$Split = \frac{Feed_2}{Feed_1} \quad (3)$$

So far, after determining parameters which caused the simulation to fail and properly adjusting their specifications, the lean loading was optimized for a base case with the high-pressure stripper at 230 kPa and a split ratio of 0.185. These operating conditions were determined to yield a minimum equivalent work for the stripper section in the previous ACM model. The optimal loading for the base case in this simulation is in Figure 19. The optimum was found to occur at a lean loading of 0.378, and the stripper dictated a rich loading of 0.500. The loadings used by the ACM model were 0.401 and 0.496, respectively. The resulting equivalent work of the system with the optimal lean loading was 25.55 kJ/mol CO_2. The equivalent work when the CO_2 product was compressed to the final pressure of 10 MPa was 34.99 kJ/mol CO_2. In comparison, the equivalent work for the previous ACM model paired with the AspenPlus absorber model, which also compressed the CO_2 to 10 MPa was 35.01 kJ/mol CO_2. The agreement between these two values was curious since the new model used a different concentration of the solvent as well as different rich and lean loadings.

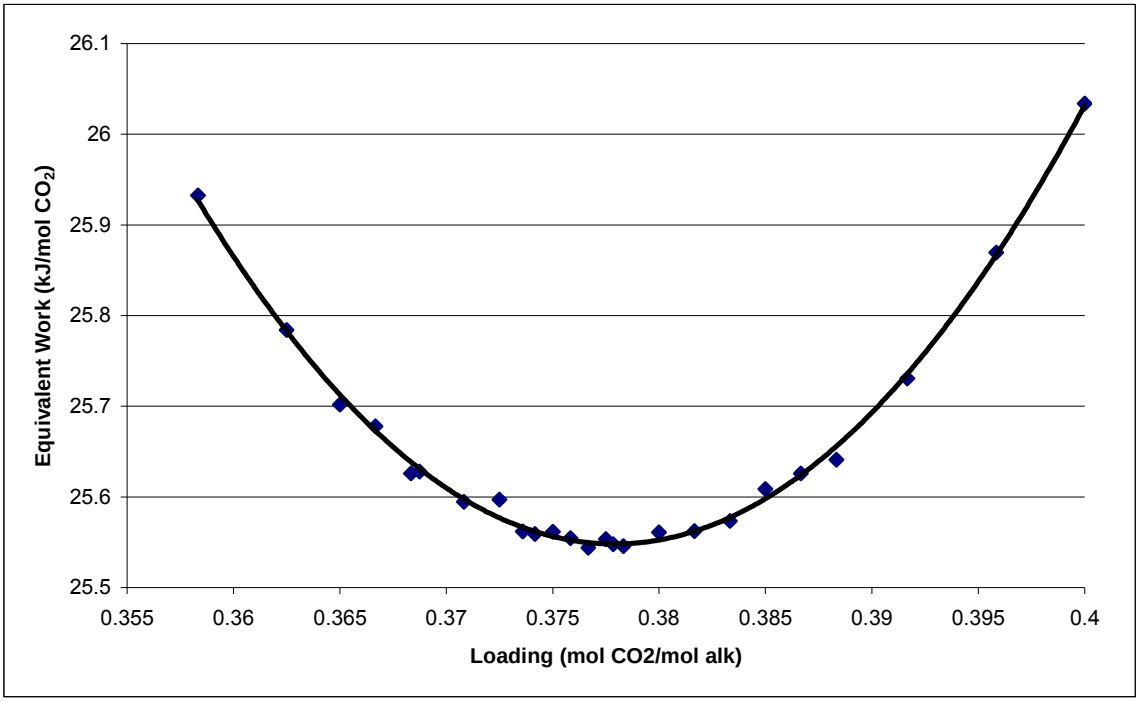

Figure 19: Optimum Lean Loading for 4 m K^+/4 m PZ, double matrix stripper (230/160 kPa, 0.185 split), 90% CO_2 removal, 15 m absorber packing.

Conclusions and Future Work

A stripper model was constructed in AspenPlus which was equivalent to the one previously designed in ACM. The model was integrated with the Ratefrac absorber model which was previously used in conjunction with the ACM stripper model. After troubleshooting the new complete model, the lean loading was optimized to yield a minimum equivalent work while maintaining 90% removal in the absorber. The optimal lean loading was slightly lower than the one used in ACM model, 0.378 compared to 0.401, but the rich loading was roughly equivalent, 0.500 compared to 0.496. At the optimized conditions the equivalent work requirement with compression to 10 MPa was 35.0 kJ/mol CO_2.

The next step for this model will be to optimize the pressure of the high-pressure stripper and split ratio while maintaining an optimal loading. The optimization tool in AspenPlus was explored with respect to optimizing the lean loading, but the model did not demonstrate enough robustness to optimize the lean loading correctly. Additionally, due to numerous convergence loops within the simulation which yield slight inaccuracies in the equivalent work, the program may locate false optima when small steps are taken. The optimization tool will be further investigated, as well as other optimization techniques. Additionally, the model with no intercooling in the absorber and a simple stripper will be optimized to its ideal lean loading and stripper pressure for comparison to the double matrix model.

Task 3 – Solvent Losses

Subtask 3.2 – Oxidative Degradation

by Andrew Sexton

(Supported by this contract and the TXU Carbon Management Program)

Introduction

This effort is an extension of work by George Goff on the oxidative degradation of MEA. Goff showed that oxidative degradation, under high catalyst conditions, is mass-transfer limited by the physical absorption of O_2 into the amine and not by reaction kinetics. Goff also theorized that the oxidative degradation of MEA produced volatile ammonia as well as a host of other proposed degradation products. The major liquid-phase degradation products among these include the heat stable salts of carboxylic acids, nitrite, and nitrate.

The oxygen stoichiometry necessary to produce these degradation products varies for each individual component; overall, it varies anywhere from 0.5 to 2.5 (Goff, 2004). It is believed that the particular degradation products are specific to certain metal catalysts present in the absorption/stripping system – specifically iron and copper. For example, the following balanced reactions illustrate the differences in oxygen consumption based upon the end products:

$$\text{MEA} + 1.5\ O_2 \rightarrow 2\ \text{Formate} + \text{Ammonia}$$
$$\text{MEA} + 3.5\ O_2 \rightarrow 2\ \text{Formate} + \text{Nitrate} + \text{Water}$$
$$\text{MEA} + O_2 \rightarrow \text{Glycolate} + \text{Ammonia}$$

Goff's work on MEA degradation was limited to analyzing MEA degradation rates via the evolution of NH_3. The ammonia evolution rates were measured using a Fourier Transform Infrared (FT-IR) analyzer.

This effort extends Goff's gas-phase analysis by applying various methods of liquid-phase analysis, specifically ion chromatography. These analytical methods will be used to quantify the rate of amine degradation as well as the rate of degradation product formation for amine systems.

Since most gas treating processes using alkanolamines for CO_2 removal are performed in the absence of oxygen, oxidative degradation is a source of solvent degradation that has not been properly quantified. Oxidative degradation is important because it can impact the environment, process economics, and decrease equipment life due to corrosion.

The environmental effects refer to the degradation products themselves: what is being produced, how much of it is being produced, and how it can be disposed of without doing significant damage to the environment. Process economics being impacted are the solvent make-up rate and design of the reclaiming operation. If amine is continually being degraded, then fresh amine must be continually added to the process at a significant cost. In addition, CO_2 loaded amine solutions corrode carbon steel equipment, which catalyzes oxidative degradation even further. It is imperative to quantify how much of this solvent make-up rate is due to oxidative degradation.

Experimental

As stated in prior reports, ion chromatography is the most extensively used liquid-phase analytical method. Anion chromatography utilizes an AS15 (a low-capacity column designed to separate low-molecular weight anions, specifically acetate, glycolate, and formate) IonPac

column and an ASRS 4-mm self-regenerating suppressor made by Dionex, while cation analysis uses a CS17 and a CSRS 4-mm self-regenerating suppressor. Anion analysis employs a linear gradient of NaOH eluent, while cation analysis uses a constant concentration methanesulfonic acid (MSA) eluent.

Some changes have been made to the analytical machines in the lab. Cation chromatography is still operated on the Dionex ICS2500, referenced in previous reports. Anion chromatography is now performed on the Dionex ICS3000. The only changes are as follows (none of which involve a change in method, only in performance):

- Eluent is generated using an EG40 Eluent Generator online, whereas before NaOH eluent was generated manually offline. This provides a consistently accurate eluent concentration.
- An IonPac ATC-3 Anion Trap column scrubs any carbonate generated by eluent production upstream of the guard column.
- A Continuously Regenerated Trap Column (CR-TC), located downstream of the suppressor before the conductivity cell, scrubs any carbonate from the amine solution (converted from loaded CO_2). The ATC-3 and CR-TC help to keep a smoother baseline for the chromatograms.
- An AS Autosampler provides automated sample handling and injection. On the ICS2500, injections are performed manually.

The sole experimental apparatus utilized in this quarter to provide samples for analysis was the low gas flow degradation apparatus. As stated in previous reports, amine solutions in the low gas flow degradation apparatus are oxidized for 12 to 14 days in a low-gas flow jacketed reactor at 55^{o}C. The solutions are agitated at 1400 RPM to produce a high level of gas/liquid mass transfer by vortexing. 98% O_2/2% CO_2 at 100 ml/min is introduced across the vortexed surface of 350 ml of aqueous amine. Samples were taken from the reactor at regular intervals in order to determine how degradation products formed over the course of the experiment. Prior quarterly reports provide a detailed explanation of the low gas flow degradation apparatus.

Two low gas flow apparatus are now operating in parallel. One system operates via the original configuration, which uses an inlet gas of 98% O_2/2% CO_2 premixed in a cylinder provided by Matheson Tri-Gas. A Cole-Parmer rotameter is used to control the flowrate at 100 mL/min. The second apparatus is set up for the modified configuration, which operates with two separate cylinders provided by Matheson Tri-Gas – a pure oxygen cylinder and a pure CO_2 cylinder. The 98% O_2/2% CO_2 mixture is achieved using a 4 channel Brose box made by Brooks and two model 5850E mass flow controllers also manufactured by Brooks. Oxygen flowrate is controlled by a 100cc flow controller, while carbon dioxide is controlled by a 20cc flow controller. The control box displays a digital readout corresponding to the % open of the valve on the mass flow controller. The valve % open corresponds to a gas flowrate, which is determined from the calibration curve constructed for each flowmeter.

The original setup is limited in the fact that the partial pressure of CO_2 over the top of the amine solution entering low gas flow apparatus is fixed. Therefore, the loading of each amine solution is fixed and corresponds to 2% CO_2 concentration in the vapor space above the amine solution. The recently constructed apparatus allows for variations in the CO_2 concentration such that a particular loading in the amine solution can be achieved by adjusting the incoming CO_2 concentration via the flow controllers. Amine loading has become a variable, whereas in the past it was constrained.

Results

Using the analytical methods for the AS15 and CS17 columns, analysis was completed on low gas flow experiments conducted during the prior quarter (α is defined as mol CO_2/mol amine):

1. March 2007 AMP experiment (Oxidative degradation of 3M AMP, α = 0.55, 55°C, 1400 RPM, 1mM Fe, 98%O_2/2%CO_2).
2. April 2007 PZ experiment (Oxidative degradation of aqueous PZ, α = 0.60, 55°C, 1400 RPM, 0.1mM Fe, 5mM Cu, 98%O_2/2%CO_2).
3. April 2007 PZ experiment (Oxidative degradation of aqueous PZ, α = 0.60, 55°C, 1400 RPM, 0.1mM Fe, 5mM Cu, 100mM "A", 98%O_2/2%CO_2).
4. May 2007 MEA experiment (Oxidative degradation of 7m MEA, α = 0.40, 55°C, 1400 RPM, 0.1mM Fe, 5mM Cu, 98%O_2/2%CO_2).
5. May 2007 PZ experiment (Oxidative degradation of aqueous PZ, α = 0.60, 55°C, 1400 RPM, 0.1mM Fe, 98%O_2/2%CO_2).
6. June 2007 MEA/PZ experiment (Oxidative degradation of 7m MEA/2m PZ, α = 0.40, 55°C, 1400 RPM, 0.1mM Fe, 100mM "A", 98%O_2/2%CO_2).
7. June 2007 MEA/PZ experiment (Oxidative degradation of 7m MEA/2m PZ, α = 0.40, 55°C, 1400 RPM, 0.1mM Fe, 5mM Cu, 100mM "A", 98%O_2/2%CO_2).

Figure 20 illustrates the degradation product formation rates for experiment 4, run in May 2007. The figure shows results from a degradation experiment for 7m MEA with low iron (0.1mM, or 5 ppm) and high copper (5mM, or 250 ppm) catalyst. Formate is the most highly concentrated degradation product, with a formation rate of 0.66 mM/hr. Nitrate and nitrite formation rates are very similar (0.13 and 0.11 mM/hr, respectively). Oxalate, glycolate and acetate are all relatively minor products – glycolate and acetate rates are less than 0.01 mM/hr.

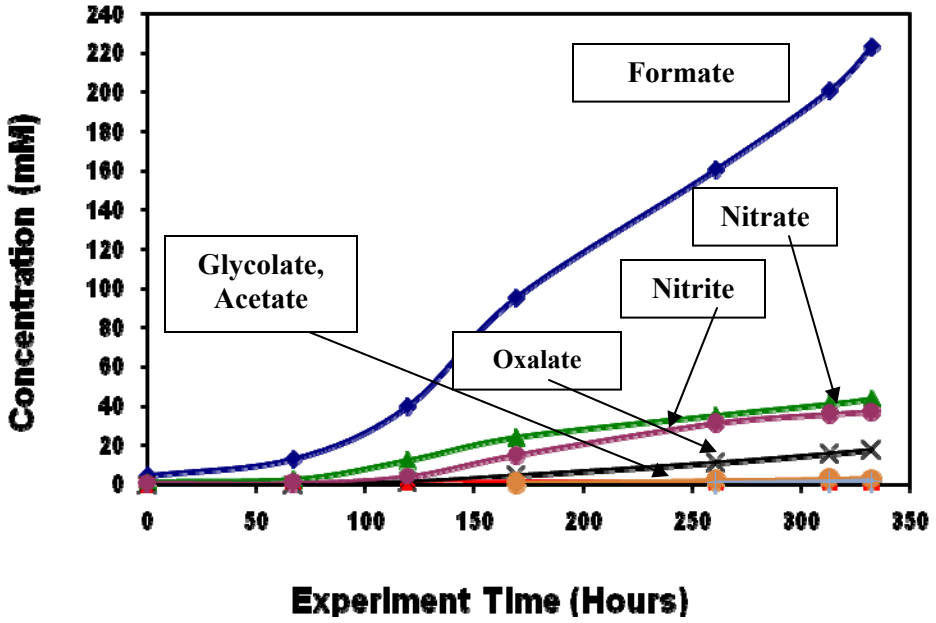

Figure 20: May 2007 MEA experiment (Oxidative degradation of 7m MEA, α = 0.40, 55°C, 1400 RPM, 0.1mM Fe, 5mM Cu, 98%O_2/2%CO_2)

Table 12 compares this MEA experiment with three prior experiments involving 7m MEA, all of which differ by the catalyst added to the system: Fe only (0.6 mM), Cu only (0.6 mM), and an equimolar mixture of Fe and Cu (both 0.6 mM).

Table 12: Rate Comparison of 7 m MEA Low Gas Flow Degradation Experiments (mM/hr)

Distinguishing Conditions	7 m MEA, 0.6 mM Fe	7 m MEA, 0.6 mM Cu	7 m MEA, 0.6 mM Cu and Fe	7m MEA, 0.1mM Fe, 5mM Cu
Formate	0.40	0.39	0.67	0.66
Oxalate	0.04	0.04	0.05	0.05
Nitrite/Nitrate	0.46	0.21	0.33	0.24
Carbon	0.73	0.75	0.85	0.78

From the information in Table 12, it appears that the equimolar Cu/Fe solution behaves similarly to a degraded 7 m MEA solution that contains minimal iron (0.1mM) and high copper (5mM), which was chosen to represent an industrial system in which copper is added to inhibit corrosion. Formate production rates are very similar, and they both exceed MEA systems which contain copper only and iron only. Oxalate rates are identical as well. Nitrate/nitrate rates for the most recent experiment are lower than for the equimolar mixture, which makes sense since the industrial catalyst combination very closely mimics a copper only system. Carbon formation rates are on the same order of magnitude as well – at this point, they are not expected to be identical because a complete material balance has not been performed yet.

Figures 21 and 22 represent experiments 2, 3, and 5, all of which involve the oxidative degradation of aqueous PZ under varying catalyst conditions. Figure 21 illustrates an aqueous PZ experiment at low iron concentration (0.1 mM), which represents catalyst conditions for an industrial system with stainless steel material of construction and continuous iron removal from the system. Figure 22 actually contains results from two experiments, both of which consisted of degraded aqueous PZ with 0.1mM Fe and 5mM Cu added. The difference was that one experiment was conducted in the presence of 100 mM of Inhibitor A, while the other was carried out in the absence of A.

Figure 21 shows that ethylenediamine (EDA) and formate are really the only two ionic degradation products present in any significant quantity (the other three products are 0.2 mM or less after 330 hours). The final concentrations of those products are less than 7 mM, which correspond to degradation rates between 0.01 and 0.02 mM/hr, both of which are very low degradation product formation rates.

Figure 22 shows all measurable degradation product formation rates for aqeuous PZ/Fe/Cu with and without Inhibitor A. Formate and EDA (not shown in Figure 22) were the most concentrated degradation products at the end of the experiment in the absence of A. Their concentrations were approximately 90 and 110 mM, respectively. Oxalate, nitrate, and nitrite were also present in final concentrations of 5 mM or less. Adding 100 mM of Inhibitor A to the solution decreased degradation greatly. EDA and formate were the only products present in detectable quantities. Final concentrations for these species were 14.5 mM and 1.5 mM, respectively, which is a significant reduction in product accumulation versus the experiment run in the absence of A.

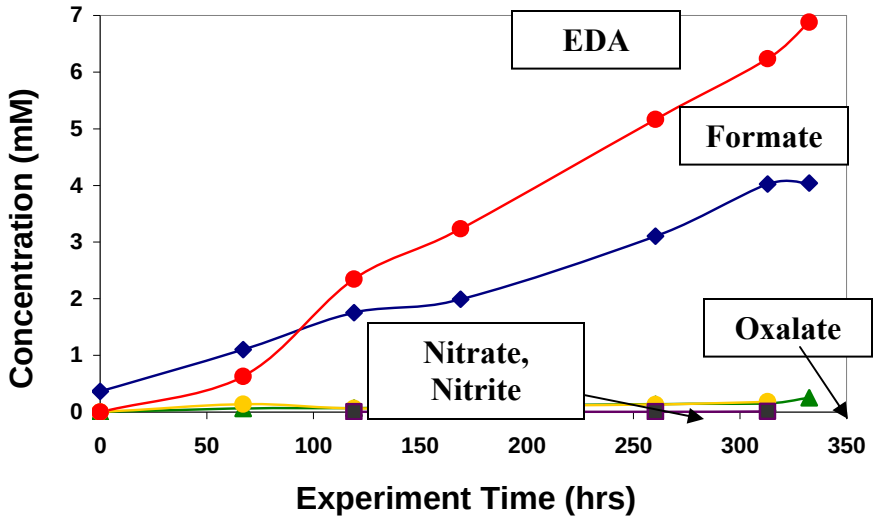

Figure 21: May 2007 PZ experiment (Oxidative degradation of aqueous PZ, α = 0.60, 55°C, 1400 RPM, 0.1mM Fe, 98%O_2/2%CO_2)

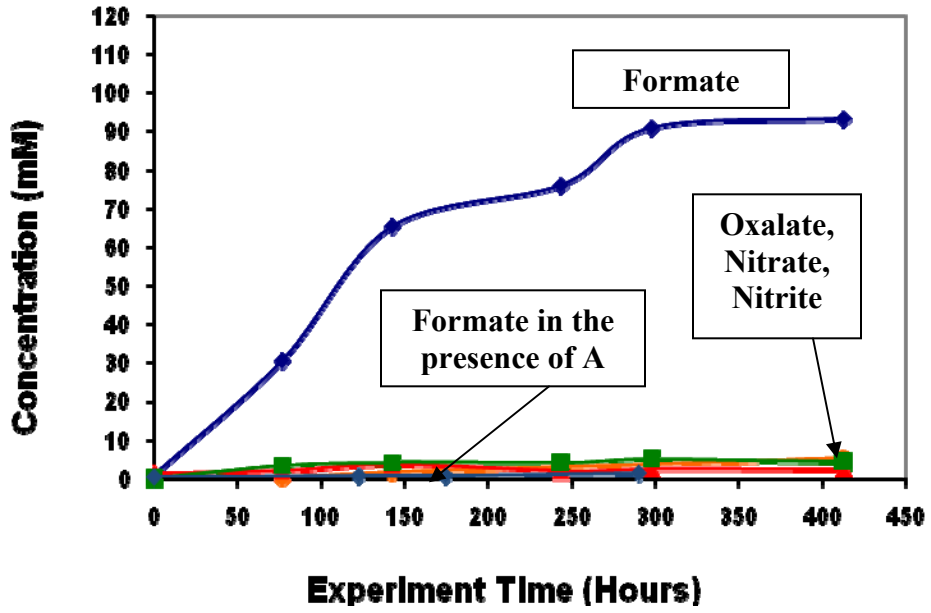

Figure 22: April 2007 PZ experiments (Oxidative degradation of aqueous PZ, α = 0.60, 55°C, 1400 RPM, 0.1mM Fe, 5mM Cu, +/- 100mM "A", 98%O_2/2%CO_2)

Table 13 shows the results of the three piperazine experiments in terms of product formation rates (mM/hr). In the absence of Inhibitor A and at high copper catalyst, a large amount of EDA was produced; however, very little nitrate or nitrite is present. This is a different trend from past piperazine experiments, all of which consisted of 2.5m PZ with vanadium added as a catalyst. The addition of 100mM of Inhibitor A significantly reduced the formation rates of formate and EDA, and lowered the other species below detection limits. An aqueous PZ system in which only a minimal concentration of iron is present produced similar results as the "A"

experiment. All degradation product formation rates are an order of magnitude lower as compared to PZ in the presence of low iron and high copper.

Table 13: Degradation Product Rate Comparison for aqueous Piperazine (mM/hr)

Distinguishing Conditions	5m PZ / 0.1mM Fe / 5mM Cu	5m PZ / 0.1mM Fe / 5mM Cu / 100mM "A"	5m PZ / 0.1mM Fe
Formate	0.22	0.004	0.01
Oxalate	0.01	0.00	0.001
EDA	0.25	0.03	0.02
Nitrate/Nitrite	0.013	0.00	0.001
Carbon	0.76	0.06	0.05
Nitrogen	0.52	0.06	0.04

Figures 23 and 24 illustrate results from experiments 6 and 7, both of which involve 7 m MEA/2 m PZ in the presence of 100 mM of Inhibitor A at differing catalyst conditions. Figure 23 depicts product formation rates when 0.1mM Fe is present along with "A". Formate is the most abundant degradation product, followed by nitrate, nitrite, and oxalate. EDA and acetate were detected, but at trace levels.

Figure 24 shows the formation of degradation products for a MEA/PZ solution in which 0.1mM Fe and 5 mM Cu were added. Formate was the degradation produced at the highest concentration, followed by EDA and nitrate. Nitrite, oxalate, glycolate acetate were all detected at trace levels. Overall, degradation of the MEA/PZ solution was higher when copper was present.

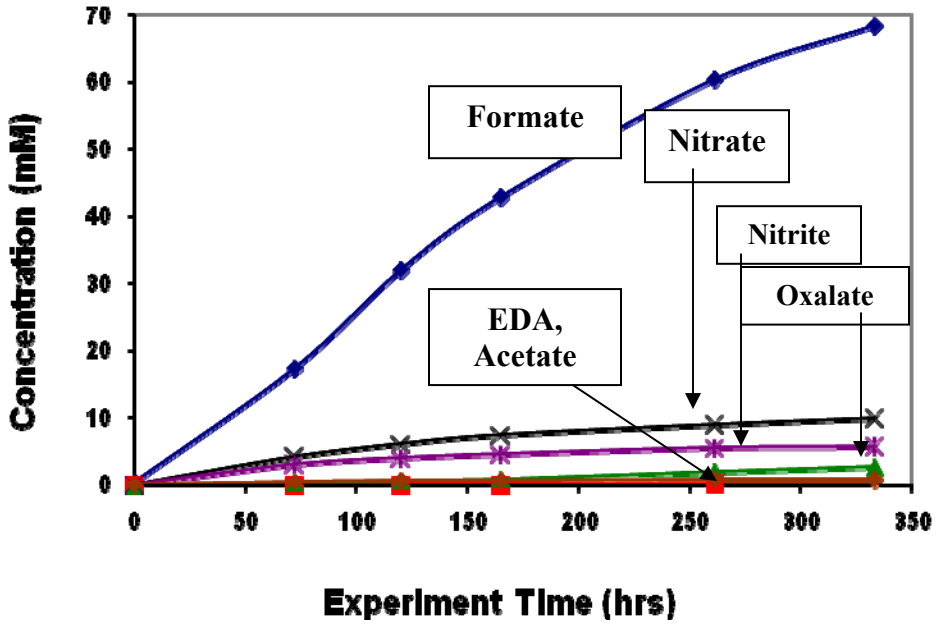

Figure 23: June 2007 MEA/PZ experiment (Oxidative degradation of 7m MEA/2m PZ, α = 0.40, 55°C, 1400 RPM, 0.1mM Fe, 100mM "A", 98%O_2/2%CO_2)

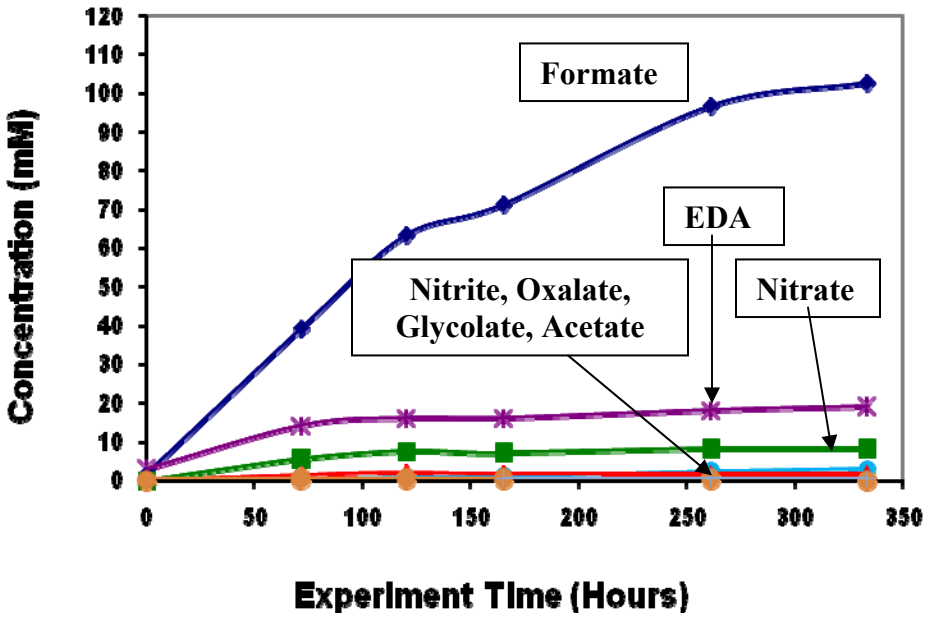

Figure 24: June 2007 MEA/PZ experiment (Oxidative degradation of 7m MEA/2m PZ, α = 0.40, 55°C, 1400 RPM, 0.1mM Fe, 5mM Cu, 100mM "A", 98%O_2/2%CO_2)

Table 14 summarizes the degradation product formation rates for MEA/PZ experiments past and present. In all cases, formate is the most abundant degradation product created. An uninhibited system with both iron and copper degrades faster than an inhibited system. Moreover, an inhibited system containing both copper and iron degrades faster than an inhibited system containing iron only. Ethylenediamine is produced at a very low rate; in the case of the MEA/PZ experiment in the presence of Fe and "A", EDA is present at trace levels.

Table 14: Rate Comparison for 7m MEA/2m PZ Low Gas Flow Experiments (mM/hr)

Distinguishing Conditions	7m MEA / 2m PZ / 0.1mM Fe / 100 mM "A"	7m MEA / 2m PZ / 0.1 mM Fe / 5mM Cu / 100 mM "A"	7m MEA / 2m PZ / 0.1 mM Fe / 5mM Cu
Formate	0.20	0.30	2.35
EDA	0.002	0.05	0.03
Nitrite/Nitrate	0.05	0.03	0.13
Carbon	0.23	0.42	2.67
Nitrogen	0.05	0.13	0.18

Figure 25 gives degradation product rates for the oxidative degradation of 3M AMP (2-amino-2-methyl-1-propanol), which is a sterically hindered amine. The methyl groups on the alpha-carbon inhibit the free radical formation necessary to initiate the amine oxidative degradation. The structure of AMP is given in Figure 26. Even at time 420 hours, formate

concentration is approximately 3 mM. All other detectable products are at 1mM or less. This corresponds to degradation product formation rates of less than 0.01 mM/hr for all detectable species.

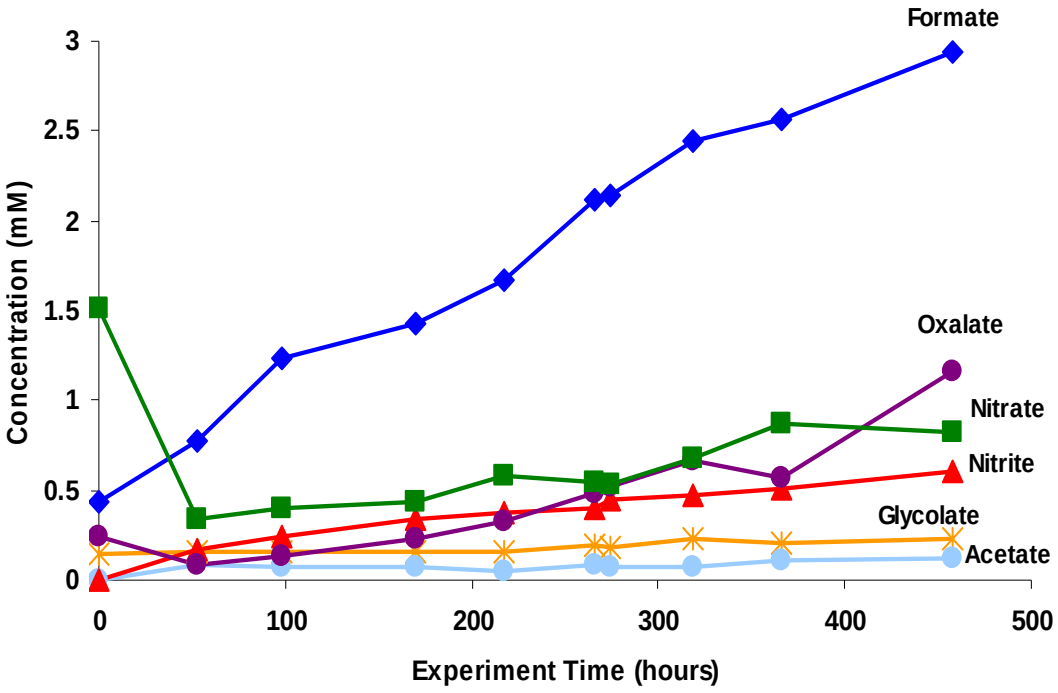

Figure 25: March 2007 AMP experiment (Oxidative degradation of 3M AMP, $\alpha = 0.55$, 55°C, 1400 RPM, 1mM Fe, 98%O_2/2%CO_2).

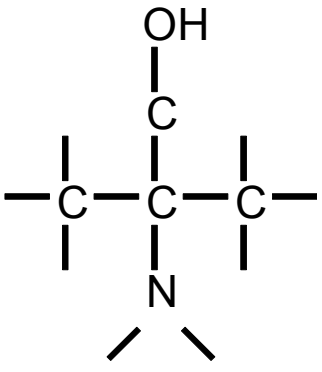

Figure 26: AMP Structure

Conclusions and Future Work

During this past quarter, anion chromatography provided some beneficial findings. With respect to 7m MEA solutions, in the absence of Inhibitor A (an oxygen scavenger), the metal catalysts of iron and copper produce different degradation product ratios depending on their presence/absence. The combination of iron and copper has an additive effect on formate production. In 7m MEA solutions in which only Fe or Cu were present at a concentration of 0.6 mM (60 ppm), formate was produced at a rate of 0.40 mM/hr. However, when Fe and Cu were added together in two completely different ratios and total concentrations (0.6mM Fe/0.6mM Cu and 0.1mM Fe/5mM Cu), formate production was 0.67 and 0.66 mM/hr, respectively. This data also suggests there may be a maximum concentration at which catalyst promotes degradation – anything beyond this concentration may be excess that has no effect on the amine degradation.

On the other hand, the presence of metal catalysts appears to have a mean effect on nitrite and nitrate production. An MEA solution with iron added produced almost double the amount of nitrate and nitrite than a solution with copper added. A degraded MEA solution containing equimolar amounts of Fe and Cu resulted in a nitrate/nitrite formation rate that was the average of the Fe-only and Cu-only experiments. Further proof was provided with an MEA experiment using a 50:1 ratio of Cu:Fe. The nitrate/nitrite production rate was very similar to the rate for the copper-only experiment.

Aqueous PZ, in the presence of low iron and high copper catalyst, degrades on the same order of magnitude as 7m MEA. Although formate production is at a lower rate and nitrate/nitrite exists at trace concentrations, high ethylenediamine concentration places the carbon degradation on par with MEA degradation and nitrogen degradation twice that of MEA. This finding is preliminary, however, because there may be other non-ionic degradation products (both liquid and vapor-phase) that may be formed from piperazine degradation. Furthermore, piperazine solutions have not yet been degraded in the high gas flow apparatus.

The oxidative degradation of aqueous PZ can be significantly reduced in two ways: keeping iron catalyst concentration low in solution in the absence of copper, or adding Inhibitor A to the system. Liquid-phase degradation product concentrations were 93% lower in an aqueous PZ system containing only 0.1mM Fe (as compared to a system with 0.1mM Fe and 5mM Cu). Likewise, the addition of 100 mM "A" to an aqueous PZ/0.1mM Fe/5mM Cu system reduced degradation by 91%. As compared to 7m MEA, these results are very favorable. The percentage reduction is greater with the addition of "A", and the absolute product formation rates are lower as well. Aqueous piperazine solution also offers the advantage of a simpler solution: continually remove the iron from the absorber/stripper system to keep the concentration low, and the same results are achieved as in a more complex system when copper and Inhibitor A must be added to the system to keep Fe concentrations low.

Inhibitor A also proved to be very effective in reducing degradation for 7m MEA/2m PZ solutions. The addition of "A" to a MEA/PZ solution with low Fe and high Cu reduced the formation of detectable degradation products by 81%. Most of this can be attributed to the reduction in formate production, which was decreased by almost an entire order of magnitude from 2.35 mM/hr to 0.30 mM/hr. The removal of 5mM Cu from an MEA/PZ solution containing Fe and "A" reduced degradation by another 50%. In all of the MEA/PZ experiments, EDA production was minimal. This leads me to believe that MEA may be oxidizing faster than the piperazine, preventing the PZ from degrading. An accurate total amine analysis method may help in determining if this hypothesis is accurate.

A fair comparison of all three amine systems is shown in Table 14. Three amine systems are compared at similar conditions: 0.1mM Fe, 5mM Cu, and 100mM "A". This composition represents an industrial aqueous absorption/stripping system utilizing copper and "A" to control corrosion and degradation. The aqueous PZ and 7m MEA systems have product formation rates about 75% lower than the 7m MEA/2m PZ. Almost all of the entire difference can be attributed to formate. In the case of aqueous PZ, the major degradation product is EDA; with 7m MEA, it is formate, nitrate, and nitrite. Overall rates are almost identical. However, neither one of these systems compare to an AMP system at low iron concentration (0.1mM Fe). Degradation in an AMP system is 83–87% lower than in the inhibited MEA and PZ systems. The steric hindrance from the structure of AMP makes it an attractive option as solvent for CO_2 removal.

Table 15: Rate Comparison of Four Different Amine Systems (mM/hr)

Distinguishing Conditions	7m MEA / 2m PZ / 0.1 mM Fe / 5mM Cu / 100 mM "A"	aq PZ / 0.1mM Fe / 5mM Cu / 100mM "A"	7m MEA / 0.1 mM Fe / 5mM Cu / 100 mM "A"	3M AMP, 1mM Fe
Formate	0.30	0.004	0.04	0.008
EDA	0.05	0.03	0.00	0.000
Nitrite/Nitrate	0.03	0.00	0.04	0.004
Carbon	0.42	0.06	0.10	0.015
Nitrogen	0.13	0.06	0.04	0.004

In the next quarter, I plan to continue my work on the oxidative degradation of various amine systems (under varying catalyst and Inhibitor conditions) using the low gas flow apparatus and ion chromatography. I am also working with Dionex on developing a robust method for amino acid detection in degraded amine solutions. A total amine method that will be more accurate than the pH titration method is being examined as well.

The high gas flow apparatus and FTIR analyzer have been repaired and are ready to be used once again. Prolonged experiments will be conducted on MEA, PZ, and AMP solutions in an effort to collect simultaneous gas-phase and liquid-phase product analysis.

Subtask 3.3 – Thermal Degradation

by Jason Davis

(Supported by this contract and the TXU Carbon Management Program)

Introduction

This subtask will be used to define future work for the development of a kinetic model for amine thermal degradation by carbamate polymerization. Monoethanolamine (MEA) will be used as the baseline for comparing amine systems, and while the initial products of MEA thermal degradation have been identified, the kinetics of the thermal degradation pathways have not been clearly defined. Currently, MEA concentrations are capped at 30 wt% to minimize thermal degradation and prevent corrosion in industrial applications; however, with a better understanding of degradation kinetics, this number can be optimized and we can better understand solvent losses by this pathway.

Piperazine (PZ) is a cyclic diamine that is being evaluated as an alternative to MEA in the absorber/stripper system. Currently, there is no literature on thermal degradation of PZ, but this

subtask will be used to define possible degradation mechanisms and to show the rate of piperazine degradation under stripper conditions.

Theory

Monoethanolamine

Polderman, Dillon and Steele[1] describe the mechanism for thermal degradation by carbamate polymerization. In CO_2 capture, MEA associates with CO_2 in the absorber to form MEA carbamate as illustrated below.

MEA MEA Carbamate

This reaction is normally reversed in the stripper, but in some cases the MEA carbamate will cyclize to form 2-oxazolidone, which is also a reversible reaction, as shown below.

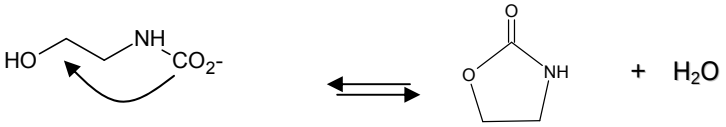

MEA Carbamate 2-Oxazolidone

MEA carbamate can also irreversibly dehydrolize to form N,N'-di(2-hydroxyethyl)urea[2].

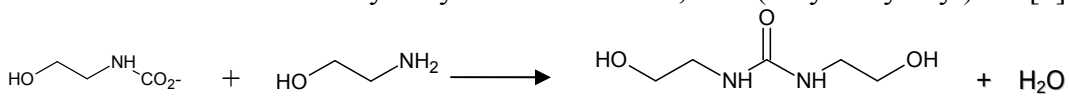

MEA Carbamate MEA N,N '-di(2-hydroxyethyl)urea

The former product, 2-Oxazolidone, can then react with another molecule of MEA to form 1-(2-hydroxyethyl)-2-imidazolidone which is sometimes referred to as HEIA.

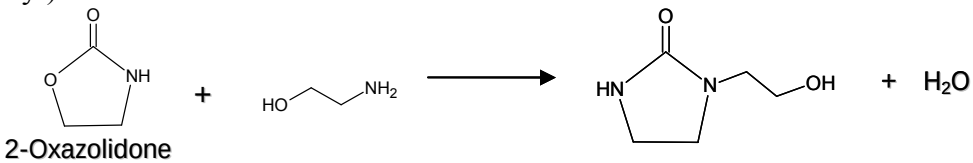

2-Oxazolidone 1-(2-hydroxyethyl)-2-imidazolidone (HEIA)

HEIA can then be hydrolyzed to form N-(2-hydroxyethyl)-ethylenediamine or HEEDA.

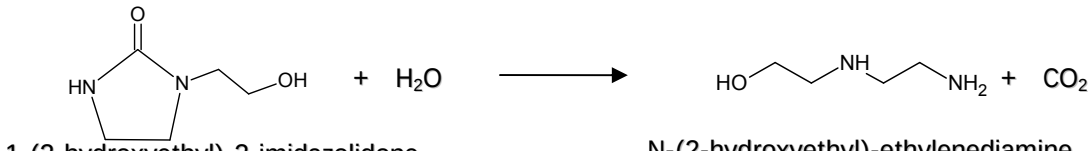

1-(2-hydroxyethyl)-2-imidazolidone (HEIA) N-(2-hydroxyethyl)-ethylenediamine (HEEDA)

These four species (2-oxazolidone, dihydroxyethylurea, HEIA and HEEDA) are believed to be the main products of thermal degradation. The rate of formation of these products is a function of temperature (faster kinetics), CO_2 loading (more carbamate present) and MEA concentration.

Piperazine

The structure of piperazine (PZ) is a cyclic diamine that is shown below.

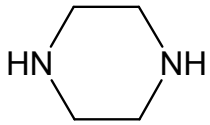

Piperazine

Since PZ does not have an alcohol group present like MEA, thermal degradation by the pathway shown for MEA above should be minimized since the initial reaction step will be eliminated. Other reaction pathways could exist like the two listed below. The first is a self forming urea between the carbamate and the protonated amine group on a single MEA molecule.

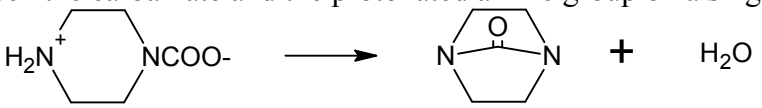

The second proposed pathway is the formation of a urea between the carbamate of one piperazine and the protonated amine of another piperazine molecule.

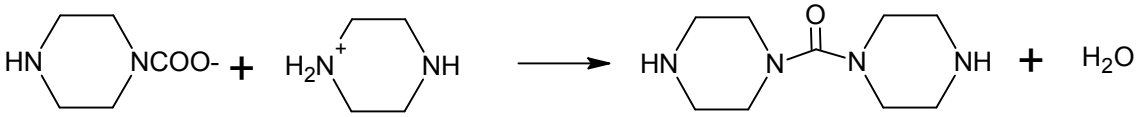

Methods

High Temperature MEA Experiment

A set of 5-2ml sample bombs were constructed using 316L SS tubing and Swagelok fittings. These bombs were filled with an amine solution and placed in a Stabil-Therm constant temperature cabinet made by Blue M for temperature control. The temperature was monitored periodically with a thermometer.

7m MEA solutions were made using Huntsman MEA and deionized water and were loaded to 0.4 mol CO_2/mol amine. 2mL of this solution were placed in each of the five sample bombs and placed in the Stabil-Therm oven and held at 150^{o}C. Samples were removed over the course of several weeks, diluted, and injected onto the GC for analysis.

MEA Full Range Temperature Experiments

A set of sample bombs were constructed similar to the high temperature experiments. This time a matrix of MEA concentrations and loadings were used. Solutions of 3.5m, 7m, and 11m MEA were loaded to 0.2, 0.4 and 0.5 moles CO_2 per mole amine and loaded into a Stabil-Therm oven held at 100^{o}C, 120^{o}C and 135^{o}C. Samples were pulled at 1, 2, 4, 6, and 8 weeks and analyzed by GC.

New sample bombs were created made of ½" tubing and Swagelok end-caps. The new sample bombs contained 10ml of sample instead of the previous 2ml sample bombs. New ovens were ordered to accommodate the scale-up in operation and were used for the 135^{o}C data. These new ovens are forced convection Imperial V ovens from Barnstead Labs with closed loop temperature control and digital read-out.

Piperazine Experiment

Aqueous PZ was loaded with CO_2 to a loading of 0.8 moles CO_2/mol PZ and then placed into a set of 2mL sample bombs like the ones used in the high temperature MEA experiment.

They were placed in Imperial V ovens at 120°C and 135°C and removed after 1, 2, 4, and 8 weeks.

GC Methods

An HP5890 gas chromatograph was acquired and reconditioned complete with a 7673A automatic sampler and equipped with FID and TCD detectors. Based on a paper by Dawodu and Meisen[3] and another paper by Supap et al[4], a polar column was selected for the method development which follows the standard practice of polarity matching of the column to the analyte of interest. Initially, an HP-Innowax column (30m x 0.25mm ID x 25um film thickness) was selected for the high-temperature experiments. The inlet and FID detector were maintained at 250°C and the oven temperature was increased from 80°C to 240°C at a rate of 7°C/min and held at the maximum temperature for 10 minutes. The carrier gas was helium and was used to maintain the pressure in the column at 25psig with a split ratio of 30:1. The split flow was determined by using a bubbler attached to the purge flow and measuring the column flow by injecting an unretained organic solvent (hexane) and dividing the known column volume by the retention time.

A second column and method was used for all the other experiments. The Agilent HP-5 column (30m x 0.53mm x 1.50um film thickness) was selected and the temperature profile was modified to start at 80°C and increase to 250°C at a rate of 10°C /min. The column pressure was maintained at 20psig and all other parameters were held constant as compared to the previous method.

HPLC Methods

A Dionex dual HPLC/IC system with an evaporative light scattering detector (ELS) is being used to develop a HPLC method for the separation of amines from their degradation products. Two methods are currently being evaluated. The first is a reverse-phased separation using a Waters T3 C18 column for separating nonpolar compounds, and the second uses a HILIC separation using a carbohydrate column from Agilent for the separation of polar compounds. The methods are still under development, but will be addressed in future reports.

pH Titration Method

A total amine analysis was performed using a pH titration method. A Mettler-Toledo autotitrator was used to titrate the degraded amine samples with sulfuric acid down to a pH of 2.5 to determine the amount of amine remaining in the sample.

Results and Discussion

MEA High Temperature Experiments

The high temperature experiments were only run at one MEA concentration and loading. Figure 27 shows a sample GC chromatogram from the 150°C MEA degradation experiments.

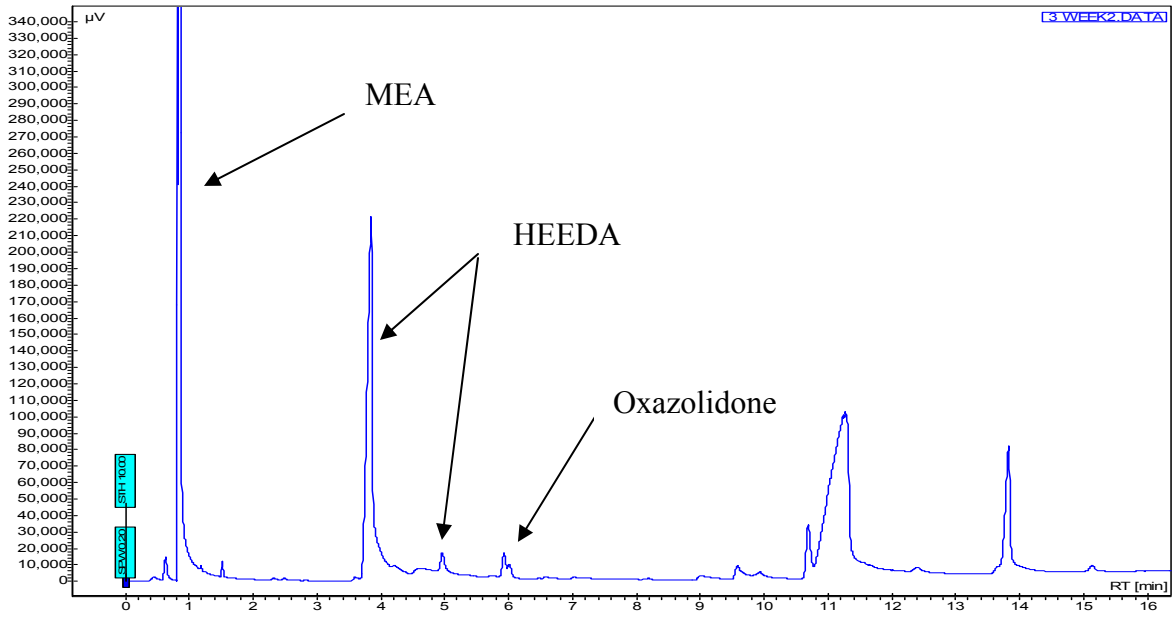

Figure 27: MEA degraded at 150°C for 3 weeks on HP-5 GC column

The MEA, HEEDA and oxazolidone have clear baseline resolution with good separation. Additional unidentified impurity peaks are present at longer retention times. The one problem with this method is that the MEA elutes at roughly column dead time. This means that any unretained species will coelute with the MEA making it difficult to say with certainty that the MEA peak is not masking potential impurities.

MEA losses were estimated based on the total MEA peak area counts for the time 0, 2, 3, 5, and 8 week samples. Figure 28 below shows the total MEA losses over time.

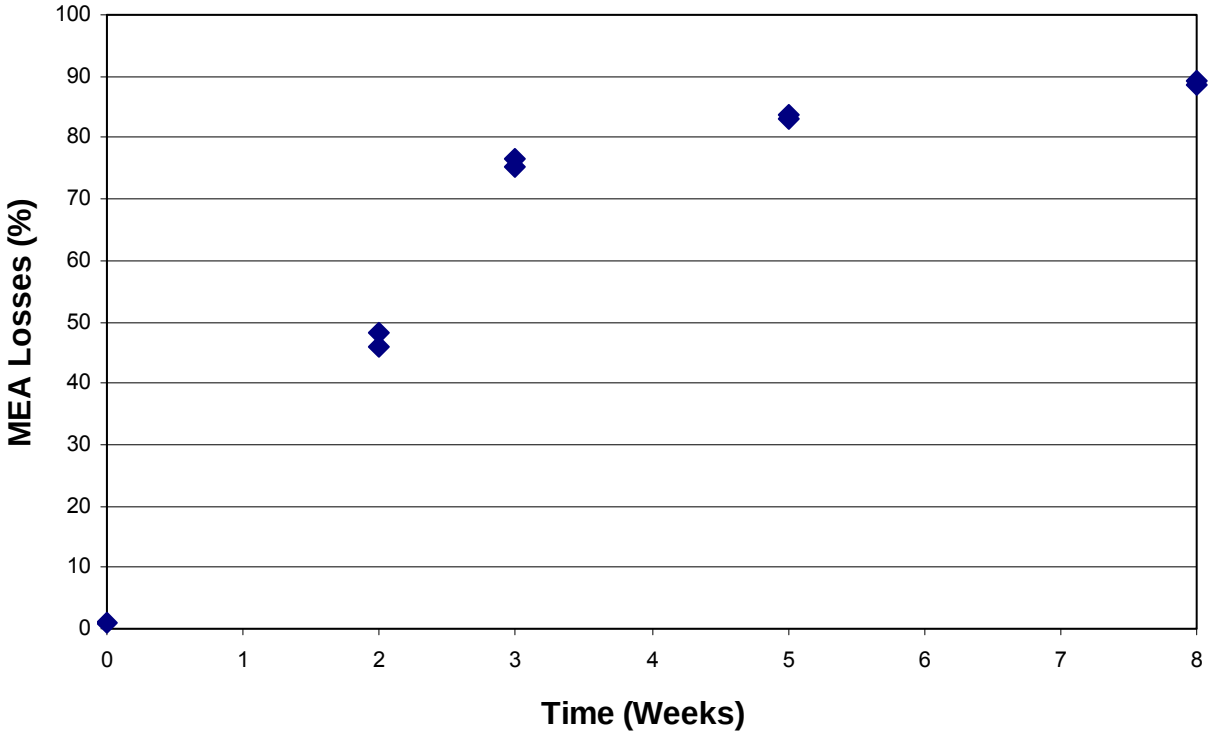

Figure 28: MEA losses at 150°C over an 8 week period

As you can see from Figure 28, the loss mechanism is an exponential decay with 75% degradation after just 3 weeks at 150°C. The amount of oxazolidone and HEEDA increased from the week 1 to week 3 samples, but actually decreased in the 5 and 8 week samples. Since the oxazolidone is in equilibrium with the amount of MEA carbamate present, it would decrease as the amount of available MEA decreased. The HEEDA would also decrease since it would further polymerize to higher molecular weight components and would be formed at a slower rate due to the disappearance of oxazolidone.

The total chromatogram area counts decreased with time indicating that some high boiling point compounds were not being vaporized properly indicating that some high molecular weight polymerization products were being formed.

MEA Full Temperature Range Experiments

A set of 45 2ml sample bombs were constructed and placed in an oven at various amine concentrations and loadings and placed in an oven at 100°C for varying amounts of time. A set of the bombs were removed at 1, 2, 4, 6, and 8 weeks. Little degradation occurred over the entire time span used. Using the HP-5 column the total degradation fell within the standard error for the experiment. Figure 29 below shows the percent losses of MEA over time.

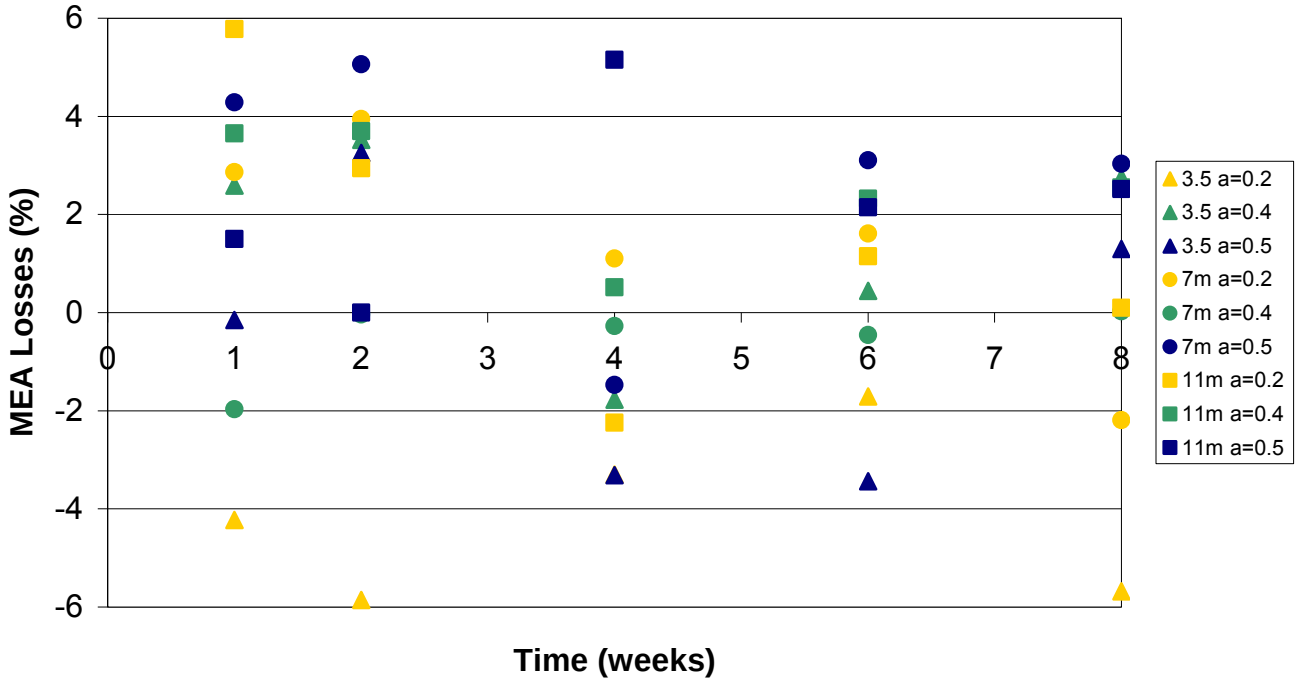

Figure 29: MEA losses over an 8 week period at 100°C

MEA degraded very little if any at 100°C based on the data shown in Figure 29. The data was all within 6% of the original solution. Averaging the 6 and 8 week samples across all loadings and concentrations, there was a slight direct correlation between loading and MEA loss as well as MEA concentration and MEA loss as shown in Tables 16 and 17 below.

Table 16: MEA losses at 100°C as a function of MEA concentration

MEA Concentration (m)	MEA Losses (%)
3.5	-1.1
7	0.9
11	1.8

Table 17: MEA losses at 100°C as a function of CO_2 loading

CO_2 Loading	MEA Losses (%)
0.2	-1.1
0.4	1.3
0.5	1.4

Figure 30 below shows the data for MEA losses at 120°C over an 8-week time span.

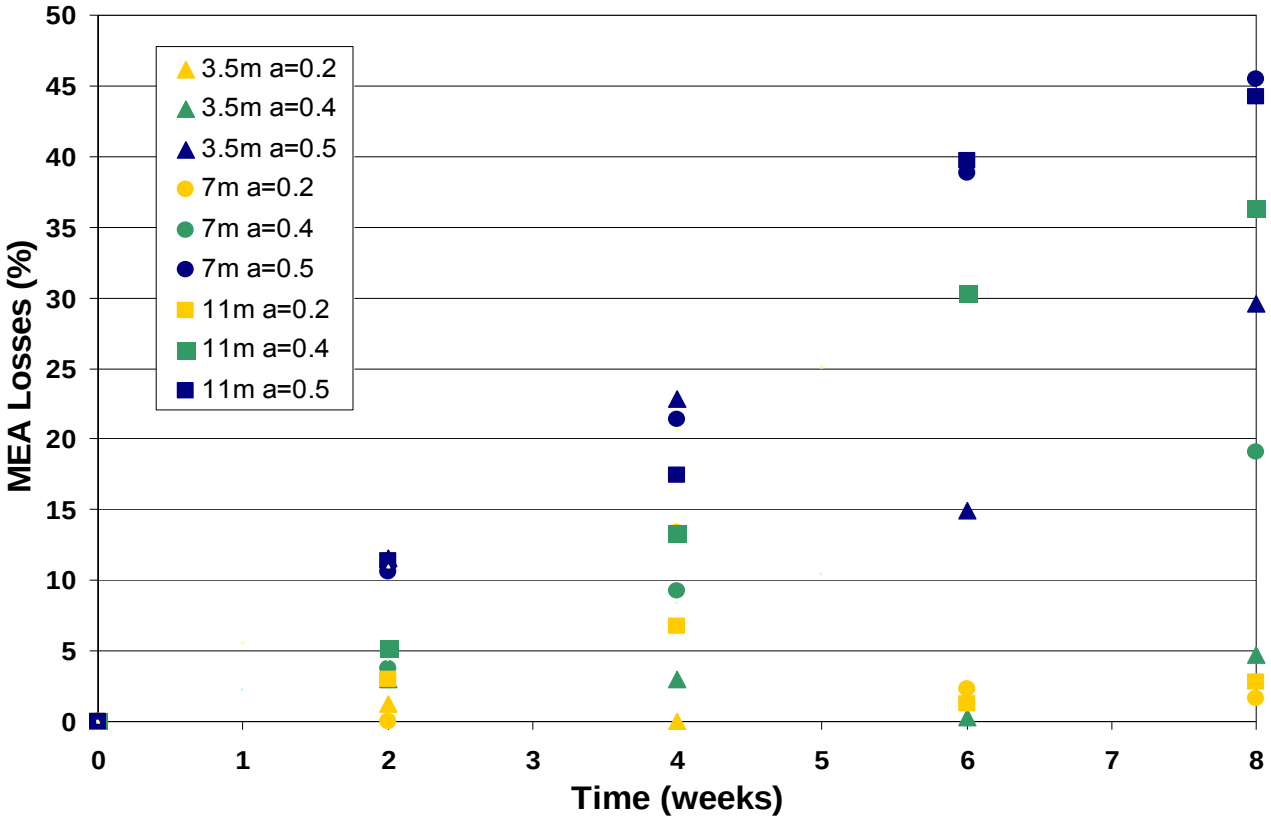

Figure 30: MEA losses at 120°C over an 8-week period

From the 120°C data it can be seen that MEA thermal degradation shows a direct correlation between CO_2 loading and amine concentration with a stronger emphasis on the former. The results for the low loading solutions showed losses that were barely measurable for all three amine concentrations whereas the high loading solutions had 30–45% solvent loss after 8 weeks. Data for MEA at 135°C was gathered in the same manner as the 120°C data and is shown in Figure 31 below.

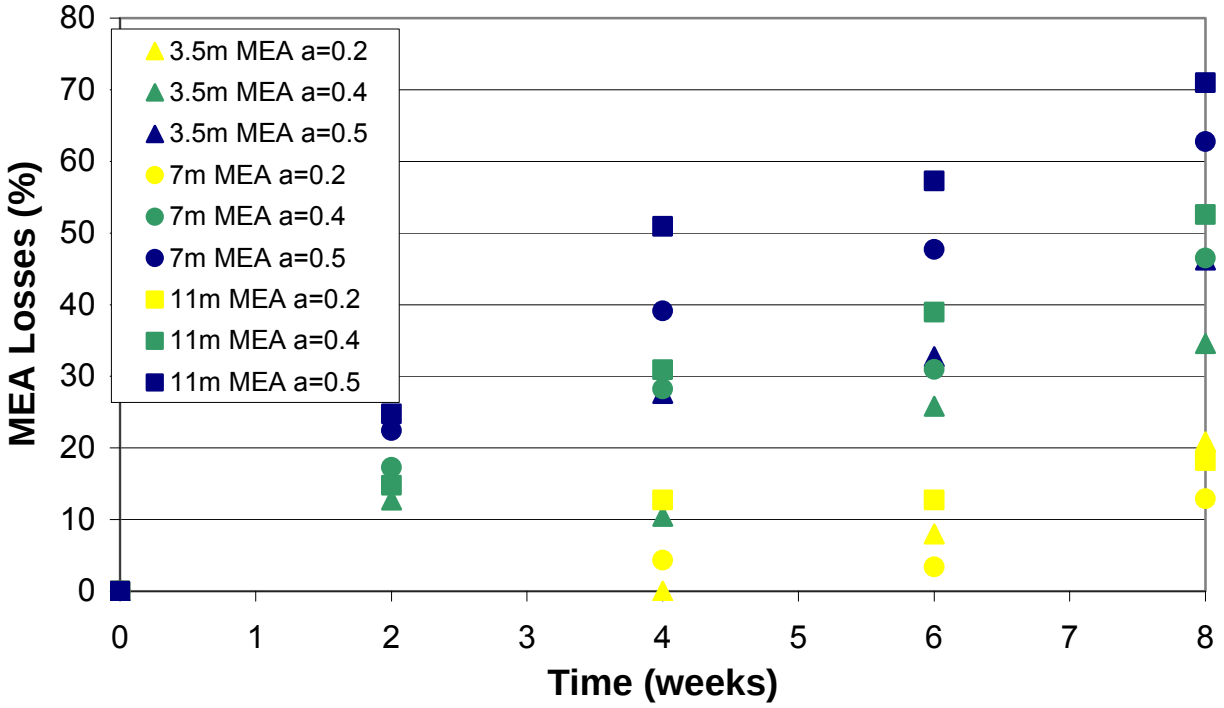

Figure 31: MEA losses at 135°C over an 8-week period

This data shows much higher amine losses than the 120°C data and really shows the strong correlation between loading and amine losses. This data also shows a much clearer correlation between solvent loss and amine concentration than was seen in the 120°C data. In this data set, a measurable amount of losses was witnessed for the low loading solutions at long times and the highly loaded solutions showed losses from 46–71% of MEA at 8 weeks.

Table 18 shows tabulated data for all of the MEA thermal degradation experiments performed to date. From this table you can see the large increase in thermal degradation that occurs from the 100°C to 120°C experiments and again from the 120°C experiments to the 150°C experiments.

Table 18: MEA Losses (%) over an 8-week time span at varying MEA concentrations, CO_2 loadings and temperatures

MEA Molality	CO_2 Loading	Temperature (^oC)	1 week	2 weeks	4 weeks	6 weeks	8 weeks
3.5	0.2	100	-4.2	-5.9	-3.3	-1.7	-5.7
3.5	0.4	100	2.6	3.5	-1.8	0.4	2.7
3.5	0.5	100	-0.2	3.3	-3.3	-3.4	1.3
7	0.2	100	2.9	3.9	1.1	1.6	-2.2
7	0.4	100	-2.0	0.0	-0.3	-0.5	0.0
7	0.5	100	4.3	5.1	-1.5	3.1	3.0
11	0.2	100	5.8	2.9	-2.2	1.1	0.1
11	0.4	100	3.7	3.7	0.5	2.3	2.5
11	0.5	100	1.5	0.0	5.2	2.1	2.5
3.5	0.2	120	2.0	1.2	0.0	-5.7	-1.7
3.5	0.4	120	6.5	3.0	3.0	0.3	4.7
3.5	0.5	120	7.8	11.6	22.8	15.0	29.6
7	0.2	120	2.4	-	13.3	2.3	1.6
7	0.4	120	1.3	3.7	9.2	-0.2	19.1
7	0.5	120	8.9	10.6	21.4	38.9	45.5
11	0.2	120	11.1	3.0	6.7	1.2	2.3
11	0.4	120	4.1	5.2	13.3	30.4	36.3
11	0.5	120	2.7	11.3	17.4	39.7	44.2
3.5	0.2	135	-	-0.7	0.0	8.0	20.1
3.5	0.4	135	-	12.7	10.5	25.8	34.6
3.5	0.5	135	-	-	27.6	32.7	46.2
7	0.2	135	-	-0.3	4.3	3.4	12.9
7	0.4	135	-	17.3	28.2	31.0	46.5
7	0.5	135	-	22.4	39.1	47.7	62.8
11	0.2	135	-	-1.0	12.7	12.7	18.2
11	0.4	135	-	14.8	30.9	39.0	52.6
11	0.5	135	-	24.7	50.9	57.2	71.0
7	0.4	150	-	47.1	75.9*	83.5*	88.9

* The 150^oC experiments were collected at weeks 2, 3, 5, and 8.

Piperazine Experiments

Aqueous piperazine samples with a loading of 0.4 were placed in ovens at 120^oC and 135^oC and removed at weeks 1, 2, and 3. They were analyzed using the GC and the HP-5 column as in the MEA work. Figure 32 below shows the results of this analysis.

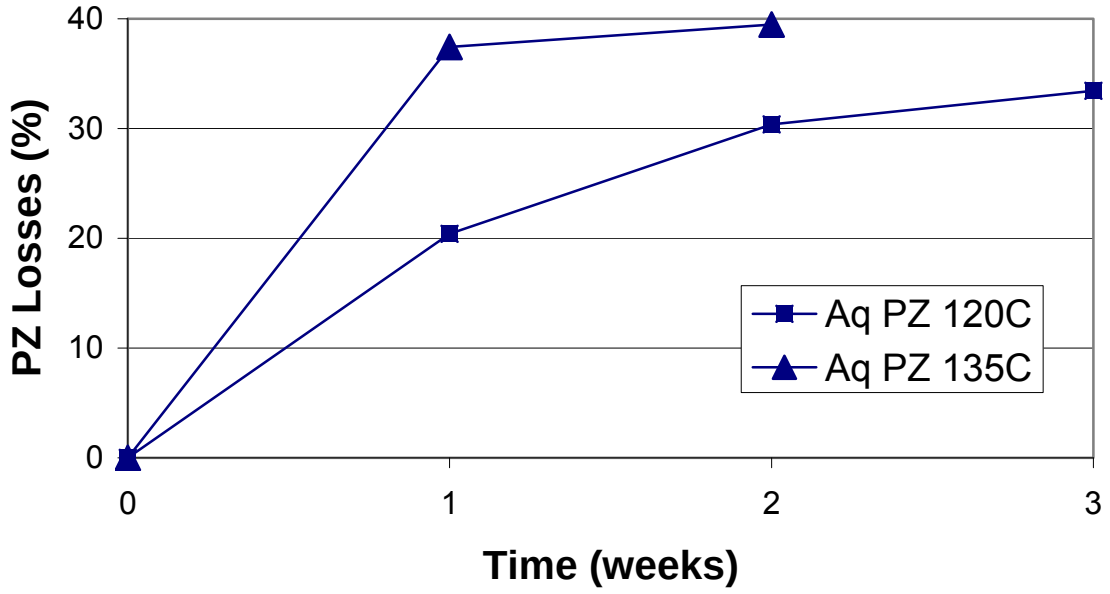

Figure 32: Piperazine losses in aqueous PZ with 0.8 moles CO_2/ over time at 120°C and 135°C

These results show rapid PZ losses at short times and some type of chemical equilibrium that is being reached within several weeks. This equilibrium is temperature dependent as well since the 135°C samples showed a faster loss rate and seem to have a higher equilibrium concentration at long times. These results go against the initial prediction that PZ would not thermally degrade.

The total amine pH titration method showed no measurable loss in amine functionality for any of the degraded samples. This would seem to indicate that while PZ losses are evident in the GC analysis, the piperazine samples are not losing their amine functionality. This data could mean several things: 1) Piperazine is not degrading at all, but is merely an artifact of the GC conditions (i.e. high temperatures in the injection port and column coupled with sample dehydration in the sample port); 2) Piperazine thermally degrades into a compound that retains the same amine functionality as the original sample; or 3) the degradation product is reversible under the titration conditions and therefore reverts to piperazine in the titrator.

Comparisons of the initial sample to the degraded samples using IC and HPLC showed no losses of piperazine as well, which further validates the titration results suggesting little, if any, degradation in the piperazine system under normal stripper conditions.

Future Work

The MEA data is currently being regressed with the intent on completing a kinetic model for the degradation of MEA at stripper conditions. An HPLC analysis is being developed to measure the amount of degradation products in each of the samples which will give more insight into the process.

A full scale piperazine experiment is currently underway and will be completed within the next month. If measurable amounts of PZ losses are detected, then a similar kinetic model regression will be applied to the PZ data.

Subtask 3.4 – Amine Volatility

by Marcus Hilliard

(Supported by the TXU Carbon Management Program)

Introduction

Extensive data have previously been collected on the thermodynamics of the system K^+/PZ/MEA/CO_2/H_2O. These data will be correlated by the AspenPlus electrolye NRTL model and reported in a dissertation by Marcus Hilliard. Two chapters have been completed and are attached to this progress report. The final report for this contract will include the complete Hilliard dissertation on this system.

Pure Component Systems: MEA, PZ, and H_2O – Chapter VIII

The critical properties of MEA were adjusted to improve estimates of the heat of vaporization. Parameters in the Watson model for the Heat of Vaporization have been adjusted so that the ElecNRTL model will accurately predict the measured heat capacities and heats of vaporization of liquid MEA and and liquid piperazine. Results of the rigorous elecNRTL model have been regressed to provide polynomial estimates of the liquid heat capacities of water, MEA, and piperazine.

Binary systems: H_2O-MEA – Chapter IX

Our new data on solution heat capacity and MEA volatility were combined with other thermodynamic data on the H_2O-MEA system determine NRTL interaction parameters with up to four terms for temperature dependence. The activity coefficient of MEA at infinite dilution in water varies from 0.15 at 25^{o}C to 0.64 at 100^{o}C. The MEA vapor pressure over 7 m MEA at 40^{o}C is 8 Pa. The heat capacity of 7 m MEA varies from 3.714 kJ/kg-K at 40^{o}C to 3.998 at 100^{o}C.

Task 4 – Solvent Reclaiming

Subtask 4.1a – Reclaiming by crystallization – potassium sulfate

by Qing Xu

(Supported by this contract and by the TXU Carbon Management Program)

Introduction

One side reaction in CO_2 capture when using MEA is the generation of sulfate from SO_2. This sulfate has to be removed so that the MEA solution can be reused for CO_2 capture. Potassium compounds can be used in the removal of sulfate. In order to determine how best to accomplish this, the solubility of potassium sulfate was measured with variable MEA concentration and CO_2 loading.

Experimental

Method 1

The first experimental method was used by a group of undergraduate students as a special project in a senior laboratory course in summer 2006 (Sachde and Sivaram, 2006).

Solutions were gravimetrically prepared with 3, 7, 11.4, and 15 m MEA (moles amine/kg water). Then 10 ml of MEA solution was mixed with 1.5 g K_2SO_4 and agitated in a water bath for about 48 hours. Four temperatures (25, 40, 60, and 80℃) were chosen within the operating range of the absorption-stripping system.

Undissolved solids were collected using vacuum filtration, dried, and weighed with a balance. The solids dissolved in the solution sample were also dried and weighed to determine residual K_2SO_4 to reduce error. The filtration process was performed quickly to prevent the filtrate from cooling down so that no K_2SO_4 would precipitate out of solution.

Method 2

The second experimental method was used by a group of undergraduate students as a special project in a senior laboratory course in fall 2006. (Abesamis et al., 2006)

7 m MEA was prepared gravimetrically as a stock solution. 100 g of this solution was agitated with stir bar. Solid K_2SO_4 was added to the system in 0.1 g increments. The conductivity of the solution was measured with each addition. Additions were continued until the solution was saturated. Then an excess of K_2SO_4 was added to the solution and the final conductivity was measured. A correlation of conductivity and K_2SO_4 concentration was developed from the data collected before saturation and the concentration at saturation was calculated with the correlation from the final measured conductivity.

In modifications of this procedure, KOH or H_2SO_4 was added to the solution before the additions of K_2SO_4.

A water bath was used to conduct these experiments at 45ºC and 60ºC.

Method 3, CO_2 loaded

This method was used to measure loaded solutions.

A bubbler was used to add CO_2 to stock amine solutions (7 m MEA, 11m MEA, 7 m MEA/2 m PZ, and 4 m PZ). The amounts of CO_2 added into the solutions were weighed by a balance. In these experiments, proper amounts of CO_2 were added to form certain molal CO_2 solutions. Another way to prepare CO_2 loading solution is by adding $KHCO_3$ to form certain molal $KHCO_3$ solutions.

50 g of the loaded solution was agitated by a stir bar during the following process. 0.1-0.4 g K_2SO_4 was sequentially added to the system and conductivity was measured with each addition until the solution was saturated. Then an excess of K_2SO_4 was added to the solution and the final conductivity was recorded. Conductivity was correlated with K_2SO_4 concentration and extrapolated to obtain the K_2SO_4 saturation concentration.

In modifications of this procedure, KOH or H_2SO_4 was added to the solution before the additions of K_2SO_4.

These experiments were carried at room temperature and 40ºC. A water bath was used to conduct these experiments at 40ºC.

Examples:

Following are experimental graph examples. Intersections of the curves are the saturation points, and solubility of K_2SO_4 is calculated from the two equations of the curves.

With an increasing solubility after saturation point:

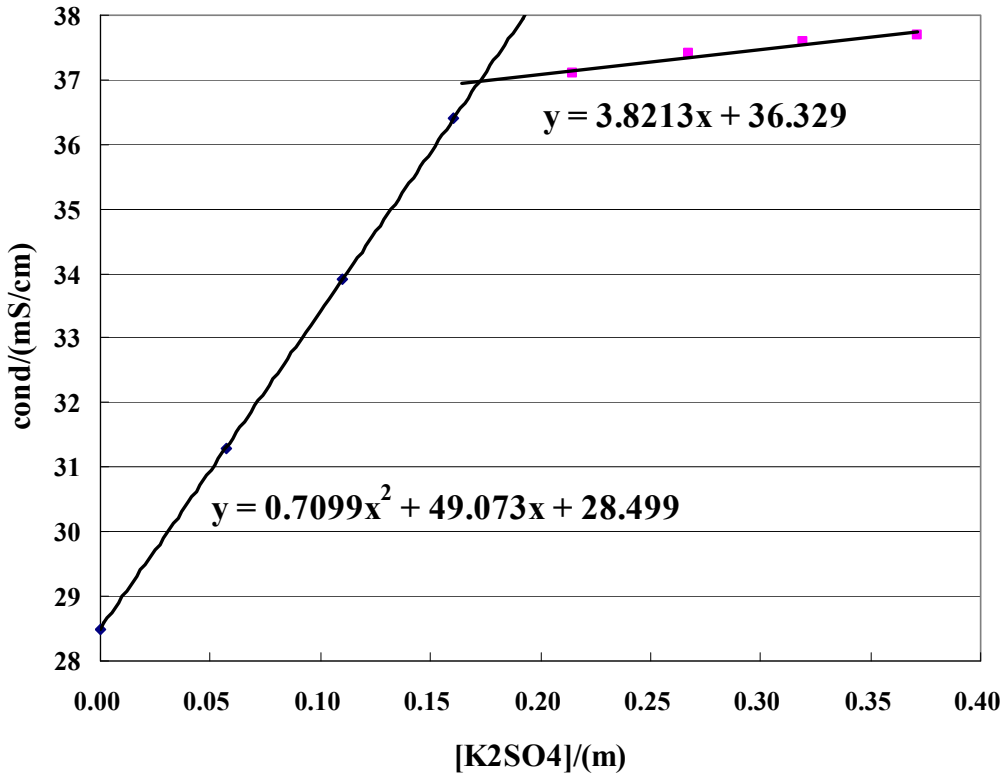

Figure 33: Conductivity dependence on concentration -1

7m MEA, $[CO_2]_t$=1.4 m, KOH=0.35m

With a decreasing solubility after saturation point:

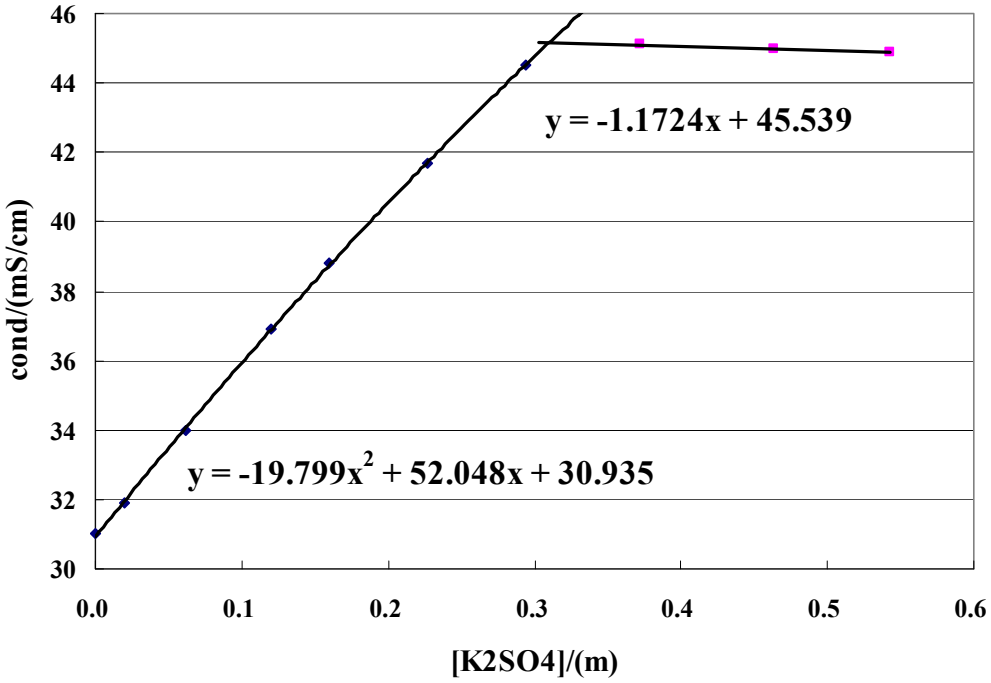

Figure 34: Conductivity dependence on concentration -2

7m MEA, $[CO_2]_t$=1.4 m, H_2SO_4=0.15m

With a flat curve after saturation point:

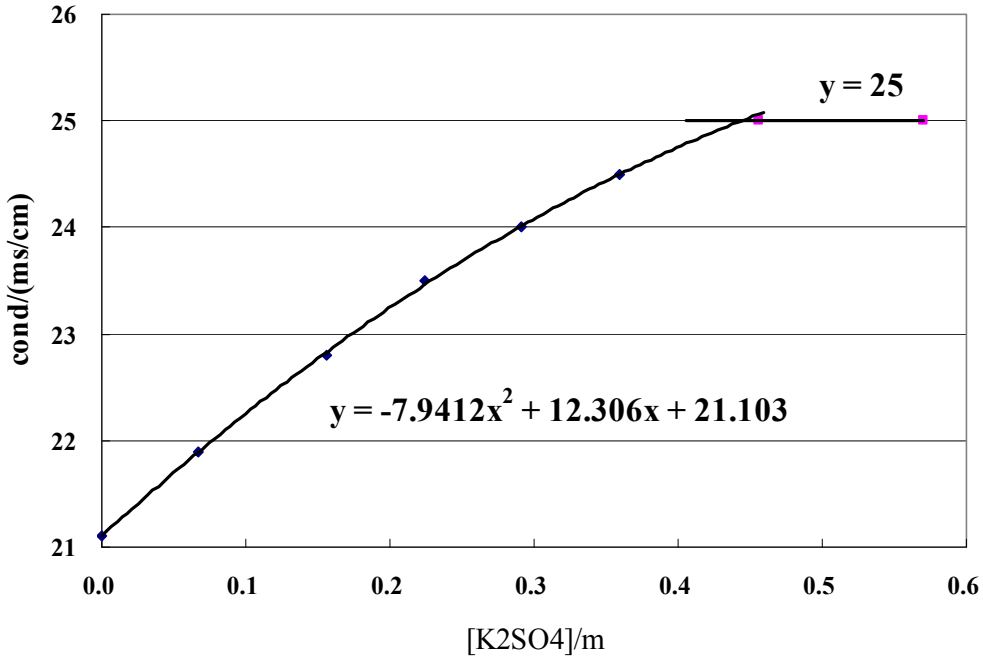

Figure 35: Conductivity dependence on concentration -3

11 m MEA, $[CO_2]_t$=5.5 m

Data:

Table 19: Solubility of K_2SO_4 in amine solution

Date	T(°C)	Concentration(m)					I^a	$Ksp_{exp}{}^b$
		K^+	$SO4^=$	CO_2	MEA	PZ		
111306	23.45	0.614	0.307	2.8	7	0	3.72	0.116
112006	22.25	0.597	0.299	2.8	7	0	3.70	0.107
112806	23.8	0.836	0.218	2.8	7	0	3.46	0.153
2006 fall	25	0.112	0.056	0	7	0	0.168	0.001
	25	0.183	0.035	0	7	0	0.162	0.001
	25	0.112	0.112	0	7	0	0.336	0.001
	45	0.190	0.095	0	7	0	0.285	0.003
	45	0.270	0.038	0	7	0	0.114	0.003
	45	0.170	0.190	0	7	0	0.570	0.005
	60	0.150	0.074	0	7	0	0.222	0.002
	60	0.260	0.057	0	7	0	0.171	0.004
	60	0.160	0.150	0	7	0	0.450	0.004
summer	25	0.250	0.125	0	7	0	0.375	0.008
	25	0.080	0.040	0	11.4	0	0.121	0.000
	25	0.097	0.049	0	15	0	0.146	0.000
	40	0.601	0.301	0	3	0	0.902	0.109
	40	0.239	0.119	0	7	0	0.358	0.007
	40	0.083	0.042	0	11.4	0	0.125	0.000
	40	0.016	0.008	0	15	0	0.024	0.000
	60	0.733	0.367	0	3	0	1.10	0.197
	60	0.302	0.151	0	7	0	0.452	0.014
	60	0.128	0.064	0	11.4	0	0.192	0.001
	60	0.017	0.008	0	15	0	0.025	0.000
	80	0.692	0.346	0	3	0	1.04	0.166
	80	0.305	0.152	0	7	0	0.457	0.014
	80	0.129	0.065	0	11.4	0	0.194	0.001
	80	0.022	0.011	0	15	0	0.033	0.000
Söhnel	20	1.268	0.634	0	0	0	1.90	1.020
	25	1.375	0.688	0	0	0	2.06	1.300

	30	1.477	0.738	0	0	0	2.22	1.610
	40	1.700	0.850	0	0	0	2.55	2.456
	50	1.899	0.950	0	0	0	2.85	3.427
	60	2.105	1.053	0	0	0	3.16	4.665
	70	2.301	1.150	0	0	0	3.45	6.091
	80	2.468	1.234	0	0	0	3.70	7.519
1.31	24.15	0.205	0.103	0	7	0	0.308	0.004
2.5	24.6	0.119	0.060	0	11	0	0.179	0.001
2.6	23.95	0.685	0.343	5.5	11	0	5.18	0.161
2.12	23.95	0.756	0.378	5.5	11	0	5.28	0.216
2.13	22.9	0.766	0.383	5.5	7	2	6.65	0.225
2.14	24.1	0.346	0.173	2.2	7	2	2.72	0.021
2.20	24.8	0.539	0.270	2	0	Aq-	2.81	0.078
2.21	22.85	0.719	0.359	4	0	Aq-	5.08	0.186
2.27	40.2	0.887	0.444	5.5	11	0	6.83	0.349
2.28	40.1	0.831	0.415	5.5	7	2	6.75	0.287
3.5	39.95	0.742	0.371	2.2	3.7	0.8	3.31	0.204
3.20	39.9	0.419	0.210	2.2	11	0	2.83	0.037
3.21	40	0.618	0.309	1.4	7	0	2.33	0.118
3.22	39.95	0.910	0.455	2.8	7	0	4.17	0.377
3.25	39.95	0.735	0.193	1.4	7	0	2.15	0.104
3.26	40	0.949	0.300	4.4	11	0	0.270	0.270
3.28	40	0.594	0.122	2.2	7	2	0.043	0.043
3.29	40	0.614	0.457	1.4	7	0	2.62	0.172
3.30	39.85	0.678	0.489	4.4	11	0	5.72	0.225
3.31	39.9	0.432	0.366	2.2	7	2	3.15	0.068
4.2	39.85	0.695	0.173	1.4	7	0	2.09	0.083
6.5	39.95	0.435	0.2175	1.88	0	aq	2.533	0.041
6.12	40	0.7753	0.3876	4.1678	0	aq	5.331	0.233

a. I: ionic strength;
b. $Ksp=[K^{+}]^{2}[SO_4^{=}]$.

Regression

The electrolyte NRTL activity coefficient model in Aspen Plus was used to regress all of the experimental data and get related parameters.

τ is the energy parameter, one of the electrolyte NRTL parameters.

$$\tau_{Ca,B} = C_{Ca,B} + \frac{D_{Ca,B}}{T} + E_{Ca,B}[\frac{T^{ref} - T}{T} + \ln\frac{T}{T^{ref}}]$$

$$\tau_{B,Ca} = C_{B,Ca} + \frac{D_{B,Ca}}{T} + E_{B,Ca}[\frac{T^{ref} - T}{T} + \ln\frac{T}{T^{ref}}]$$

GMELCC and GMELCD are C and D, separately. They are Electrolyte-Molecule Pair Parameters,

All the GMELCD were set to be the default value of zero. The experiment data were regressed to get GMELCC of all the different electrolyte pairs and K-SALT of K_2SO_4.

GMELCC values were selected that had little correlation with the others. Other parameters were excluded as possible to get small standard deviations and small sum of squares.

The final regression result is given in Table 20.

Table 20: Regression result

Parameter	Component i	Component j	Value (SI units)	Standard deviation
GMELCC/1	H_2O	(MEA^+,$SO_4^=$)	3.31	0.34
GMELCC/1	(MEA^+,$SO_4^=$)	MEA	-9.40	0.31
GMELCC/1	MEA	(K+,$SO_4^=$)	44.6	3.21
K-SALT/1	K_2SO_4(s)		141	6.08
K-SALT/2	K_2SO_4(s)		-7006	258
K-SALT/3	K_2SO_4(s)		-23.97	0.93

Compared with parameter values, the standard deviations are small.

The correlation matrix is:

Table 21: Correlation matrix

Parameter	1	2	3	4	5	6
1	1					
2	-0.26	1				
3	-0.94	0.12	1			
4	0.73	-0.09	-0.59	1		
5	-0.82	0.10	0.66	-0.89	1	
6	-0.70	0.08	0.57	-0.997	0.86	1

The sum of squares of this regression result is 7011.

Residual root mean square error is 14.8.

To test the result, if one of the parameters was excluded from regression, we get different sum of squares:

Table 22: Sum of squares

Parameter excluded	Sum of squares
none	7011
GMELCC/1, H_2O, (MEA^+,$SO_4^=$)	6992
GMELCC/1, (MEA^+,$SO_4^=$), MEA	6984
GMELCC/1, MEA, (K^+,$SO_4^=$)	9294
K-SALT/1	8758
K-SALT/2	18017
K-SALT/3	6740

When GMELCC/1(H_2O, (MEA^+, $SO_4^=$)), GMELCC/1((MEA^+, $SO_4^=$), MEA) and K-SALT/3 are excluded, respectively, the sum of squares decreases a little. But the standard deviations of each parameter increase a lot when one of them is excluded. Compared with the decrease of sum of squares, this change gives more effect on the regression result. When GMELCC/1(MEA, (K^+, $SO_4^=$)), K-SALT/1 and K-SALT/2 are excluded, respectively, the sum of squares increases by a large number. Thus in general, the 6 parameters give a good result.

Dependence of activity coefficient on T, CO_2 loading and MEA concentration

The electrolyte NRTL model in Aspen Plus was used in a flash simulation with each of the experimental conditions to get the activity coefficients of K^+ and $SO_4^=$ and to calculate mole fractions of K^+ and $SO_4^=$, the product of activity coefficient, and the relative saturation of K_2SO_4. The product of activity coefficient is calculated from the equation bellow:

$$\text{product of } \gamma = \gamma_{K^+}^2 \cdot \gamma_{SO_4^{2-}}$$

The relative saturation is calculated from the equation below:

$$\text{R.S.} = \frac{\text{Ksp(from mole fraction and activity coefficient)}}{\text{Ksp(from K - SALT)}}$$

$$= \frac{x^2(K^+) \cdot \gamma^2(K^+) \cdot x(SO_4^{2-}) \cdot \gamma(SO_4^{2-})}{\text{Ksp(T)}}$$

$$= \frac{\alpha^2(K^+) \cdot \alpha(SO_4^{2-})}{\text{Ksp(T)}}$$

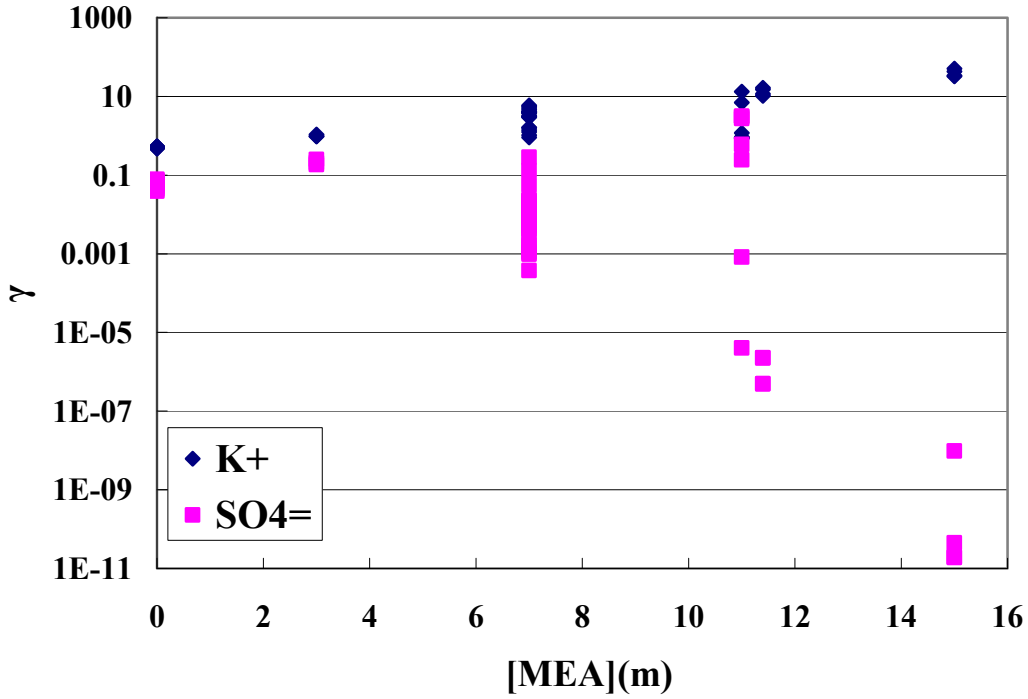

Figure 36: Activity coefficient of K^+ and $SO_4^=$, effect of MEA concentration

As the concentration of MEA increases, the activity coefficient of K^+ increases. The activity coefficient of $SO_4^=$ decreases dramatically.

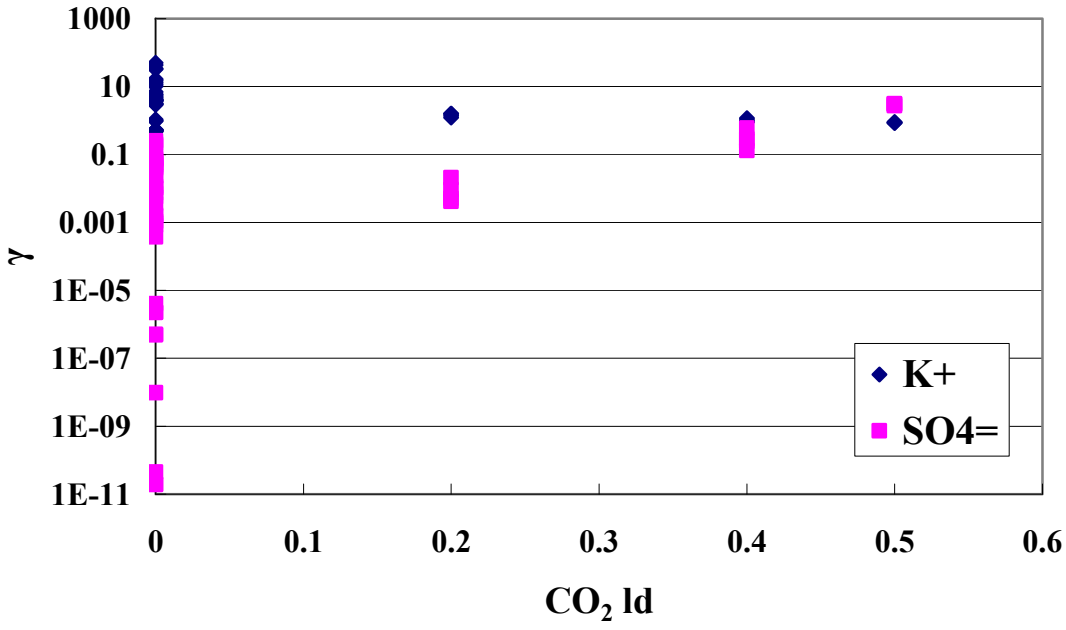

Figure 37: Activity coefficient of K+ and SO4=, effect of CO2 loading

When CO_2 loading is 0, the activity coefficient varies mainly because of other conditions. The activity coefficient of $SO_4^=$ increases dramatically with loading.

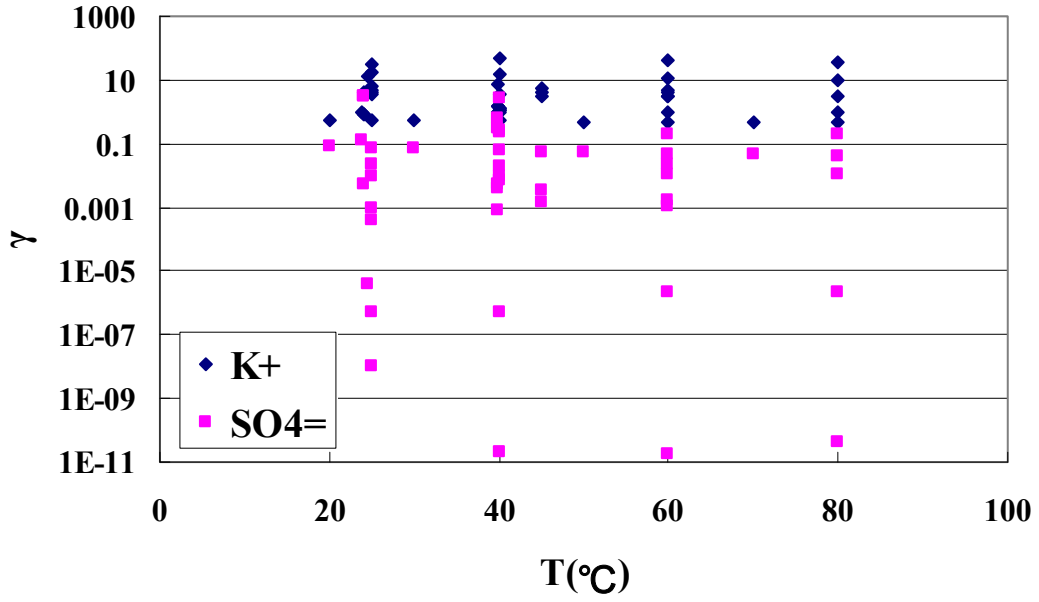

Figure 38: Activity coefficient of K+ and SO4=, effect of T

There is no big difference among different temperatures. And activity coefficient of K^+ has a larger range than that of $SO_4^=$.

Dependence of the product of activity coefficient on T, CO_2 loading and MEA concentration

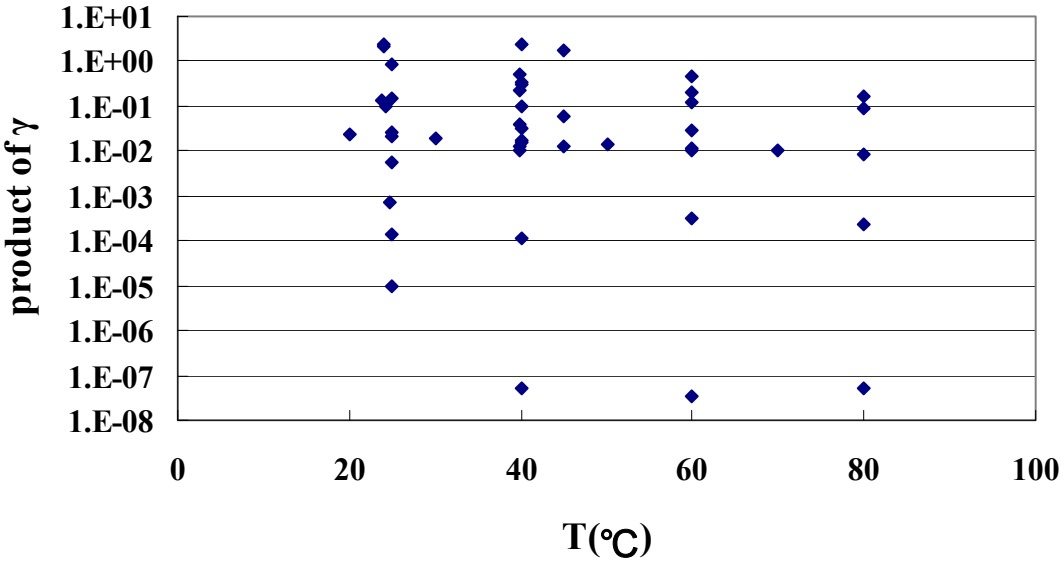

Figure 39: Product of γ, effect of temperature

There is no big difference among different temperatures.

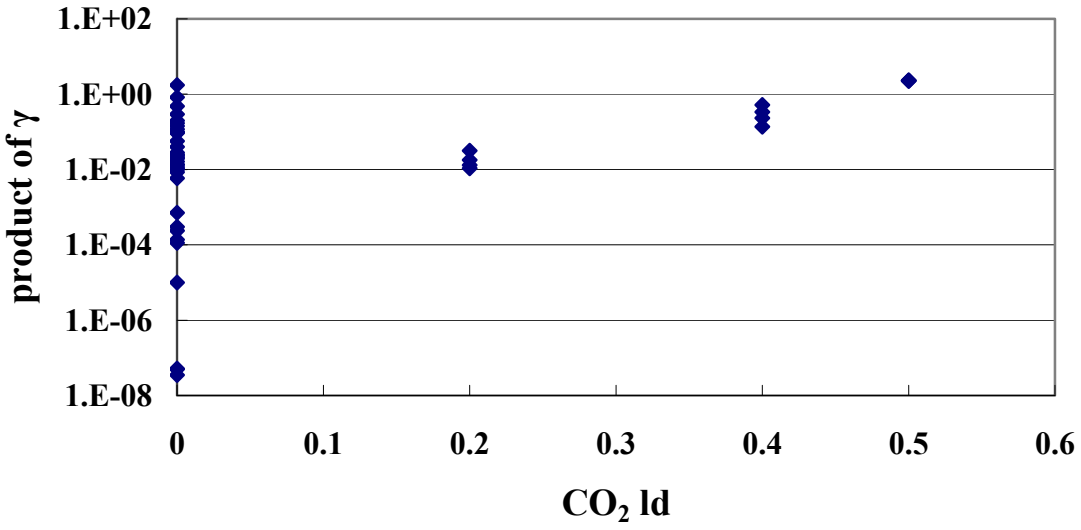

Figure 40: Product of γ, effect of CO_2 loading

The product of γ has a large range when CO_2 loading is 0. It varies because of other conditions.

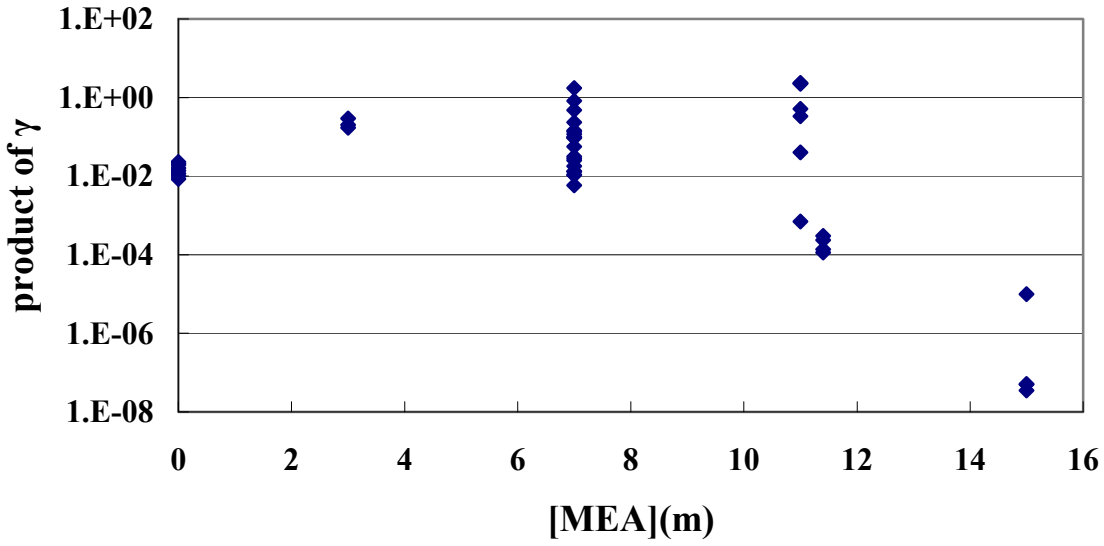

Figure 41: Product of γ, effect of MEA concentration

The product of γ increases a little and then decreases when MEA concentration increases.

Dependence of relative saturation on T, CO_2 loading and MEA concentration

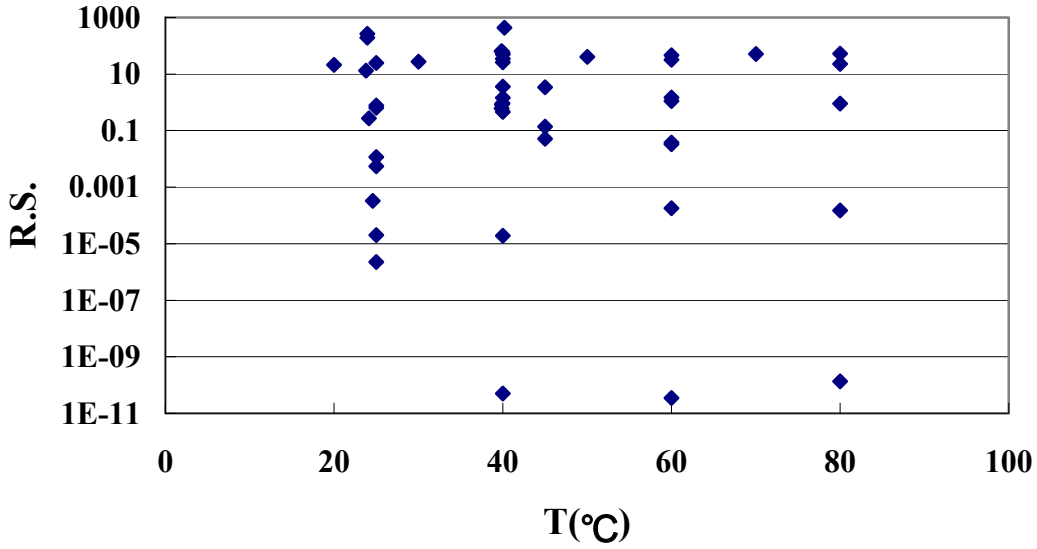

Figure 42: Relative Saturation, effect of T

There is no big difference among different temperatures.

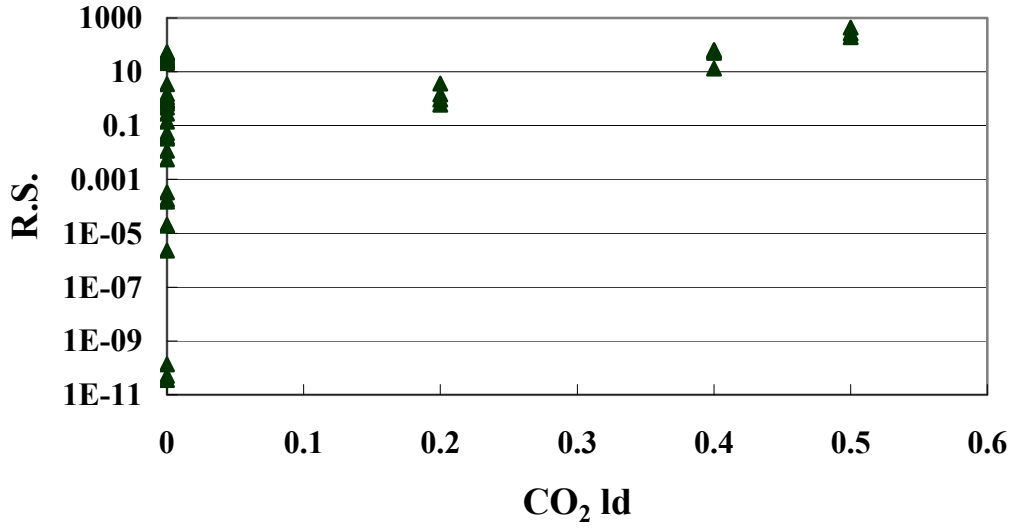

Figure 43: Relative Saturation, effect of CO_2 loading

Similar to the dependence of activity coefficients on CO_2 loading, when loading is 0, the R.S. has a large range. That may result from other conditions.

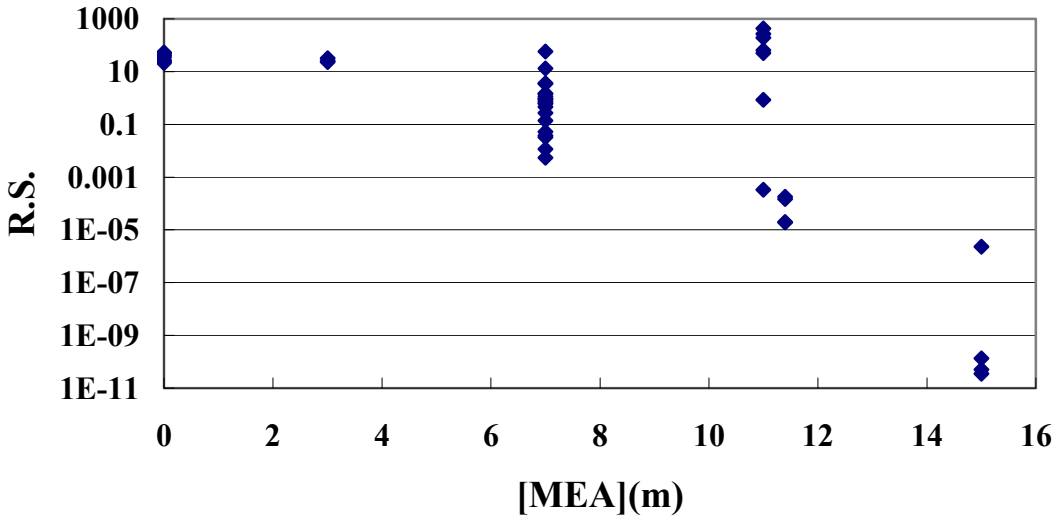

Figure 44: Relative Saturation, effect of MEA concentration

As the concentration of MEA increases, the relative saturation decreases. The data from which this model is regressed includes only a few high MEA concentration sets and they take low weight in the regression, so higher MEA concentration results in bigger error in this model.

ΔH calculation

ΔH is the heat of solution. Its relation with Ksp is as follows:

$$\frac{d\ln Ksp}{d(\frac{1}{T})} = -\frac{\Delta H_{rxn}}{R}$$

From the result of regression, we can get K_{sp} dependence on T:

$$\ln Ksp = A + B/T + C * \ln T$$

A is the K-SALT/1, B is the K-SALT/2, C is the K-SALT/3.

$$\frac{d\ln Ksp}{d(\frac{1}{T})} = B + C \cdot \frac{d\ln T}{d(\frac{1}{T})} = B - C \cdot T$$

$$\therefore \Delta H = -R \cdot (B - C \cdot T) = -8.314 \times (-7006 + 23.972T)$$

When T=25°C, $\Delta H = -8.314 \times (-7006 + 23.972 \times 298.15) = -1174.37(J/mol)$

Conclusions

From data regression, we get the electrolyte parameters and Ksp dependence on T. When the concentration of MEA increases, the activity coefficient and relative saturation increase. There is no big difference among different T or CO_2 loading. The activity range of K^+ is much larger than that of $SO_4^=$.

Future work

We will prepare an energy and material balance of the reclaiming process using Aspen Plus to simulate.

Attachment

Raw data:

date	T/°C	Concentrations (m)						I
		Sat. K_2SO_4	MEA	PZ	CO_2	KOH	H_2SO_4	
111306	23.45	0.3069	7	0	2.8	0	0	3.721
112006	22.25	0.2987	7	0	2.8	0	0	3.696
112006	22.6	0	7	0	2.8	2.79	0	2.800
112806	23.8	0.2182	7	0	2.8	0.4	0	3.455
1.31	24.15	0.1025	7	0	0	0	0	0.308
2.5	24.6	0.0597	11	0	0	0	0	0.179
2.6	23.95	0.3426	11	0	5.5	0	0	5.178
2.12	23.95	0.3781	11	0	5.5	0	0	5.284
2.13	22.9	0.3829	7	2	5.5	0	0	6.649
2.14	24.1	0.1728	7	2	2.2	0	0	2.718
2/20	24.8	0.2695	0	Aq-	2	0	0	2.809
2.21	22.85	0.3594	0	Aq-	4	0	0	5.078
2.27	40.2	0.4437	11	0	5.5	0	0	6.831
2.28	40.1	0.4153	7	2	5.5	0	0	6.746
3.5	39.95	0.3710	3.7	0.8	2.2	0	0	3.313
3.20	39.9	0.2097	11	0	2.2	0	0	2.829
3.21	40	0.3091	7	0	1.4	0	0	2.327
3.22	39.95	0.4551	7	0	2.8	0	0	4.165
3.25	39.95	0.1927	7	0	1.4	0.35	0	2.153
3.26	40	0.2995	11	0	4.4	0.35	0	5.474
3.28	40	0.1219	7	2	2.2	0.35	0	2.741
3.29	40	0.3070	7	0	1.4	0	0.15	2.621
3_30	39.85	0.3392	11	0	4.4	0	0.15	5.718
3.31	39.9	0.2158	7	2	2.2	0	0.15	3.147
4.2	39.85	0.1726	7	0	1.4	0.35	0	2.093

Task 5 – Corrosion

Subtask 5.3 – Corrosion MEA/PZ with Oxidtion Inhibitor A

by Amorvadee (Amy) Veawab, University of Regina

(Supported by subcontract)

For the past three months, we have made significant progress on our corrosion experiments. We examined the corrosiveness of carbon steel in the aqueous solutions of blended monoethanolamine (MEA) and piperazine (PZ) containing the proprietary oxidative degradation inhibitor (Inhibitor A) provided by Dr. G. Rochelle, University of Texas at Austin. The following provides summary and discussion of these results.

Corrosion due to oxidative degradation Inhibitor A

A series of electrochemical corrosion tests were carried out to investigate the corrosiveness of oxidative degradation Inhibitor A. Results in Figure 44 show that the corrosion behavior of carbon steel in the aqueous solution MEA/PZ containing Inhibitor A is similar to that in the solution containing no Inhibitor A. That is, the carbon steel typically exhibits active, passive, and transpassive states depending on the system's potential. However, under the tested condition, the carbon steel is in the active state where corrosion takes place on the free-film metal surface. No pitting tendency is observed as the cyclic polarization curve exhibits negative hysteresis, i.e. the reverse polarization curve is on the left of the forward curve.

In addition to the above general corrosion behavior, the presence of Inhibitor A appears to make the blended MEA/PZ solution more corrosive. As shown in Figure 45, the addition of Inhibitor A shifts the polarization curve of carbon steel to the right where both anodic and cathodic corrosion reactions are expedited. The increase in corrosion rate is attributed to mechanism changes of iron dissolution and reduction of oxidizing agents. From the electrochemical kinetic data obtained, such mechanism is predominant at the anode site where the iron dissolution takes place. This is evidenced by a more pronounced variation in the anodic Tafel slope.

Effect of Inhibitor A concentration on corrosion

The effect of Inhibitor A concentration was studied in the corrosion experiments using aqueous solutions of blended MEA/PZ (5.0/1.2 kmol/m^3) containing 0.20 mol/mol CO_2 loading, 1% acetic acid and the Inhibitor A with various concentrations in the presence and absence of oxygen (O_2). The acetic acid was chosen to represent the anions of heat-stable salt in the blended MEA/PZ solution since it is the most corrosive salt according to our previous results. Results in Figure 46 show that the corrosion rate of carbon steel decreases with the increasing concentration of Inhibitor A as illustrated by the shifts of polarization curves to left where the anodic and cathodic current densities are reduced (Figure 45). Such decrease is attributed to changes in the mechanisms of iron dissolution as evidenced by the increasing anodic Tafel slope of the system. Note that since the cathodic Tafel slope does not change with the concentration of Inhibitor A, the reduction mechanism of oxidizing agents on the cathode site is speculated to remain unchanged.

Effect of oxygen on corrosion in the presence of Inhibitor A

The effect of oxygen on corrosion was examined using aqueous solutions of blended MEA/PZ (5.0/1.2 kmol/m^3) containing 0.20 mol/mol CO_2 loading, 1 wt % acetic acid and the

oxidative degradation Inhibitor A. Results in Figure 46 show that the corrosion rates of carbon steel in the aerated solutions are less than those in the de-aerated solutions in the presence of Inhibitor A. This could be attributed to changes in the mechanisms of iron dissolution. From the electrochemical kinetic data obtained, the anodic Tafel slopes of the aerated system are far greater than those in the de-aerated system. The cathodic Tafel slopes vary slightly indicating no significant changes in the cathodic reactions.

Effect of solution temperature on corrosion in the presence of Inhibitor A

The effect of solution temperature was studied using blended MEA/PZ (5.0/1.2 kmol/m^3) solution containing 0.20 mol/mol CO_2 loading, 1 wt % acetic acid and 1000 ppm Inhibitor A at 40 and 80°C. Results in Figure 47 show that the presence of Inhibitor A does not alter the effect of solution temperature on the corrosion rate of carbon steel. The trend of corrosion rate is similar to that in the system without Inhibitor A, i.e. the corrosion rate increases with the solution temperature. This behavior is attributed to the dependence of kinetics of both iron dissolution and reduction of oxidizing agents on the solution temperature as illustrated from the shifts of anodic and cathodic polarization curves to greater values of current densities (Figure 48).

Inhibition performance of copper carbonate in the presence of Inhibitor A

The performance of a corrosion inhibitor, namely copper carbonate ($CuCO_3$), was evaluated using the aqueous solutions of blended MEA/PZ (5.0/1.2 kmol/m^3) containing 0.20 mol/mol CO_2 loading, 1 wt % acetic acid, the oxidative degradation Inhibitor A, and 250ppm $CuCO_3$ in the presence and absence of O_2. It is apparent from Figure 49 that the Inhibitor A has no effect on the inhibition mechanism of $CuCO_3$. The $CuCO_3$ functions as an anodic corrosion inhibitor shifting the corrosion potential of the metal from active to passive state where a passive film is developed on the metal surface. The passive film acts as a separator of metal surface and solution, thus retarding the diffusion of ferrous ion (Fe^{2+}) and electrons from the metal surface to the bulk solution and at the same time retarding the diffusion of oxidizing agents from the bulk solution to the metal surface, thus slowing down the corrosion rate.

The performance of $CuCO_3$ is not greatly affected by Inhibitor A, solution temperature, and CO_2 loading of solution. The Inhibitor A has an insignificant impact on the inhibition performance of $CuCO_3$. As shown in Figures 49–50, the $CuCO_3$ reduces the corrosion rates of carbon steel significantly regardless of Inhibitor A concentration. The inhibition performance of $CuCO_3$ is reduced slightly as the solution temperature increases (Figures 51–52). This could be because of the fact that the increase in temperature accelerates both anodic and cathodic reactions, thus increasing the corrosion rate. The $CuCO_3$ inhibits well even under high CO_2 loading of solution. From Figures 53–54, the corrosion rate of the inhibited system containing 0.20 mol/mol CO_2 loading is 0.043 mmpy while that containing 0.40 mol/mol CO_2 loading is 0.058 mmpy.

The performance of $CuCO_3$ is, however, greatly affected by the presence of dissolved O_2. The $CuCO_3$ was found to perform well under all aerated conditions, but this was not necessarily the case for the de-aerated conditions. The corrosion rates of carbon steel were successfully reduced by $CuCO_3$ under aerated conditions to below an acceptable level (10 mpy or 0.254 mmpy). No pitting tendency was observed from the cyclic polarization curves. The presence of oxygen is required in the inhibited system with $CuCO_3$ to maintain Cu^{2+} from plating out to be Cu.

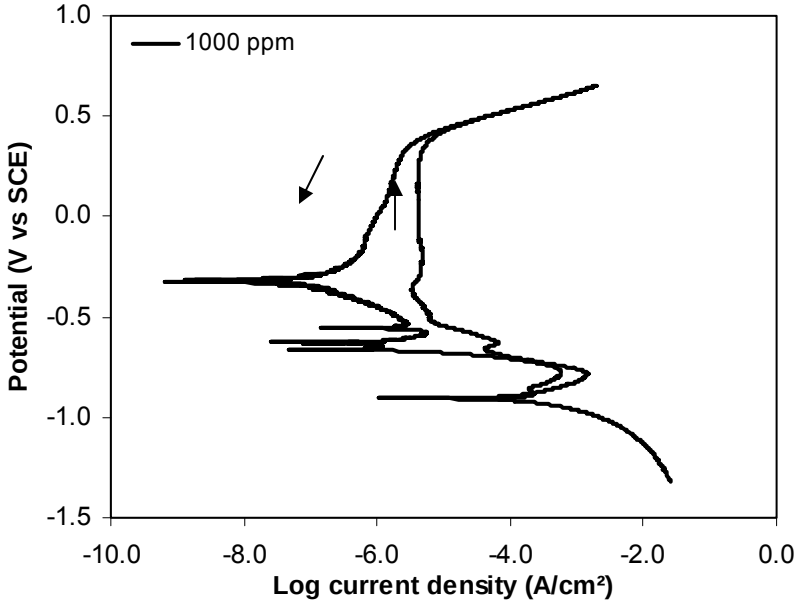

Figure 45: Cyclic polarization curve of an aqueous solution of MEA/PZ (5/1.2 kmol/m^2) containing the oxidative degradation Inhibitor A and 0.20 mol/mol CO_2 loading at 80^{o}C under 10.13 kPa O_2.

(a)

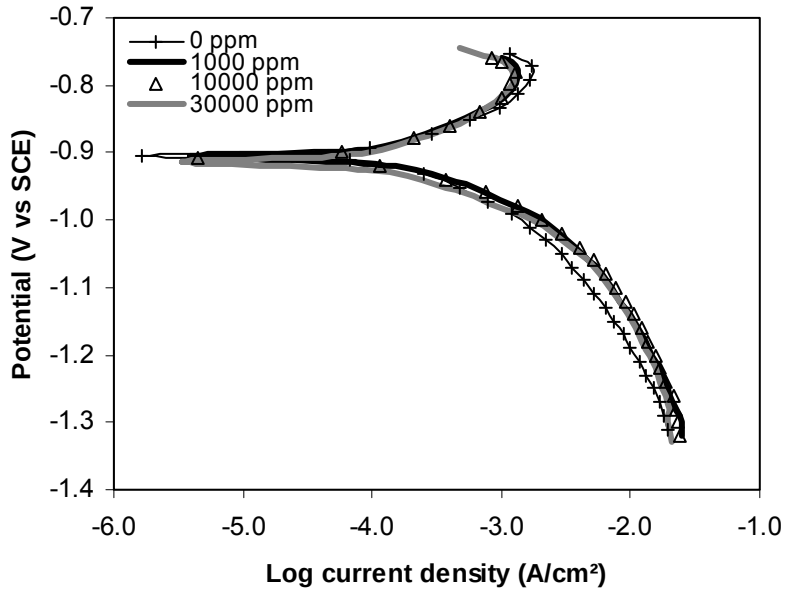

(b)

Figure 46: Effect of concentration of the oxidative degradation Inhibitor A on polarization behavior of carbon steel in aqueous solutions of MEA/PZ (5/1.2 kmol/m^3) containing the oxidative degradation Inhibitor A with the concentrations of 0, 1,000, 10,000 and 30,000 ppm, 0.20 mol/mol CO_2 loading, 1 wt % acetic acid at 80^{o}C under (a) 0.00 kPa O_2 and (b) 10.13 kPa O_2.

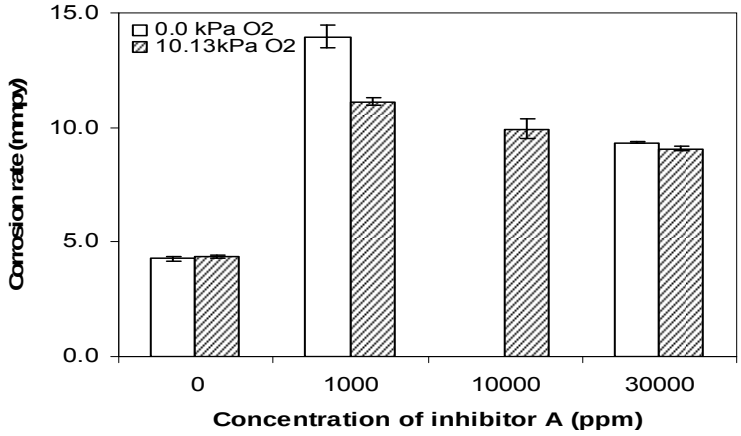

Figure 47: Effect of concentration of the oxidative degradation Inhibitor A on corrosion rates of carbon steel in aqueous solutions of blended MEA/PZ (5/1.2 kmol/m^3) containing 0.20 mol/mol CO_2 loading, 1 wt % acetic acid, and various concentrations of Inhibitor A at 80°C.

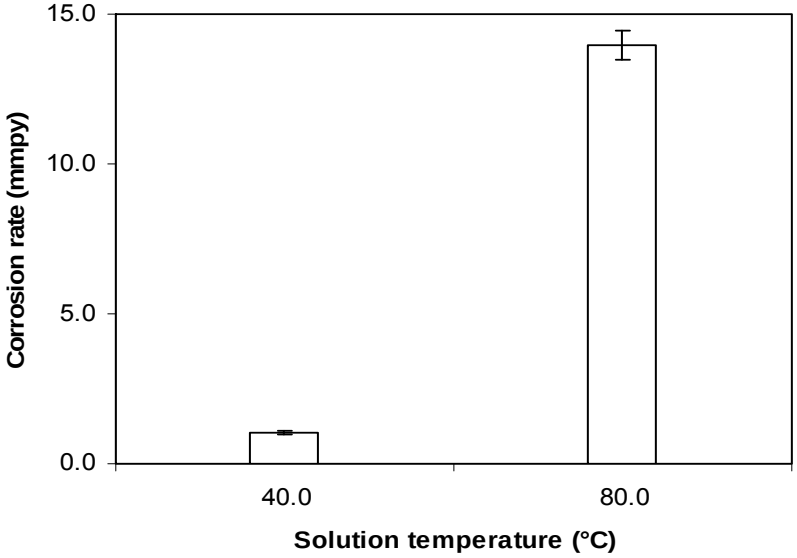

Figure 48: Effect of solution temperature on polarization behavior of carbon steel in blended MEA/PZ (5/1.2 kmol/m^3) solution containing 0.20 mol/mol CO_2 loading, 1 wt % acetic acid and 1000ppm Inhibitor A.

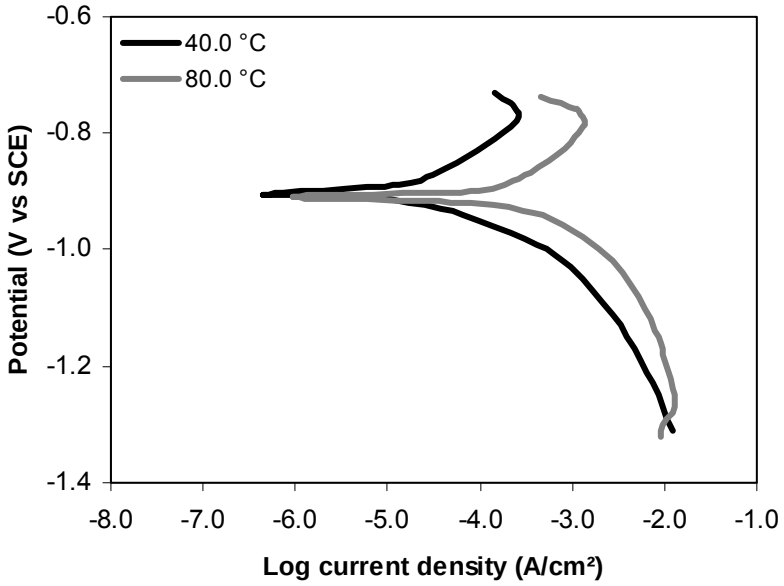

Figure 49: Effect of solution temperature on polarization behavior of carbon steel in blended MEA/PZ (5.0/1.2 kmol/m^3) solution containing 0.20 mol/mol CO_2 loading, 1 wt % acetic acid and 1000ppm Inhibitor A.

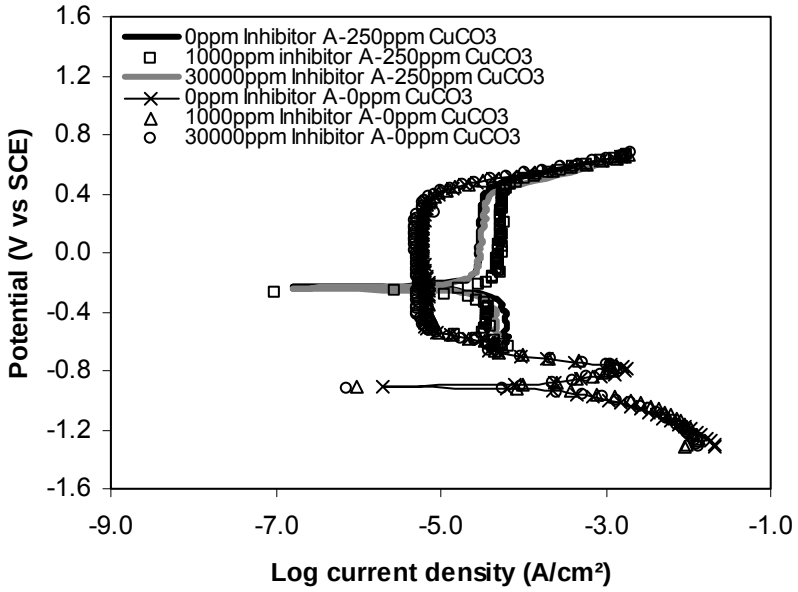

(a)

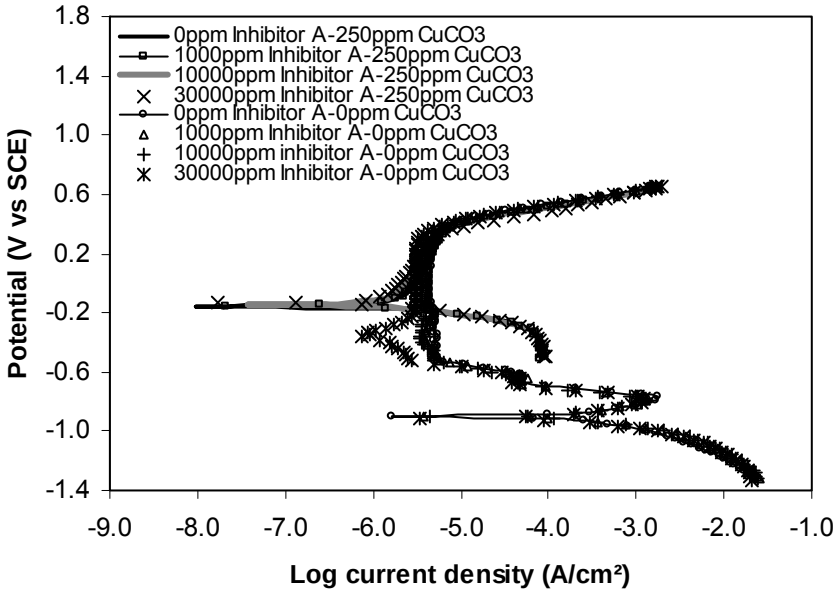

(b)

Figure 50: Effect of $CuCO_3$ on polarization behavior of carbon steel in blended MEA/PZ (5/1.2 kmol/m^3) solutions containing 0.20 mol/mol CO_2 loading, 1 wt % acetic acid, the oxidative degradation Inhibitor A with concentrations of 0, 1,000, 10,000 and 30,000 ppm, and $CuCO_3$ with concentrations of 0 and 250 ppm at 80^{o}C under (a) 0.00 kPa O_2 and (b) 10.13 kPa O_2.

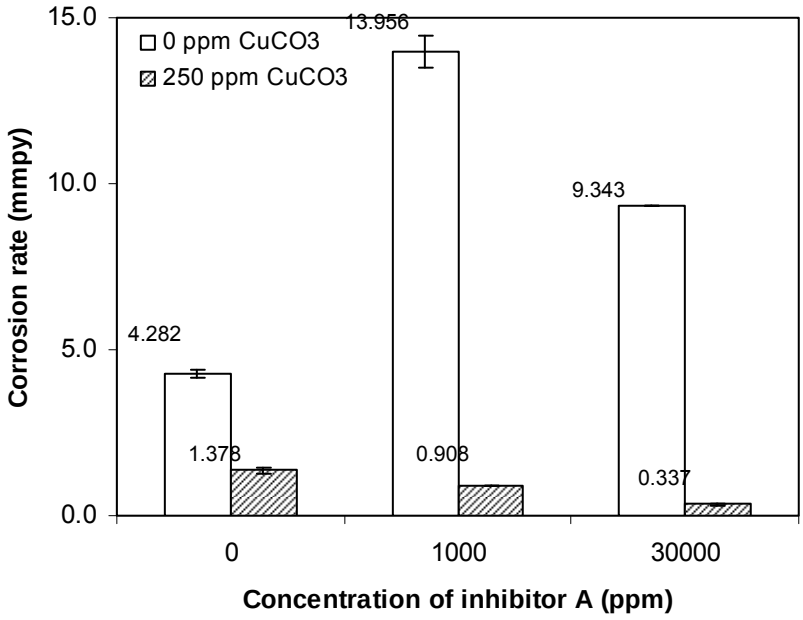

(a)

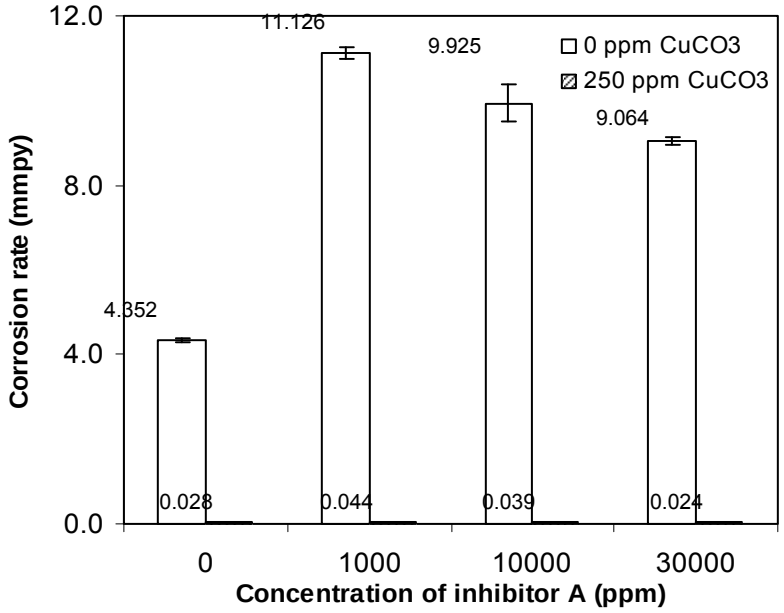

(b)

Figure 51: Effect of $CuCO_3$ on corrosion rate of carbon steel in blended MEA/PZ (5/1.2 kmol/m^3) solution containing 0.20 mol/mol CO_2 loading, 1 wt % acetic acid and various concentrations of Inhibitor A and $CuCO_3$, at 80°C (a) 0.00 kPa O_2 and (b) 10.13 kPa O_2.

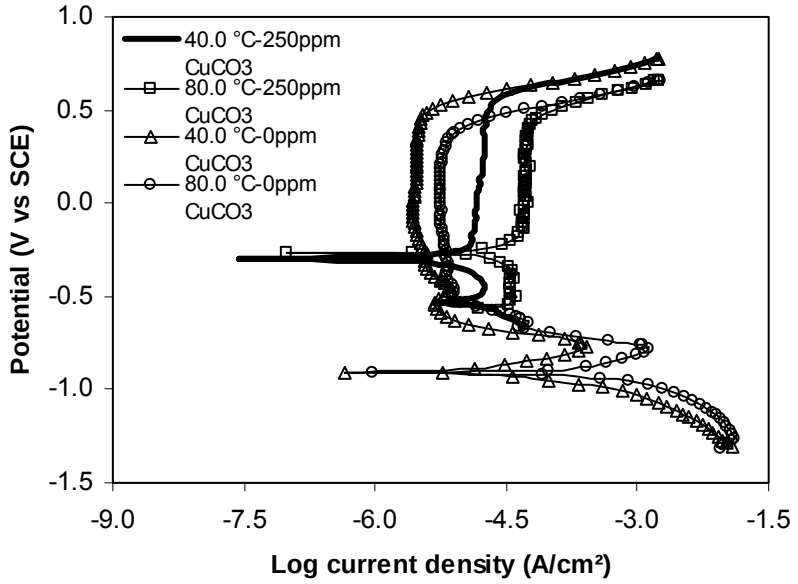

Figure 52: Effect of solution temperature on polarization behavior of carbon steel in blended MEA/PZ (5/1.2 kmol/m^3) solutions containing 0.20 mol/mol CO_2 loading, 1 wt % acetic acid, 1000ppm Inhibitor A, and $CuCO_3$ with concentrations of 0 and 250 ppm at 40 and 80^{o}C in the absence of O_2.

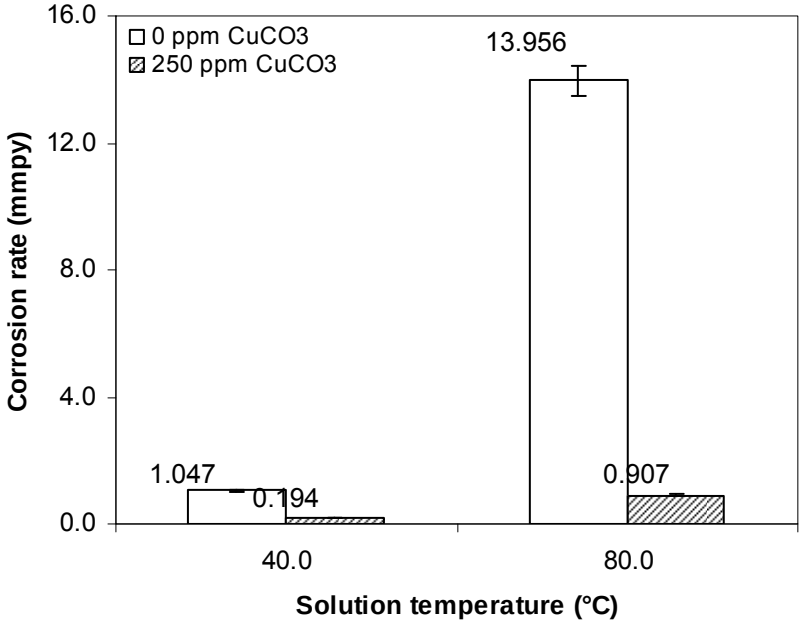

Figure 53: Comparison of corrosion rates of carbon steel in blended MEA/PZ (5/1.2 kmol/m^3) solution containing 0.20 mol/mol CO_2 loading, 1 wt % acetic acid, 1000ppm Inhibitor A and $CuCO_3$ with concentrations of 0 and 250 ppm, at 40 and 80°C in the absence of O_2.

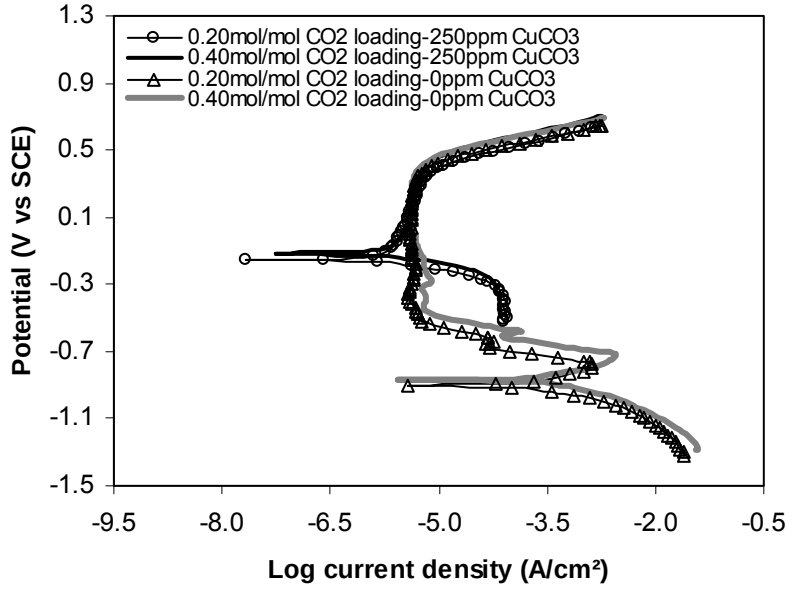

Figure 54: Effect of CO_2 loading on polarization behavior of carbon steel in blended MEA/PZ (5/1.2 kmol/m^3) solutions containing 1 wt % acetic acid, 1000ppm Inhibitor A and $CuCO_3$ with concentrations of 0 and 250 ppm under 10.13 kPa O_2 and CO_2 loadings of 0.20 and 0.40 mol/mol at 80°C.

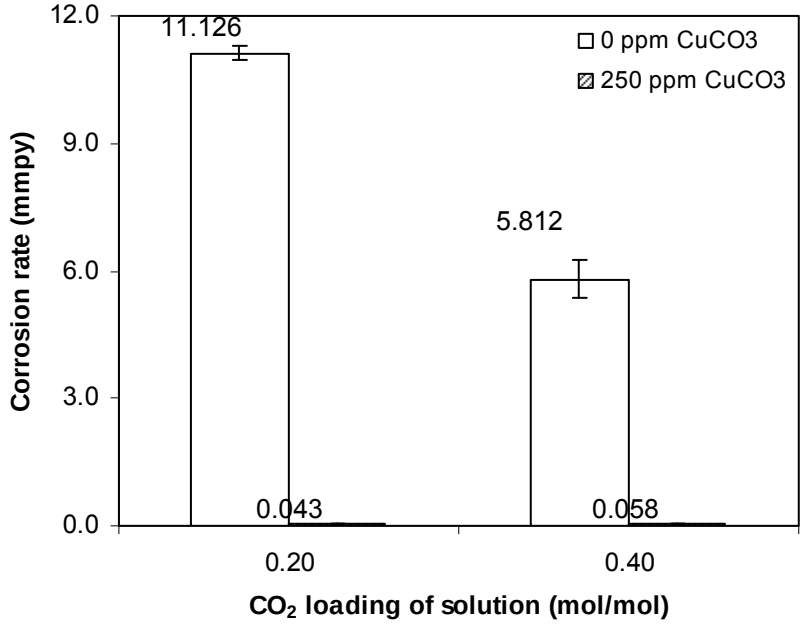

Figure 55: Effect of CO_2 loading on corrosion rate of carbon steel in blended MEA/PZ (5/1.2 kmol/m^3) solutions containing 1 wt % acetic acid, 1000ppm Inhibitor A, $CuCO_3$ with 0 and 250 ppm under 10.13 kPa O_2 at 80°C.

References

Abesamis A, Bayer B, Hai R. "Crystallization of Potassium Sulfate." ChE 264 special project report. Fall 2006, University of Texas at Austin.

Alletag, A. and A. Brown (2006). "Report on Project 06-303: Viscosity of MEA/PZ/CO_2." ChE 264 special project, University of Texas at Austin.

Bocard, J.P. and BJ. Mayland (1962). "New Charts for Hot Carbonate Process." *Hydrocarbon Processing and Petroleum Refiner* **41**(4): 128–132.

Cook, H.L. and B.M. Lowe (1976). "Viscosity B-Coefficients for Pinacal and Piperazine in Aqueous Solutions at 25 and 35°C." *Electrochimica Acta* **21**: 153–154.

CRC Handbook of Chemistry and Physics, 87th edition, online, section 8-114, http://www.hbcpnetbase.com/articles/08_21_86.pdf

Cullinane, JT. "Thermodynamics and Kinetics of Aqueous Piperazine with Potassium Carbonate for Carbon Dioxide Absorption," PhD dissertation, University of Texas, Austin, 2005.

Dawodu OF, Meisen A. "Gas chromatographic analysis of alkanolamine solutions using capillary and packed columns." *J Chrom*. 1993;629(2):297-307.

Derks, P.W., K.J. Hogendoorn and G.F. Versteeg (2005). "Solubility of N_2O in and Density, Viscosity, and Surface Tension of Aqueous Piperazine Solutions." *Journal of Chemical and Engineering Data*.

Dugas, R.E. (2006). "Pilot Plant Study of Carbon Dioxide Capture by Aqueous Monoethanolamine." Topical Report Prepared for DOE Award No. DE-FC26-02NT41440. Chemical Engineering, Austin TX, University of Texas at Austin.

Freguia S, Rochelle GT. "Modeling of CO_2 Capture by Aqueous Monoethanolamine," *AIChE J*. 2003;49:1676–1686.

Goff GS, Rochelle, GT. "Monoethanolamine Degradation: O_2 Mass Transfer Effects under CO_2 Capture Conditions." *Ind Eng Chem Res.* 2004;43(20):6400–6408.

Gonclaves, F.A. and J. Kestin (1981). "The Viscosity of Na_2CO_3 and K_2CO_3 Aqueous Solutions in the Range 20-60°C." *International Journal of Thermophysics* **2**(4): 315–322.

Hilliard M. "Thermodynamics of Aqueous Piperazine/ Potassium Carbonate/ Carbon Dioxide Characterized by the Electrolyte NRT Model in AspenPlus®." MS thesis, University of Texas, Austin, 2005.

Hitchcock, L.B. and J.S. McIlhenny (1935). "Viscosity and Density of Pure Alkaline Solutions and Their Mixtures." *Industrial and Engineering Chemistry* **27**(4): 461–466.

Lee, Jang. Oxidative Degradation of 5 Molal Piperazine (CHE 377 Report). Submitted May 15, 2007.

Mellin, Jon. Oxidative Degradation of 2-amino-2-methyl-1-propanol (CHE 264 Report). Submitted May 1, 2007.

O'Connor, R. *Fundamentals of Chemistry*. 2nd Ed. Harper and Row Publishing. 1977. 612–616.

Oyenekan BA, Rochelle GT. "Alternative Stripper Flow Schemes for CO2 Capture by Aqueous Amines." Submitted to *AIChE J*. 2007.

Polderman LD, Dillon CP, Steele AB. "Why monoethanolamine solution breaks down in gas-treating service." *Oil Gas J*. 1955;54(2):180-183.Waters LC/MS: Interfacing HPLC and MS. http://www.waters.com/WatersDivision/ContentD.asp?watersit=EGOO-66YNU9. (Accessed March 2007).

Sachde D, Sivaram S. "CO_2 capture: Solubility of Potassium Sulfate in Amine Solutions" ChE 264 special project report. Summer 2006.

Söhnel O, Novotny P. *Densities of Aqueous Solutions of Inorganic Substances*. Elsevier, Amsterdam, 1985.

Supap T, et al. "Analysis of Monoethanolamine and its Oxidative Degradation Products During CO_2 Absorption from Flue Gases: A Comparative Study of GC-MS, HPLC-RID and CE-DAD Analytical Techniques and Possible Optimum Combinations." *Ind Eng Chem Res.* 2006;45(8):2437–2451.

Yazvikova NV, Zelenskaya LG, Balyasnikova LV. "Mechanism of Side Reactions during removal of Carbon Dioxide from Gases by Treatment with Monoethanolamine." *Zhurnal Prikladnoi Khimii.* 1975;48(3):674–676.

Ziaii, S. "Modeling of an Absorber with a Double Matrix Stripper for CO_2 Capture with 11 m Monoethanolamine." *First Quarterly Progress Report, 2007*. University of Texas at Austin.

Ziaii, S. "CO_2 Removal with 7m monoethanolamine MEA – AspenPlus® model for base case." *Fourth Quarterly Progress Report, 2006*. University of Texas at Austin.

Attachment 1

A Predictive Model for Aqueous Potassium Carbonate/Piperazine/Monoethanolamine for Carbon Dioxide Removal from Flue Gas

Draft Chapters

Ph.D. dissertation

by

Marcus Hilliard

CHAPTER VIII

Pure Component Systems: MEA, PZ, and H_2O

Preface for the User

We start this chapter with a warning to the end user: The foundations of the NRTL model and the electrolyte-NRTL (elecNRTL) within Aspen Plus™ are not transparent with respect to each other; where the calculation methods and scalar pure component proprieties (as stated in Chapter VII) are different between each model. This chapter has been segmented into two parts: part one describes the heat of vaporization corrections to the NRTL model to predict the specific heat capacity of the pure component. Part two describes corrections to the elecNRTL model to predict the specific heat capacity of the pure component.

In the end, we will be using the elecNRTL property model for all future chapters to describe molecular and ionic interactions. Therefore, part one of this chapter will not be included in the final elecNRTL code and is included as a supplement to the end user.

— Part One —

8.1 NRTL Introduction

The development of any thermodynamic model starts with the basic scalar and temperature dependant physical properties of the molecular components. At this point in the model development, we are building the foundation of our model, which represents the values of the basic properties used in Aspen Plus™. This chapter describes the data regression and model predictions to correct the specific heat capacity (heat capacity) of monoethanolamine (MEA), piperazine (PZ), and water (H_2O) based on previous literature data and experimental results from this work. Coefficients for the heat of vaporization and solid heat capacity polynomial associated with these systems are then regressed in the NRTL model. Overall, the new parameters adequately describe the specific heat capacity of MEA, PZ, and H_2O within an average absolute relative error of ± 0.41, 0.83, and 0.39 percent, respectively.

8.2 Specific Heat Capacity of MEA

As stated in Chapter 6, Aspen Plus™ calculates the liquid phase heat capacity of a *pure component* by taking the derivative of the liquid enthalpy departure, which is a function of the ideal gas enthalpy and the heat of vaporization. Six data sets have been regressed with the NRTL model to correct the liquid phase heat capacity of MEA. Coefficients of the DIPPR heat of vaporization equation were adjusted to account for the heat of vaporization [Clapeyron (1834) and Riddick and Bunger (1970)] and liquid heat capacity [The Dow

Chemical Company (1981), Swanson and Chueh (1973), Chiu et al. (1999), and this work] of pure MEA.

8.2.1 *Standard Enthalpy of Vaporization*

According to Atkins and de Paula (2002) the standard enthalpy of vaporization, also know, as the heat of vaporization is the energy required to transform a given quantity of a substance into a gas. Aspen Plus™ relates the specific heat capacity to the ideal gas enthalpy and the heat of vaporization to eliminate errors associated with accurate thermal properties of both phases by the following method:

$$H_i^l - H_i^l\left(T^{ref}\right) = \int_{T^{ref}}^{T} C_{p,i}^l dT \qquad 8\text{-}1$$

$$H_i^l\left(T^{ref}\right) = H_i^{ig} + \left(H_i^v - H_i^{ig}\right) - \Delta H_i^{vap} \qquad 8\text{-}2$$

Where

$H_i^l\left(T^{ref}\right)$ is the reference enthalpy of component i at $T^{ref} = 298.15K$,

H_i^{ig} is the ideal gas enthalpy of component i,

$H_i^v - H_i^{ig}$ is the vapor enthalpy departure of component i,

ΔH_i^{vap} is the heat of vaporization of component i.

Table 8.2-1 gives the coefficients for the DIPPR heat of vaporization equation for MEA used in Aspen Plus™ based on the following expression:

$$\Delta H_i^{vap}\left(\frac{J}{kmol}\right) = C_{1i}\left(1 - T_{ri}\right)^{\left(C_{2i} + C_{3i}T + C_{4i}T^2\right)} \qquad 8\text{-}3$$

Where

T_{ri} is the reduced temperature, T / T_{ci},

T_{ci} is the critical temperature of component i,

T is the temperature, °C.

Table 8.2-1. DIPPR Heat of Vaporization Default Coefficients for MEA from 10.5 – 405.05 °C.

Parameter	Symbol	Default value
DHVLPD-1	C_1	8.5465E+7
DHVLDP-2	C_2	0.5102
DHVLDP-3	C_3	0.0
DHVLDP-4	C_4	0.0

Experimental heat of vaporization data used in this work from the above two sources is shown in Figure 8.2-1.

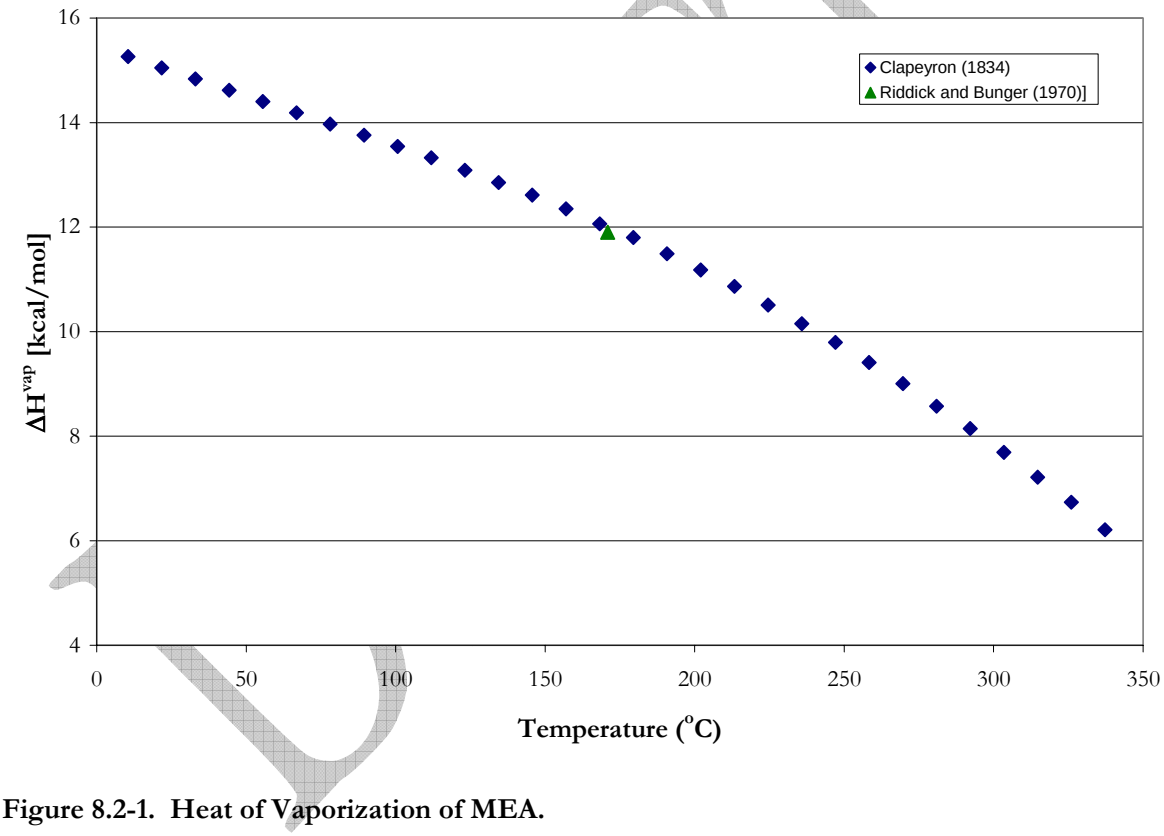

Figure 8.2-1. Heat of Vaporization of MEA.

We decided to limit the heat of vaporization data to values under 171 °C to capture successfully the experimental specific heat capacity trends within the current work.

Using the Clausius-Clapeyron equation, we can verify the consistency between the DIPPR Heat of Vaporization Equation given for MEA versus the DIPPR Extended Antoine Vapor Pressure Equation based on the following expression:

$$\ln P_i^{*,l}\left(kPa\right) = C_{1i} + \frac{C_{2i}}{T\left(K\right)+C_{3i}} + C_{4i}T\left(K\right) + C_{5i}\ln T\left(K\right) + C_{6i}T\left(K\right)^{C_{7i}} \qquad 8\text{-}4$$

where coefficients for MEA are given in Table 8.2-2.

Table 8.2-2. DIPPR Extended Antoine Vapor Pressure Default Coefficients for MEA from 10.0 – 365.0 °C.

Parameter	Symbol	Default value
PLXANT-1	C_1	165.87
PLXANT-2	C_2	-13492
PLXANT-3	C_3	0.0
PLXANT-4	C_4	0.0
PLXANT-5	C_5	-21.9
PLXANT-6	C_6	1.38E-05
PLXANT-7	C_7	2.00

The Clausius-Clapeyron equation, relates the heat of vaporization directly to the vapor pressure curve based on the following equation:

$$\Delta H_i^{vap} = -R\frac{d\ln P_i^{*,l}}{d\left(1/T\right)} \qquad 8\text{-}5$$

and valid only at low pressures, approximately below 2 atm. Using Equation 8-5, Equation 8-4 yields

$$\Delta H_i^{vap} = -R\left\{\left(\frac{-T\left(K\right)}{\left(T\left(K\right)+C_{3i}\right)^2}\right)\left[\begin{array}{l} C_{6i}C_{7i}\left(T\left(K\right)+C_{3i}\right)^2 T\left(K\right)^{C_{7i}} + \\ C_{4i}T\left(K\right)^3 + \left(2C_{3i}C_{4i}+C_{5i}\right)T\left(K\right)^2 - \\ \left(C_{2i} - C_{3i}\left(C_{3i}C_{4i}+2C_{5i}\right)\right)T\left(K\right) + \\ C_{3i}^2 C_{5i} \end{array}\right]\right\} \qquad 8\text{-}6$$

Since C_{3i} = 0.0 for MEA, we can simplify Equation 8-6 to yield

$$\Delta H_i^{vap} = R\left(C_{6i}C_{7i}T(K)^{C_{7i}+1} + C_{4i}T(K)^2 + C_{5i}T(K) - C_{2i}\right) \qquad 8\text{-}7$$

Based on Equation 8-7, we can compare the coefficients for the DIPPR Extended Antoine Vapor Pressure for MEA given in Table 8.2-2 to literature heat of vaporization as shown in Figure 8.2-2. Deviations at high pressures appear above 200 °C between cited and predicted values due to the approximate linear nature of the Clausius-Clapeyron equation.

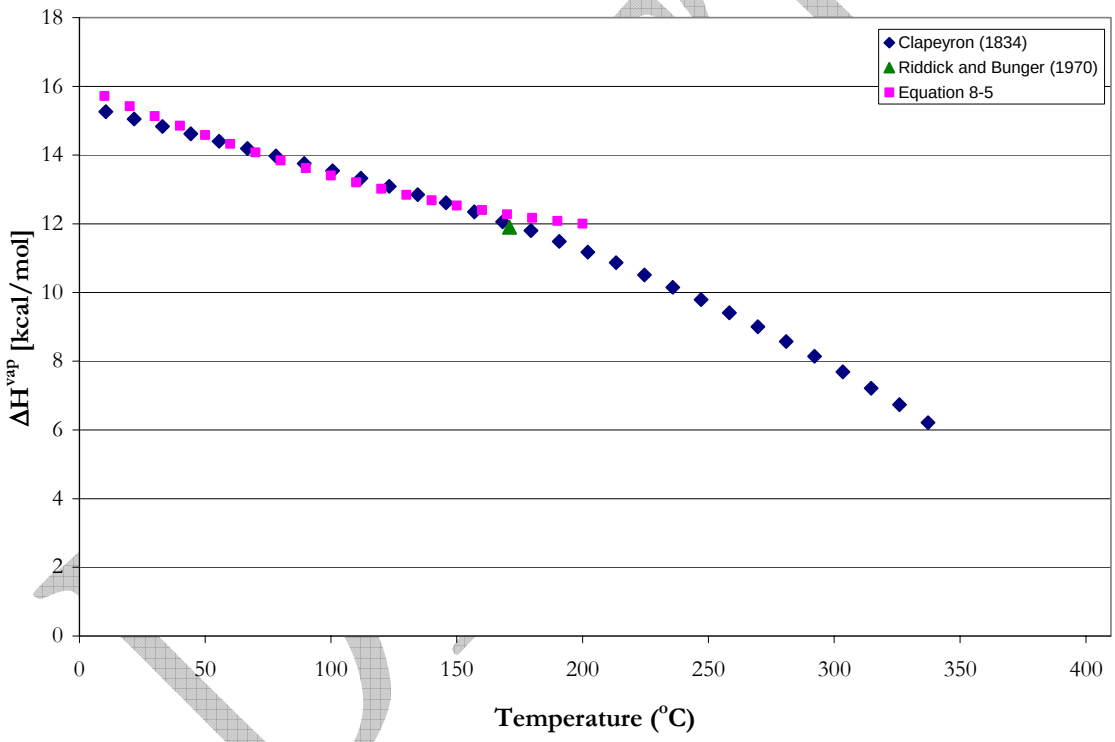

Figure 8.2-2. Comparison of the Heat of Vaporization based on Equation 8-5 to Literature Values for MEA.

8.2.2 *Data Regression*

Through simultaneous regression, the coefficients for the DIPPR heat of vaporization equation were determined by DRS in Aspen Plus utilizing the maximum

likelihood principle of Britt and Luecke (1973) through the minimization of the following objective function:

$$f = \sum_{k=1}^{n} W_{U_k} \left(\frac{\left(U_{k,adj} - U_{k,obs}\right)^2}{\sigma_{U_k}^2} \right) + \sum_{k=1}^{n} W_{P_k} \left(\frac{\left(P_{k,adj} - P_{k,obs}\right)^2}{\sigma_{P_k}^2} \right) \qquad 8\text{-}8$$

where the measurable variables, U_k (e.g. state variables: T, P, x, y), and property variables, P_k (e.g. heat of vaporization and heat capacity) are weighted by their standard error, σ. The objective function is then minimized using Lagrange multipliers to adjust the measurable variables and the model parameters within parameter bounds. A list of the pure component data sets that were examine in this work is given in Figure 8.2-3. The column labels σ_T, σ_{DHVL}, σ_{CPL-M} gives standard error associated with the temperature, heat of vaporization, and the heat capacity, respectively, with each data set.

Table 8.2-3. Experimental data used in the regression of Heat of Vaporization Coefficients for MEA.

	Obs.	T (°C)	σ_T	σ_{DHVL}	Source
ΔH^{vap}	1	170.95	0.1	1%	Riddick and Bunger (1970)
	15	10.50 – 337.23	0.1	1%	Clapeyron (1834)

	Obs.	T (°C)	σ_T	σ_{CPL-M}	Source
C_p	1	30.0	0.1	1%	The Dow Chemical Company (1981)
	1	20.0	0.1	1%	Swanson and Chueh (1973)
	11	30.0 – 80.0	0.1	1%	Chiu et al. (1999)
	17	40.0 – 120.0	0.1	1%	This work

Table 8.2-4 shows the following regression summary statistics output for estimates of the heat of vaporization coefficients after performing a nonlinear regression for the full

model using DRS. To account for the temperature dependant nature of heat capacity in the heat of vaporization equation, we include the third term into the full model regression.

Table 8.2-4. DRS Regression Output for Full MEA Model.

Parameter	Estimate	σ wrt Estimate
DHVLPD-1	8.8033E+07	8.2460E+09
DHVLDP-2	0.7078	0.0055
DHVLDP-3	-0.2813	0.0058

Residual Sum of Squares: 29.2382
Residual Root Mean Square: 3.707

Recall that the standard error of an estimate is the estimated standard deviation of that statistic. Notice that all of the estimates are large relative to their standard errors with the exception of the first coefficient. A complete description of the variability of the coefficient estimates requires examining the correlations between the estimates is shown in Table 8.2-5.

Table 8.2-5. Correlation Matrix of the Coefficient Estimates for the Full MEA Model.

Parameter	1	2	3
1	1.00		
2	0.00	1.00	
3	0.00	-0.98	1.00

Each correlation coefficient is a summary statistic for a 2D scatterplot of the variables used in the correlation and is a measure of the linear relationship between the variables. The correlation coefficient is a unitless number that always falls between -1 and 1. If the correlation coefficient equals 1 or -1, then the parameters can be described by a linear line with either a positive or negative slope. If the correlation coefficient equals 0, then the parameters are said to be uncorrelated and independent. The correlation matrix is

symmetric because the covariance between parameters $\hat{\eta}_j$ and $\hat{\eta}_k$ is the same as the covariance between parameters $\hat{\eta}_k$ and $\hat{\eta}_j$.

Table 8.2-5 shows a high negative correlation between $\hat{\eta}_{3\to2}$ for the third parameter, but the correlation between $\hat{\eta}_{3\to1}$ and $\hat{\eta}_{2\to1}$ is independent due to the non-linear nature of Equation 8-3. Table 8.2-5 suggests that the third parameter might be usefully removed from the model without significant loss of information.

8.2.3 *Full MEA Model Results*

With the determination of the estimates for the heat of vaporization parameters known for the full model, a simple Aspen Plus™ Flash model was used to test the predictive capability of the MEA model against literature data. For each data point, the deviation between the experimental and estimated values is expressed in terms of the absolute average relative deviation (AARD), as given by the following equation:

$$AARD(\%) = \frac{100}{N}\sum_i \frac{|\exp_i - \mathrm{est}_i|}{\exp_i} \qquad 8\text{-}9$$

Where
N is the number of experimental data points.

Table 8.2-6 gives the AARD and the maximum AARD for the model predictions.

Overall, the model adequately describes the MEA property data listed above within an average absolute relative error of ±0.41 percent, with the exception of a few outliers.

We found that parameters regressed for the above two systems with heat of vaporization data above 171 °C did not accurately describe significant systematic trends presented in the specific heat capacity data.

Table 8.2-6. Absolute Percent Relative Error for the MEA Full Model.

		AARD(%)	Max. AARD
ΔH^{vap}	Riddick and Bunger (1970)	1.22	-
	Clapeyron (1834)	0.16	0.37
C_p	The Dow Chemical Company (1981)	2.10	-
	Swanson and Chueh (1973)	2.62	-
	Chiu et al. (1999)	0.87	1.80
	This work	0.20	0.60
Overall		**0.41**	**1.80**

8.2.4 *MEA Model Predictions*

With the determination of the estimates for the heat of vaporization coefficients known for the full model, a simple Aspen Plus™ Flash model was used to test the predictive capability of the MEA heat of vaporization coefficients against literature data. Figure 8.2-3 compares estimated and experimental heat of vaporization from Riddick and Bunger (1970) and Clapeyron (1834) for MEA from 10.50 to 337.23 °C. The full model overpredicts the heat of vaporization above 202.03 °C with a maximum error of 17.0 % at 337.23 °C. However, this error is well beyond the operating range of present carbon capture technology and is negligible overall since the full model is consistent with the critical temperature of MEA (405.05 °C).

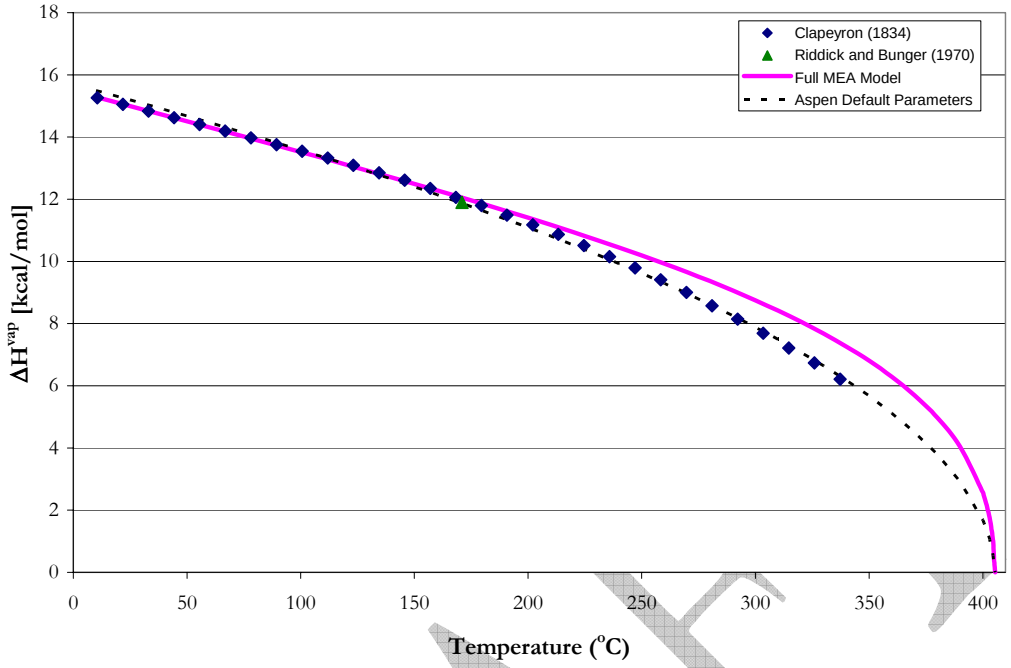

Figure 8.2-3. Comparison of Model Predictions with Experimental Data from Riddick and Bunger (1970) and Clapeyron (1834) for the ΔH^{vap} of MEA from 10.50-337.23 °C.

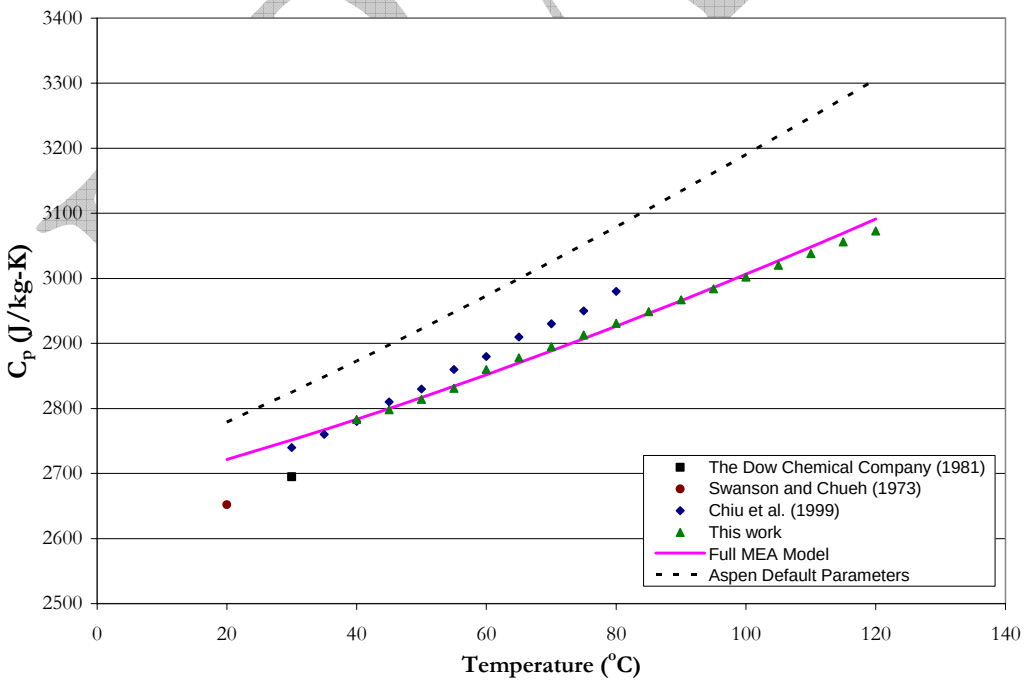

Figure 8.2-4. Comparison of Model Predictions with Experimental Data for the Specific Heat Capacity of MEA from 20 – 120 °C

Figure 8.2-4 compares estimated and experimental specific heat capacity from The Dow Chemical Company (1981), Swanson and Chueh (1973), Chiu et al. (1999) and from this work for pure MEA from 20 – 120 °C. The full model overestimates the specific heat capacity at low temperatures as compared to Swanson and Chueh (1973) and The Dow Chemical Company (1981), even though all of the predictions for the model were within an AARD of ± 0.59 %. Figure 8.2-4 illustrates a 5.19 % decrease for the prediction of the specific heat capacity as compared to Aspen default parameters.

8.3 Specific Heat Capacity of PZ

Two data sets have been regressed with the NRTL model to correct the liquid phase heat capacity of PZ. Coefficients of the DIPPR heat of vaporization equation were adjusted to account for the heat of vaporization [Clapeyron (1834)] and liquid heat capacity [Swanson and Chueh (1973)] of pure PZ. Coefficients for the solid heat capacity equation were not adjusted since predictions from the Aspen default parameters accurately described literature data from Steele et al. (1997) and from this work with an AARD of ± 0.54 and 1.28 %, respectively.

8.3.1 *Standard Enthalpy of Vaporization*

As stated in section 8.2, Aspen Plus™ relates the liquid phase specific heat capacity to the ideal gas enthalpy and the heat of vaporization through equations 8-1 to 8-3. Table 8.3-1 gives the coefficients for the DIPPR heat of vaporization equation for PZ used in Aspen Plus™ based on equation 8-3:

Table 8.3-1. DIPPR Heat of Vaporization Default Coefficients for PZ from 106 – 364.85 °C.

Parameter	Symbol	Default value
DHVLPD-1	C_1	6.5323E+7
DHVLDP-2	C_2	0.4158
DHVLDP-3	C_3	0.0
DHVLDP-4	C_4	0.0

Experimental heat of vaporization data used in this work from Clapeyron (1834) is shown in Figure 8.3-1.

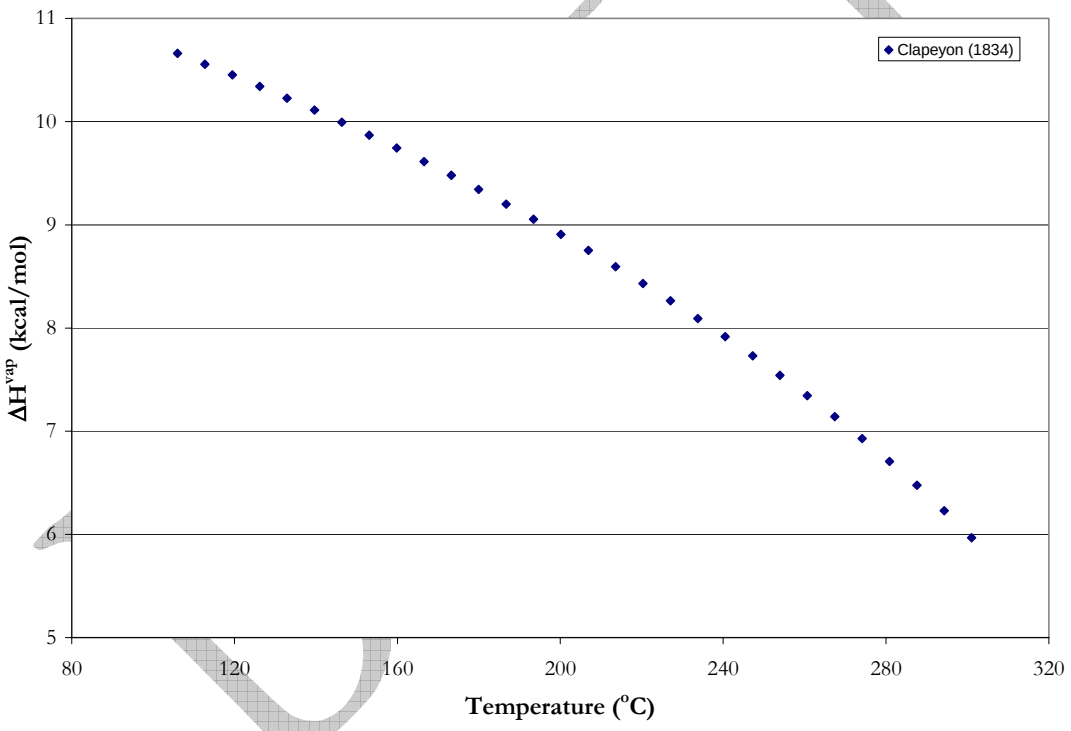

Figure 8.3-1. Heat of Vaporization of PZ.

Using the Clausius-Clapeyron equation, we can verify the consistency between the DIPPR Heat of Vaporization Equation given for PZ versus the DIPPR Extended Antoine Vapor Pressure Equation based on Equation 8-4 and Table 8.3-2.

Table 8.3-2. DIPPR Extended Antoine Vapor Pressure Default Coefficients for PZ from 106 – 364.85 °C.

Parameter	Symbol	Default value
PLXANT-1	C_1	63.60
PLXANT-2	C_2	-7915
PLXANT-3	C_3	0.0
PLXANT-4	C_4	0.0
PLXANT-5	C_5	-6.65
PLXANT-6	C_6	5.21E-18
PLXANT-7	C_7	6.00

Based on Equation 8-7, we can compare the coefficients for the DIPPR Extended Antoine Vapor Pressure for PZ given in Table 8.3-2 to literature heat of vaporization as shown in Figure 8.3-2. Deviations at high pressures appear above 150 °C between cited and predicted values due to the approximate linear nature of the Clausius-Clapeyron equation.

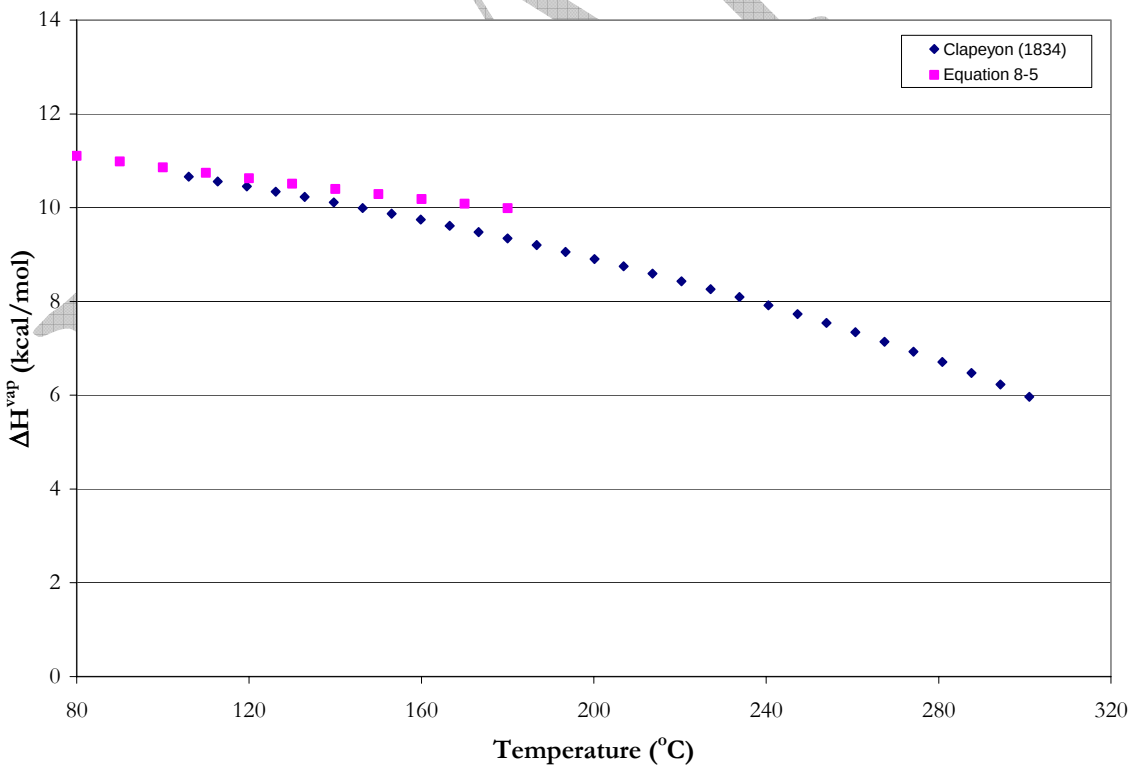

Figure 8.3-2. Comparison of the Heat of Vaporization based on Equation 8-5 to Literature Values for PZ.

8.3.2 *Solid Specific Heat Capacity*

Aspen Plus™ calculates the solid phase specific heat capacity for PZ by the DIPPR solid heat capacity equation based on the following expression:

$$C_{p,i}^{s}\left(\frac{J}{kmol-K}\right)=C_{1i}+C_{2i}T \qquad 8\text{-}10$$

Where
T is the temperature, K.

Parameters for equation 8-6 are given in Table 8.3-3.

Table 8.3-3. DIPPR Solid Heat Capacity Default Coefficients for PZ from 21.85 – 106.0 °C

Parameter	Symbol	Default value
CPSDIP-1	C_1	-46900.0
CPSDIP-2	C_2	542.0

Experimental solid phase specific heat capacity data, based on equation 8-6, from Swanson and Chueh (1973) is shown in Figure 8.3-3. Note that the solid phase specific heat capacity from this work was not regressed.

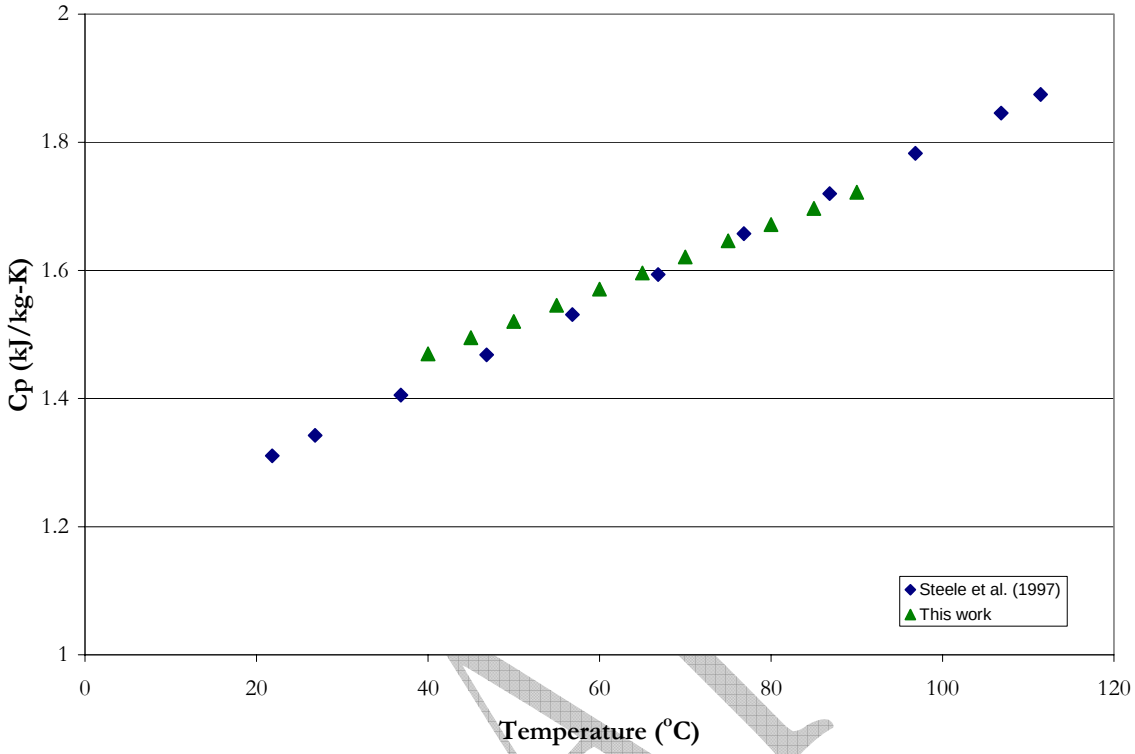

Figure 8.3-3. Solid Phase Specific Heat Capacity of PZ.

8.3.3 *Data Regression*

Through simultaneous regression, the coefficients for the DIPPR heat of vaporization equation were obtained through the regression of the heat of vaporization [Clapeyron (1834)] and liquid heat capacity [Swanson and Chueh (1973)] of pure PZ as determined by DRS in Aspen Plus™. A list of the pure component data sets that were examine in this work is given in Table 8.3-4.

Table 8.3-4. Experimental data used in the regression of Heat of Vaporization Coefficients for PZ.

	Obs.	T (°C)	σ_T	σ_{DHVL}	Source
ΔH^{vap}	30	106 – 301.05	0.1	1%	Clapeyron (1834)

	Obs.	T (°C)	σ_T	σ_{CPL-M}	Source
C_p (l)	7	105.85 – 195.85	0.1	1%	Swanson and Chueh (1973)

Table 8.3-5 shows the following regression summary statistics output for estimates of the heat of vaporization coefficients after performing a nonlinear regression for the full model using DRS. As stated in section 8.2.2, we also include an additional term into the full model regression to account for the temperature dependant of the liquid phase specific heat capacity within the heat of vaporization equation.

Table 8.3-5. DRS Regression Output for Full PZ Model.

Parameter	Estimate	σ wrt Estimate
DHVLPD-1	6.4715E+07	1.8074E+06
DHVLDP-2	0.4673	0.0727
DHVLDP-3	-0.0734	0.0693

Residual Sum of Squares: 83.8909
Residual Root Mean Square: 1.5708

Notice that all of the estimates are large relative to their standard errors. A complete description of the variability of the coefficient estimates requires examining the correlations between the estimates as shown in Table 8.3-6.

Table 8.3-6. Correlation Matrix of the Coefficient Estimates for the Full PZ Model.

Parameter	1	2	3
1	1.00		
2	0.99	1.00	
3	-0.99	-1.00	1.00

Table 8.3-6 shows highly negative and positive correlations between all of the parameters. This suggests that some of the parameters might be usefully removed from the model without significant loss of information.

8.3.4 *Full PZ Model Results*

With the determination of the estimates for the heat of vaporization parameters known for the full model, a simple Aspen Plus™ Flash model was used to test the predictive capability of the PZ model against literature data. Table 8.3-7 gives the deviation between the experimental values and model predictions expressed in terms of the absolute average relative deviation (AARD) and the maximum AARD.

Table 8.3-7. Absolute Percent Relative Error for the PZ Full Model.

		AARD(%)	Max. AARD
ΔH^{vap}	Clapeyron (1834)	1.05	2.74
C_p (l)	Swanson and Chueh (1973)	0.95	2.39
C_p (s)	Steele et al. (1997)	0.05	0.08
	This work	1.28	3.09
TOTAL		**0.83**	**3.09**

Overall, the model adequately describes the PZ property data listed above within an average absolute relative error of ± 0.83 percent, with the exception of a few outliers.

8.3.5 *PZ Model Predictions*

With the determination of the estimates for the heat of vaporization coefficients known for the full model, a simple Aspen Plus™ Flash model was used to test the predictive capability of the PZ heat of vaporization coefficients against literature data. Figure 8.3-4 compares estimated and experimental heat of vaporization from Clapeyron (1834) for PZ from 106 to 301.05 °C. The full model accurately predicts the heat of vaporization over the full temperature range. In addition, the full model demonstrates its consistency with the critical temperature of PZ (364.85 °C).

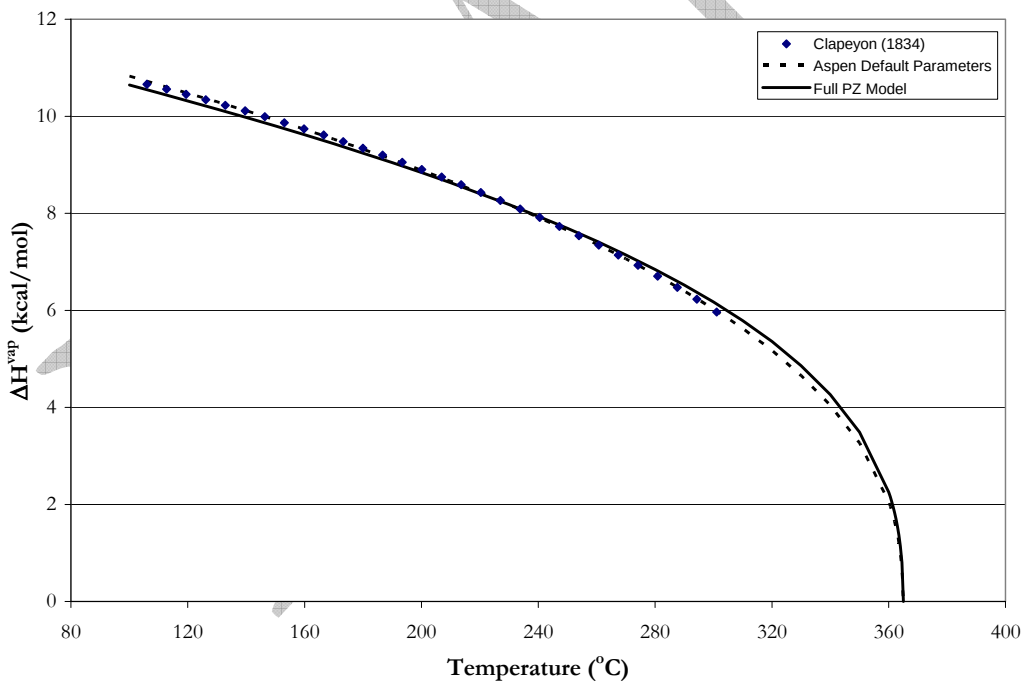

Figure 8.3-4. Comparison of Model Predictions with Experimental Data from Clapeyron (1834) for the Heat of Vaporization of PZ from 106 – 301.05 °C

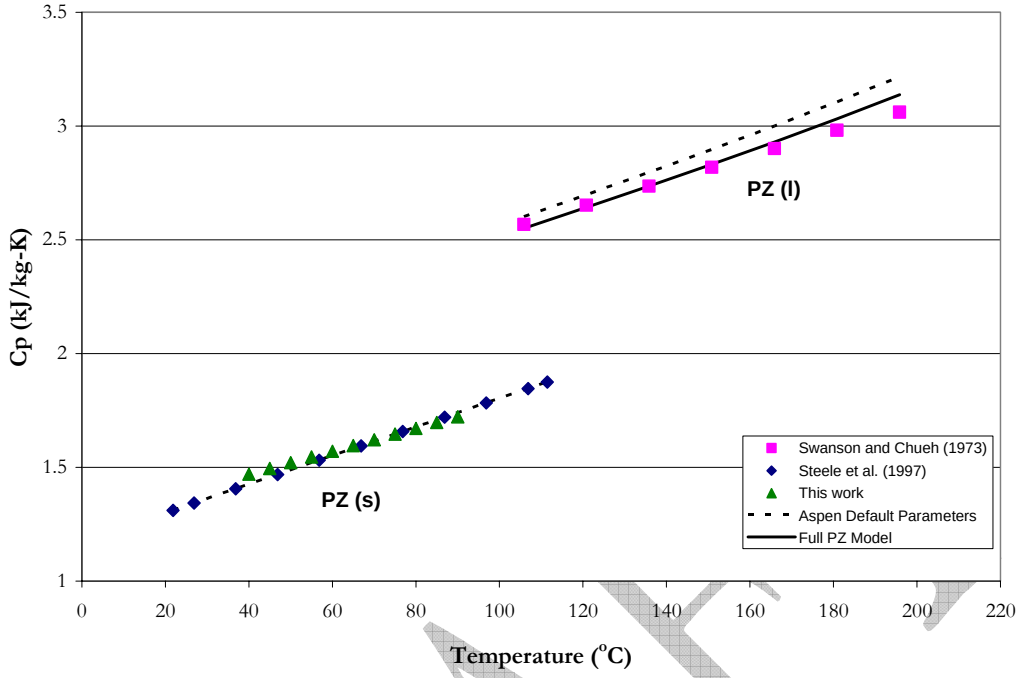

Figure 8.3-5. Comparison of Model Predictions with Experimental Data for the Specific Heat Capacity of PZ from 20 – 200 °C.

Figure 8.3-5 compares estimated and experimental specific heat capacity from Swanson and Chueh (1973), Steele et al. (1997) and from this work for pure PZ from 20 – 200 °C. The full model overestimates the specific heat capacity at high temperatures (> 200 °C) as compared to Swanson and Chueh (1973) even though all of the predictions for the model were within an AARD of ± 0.95 %. Figure Figure 8.3-5 illustrates an AARD of ± 1.28 % for the predictions of the solid phase specific heat capacity as compared to this work.

8.4 Specific Heat Capacity of H_2O

Four data sets have been regressed with the NRTL model to correct the liquid phase heat capacity of H_2O. Coefficients of the DIPPR heat of vaporization equation were

adjusted to account for the heat of vaporization [Moore et al. (1969) and Kell et al. (1984)] and liquid heat capacity [Osborne et al. (1939) and Kell et al. (1984)] of pure H_2O.

8.4.1 *Standard Enthalpy of Vaporization*

As stated in section 8.2, Aspen Plus™ relates the liquid phase specific heat capacity to the ideal gas enthalpy and the heat of vaporization through equations 8-1 to 8-3. Table 8.4-1 gives the coefficients for the DIPPR heat of vaporization equation for H_2O used in Aspen Plus™ based on equation 8-3:

Table 8.4-1. DIPPR Heat of Vaporization Default Coefficients for H_2O from 0.01 – 373.95 °C.

Parameter	Symbol	Default value
DHVLPD-1	C_1	5.2053E+07
DHVLDP-2	C_2	0.3199
DHVLDP-3	C_3	-0.2120
DHVLDP-4	C_4	0.2580

Experimental heat of vaporization data used in this work from Moore et al. (1969) and Kell et al. (1984) is shown in Figure 8.4-1.

We decided not to include the work by Clapeyron (1834) due to deviations at high temperatures as compared to previous authors. In addition, we decided to limit the heat of vaporization data to values under 200 °C to capture successfully the experimental specific heat capacity trends within the current work.

Using the Clausius-Clapeyron equation, we can verify the consistency between the DIPPR Heat of Vaporization Equation given for H_2O versus the DIPPR Extended Antoine Vapor Pressure Equation based on Equation 8-4 and Table 8.4-2.

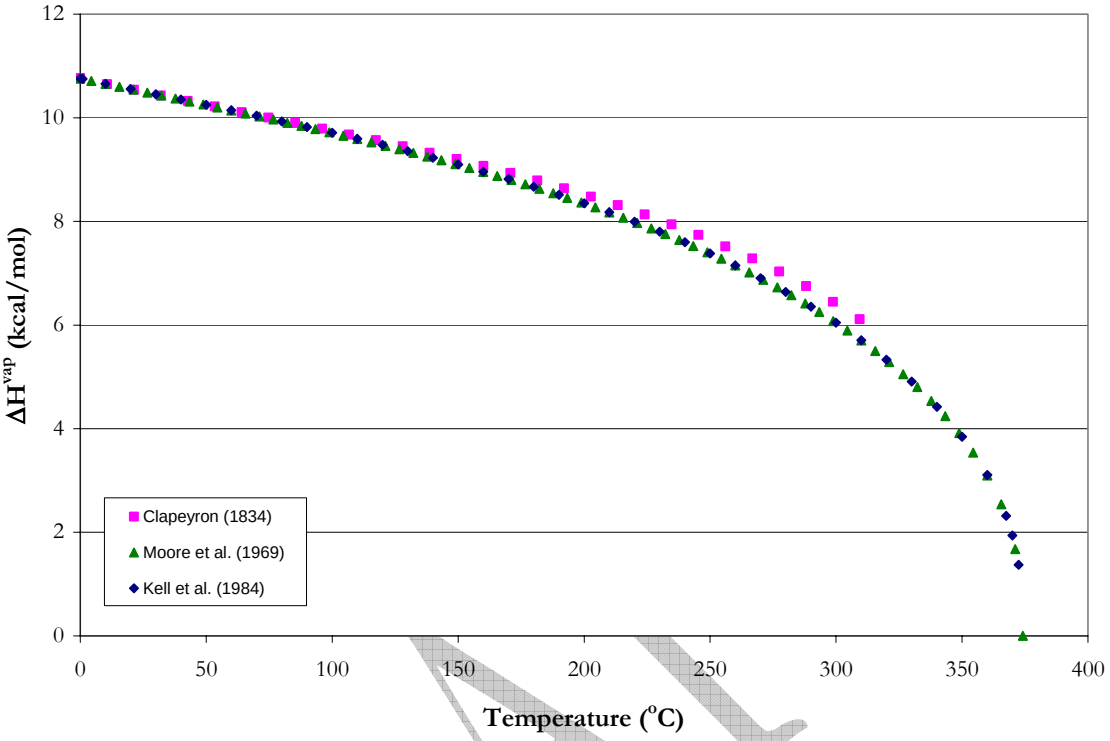

Figure 8.4-1. Heat of Vaporization of H_2O.

Table 8.4-2. DIPPR Extended Antoine Vapor Pressure Default Coefficients for H_2O from 0.01 – 373.95 °C.

Parameter	Symbol	Default value
PLXANT-1	C_1	65.64
PLXANT-2	C_2	-7207
PLXANT-3	C_3	0.0
PLXANT-4	C_4	0.0
PLXANT-5	C_5	-7.14
PLXANT-6	C_6	4.05E-06
PLXANT-7	C_7	2.00

Based on Equation 8-7, we can compare the coefficients for the DIPPR Extended Antoine Vapor Pressure for H_2O given in Table 8.4-2 to literature heat of vaporization as

shown in Figure 8.4-2. Deviations at high pressures appear above 130 °C between cited and predicted values due to the approximate linear nature of the Clausius-Clapeyron equation.

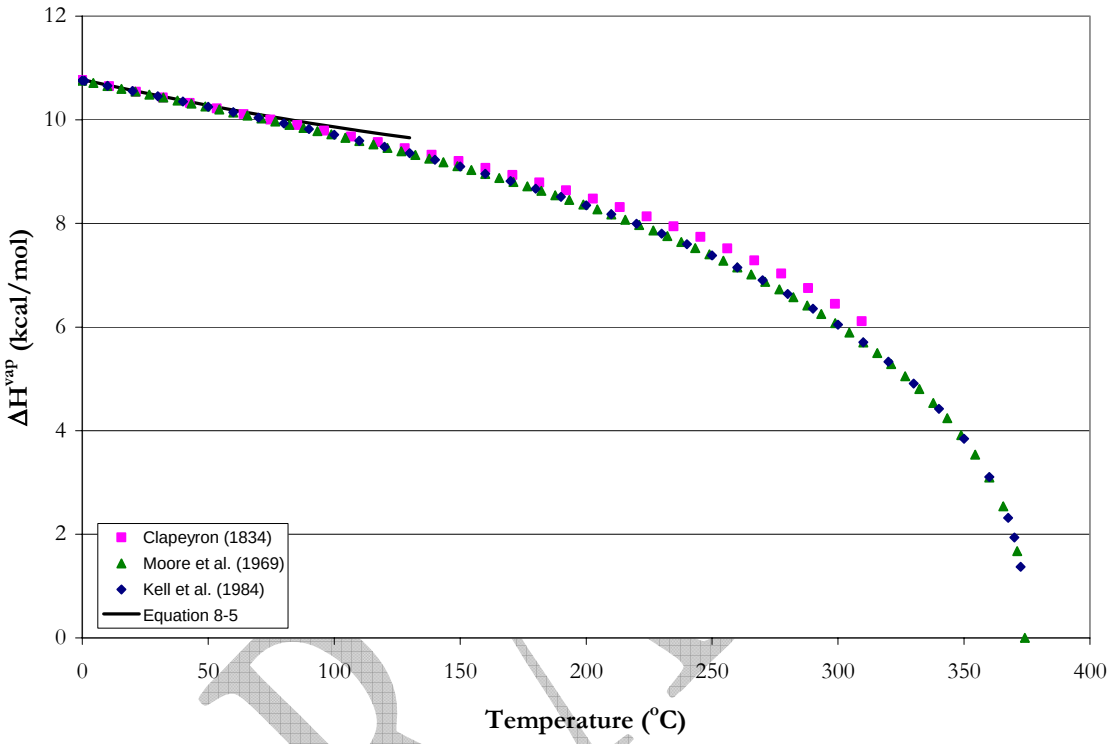

Figure 8.4-2. Comparison of the Heat of Vaporization based on Equation 8-5 to Literature Values for H_2O.

8.4.2 *Data Regression*

Through simultaneous regression, the coefficients for the DIPPR heat of vaporization equation were obtained through the regression of the heat of vaporization [Moore et al. (1969) and Kell et al. (1984)] and liquid heat capacity [Osborne et al. (1939) and Kell et al. (1984)] of pure H_2O as determined by DRS in Aspen Plus™. A list of the pure component data sets that were examine in this work is given in Table 8.4-3.

Table 8.4-3. Experimental data used in the regression of Heat of Vaporization Coefficients for H_2O.

	Obs.	T (°C)	σ_T	σ_{DHVL}	Source
ΔH^{vap}	37	0.01 – 198.89	0.1	1%	Moore et al. (1969)
	22	0.01 – 200.00	0.1	1%	Kell et al. (1984)

	Obs.	T (°C)	σ_T	σ_{CPL-M}	Source
C_p (l)	101	0.0 – 100.0	0.1	0.5%	Osborne et al. (1939)
	17	0.0 – 260.0	0.1	0.5%	Kell et al. (1984)

Table 8.4-4 shows the following regression summary statistics output for estimates of the heat of vaporization coefficients after performing a nonlinear regression for the full model using DRS.

Table 8.4-4. DRS Regression Output for Full H_2O Model.

Parameter	Estimate	σ wrt Estimate
DHVLPD-1	5.9101E+07	5.0137E+09
DHVLDP-2	0.7687	0.0024
DHVLDP-3	-0.7479	0.0045
DHVLDP-4	0.3079	0.0027

Residual Sum of Squares: 43.4867
Residual Root Mean Square: 0.5014

Notice that all of the estimates are large relative to their standard errors with the exception for the first coefficient. A complete description of the variability of the coefficient estimates requires examining the correlations between the estimates as shown in Table 8.4-5.

Table 8.4-5. Correlation Matrix of the Coefficient Estimates for the Full H_2O Model.

Parameter	1	2	3	4
1	1.00			
2	0.00	1.00		
3	0.00	-0.98	1.00	
4	0.00	0.91	-0.97	1.00

Table 8.4-5 shows both highly positive and highly negative correlations between $\hat{\eta}_{3\to2}$, $\hat{\eta}_{4\to2}$, and $\hat{\eta}_{4\to3}$ for the second and third parameters, but the correlations between $\hat{\eta}_{4\to1}$, $\hat{\eta}_{3\to1}$, and $\hat{\eta}_{2\to1}$ are independent due to the non-linear nature of Equation 8-3. Table 8.4-5 suggests that the fourth parameter might be usefully removed from the model without significant loss of information.

8.4.3 *Full H_2O Model Results*

With the determination of the estimates for the heat of vaporization parameters known for the full model, a simple Aspen Plus™ Flash model was used to test the predictive capability of the H_2O model against literature data. Table 8.4-6 gives the deviation between the experimental values and model predictions expressed in terms of the absolute average relative deviation (AARD) and the maximum AARD.

Table 8.4-6. Absolute Percent Relative Error for the H_2O Full Model.

		AARD(%)	Max. AARD
ΔH^{vap}	Moore et al. (1969)	0.59	1.77
	Kell et al. (1984)	0.63	1.78
C_p (l)	Osborne et al. (1939)	0.06	0.37
	Kell et al. (1984)	0.28	1.11
TOTAL		**0.39**	**1.78**

Overall, the model adequately describes the H_2O property data listed above within an average absolute relative error of ± 0.39 percent, with the exception of a few outliers.

8.4.4 *H_2O Model Predictions*

With the determination of the estimates for the heat of vaporization coefficients known for the full model, a simple Aspen Plus™ Flash model was used to test the predictive

capability of the H_2O heat of vaporization coefficients against literature data. Figure 8.4-3 compares estimated and experimental heat of vaporization from Moore et al. (1969), Kell et al. (1984) and Clapeyron (1834) for H_2O from 0.01 to 373.95 ^oC. The full model over predicts the heat of vaporization above 204.44 ^oC with a maximum error of 21.7 % at 348.98 ^oC. However, this error is well beyond the operating range of present carbon capture technology and is negligible overall since the full model is consistent with the critical temperature of H_2O (373.95 ^oC).

Figures 8.4-3 and 8.4-4 compares estimated and experimental specific heat capacity from Osborne et al. (1939), Engineering Sciences Data (1966), Kell et al. (1984), Chiu et al. (1999) and from this work for pure H_2O from 0 – 260 ^oC. The full model underestimates the specific heat capacity as compared to Kell et al. (1984) even though all of the predictions for the model were within an AARD of ± 0.17 %. Figure 8.4-5 illustrates a 0.27 % difference for the prediction of the specific heat capacity from this work as compared to the Full H_2O Model.

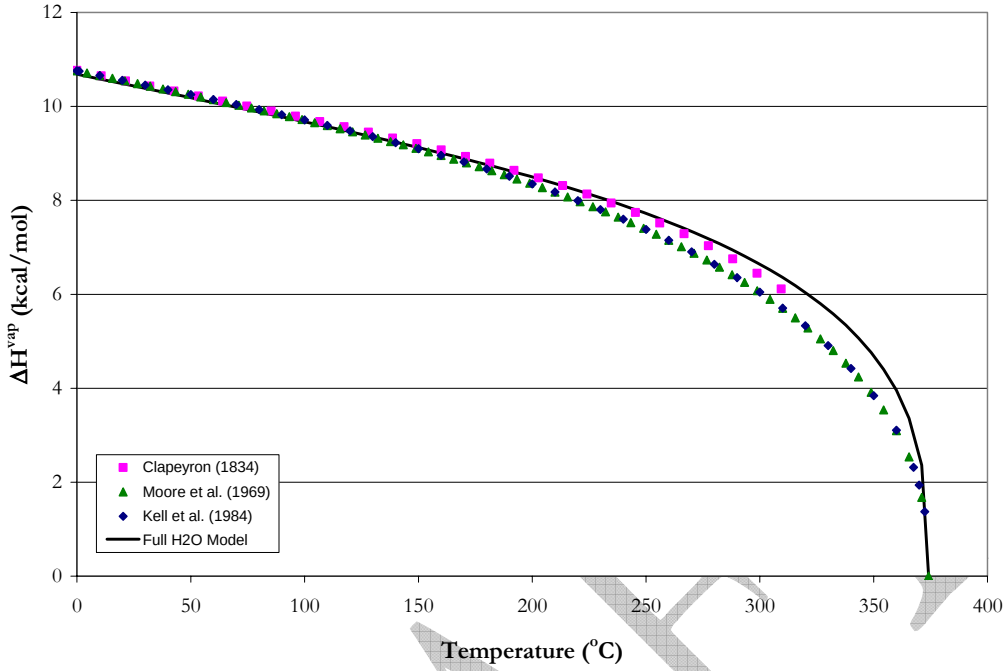

Figure 8.4-3. Comparison of Model Predictions with Experimental Data for the Heat of Vaporization of H_2O from 0.01 – 373.95 °C.

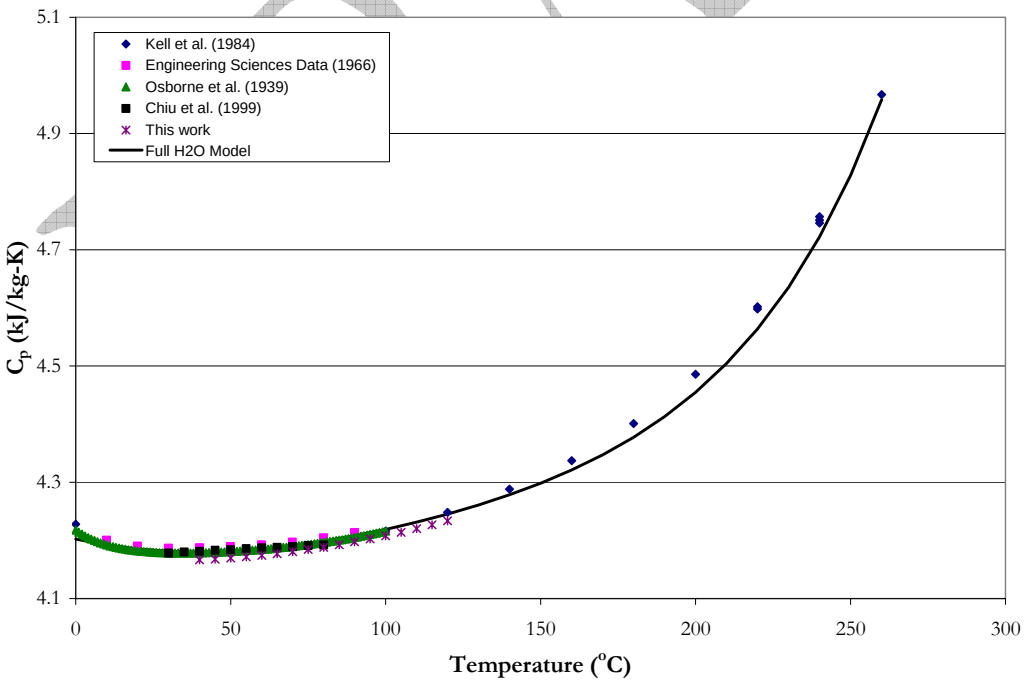

Figure 8.4-4. Comparison of Model Predictions with Experimental Data for the Specific Heat Capacity of H_2O from 0 – 260 °C.

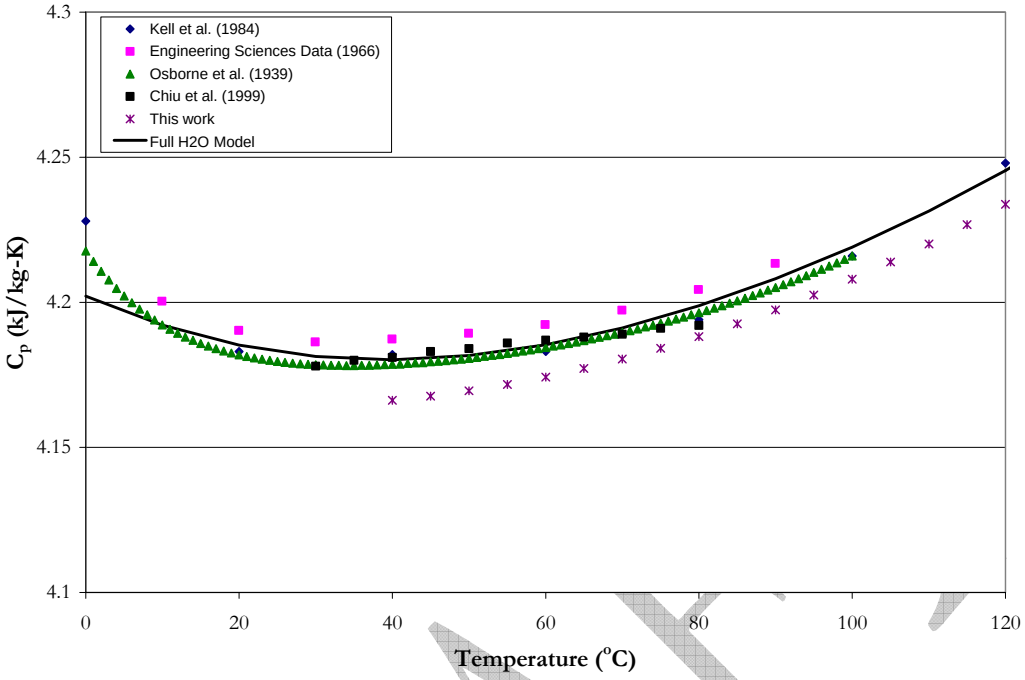

Figure 8.4-5. Expansion of Figure 8.4-3 from 0 – 120 °C for the Comparison of Model Predictions with Experimental Data for the Specific Heat Capacity of H_2O.

8.5 NRTL Conclusions

Results presented above indicate that the NRTL model, through simultaneous regression gave a set of heat of vaporization coefficients to describe liquid phase specific heat capacity for MEA, PZ, and H_2O. In addition, the model adequately represents the solid phase specific heat capacity for pure PZ.

— Part Two —

8.6 elecNRTL Introduction

Within the NRTL model, Aspen Plus calculates the liquid phase specific heat capacity for a pure component (CP) based on the heat of vaporization as stated in Section 8.2.1. Predictions for the liquid phase heat capacity of a *mixture* (CPMX), based on the

derivative of the liquid enthalpy at constant pressure, are consistent with values for CP for the pure component. On the contrary, predictive values for CP and CPMX within the elecNRTL model are inconsistent with respect to one other. In this part of the chapter, we will explain the calculation method for CP and CPMX with respect to H_2O, MEA and PZ associated with the elecNRTL model. In addition, we will try to improve upon existing parameters in order to agree with literature data.

8.7 Specific Heat Capacity for a Mixture (CPMX)

The elecNRTL model, within Aspen Plus™, calculates the liquid phase heat capacity of a *mixture* (CPMX) by taking the derivative of the liquid enthalpy at constant pressure as shown by the following expression:

$$H_i^l\left(T+\Delta T\right)-H_i^l\left(T\right)=\int_T^{T+\Delta T} C_{p,i}^l dT \qquad 8\text{-}11$$

where the liquid enthalpy of a mixture is calculated by the following equation:

$$H_i^l\left(T\right)=\sum_i x_i H_i + H_i^E \qquad 8\text{-}12$$

$$H_i\left(T\right)=\Delta H_{f,i}^{ig}\left(T^{ref}\right)+\int_{T^{ref}}^{T} C_{p,i}^{ig} dT+\left[H_i\left(T,p\right)-H_i^{ig}\left(T,p\right)\right] \qquad 8\text{-}13$$

Where
ΔT is the perturbation in temperature from *T*,
H_i^E is the excess enthalpy of component i,
$\Delta H_f^{ig}\left(T^{ref}\right)$ is the standard enthalpy of formation of component i at T^{ref},
T^{ref} is the reference temperature, 25.0 °C,
C_p^{ig} is the ideal gas heat capacity of component i,
H_i^{ig} is the ideal gas enthalpy of component i.

Liquid solutions are often described with through properties that measure their deviations from ideal-solution behavior and not from ideal behavior.

$$M^E = M - M^{id} \tag{8-14}$$

Thus, an excess property (e.g. excess enthalpy) is defined as the difference between the value of the actual property of a solution and the value the property would have as an ideal solution at the same temperature, pressure, and composition. However, excess properties have no physical meaning for pure components, because there is no deviation. Thus, equations 8-8 and 8-9 would reduce to the following functional form.

$$H_i^l(T) = \Delta H_{f,i}^{ig}(T^{ref}) + \int_{T^{ref}}^{T} C_{p,i}^{ig} dT + \left[H_i(T,p) - H_i^{ig}(T,p) \right] \tag{8-15}$$

8.8 Specific Heat Capacity of H_2O

For H_2O, Aspen Plus™ calculates CP through equations 8-1 and 8-2, but the heat of vaporization for H_2O is based on the Watson equation.

$$\Delta H_i(T) = \Delta H_i(T_1)\left(\frac{1-T/T_{ci}}{1-T_1/T_{ci}}\right)^{a_i+b_i(1-T/T_{ci})} \tag{8-16}$$

where the Watson equation can estimate the heat of vaporization of a pure liquid component at any temperature from the known value at a single temperature $\left(\Delta H_i(T_1)\right)$. Table 8.8-1 gives the coefficients for the Watson heat of vaporization equation for H_2O in the elecNRTL model within Aspen Plus™ based on equation 8-12.

Table 8.8-1. Watson Heat of Vaporization Default Coefficients for H_2O in the elecNRTL model from 0.05 – 373.95 °C [J/kmol].

Parameter	Symbol	Default value
DHVLWT-1	$\Delta H_1(T_1)$	40655000
DHVLWT -2	T_1	100.0
DHVLWT -3	a_i	0.3106
DHVLWT -4	b_i	0

Figure 8.8-1 illustrates the prediction of the heat of vaporization for H_2O from equation 8-12 within the elecNRTL model. Note, one of the deficiencies of a two parameter heat of vaporization model, vis-à-vis Watson equation, is apparent with the prediction of CP for H_2O as shown in Figure 8.8-2. Figure 8.8-2 demonstrates a known issue within the elecNRTL model where the liquid phase specific heat capacity of H_2O is calculated from the Watson heat of vaporization equation for CP and from the ASME Steam Table (1967) Equation-of-State for CPMX.

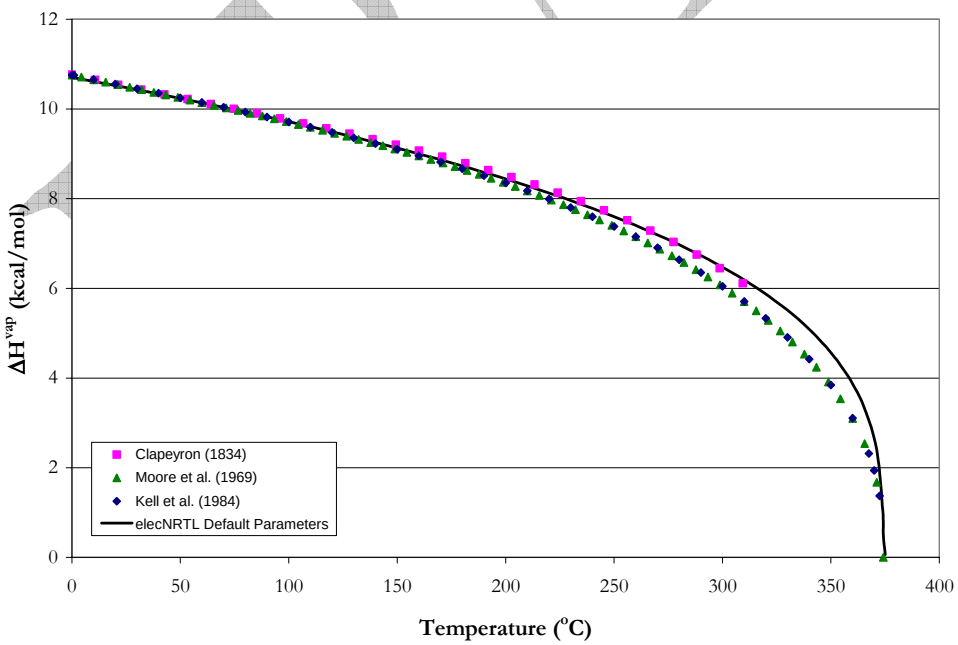

Figure 8.8-1. Predictions for the Watson Heat of Vaporization for H_2O from default values in the elecNRTL model.

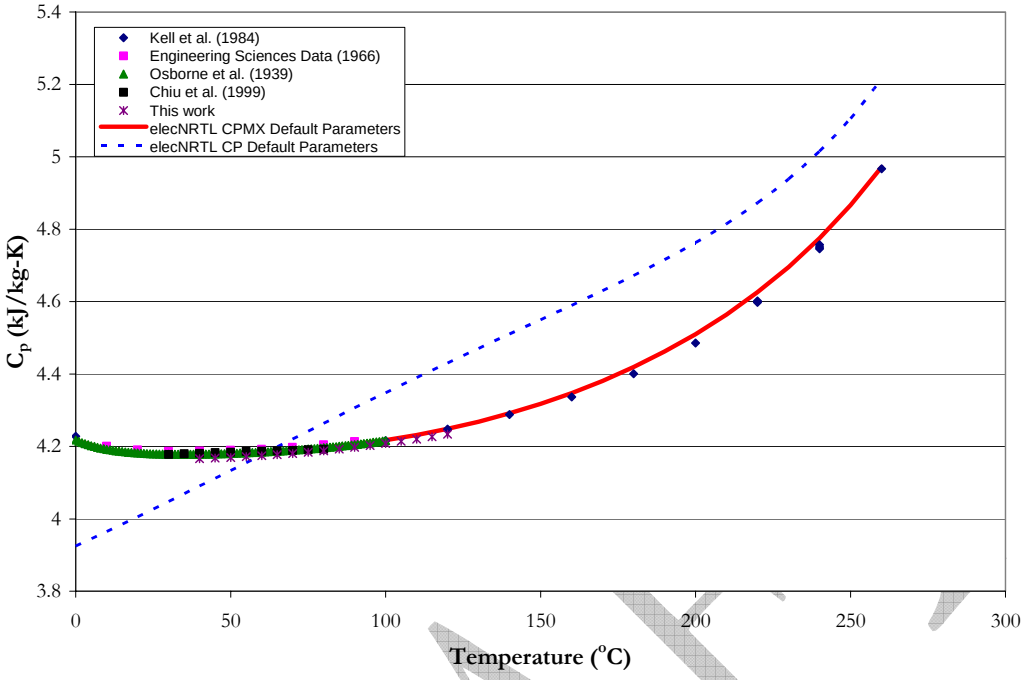

Figure 8.8-2. Predictions for CP and CPMX for H_2O from default values in the elecNRTL model.

Due to the large deviations between CP and CPMX for H_2O, we attempted to adjust the a and b terms of equation 8-12 implementing a similar procedure as described in section 8.4.2, but we were only able to improve the fit slightly as shown in Figure 8.8-3.

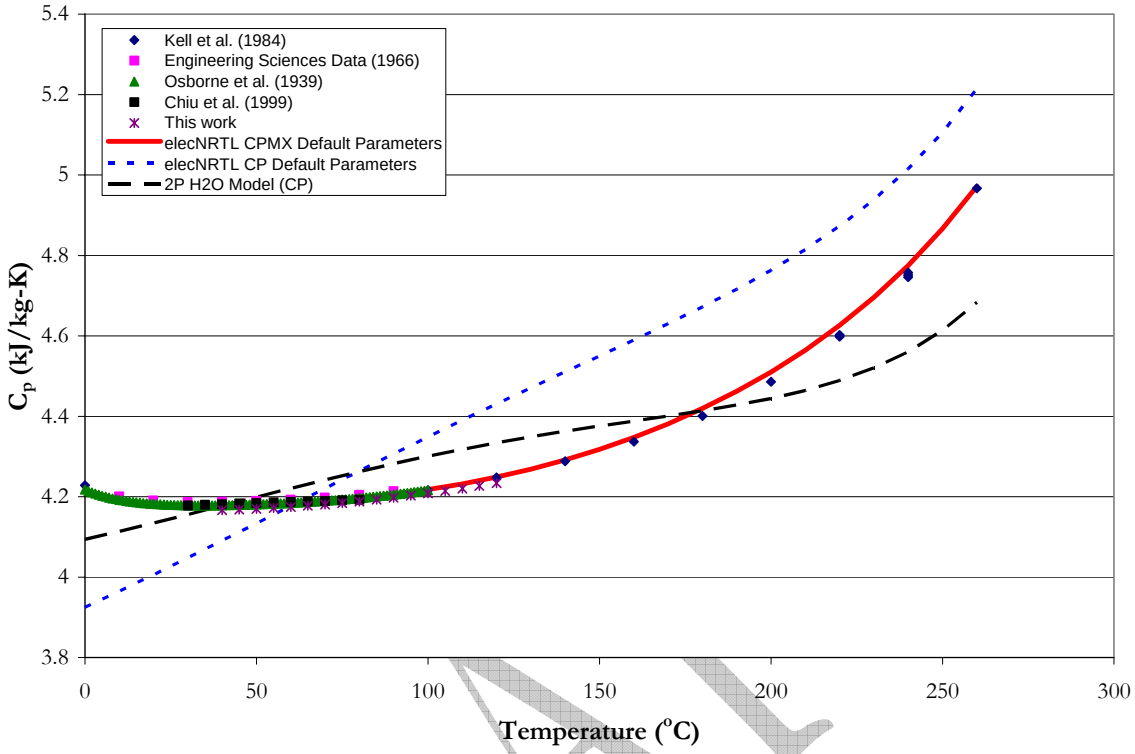

Figure 8.8-3. Comparison of elecNRTL Model Predictions (v3) with Experimental Data for the Specific Heat Capacity of H_2O from 0 – 260 °C.

Resulting in the following regression summary statistics output for estimates of the heat of vaporization coefficients as shown in Table 8.8-2.

Table 8.8-2. DRS Regression Output for 2P H_2O Model for CP.

Parameter	Estimate	σ wrt Estimate
DHVLWT -3	0.2662	0.0019
DHVLWT -4	0.0911	0.0036

Figure 8.8-4 compares estimated and experimental heat of vaporization based on parameters in Table 8.8-2 to literature data from Moore et al. (1969), Kell et al. (1984) and Clapeyron (1834) for H_2O from 0.01 to 373.95 °C. The two parameter (2P) model over predicts the heat of vaporization above 254.44 °C with a maximum error of 30.2 % at 348.98

°C. However, this error is well beyond the operating range of present carbon capture technology and is negligible overall since the full model is consistent with the critical temperature of H_2O (373.95 °C).

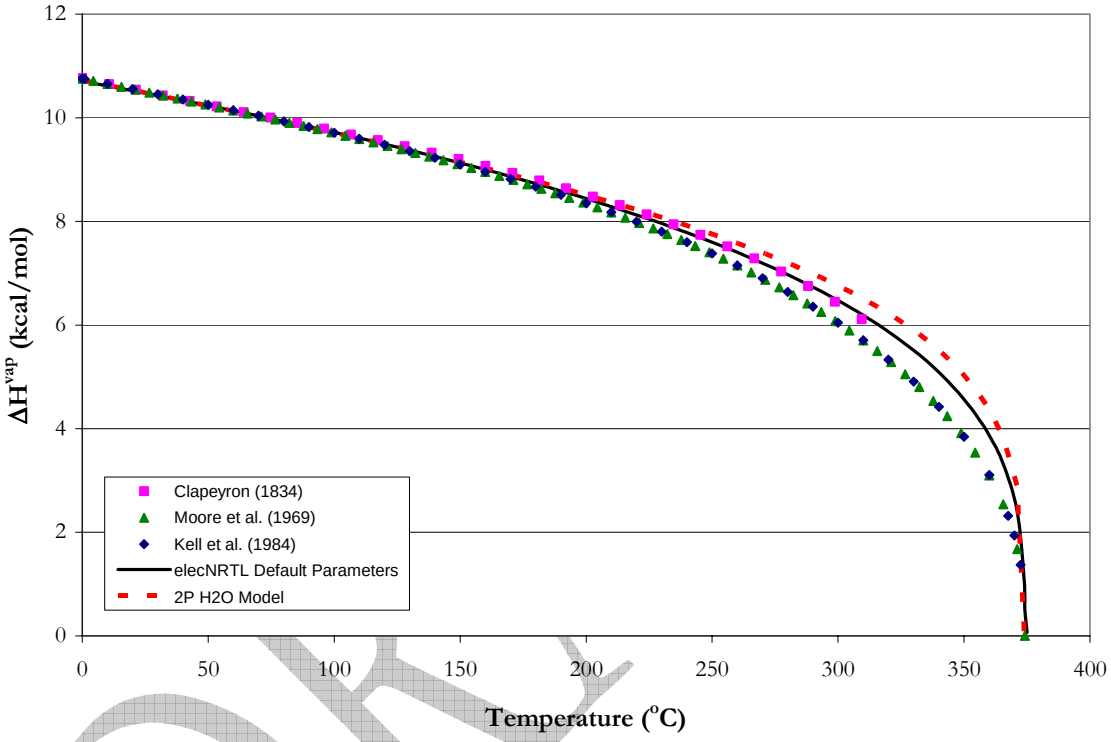

Figure 8.8-4. Comparison of Model Predictions (v3) with Experimental Data for the Heat of Vaporization of H_2O from 0.01 – 373.95 °C.

The above results attempted to improve upon the correlation for the specific heat capacity by adjusting the heat of vaporization of H_2O, but were unable to achieve satisfactory results as previously discussed in section 8.4.4. In solution mixtures, the elecNRTL model will use the ASME Steam Table (1967) Equation-of-State for H_2O in the calculation of CPMX and hence, the CP value will not affect future calculations, but we do not feel this to be a satisfactory solution. We will then recommend to AspenTech to change

the calculation structure within the elecNRTL model to reflect the heat of vaporization of H_2O based on the DIPPR equation and results as described in section 8.4.2.

8.9 Specific Heat Capacity of MEA

Table 8.9-1 gives the coefficients for the Watson heat of vaporization equation for MEA in the elecNRTL model within Aspen Plus™ based on equation 8-12.

Table 8.9-1. Watson Heat of Vaporization Default Coefficients for MEA in the elecNRTL model from 10.5 – 405.05 °C [J/kmol].

Parameter	Symbol	Default value
DHVLWT-1	$\Delta H_1(T_1)$	54835800
DHVLWT -2	T_1	126.67
DHVLWT -3	a_i	0.3288
DHVLWT -4	b_i	-0.0857

Figure 8.9-1 illustrates the prediction of the heat of vaporization for MEA from equation 8-12 within the elecNRTL model. Figure 8.9-1 demonstrates an issue between the NRTL and the elecNRTL model where the critical temperature of MEA reported in the elecNRTL model is from the work by Austgen (1989). The liquid phase specific heat capacity of MEA is calculated from the Watson heat of vaporization equation for CP and CPMX, but there is a 1 % deviation between CP and CPMX for temperatures above 120 °C as shown in Figure 8.9-2. Even though there is a minimum AARD of 5 % at 140 °C between predictions from the elecNRTL model and current literature data.

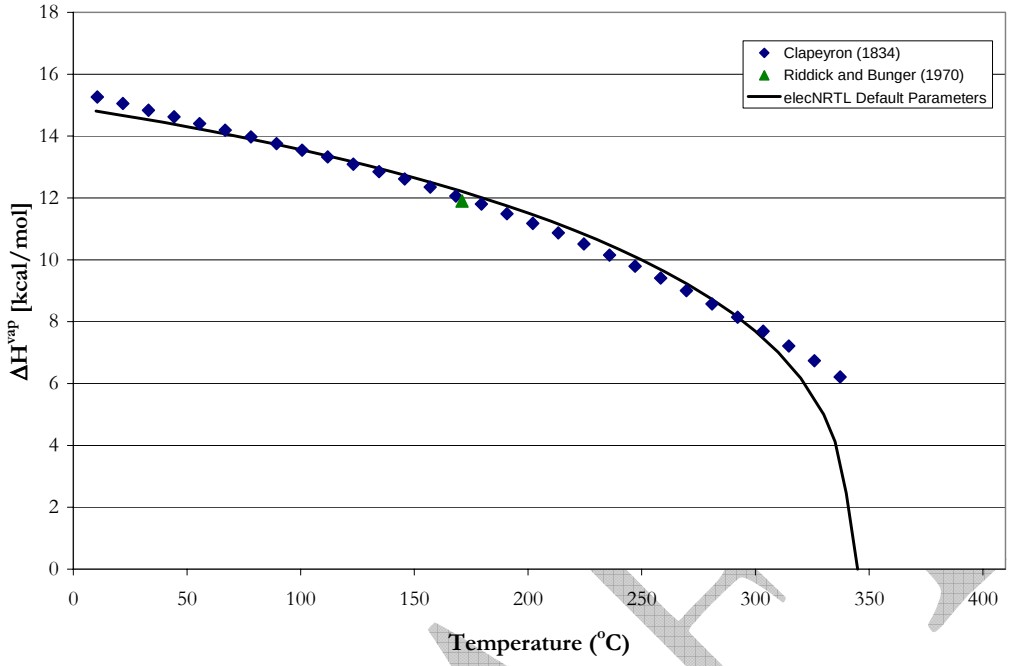

Figure 8.9-1. Predictions for the Watson Heat of Vaporization for MEA from default values in the elecNRTL model.

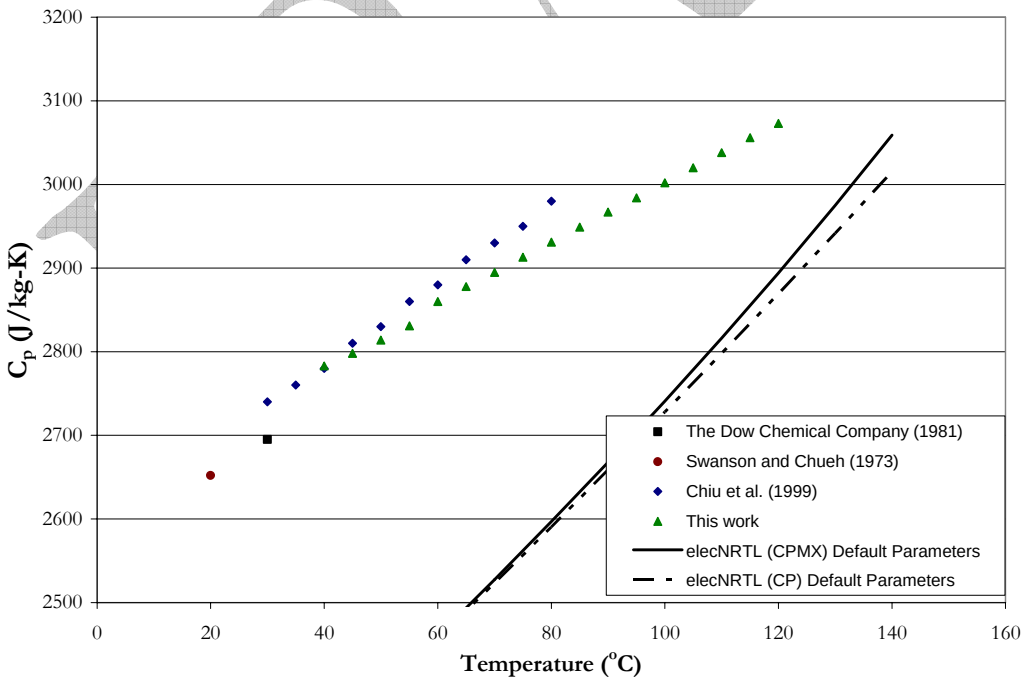

Figure 8.9-2. Predictions for CP and CPMX for MEA from default values in the elecNRTL model.

Due to the large deviations between predictions from the elecNRTL model and current literature data, we also regressed the a and b terms of equation 8-12 implementing a similar procedure as described in section 8.2.2, however in this case, we successfully matched the specific heat capacity for MEA (AARD = 0.6 %) as shown in Figure 8.9-3. Even though, the liquid phase specific heat capacity of MEA calculated from the regressed parameters of the Watson heat of vaporization equation displays approximately 1 % deviation between CP and CPMX for temperatures above 130 °C.

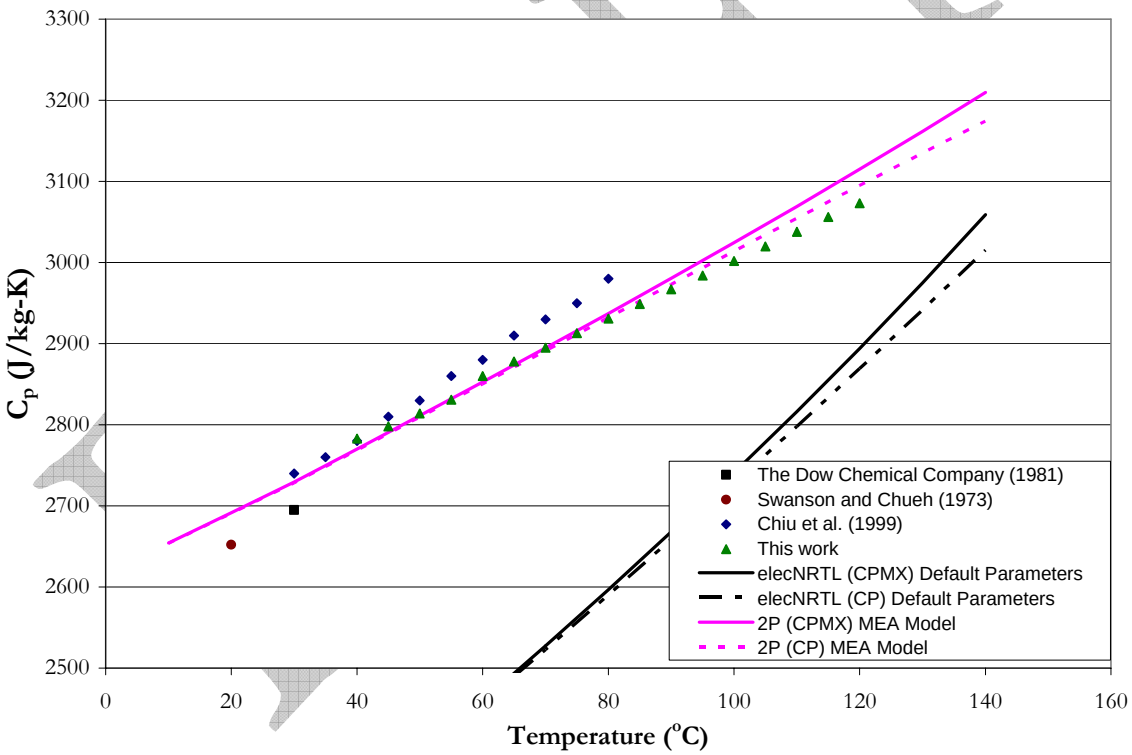

Figure 8.9-3. Comparison of elecNRTL Model Predictions (v4) with Experimental Data for the Specific Heat Capacity of MEA from 20 – 140 °C

Resulting in the following regression summary statistics output for estimates of the heat of vaporization coefficients as shown in Table 8.9-2.

Table 8.9-2. DRS Regression Output for 2P MEA Model for CP.

Parameter	Estimate	σ wrt Estimate
DHVLWT -3	0.4041	0.0077
DHVLWT -4	0.1101	0.0138

Figure 8.9-4 compares estimated and experimental heat of vaporization based on parameters in Table 8.9-2 to literature data from Riddick and Bunger (1970) and Clapeyron (1834) for MEA from 10.50 to 337.23 °C. The two parameter (2P) model overpredicts the heat of vaporization above 213.30 °C with a maximum error of 15.0 % at 337.23 °C. However, this error is well beyond the operating range of present carbon capture technology and is negligible overall since the full model is now consistent with the critical temperature of MEA (405.05 °C).

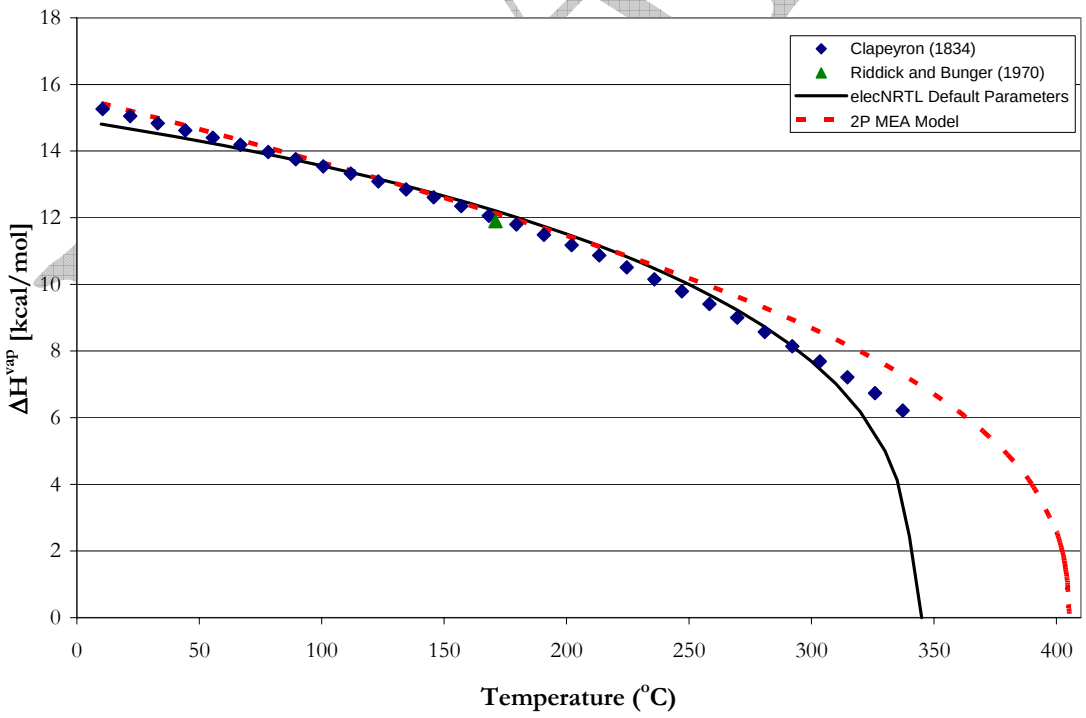

Figure 8.9-4. Comparison of Model Predictions (v4) with Experimental Data for the Heat of Vaporization of MEA from 10.5 – 405.05 °C.

The above results indicate an improvement upon the default elecNRTL parameters for the Watson heat of vaporization equation to predict the specific heat capacity of MEA. Critical properties in the elecNRTL model were adjusted to match correctly the critical temperature of MEA and to improve the heat of vaporization correlation between predicted values and current literature data.

8.10 Specific Heat Capacity of PZ

In section 8.3, we were able to illustrate that predictions for the liquid phase specific heat capacity of PZ could improve by adjusting the coefficients of the DIPPR heat of vaporization equation. In the elecNRTL model, Aspen Plus™ calculates the solid and liquid phase specific heat capacity by the same method as described in section 8.3, however, as shown in Figure 8.10-2, there is an AARD of ±2.58 % between predictions of CP and CPMX for the liquid phase specific heat capacity of PZ.

Due to deviations between the predictions from the elecNRTL model and current literature data, we regressed coefficients for the heat of vaporization of PZ implementing a similar procedure as described in section 8.3.3. In this case, we successfully matched the pure and mixture specific heat capacities for PZ (AARD = 0.0 and 0.0 %, respectively) as shown in Figures 8.10-3 and 8.10-4. Resulting in the following regression summary statistics output for estimates of the heat of vaporization coefficients as shown in Table 8.10-1.

Table 8.10-1. DRS Regression Output for 3P PZ Model for CP.

Parameter	Estimate	σ wrt Estimate
DHVLPD-1	64355423	263643
DHVLDP-2	0.3857	0.0107
DHVLDP-3	0.0257	0.0102

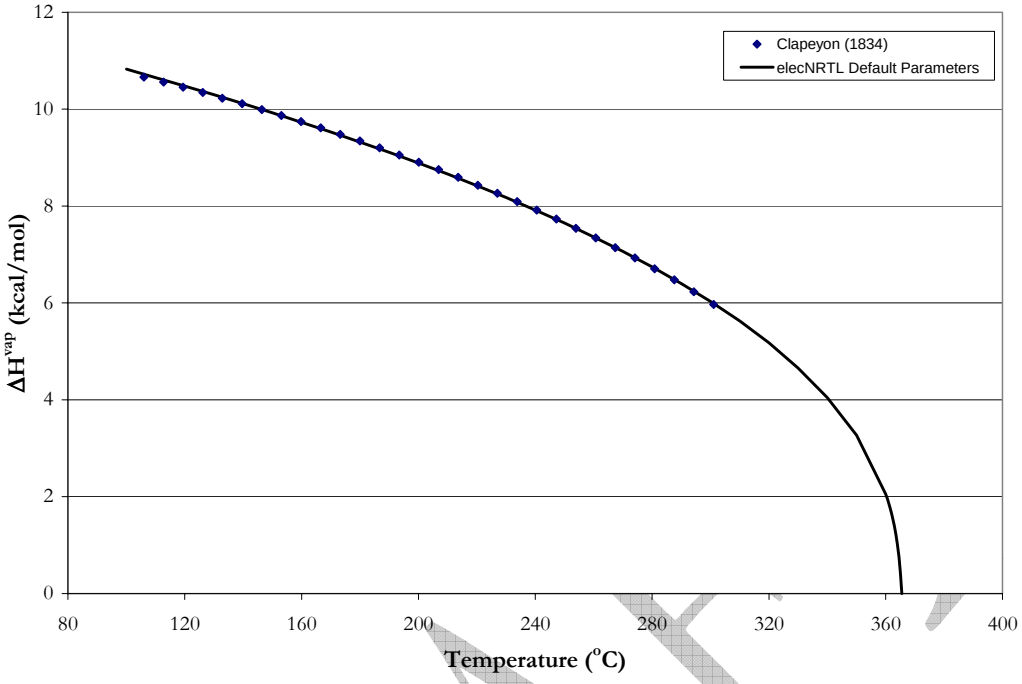

Figure 8.10-1. Comparison of elecNRTL Model Predictions with Experimental Data from Clapeyron (1834) for the Heat of Vaporization of PZ from 106 – 301.05 °C.

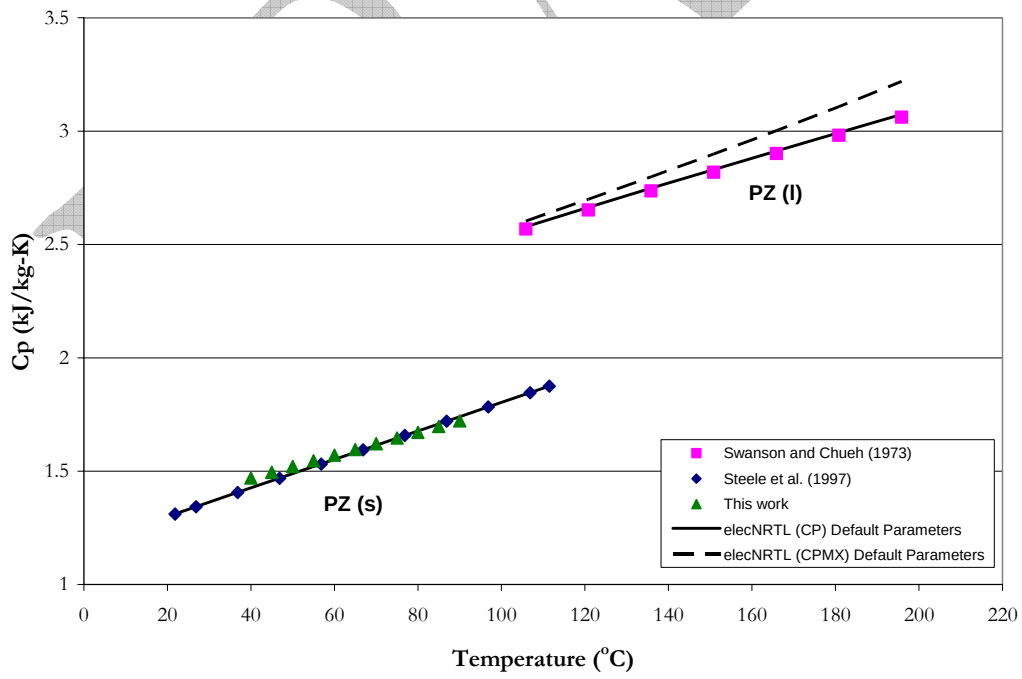

Figure 8.10-2. Comparison of elecNRTL model Predictions with Experimental Data for the Specific Heat Capacity of PZ from 20 to 200 °C.

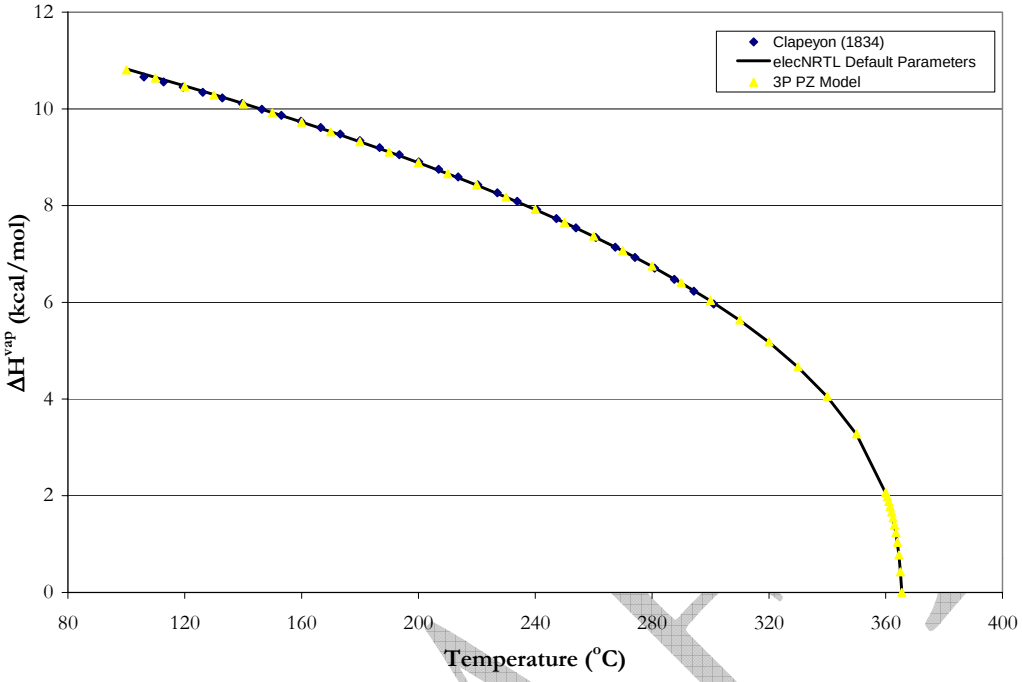

Figure 8.10-3. Comparison of Model Predictions (v2) with Experimental Data from Clapeyron (1834) for the Heat of Vaporization of PZ from 106 – 301.05 °C.

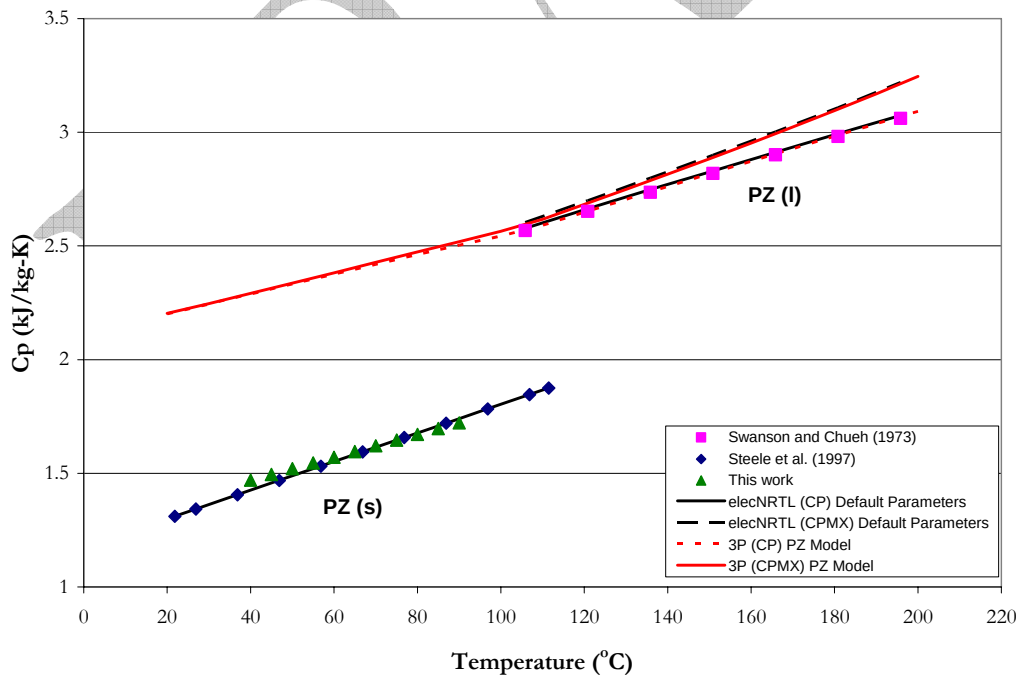

Figure 8.10-4. Comparison of elecNRTL Model Predictions (v2) with Experimental Data for the Specific Heat Capacity of PZ from 20 to 200 °C.

By adjusting the coefficients of the DIPPR heat of vaporization equation, we were unable to decrease the deviation between the prediction of CP and CPMX. As shown in Figure 8.10-4, there is an AARD of ±2.69 % between predictions of CPMX and Swanson and Chueh (1973) for the liquid phase specific heat capacity of PZ. Due to this relatively small error between CP and CPMX and the slight improvement for the prediction of the heat of vaporization based on the 3P PZ model, the above analysis is satisfactory given the lack of documentation from Aspen Plus™ to describe the calculation methods of CP and CPMX for PZ. We will then recommend to limit predictions for the specific heat capacity of pure PZ to temperatures below 140 °C.

8.11 Abridged elecNRTL Predictive Correlations

To anticipate installation difficulties with the implementation of our model on future platforms, we have developed specific correlations based on predictive results from our rigorous thermodynamic model for the liquid phase specific heat capacity of H_2O, MEA, and PZ. We chose to relate the liquid phase specific heat capacity by the following relation:

$$C_{p,i}^{l,*}\left(\frac{kJ}{kg\cdot K}\right) = C_{1i} + C_{2i}T + C_{3i}T^2 + C_{4i}T^3 + C_{5i}T^4 \qquad 8\text{-}17$$

Where
$C_{p,i}^{l,*}$ is the predictive liquid phase specific heat capacity for component i,
T is the temperature, °C.

In this case of H_2O, we successfully matched the liquid phase specific heat capacity (CPMX) (AARD = 0.04 %) as shown in Figure 8.11-1. Resulting in the following regression

summary statistics output for estimates of the abridge model correlation coefficients as shown in Table 8.11-1.

Table 8.11-1. DRS Regression Output for the Abridge Model Correlation for H_2O.

Parameter	Estimate	σ wrt Estimate
C_1	4.2107	0.0020
C_2	-1.696E-03	1.0874E-04
C_3	2.568E-05	1.7486E-06
C_4	-1.095E-07	1.0198E-08
C_5	3.038E-10	1.9449E-11

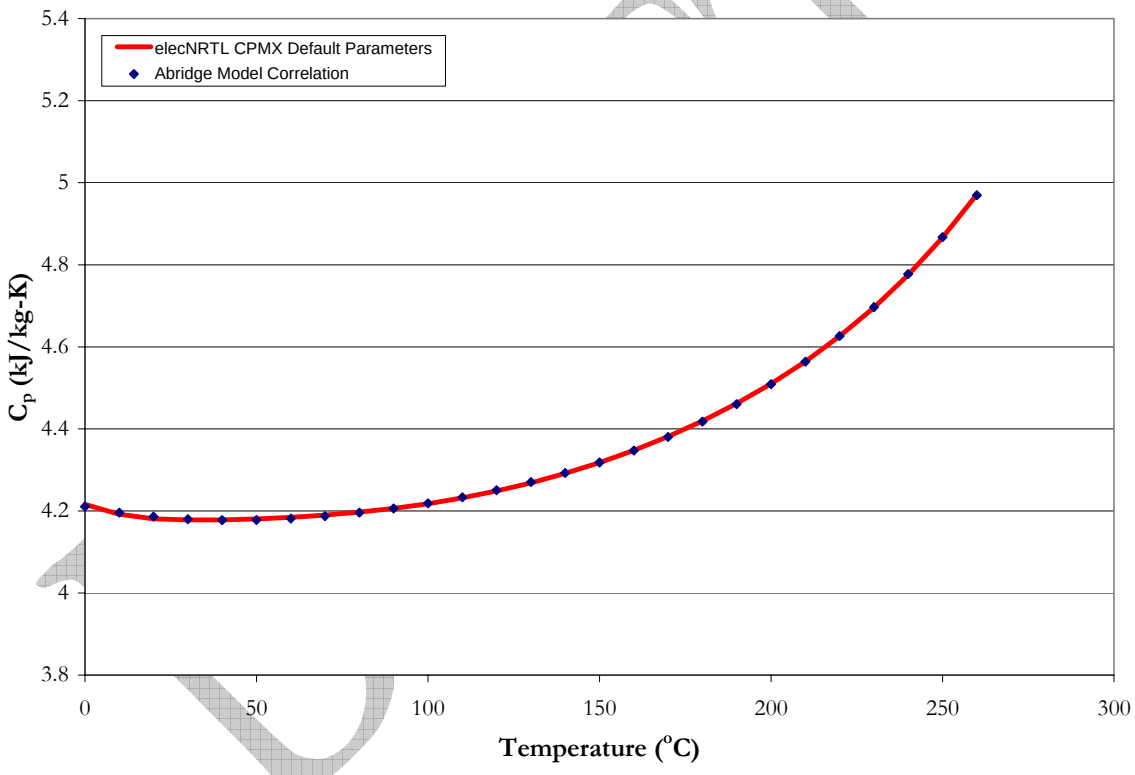

Figure 8.11-1. Comparison of elecNRTL model Predictions with the Abridge Model Correlation for the Specific Heat Capacity of H_2O from 0 to 260 °C.

For MEA, we successfully matched the liquid phase specific heat capacity (CPMX) (AARD = 0.02 %) as shown in Figure 8.11-2. Resulting in the following regression

summary statistics output for estimates of the abridge model correlation coefficients as shown in Table 8.11-2.

Table 8.11-2. DRS Regression Output for the Abridge Model Correlation for MEA.

Parameter	Estimate	σ wrt Estimate
C_1	2.6161	0.0006
C_2	3.706E-03	1.8487E-05
C_3	3.787E-06	1.1989E-07
C_4	0.0	-
C_5	0.0	-

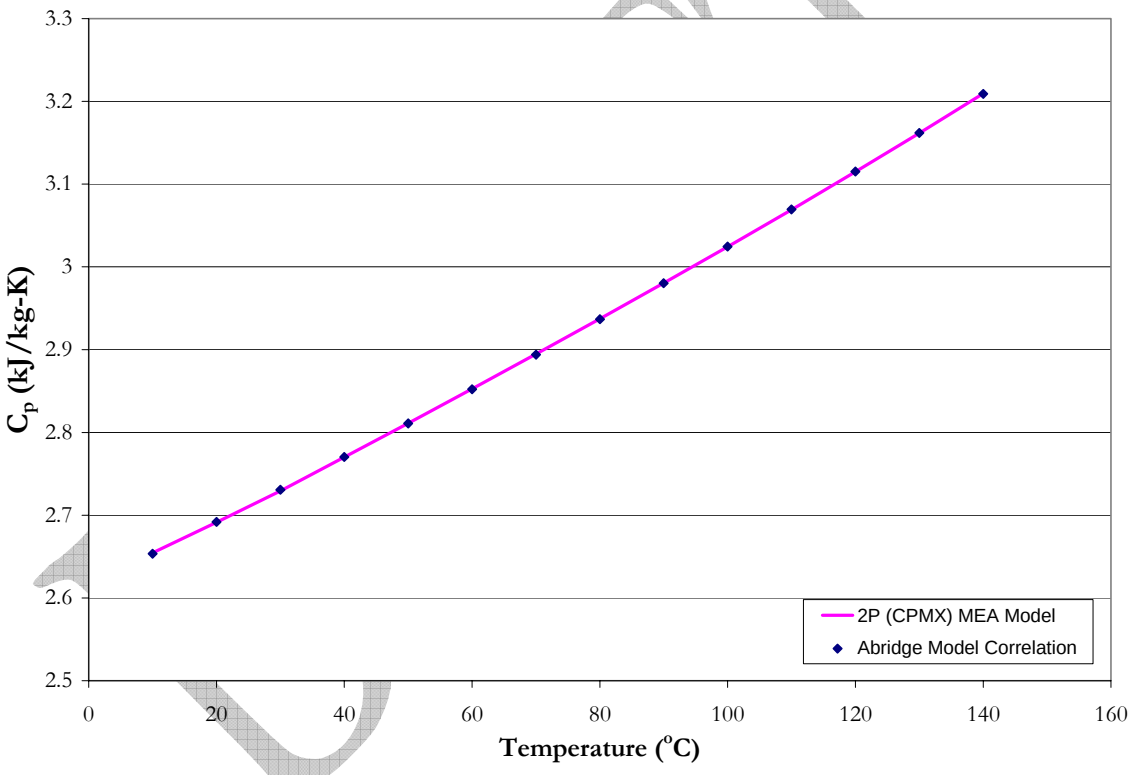

Figure 8.11-2. Comparison of elecNRTL model Predictions with the Abridge Model Correlation for the Specific Heat Capacity of MEA from 10 to 140 °C.

In this case of PZ, we successfully matched the liquid phase specific heat capacity (CPMX) (AARD = 0.23 %) as shown in Figure 8.11-3. Resulting in the following regression

summary statistics output for estimates of the abridge model correlation coefficients as shown in Table 8.11-3.

Table 8.11-3. DRS Regression Output for the Abridge Model Correlation for PZ.

Parameter	Estimate	σ wrt Estimate
C_1	2.1470	0.0061
C_2	3.038E-03	1.2548E-04
C_3	1.234E-05	5.5684E-07
C_4	0.0	-
C_5	0.0	-

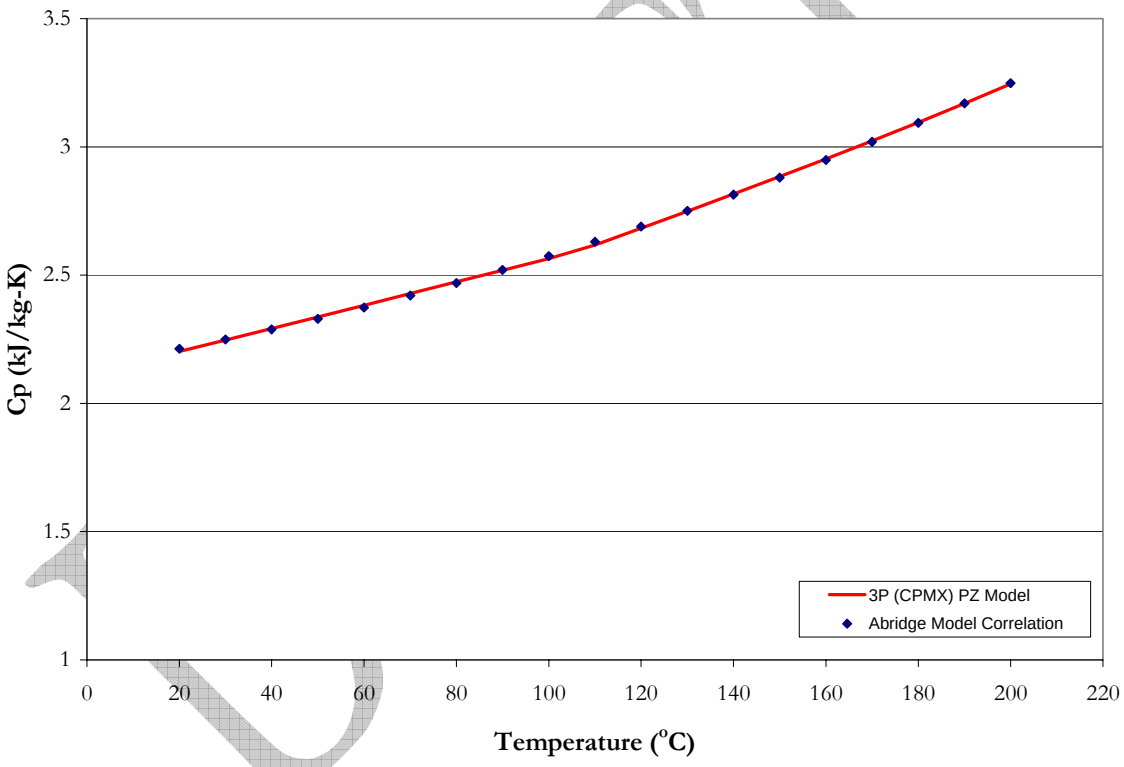

Figure 8.11-3. Comparison of elecNRTL model Predictions with the Abridge Model Correlation for the Specific Heat Capacity of PZ from 20 to 200 °C.

8.12 elecNRTL Conclusions

With reference to H_2O, the above results attempted to improve upon the correlation for the specific heat capacity by adjusting the heat of vaporization of H_2O, but were unable to achieve satisfactory results as previously discussed in section 8.4.4. In solution mixtures, the elecNRTL model will use the ASME Steam Table (1967) Equation-of-State for H_2O in the calculation of CPMX and hence, the CP value will not affect future calculations, but we do not feel this to be a satisfactory solution. We will then recommend to AspenTech to change the calculation structure within the elecNRTL model to reflect the heat of vaporization of H_2O based on the DIPPR equation and results as described in section 8.4.2.

With reference to MEA, the above results indicate an improvement upon the default elecNRTL parameters for the Watson heat of vaporization equation to predict the specific heat capacity of MEA. Critical properties in the elecNRTL model were adjusted to correctly match the critical temperature of MEA and to improve the heat of vaporization correlation between predicted values and current literature data.

With reference to PZ, we were unable to decrease the deviation between the prediction of CP and CPMX by adjusting the coefficients of the DIPPR heat of vaporization equation. As shown in Figure 8.10-4, there is an AARD of ±2.69 % between predictions of CPMX and Swanson and Chueh (1973) for the liquid phase specific heat capacity of PZ. Due to this relatively small error between CP and CPMX and the slight improvement for the prediction of the heat of vaporization based on the 3P PZ model, the above analysis is satisfactory given the lack of documentation from Aspen Plus™ to describe the calculation

methods of CP and CPMX for PZ. We will then recommend to limit predictions for the specific heat capacity of pure PZ to temperatures below 140 °C.

Using an abridge model correlation, we were successful in matching the liquid phase specific heat capacity for H_2O, MEA, and PZ over the respective temperature ranges for each component.

Overall, results presented above indicate that the elecNRTL model, through simultaneous regression gave a set of heat of vaporization coefficients to describe liquid phase specific heat capacity for MEA, PZ, and H_2O. In addition, the model adequately represents the solid phase specific heat capacity for pure PZ as compared to the NRTL model and current literature data.

References

1. (1966). Engineering Sciences Data. London.
2. Atkins, P. and J. de Paula (2002). Physical Chemistry. New York, W. H. Freeman and Company.
3. Chiu, L. F. and M. H. Li (1999). "Heat Capacity of Alkanolamine Aqueous Solutions." Journal of Chemical Engineering Data 44(6): 1396-1401.
4. Chiu, L. F., H. F. Liu, et al. (1999). "Heat Capacity of Alkanolamines by Differential Scanning Calorimetry." Journal of Chemical Engineering Data 44(4): 631-636.
5. Clapeyron, E. J. (1834). "Memoirs on the Motive Power of Heat." L'ecole Polytechnique 14(23): 153.
6. Company, T. D. C. (1981). The Alkanolamines Handbook. Midland, Michigan.
7. Kell, G. S., L. Haar, et al. (1984). NBS/NRC Steam Tables. Thermodynamic and Transport Properties and Computer Programs for Vapor and Liquid States of Water in SI Units. Washington, Hemisphere Publishing Corporation.
8. Moore, J. G., F. G. Keyes, et al. (1969). Steam Tables. Thermodynamic Properties of Water Including Vapor, Liquid, and Solid Phases. New York, John Wiley & Sons, Inc.
9. Osborne, N. S., H. F. Stimson, et al. (1939). "Measurements of Heat Capacity and Heat of Vaporization of Water in the Range 0 oC to 100 oC." Journal of Research of the National Bureau of Standards 23: 197-260.

10. Riddick, J. A. and W. B. Bunger (1970). Organic Solvents: Physical Properties and Methods of Purification. New York, Wiley Interscience.
11. Rowley, R. L., W. V. Wilding, et al. (2004). DIPPR® Data Compilation of Pure Chemicals Properties, Design Institute for Physical Properties, Brigham Young University. Provo, Utah.
12. Sada, E. and S. Kito (1972). "Solubilities of Gases in Aqueous Monoethanolamine Solutions." Kagaku Kogaku 36(2): 218-220.
13. Steele, W. V., N. K. Smith, et al. (1997). "Thermodynamic Properties and Ideal-Gas Enthalpies of Formation for Dicyclohexyl Sulfide, Diethylenetriamine, Di-n-octyl Sulfide, Dimethyl Carbonate, Piperazine, Hexachloroprop-1-ene, Tetrakis(dimethylamino)ethylene, N,N'-Bis-(2-hydroxyethyl)ethylene." Journal of Chemical Engineering Data 42: 1037-1052.
14. Swanson, A. C. and C. F. Chueh (1973). "Estimating Liquid Heat Capacity." Chemical Engineering Progress 69: 83.

CHAPTER IX

Binary Systems: H_2O-MEA

9.1 Introduction

We continue the thermodynamic model development by describing the molecule-molecule interactions between water and monoethanolamine. Interactions between water and piperazine will be addressed in Chapter X. This chapter describes the data regression and model predictions for the H_2O-Monoethanolamine (MEA) system based on previous literature data and experimental results from this work. The results for the binary interaction parameters for the electrolyte-NRTL (elecNRTL) model in Aspen Plus™ are then presented; showing good statistical fit to the literature data with an average absolute relative error of ± 2.62 % with the exception of a few outliers.

9.2 H_2O-MEA System

Recall from Chapter VII that as the concentration of ions in an electrolyte solution approaches zero, the elecNRTL model reduces in theory to the NRTL Model of Renon and Prausnitz (1968). As shown in Chapter 8, the calculation routes for physical properties between the NRTL and the elecNRTL property models are different. In this section, we present background on the NRTL model for clarification purposes only since we will be using the elecNRTL property model for all future chapters to describe molecular and ionic interactions

The NRTL model is an excess Gibbs energy model given by the following form for a binary system:

$$\frac{G^{ex}}{RT} = x_1 x_2 \left(\frac{\tau_{21} G_{21}}{x_1 + x_2 G_{21}} + \frac{\tau_{12} G_{12}}{x_2 + x_1 G_{12}} \right) \qquad 9\text{-}1$$

Where
i is the species index, 1: H_2O and 2: MEA,
j is the species index, 1: H_2O and 2: MEA,
x_i is the liquid mole fraction of component i,
τ_{ij} is the binary interaction parameter between component i and j,
α_{ij} is the molecule-molecule nonrandomness factor, 0.2,
$G_{12} = e^{-\alpha_{12}\tau_{12}}$,
$G_{21} = e^{-\alpha_{21}\tau_{21}}$.

The molecule-molecule binary interaction parameters were assumed to be temperature dependent and were fitted to the following function of temperature:

$$\tau_{12} = A_{12} + \frac{B_{12}}{T} + C_{12} \ln(T) + D_{12} T \qquad 9\text{-}2$$

$$\tau_{21} = A_{21} + \frac{B_{21}}{T} + C_{21}\ln(T) + D_{21}T \qquad 9\text{-}3$$

Taking the appropriate derivative of Equation 9-1, an expression for the activity coefficient of MEA can then be derived from thermodynamic relationships.

$$\ln\gamma_i = \left[\frac{\delta\left(nG^{ex}/RT\right)}{\delta n_i}\right] \qquad 9\text{-}4$$

$$\ln\gamma_2 = x_1^2\left[\tau_{12}\left(\frac{G_{12}}{x_2 + x_1 G_{12}}\right)^2 + \frac{\tau_{21}G_{21}}{\left(x_1 + x_2 G_{21}\right)^2}\right] \qquad 9\text{-}5$$

By taking the limit as the mole fraction of MEA (x_2) approaches zero, we get an explicit form of Equation 9-5 for the infinite dilution activity coefficient of MEA as given below:

$$\ln\gamma_2^{\infty} = \tau_{12} + \tau_{21}e^{-\alpha_{12}\tau_{21}} \qquad 9\text{-}6$$

Where
γ_2^{∞} is the infinite dilution activity coefficient for monoethanolamine.

From Equation 9-6, we can see how excess Gibbs energy and activity coefficients are related through model parameters. The creation of the H_2O-MEA model begins with the regression of literature data. Twelve data sets have been regressed with the elecNRTL model to represent the phase equilibrium of a single solvent system through regression of total vapor pressure [Nath and Bender (1983) and Touhara et al. (1982)], vapor-liquid equilibrium [Park and Lee (1997), Tochigi et al. (1999), Cai et al. (1996), and from this work], specific heat capacity [Pagé et al. (1993), Chiu and Li (1999), Weiland et al. (1997), and from this work], and freezing point depression [Chang et al. (1993)] data over monoethanolamine

solutions. The elecNRTL model was never designed to regress excess enthalpy data thus we will reserve literature data from Touhara et al. (1982) and Posey (1996) until a comparison can be made from predictions based on an optimum set of binary interaction parameters. For more information, please refer to Section 9.4.5.

The following stoichiometric chemical equilibrium expression (Equation 9-7) for the dissociation of monoethanolamine is given below:

$$MEAH^+ \leftrightarrow MEA(l) + H^+ \qquad 9\text{-}7$$

Equation 9-7 describes the dissociation of protonated monoethanolamine $\left(MEAH^+\right)$ ion to aqueous monoethanolamine and proton $\left(H^+\right)$ ion. The chemical equilibrium constant for the above reaction was determined analytically from pKa data reported by Bates and Pinching (1951) and corrected, based on the optimum binary interaction model parameters, for the symmetric reference state for the activity coefficient of monoethanolamine from infinite dilution in water to infinite dilution in amine solvent. We were then able to determine the following standard state properties: the infinite dilution aqueous phase free energy of formation $\left(\Delta G_f^{\infty,aq}\right)$ and the infinite dilution aqueous phase enthalpy of formation $\left(\Delta H_f^{\infty,aq}\right)$ for protonated monoethanolamine.

The following section describes the different types of data used in the creation of the binary H_2O-MEA elecNRTL model.

9.2.1 *Total Vapor Pressure*

Data in the form of total vapor pressure from aqueous monoethanolamine solutions as a function of concentration and temperature was used to adjust the activity coefficients of

monoethanolamine and water through the simultaneous regression of the binary interaction parameters in the elecNRTL model. For the binary system, the following equation can be used to represent the equilibrium for the total vapor pressure data.

$$P = x_{MEA}\gamma_{MEA}P^0_{MEA} + x_{H_2O}\gamma_{H_2O}P^0_{H_2O} \quad 9\text{-}8$$

Where
P is the total pressure of the system,
x_i is the apparent mole fraction of component i,
γ_i is the symmetric activity coefficient of component i,
P_i^0 is the Extended Antoine pure vapor pressure of component i.

Note, total vapor pressure data does not allow for the direct calculation of individual component activity coefficients or extrapolation to infinite dilution. Therefore, activity coefficients regressed from total pressure data cannot be accurately determined. An example of the experimental total vapor pressure data used in this work by Nath and Bender (1983) and Touhara et al. (1982) from 333 – 393 K at 2 m PZ and from 353 – 393 K at 4 m PZ are shown in Figures 9.2-1 and 9.2-2, respectively.

9.2.2 *Vapor-Liquid Equilibrium*

Data in the form of vapor-liquid equilibrium (VLE), which measures the vapor and liquid compositions in aqueous monoethanolamine solutions, as a function of concentration and temperature were also used to adjust the activity coefficients of monoethanolamine and water through the simultaneous regression of the binary interaction parameters in the NRTL model. For the binary system, Equation 9-9 can be used to represent the vapor-liquid equilibrium data.

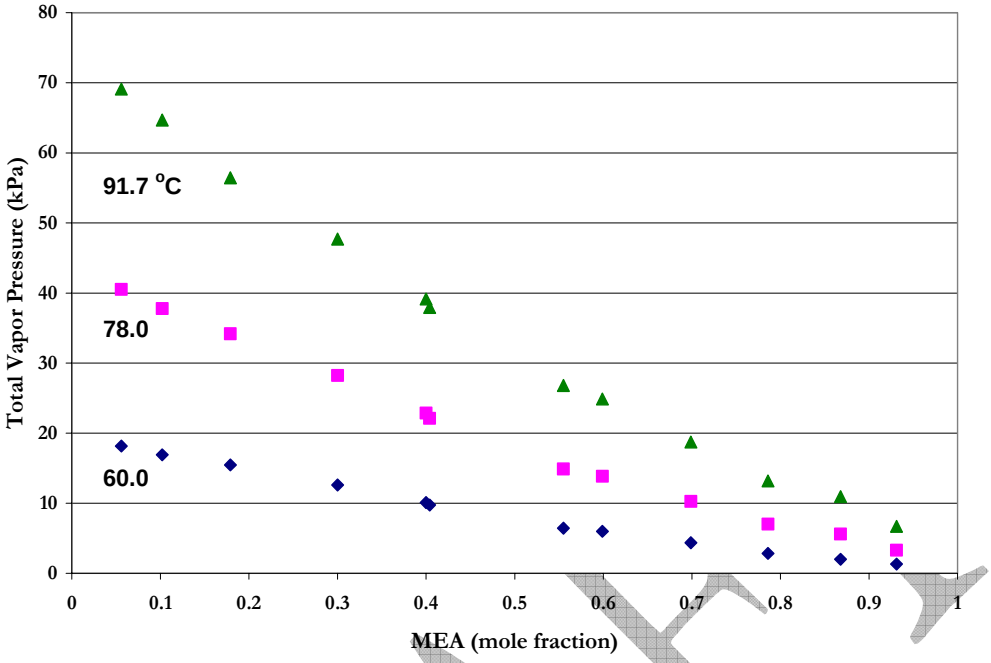

Figure 9.2-1. Total Vapor Pressure at 60, 78, and 91.7 °C. Points: Nath and Bender (1983).

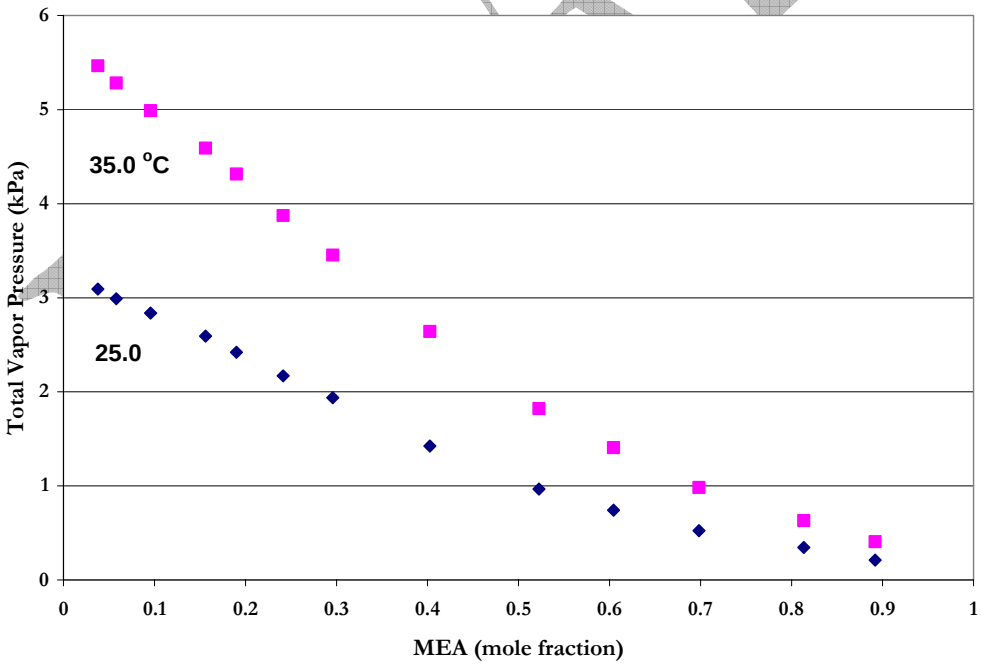

Figure 9.2-2. Total Vapor Pressure at 25.0 and 35.0 °C. Points: Touhara et al. (1982).

$$y_i P = x_i \gamma_i P_i^0 \qquad 9\text{-}9$$

Where

y_i is the vapor mole fraction of component i,

P is the total pressure of the system,

x_i is the liquid mole fraction of component i,

γ_i is the symmetric activity coefficient of component i,

P_i^0 is the Extended Antoine pure vapor pressure of component i.

Examples of experimental isobaric vapor-liquid equilibrium used in this work from Park and Lee (1997) and Cai et al. (1996) are shown in Figure 9.2-3 and for isothermal vapor-liquid equilibrium from Tochigi et al. (1999) in Figure 9.2-4. As previously shown in Chapter II, amine volatility from this work between 3.5 and 23.8 m MEA is presented in Figure 9.2-5.

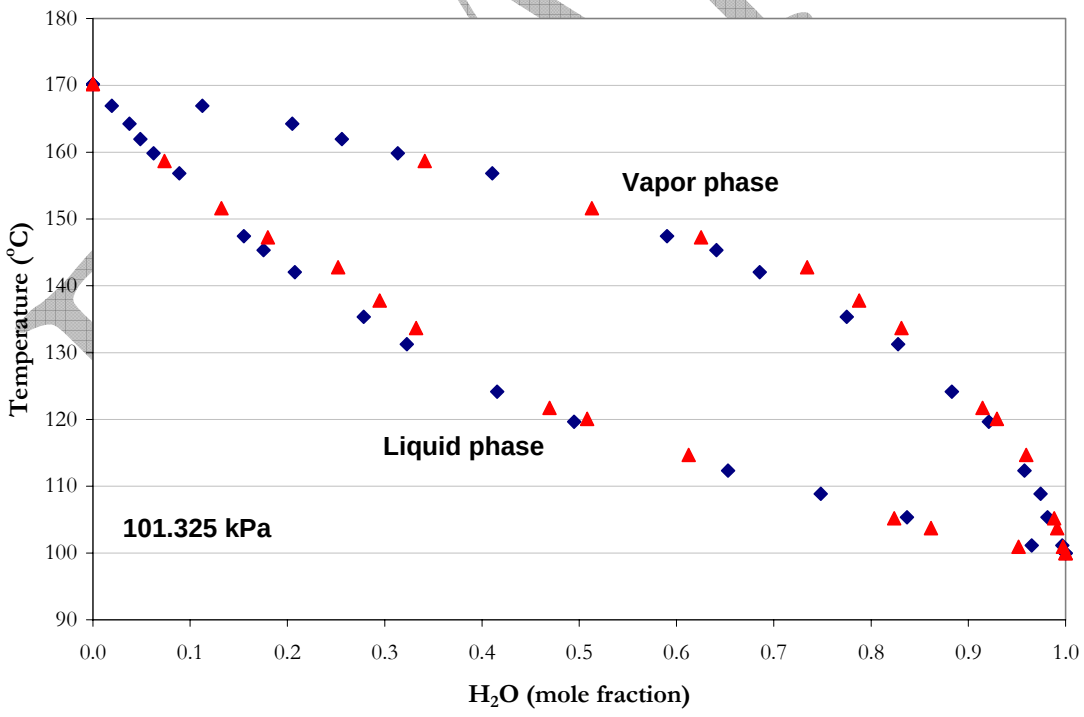

Figure 9.2-3. Isobaric VLE at 101.325 kPa. Points: ♦, Park and Lee (1997) and ▲, Cai et al. (1996).

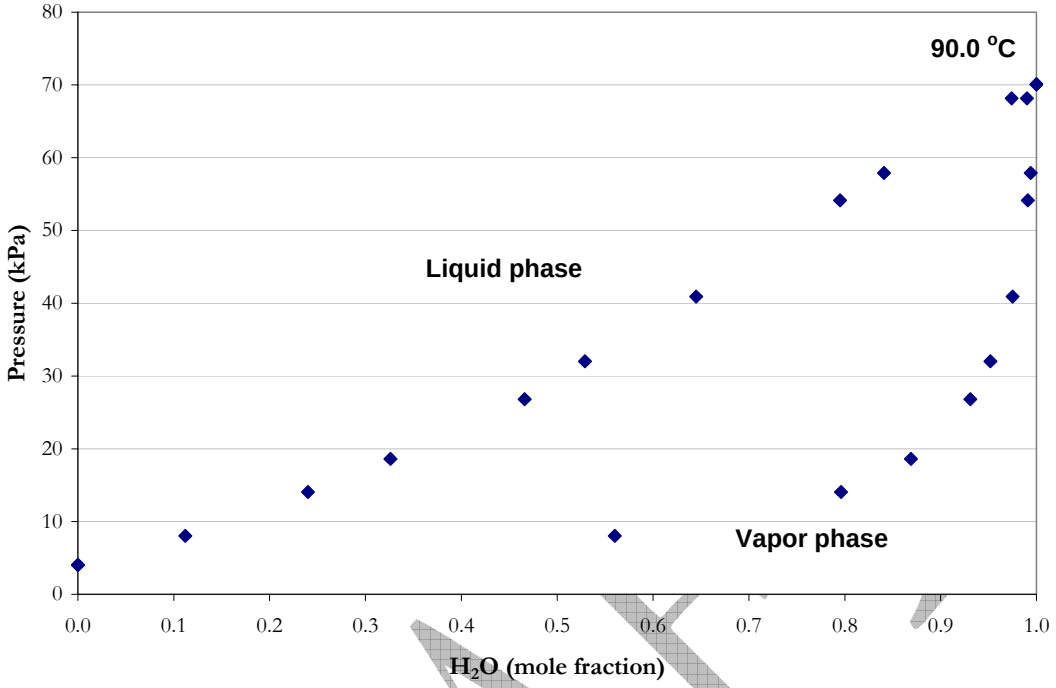

Figure 9.2-4. Isothermal VLE at 90.0 °C. Points: ◆,Tochigi et al. (1999).

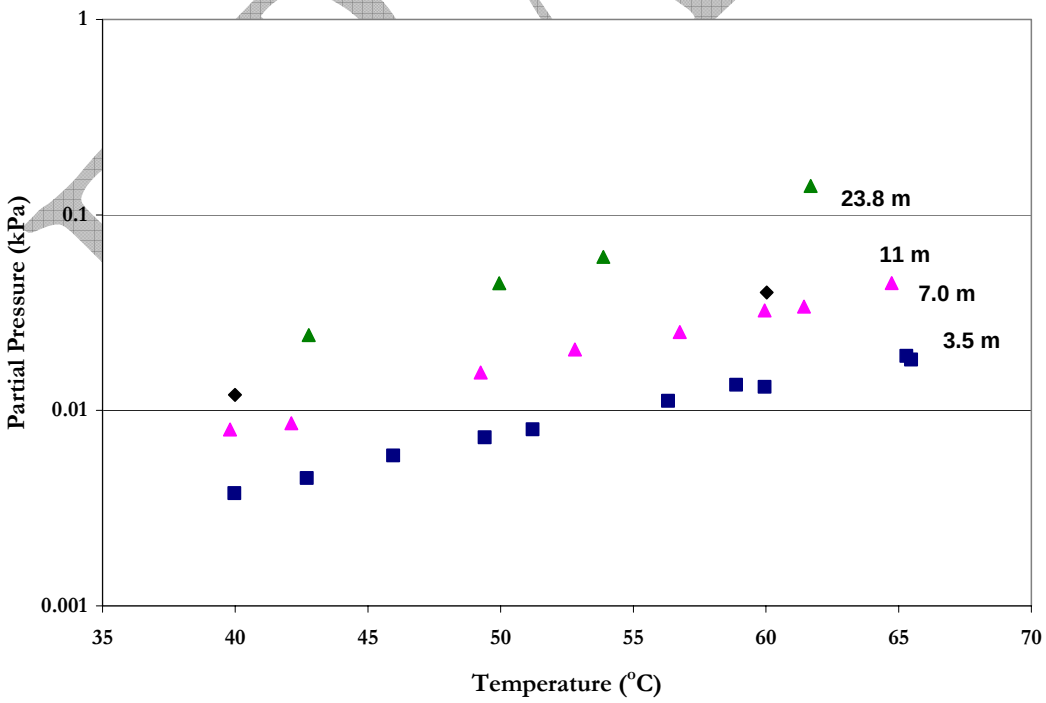

Figure 9.2-5. Amine Volatility for 3.5, 7, 11, and 23.8 m MEA from this work.

9.2.3 *Specific Heat Capacity*

As stated in Chapter VIII, Aspen Plus™ calculates the liquid phase heat capacity of a *mixture* (CPMX) by taking the derivative of the liquid enthalpy at constant pressure:

$$H_i^l\left(T+\Delta T\right)-H_i^l\left(T\right)=\int_T^{T+\Delta T} C_{p,i}^l dT \qquad 9\text{-}10$$

where the liquid enthalpy of a mixture is calculated by the following equation:

$$H_i^l\left(T\right)=\sum_i x_i H_i + H_i^E \qquad 9\text{-}11$$

$$H_i\left(T\right)=\Delta H_f^{ig}\left(T^{ref}\right)+\int_{T^{ref}}^{T} C_p^{ig} dT+\left[H_i\left(T,p\right)-H_i^{ig}\left(T,p\right)\right] \qquad 9\text{-}12$$

Where
ΔT is the perturbation in temperature from T,
H_i^E is the excess enthalpy of component i,
$\Delta H_f^{ig}\left(T^{ref}\right)$ is the standard enthalpy of formation of component i at T^{ref},
T^{ref} is the reference temperature, 25.0 °C,
C_p^{ig} is the ideal gas heat capacity of component i,
H_i^{ig} is the ideal gas enthalpy of component i.

Data in the form of specific heat capacity of a mixture as a function of concentration and temperature were used to adjust the activity coefficients of monoethanolamine and water through the simultaneous regression of the binary interaction parameters by taking the derivative of the NRTL model, vis-à-vis excess enthalpy. Thus, specific heat capacity effects are limited only to the second and third terms of Equations 9-2 and 9-3. Examples of experimental specific heat capacity used in this work are from: Pagé et al. (1993) and Weiland et al. (1997) at 25 °C, Pagé et al. (1993), Chiu and Li (1999), and from this work at

40 °C, and from Chiu and Li (1999) and from this work at 60 °C, as shown in Figures 9.2-6, 9.2-7, and 9.2-8, respectively.

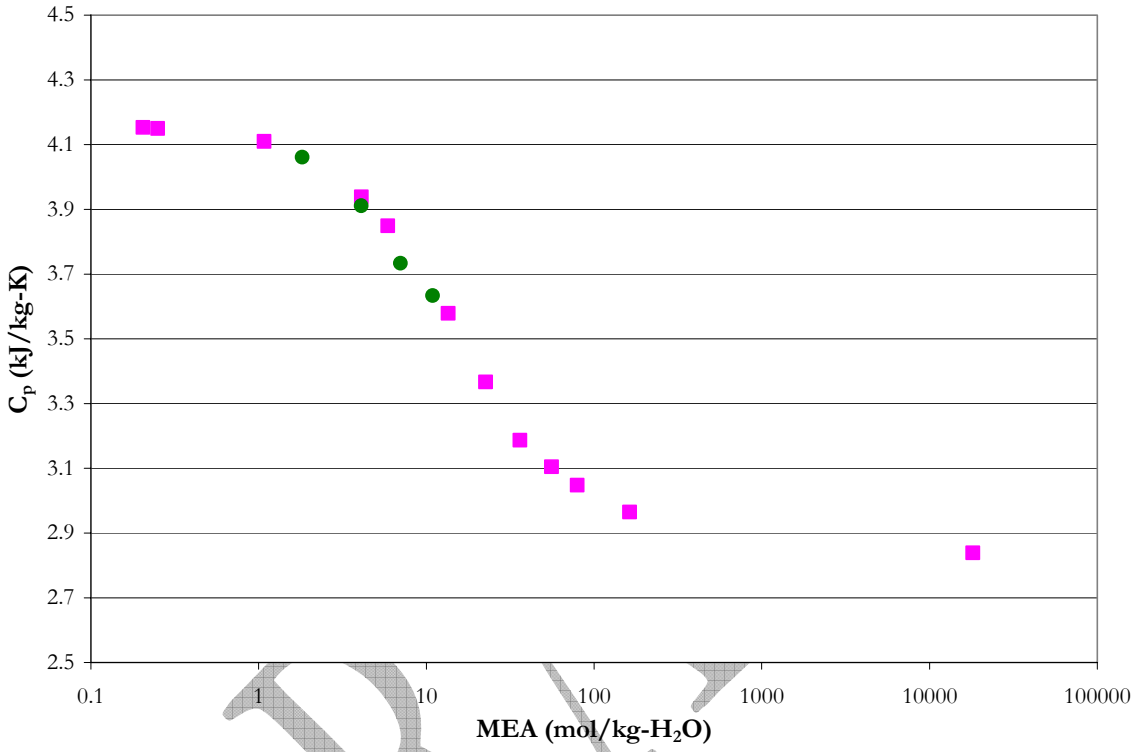

Figure 9.2-6. Specific Heat Capacity at 25.0 °C. Points: ■, Pagé et al. (1993) and ●, Weiland et al. (1997).

9.2.4 *Excess Enthalpy*

Prausnitz et al. (1999) noted that the behavior of a real binary mixture is frequently described using excess properties. In the electrolyte-NRTL model, one of the main goals is the ability to describe the excess Gibbs energy of a system, including temperature derivatives, to accurately represent deviations from ideal solution behavior. In this case, the excess enthalpy of mixing is referred to more commonly as the heat of mixing through Equation 9-13.

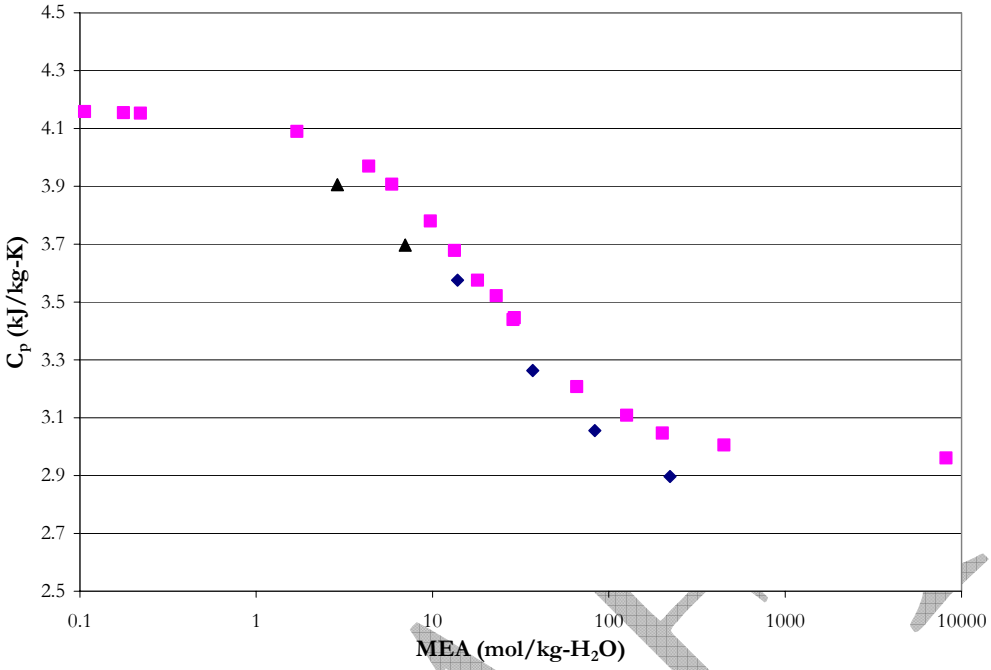

Figure 9.2-7. Specific Heat Capacity at 40.0 °C. Points: ■, Pagé et al. (1993), ♦, Chiu and Li (1999), and ▲, this work.

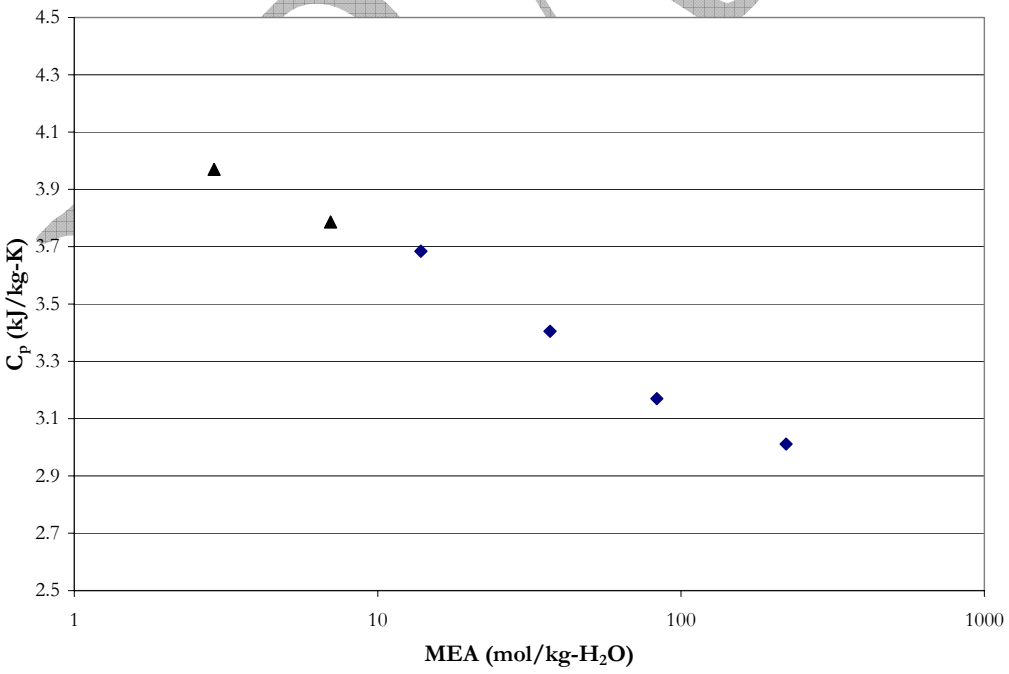

Figure 9.2-8. Specific Heat Capacity at 60.0 °C. Points: ♦, Chiu and Li (1999) and ▲, this work.

$$-\frac{H_i^E}{RT^2}=\left(\frac{\partial G_i^E / RT}{\partial T}\right)_{P,x_i} \qquad 9\text{-}13$$

By apply the partial molar property to Equation 9-13, an expression describing the relationship between the temperature dependence of the activity coefficient and the excess Gibbs energy is given by Equation 9-14.

$$\left(\frac{\partial \ln \gamma_i}{\partial T}\right)_{P,x} = -\frac{H_i^E}{RT^2} \qquad 9\text{-}14$$

For a binary mixture, the molar excess enthalpy can be described by the following expression:

$$H_m^{E,l} = -RT^2 \sum_i x_i \left(\frac{\partial \ln \gamma_i}{\partial T}\right) \qquad 9\text{-}15$$

Where
$H_m^{E,l}$ is the liquid molar excess enthalpy of the mixture,
x_i is the mole fraction of component i,
γ_i is the symmetric activity coefficient of component i.

An example of experimental excess enthalpy data from Touhara et al. (1982) and Posey (1996) at 25 and 70 °C is shown in Figure 9.2-9.

9.2.5 *Freezing Point Depression*

Freezing point depression of aqueous MEA mixtures from Chang et al. (1993) were transformed to represent the partial pressure of water, P^{H_2O}. Harned and Owen (1950) related the activity of water to the freezing point depression of water through Equation 9-15.

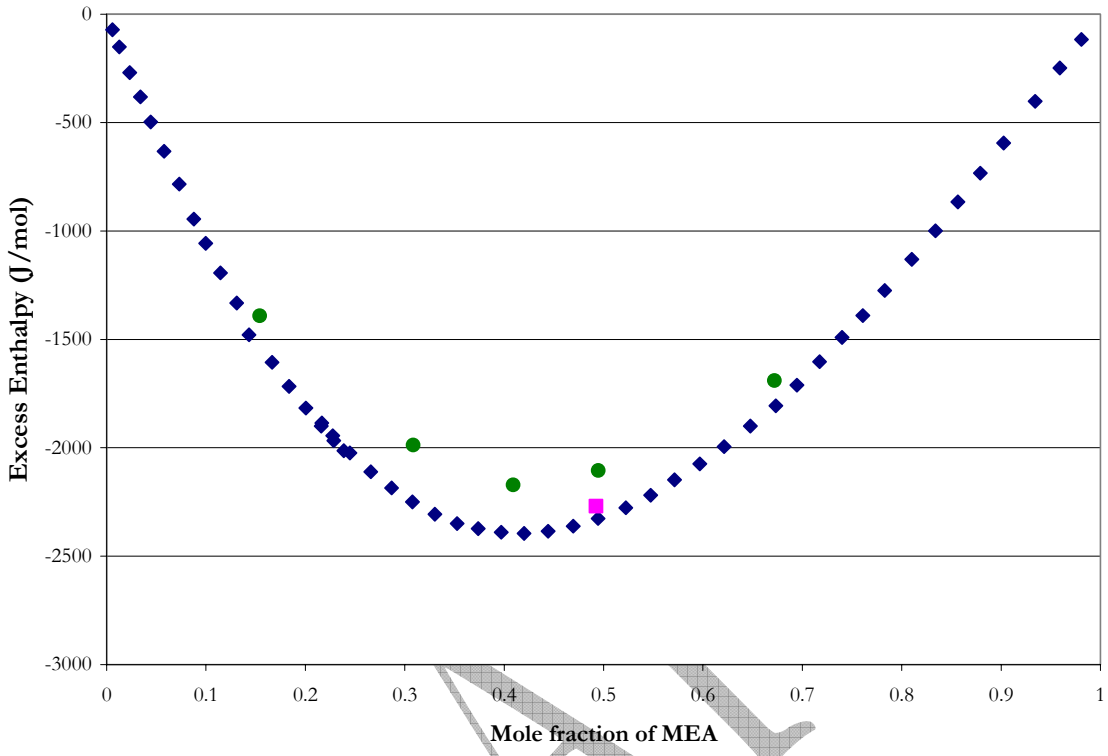

Figure 9.2-9. Excess Enthalpy at 25.0 and 70.0 °C. Points: ♦, Touhara et al. (1982), ■, Posey (1996) at 25 °C, and ●,Posey (1996) at 75 °C.

$$-\ln\left(a_w\right)=\Delta T_f\left(\frac{\Delta H_f}{R\cdot T_o^2}\right)+\frac{\Delta T_f^2}{T_o^2}\left(\frac{\Delta H_f}{R\cdot T_o}-\frac{\Delta C_p}{2\cdot R}\right) \qquad 9\text{-}16$$

simplifying and substituting Equation 9-16 into Equation 9-9, an expression for the partial pressure of water as a function of the freezing point depression vis-à-vis activity of water, is given below

$$P_{H_2O}=\exp\left(\frac{-0.018\cdot\Delta T_f}{1.858}\right)P^o_{H_2O} \qquad 9\text{-}17$$

Where

a_w is the activity of water,

R is the universal gas constant, 8.314 J/mole-K,

T_o is the melting point of ice, 0.0 °C,

ΔT_f is the freezing point depression, $T_o - T_f$,

T_f is the mixture freezing point, °C,

ΔH_f is the heat of fusion of water, -6.008 kJ/mole,

ΔC_p is the heat capacity difference between water and ice, 37.6 J/mole-K.

Freezing point depression in the form of vapor pressure of water, as a function of molality and temperature, was used to adjust the activity coefficient of water for the H_2O-MEA system through the simultaneous regression of the binary interaction parameters in the electrolyte NRTL model.

An example of the vapor pressure of water based on Equation 9-17 from literature of Chang et al. (1993) is shown in Figure 9.2-10 from -20.0 to -5.0 °C.

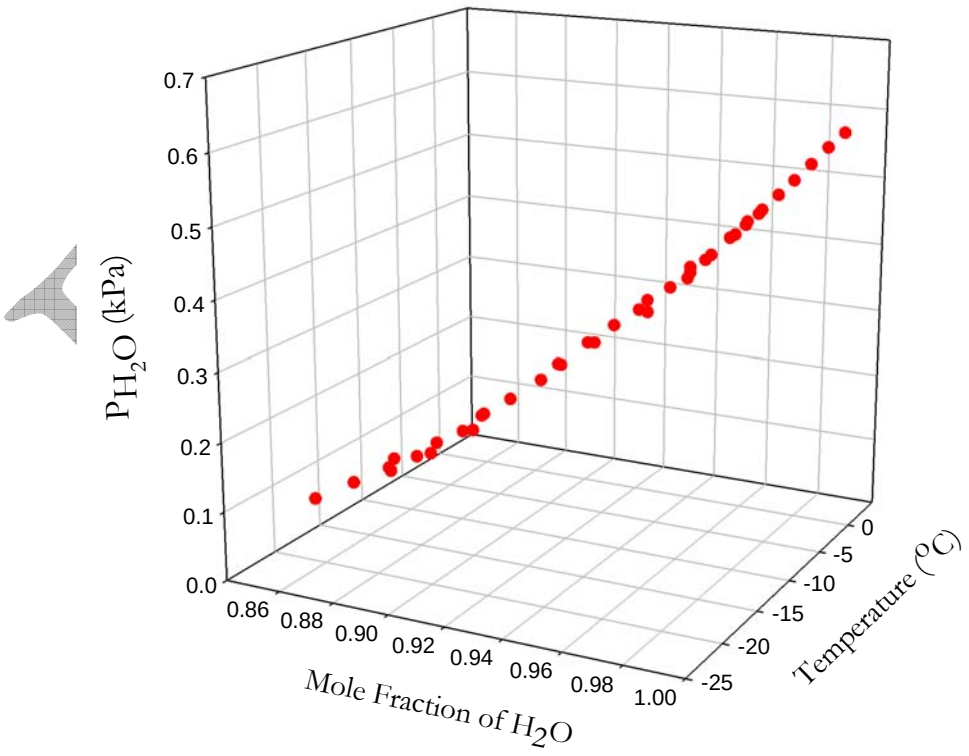

Figure 9.2-10. Partial Pressure of H_2O based on Equation 9-17 from Freezing Point Depression Data by Chang et al. (1993) from -20.0 to -5.0 °C.

9.2.6 *Dissociation Constant of Monoethanolamine*

Recall from Chapter VII that the chemical equilibrium or dissociation constant for Equation 9-7 in terms of the activity is given by the following relationship:

$$K^* = \frac{a_{MEA} \cdot a_{H_3O^+}}{a_{MEAH^+} \cdot a_{H_2O}} \qquad 9\text{-}18$$

where the thermodynamic equilibrium constant can be defined as

$$\ln K^* = \left(\frac{-\Delta G_m^o}{RT} \right) \qquad 9\text{-}19$$

$$\Delta G_m^o = \sum_i \nu_i \mu_i^o \qquad 9\text{-}20$$

Where
K^* is the asymmetric chemical equilibrium constant for Equation 9-7 (molality based),
a_i is the activity of component i,
ΔG_m^o is the standard molar Gibbs free energy change for Equation 9-7,
ν_i is the stoichiometric coefficient of component i,
μ_i^o is the reference chemical potential for component i.

The chemical equilibrium constant vis-à-vis component activities provides the connection between the standard Gibbs free energy change of reaction to the standard (reference) states of the individual species activities in a given reaction. In this work, H_2O and MEA were regarded as solvents and the solution was treated as a mixed-solvent system and described by the symmetric reference state convention where the activity coefficient approaches one as the mole fraction of the species approaches its pure liquid state.

Experimental pKa data from Bates and Pinching (1951) (Figure 9.2-11) were used analytically, to determine the chemical equilibrium constant for Equation 9-7 for the

dissociation constant of monoethanolamine. We were then able to determine the following standard state infinite dilution aqueous phase properties: the free energy of formation $\left(\Delta G_f^{\infty,aq}\right)$, the enthalpy of formation $\left(\Delta H_f^{\infty,aq}\right)$, and coefficients for the temperature dependent heat capacity $\left(\Delta C_p^{\infty,aq}\right)$ of protonated monoethanolamine.

Chemical equilibria reported in literature are normally referenced to infinite dilution in water (molality based), treating monoethamine as a solute. Solute and ionic activity coefficients are described by the asymmetric reference state convention which states that as the activity coefficient approaches one, the mole fraction of the species approaches zero in pure water.

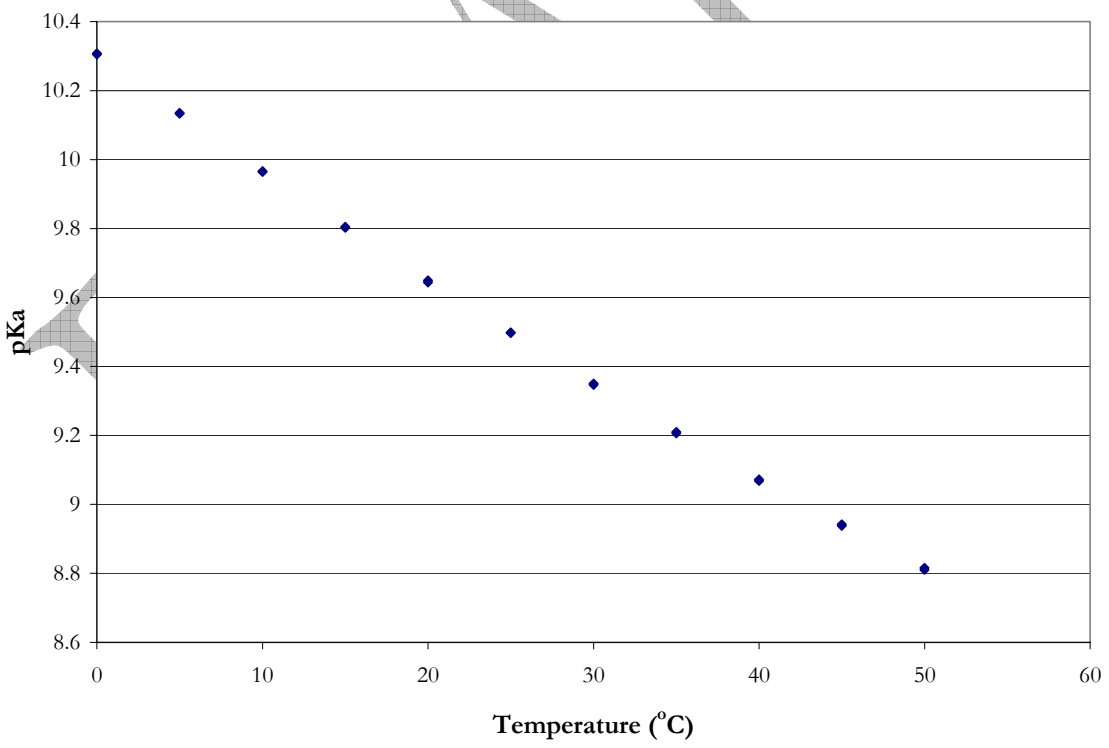

Figure 9.2-11. Experimental pKa from Bates and Pinching (1951) for the Dissociation Constant of Monoethanolamine (molality based) from 0 to 50 °C.

Bates and Pinching (1951) found it helpful to express the chemical equilibrium as a p-function where the p-function is the negative logarithm (base 10) of the number as given by the following expression:

$$pK = -\log_{10}(K) \tag{9-21}$$

Where
p is the p-function of a numerical datum.

In this work, chemical equilibrium constants are defined in terms of mole fractions; therefore the chemical equilibrium constant reported by Bates and Pinching (1951) has to be converted. However, due to the asymmetric reference state convention, the chemical equilibrium constant of monoethanolamine requires an additional conversion to the symmetric reference state convention since all subsequent monoethanolamine based ionic equilibrium constants are determined based on the asymmetric reference state convention referenced to infinite dilution in monoethanolamine. These two reference state conventions are related for monoethanolamine by the following expression:

$$\frac{\gamma_{MEA}}{\gamma^{*}_{MEA}} = \lim_{x_{MEA}\to 0} \gamma_{MEA} = \gamma^{\infty}_{MEA} \tag{9-22}$$

Where
γ_{MEA} is the symmetric activity coefficient for monoethanolamine,
γ^{*}_{MEA} is the asymmetric activity coefficient for monoethanolamine as the solution approaches its pure solute reference state.

Thus, the chemical equilibrium constant of monoethanolamine (Equation 9-7) referenced to the symmetric reference state convention used in this work is related by the following expression:

$$\ln K^* = \ln K + \ln\left(\frac{1000}{MW_w}\right)\sum_{i\neq w}\nu_i + \ln\gamma^{\infty}_{MEA} \qquad 9\text{-}23$$

Where
MW_w is the molecular weight of H_2O, 18.01528 gm/mole,
K is the symmetric chemical equilibrium constant (mole fraction based).

The infinite dilution activity coefficient of monoethanolamine is calculated from the binary interaction parameters for the water-monoethanolamine system using the elecNRTL model. The resulting values were then re-regressed to the standard temperature dependent form of the chemical equilibrium constant given in Chapter VII and compared to Equation 9-6. This modified chemical equilibrium constant for monoethanolamine was then utilized in the elecNRTL model within Aspen Plus™ to specify the infinite dilution standard state free energy and enthalpy of formation, respectively, for protonated monoethanolamine. Therefore, chemical equilibrium constants reported in this work must be corrected for the infinite dilution activity coefficient of monoethanolamine prior to comparison with other work.

9.3 Data Regression

For the elecNRTL model, binary interaction parameters for molecule-molecule interactions were given a default value of zero.

Through simultaneous regression, the molecule-molecule binary interaction parameters for the H_2O-MEA system were obtained through the regression of total vapor pressure [Nath and Bender (1983) and Touhara et al. (1982)], vapor-liquid equilibrium [Park and Lee (1997), Tochigi et al. (1999), Cai et al. (1996), and from this work], specific heat

capacity [Pagé et al. (1993), Chiu and Li (1999), Weiland et al. (1997), and from this work], and freezing point depression [Chang et al. (1993)] data over monoethanolamine solutions.

A list of the aqueous electrolyte data sets that were examined in this work is given in Table 9.3-1. The column labels σ_T, σ_P, σ_{Cp}, σ_{x_i}, σ_{y_i}, give standard error associated with the temperature, pressure, specific heat capacity, liquid mole fraction, and the vapor mole fraction, respectively, with each data set. DRS suggested standard error default values were assigned unless otherwise stated by the author.

Table 9.3-1. Experimental data used in the regression of the H_2O-MEA system.

	Obs.	T (°C)	σ_T	σ_P	σ_x	σ_y	Source
TP	36	60.0 – 91.7	0.05	0.25%	0.1%	10%	Nath and Bender (1983)
	26	25.0 – 35.0	0.01	0.25%	0.1%	10%	Touhara et al. (1982)
	Obs.	T (°C)	σ_T	σ_P	σ_x	σ_y	Source
VLE	16	101.2 – 167.0	0.1	0.1%	0.5%	0.5%	Park and Lee (1997)
	9	90.0	0.01	0.03	0.7%	0.7%	Tochigi et al. (1999)
	25	89.7 – 158.7	0.01	0.133	0.1%	0.1%	Cai et al. (1996)
	25	39.8 – 72.7	0.01	0.1%	0.1%	0	This work
	Obs.	T (°C)	σ_T	σ_x	σ_{Cp}		Source
Cp	48	10.0 – 40.0	0.01	0.1%	0.1%		Pagé et al. (1993)
	44	30.0 – 80.0	0.01	0.1%	0.1%		Chiu and Li (1999)
	4	25.0	0.01	0.1%	0.1%		Weiland et al. (1997)
	34	40.0 – 120.0	0.01	0.1%	0.1%		This work
	Obs.	T (°C)	σ_T	σ_P	σ_x	σ_y	Source
P^{H2O}	40	-20.5 – (-0.5)	0.01	2.0%	0.1%	0	Chang et al. (1993)

After performing a nonlinear regression for the full model using DRS, the following regression summary statistics output for estimates of the adjustable binary parameter coefficients are shown in Table 9.3-2.

Table 9.3-2. DRS Regression Output for Full H_2O-MEA System Model.

Parameter	Interacting Species i	Interacting Species j	Estimate	σ wrt Estimate
1-$A_{m,m}$	H_2O	MEA	-434	23.1
2-$B_{m,m}$	H_2O	MEA	11272	778
3-$C_{m,m}$	H_2O	MEA	75.8	3.97
4-$D_{m,m}$	H_2O	MEA	-0.1111	0.0069
5-$A_{m,m}$	MEA	H_2O	115	12.1
6-$B_{m,m}$	MEA	H_2O	-3483	406
7-$C_{m,m}$	MEA	H_2O	-20.2	2.04
8-$D_{m,m}$	MEA	H_2O	0.0308	0.0031

Residual Sum of Squares:	724,121
Residual Root Mean Square:	49.294
Degree of Freedom:	299

Recall that the standard error of an estimate is the estimated standard deviation of that statistic. Notice that all of the estimates are large relative to their standard errors. A complete description of the variability of the coefficient estimates requires examining the correlations between the estimates as shown in Table 9.3-3.

Table 9.3-3. Correlation Matrix of the Coefficient Estimates, for the Full H_2O-MEA Model.

Parameter	1	2	3	4	5	6	7	8
1	1.00							
2	-0.87	1.00						
3	*-0.99*	0.82	1.00					
4	0.83	-0.47	-0.88	1.00				
5	-0.79	0.77	0.76	-0.57	1.00			
6	0.68	-0.86	-0.61	0.26	*-0.91*	1.00		
7	0.80	-0.74	-0.78	0.62	*-1.00*	0.86	1.00	
8	-0.77	0.50	0.79	-0.84	0.86	-0.57	*-0.90*	1.00

Table 9.3-3 shows a high negative correlation between $\hat{\eta}_{3\to1}$ for the first energy parameter estimate, $\tau_{H_2O/MEA}$, but the correlation between other coefficients is relatively small, suggesting that $\hat{\eta}_3$ might be usefully removed from the model without significant loss

of information. On the other hand, Table 9.3-3 shows three highly correlated coefficients for τ_{MEA/H_2O} where a submodel containing fewer coefficients for the τ_{MEA/H_2O} expression might be useful without a significant loss of information.

After performing backward elimination using DRS, the following optimum model regression summary statistics output for estimates of the adjustable binary parameter coefficients are shown in Table 9.3-4. Please refer to Appendix O for more information about the backward elimination procedure to determine the optimal set of binary interaction parameters for the H_2O-MEA system.

Table 9.3-4. DRS Regression Output for Optimum H_2O-MEA Model.

Parameter	Interacting Species i	Interacting Species j	Estimate	σ wrt Estimate
1-$A_{m,m}$	H_2O	MEA	-123	9.65
2-$B_{m,m}$	H_2O	MEA	2575	306
3-$C_{m,m}$	H_2O	MEA	22.1	1.65
4-$D_{m,m}$	H_2O	MEA	-0.0297	0.0022
5-$A_{m,m}$	MEA	H_2O	-1.71	0.149
6-$B_{m,m}$	MEA	H_2O	-214	66.3

Residual Sum of Squares: 740,215
Residual Root Mean Square: 49.673
Degree of Freedom: 301

Notice that all of the estimates are larger relative to their standard errors. Comparing the estimates from the full model to the optimum model, there was relatively little difference between the estimated values. The proposed optimum model provides the following correlations between the estimates as shown in Table 9.3-5.

Table 9.3-5. Correlation Matrix of the Coefficient Estimates, for the Optimum H_2O-MEA Model.

Parameter	1	2	3	4	5	6
1	1.00					
2	*-0.96*	1.00				
3	*-1.00*	*0.96*	1.00			
4	*0.99*	*-0.95*	*-0.99*	1.00		
5	-0.14	0.34	0.13	-0.10	1.00	
6	0.26	-0.46	-0.25	0.19	*-0.91*	1.00

Table 9.3-5 again shows highly negative correlations between all of the $\tau_{H_2O/MEA}$ parameters suggesting that some of the remaining parameters might be usefully removed from the model without significant loss of information.

Results from the previous section show that dropping a term from the full model may provide a submodel that may have a decrease in the correlation between the estimate coefficients and improve the reliability of the model. Testing whether any subset of the regression estimate coefficients may be zero plays an important role in many analyses which leads to the following hypotheses:

NH: $3C_{m,m} = 7C_{m,m} = 0$ Submodel function applies

AH: At lease one $3C_{m,m}, 7C_{m,m} \neq 0$ Full model function applies

We can perform an F-Test to compare the purposed submodel with the full model. Significance levels for this test are obtained by comparing the observed value of F to the $F_{df_{NH}-df_{AH},df_{AH}}$ distribution. The p-value is then computed as an upper-tail test and gives the probability associated with evidence to reject the null hypothesis which will then be compared to the results given by the submodel.

If we were to remove the highly correlated parameters from the full model, the following submodel regression summary statistics output for estimates of the adjustable binary parameter coefficients is shown in Table 9.3-6.

Table 9.3-6. DRS Regression Output for H_2O-MEA Submodel.

	Interacting Species			
Parameter	i	j	Estimate	σ wrt Estimate
1-$A_{m,m}$	H_2O	MEA	-4.46	0.67
2-$B_{m,m}$	H_2O	MEA	-85.3	174
3-$D_{m,m}$	H_2O	MEA	0.0149	0.0011
4-$A_{m,m}$	MEA	H_2O	2.90	0.72
5-$B_{m,m}$	MEA	H_2O	-456	190
6-$D_{m,m}$	MEA	H_2O	-0.0079	0.0007

Residual Sum of Squares: 831,795
Residual Root Mean Square: 52.656
Degree of Freedom: 301

Notice that only one of the estimates is smaller relative to the standard error. Comparing the estimates from the submodel to the full model, there was large difference between the estimated values with respect to the order of magnitude. The residual sum of squares and the standard errors for the submodel have increased as compared to the full model. The proposed submodel provides the following estimated covariances between the estimates as shown in Table 9.3-7.

Table 9.3-7 shows parameter $\left(2B_{m,m}\right)$ is highly correlated to the first coefficient, $\left(1A_{m,m}\right)$, suggesting that $\hat{\eta}_2$ might be usefully removed from the model without significant loss of information.

Table 9.3-7. Correlation Matrix of the Coefficient Estimates for the H_2O-MEA Submodel.

Parameter	1	2	3	4	5	6
1	1.00					
2	*-0.91*	1.00				
3	-0.86	0.77	1.00			
4	-0.82	0.80	0.50	1.00		
5	0.79	*-0.91*	-0.60	*-0.91*	1.00	
6	*0.90*	-0.79	-0.61	*-0.97*	0.83	1.00

The two models were then compared using the test statistic F applied to the null hypothesis versus the alternative:

$$\frac{\left[\frac{831795-724121}{301-299}\right]}{\left[\frac{724121}{299}\right]} \sim 22.4355(2,299)$$

We can then calculate the probability for a F-distribution, df = 2, 299, upper-tail.

F dist. with (2, 299) df, value = 22.4355, upper-tail probability = 8.35122e-10

The finding of $p \approx 0$ provides strong evidence against the null hypothesis that $3C_{m,m} = 7C_{m,m} = 0$. Since a value of F this strong would be observed 0 times out of a hundred if the null hypothesis were true, the submodel will not give an adequate description of the data over the range of temperatures and concentration available in the data.

9.3.1 *Optimum Model Results*

With the determination of the estimates for the binary interaction parameters known for the optimum model, a simple Aspen Plus™ Flash model was used to test the predictive capability of the H_2O-MEA model against literature data. For each data point, the deviation between the experimental and estimated values is expressed in terms of the average absolute

relative deviation (AARD). Table 9.3-8 gives the percent AARD and the maximum percent AARD for the model predictions.

Table 9.3-8. Absolute Percent Relative Error for the H_2O-MEA Optimum Model.

		AARD(%)	Max. AARD
TP	Nath and Bender (1983)	2.01	6.94
	Touhara et al. (1982)	2.40	11.78
VLE	Park and Lee (1997)	6.99	11.79
	Tochigi et al. (1999)	5.49	11.59
	Cai et al. (1996)	4.81	11.27
	This work	4.28	7.02
C_p	Pagé et al. (1993)	1.95	6.26
	Chiu and Li (1999)	1.20	2.51
	Weiland et al. (1997)	2.20	2.79
	This work	0.16	0.48
P^{H2O}	Chang et al. (1993)	0.35	0.67
Overall		**2.62**	**11.79**

Overall, the model adequately describes the H_2O-MEA property data listed above within an average absolute relative error of ± 2.62 percent, with the exception of a few outliers.

9.3.2 *Chemical Equilibrium Constant*

With the determination of the estimates for the binary interaction parameters known for the optimum model, we can directly evaluate the infinite dilution activity coefficient of monoethanolamine (Equation 9-6) as given by the following expression:

$$\ln \gamma_{MEA}^{\infty} = \left(-123 + \frac{2575}{T(K)} + 22.1 \ln T(K) - 0.0297 T(K) \right) + \left(-1.71 - \frac{214}{T(K)} \right) e^{-0.2\left(-1.71 - \frac{214}{T(K)}\right)} \qquad 9\text{-}24$$

Previous authors chose to linearize the above expression into the temperature dependent form used for the chemical equilibrium constants as given by the following

expression from the ARC (2004) summary statistics output for estimates of the temperature dependent coefficients shown in Table 9.3-9:

$$\ln \gamma_{MEA}^{\infty} = -8.95 - \frac{1296}{T(K)} + 2.016 \ln T(K) \qquad 9\text{-}25$$

Table 9.3-9. ARC Regression Output for the Infinite Dilution Activity Coefficient for Monoethanolamine.

Data set = Dataset, Name of Fit = L1
Normal Regression
Kernel mean function = Identity
Response = LNMEA
Terms = (1T LNT)
Coefficient Estimates

Label	Estimate	Std. Error	t-value	p-value
Constant	-8.95461	0.735950	-12.137	0.0000
1T	-1295.89	35.7499	-36.725	0.0000
LNT	2.01628	0.108184	18.689	0.0000

R Squared:	0.999995
Sigma hat:	0.00108305
Number of cases:	17
Degrees of freedom:	14

Summary Analysis of Variance Table

Source	df	SS	MS	F	p-value
Regression	2	3.32927	1.66464	1419139.54	0.0000
Residual	14	0.0000164219	1.172989E-6		

We can then compare the two expressions as shown in Table 9.3-10. Table 9.3-10 illustrates how linearization of Equation 9-24 may cause minor errors at elevated temperatures. In this work, we chose to use Equation 9-24 to represent the infinite dilution activity coefficient of monoethanolamine due to the small variations between Equation 9-24 and Equation 9-25.

Table 9.3-10. Comparison between Equations 9-24 and 9-25 for the Natural Log Infinite Dilution Activity Coefficient for Monoethanolamine in Water.

LN Infinite Dilution Activity Coefficient for MEA			
Temp (°C)	Equation 9-24	Equation 9-25	AARD(%)
25	-1.8128	-1.8131	0.02
30	-1.7085	-1.7079	0.04
35	-1.6066	-1.6056	0.07
40	-1.5072	-1.5060	0.08
45	-1.4100	-1.4090	0.07
50	-1.3152	-1.3145	0.05
55	-1.2227	-1.2225	0.02
60	-1.1325	-1.1327	0.02
65	-1.0445	-1.0451	0.06
70	-0.9588	-0.9597	0.10
75	-0.8752	-0.8763	0.13
80	-0.7937	-0.7949	0.14
Overall			**0.07**

Since there are only minor differences between Equation 9-24 and 9-25, we can illustrate thermal effects of the solution equivalent to the infinite dilution excess enthalpy given by the following equation for MEA:

$$-\frac{\Delta H^E}{R} = \frac{d \ln \gamma_{MEA}^{\infty}}{d1/T} = -1296 + 2.016 \cdot T\left(K\right) \qquad 9\text{-}26$$

At 25 and 80 °C, the infinite dilution excess enthalpy (kJ/mol) is -12.46 and -11.34, respectively. Figure 9.3-1 illustrates experimental [Touhara et al. (1982) and Kim et al. (1987)] and predicted [Austgen et al. (1991), Posey (1996), and this work] values for the infinite dilution excess enthalpy for MEA from 20 to 100 °C.

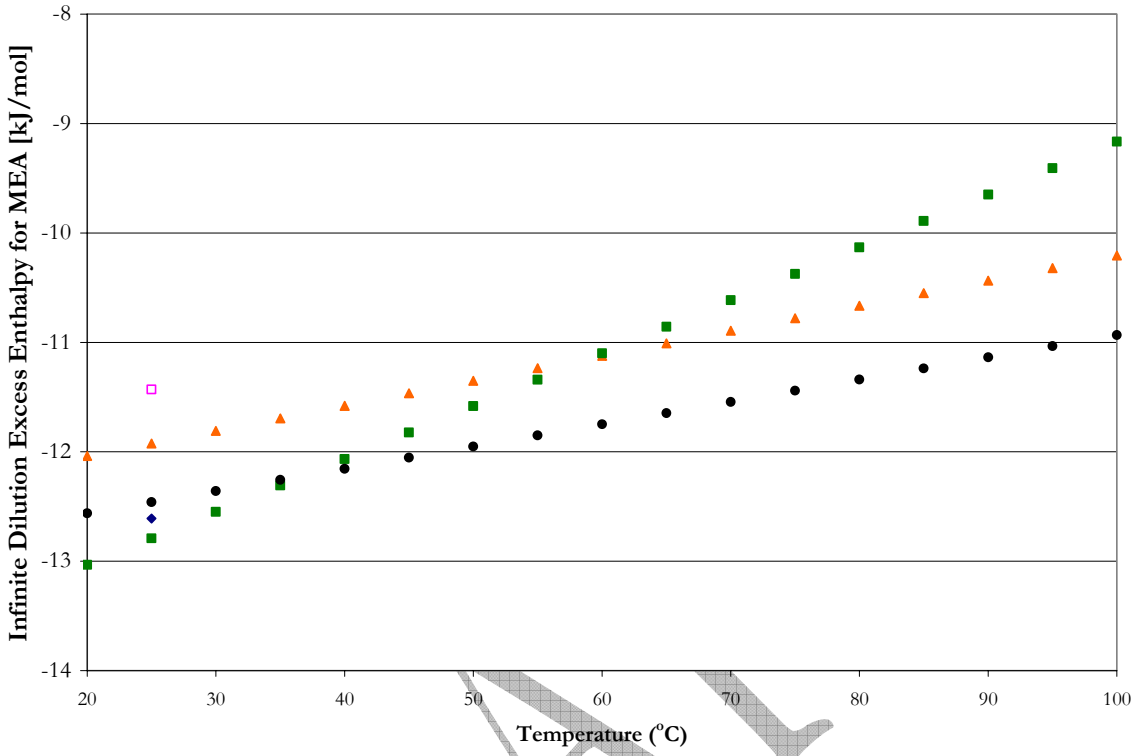

Figure 9.3-1. Infinite Dilution Excess Enthalpy for MEA from 20 to 100 °C. Points: ♦, Touhara et al. (1982), □, Kim et al. (1987), ▲, Austgen et al. (1991), ■, Posey (1996), an ●, this work.

Experimental values for the infinite dilution excess enthalpy for MEA from Touhara et al. (1982) and Kim et al. (1987) differ by ± 10% from one another. As compaired to model predictions from Posey (1996) and from this work, differ by ± 2% from Touhara et al. (1982), whereas, Austgen et al. (1991) differs from Kim et al. (1997) by ± 5%. One striking feature of Figure 9.3-1 is the temperature dependence of the infinite dilution excess enthalpy. This difference is a magnification of the temperature effect on the infinite dilution activity coefficient of MEA as shown in Figure 9.3-2.

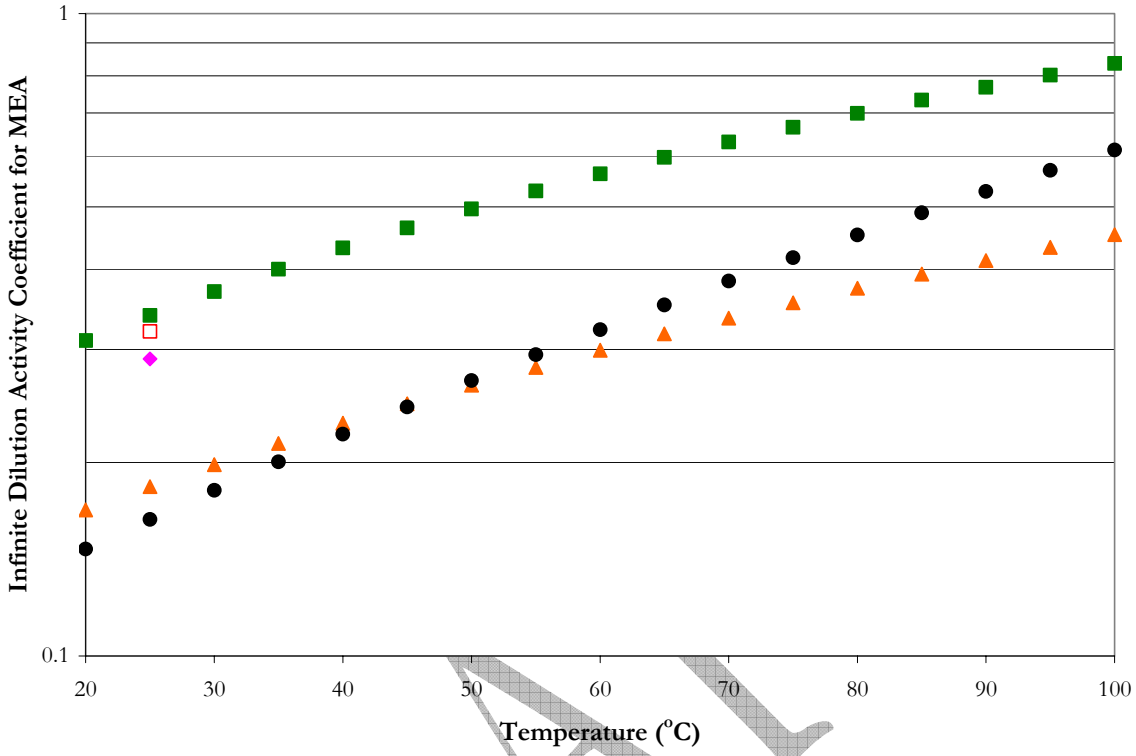

Figure 9.3-2. Infinite Dilution Activity Coefficient for MEA from 20 to 100 °C. Points: ▲, Austgen et al. (1991), □, Lee (1996), ■, Posey (1996), ♦, Poplsteinova (2004), and ●, this work.

For most activity coefficient models, the reference state for solutes is defined as infinite dilution in pure solvent; at 25 °C we can see that there is a large degree of scatter even at this temperature. The optimum model parameters were fitted to a more extensive database than previous authors, thus infinite dilution activity coefficients predicted with the optimum model may give more realistic activity coefficients as a function of temperature and composition as compared to data found in the literature.

With the determination of the above expression known, we can then regress Equation 9-23 to the standard temperature dependent form of the chemical equilibrium

constant given in Chapter VII based on experimental data reported by Bates and Pinching (1951) using ARC (2004) as shown in Table 9.3-11.

Table 9.3-11. Estimates for the Chemical Equilibrium Coefficients for the H_2O-MEA System.

Reference State	Concentration Basis	A	σ_A	B	σ_B	C	σ_C	D	σ_D
Asymmetric	Molality	3.17	6.33	-6286	281	-0.694	0.946	0.0	-
Asymmetric	Mole Fraction	-0.844	6.33	-6286	281	-0.694	0.946	0.0	-
Symmetric	Mole Fraction	-22.82	6.46	-6997	286	3.26	0.965	0.0	-

Data Reference: Bates and Pinching (1951)
$\ln K = A + B/T(K) + C \cdot \ln T(K) + D \cdot T(K)$

We can now compare our linear equilibrium constant expression for the dissociation of MEA to coefficients reported by Austgen et al. (1989) as shown in Figure 9.3-3.

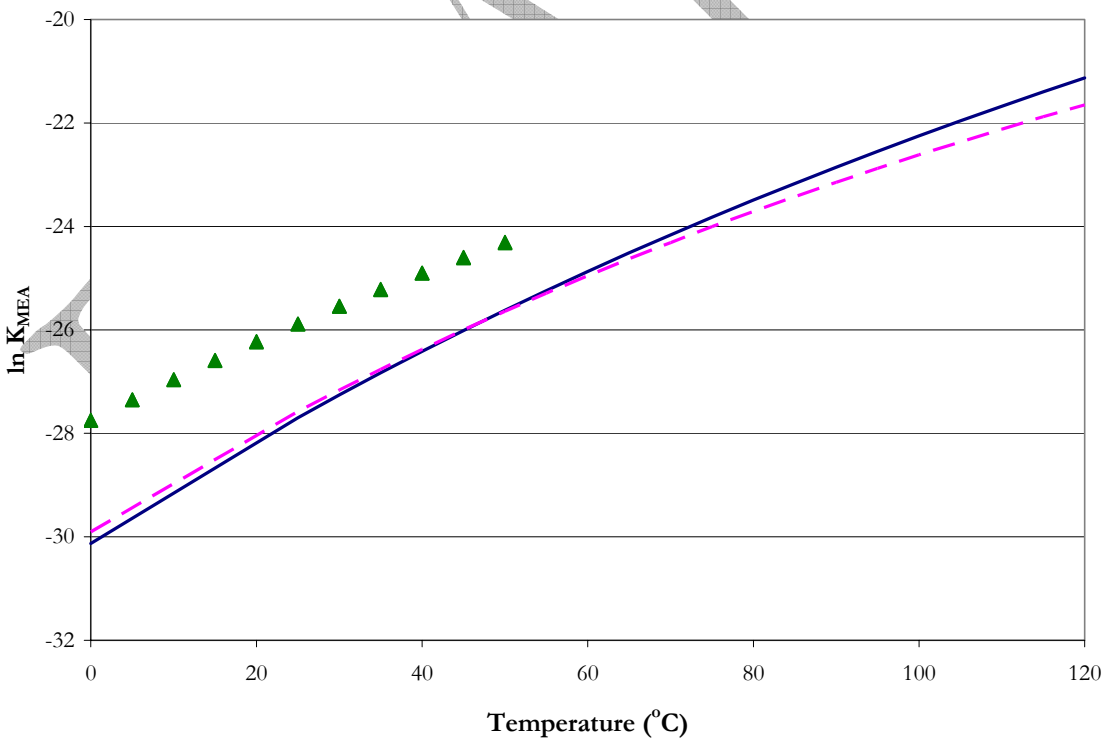

Figure 9.3-3. Comparison of the Dissociation Equilibrium Constant for MEA (mole fraction based) from 0 – 120 °C. Points: ▲, Bates and Pinching (1951). Lines: – –, Austgen et al. (1989), —, this work.

Figure 9.3-3 illustrates similar trends presented in Figure 9.3-2 where predictions for the infinite dilution activity coefficient for MEA reported by Austgen et al. (1989) as compared to predictions from this work crossed at 45 °C. Since both works utilized Bates and Pinching (1951) to describe the dissociation of MEA, the only differences between the two reported K-values would be in the treatment of the infinite dilution activity coefficient of MEA applied to the linearization of the chemical equilibrium constant to the temperature dependent functional form. Over the range (0 – 50 °C) where the experimental data are valid, the two expressions adequately describe similar trends but tend to diverge at high temperatures.

As stated previously, Equation 9-19 relates the equilibrium constant for the dissociation of MEA to the standard Gibbs free energy change of reaction.

$$\frac{\Delta G^o}{RT} = -\ln K \tag{9-27}$$

$$\frac{\Delta G^o}{RT} = -\left(A + \frac{B}{T(K)} + C \cdot \ln T(K) + D \cdot T(K) \right) \tag{9-28}$$

By taking the partial derivative of Equation 9-28 with respect to temperature; Equation 9-29 relates the standard enthalpy of reaction to the standard Gibbs free energy.

$$-\frac{\Delta H^o}{RT} = \frac{d\left(\Delta G^o / RT\right)}{dT} \tag{9-29}$$

$$\Delta H^o = RT^2 \frac{d \ln K}{dT} = RT^2 \frac{d}{dT}\left(A + \frac{B}{T(K)} + C \cdot \ln T(K) + D \cdot T(K) \right) \tag{9-30}$$

$$\Delta H^o = RT^2 \left(-\frac{B}{T(K)^2} + \frac{C}{T(K)} + D \right) \tag{9-31}$$

$$\Delta H^o = R\left(-B + C\cdot T\left(K\right) + D\cdot T\left(K\right)^2\right) \qquad 9\text{-}32$$

Where the standard property changes of reaction (e.g. Gibbs free energy and enthalpy) are defined as the difference between the standard property change of the products and reactants, weighted by their stoichiometric coefficients.

$$\Delta M^o = \sum_i \nu_i M_i^o \qquad 9\text{-}33$$

For ionic species the aqueous phase infinite dilution molar heat capacity is described by the following equation:

$$C_{p,i}^{\infty,aq}\left(\frac{J}{kmol\cdot K}\right) = C_{1,i} + C_{2,i}T\left(K\right) + C_{3,i}T\left(K\right)^2 + \frac{C_{4,i}}{T\left(K\right)} \qquad 9\text{-}34$$

The molar heat capacity of MEA was described in Chapter VIII by the following equation:

$$C_{p,MEA}^{l,*}\left(\frac{J}{kmol\cdot K}\right) = 115228 + 99.98\cdot T\left(K\right) + 0.231\cdot T\left(K\right)^2 \qquad 9\text{-}35$$

Based on Equations 9-27 to 9-32, Table 9.3-12 reports the standard property changes of formation as compare to literature values and Table 9.3-13 reports the coefficients for the aqueous phase infinite dilution heat capacity for a proton.

Table 9.3-12. Standard Property Changes of Formation at 298.15 K for Molecular and Ionic Components.

		This work.		DIPPR Literature*	
Component	ν_i	ΔG^o (kcal/mol)	ΔH^o (kcal/mol)	ΔG^o (kcal/mol)	ΔH^o (kcal/mol)
$MEAH^+$	-1	-43.2255†	-80.4807†		
MEA	1	-29.2059‡	-64.5427‡	-30.2103*	-65.5999*
H^+	1	0.0	0.0		

*Rowley et al. (2004) – DIPPR: Model Predictions.
†Calculated based on Equation 9-23.
‡Based on Chapter VIII.

Table 9.3-13. Coefficients for the Aqueous Phase Infinite Dilution Heat Capacity (J/kmol·K).

Component	C_1	C_2	C_3	C_4
H^+	0.0	0.0	0.0	0.0

For a given temperature, the molar aqueous phase infinite dilution heat capacity of $MEAH^+$ can then be determined analytically. A starting point for a rigorous development starts with the following equation:

$$\Delta G_m^o = \Delta H_m^o - T\Delta S_m^o \tag{9-36}$$

Equation 9-36 is from the definition of the molar Gibbs free energy applied to each component in a chemical reaction evaluated at the standard state. By applying Equation 9-33 to Equation 9-36 yields

$$\sum_i \nu_i G_{m,i}^o = \sum_i \nu_i H_{m,i}^o - T\sum_i \nu_i S_{m,i}^o \tag{9-37}$$

where the standard molar heat of reaction and standard molar entropy change of reaction are related to temperature by the following expressions

$$\Delta H_m^o = \Delta H_{0,m}^o + R\int_{T_0}^{T} \frac{\Delta C_{p,m}^o}{R}\, dT \tag{9-38}$$

$$\Delta S_m^o = \Delta S_{0,m}^o + R\int_{T_0}^{T} \frac{\Delta C_{p,m}^o}{R}\frac{dT}{T} \tag{9-39}$$

Equations 9-36, 9-38, and 9-39 are combined to yield

$$\Delta G_m^o = \Delta H_{0,m}^o + R\int_{T_0}^{T} \frac{\Delta C_{p,m}^o}{R}\, dT - T\Delta S_{0,m}^o - RT\int_{T_0}^{T} \frac{\Delta C_{p,m}^o}{R}\frac{dT}{T} \tag{9-40}$$

However,

$$\Delta S_{0,m}^o = \frac{\Delta H_{0,m}^o - \Delta G_{0,m}^o}{T_0} \tag{9-41}$$

hence

$$\Delta G_m^o = \Delta H_{0,m}^o - \frac{T}{T_0}\left(\Delta H_{0,m}^o - \Delta G_{0,m}^o\right) + R\int_{T_0}^{T}\frac{\Delta C_{p,m}^o}{R}dT - RT\int_{T_0}^{T}\frac{\Delta C_{p,m}^o}{R}\frac{dT}{T} \qquad 9\text{-}42$$

Finally, division by RT yields

$$-\ln K_i = \frac{\Delta G_m^o}{RT} = \frac{\Delta G_{0,m}^o - \Delta H_{0,m}^o}{RT_0} + \frac{\Delta H_{0,m}^o}{RT} + \frac{1}{T}\int_{T_0}^{T}\frac{\Delta C_{p,m}^o}{R}dT - \int_{T_0}^{T}\frac{\Delta C_{p,m}^o}{R}\frac{dT}{T} \qquad 9\text{-}43$$

The change in heat capacity for the mixture can be expressed as

$$\Delta C_p^o\left(\frac{J}{kmol\cdot K}\right) = \Delta A + \Delta B\cdot T(K) + \Delta C\cdot T(K)^2 + \Delta D\cdot T(K)^3 + \Delta E\cdot T(K)^4 \qquad 9\text{-}44$$

with

$$\Delta A = \sum_i \nu_i A_i \qquad 9\text{-}45$$

With analogous definitions for ΔB, ΔC, ΔD, and ΔE. Using Equation 9-43 and the coefficients for the chemical equilibrium constant given in Table 9.3-11, we can determine the coefficients for the aqueous phase infinite dilution molar heat capacity of $MEAH^+$.

Table 9.3-14. Coefficients for the Aqueous Phase Infinite Dilution Heat Capacity (J/kmol·K) of $MEAH^+$ from 0 – 200 °C based on Equation 9-44.

Coefficient	Estimate
C_1	0.0001
C_2	0.0256
C_3	4.5343
C_4	-0.0089

Coefficients for the aqueous phase infinite dilution molar heat capacity of $MEAH^+$ were adjusted to match the form of Equation 9-34.

Table 9.3-15. Coefficients for the Aqueous Phase Infinite Dilution Heat Capacity (J/kmol·K) of $MEAH^+$ from 0 – 200 °C based on Equation 9-34.

Coefficient	Estimate	Aspen Plus Default Estimate
C_1	-1710760	0.0
C_2	7136	295.12
C_3	-8.547	0.0
C_4	1.5206E+08	0.0

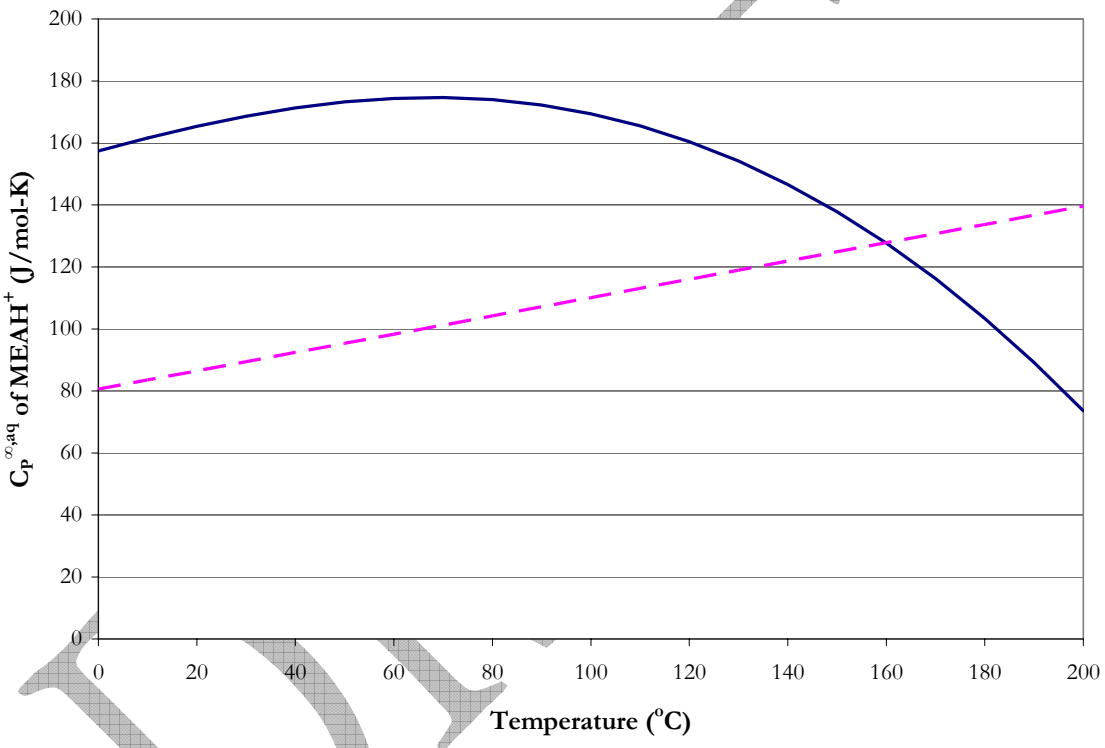

Figure 9.3-4. Comparison of the Coefficients for the Aqueous Phase Infinite Dilution Heat Capacity (J/kmol·K) of $MEAH^+$ from 0 – 200 °C based on Equation 9-34 to Aspen Plus™ Default Parameters. Lines: ——, This work, – – –, Aspen Plus™ Default Parameters.

Aspen Tech does not provide source documentation for the coefficients assigned to $MEAH^+$, but does reference Austgen et al. (1989), even though Austgen et al. (1989) did not provide documentation. In this work, we have compiled a consistent database for experimental H_2O-MEA data as compared to the work by Austgen et al. (1989). The

difference between the two predictions for the aqueous phase infinite dilution heat capacity of $MEAH^+$ accounts for differences is in the model framework. Austgen et al. (1989) chose to describe the liquid phase chemical equilibrium through linear temperature dependent functions. In this work, we chose not to provide the chemical equilibrium constants, but rather determine the chemical equilibrium from the reference state free energy of the system. Thus, Austgen et al. (1989) was never required to fully describe the standard property changes for each ionic species because Aspen Plus™ would rely on the provided chemical equilibrium constants for the necessary ionic information (e.g. ΔG, ΔH, ΔC_p) as shown in Figure 9.3-5.

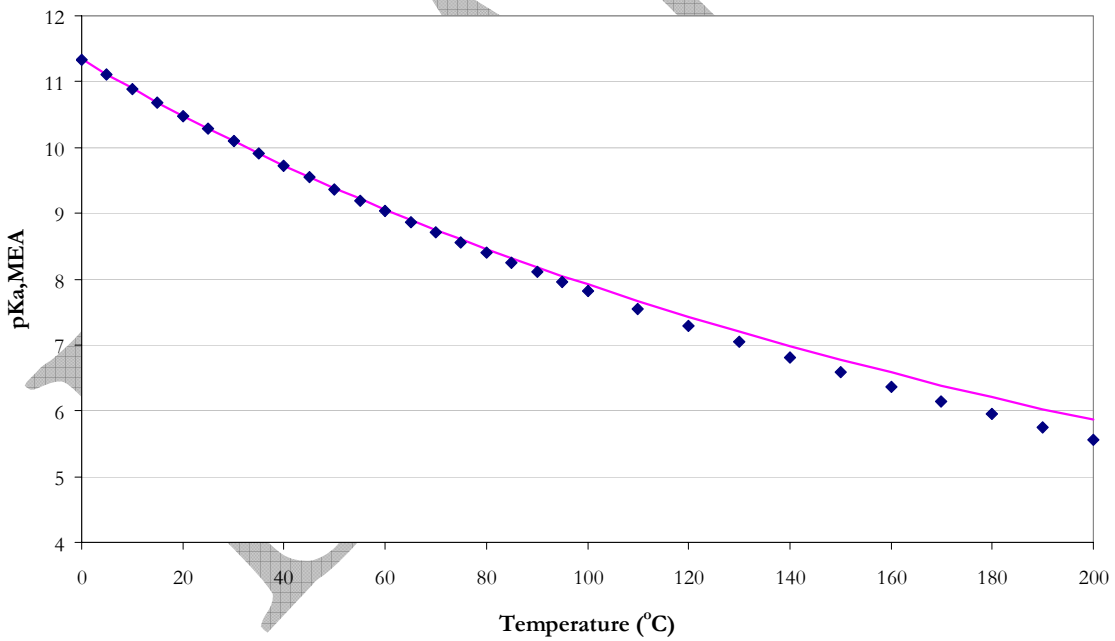

Figure 9.3-5. Comparison of the Dissociation Equilibrium Constant for MEA (mole fraction based) from 0 – 200 °C. Points: ♦, Austgen et al. (1989). Lines: —, Corrected Bates and Pinching (1951) based on Table 9.3-11.

By determining the coefficients for the aqueous phase infinite dilution molar heat capacity of $MEAH^+$ analytically, this work is thermodynamically consistent with published literature for the dissociation constant of MEA as shown in Figure 9.3-6.

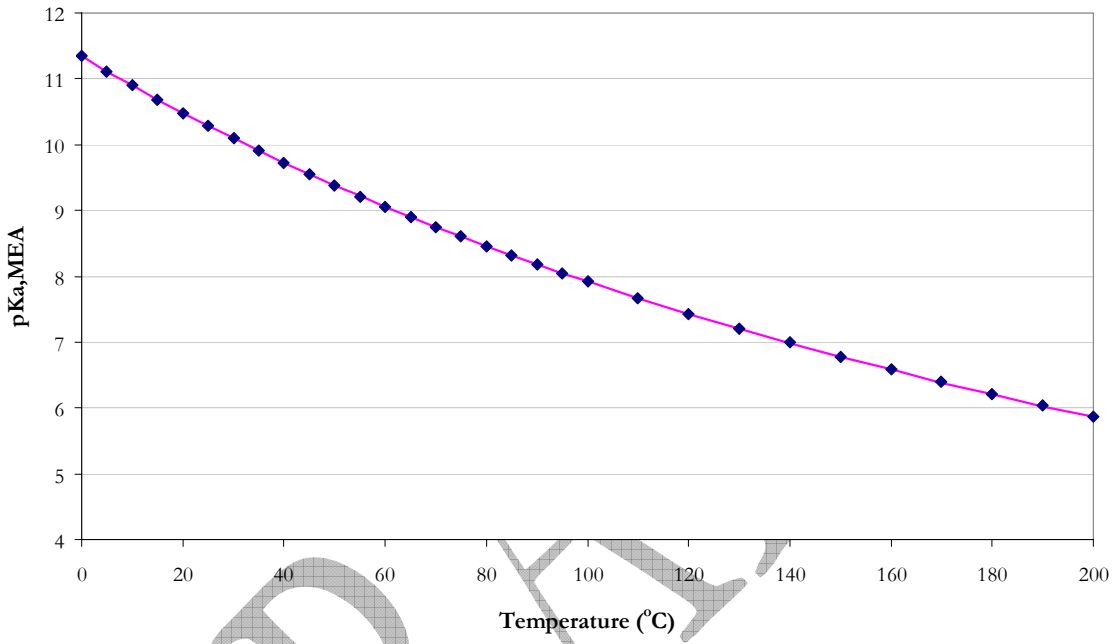

Figure 9.3-6. Comparison of the Dissociation Equilibrium Constant for MEA (mole fraction based) from 0 – 200 °C. Points: ♦, This work. Lines: —, Corrected Bates and Pinching (1951) based on Table 9.3-11.

9.4 Optimum Model Predictions

In this work, we have compiled a large database of consistent high quality data needed to obtain a unique set of binary interaction parameters to describe the H_2O-MEA system. The remainder of this chapter will be devoted to using our model as a predictive tool as described in the subsequent sections.

9.4.1 *Total Vapor Pressure*

With the determination of the estimates for the energy parameter coefficients known for the optimum model, a simple Aspen Plus™ Flash model was used to test the predictive capability of the H_2O-MEA energy parameter coefficients against literature data. Figures 9.4-1 and 9.4-2 compare estimated and experimental total pressure measurements from Nath and Bender (1983) and Touhara et al. (1982), for aqueous MEA mixtures from 25.0 – 91.7 ^oC. The optimum model exhibits systematic error and under predicts the total vapor pressure with a maximum error of ± 6.99 % for concentrations less than 40 mole percent of MEA even though all the predictions of the model were within an AARD of ± 2.01 %, with the exception of a few outliers. Figure 9.4-1 and Figure 9.4-2 illustrates the departure from an ideal solution behavior vis-à-vis Raoult's Law as compared to predictions from the elecNRTL model. Over the temperature range from 25 to 91.7 ^oC, Raoult's Law adequately describes the vapor pressure of H_2O-MEA mixtures below $x_{MEA} = 0.1$, but as the concentration of MEA increases so does the importance of including activities to describe the vapor-liquid equilibrium.

Overall, the optimum model adequately describes the total vapor pressure data in MEA mixtures within an average absolute relative error of ± 2.21 percent.

9.4.2 *Vapor-Liquid Equilibrium*

Figure 9.4-3 gives the results of fit for experimental isobaric (*Txy*) vapor-liquid equilibrium (VLE) data from Park and Lee (1997) and Cai et al. (1996) versus the concentration of water at 101.325 kPa. To describe the *Txy* behavior of H_2O-MEA mixtures

at atmospheric pressure given the degree of scatter between Park and Lee (1997) and Cai et al. (1996) allows Raoult's Law and the elecNRTL model to describe systematic trends presented in both data sets adequately. Overall, the optimum model adequately describes the *Txy* data within an average absolute relative error of ± 2.82 percent.

Figure 9.4-4 compares estimated and experimental isothermal (*Pxy*) VLE data from Tochigi et al. (1999) versus the concentration of water at 90.0 °C. To describe the liquid phase we see from Figure 9.4-4 the extent of this departure from an ideal solution to a real solution as illustrated by predictions from the elecNRTL model.

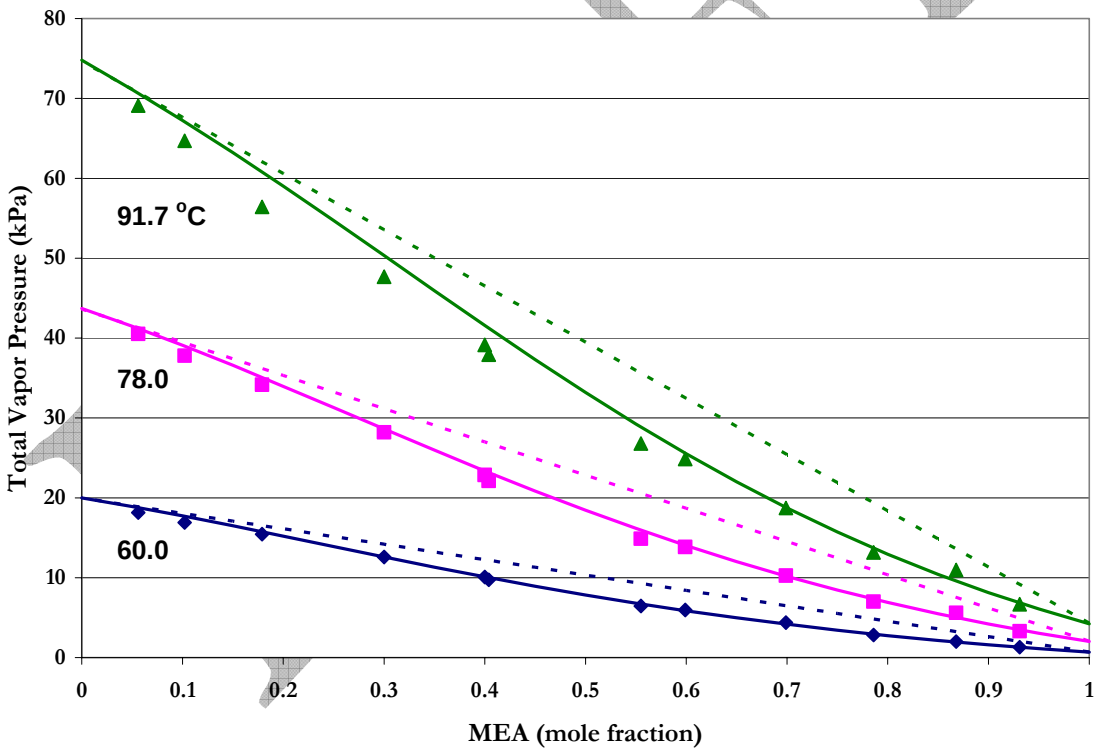

Figure 9.4-1. Comparison of Nath and Bender (1983) Total Pressure data to elecNRTL Model Predictions from 60.0 – 91.7 °C. Lines: ▬, elecNRTL Predictions, - - - , Raoult's Law.

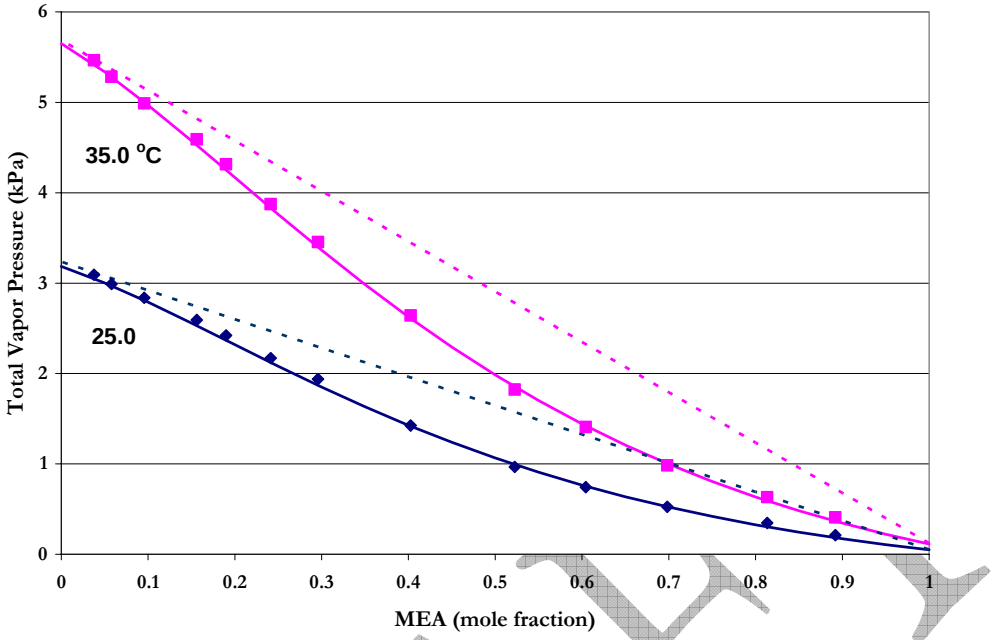

Figure 9.4-2. Comparison of Touhara (1982) Total Pressure data to elecNRTL Model Predictions from 25.0 – 35.0 °C. Lines: ▬, elecNRTL Predictions, - - - , Raoult's Law.

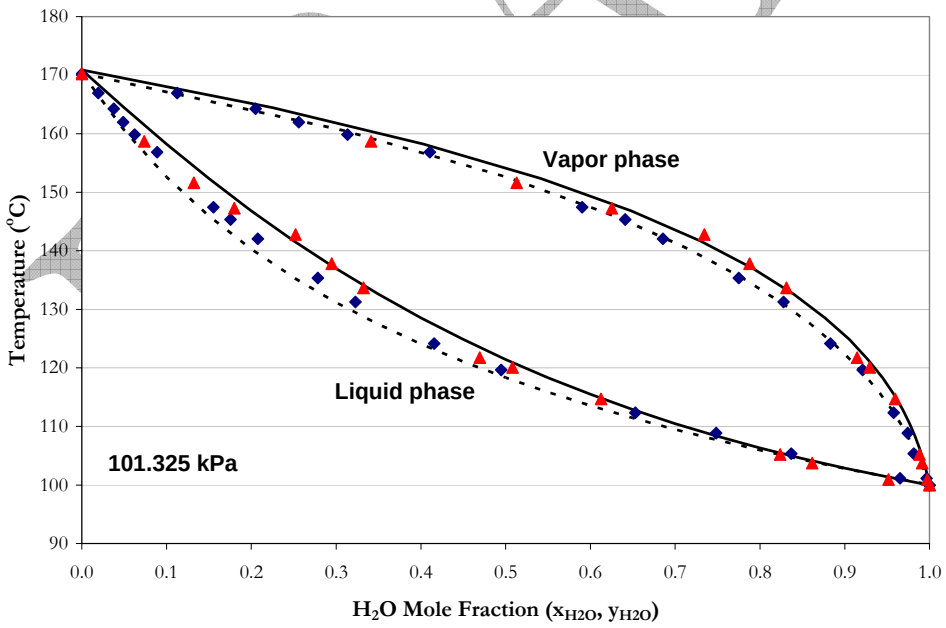

Figure 9.4-3. Comparison of Park and Lee (1997) and Cai et al. (1996) Isobaric *Txy* data to elecNRTL Model Predictions at 101.325 kPa. Points: ♦, Park and Lee (1997) and ▲, Cai et al. (1996). Lines: ▬, elecNRTL Predictions, - - - , Raoult's Law.

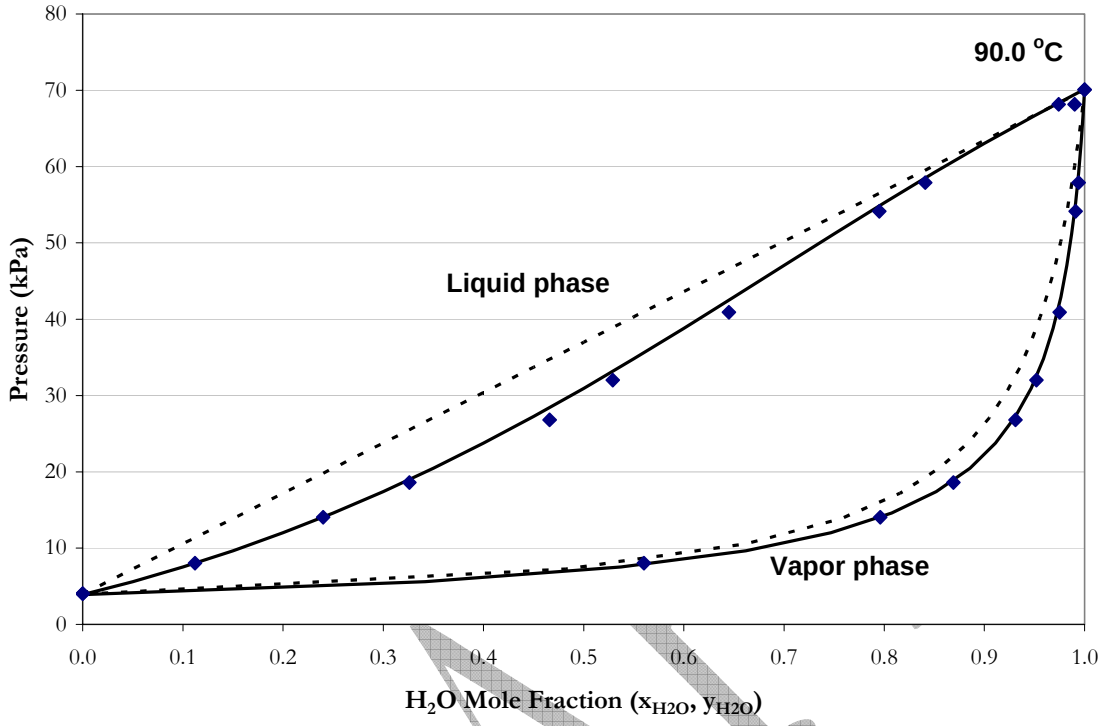

Figure 9.4-4. Comparison of Tochigi et al. (1999) Isothermal *Pxy* data to elecNRTL Model Predictions at 90.0 °C. Points: ♦, Tochigi et al. (1999). Lines: ═, elecNRTL Predictions, - - - , Raoult's Law.

Overall, the optimum model adequately describes the *Pxy* data within an average absolute relative error of ± 4.81 percent.

One of the main goals of this work was to describe the amine volatility at absorber and stripper conditions. Figure 9.4-5 and Figure 9.4-6 compares estimated and experimental amine volatility data from this work to predictions from the elecNRTL model up to 120 °C.

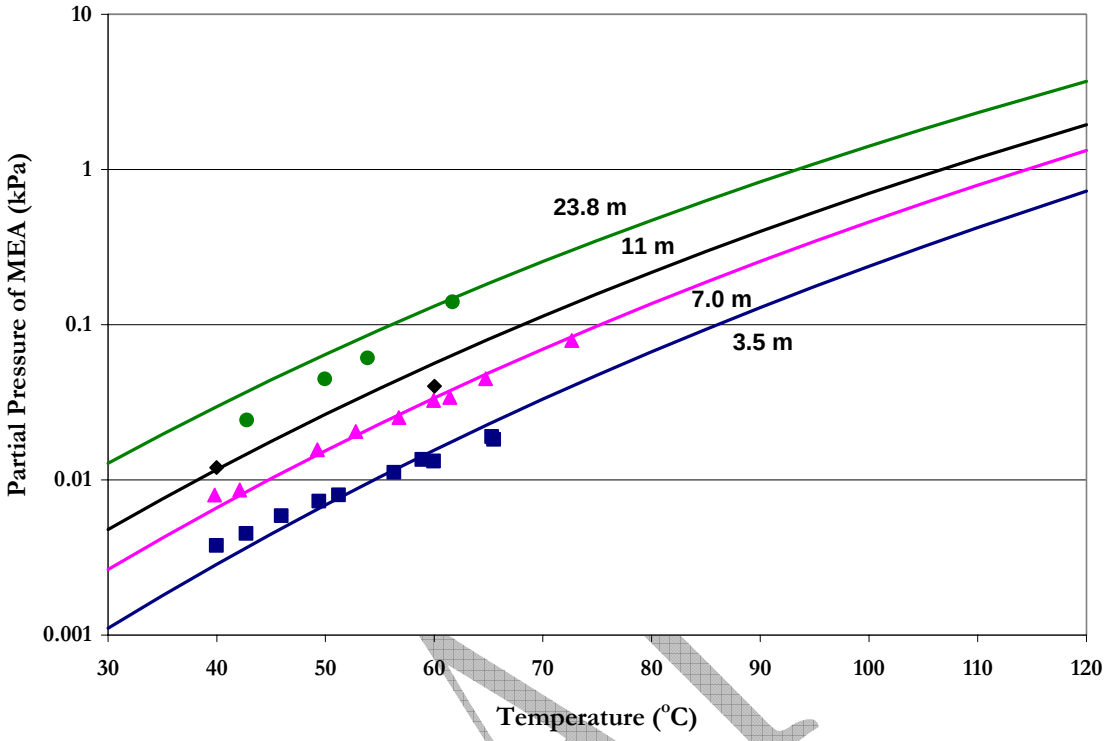

Figure 9.4-5. Comparison of Amine Volatility (e.g. Partial Pressure of MEA) from this work to elecNRTL Model Predictions from 30 – 120 °C. Points: experimental data from this work ■, 3.5 m (mole/kg-H_2O), ▲, 7 m, ◆, 11 m, ●, 23.8 m. Lines: —, elecNRTL Predictions.

We chose to concentrate our modeling efforts to describe the partial pressure of MEA between 3.5 and 7.0 m MEA due to limited data at 11.0 and 23.8 m MEA. Overall, the optimum model adequately describes the partial pressure of MEA within an average absolute relative error of ± 4.28 percent, with the exception of a few outliers. In addition, the optimum model adequately described the partial pressure of water within an average absolute relative error of ± 6.64 percent, with the exception of a few outliers. We would recommend that future work should endeavor to describe the binary system at stripper conditions (e.g. temperatures between 80 - 120 °C) to complete this analysis. Modifications

to the reactor used in this work would need the ability to perform at high temperatures and high pressures to obtain high quality data.

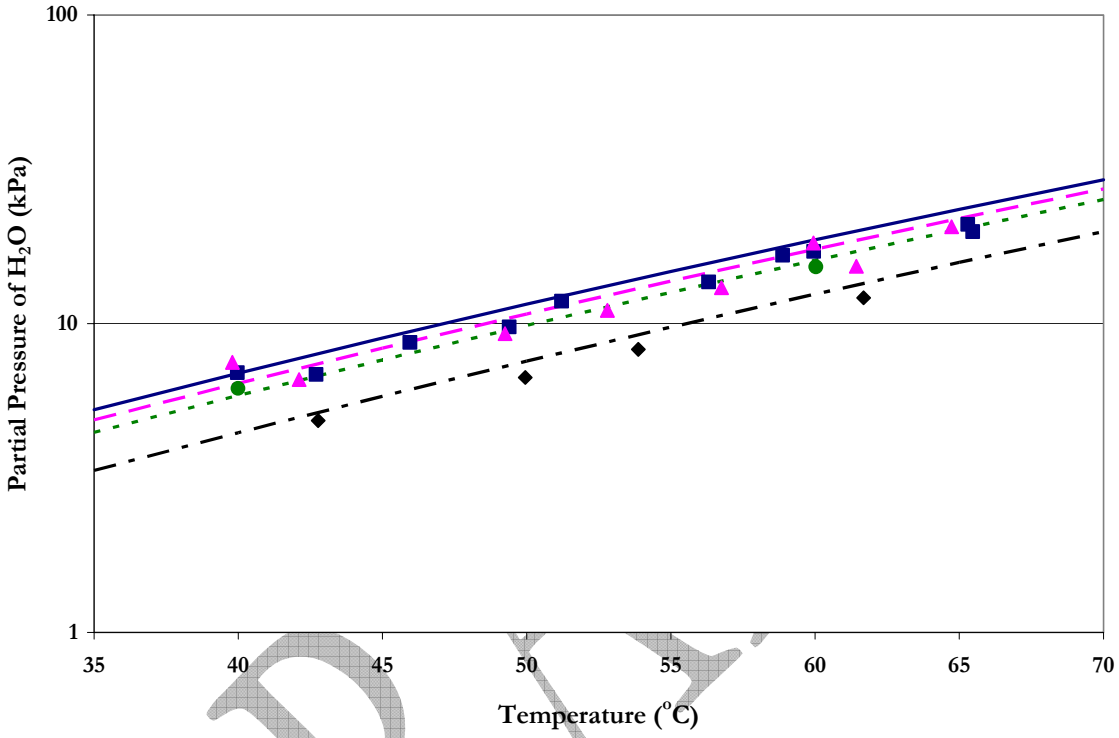

Figure 9.4-6. Comparison of Amine Volatility (e.g. Partial Pressure of Water) from this work to elecNRTL Model Predictions from 30 – 120 °C. Points: experimental data from this work ■, 3.5 m (mole/kg-H_2O), ▲, 7 m, ●, 11 m, ♦, 23.8 m. Lines: ▬, 3.5 m (mole/kg-H_2O) elecNRTL Predictions, – –, 7 m, - - -, 11 m, ─ ·, 23.8 m.

9.4.3 *Specific Heat Capacity*

To describe the specific heat capacity of H_2O-MEA solutions, we chose to concentrate our modeling efforts to describe the specific heat capacity from Chiu and Li (1999) and from this work due to the agreement between the two sources where specific

heat capacity from Pagé et al. (1993) and Weiland et al. (1997) were limited to temperatures below 40 °C.

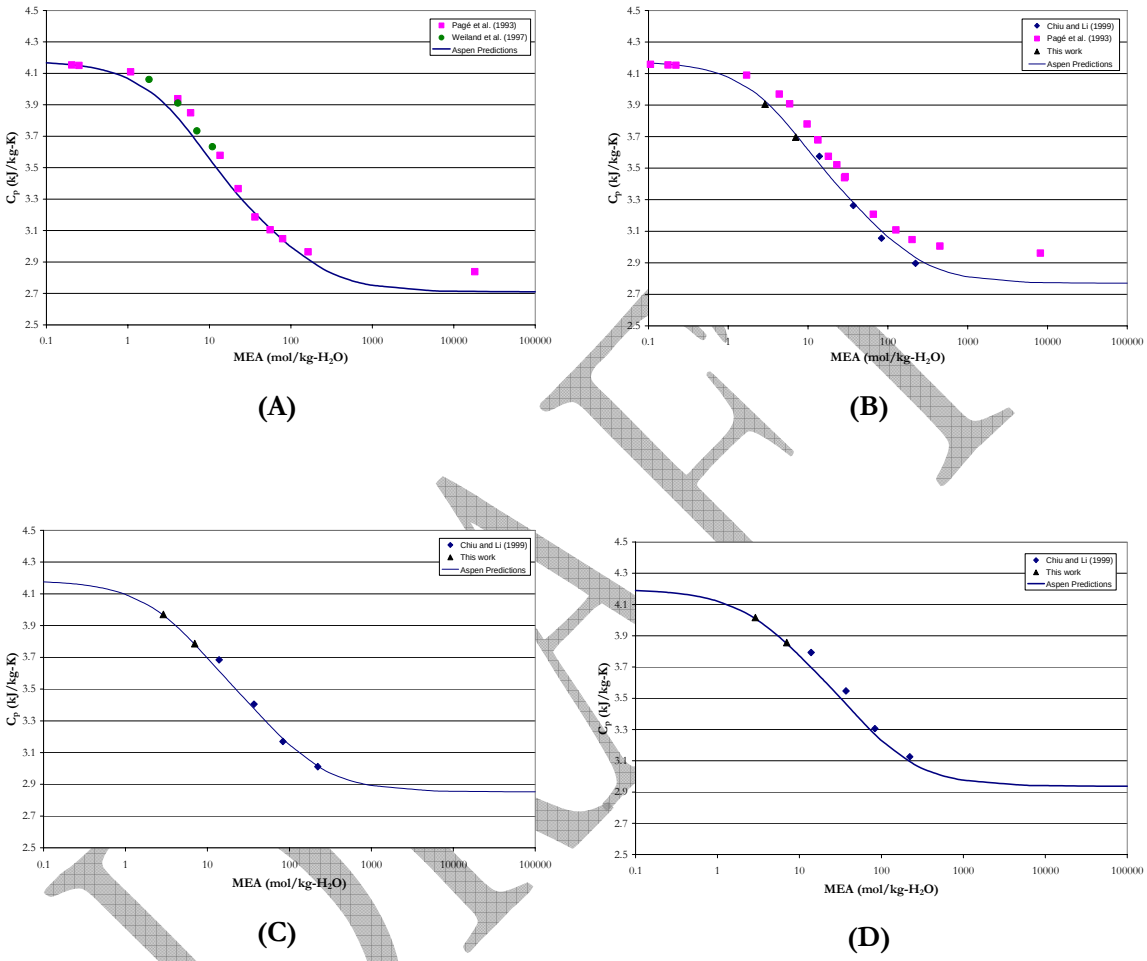

Figure 9.4-7. Comparison of Specific Heat Capacity from Pagé et al. (1993), Chiu and Li (1999), Weiland et al. (1997), and from this work to elecNRTL Model Predictions at 25.0 (A), 40.0 (B), 60.0 (C), and 80.0 °C (D).

Figure 9.4-7 compares estimated and experimental specific heat capacities from 25 to 80 °C over the full range of concentrations. Figure 9.4-7 also illustrates that the optimum model is consistent with the pure component specific heat capacities as discussed in Chapter VIII. To use the H_2O and MEA parameters for an NRTL property model, please refer to

Chapter VIII for more information on the pure component parameters. Otherwise, the specific heat capacity for the mixture will not have the correct pure component specific heat capacity for water as shown in Figure 9.4-8.

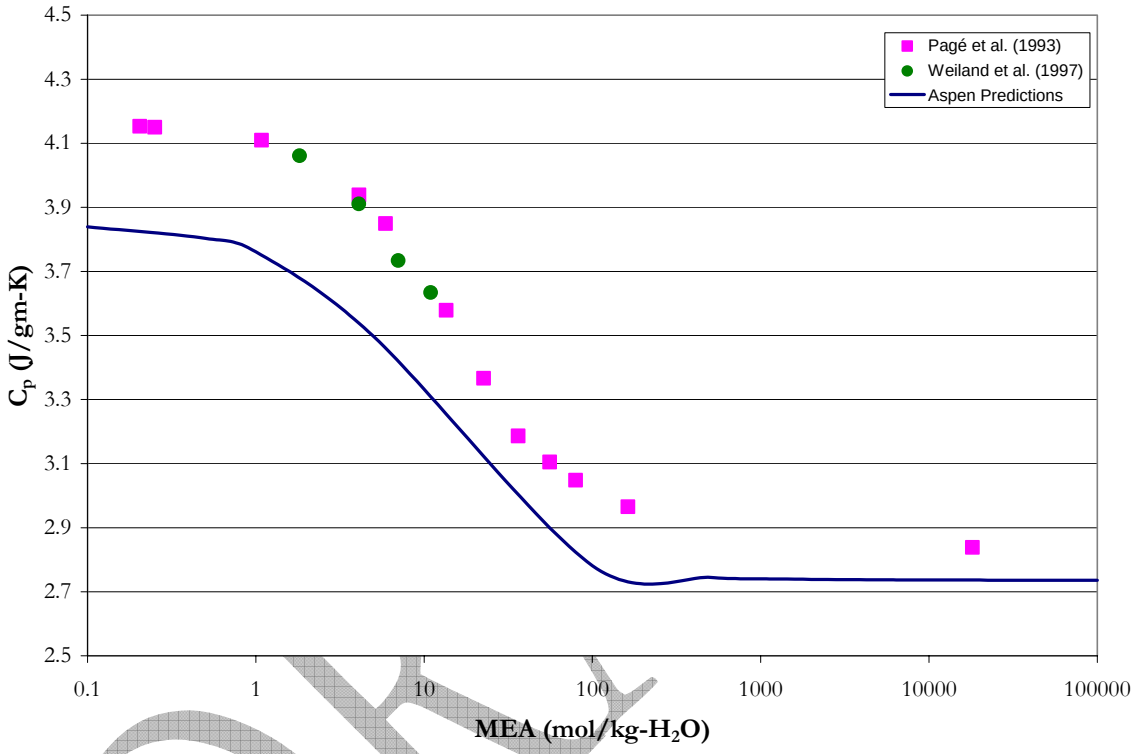

Figure 9.4-8. Comparison of Specific Heat Capacity from Pagé et al. (1993) and Weiland et al. (1997) to NRTL Model Predictions at 25.0 °C based on the default parameters for the DIPPR Heat of Vaporization Equation for H_2O.

Specific heat capacity predictions from this work are shown in Figure 9.4-9. Overall, the optimum model adequately describes the specific heat capacity for aqueous mixtures of MEA within an average absolute relative error of ± 1.38 percent, with the exception of a few outliers.

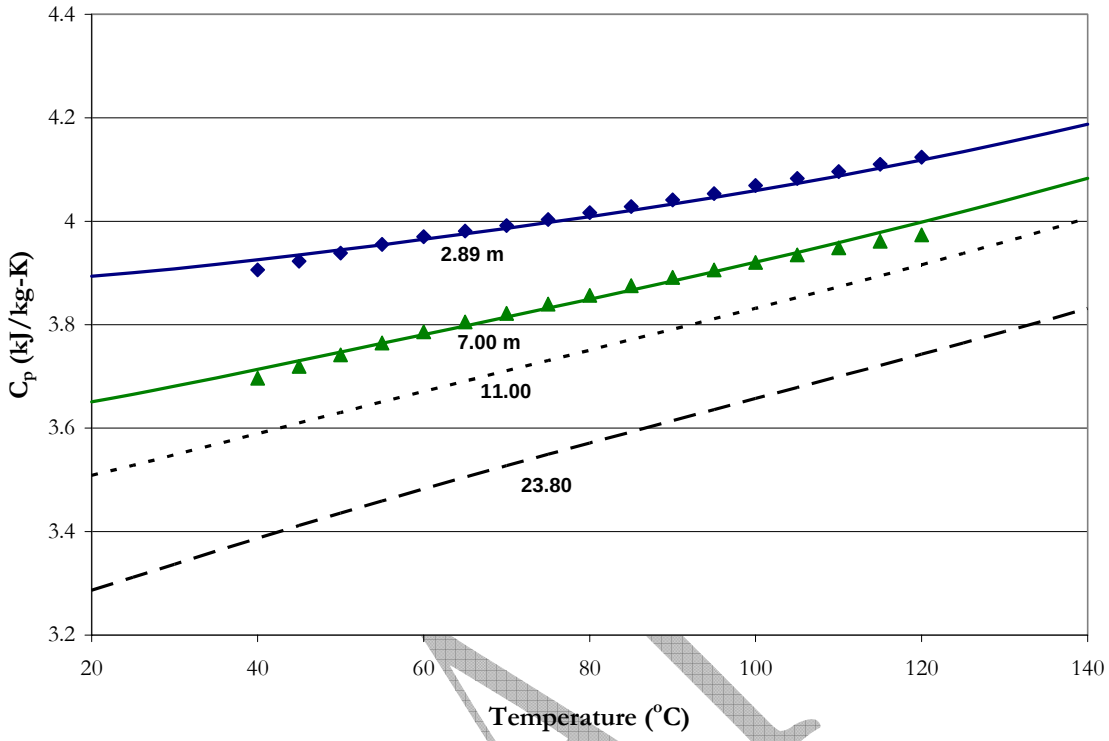

Figure 9.4-9. Comparison of Specific Heat Capacity from this work to elecNRTL Model Predictions for 2.89 – 23.80 m MEA.

9.4.4 *Freezing Point Depression*

Figure 9.4-10 compares estimated and experimental freezing point depression vis-à-vis vapor pressure of water from Chang et al. (1993) for aqueous MEA mixtures over the concentration range 0.86 – 0.995 mole fraction of H_2O from -20.5 to -0.5 °C. The optimum model reproduces the vapor pressure of water within an AARD of ± 0.35 percent.

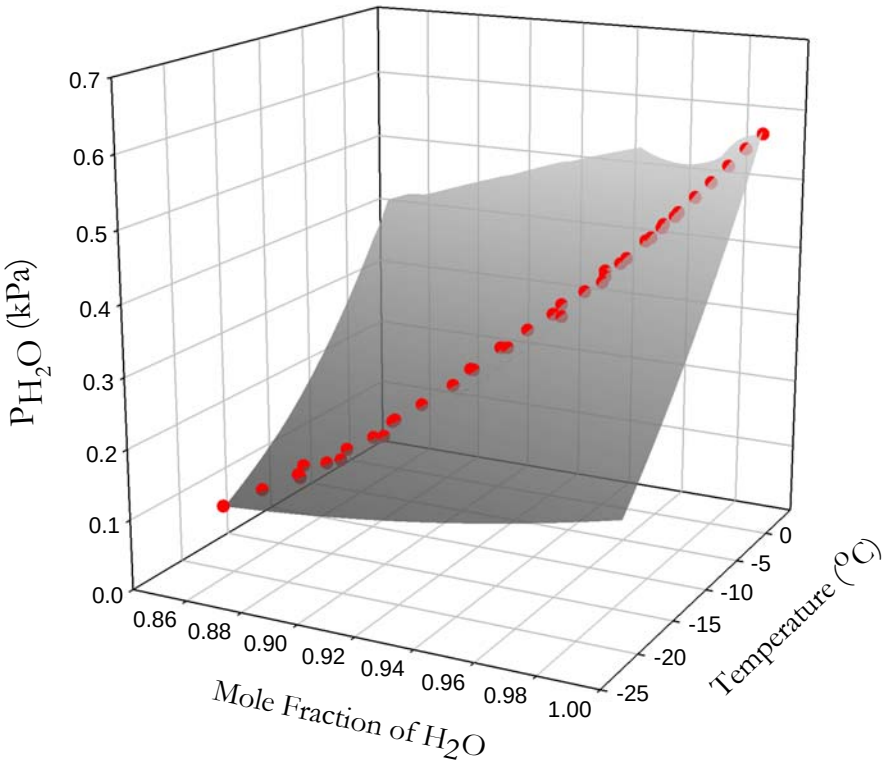

Figure 9.4-10. Comparison of Model Predictions with Experimental Data for Chang et al. (1993) Vapor Pressure Depression from - 20.5 to -0.5 °C.

9.4.5 *Excess Enthalpy Predictions for H_2O-MEA*

As stated at the beginning of this chapter, the elecNRTL model was never designed to regress excess enthalpy data thus we were required to reserve literature data from Touhara et al. (1982) and Posey (1996) until a comparison can be made from predictions based on an optimum set of binary interaction parameters. Thus, using the optimum model as a purely predictive model, the excess enthalpy for aqueous MEA mixtures were calculated based on Equation 9-15. On the other hand, Aspen Plus™ gives the following equation as an

alternative procedure to calculate the excess enthalpy. Results based on the two methods are presented in Figures 9.4-11 and 9.4-12.

$$H_m^{E,l} = H_m^l - \sum_i x_i H_i^{*,l} \qquad 9\text{-}46$$

Where

$H_m^{E,l}$ is the liquid molar excess enthalpy of the mixture,

H_m^l is the liquid molar enthalpy of the mixture,

x_i is the mole fraction of component i,

$H_m^{*,l}$ is the pure liquid molar enthalpy of component i.

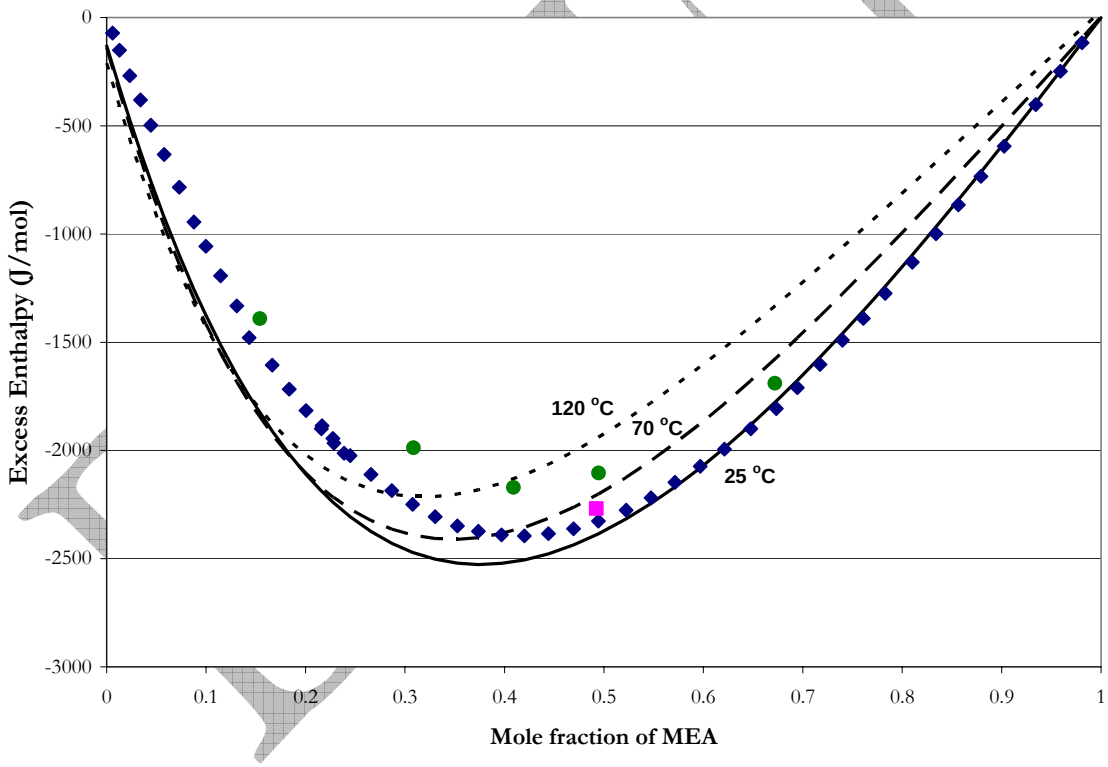

Figure 9.4-11. Comparison of Model Predictions with Experimental Excess Enthalpy Data for Touhara et al. (1982) and Posey (1996) at 25 and 70 °C Based on Equation 9-23. Points: ♦, Touhara et al. (1982) and ■, Posey (1996) at 25 °C, ●, Posey (1996) at 70 °C.

Figure 9.4-11 illustrates two important issues: one, the model was unable to predict the liquid enthalpy of pure water; two, the model does under predict the temperature

dependence of the activity coefficients for MEA and H_2O. The above results would then contradict the previous discussion, vis-à-vis the representation of the optimum model to adequately represents the regressed literature data. Figure 9.4-12 validates previous work by demonstrating Equation 9-15 to calculate the excess enthalpy.

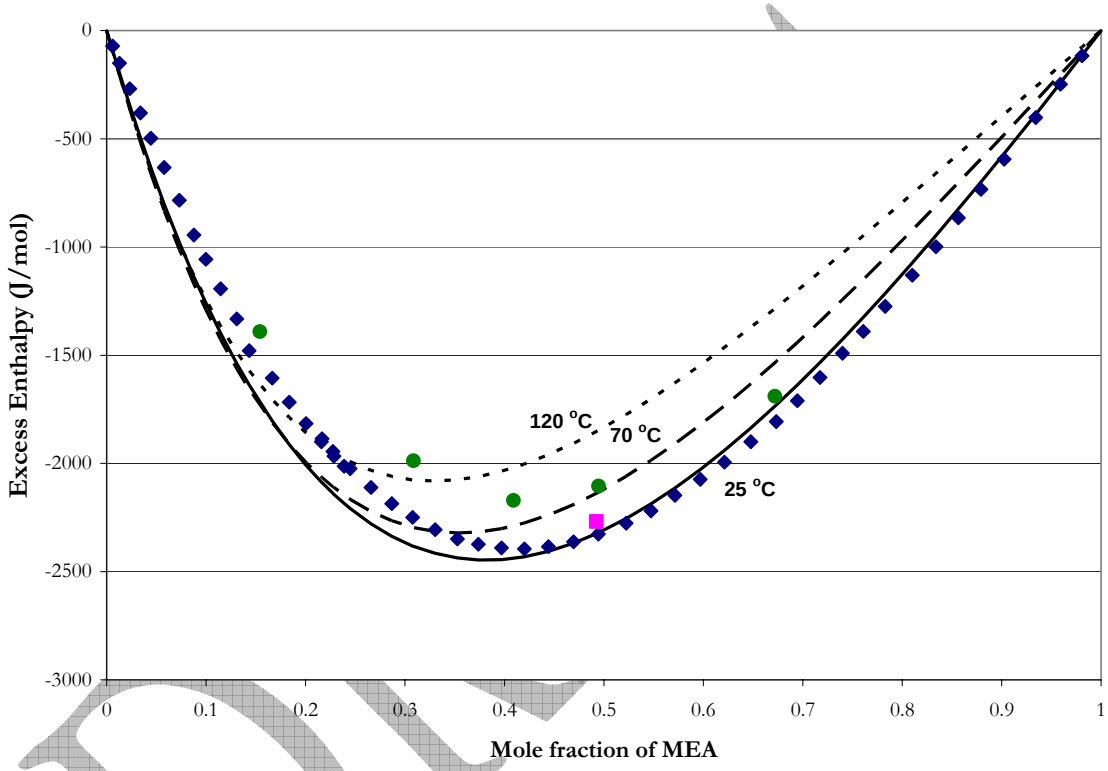

Figure 9.4-12. Comparison of Model Predictions with Experimental Excess Enthalpy Data for Touhara et al. (1982) and Posey (1996) at 25 and 70 °C Based on Equation 9-15. Points: ♦, Touhara et al. (1982) and ■, Posey (1996) at 25 °C, ●, Posey (1996) at 70 °C.

Even though the optimum model does not capture the excess enthalpy temperature dependence, the model does characterize the experimental data within an average absolute relative error of ± 9.17 percent. We would then recommend to Aspen Plus™ to include the excess enthalpy calculation routes, based on equation 9-15, as part of the simulation package in the elecNRTL model.

9.4.6 *Activity Coefficient Predictions for H_2O-MEA*

Several authors have presented activity-based models to calculate the activity coefficient of MEA in aqueous MEA mixtures. Works include:

Author	Model
Deshmukh and Mather (1981)	Applying Guggenheim extension of the Debye-Hückel theory
Austgen et al. (1989)	Electrolyte-NRTL (Aspen Plus)
Weiland et al. (1993)	Applying Deshmukh-Mather Model
Li and Mather (1994)	Pitzer Equation
Lee (1996)	UNIFAC Group Contribution Method
Posey (1996)	Electrolyte-NRTL (Aspen Plus)
Kaewsichan et al. (2001)	Electrolyte-UNIQUAC Model
Poplsteinova (2004)	UNIFAC Group Contribution Method

All of the above authors had a limited database of experimental literature data to describe interactions between H_2O and MEA. In this work, we have compiled an extensive database of consistent high quality literature data. Thus, the subsequent discussion on predicting the activity coefficients for MEA in aqueous MEA mixtures will provide the most realistic values to date. Figure 9.4-13 compares activity coefficient predictions based on the works by Lee (1996), Prausnitz et al. (1999), and Poplsteinove (2004) described by the UNIFAC Group Contribution Method and the Wilson Equation as presented by Poplsteinove (2004).

Poplsteinove (2004) described predictions from Lee (1996) as producing a concentration dependent minimum with respect to the activity coefficient of MEA indicating an "azeotropic behavior." Lee (1996) based his work on excess enthalpy [Touhara et al. (1982) and Posey (1996)], vapor-liquid equilibrium [The Dow Chemical Company (1981)], and total pressure [Nath and Bender (1983) and Touhara et al. (1982)] data. In this work, we have increased the amount of literature data by including additional vapor-liquid

equilibrium, amine volatility, specific heat capacity, and water vapor pressure depression data. In the end, Poplsteinove (2004) decided to adopt parameters from Lee (1996) into her work based on the agreement with predictions from his model to data found in the literature.

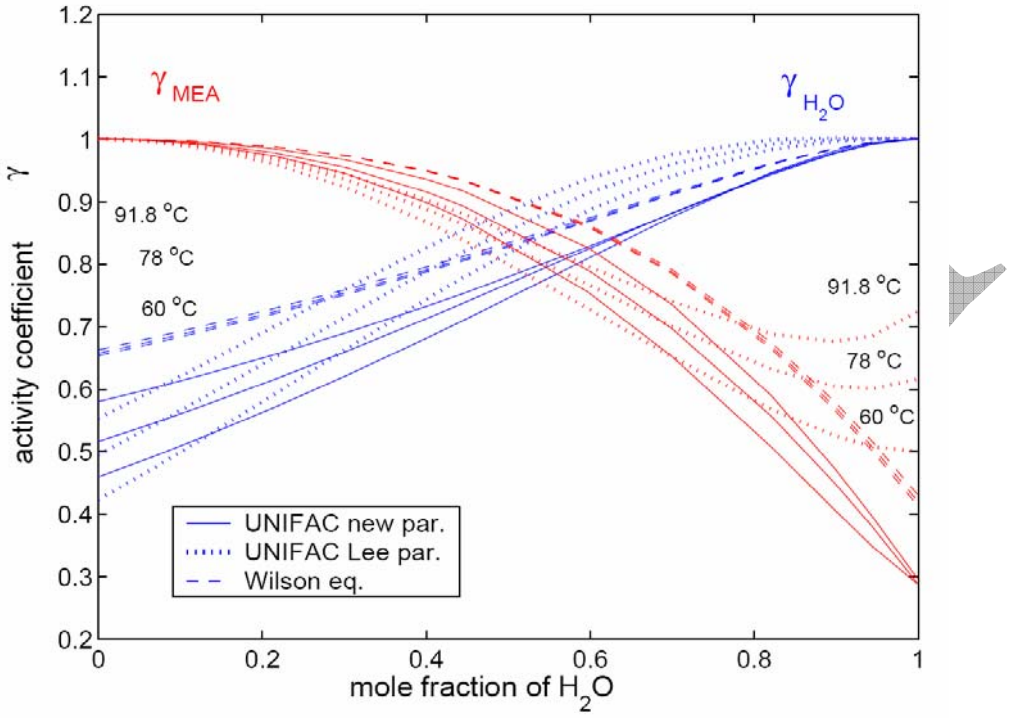

Figure 9.4-13. Predictions of Activity Coefficients for MEA and H2O as Presented by Poplsteinove (2004).

In this work, the optimum model also predicted a minimum value for the activity coefficient of MEA (x_{H2O} = 0.86, T = 120 °C) as shown in Figure 9.4-14, but the phase diagram at this temperature does not indicate the presence of an azeotrope (Figure 9.4-15). If we vary the temperature or pressure, results do not indicate the presence of an azeotropic state. Thus, the azeotropic behavior for the activity coefficient of MEA, as reported in Poplsteinove (2004), may not adequately describe this situation.

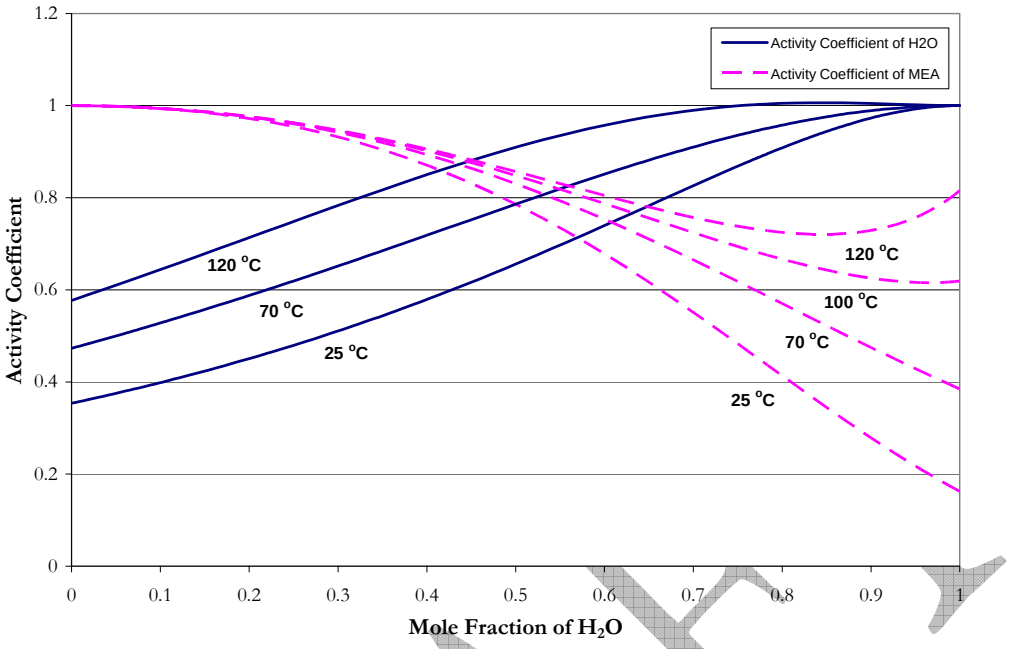

Figure 9.4-14. Model Predictions for the Activity Coefficient of Water and Monoethanolamine at 25, 70 and 120 °C.

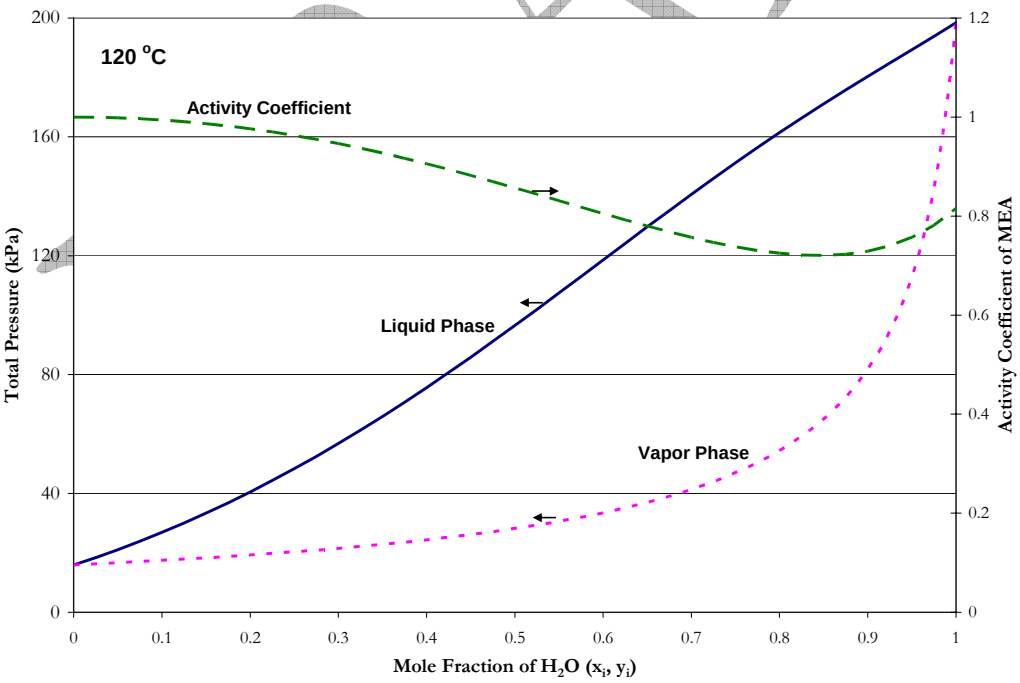

Figure 9.4-15. Pxy Diagram at 120 °C for H_2O-MEA mixtures based on the elecNRTL Model.

9.5 Abridged elecNRTL Predictive Correlations

To anticipate installation difficulties with the implementation of our model on future platforms, we have developed specific correlations based on predictive results from our rigorous thermodynamic model for the partial pressure of MEA and liquid phase specific heat capacity of H_2O-MEA based on experimental results from this work.

Correlations for the Partial Pressure of MEA

Predictions for the partial pressure of MEA for 3.5, 7, 11, and 23.8 m MEA based on the elecNRTL model, as shown in Figure 9.4-5, where related to the natural logarithm of the partial pressure of MEA by the following relation for two predictors:

$$\ln P_{MEA} = C_1 + \frac{C_2}{T} + C_3 \ln(T) + C_4 T + \frac{C_5}{[MEA]} + C_6 \ln([MEA]) + C_7 [MEA] + C_8 [MEA] T \qquad 9\text{-}47$$

Where
T is the temperature, K,
$[MEA]$ is the concentration of MEA, m (mole/kg-H_2O).

Equation 9-47 allows for nonlinearity in the temperature and concentration dependence. The interaction term $([MEA]T)$ allows for twisting of the predictive surface versus the two predictors. Predictions from the elecNRTL model for the partial pressure of MEA are tabulated in Table 9.5-1.

Performing ordinary least squares (OLS) regression for the full model using ARC (2004), the following regression summary statistics output for coefficient estimates in Equation 9-47 are shown in Table 9.5-2.

Table 9.5-1. Tabulated Predictions for the P_{MEA} (kPa) from the elecNRTL Model.

	MEA Concentration (mole/kg-H_2O)			
Temperature (°C)	3.5	7	11	23.8
30	0.00111	0.002649	0.00479	0.0128
35	0.00180	0.004225	0.00754	0.0196
40	0.00286	0.006617	0.0117	0.0297
45	0.00448	0.0102	0.0177	0.0440
50	0.00689	0.0154	0.0264	0.0644
55	0.0104	0.0230	0.0389	0.0927
60	0.0156	0.0337	0.0564	0.13
65	0.0229	0.0488	0.0805	0.18
70	0.0331	0.0696	0.11	0.26
75	0.0474	0.0981	0.16	0.35
80	0.0669	0.14	0.22	0.47
85	0.0935	0.19	0.30	0.63
90	0.13	0.26	0.40	0.83
95	0.18	0.34	0.53	1.09
100	0.24	0.46	0.70	1.42
105	0.32	0.61	0.92	1.82
110	0.42	0.79	1.19	2.33
120	0.72	1.33	1.95	3.70

Table 9.5-2. ARC Regression Output for the Predictive Full P_{MEA} Correlation.

Parameter	Estimate	σ wrt Estimate
C_1	222	258
C_2	-15856	7607
C_3	-33.0	24.2
C_4	0.0346	0.0239
C_5	0.447	0.548
C_6	1.193	0.139
C_7	0.138	0.00826
C_8	-0.000420	0.000014

Residual Sum of Squares: 0.0385
Degree of Freedom: 64

Recall that the standard error of an estimate is the estimated standard deviation of that statistic. Notice that only one of the estimates (C_5) is smaller relative to the standard error. This term might be usefully removed from the model without significant loss of

information. A complete description of the variability of the coefficient estimates requires examining the correlations between the estimates as shown in Table 9.5-3.

Table 9.5-3. Correlation Matrix of the Coefficient Estimates, for the Full P_{MEA} Model.

Parameter	1	2	3	4	5	6	7	8
1	1.00							
2	-0.97	1.00						
3	-0.97	*0.99*	1.00					
4	0.96	-0.97	*-0.99*	1.00				
5	-0.24	0.00	0.00	0.00	1.00			
6	-0.24	0.00	0.00	0.00	*0.99*	1.00		
7	0.23	0.00	0.00	0.01	-0.97	-0.98	1.00	
8	0.01	0.00	0.00	-0.07	0.00	0.00	-0.15	1.00

Table 9.5-3 shows three highly correlated coefficients between parameter estimates, $\hat{\eta}_{3\to 2}$, $\hat{\eta}_{3\to 2}$, and $\hat{\eta}_{3\to 2}$, but the correlation between other coefficients is relatively small, suggesting that C_3, C_4, and C_6, might be usefully removed from the model without significant loss of information. Using the Full Model as our base case, we can perform backward elimination using ARD to determine the optimum model as shown in Table 9.5-4.

From Table 9.5-4, the deletion of parameter C_5 from the Full Model gives the smallest change in the residual sum of squares (RRS) as compared to the other regression cases. We then chose Case 1 as the optimum model; the regression summary statistics output for coefficient estimates in Equation 9-47 based on Case 1 are shown in Table 9.5-4.

Table 9.5-4. P_{MEA} Backward Elimination Case Summary Results.

FULL MODEL			RSS	0.039	
Case	Current terms: (C_2 C_3 C_4 C_5 C_6 C_7 C_8)				
			df	RSS	AARD (%)
1	Delete:	C_5	65	0.039	1.0
2	Delete:	C_7	65	0.045	17.9
3	Delete:	C_4	65	0.076	98.5
4	Delete:	C_6	65	0.081	111.0
5	Delete:	C_2	65	0.087	124.7
6	Delete:	C_3	65	0.189	390.4
7	Delete:	C_8	65	0.561	1356.1
Case	Current terms: (C_2 C_3 C_4 C_6 C_7 C_8)				
			df	RSS	AARD (%)
8	Delete:	C_4	66	0.077	99.5
9	Delete:	C_2	66	0.087	125.7
10	Delete:	C_3	66	0.189	391.4
11	Delete:	C_7	66	0.209	441.5
12	Delete:	C_8	66	0.561	1357.1
13	Delete:	C_6	66	3.194	8195.6
Case	Current terms: (C_2 C_3 C_6 C_7 C_8)				
			df	RSS	AARD (%)
14	Delete:	C_7	67	0.240	524.1
15	Delete:	C_8	67	0.583	1413.4
16	Delete:	C_2	67	2.691	6890.2
17	Delete:	C_6	67	3.232	8294.1
18	Delete:	C_3	67	17.390	45065.6
Case	Current terms: (C_2 C_3 C_6 C_8)				
			df	RSS	AARD (%)
19	Delete:	C_8	68	0.584	1416.6
20	Delete:	C_2	68	2.716	6953.9
21	Delete:	C_6	68	10.644	27545.5
22	Delete:	C_3	68	18.057	46798.4
Case	Current terms: (C_2 C_3 C_6)				
			df	RSS	AARD (%)
23	Delete:	C_2	69	2.789	7143.9
24	Delete:	C_3	69	19.375	50219.7
25	Delete:	C_6	69	39.844	103383.1

Table 9.5-5. ARC Regression Output for the Predictive Optimum P_{MEA} Correlation.

Parameter	Estimate	σ wrt Estimate
C_1	222	157
C_2	-15856	7587
C_3	-33.0	24.1
C_4	0.0346	0.0238
C_6	1.0804	0.0146
C_7	0.143	0.00501
C_8	-0.000420	0.0000140

Residual Sum of Squares: 0.0388
Degree of Freedom: 65

Notice that all of the estimates are larger relative to their standard errors. Comparing the estimates from the full model to the optimum model, there was relatively little difference between the estimated values. The proposed optimum model provides the following correlations between the estimates as shown in Table 9.3-5.

Table 9.5-6. Correlation Matrix of the Coefficient Estimates, for the Optimum P_{MEA} Model.

Parameter	1	2	3	4	5	6	7
1	1.00						
2	*-1.00*	1.00					
3	*-1.00*	*0.99*	1.00				
4	*0.99*	*-0.97*	*-0.99*	1.00			
5	-0.01	0.00	0.00	0.00	1.00		
6	0.00	0.00	0.00	0.04	-0.76	1.00	
7	0.01	0.00	0.00	-0.07	0.00	-0.61	1.00

Table 9.5-6 shows highly negative correlations between all of the temperature dependent parameters suggesting that some of the remaining parameters might be usefully removed from the model without significant loss of information. From Table 9.5-4 illustrated the point with further parameter elimination the deviation between the submodel and the full model increases beyond an adequate level for the predictive correlation to describe systematic trends in the smoothed data. Figure 9.5-1 demonstrates the predictive

quality of Equation 9-44 based on coefficients from Table 9.5-5 for the optimum model. The functional form of Equation 9-45 adequately describes the predictions from the elecNRTL model within an average absolute relative error of ± 1.83 percent., presented in Figure 9.5 1.

$$\ln P_{MEA}(kPa) = 222 - \frac{15856}{T(K)} - 33.0\ln T(K) + 0.0346T(K) + 1.08\ln([MEA]) + \ldots$$
$$\ldots + 0.143[MEA] - 0.000420[MEA]T(K) \qquad 9\text{-}48$$

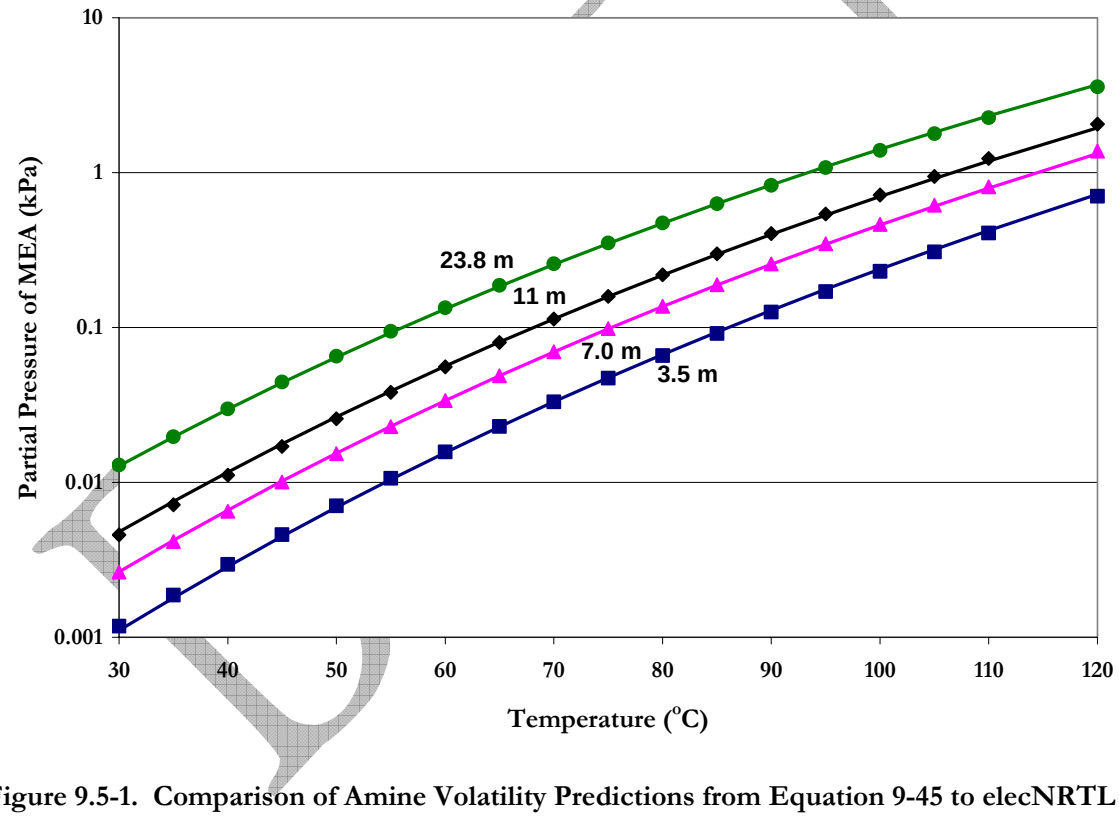

Figure 9.5-1. Comparison of Amine Volatility Predictions from Equation 9-45 to elecNRTL Model Predictions from 30 – 120 °C. Points: Smooth Prediction at ■, 3.5 m (mole/kg-H_2O), ▲, 7 m, ♦, 11 m, ●, 23.8 m. Lines: ▬, original elecNRTL Predictions.

Since there are only minor differences between Equation 9-45 and the predictions from the elecNRTL model, we can illustrate thermal effects of the solution equivalent to the effective heat of vaporization of MEA from water given by the following equation:

$$-\frac{\Delta H}{R} = \frac{d \ln P_{MEA}}{d1/T} \qquad 9\text{-}49$$

Substituting Equation 9-45 into Equation 9-46 and evaluating the derivative gives the following relationship for the effective heat of vaporization of MEA from water.

$$-\frac{\Delta H}{R} = \frac{d \ln P_{MEA}}{d1/T} = -15856 + 33.0T(K) - \left(0.0346 + 0.000420[MEA]\right)T(K)^2 \qquad 9\text{-}50$$

Over absorber and stripper conditions, the effective heat of vaporization of MEA from water (kJ/mol) at 3.5, 7, 11, and 23.8 m MEA is given in Table 9.5-7.

Table 9.5-7. Effective Heat of Vaporization of MEA from H_2O (kJ/mol-MEA).

	MEA Concentration (mole/kg-H_2O)			
Temperature (°C)	3.5	7	11	23.8
40	-73.01	-71.81	-70.44	-66.04
80	-69.40	-67.88	-66.13	-60.55
120	-66.68	-64.79	-62.63	-55.71

The effective heat of vaporization of MEA from H_2O given in Table 9.5-7 reflects a relatively high heat of solution associated with strong interactions between H_2O and MEA. Thus, to evolve MEA from the liquid phase requires the heat of vaporization of pure MEA plus the effective heat of vaporization of MEA from H_2O. Recovery of MEA in industrial applications (i.e. absorber water washing) would require an additional parameter, in this case temperature, to design an effective process.

Correlations for the Specific Heat Capacity

Predictions for the specific heat capacity for 2.89, 7, 11, and 23.8 m MEA based on the elecNRTL model, as shown in Figure 9.4-9, where related to the following relation for two predictors:

$$C_p^l\left(\frac{kJ}{kg\cdot K}\right) = C_1 + C_2T + C_3T^2 + C_4\left[MEA\right] + C_5\left[MEA\right]^2 + C_6\left[MEA\right]T \qquad 9\text{-}51$$

Where
T is the temperature, °C,
$\left[MEA\right]$ is the concentration of MEA, m (mole/kg-H_2O).

Equation 9-51 allows for nonlinearity in the temperature and concentration dependence. The interaction term $\left(\left[MEA\right]T\right)$ allows for twisting of the predictive surface versus the two predictors. Predictions from the elecNRTL model for the partial pressure of MEA are tabulated in Table 9.5-8.

Table 9.5-8. Specific Heat Capacity Predictions (kJ/kg-K) from the elecNRTL model.

	MEA Concentration (mole/kg-H_2O)			
Temperature (°C)	2.89	7.0	11.0	23.8
40	3.926	3.714	3.589	3.387
50	3.945	3.747	3.630	3.436
60	3.965	3.781	3.671	3.482
70	3.986	3.815	3.711	3.527
80	4.009	3.849	3.751	3.571
90	4.033	3.885	3.791	3.614
100	4.059	3.921	3.832	3.657
110	4.088	3.959	3.873	3.700
120	4.118	3.998	3.916	3.743

Performing ordinary least squares (OLS) regression for the full model using ARC (2004), the following regression summary statistics output for coefficient estimates in Equation 9-48 are shown in Table 9.5-9.

Table 9.5-9. ARC Regression Output for the Predictive Full CPMX Correlation.

Parameter	Estimate	σ wrt Estimate
C_1	3.93	0.0188
C_2	0.00229	0.000455
C_3	0.000002	0.000003
C_4	-0.0519	0.00114
C_5	0.000904	0.000034
C_6	0.000084	0.000008

Residual Sum of Squares: 0.0092
Degree of Freedom: 62

Recall that the standard error of an estimate is the estimated standard deviation of that statistic. Notice that only one of the estimates (C_3) is smaller relative to the standard error. This term might be usefully removed from the model without significant loss of information. A complete description of the variability of the coefficient estimates requires examining the correlations between the estimates as shown in Table 9.5-3.

Table 9.5-10. Correlation Matrix of the Coefficient Estimates, for the Full P_{MEA} Model.

Parameter	1	2	3	4	5	6
1	1.00					
2	-0.93	1.00				
3	0.85	-0.97	1.00			
4	-0.40	0.10	*0.00*	1.00		
5	0.23	*0.00*	*0.00*	-0.83	1.00	
6	0.37	-0.19	*0.00*	-0.54	*0.00*	1.00

Table 9.5-3 shows five independent coefficients between parameter estimates, $\hat{\eta}_{4\to3}$, $\hat{\eta}_{5\to2}$, $\hat{\eta}_{5\to3}$, $\hat{\eta}_{6\to3}$, and $\hat{\eta}_{6\to5}$, but the correlation between other coefficients is relatively small, suggesting that C_3 and C_5, might be usefully removed from the model without significant loss of information. Using the Full Model as our base case, we can perform

backward elimination using ARC (2004) to determine the optimum model as shown in Table 9.5-11.

With the deletion of parameter C_3 from the Full Model gives the smallest change in the RRS as compared to the other regression cases. We then chose Case 1 as the optimum model; Table 9.5-12 gives the regression summary statistics output for coefficient estimates in Equation 9-51 based on Case 1.

Table 9.5-11. CPMX Backward Elimination Case Summary Results.

FULL MODEL			RSS	0.0092	
Case	Current terms: (C_2 C_3 C_4 C_5 C_6)				
			df	RSS	AARD (%)
1	Delete:	C_3	63	0.0093	1.2
2	Delete:	C_2	63	0.0130	40.9
3	Delete:	C_6	63	0.0267	190.0
4	Delete:	C_5	63	0.1162	1162.3
4	Delete:	C_4	63	0.3165	3339.9
Case	Current terms: (C_2 C_4 C_5 C_6)				
			df	RSS	AARD (%)
6	Delete:	C_6	64	0.0268	191.1
7	Delete:	C_2	64	0.1048	1039.4
8	Delete:	C_5	64	0.1163	1163.4
9	Delete:	C_4	64	0.3166	3341.1
Case	Current terms: (C_2 C_4 C_5)				
			df	RSS	AARD (%)
10	Delete:	C_5	65	0.1337	1353.4
11	Delete:	C_4	65	0.3561	3769.8
12	Delete:	C_2	65	0.5552	5933.7
Case	Current terms: (C_2 C_4)				
			df	RSS	AARD (%)
13	Delete:	C_2	66	0.6622	7096.0
14	Delete:	C_4	66	1.7944	19401.0

Table 9.5-12. ARC Regression Output for the Predictive Optimum CPMX Correlation.

Parameter	Estimate	σ wrt Estimate
C_1	3.92	0.010
C_2	0.00267	0.000105
C_4	-0.0519	0.00114
C_5	0.000904	0.000034
C_6	0.000084	0.000008

Residual Sum of Squares: 0.0093
Degree of Freedom: 63

Notice that all of the estimates are larger relative to their standard errors. Comparing the estimates from the full model to the optimum model, there was relatively little difference between the estimated values. The proposed optimum model provides the following correlations between the estimates as shown in Table 9.5-6.

Table 9.5-13. Correlation Matrix of the Coefficient Estimates, for the Optimum P_{MEA} Model.

Parameter	1	2	3	4	5
1	1.00				
2	-0.86	1.00			
3	-0.78	0.44	1.00		
4	0.43	*0.00*	-0.83	1.00	
5	0.71	-0.82	-0.54	*0.00*	1.00

Table 9.5-6 shows only two independent correlations between all of the parameter estimates suggesting that some of the remaining parameters might be usefully removed from the model without significant loss of information. Table 9.5-5 demonstrated that with further elimination of parameters, the deviation between the possible submodels and the full model increases beyond an adequate level for the predictive correlation to describe systematic trends in the smoothed data.

Figure 9.5-2 demonstrates the predictive quality of Equation 9-48 based on coefficients from Table 9.5-12 for the optimum model. The functional form of Equation 9-

48 adequately describes the predictions from the elecNRTL model within an average absolute relative error of ± 0.25 percent.

Since there are only minor differences between Equation 9-48 and the predictions from the elecNRTL model, we can illustrate nonideality of the solution equivalent to the excess specific heat capacity using the Redlich-Kister equation to represent the concentration dependence as shown in Equation 9-49.

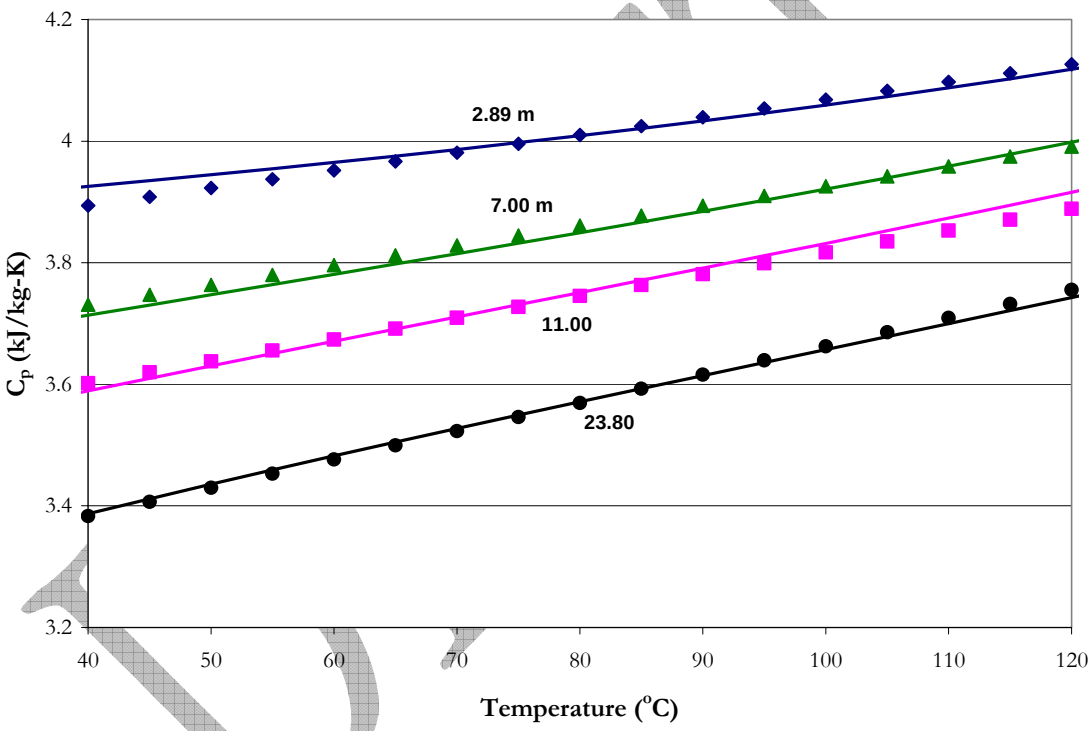

Figure 9.5-2. Comparison of Specific Heat Capacity Predictions from Equation 9-48 to elecNRTL Model Predictions from 40 – 120 °C. Points: Smooth Prediction at ♦, 2.89 m (mole/kg-H_2O), ▲, 7 m, ■, 11 m, •, 23.8 m. Lines: —, original elecNRTL Predictions.

$$C_p^E = C_p^l - \left(x_{H_2O} C_{p,H_2O}^* - x_{MEA} C_{p,MEA}^* \right) \qquad 9\text{-}52$$

Where

C_p^E is the excess specific heat capacity, kJ/kmol-K,

C_p^l is the molar heat capacity of the mixture, Equation 9-48,

x_i is the mole fraction of component i,

$C_{p,i}^*$ is the pure component molar heat capacity (ref. Chapter VIII).

In general, the value of the excess specific heat capacity will indicate the degree of nonideality of the binary mixture; as the value of the excess specific heat capacity decreases, the closer the binary mixture will approach an ideal solution. Figure 9.5-3 illustrates the departure from ideal behavior as compared to predictions from the elecNRTL model.

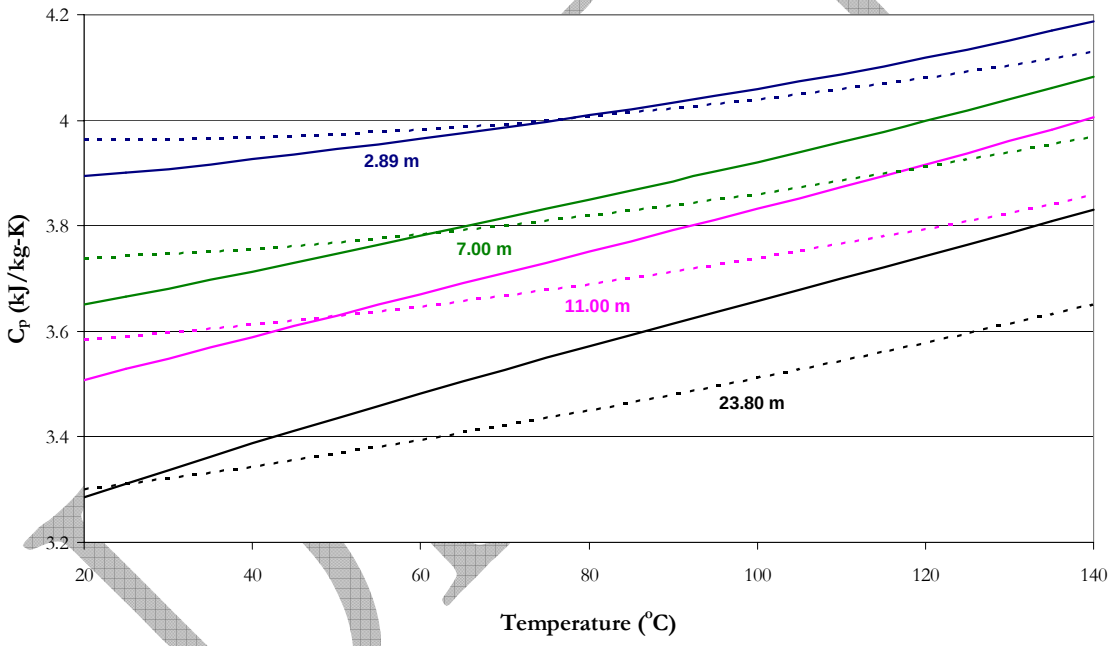

Figure 9.5-3. Comparison of elecNRTL Model Predictions of Ideal and Solution Specific Heat Capacity from 20 – 140 °C. Lines: - - -, Ideal Behavior, ═, Solution Behavior.

Figure 9.5-3 demonstrates that as the concentration of MEA increases, the nonideality of the solution also increases. An ideal solution can adequately describe the specific heat capacity for 2.89 m MEA within ± 1.0 %, but for concentrations greater than 7 m MEA, this ability breaks down. As far as the degree of nonideality, the ratio of the excess

specific heat capacity to the solution specific heat capacity has been shown to be a suitable replacement factor for the absolute value of the excess heat capacity (Chiu and Li (1999)).

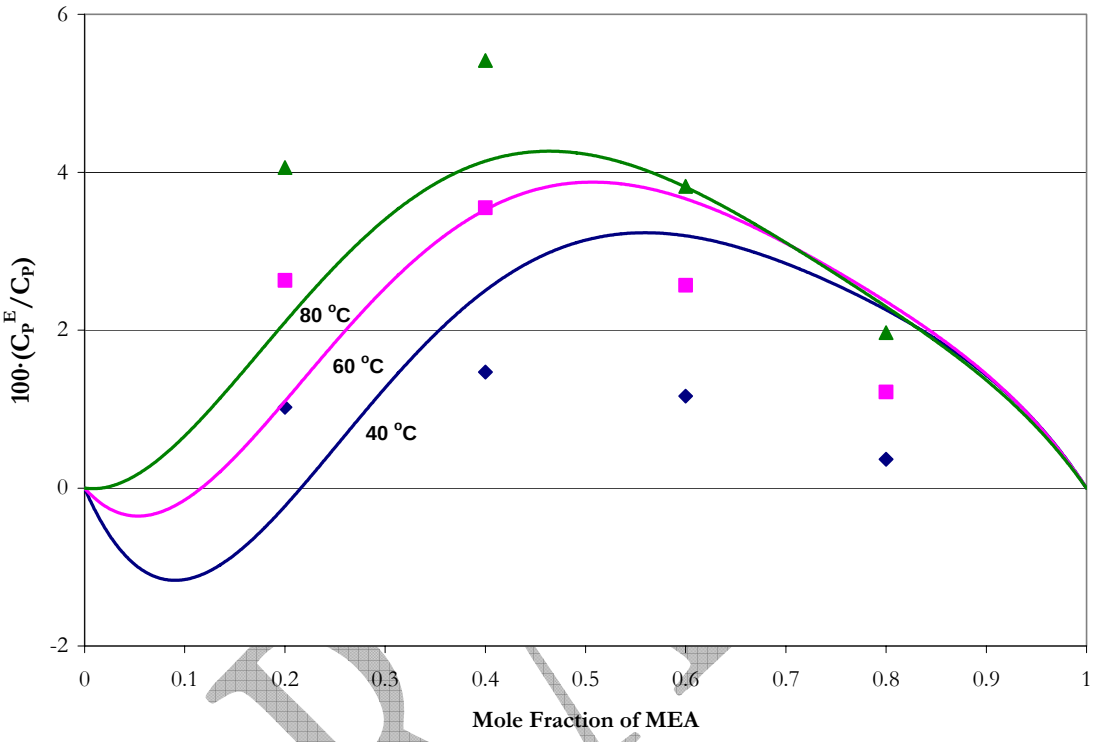

Figure 9.5-4. The Ratio of the Excess Specific Heat Capacity to the Mixture Specific Heat Capacity based on Predictions from the elecNRTL Model as compared to Chiu and Li (1999) at 40, 60, and 80 °C. Points: Chiu and Li (1999) ♦, 40 °C, , ■, 60 °C, and ▲, 80 °C. Lines: ━, elecNRTL Predictions.

Figure 9.5-4 illustrates the differences between the two authors to describe the ideal solution since we have already shown the elecNRTL model to match the specific heat capacity of the solution within ± 1.37 %. As shown in Chapter XIII, Chiu and Li (1999) over predicted the specific heat capacity of H_2O and MEA as compared to previous authors. This discrepancy would explain the difference shown in Figure 9.5-4 in addition to the behavior shown in Figure 9.5-3. Chiu and Li (1999) described the excess specific heat

capacity with a Redlich-Kister expansion taking into account concentration and temperature dependences. Chiu and Li (1999) noted a 60 % AARD between the model predictions and calculated results for the excess specific heat capacity, but concluded the calculated values looked reasonable.

Using the elecNRTL model, we can extend the description of the behavior of excess properties of liquid H_2O-MEA mixtures. Those of primary interest are the excess Gibbs free energy $\left(G^E / RT\right)$ in addition to the excess enthalpy or heat of mixing $\left(H^E / RT\right)$ which is related to the temperature derivative of the excess Gibbs free energy, where the excess entropy is normally calculated from the following equation

$$G^E = H^E - TS^E \qquad 9\text{-}53$$

Figure 9.5-5 demonstrates the composition dependence of G^E, H^E, TS^E, and $C_p{}^E$ for H_2O-MEA mixtures at 40 °C. Even though the system exhibits a diverse behavior, we can note some common features for excess properties:

1. All excess properties are zero for each pure component.
2. G^E may exhibit a parabolic shape, the structure of H^E and TS^E predictions are concentration dependent.

Figure 9.5-5 exhibits only one sign for the value of the excess properties, but the relative magnitudes of these quantities are useful for describing the solution behavior, in particular, the behavior of G^E in relation to H^E contributions. Abbott et al. (1994) presented a visual scheme to identify patterns in different mixture types based on a dimensionless form of Equation 9-50

$$\frac{G^E}{RT} = \frac{H^E}{RT} - \frac{S^E}{R} \qquad 9\text{-}54$$

where each contribution for the three excess properties defined a region on a plot of G^E/RT versus H^E/RT.

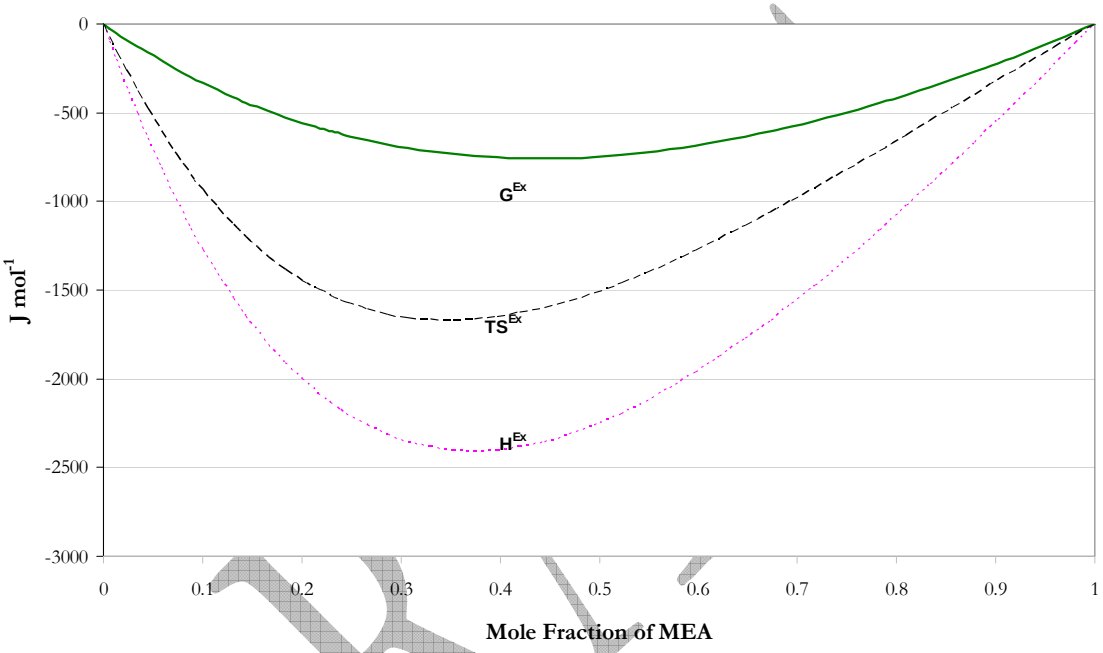

Figure 9.5-5. Excess Properties for H_2O-MEA Mixtures at 40 °C. Lines: ——, G^{Ex}, — —, TS^{Ex}, and - - -, H^{Ex}.

For mixtures of H_2O-MEA, Figure 9.5-6 illustrates the enthalpy dominates the solution behavior over the absorption and regeneration temperature range because, mixtures of H_2O-MEA offer a variety of opportunities for hydrogen-bonded dimers by either solvation or by association with respect to the molecular functional groups.

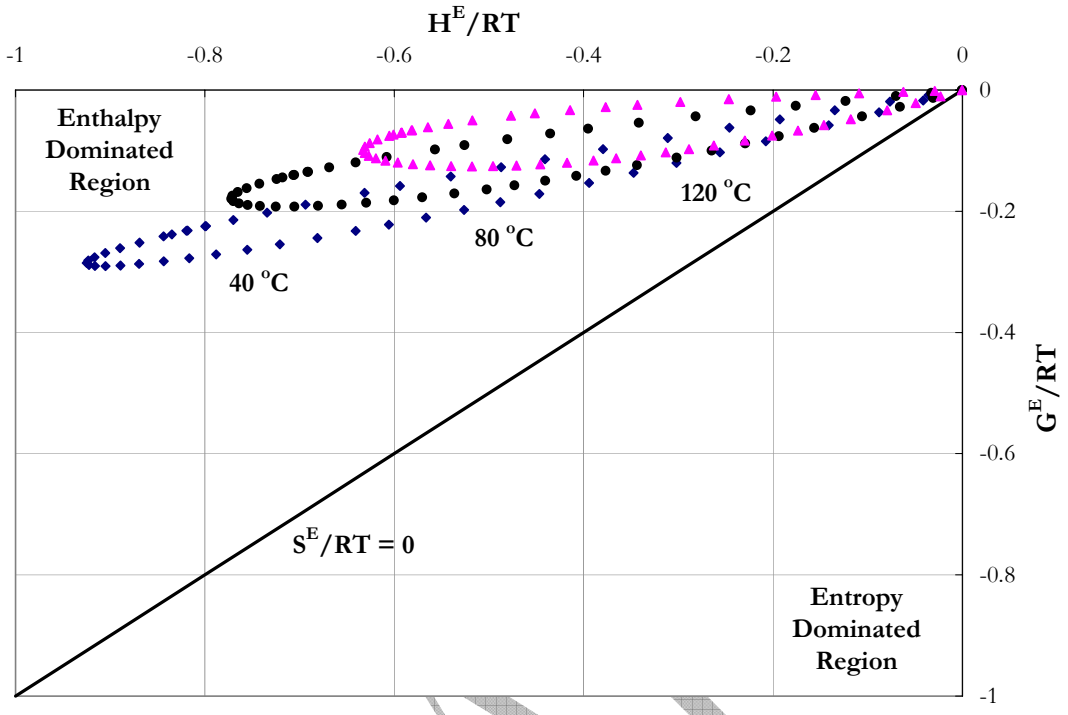

Figure 9.5-6. Equimolar Excess Properties for H2O-MEA Mixtures at 40, 80 and 120 °C.

9.6 Conclusions

To sum up, in this work we chose to use Equation 9-24 to represent the infinite dilution activity coefficient of monoethanolamine due to the small variations between Equation 9-24 and Equation 9-25. Based on the optimum model, parameters were fitted to a more extensive database than previous authors, thus infinite dilution activity coefficients predicted with the optimum model may give more realistic activity coefficients as a function of temperature and composition as compared to data found in the literature.

We saw that Figure 9.3-3 illustrated similar trends presented in Figure 9.3-2 where predictions for the infinite dilution activity coefficient for MEA reported by Austgen et al. (1989) as compared to predictions from this work crossed at 45 °C. Since both works used

Bates and Pinching (1951) to describe the dissociation of MEA, the only differences between the two reported K-values would be in the treatment of the infinite dilution activity coefficient of MEA applied to the linearization of the chemical equilibrium constant to the temperature dependent functional form.

In addition, the difference between the two predictions for the aqueous phase infinite dilution heat capacity of $MEAH^+$ accounted for differences is in the treatment of the activity coefficient of MEA at infinite dilution as shown in Figure 9.3-2 and in the linearization of the equilibrium constant for MEA.

Figure 9.4-1 and Figure 9.4-2 illustrated the departure from an ideal solution behavior vis-à-vis Raoult's Law as compared to predictions from the elecNRTL model. Over the temperature range from 25 to 91.7 °C, Raoult's Law adequately described the vapor pressure of H_2O-MEA mixtures below $x_{MEA} = 0.1$, but as the concentration of MEA increases so does the importance of including activities to describe the vapor-liquid equilibrium.

Figure 9.4-3 gave the results of fit for experimental isobaric (*Txy*) vapor-liquid equilibrium (VLE) data from Park and Lee (1997) and Cai et al. (1996) versus the concentration of water at 101.325 kPa. Given the degree of scatter between Park and Lee (1997) and Cai et al. (1996) to describe *Txy* behavior of H_2O-MEA mixtures at atmospheric pressure allowed Raoult's Law and the elecNRTL model to describes systematic trends presented in both data sets adequately. Overall, the optimum model adequately describes the *Txy* data within an average absolute relative error of ± 2.82 percent.

We chose to concentrate our modeling efforts to describe the partial pressure of MEA (amine volatility) between 3.5 and 7.0 m MEA due to limited data at 11.0 and 23.8 m MEA. Overall, the optimum model adequately describes the partial pressure of MEA within an average absolute relative error of ± 4.28 percent, with the exception of a few outliers. In addition, the optimum model adequately described the partial pressure of water within an average absolute relative error of ± 6.64 percent, with the exception of a few outliers. We would recommend that future work should endeavor to describe the binary system at stripper conditions (e.g. temperatures between 80 - 120 °C) to complete this analysis.

In terms of excess enthalpy, Figure 9.4-11 illustrated two important issues: one, the proposed Aspen method was unable to predict the liquid enthalpy of pure water; two, the method under predicted the temperature dependence of the activity coefficients for MEA and H_2O. The above results would then contradict the previous discussion, vis-à-vis the representation of the optimum model to adequately represent the regressed literature data. Figure 9.4-12 validated previous work by demonstrating Equation 9-15's ability to calculate the excess enthalpy. Even though the optimum model does not capture the excess enthalpy temperature dependence, the model does characterize the experimental data within an average absolute relative error of ± 9.17 percent.

In this work, the optimum model predicted a minimum value for the activity coefficient of MEA (x_{H2O} = 0.86, T = 120 °C) as shown in Figure 9.4-14, but the phase diagram at this temperature did not indicate the presence of an azeotrope (Figure 9.4-15). If we vary the temperature or pressure, results do not indicate the presence of an azeotropic

state. Thus, the azeotropic behavior for the activity coefficient of MEA, as reported in Poplsteinove (2004), may not adequately describe this situation.

The effective heat of vaporization of MEA from H_2O given in Table 9.5-7 reflects a relatively high heat of solution associated with strong interactions between H_2O and MEA. Thus, to evolve MEA from the liquid phase requires the heat of vaporization of pure MEA plus the effective heat of vaporization of MEA from H_2O. Recovery of MEA in industrial applications (i.e. absorber water washing) would require an additional parameter, in this case temperature, to design an effective process.

Figure 9.5-4 illustrated the differences between Chiu and Li (1999) and this work to describe the ideal. As shown in Chapter XIII, Chiu and Li (1999) over predicted the specific heat capacity of H_2O and MEA as compared to previous authors. This discrepancy would explain the difference shown in Figure 9.5-4 in addition to the behavior shown in Figure 9.5-3. Chiu and Li (1999) described the excess specific heat capacity with a Redlich-Kister expansion taking into account concentration and temperature dependences, but noted a 60 % AARD between the model predictions and calculated results for the excess specific heat capacity. They concluded the calculated values looked reasonable.

For mixtures of H_2O-MEA, Figure 9.5-6 illustrated that as compared to the excess Gibbs free energy the enthalpy dominates the solution behavior over the absorption and regeneration temperature range because, mixtures of H_2O-MEA offer a variety of opportunities for hydrogen-bonded dimers by either solvation or by association.

Overall, the results presented above indicate that the elecNRTL model, through simultaneous regression gave a set of optimum binary interaction parameters for the H_2O-

MEA system. The optimum model adequately represents the literature data for aqueous MEA mixtures.

References

1. The Alkanolamines Handbook. 3rd ed.; The Dow Chemical Company: Midland, Michigan, 1981.
2. Arc Version 1.06, http://www.stat.umn.edu/arc/: 2004.
3. Abbott, M. M.; O'Connell, J. P., Chemical Engineering Education 1994, 28, 18-23 and 77.
4. Austgen, D. M.; Rochelle, G. T.; Chen, C. C., Model of Vapor-Liquid Equilibria for Aqueous Acid Gas-Alkanolamine Systems. 2. Representation of H2S and CO2 Solubility in Aqueous MDEA and CO2 Solubility in Aqueous Mixtures of MDEA with MEA or DEA. Ind. Eng. Chem. Res. 1991, 30, (3), 543-555.
5. Austgen, D. M.; Rochelle, G. T.; Peng, X.; Chen, C. C., Model of Vapor-Liquid Equilibria for Aqueous Acid Gas-Alkanolamine Systems Using the Electrolyte-NRTL Equation. Ind. Eng. Chem. Res. 1989, 28, 1060-1073.
6. Bates, R. G.; Pinching, G. D., Acidic Dissociation Constant and Related Thermodynamic Quantities for Monoethanolammonium Ion in Water From 0 to 50 oC. Journal of Research of the National Bureau of Standards 1951, 46, (5), 349352.
7. Cai, Z.; Xie, R.; Wu, Z., Binary Isobaric Vapor-Liquid Equilibria of Ethanolamines + Water. Journal of Chemical Engineering Data 1996, 41, (5), 1101-1103.

8. Chang, H. T.; Posey, M.; Rochelle, G. T., Thermodynamics of Alkanolamine-Water Solutions from Freezing Point Measurements. Ind. Eng. Chem. Res. 1993, 32, (10), 2324-2335.
9. Chiu, L. F.; Li, M. H., Heat Capacity of Alkanolamine Aqueous Solutions. Journal of Chemical Engineering Data 1999, 44, (6), 1396-1401.
10. Chiu, L. F.; Liu, H. F.; Li, M. H., Heat Capacity of Alkanolamines by Differential Scanning Calorimetry. Journal of Chemical Engineering Data 1999, 44, (4), 631-636.
11. Deshmukh, R. D.; Mather, A. E., A Mathematical Model for Equilibrium Solubility of Hydrogen Sulfide and Carbon Dioxide in Aqueous Alkanolamine Solutions. Chemical Engineering Science 1981, 36, 355-362.
12. Harned, H. S.; Owen, B. B., The Physical Chemistry of Electrolyte Solutions. 3rd ed.; Reinhold: New York, 1958.
13. Kaewsichan, L.; Al-Bofersen, O.; Yesavage, V. F.; Selim, M. S., Predictions of The Solubility of Acid Gases in Monoethanolamine (MEA) and Methyldiethanolamine (MDEA) Solutions Using the Electrolyte-UNIQAC Model. Fluid Phase Equilibria 2001, 183-184, 159-171.
14. Kim, J. H.; Dobrogowska, C.; Hepler, L. G., Thermodynamics of Ionization of Aqueous Alkanolamines. Canadian Journal of Chemistry 1987, 65, 1726-1728.
15. Lee, L. J. B. A Vapor-Liquid Equilibrium Model for Natural Gas Sweetening Process. The University of Oklahoma, Norman, Oklahoma, 1996.
16. Li, Y. G.; Mather, A. E., Correlation and Prediction of The Solubility of CO2 in a Mixed Alkanolamine Solution. Ind. Eng. Chem. Res. 1994, 33, 2006-2015.

17. Nath, A.; Bender, E., Isothermal Vapor-Liquid Equilibrium of Binary and Ternary Mixtures Containing Alcohol, Alkanolamine, and Water with a New Static Device. Journal of Chemical Engineering Data 1983, 28, (4), 370-375.
18. Page, M.; Huot, J. Y.; Jolicoeur, C., A Comprehensive Thermodynamic Investigation of Water-Ethanolamine Mixtures at 10, 25, and 40 oC. Canadian Journal of Chemistry 1993, 71, (7), 1064-1072.
19. Park, S. B.; Lee, H., Vapor-Liquid Equilibria For the Binary Monoethanolamine + Water and Monoethanolamine + Ethanol Systems. Korean Journal of Chemical Engineering 1997, 14, (2), 146-148.
20. Poplsteinova, J. Absorption of Carbon Dioxide - Modeling and Experimental Characterization. Norwegian University of Science and Technology, Trondheim, Norway, 2004.
21. Posey, M. L. Thermodynamic Model for Acid Gas Loaded Aqueous Alkanolamine Solutions. The University of Texas at Austin, Austin, 1996.
22. Prausnitz, J. M.; Lichtenthaler, R. N.; de Azevedo, E. G., Molecular Thermodynamics of Fluid Phase Equilibria. 3rd ed.; Prentice Hall PTR: New York, 1999.
23. Renon, H.; Prausnitz, J. M., Local Compositiions in Thermodynamic Excess Functions for Liquid Mixtures. AICHE J. 1968, 14, (1), 135-44.
24. Rowley, R. L.; Wilding, W. V.; Oscarson, J. L.; Yang, Y.; Zundel, N. A., DIPPR® Data Compilation of Pure Chemicals Properties, Design Institute for Physical Properties. In Brigham Young University. Provo, Utah.: 2004.

25. Tochigi, K.; Akimoto, K.; Ochi, K.; Liu, F.; Rawase, Y., Isothermal Vapor-Liquid Equilibria for Water + 2-Aminoethanol + Dimethyl Sulfoxide and Its Constituent Three Binary Systems. Journal of Chemical Engineering Data 1999, 44, (3), 588-590.
26. Touhara, H.; Okazaki, S.; Okino, F.; Tanaka, H.; Ikari, K.; Nakanishi, K., Thermodynamic Properties of Aqueous Mixtures of Hydrophilic Compounds 2. Aminoethanol and its Methyl Derivatives. Journal of Chemical Thermodynamics 1982, 14, 145-156.
27. Weiland, R. H.; Chakravarty, T.; Mather, A. E., Solubility of Carbon Dioxide and Hydrogen Sulfide in Aqueous Alkanolamines. Ind. Eng. Res. 1993, 32, 1419-1430.
28. Weiland, R. H.; Digman, J. C.; Cronin, D. B., Heat Capacity of Aqueous Monoethanolamine, Diethanolamine, N-Methyldiethanolamine, and N-Methyldiethanolamine-Based Blends with Carbon Dioxide. Journal of Chemical Engineering Data 1997, 42, (5), 1004-1006.

Attachment 2

Carbon Dioxide Absorption into Piperazine Promoted Potassium Carbonate using Structured Packing

Draft Chapters

Ph.D. dissertation

Eric Chen

Chapter 1: Pilot Plant Experimental Setup, Methods, and Results

The experiments for this work were conducted at the pilot plant facility operated by the Separations Research Program (SRP) of The University of Texas at Austin (UT). The facility is located at the J.J. Pickle Research Center, 20 minutes north of the main UT campus. SRP typically uses the facility to conduct distillation and extraction experiments for industrial companies and also aids UT graduate students with pilot-scale work.

As part of this work, the existing pilot plant facility was extensively modified and converted to an absorber/stripper system prior to the startup of the first CO_2 capture campaign. New analytical equipment, process instrumentation, stainless steel process equipment and piping were added as part of the modification. A total of four pilot plant campaigns were conducted; three pilot plant campaigns that used aqueous piperazine promoted potassium carbonate and one campaign with monoethanolamine (MEA) to establish a base case for comparison. The four campaigns were completed over a period of four years. When the pilot plant was not being used for this work, it was reconfigured back to the original setup and used to run distillation and extraction experiments.

This work will focus on the three potassium carbonate and piperazine campaigns. The results of the MEA campaign can be found in Dugas (2006). Incremental improvements and modifications to the pilot absorber/stripper system were made over the course of the four

campaigns. This chapter details the pilot plant equipment and setup, the modifications that were made for each campaign, sampling and analytical methods developed by this work, and the results from each of the campaigns. An overview of the four campaigns is given by Table 1-1.

Table 1-1. Summary of the 4 Pilot Plant Campaigns

Campaign	Solvent	Absorber Packing	Stripper Packing
1	5m K^+/2.5m PZ	Flexipac 1Y	Sieve Trays
2	5m K^+/2.5m PZ	Flexipac 1Y	IMTP#40
3	7m MEA	Flexipac 1Y	IMTP#40
	7m MEA	IMTP#40	Flexipac 1Y
4	5m K+/2.5m PZ	Flexipac AQ Style 20	Flexipac AQ Style 20
	6.4m K+/1.6m PZ	Flexipac AQ Style 20	Flexipac AQ Style 20

1.1 EXECUTIVE SUMMARY OF PILOT PLANT CAMPAIGNS

This section presents a summary of the major issues that were resolved, through trial and error, over the course the four pilot plant campaigns. Preheating the stripper feed solvent was most efficiently done with a plate and frame heat exchanger in terms of performance and relative cost. The cross exchanger is a critical part of the absorption and stripping system. Preheating and saturating the absorber inlet gas was performed most effectively with a steam injector. The in-situ CO_2 analyzers needed be protected from non-condensing water and the extractive sampling system performed best when the sample lines were heated to prevent condensation of water. Liquid sampling was best done using sample bombs to minimize the flashing of CO_2 especially at rich loadings and high temperatures. It is also recommended to allow the hot sample bombs to be cooled prior to sample extraction. The liquid analytical techniques need to be fully developed prior to the start of pilot plant experiments and sample quality assurance and control is extremely important. Due to the inherent variability of a pilot plant, all the possible unknowns must be eliminated for proper interpretation of critical data. The calibration of the process equipment for to validate the measured flow rates is critical and introduces addition

unknown if not done. Gas flow measurements are difficult and expensive, but are critical if any data is to be extracted. Measurement of water concentration in the gas may be critical in data interpretation because the transfer of enthalpy between the liquid and vapor is dependent on the water content of the inlet gas and the temperature of the inlet liquid. In the pilot plant, the inlet liquid temperature may not have been adequately measured because the nearest temperature measurement was 15 meters away from the absorber inlet. Heat loss from the 5.1 cm pipe may have resulted in slightly lower temperatures than that measured. The titration and ion chromatography methods developed for measuring piperazine and potassium concentration needed to be reconciled. The difference in CO_2 loading between the on-campus inorganic carbon analyzer and that of the Shimadzu Total Organic Carbon analyzer should also be reconciled, possibly using standard made up of both sodium bicarbonate and carbonate and also standards that contain only of each. Also, the inlet CO_2 gas concentration appeared to cycle with the stripper valve opening and closing. A new process control technique should be developed to address this issue. An efficient analysis of the CO_2 loading in the liquid is needed to allow a rapid material and heat balance during actual operation. The maintenance of the water balance, temperature, and CO_2 loading is extremely important for the piperazine and potassium carbonate system in order to avoid solubility issues, which can result in instrument and equipment failure and possible plant shutdown.

1.2 TIMELINE OF PILOT PLANT CAMPAIGNS

Quarter	Action
2002 Q4	▪ Start of project
2003 Q1	▪ Order solvent cooler
2003 Q2	▪ Piping demolition ▪ Piping iso drawn ▪ Created Welding bid ▪ Solvent cooler procured ▪ Ordered air cooler, 5 Micro Motion® flowmeters, Vaisala CO_2 analyzers,

	raw materials
2003 Q3	▪ Test Plan ▪ Begin welding ▪ Air cooler procured ▪ Analytical method development, ▪ Purchased for RTD for absorber ▪ Installation of solvent heater, solvent cooler, control valves, Micro Motion® flowmeters, and filters on support racks
2003 Q4	▪ Pipe welding
2004 Q1	▪ Welding completed ▪ Installation of instrumentation 90% complete ▪ Excel absorber model completed ▪ Gas line
2004 Q2	▪ Campaign 1 commenced in May ▪ Measured effective interfacial area for Flexipac 1Y ▪ Load chemicals ▪ Begin operation mid-June for 7 days
2004 Q3	▪ Campaign 1 Data analysis ▪ Campaign 2 modifications ▪ Test plan
2004 Q4	▪ Build sample bombs ▪ Construct bypass around blower to heat up gas ▪ Campaign 2 (mid-October to mid-November) ▪ Campaign 2 loading and data analysis
2005 Q1	▪ Loading analysis resolution ▪ MEA modifications ▪ Built new CO_2 makeup heater and 0-5%Horiba sampling unit ▪ Ordered new stainless steel reboiler ▪ Campaign 3 (MEA, mid-March to mid-April)
2005 Q2	▪ Replaced PVC airline stainless steel ▪ Designed new air heater and cross-exchanger ▪ New reboiler procured ▪ Data analysis
2005 Q3	▪ Design carbon filter ▪ Procure parts for FTIR ▪ Installation of reboiler ▪ Test plan ▪ Solubility experiments.
2005 Q4	▪ Bench-scale density and pH measurements ▪ IC method development ▪ Installation of cross-exchanger, carbon filter, heat lines, FTIR
2006 Q1	▪ Campaign 4 (January to February)

1.3 CAMPAIGN ONE – PILOT PLANT SETUP AND TROUBLESHOOTING

The main objectives of the first campaign were the design, modification, startup and troubleshooting of the pilot absorber/stripper system. The existing distillation and extraction pilot plant was converted into an absorber and stripper system. The modifications were made such that the pilot plant could be easily converted between the two modes of operation. The second objective was to obtain characterization data for the absorber and stripper with FLEXIPAC® 1Y structured packing and sieve trays, respectively.

1.3.1 Existing Major Equipment

The pilot plant facility was constructed in 1986 and originally designed for distillation and extraction experiments. The pilot plant consists of two columns, each with an internal diameter of 0.43 m and constructed from 18-inch schedule 40 carbon steel pipe. Both columns have a number of penetration points, manways, and sight glass windows along the entire length of the vessel. The height of each column is approximately 13.3 meters. The column that is used typically for distillation experiments is insulated with calcium silicate, while the extraction column is not insulated. In the CO_2 absorption campaigns, the distillation column was used as the stripper and the extraction column was used as the absorber. The absorption column is packed with 6.1 m of packing, which are divided into two beds of 3.05 m. In between each packed bed, there is a spool piece that swings out to facilitate packing change-outs. Also, within each spool piece, there is a chimney tray and a redistributor just below. There is no water wash section above the top of the absorber packing, as in conventional plants. When trays are used, it is installed as one continuous section from the top of the column to bottom. A picture of the pilot plant facility is shown in Figure 1-1 and a schematic of the absorber and stripper is given by

Figure 1-2. A process and instrumentation diagram of the absorber and stripper are shown in Figure 1-3 and Figure 1-4, respectively.

Figure 1-1. Pilot Plant Facility Located at UT SRP with the Stripper Column and Reboiler on the Left Side, Absorber Column on the Right Side, Absorber Feedtank and Overhead Gas Accumulator on the First Platform (Picture Taken by C. Lewis)

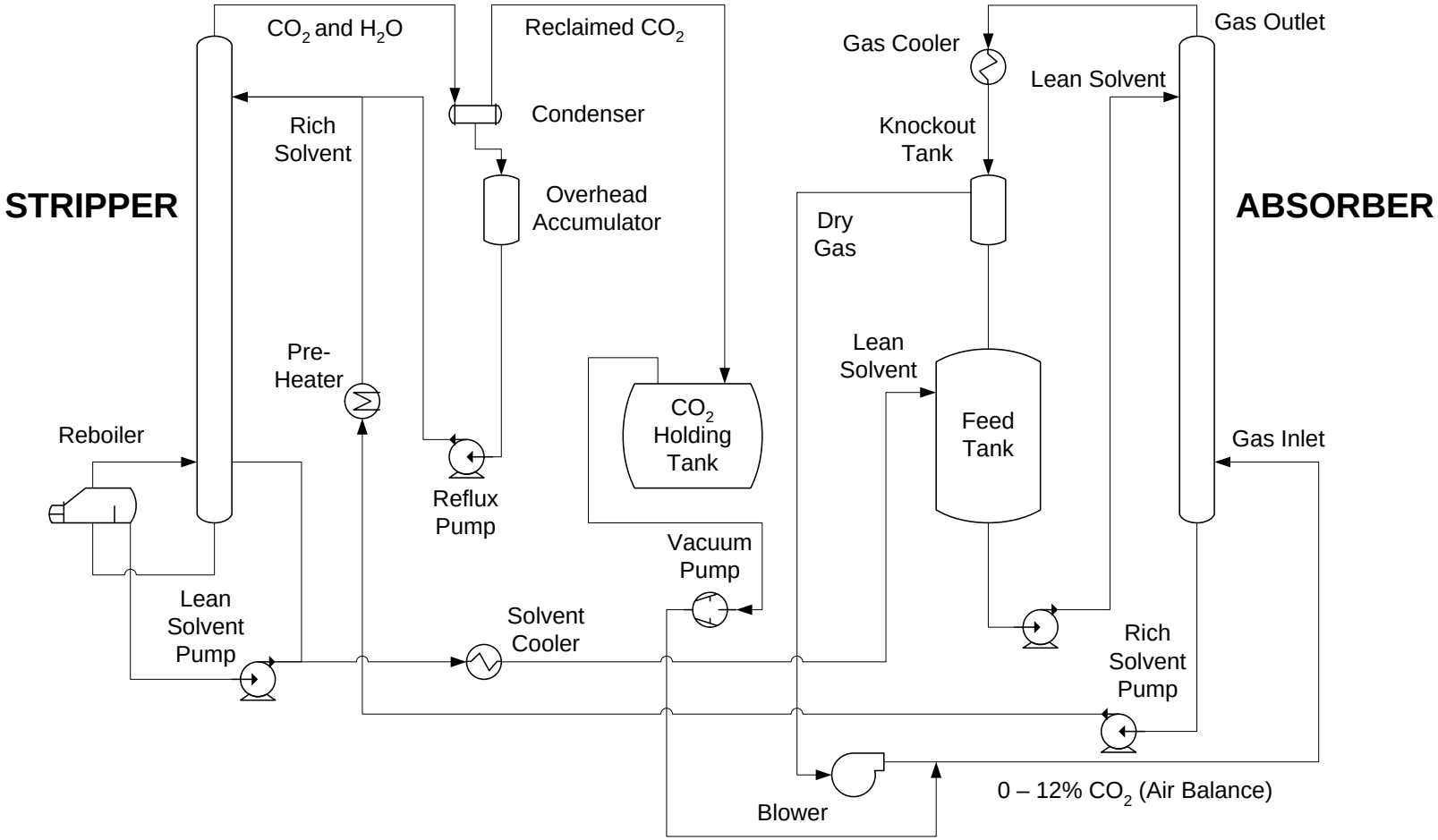

Figure 1-2. Process Flowsheet of Absorber/Stripper Pilot Plant for Campaign 1

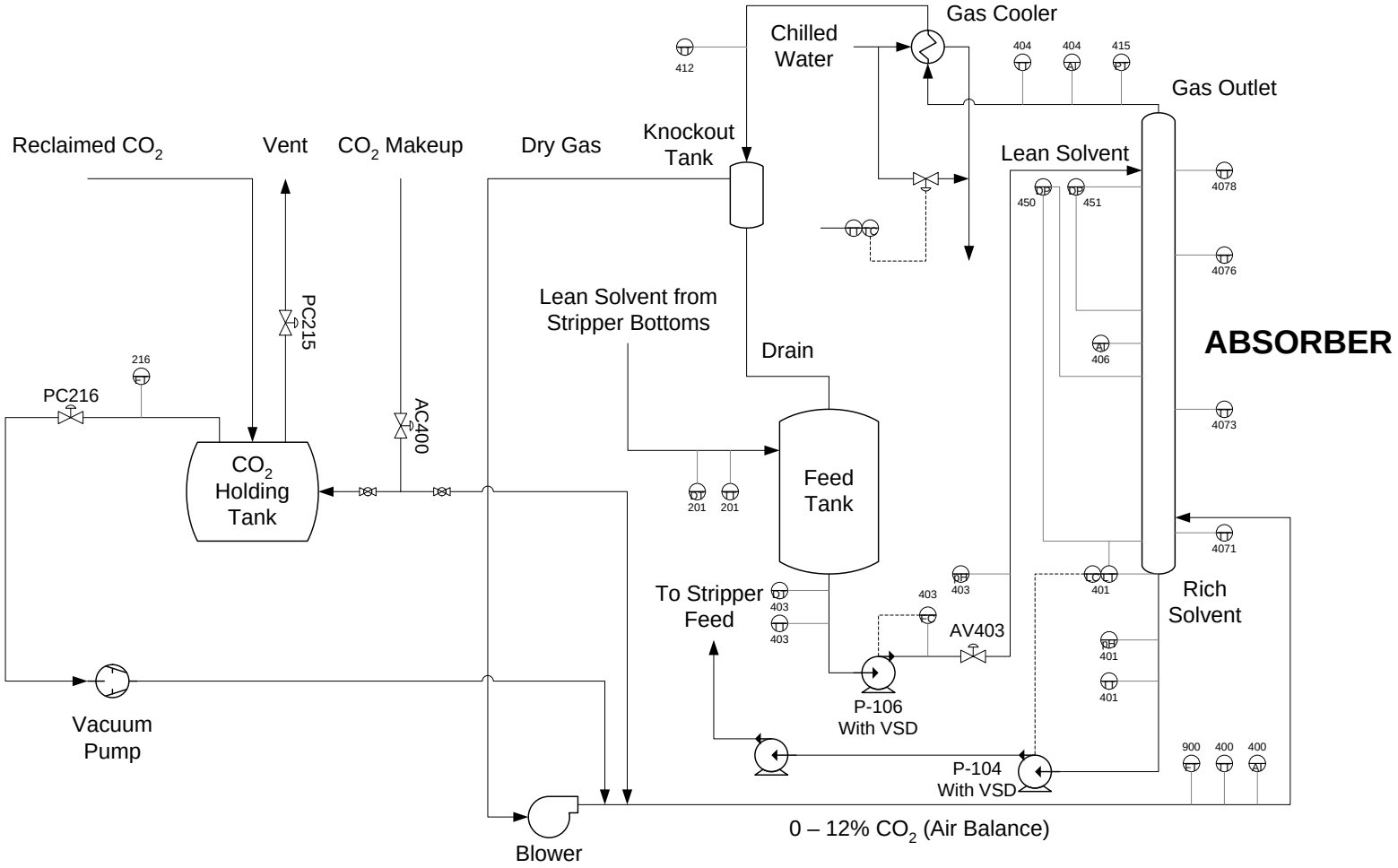

Figure 1-3. Process and Instrumentation Diagram of the Absorber for Campaign 1

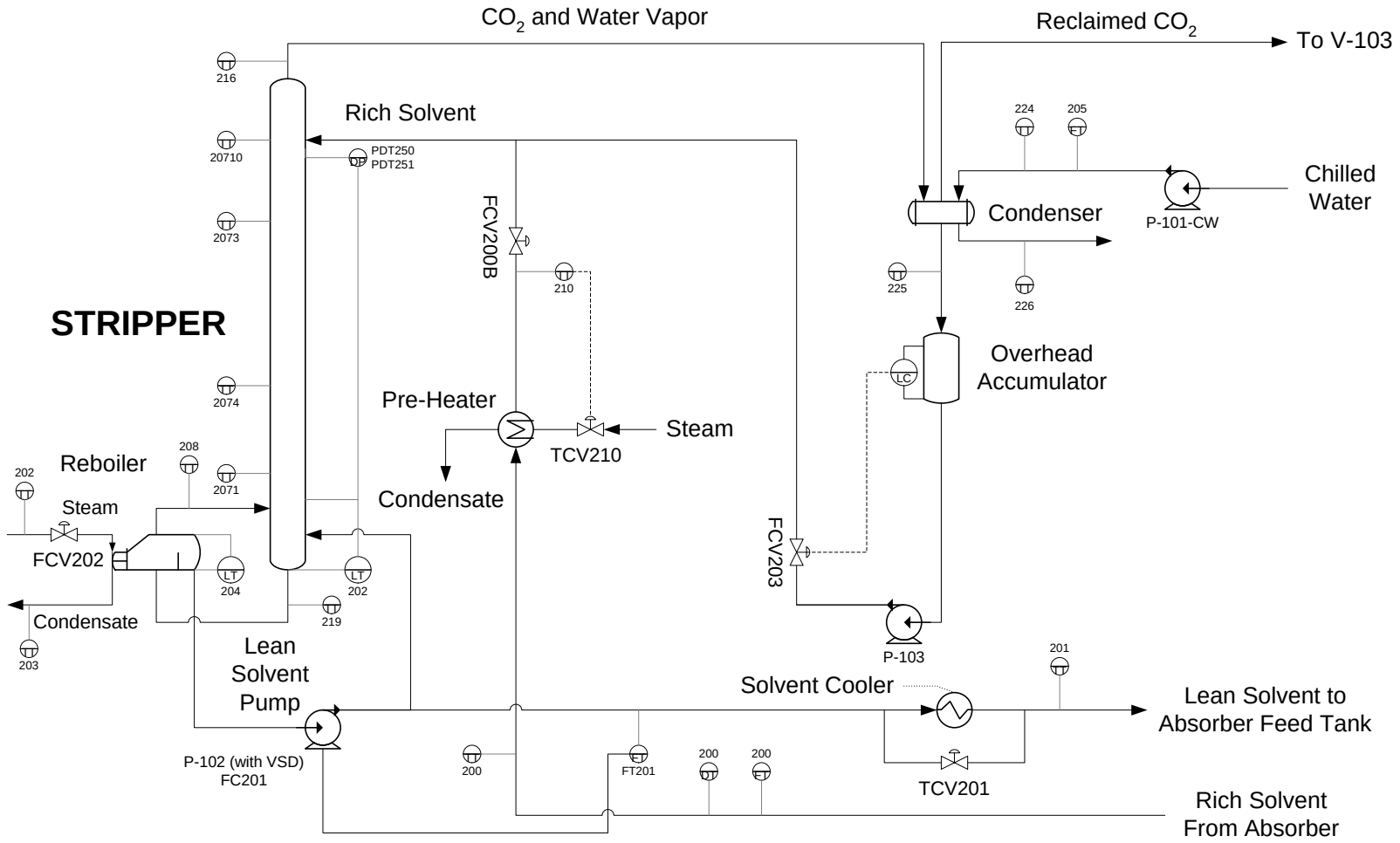

Figure 1-4. Process and Instrumentation Diagram of the Stripper for Campaign 1

The majority of the existing equipment was retained, which included a blower, 6 centrifugal pumps, several feed tanks, a reboiler, condenser, and vacuum pump (Table 1-2). The blower (C-103) is normally operated as a standalone unit and used to provide ambient air to an air-water column. During the operation of the CO_2 capture campaigns, the blower was used to recycle the gas from the top of the absorber to back to inlet. The silencer of the blower was removed and a new piping was installed to connect the blower inlet to the outlet of the water knockout. The blower is also equipped with a variable speed drive.

In the first campaign, only four of the centrifugal pumps were used. The pumps have capacities that range from 3.4 to 22.7 m^3/hr (15 to 100 gpm). The impellers of the pumps are made of carbon steel. During the course of the campaigns, it was discovered that the pump seals needed to be made out of Ethylene-Propylene-Diene Monomer (EDPM) rubber. Other types of rubber seals eventually resulted in leaks. There are two pumps associated with absorber, one that pumps lean solvent absorber feed tank to the top of the absorber (P-106) and one that pumps rich solvent from the bottom of the absorber to the stripper (P-104). There are two pumps associated with the stripper. One pump is used to pump liquid solvent from the bottom stripper reboiler to the solvent cooler (P-102). The other pump is used to pump the reflux from the overhead liquid condenser back to the stripper feed (P-103). Most of the pumps have variable speed drives, which eliminates the need for control valves and dramatically improves flow control.

In the existing facility, there are two identical liquid feed-tanks, one for each of the columns. For the CO_2 capture campaigns, only the absorber feed-tank was used (V-105). The feed tank is constructed out of carbon steel and has a volume of 3.6 m^3. The top of the feed-tank vented to the atmosphere to prevent a vapor lock. In addition, a portion of the solvent in the absorber feed-tank is continuously re-circulated. There is also another large feed-tank, the overhead gas accumulator, which is used to store the CO_2 gas from the condenser (V-103). The overhead gas accumulator has a volume of 2.4 m^3 and is made of carbon steel. A control valve was installed downstream of the gas accumulator to regulate the pressure in the stripper column. There is also vent on the gas accumulator which is regulated by a control valve. Water from condenser is stored in the overhead liquid accumulator (V-106) before it is pumped back to stripper feed as reflux. The overhead liquid accumulator has a volume of 0.2 m^3 and is made of carbon steel.

Table 1-2. Pilot Plant Equipment Specifications

Equipment	Function	Status	Equipment Specification				MOC	T_{DSGN} (°C)	P_{DSGN} (kPag)	Phase
Vessels			Vol (m^3)	ID (cm)	No. Bed	Bed Ht (m)				
V-102	Stripper	Existing	-	42.7	2	3.05	CS	200	520	G/L
V-104	Absorber	Existing	-	42.7	2	3.05	CS	180	520	G/L
V-103	OVHD Horiz. Acc.	Existing	2.4	-	-	-	CS	200	520	G
V-105	Absorber Feed Tank	Existing	3.6	-	-	-	CS	230	520	L
V-106	OVHD Liq. Acc.	Existing	0.2	-	-	-	CS	150	520	L

Heat Exchangers			Type	Duty (MJ/hr)	Area (m^2)	Passes	Shell	Tube	Shell	Tube	Shell	Tube	Shell	Tube
H-101A	Feed Heater	New	Hairpin	840	9.9	1-1	CS	316	340	200	3450	3450	STM	L
H-101B	Feed Heater	New	Hairpin	840	9.9	1-1	CS	316	340	200	3450	3450	STM	L
H-107	Solvent Cooler	New	Fixed	1800	13.4	1-2	316	316	230	230	1550	1030	L	CW
H-111	Condenser Preheater	Existing	Fixed	230	1.5	1-4	316	316	230	230	1550	1030	STM	L
H-112	Air Cooler	New	Fixed	490	19.8	-	316	316	-	-	-	-	G	CW

Condensers/Reboilers			Type	Duty (MJ/hr)	Area (m^2)	Passes	Shell	Tube	Shell	Tube	Shell	Tube	Shell	Tube
H-102	Reboiler	Existing	Fixed	2500	18.6	1-2	CS	CS	200	200	690	1210	G/L	STM
H-104	Condenser	Existing	Fixed	2480	14.3	1-1	CS	CS	150	180	1030	1030	G/L	CW

Pumps			Cap (m^3/hr)	Diff Hd (m)	Eff. (%)	Type	Power (kW)				
P-102-DI	Stripper Bottoms Pump	Existing	6.8	59.4	27	Centrifugal	5.6	CS	180	1310	L
P-103-DI	OVHD Acc Pump	Existing	3.4	61.0	15	Centrifugal	5.6	CS	180	1310	L
P-104-DI	Absorber Pump	Existing	22.7	36.6	59	Centrifugal	5.6	CS	180	1660	L
P-105-DI	Absorber Pump	Existing	3.4	36.6	16	Centrifugal	3.7	CS	180	1660	L
P-106-DI	Absorber Feed Pump	Existing	11.4	41.1	42.5	Centrifugal	3.7	CS	180	1660	L

Blower/Vacuum Pump			Cap (m^3/hr)	DP (kPa)	Power (kW)				
C-102A	Vacuum Pump	Existing	730	100	11.2	CS	-	70	G
C-103	Blower	Existing	2550	20	29.8	CS	650	35	G

Notes:
DSGN = Design
ID = Inner Diameter
MOC = Material of Construction
OVHD = Overhead

The carbon steel reboiler (H-102) on the stripper is a kettle-type boiler and has a surface area of 18.6 m^2. Liquid is circulated from the bottom of the stripper to the bottom of the reboiler. Liquid is pumped from the bottom of the reboiler, on the opposite end of the feed nozzle. Vapor generated by the reboiler is fed through a nozzle on the side of the stripper, just above the liquid level in the sump. The reboiler and associated piping are all insulated. Low pressure steam from the university gas-fired steam boiler at 930 kPa (135 psi) is used to heat the reboiler. The reboiler is located adjacent to the stripper and the reboiler level varied from 14 to 37 cm (5.4 – 15 in.).

The two phase condenser (H-104) for the stripper is located on the top level of the pilot plant structure. The 1-1 single pass condenser has a surface area of 14.3 m^2 and is constructed out of carbon steel. In the condenser, water and CO_2 from the overhead vapor of the stripper are separated. Water is condensed as liquid and fed to the overhead liquid accumulator from the bottom of the condenser. The non-condensable CO_2 vapor is sent to the overhead gas accumulator, before being recycled back to the feed gas.

The vacuum pump (C-102A) is used when the stripper is configured for vacuum operation. The vacuum pump is connected to a 2.5 cm (1 in.) nozzle on the CO_2 vapor outlet of the condenser. Due to the size of the nozzle, there is a limitation in the amount of CO_2 that could be stripped, which dictated certain flow ranges for vacuum operation of the pilot plant. During the operation of the vacuum pump, the CO_2 vapor comes into intimate contact with the lubricating oil. An oil separator is installed downstream to minimize the amount of entrainment. The vacuum pump is made of carbon steel.

Figure 1-5. Vaccum Pump (C-102A) Draws Gas from the Right Side and Discharges from the Top of the Oil Reservoir (Picture Taken by C. Lewis)

A reflux heater (H-111) is available, but is not used. The condensed water from the overhead liquid accumulator is pumped through the reflux before being mixed with the stripper feed stream.

The cooling water system consists of a feed-tank (T-101-CW), a heat exchanger (H-101-CW), and two pumps (P-101-CW and P-102-CW). The cooling water system is design so that it isolated from the university cooling water system. The pilot plant cooling water is cross-exchanged with the cooling water from the university and then stored in the cooling water feed-tank. Cooling water from the feed-tank is then pumped through the pilot plant system, in this case to the condenser of the stripper and/or the air

cooler. If there is ever a leak in one of the process exchangers, only the pilot plant cooling water system becomes contaminated.

1.3.2 New Major Equipment

In a typical industrial application, the rich solvent from the absorber is preheated by the lean stream leaving the stripper bottom through a plate and frame cross-exchanger. The exchanger is typically designed to achieve a temperature approach of 5 to 10 °C with the temperature of the reboiler. Preheating the rich solvent minimizes the reboiler heat duty. Due to the constraints of the pilot plant being a multi use facility, the solvent preheater and cooler were kept as separate pieces of equipment. As part of this work, the existing solvent cooler and preheater were replaced and a new air cooler was purchased.

The existing solvent preheater was undersized and was replaced with two Brown Fintube heat exchangers (H-101A and H-101B) that were installed in parallel (Figure 1-6). The hairpin exchangers were donated by Huntsman Chemical from an existing facility nearby. The U-tube heat exchangers each have a surface area of 9.9 m^2, 2.5 cm OD tubes, 7.6 cm shells, and 2.4 cm longitudinal fins. Exchanger drawings obtained from a local distributor showed that the tube side was constructed from stainless steel and the shell side was constructed of carbon steel. Therefore, in all of the CO_2 capture campaigns, the preheater exchangers were operated with the process stream on the tube side and 930 kPa (135 psi) low pressure steam was used on the shell side.

Figure 1-6. Solvent Preheater (H-101A & B) as Installed on Support Rack, along with Micro Motion® Flowmeters, and Control Valves (Picture Taken by C. Lewis)

An ITT standard model 08084 SSCFC heat exchanger was purchased and used as the new solvent cooler (H-107). The BEM type heat exchanger is constructed from type-316 stainless steel and has an area of 144 ft^2 (Figure 1-7). The exchanger has a total of 210 tubes and is designed as a single pass on the shell side and 2 passes on the tube side. In the solvent cooler, the process stream was flowed on the shell side and cooling water at 10 °C flowed on the tube side. The lean solvent from the stripper bottoms was cooled to approximately 40 °C before being pumped into the lean solvent feed tank. The solvent cooler and solvent heaters were mounted on custom built support racks to centralize

operational procedures and to minimize the footprint. The support racks were fabricated by the welding shop at the PRC campus.

Figure 1-7. Solvent Cooler (H-107) as Installed on Support Rack. Cooling Water Piping is Painted Green and Flows Tubeside (Picture Taken by C. Lewis)

The water in the saturated gas leaving the top of the absorber column needed to be removed in order to protect the downstream blower and CO_2 analyzer. A new air cooler (H-112) was purchased from Super Radiator Coils, model number 27x27-12R-58/156. The air cooler was sized to remove approximately 490 MJ/hr and has an area of 19.8 m^2. The cooler is constructed much like a radiator with a large number of coils, which were made out of 1.6 cm (5/8 in.) OD 316L stainless steel tubing. The rest of the structure is constructed from type 316 stainless steel. Cooling water at 10 °C was used to cool the

process gas. Water condensed from the air cooler was drained back to the absorber feed tank.

Figure 1-8. Air Cooler (H-112) as Installed on Top Platform of Structure. Radiator Coils are Located on the Oppoite Side (Picture Taken by C. Lewis)

Downstream of the air cooler, a new water knockout was purchased and installed. The water knockout was used to remove entrained water that may have bypassed the air cooler and prevent water droplets from damaging the impeller of the blower that was located downstream. The water knockout works as centrifugal type separator. Gas enters the vessel tangentially near the bottom and exits out the top. The condensed liquid drains from the bottom of the knockout and to the lean feed tank.

Rosedale bagged filters were used to removed rust and debris in order to protect the Micro Motion® flowmeters downstream of the filters. The filter housing is made of

type 316 stainless steel and bagged filter made of cotton were used. There is another bagged filter that is located on the stripper, used to filter the solvent from the reboiler. It was discovered through trial and error, that only the filter bag made of cotton could withstand the high temperature and corrosiveness of the piperazine and potassium carbonate solvent. The bag filters made of polypropylene eventually dissolved in the system. It is also important to point out that while the bag filter is made of cotton, the manufacturer may use stitching made of synthetic material. This also resulted in failure of the bagged filters. Therefore, cotton filter with cotton stitching was requested for all of the bagged filters used in the campaigns.

1.3.3 Piping Modification

Due to the corrosive nature of the aqueous piperazine promoted potassium carbonate solvent, all of the carbon steel piping was replaced type 304L stainless steel pipe. As part of this work, a demolition of a portion of the carbon steel piping was performed as well installation of the new stainless piping. The personnel at SRP performed the layout of the new piping iso and also purchased the new stainless steel pipe, flanges, and gaskets. Schedule 10 304L stainless steel pipe, 150# flanges, and Garlock gaskets were used for construction. The majority of the new stainless steel piping was welded by an outside contractor and was completed in approximately 6 months.

1.3.4 CO_2 Delivery System

A carbon dioxide delivery system was required to initially charge the liquid solvent with CO_2 prior to startup and also for CO_2 makeup during the operation of the

pilot plant. As part of this work, a steam heated CO_2 pressure regulator was purchased from Andon Specialties, model number H2-1A55Q5G114, and a storage rack was constructed out of unistrut to house up to three large CO_2 cylinders. The capacity of the cylinders varied in size from 150, 200, and up to 300 L. The CO_2 delivery system was housed indoors.

The steam heated regulator was later found to be inadequate. As the liquid carbon dioxide from the cylinder was being released, over time the lines would begin to freeze and eventually stop flowing. A simple shell and tube heat exchanger was built using 1.3-cm and 1.9-cm OD type 316 stainless steel tubing and stainless steel fitting from Swagelok. University steam was used to vaporize the liquid carbon dioxide from the shell side. A steam trap was also installed. The preheater worked adequately for makeup, but the initial charging of the liquid solvent required patience. Stainless steel tubing (1.3-cm OD) was ran from the steam regulator to a control valve located outside. Initially, the makeup CO_2 was discharged directly into the blower discharge. Later, it was found better control was obtained when the CO_2 makeup was discharged into the overhead gas accumulator.

1.3.5 Process Flowsheet

The pilot plant was operated as a closed-loop system, where both the gas and solvent was continuously recycled. The aqueous piperazine and potassium carbonate solvent was stored in the absorber feed tank. The feed tank was used to maintain a constant lean loading and minimize any flow interruptions in the system. The residence time in the feed tank varied from 0.5 hr to 1.5 hr depending on the liquid flow rate. Lean

solvent from the feed tank was pumped through a filter and then through a Micro Motion® flowmeter before being pumped to the top of the absorber column.

The liquid is evenly distributed on the top of the packing by a distributor. The solvent flows downward by gravity along the surface of the first section of packing, promoting gas liquid contact area. Carbon dioxide from the upwardly flowing gas is absorbed by the liquid solvent at the gas-liquid interface of the wetted packing surface. At the middle of the column there is a chimney tray to recollect the liquid and a redistributor for spreading the liquid over the second section of packing.

The solvent rich in CO_2 exits out the bottom of the absorber and is then pumped to another filter before passing through a second Micro Motion® flowmeter. After the flowmeter, the solvent flow is split and passes through the two solvent pre-heaters. Near the top of the column, the preheated stripper feed is mixed with the reflux and then fed at the top of the stripper column to a distributor. In the first campaign, sieve trays were used in the stripper. In later campaigns, random and structured packing were used. A chimney tray and distributor similar to the one in the absorber was used only when there was packing in the stripper. The rich solvent flows downward and the CO_2 is stripped by the steam generated from the solvent by the reboiler.

The lean liquid at the bottom of the stripper is circulated through the reboiler before being pumped to the solvent cooler. Instead of passing through the cooler, a portion of the lean solvent is diverted and pumped to the stripper sump. The solvent is cooled to approximately 40 °C and flows back into the absorber feed tank where the entire process is repeated.

The gas consists of ambient air with the addition of CO_2 from large compressed gas cylinders. The CO_2 concentration in the gas was varied from 3 to 17 mol%. The CO_2 rich gas enters the bottom of the absorber and counter-currently contacts the liquid solvent. The absorber column contains structured packing to maximize the amount of effective interfacial area and minimize pressure drop. Carbon dioxide is absorbed by the liquid solvent at the gas –liquid interface. The "clean" gas then exits out the top the absorber and passes through the air cooler, where it chilled to approximately 10 °C and most of the moisture is removed to protect the CO_2 analyzers and the blower located downstream.

The cooled gas then passes through the water knockout drum where any residual water that may have been entrained is finally removed. The gas is then mixed with the CO_2 from the overhead gas accumulator and recycled back to the blower, where the gas is the process is repeated. During the operation of the pilot plant, makeup CO_2 was added into the overhead gas accumulator. The overhead gas accumulator has a split vent valve. When the vent is 0-50%, the accumulator is vented where the vent is fully open at 0%. For 50-100%, nitrogen is added to the system, where at 100%, the vent is fully open for nitrogen addition. When the vent is 50%, both the vent and nitrogen valves are closed. In all of the campaigns, although the vent was at 100%, the gate valve for the nitrogen was closed shut, which resulted in zero nitrogen addition. There is a vent on the impeller housing of the blower; the casing around the hub has an opening that is approximately 2.5 cm in width. The absorber feed tank is vented to the absorber in order to equalize the pressure. During the steady state operation of the pilot plant, it was assumed that there

was no leakage. Only when the process conditions were change, was there expected to be any leakage through blower vent.

The vapor exiting the top of stripper contains carbon dioxide and water and flows to two phase condenser. The water is condensed out as liquid and flows into the overhead liquid accumulator. The water is then pumped through the reflux heater and mixed with the stripper feed. In all of the campaigns, the reflux heater was not used and therefore the reflux was cooler the stripper feed. The CO_2 gas exits the top of the condenser and then flows to the overhead gas accumulator. The CO_2 in the gas accumulator was mixed with the "clean" air that had passed through the absorber. A control valve downstream of the accumulator controlled the CO_2 concentration in the inlet gas to the absorber. Makeup CO_2 was added to the overhead gas accumulator. During vacuum operation, the vacuum pump was used to draw suction from the gas accumulator.

1.3.6 Online Process Instrumentation

As part of the pilot plant modification, a number of upgrades were made to the measurements of gas and liquid flow, pressure, and temperature. In addition, the capability of online pH measurement and gas phase CO_2 analysis were added. A list of process instrumentation used in the CO_2 capture pilot plant is given by Table 1-3.

Table 1-3. Pilot Plant Instrumentation Specification

Manufacturer	Model Number	Function	Range	Method	Accuracy
Dietrich Standard	AN-75	Gas Flow – Abs Inlet (C1/C2)	-	DP	±1% Actual Value
Dietrich Standard	Diamond II Annubar - GCR 15	Gas Flow – Abs Inlet (C3/C4)	-	DP	±1% Actual Value
Horiba	PIR-2000	CO_2 Conc - Abs Gas Mid	0-5/10/20 %	NDIR	±1% Full-Scale
Horiba	PIR-2000	CO_2 Conc - Abs Gas Out	0-1/3/5 %	NDIR	±1% Full-Scale
Micro Motion®	F-Series	Liquid Flow Rate	0 - 32650 L/hr	Coriolis	±0.20 Vol %
Micro Motion®	F-Series	Liquid Density	0 - 5000 kg/m3	-	±2.0 kg/m3
Micro Motion®	F-Series	Liquid Temperature	-100 to 180 ºC	-	±1 ºC
Rosemount	3095MFA Mass Probar Flowmeter	Gas Flow - CO_2 Recycle	-	DP	±0.9%
Rosemount	389VP pH/ORP Sensor	pH - Abs Inlet/Outlet	9 - 12	-	99% Linearity
Rosemount	5081-P pH/ORP Transmitter	pH - Abs Inlet/Outlet	-	-	±1 mV @ 25ºC, ±0.01 pH
Rosemount	68 Series Platinum RTD	Temperature Sensor	-50 to 400C	Resistance	±0.6 ºC
Rosemount	848T 8-Input Temp Transmitter	Temperature Transmitter	-	-	-
Rosemount	3051 Series - DP/GP/AP/LT	Pressure Transmitter	0-3/25/40 inch of H_2O	-	±0.1% Reading
Rosemount	1151 Series - DP/GP/AP/LT	Pressure Transmitter	0-5/30/150 inch of H_2O	-	±0.5% Calib Span (0.1% Smart)
Temet Instruments	Gasmet DX-4000 FTIR	CO_2 Conc - Abs Gas Inlet/Outlet	0-100 %	FTIR	<2% Measuring Range
Vaisala	GMT221	CO_2 Conc - Abs Gas Outlet	0-5 % CO_2	NDIR - CarboCap	<±[0.02% CO_2 + 2% Reading] @ 25ºC
Vaisala	GMT221	CO_2 Conc - Abs Gas Inlet	0-20 % CO_2	NDIR - CarboCap	<±[0.02% CO_2 + 2% Reading] @ 25ºC
Vaisala	GMT222	CO_2 Conc - Abs Gas Outlet	0-10,000 ppm	NDIR - CarboCap	<±[20 ppm CO_2 + 2% Reading] @ 25ºC

Notes:
AP = Absolute Pressure
DP = Differential Pressure
GP = Gauge Pressure
LT = Level Transmitter
FTIR = Fourier Transform Infrared Sensor
NDIR = Nondispersive Infrared Sensor
RTD = Resistance Temperature Detector

Pressure measurements were performed using Ashcroft, Rosemount 1151 and Rosemount 3051 Series pressure transmitters. The Ashcroft pressure transmitters were used with the AN-75 Dietrich Standard annubar for gas flow measurements in Campaign 1 and 2. The 3051 Series transmitters are smart transmitters and contain a microprocessor that allows communication through the HART protocol. The 3051 transmitters have an accuracy of ±0.1% of the reading and ranged from 0-3, 0-25, and 0-40 inches of water. The 1151 Series transmitters are analog and have a 4-20 mA output. The 1151 transmitters have an accuracy of ±0.5% of the calibrated span and ranged from 0-5, 0-30, and 0-150 inches of water. The pressure transmitters were used to measure absolute, differential, and gauge pressure throughout the pilot plant. The pressure transmitters were also used to measure liquid level in the sump of the two columns, the absorber feed tank, overhead liquid accumulator and the reboiler.

Temperature measurements of the process streams and column profiles were made using K-type thermocouples and Rosemount Series 68 Platinum Resistance Temperature Detector (RTD) sensors. Rosemount 848T 8-Input temperature transmitters were used in conjunction with the RTD sensors. The RTD sensors have an accuracy ±0.6 °C. In the first campaign, the temperature measurements on the stripper side were performed with thermocouples and on the absorber side, the thermocouples were replaced with RTD sensors. In later campaigns, all of the thermocouples in the pilot plant were gradually replaced with the Rosemount RTD sensors. As part of this work, some of the conduit and cabling associated with the RTD sensors were installed. Also, in campaign 1,

an infrared temperature gun was used to measure the surface temperature of the absorber column.

The liquid flow rate, temperature and density of the absorber lean and rich solvent streams were measured using Micro Motion® F-series coriolis flowmeters and are manufactured by Emerson Process Management. The F-series flowmeters have an accuracy of ±0.20 vol% for the flow rate, ±2.0 kg/m^3 for the density, and ±1 °C for the temperature. The Micro Motion® flowmeters were used to measure the flow rates of the absorber inlet, stripper inlet, stripper reflux, and absorber feed tank inlet. The density measurement was used to monitor changes in the water balance.

In Campaign 1, the inlet gas line to the absorber was 20.3 cm and made of PVC. The gas flow rate was measured using a Dietrich Standard AN-75 annubar, differential pressure transmitters with varying pressure ranges, and a temperature measurement. The flowmeter has an accuracy of ±1% of the actual value. The flow meter was calibrated for air and density corrections were made in the calculations of the actual gas rate to include CO_2 and water. The steam flow to the reboiler was measured using an orifice plate and Rosemount differential pressure transmitters.

The pH of the absorber inlet and outlet solvent streams were continuously measured with Rosemount 389VP pH/ORP sensors and Rosemount 5081-P pH/ORP transmitters. The 389VP pH sensor has a measuring range of 9–12 pH units and a linearity of 99%. The 5081-P transmitters have an accuracy of ±0.01 pH units or ±1 mV at 25 °C. The connection cable is hardwired to the Rosemount transmitter and attached to the pH sensor on the other end via a quick-connect adapter. As discovered just before

the startup of the first campaign, the quick-connect cables may not be waterproof and needed to be shielded by a shelter. Lean loading measurements were correlated to bench-scale pH measurements. The online pH measurements were used to monitor the lean loading and rich loading of the solution. The lean loading of the solution was changed by adjusting reboiler heat duty and CO_2 makeup flow rate.

The concentration of CO_2 in the gas was measured at the inlet, middle and outlet of the absorber column. The inlet and outlet concentration was measuring in situ using Vaisala GMT 221 and GMT 222 CO_2 analyzers. In the first campaign, the absorber inlet Vaisala probe was located downstream of the blower, while the absorber outlet probe was located just upstream of the air cooler. In later campaigns, the absorber outlet probe was moved downstream of the water knockout. The Vaisala CO_2 analyzers use a new silicon based non-dispersive infrared (NDIR) sensor and uses single-beam dual-wavelength NDIR. The probes are interchangeable with the transmitters. The inlet CO_2 concentration was measured with a 0–20 mol% probe and the outlet concentration was measured with either a 0–10,000 ppm or 0–5 mol% probe, depending on the range of the outlet gas. The analyzers have an accuracy $<\pm$(0.02% CO_2 + 2% of the reading) at 25 °C, an operating of limit of 60 °C and 0–100% relative humidity. The Vaisala analyzers have a temperature dependence of -0.1% of %full-scale/°C and a pressure dependence of +0.15% reading/hPa.

The concentration of CO_2 in the middle of the absorber column was measured with a Horiba PIR-2000 CO_2 analyzer with a range of 0–1, 0–3, and 0–5 mol%. The Horiba is also a NDIR analyzer and has an accuracy of ±1% full-scale. Unlike the in situ

Vaisala analyzers, the middle gas samples use an extractive sampling system. The gas is extracted from the space between the chimney tray and redistributor in the spool piece, where there is no liquid. A diaphragm sample pump extracts the gas and it passes through a water knockout immediately after it exits the column (Figure 1-9). The gas then flows through approximately 30 meters of 0.6 cm polyethylene tubing and into a coalescing filter that removes water and excess gas, which is adjusted by a downstream needle valve. Next, the gas passes through a membrane filter before it flows to the PIR-2000 CO_2 analyzer. A rotameter on the outlet of the analyzer was adjusted to maintain a constant flow rate to the analyzer during online operation and the calibration process. The sampled gas was then discharged outside.

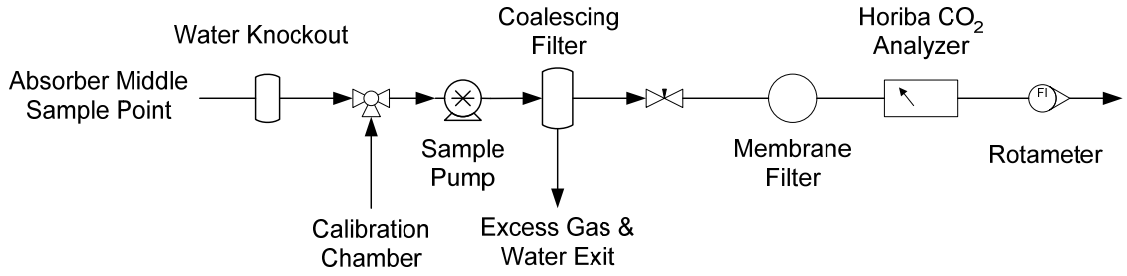

Figure 1-9. Schematic of Extractive Sampling System for Horiba CO_2 Analyzer

1.3.7 DeltaV Process Control System

The DeltaV digital automation system version 7.2 was used to log all the process data and control the operations of the pilot absorber/stripper system. DeltaV is a distributed control system (DCS) based on PlantWeb® digital plant architecture and is manufactured by Emerson Process Management. HART® and FOUNDATION™ field bus process instrumentation as well as 4–20 mA analog signals were fully integrated into the DeltaV system. The DeltaV consists of an operator interface, control hardware, and

control software. DeltaV Operate, the operator interface, is run directly on standard PC hardware and operating system and allows the user to monitor and make changes to the process. The control hardware consists of I/O modules connected to a digital control computer, which are attached to a larger redundant DeltaV plant-wide network. The DeltaV control software can be configured to provide model predictive control, neural networks, fuzzy logic, and variability analysis. A schematic of the DeltaV architecture is shown in Figure 1-10.

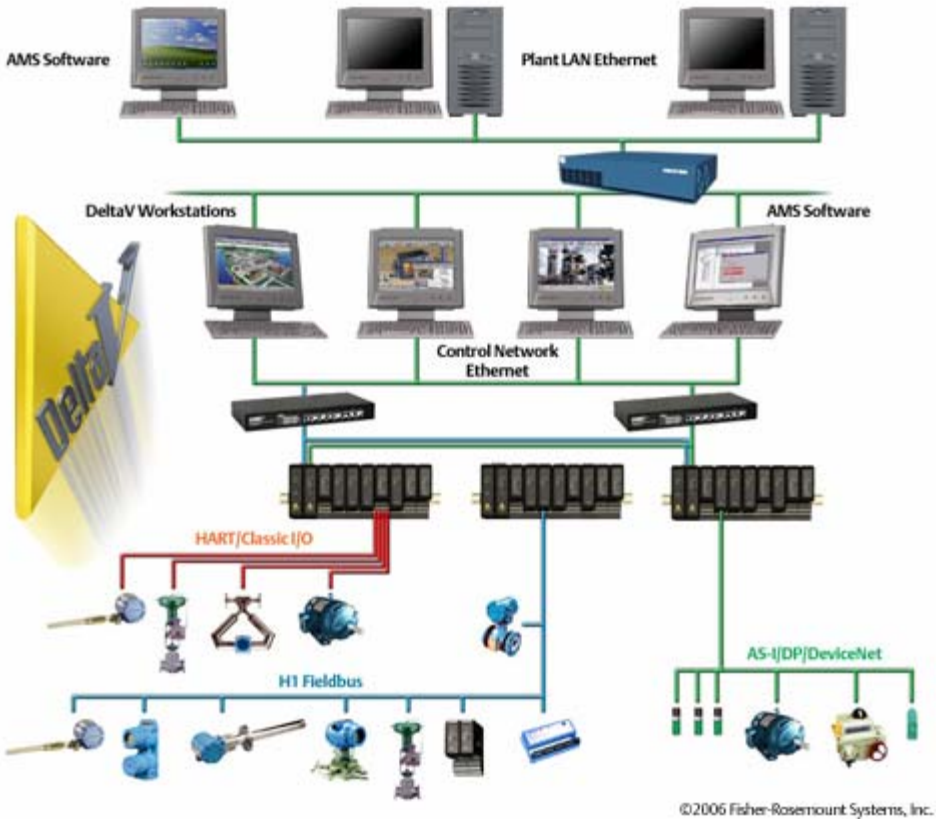

Figure 1-10. Schematic of DeltaV architecture

1.3.8 Instrument Calibration

The Vaisala and Horiba CO_2 analyzers were calibrated approximately once every 24 to 48 hours with primary standards. In the first campaign, a total of four primary standards were used: 0, 1, 4, and 12 mol% CO_2. In later campaigns, calibration standards of 4.9 and 16.9 mol% CO_2 were added. An onsite nitrogen source was used as the zero calibration gas. The calibration gases consisted of air and carbon dioxide and were purchased from Praxair Inc. The cylinders were filled gravimetrically and have an analytical accuracy of ±0.02 %. Certificates of analysis for the calibration gases provide by the vendor are listed in the appendix.

The calibration system consisted of a calibration panel and two calibration chambers, which are located at the inlet and outlet sample points. The calibration chamber is made of 5.1 cm PVC pipe and several tees. Calibration gas is flows into the calibration apparatus at one end and exits out the opposite end. The Vaisala probe and 0.64 cm tubing for the Horiba are inserted into the penetrations along the length of the calibration chamber. The calibration panel consists of several on-off ball valves, a rotameter, the CO_2 gas standards and the respective regulators, and needle valves for each of the CO_2 gas cylinders. The needle valves control the flow of the calibration gas from the individual cylinders and the rotameter is used to adjust the flow calibration chamber. The ball valves control which calibration chambers the calibration gas is directed. The Horiba for absorber middle sample point is calibrated from the inlet calibration chamber. Sampling for the Horiba is switched from calibration chamber and absorber middle sample location at the calibration panel.

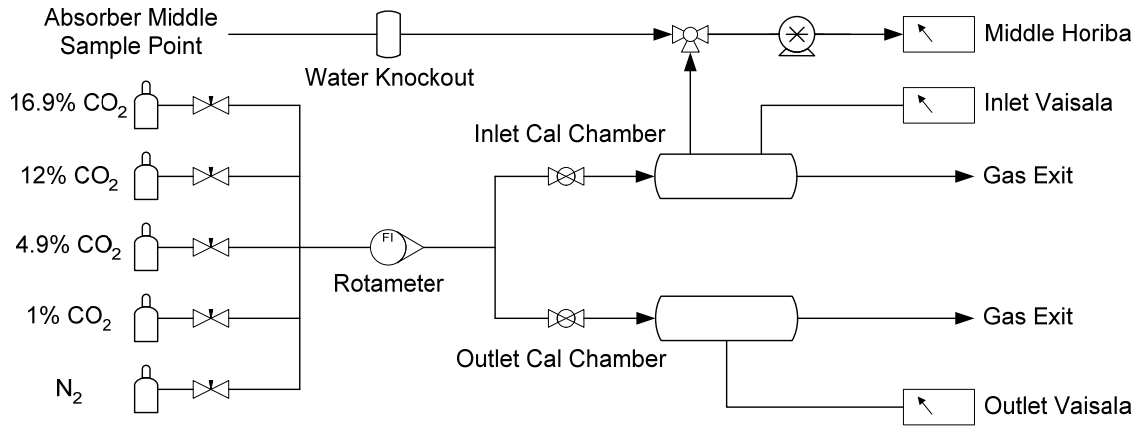

Figure 1-11. Schematic of Calibration Panel for CO_2 Analyzers

During the calibration process, the Vaisala probes were removed from the process line and insert into a calibration chamber. The sample line of the Horiba was disconnected from the absorber and also connected to calibration chamber. The CO_2 calibration gas was metered to the calibration chamber using a rotameter on the calibration panel. The raw output signals from the analyzers were recorded and a calibration curve was fitted to a linear equation. The results of the calibration curve were then inputted into DeltaV. The process to calibrate the Horiba analyzer took approximately 20–30 minutes, due to the extractive sampling system that was used. The in situ Vaisala had much quicker response time and could be calibrated in less than 10 minutes. The standard operating procedure for the calibration of CO_2 analyzers is listed in the appendix.

The Micro Motion® and orifice flowmeters are factory calibrated and are periodically checked by measuring the time it takes to fill a known volume. The Deitrich Standard annubar was calibrated using the pitot tube traverse method. The Rosemount

pressure transmitters are calibrated approximately once per month using manometers and pressure gauges. The Rosemount RTD sensors are calibrated before installation in the pilot plant with a dry block calibrator. The pH meters were calibrated with 7 and 10 pH standard solutions prior the startup of each campaign.

1.3.9 Offline Analytical Methods

In this campaign, an acid-base titration method was used to determine the concentration of piperazine and potassium. The standard operating procedure for the titration procedure is listed in the appendix. An abbreviated summary of the method is enumerated as follows:

1. Add methyl orange to the undiluted sample
2. Titrate with 2N hydrochloric acid (HCl) until the endpoint is reached
3. Heat the solution to release residual CO_2 and allow the solution to cool
4. Titrated with 2N sodium hydroxide (NaOH) until the pH is approximately -265 mV.

The first endpoint represents the total alkalinity of solution and given by the following equation:

$$Total\ Alkalinity = mol\ K^+ + 2\ mol\ PZ \tag{1.1}$$

The back-titration endpoint represents the concentration of piperazine in the solution. The concentration of piperazine is calculated by dividing the amount of HCl that is added by two because piperazine contains two nitrogen. The potassium concentration was calculated by taking the difference between the total alkalinity and piperazine concentration. The concentration measurements for K^+ and PZ are reported in units of

mol/kg of solution, not mol/kg of H_2O. For CO_2 loading measurements, the piperazine and potassium concentrations were reported as total alkalinity.

The concentration of carbon dioxide (CO_2 loading) in the solution was measured using the Shimadzu TOC-5050A Total Organic Carbon Analyzer (TOC). The Shimadzu TOC can be used to measure both inorganic (IC) and total organic carbon (TC). For the measurements of inorganic carbon, 25 wt% phosphoric acid is used to evolve the CO_2 gas from the solvent. The stream of CO_2 is analyzed with a NDIR detector. For total organic carbon analysis, a precisely metered slipstream of the sample is combusted over platinum catalyst at 680 °C with ultra pure air. The resulting CO_2 is measured with the NDIR detector. The Shimadzu has a detection limit of four ppb and a range up to 4000 ppm for TOC and 5000 ppm for IC. The TOC analyzer has an autosampler, which allows it to perform up 89 analyses in one run. A 1000 ppm IC standard was prepared from a mixture of Na_2CO_3, $NaHCO_3$ and deionized (DI) water. The Na_2CO_3 was heated in an oven at 225 °C for several hours and allowed to cool in a desiccator jar. The sodium bicarbonate and carbonate were stored in sealed glass bottles in the desiccator jar when not being used. The 1000 ppm standard was further diluted to make 50, 100, 150 and 200 ppm IC standards for the calibration curve. A new 1000 ppm standard was prepared each month.

In the first campaign, the total carbon standard was made from a solution of piperazine and potassium carbonate. The recommended total carbon standard by Shimadzu is made using hydrogen potassium phthalate (KHP). Total carbon calibration curves were generated with 50, 100, 200, and 300 ppm TC standards. The TOC has an

auto sampler that allows the analyzer to be continuously operated without user intervention. However, the DI rinse water for the auto-sampler and phosphoric acid for the IC analysis needed to be periodically monitored and replenished when necessary.

In the first campaign, the CO_2 loading was determined by the inorganic carbon analysis and the concentration of piperazine was determined by the taking the difference between the organic carbon and inorganic carbon analyses.

$$Total\ Carbon = Inorganic\ Carbon + Piperazine\ Carbon \tag{1.2}$$

Prior to analysis, approximately 0.9 grams of liquid sample was weighed and then diluted with to 1000 mL with DI water. The samples were then pipetted into 8 mL vials and placed in the auto-sampler. It was noticed that the TOC measurements seemed drift over time. IC standards (100 ppm) were analyzed every 10^{th} sample in the matrix. The standards appeared to trend upward in concentration at consistent rate over time. After the loading analysis of Campaign 1 had been completed, it was found that the 100 ppm IC standards absorbed CO_2 from the atmosphere, up to 30% was observed in some cases. The 200 ppm IC standards seemed to absorb CO_2 at a much slower rate. It is also entirely possible that the diluted sample solutions may have absorbed CO_2 from the air. This problem was rectified in Campaign 2, when a new liquid sampling and new TOC analysis method was developed. In later campaigns, all of vials were covered with parafilm to eliminate atmospheric absorption of CO_2.

In campaign 1, Inductively Coupled Plasma (ICP) emission spectroscopy was used to determine the concentration of potassium, vanadium and total iron in the solution. Due to the presence of carbon steel equipment in the system, 1000 ppm of vanadium

(V^{5+}) was added to the solvent as a corrosion inhibitor. The iron concentration indicated the amount of rust that was being produced from carbon steel equipment in the pilot plant and was used to indirectly evaluate corrosion. The ICP analysis was performed by another member in our research group using the ICP analyzer that belonged to the UT Austin Civil Engineering Department.

1.3.10 Raw Materials Inventory

In campaign 1, the effective interfacial area of the FLEXIPAC® 1Y structured packing was determined by absorbing CO_2 from ambient air into 0.1 N KOH. The solution was made up from city water (CAS No. 7732-18-5) and KOH (CAS No. 1310-58-3) pellets in 22.7 kg bags purchased from UNIVAR USA. The starting 5m K+/2.5m PZ solution was made by removing several drums of the KOH solution and adding 68 wt% aqueous piperazine (CAS No. 111-85-0) and 47 wt% aqueous potassium carbonate (CAS No. 584-08-7) from 300 kg drums. In addition, 4 bags of 22.7 kg bags of U.S.P. grade potassium bicarbonate (CAS No. 298-14-6) were purchased for makeup. The piperazine was donated by DOW Chemical and the potassium bicarbonate and carbonate were purchased from UNIVAR USA. The makeup CO_2 (CAS No. 124-38-9) was purchased from Texas Welding Supply and was dispensed from 150, 200, and 300L cylinders containing liquid carbon dioxide. Vanadium (V^{5+}) was added as a corrosion inhibitor in the form of potassium metavanadate (KVO_3). The metavanadate (CAS No. 13769-43-2) is commercially sold under the trade name HotPot-922 by Pechiney World Trade USA is typically used in hot potassium carbonate systems for inhibiting corrosion.

In the December of 2003, the purchased cost from UNIVAR USA for 6 drums of 47 wt% aqueous potassium carbonate, 45.5 kg of KOH pellets, and 90.9 kg of U.S.P. grade $KHCO_3$ was \$0.7/kg, \$3.04/kg, and \$3.85/kg. Per the Armand Products July 1, 2006 truckload price list, 47% K_2CO_3 solution costs \$0.45/kg for bulk and \$0.62/kg for 300 kg drums, FOB Muscle Shoals, Alabama. For U.S.P. grade potassium bicarbonate in 22.7 kg bags from Armand Products, the cost is \$6.53/kg for quantities less than 455 kg. The cost per pound decreases with increasing quantities. For quantities greater than 4546/kg, the cost of $KHCO_3$ is \$2.10/kg. Piperazine costs were estimated to be on the order of \$5.50/kg, while MEA costs are estimated to be about 5 times less than piperazine. The cost of the CO_2 gas from Texas Welding Supply was approximately \$0.37/kg.

1.3.11 Liquid Sample Collection

In Campaign 1, the liquid samples were taken at the inlet, middle, and outlet of the absorber. Erlenmeyer flasks with glass stoppers were used to take the samples. The sampling procedure involved opening a valve at the sample point and allowing the solution to flow out into the Erlenmeyer flasks. The pH and temperature was recorded for each liquid sample with a handheld pH meter. The sample was then poured into a glass 40-mL sample vial and capped. Samples were collected once the pilot operation had reached steady state for one hour. Two sets of liquid samples were taken for each run condition. It was later discovered that the sampling process made have resulted in the loss of CO_2 from the samples due to flashing. In the second campaign, the liquid sample collection procedure incorporated the use of sample bombs, which minimized flashing.

1.3.12 Campaign 1 Plant Operation

Pilot plant operations commenced at the end of May 2004. First, the effective interfacial area of the FLEXIPAC® 1Y structured packing in absorber was determined by absorbing CO_2 from ambient air into a solution of 0.1 N potassium hydroxide (KOH). The gas and liquid flow rates were varied from 300 to 770 m^3/hr and 8 to 40 m/hr, respectively. The starting solution inventory was 2.9 m^3 (14 drums). A Horiba VIA510 CO_2 gas analyzer was used to measure the outlet CO_2 concentration.

Upon completion of the effective area tests, 5 drums of the 0.1 N KOH solution were removed. The remaining solution was mixed with 3 drums of 68% piperazine AQ, 2 drums of water, 5 drums of 47% liquid K_2CO_3, and 0.03 m^3 (50 kg) of the HotPot-922 solution to give a vanadium concentration of 1000 ppm. Piperazine has a freezing point of 54 °C and is solid at room temperature. Drum heaters were used unsuccessfully to liquefy the solid piperazine. Numerous attempts to solubilize piperazine in the potassium carbonate solution were also unsuccessful. The piperazine was eventually added into the system by first adding CO_2 into the relatively lean starting potassium solution. Once the solution was loaded, it was heated in the reboiler. Then via a batch process, hot bicarbonate solution was pumped into the piperazine drum and the mixture was charged into the absorber feed tank. While the solvent was circulating, 40 mL of anti-foam was added to the system to correct the foaming issue. The process of charging the piperazine and potassium carbonate took approximately two weeks. Once the chemicals were loaded, troubleshooting on the absorber and stripper began. During startup, solids were discovered at the bottom of the absorber feed tank. It was speculated that piperazine had

precipitated. Hot solvent was circulated through the entire system to dissolve the piperazine and the absorber feed was withdrawn from the side of the absorber feed tank, instead of the bottom.

The pilot plant was operated for a total of 7 days, beginning in mid June. A total of 35 runs and 19 operating conditions were conducted with three solvent K^+/PZ compositions at a ratio of 2:1. The potassium and piperazine concentrations were 2.3, 2.9, and 3.1 mol K^+/kg soln and 1.15, 1.45, and 1.55 mol PZ/kg soln, respectively. The gas and liquid flow rates were varied from 0.5 to 3 kg/m^2-s and 1.3 to 5.1 kg/m^2-s, respectively. The L/G ratio was varied from 0.9 to 5.6 kg/kg. The synthetic flue gas contained 3 and 13 % CO_2 in air at 25 to 50 °C. The temperature of the solvent to the absorber varied from 35 to 45 °C. The absorber pressure was operated at 1 atm. The stripper pressure varied from 1 to 1.7 atm. The absorber contained 6.1 m of FLEXIPAC® 1Y structured packing and the stripper contained 14 sieves trays with 18-inch tray spacing. Lean loading and CO_2 removal varied from 0.41 to 0.54 mol CO_2/mol K+2PZ and from 84.5 to 99.8%, respectively. Vanadium concentrations were maintained at approximately 18 mmol/kg soln (1000 ppm). Dissolved iron concentration varied from 0.3 to 0.6 mmol/kg soln.

Table 1-4. Campaign 1 Absorber Operation

Parameter	Value
Inlet CO_2 (mol %)	3 – 12
PZ Concentration[1] (mol/kg)	1.2 – 1.6
K^+/PZ Ratio	2.0 – 2.05
Lean Loading[2] (mol CO_2/TAlk)	0.39 – 0.50
G (kg/m^2-s)	0.5 – 3.0
L/G (kg/kg)	2.2 – 5.6
$T_{GAS,IN}$ (°C), Typical	32
T_{LEAN} (°C), Typical	40

1. Concentration in mol/kg of solvent
2. TAlk = Total alkalinity (mol K+2 mol PZ)

Foaming was observed in the absorber after several days of operation. Three hundred and seventy-five milliliters of silicone based GE antifoam were added throughout the duration of pilot plant operations. The online Rosemount pH meters failed after the first day of the operation. The rain may have short-circuited the probes because the quick-connect cables on pH meter are not designed for outdoor use.

There were also solubility issues with both the piperazine and the potassium carbonate. The absorber and stripper filters both eventually became plugged up and had to be bypassed. Based on visual inspection, the stripper filter had plugged up with potassium carbonate and the absorber filter was filled precipitated piperazine. When the solution is too lean, piperazine will precipitate and tends to float. Potassium carbonate precipitates when the solution becomes too rich and sinks to the bottom. Also, both potassium carbonate and piperazine were near their respective solubility limits. After the loss of the filters, it was finally realized that the additional water needed to be added to the system and that the liquid holdup in the overhead liquid accumulator should be minimized because there would always be a water inventory in the accumulator. The loss

of water from the solution resulted in the precipitation of both components and wreaked havoc on the plant operation. In addition, the some of the samples for the stripper lean, which tended to be slightly cooler, contained precipitate.

In the first campaign, the solvent was not adequately preheated by the heat exchanger. It was discovered that the steam traps were undersized and that the condensate eventually backed up into the exchanger resulting in poor performance. This issue was address in the next campaign. The inlet gas temperature was also too low. To much cooling occurred at that air cooler and mechanical work from the blower could not get the temperature up to 40 °C. A control valve was not installed for the cooling water to the air cooler cooling and thus the flow rate could not be turned off. In addition, the inlet gas was not saturated with water as would be expected in an industrial process.

Also, the orifice meter measuring the steam flow to the reboiler was too small. In some cases, the reboiler steam rate was operated beyond the measurement range. Finally, the middle absorber CO_2 gas sampling system was plugged up with water due to condensation from the saturated gas. The water knock-out filters for the Horiba sampling system were replaced and the entire sampling line was blown out with compressed air.

1.3.13 Campaign 1 Results

The results from the KOH test showed that the maximum effective area was approximately 49% of the total packing surface area. The specific area of the FLEXIPAC® 1Y structured packing is 410 m^2/m^3. The results are plotted in Figure 1-12. The figure shows that at higher gas rates, the effective area appears to approach a

maximum. These results are consistent with that obtained by UT-SRP (Separations Research Program) for a high surface area structured packing.

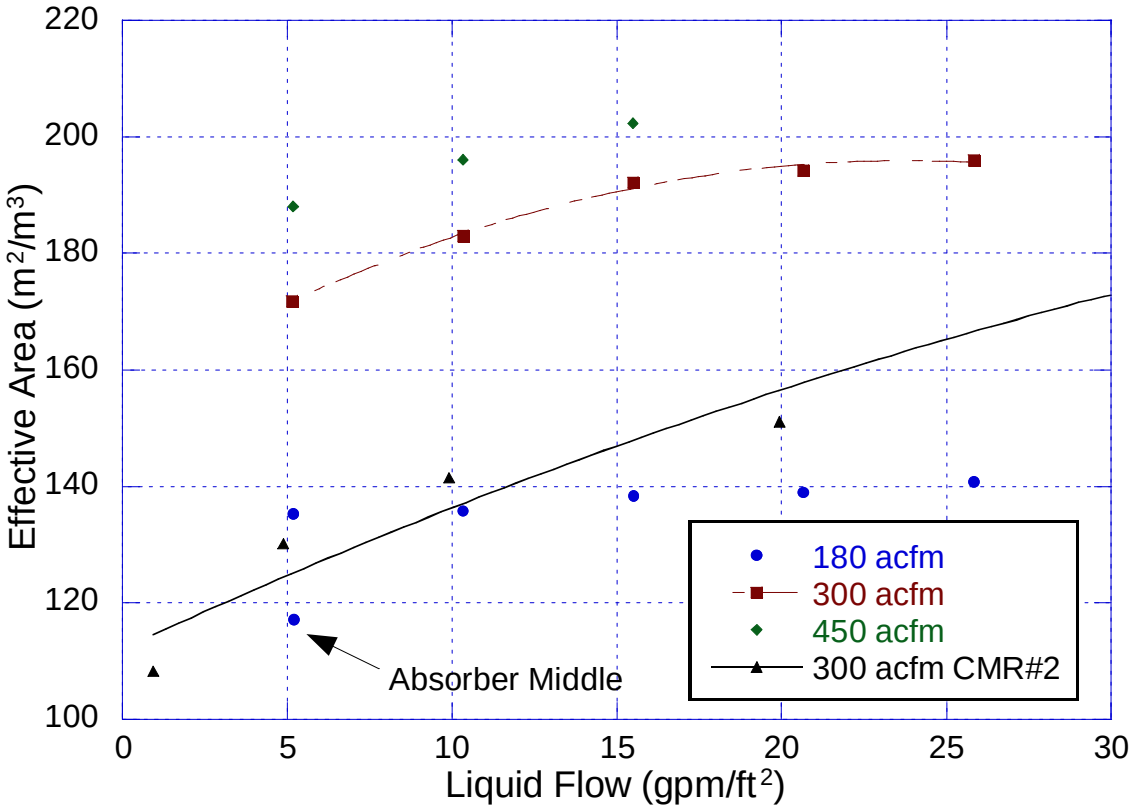

Figure 1-12. FLEXIPAC® 1Y effective area for CO_2 absorption in 0.1 N KOH

The DeltaV control system was used to log the process data real-time. Measurements included the temperature, pressure, flow rate, density, CO_2 concentration, liquid level, steam flow, and cooling water flow. The logged data was retrieved from DeltaV and imported into Excel spreadsheets on a daily basis. The data points were recorded once per minute. The reported process conditions were generated by averaging the points 10 minutes before and after the specified sample point. This reduces the effect from the disturbances caused by the liquid sample collection process.

Titrations and ICP analyses were performed only at the beginning and end of each concentration change (Table 1-5). CO_2 loading and piperazine analysis was performed for absorber lean, middle, and rich solutions using the Shimadzu TOC. Some of the rich samples had precipitate in and these samples were later diluted with water and re-analyzed. Parafilmed 100-ppm IC standards were placed in between every 10 samples, however the samples themselves were not parafilmed. Therefore, some of the samples may have absorbed CO_2 from the atmosphere before analysis and the inorganic carbon analysis may be erroneously higher. The piperazine was calculated by subtracting the contribution of the inorganic carbon portion of the analysis. Therefore, the loading and piperazine data reported in Campaign 1 should be used with caution. In addition, ion chromatography was used to analyze the concentration of piperazine and potassium prior to the start of Campaign 4. The results show that ion chromatography results are 15 to 20% higher than that obtained by the titration analysis.

In Run 1.1.1, the concentration of potassium carbonate was slightly low. Therefore, an additional three-quarter drum of potassium carbonate was added to the system. In Run 1.2.1 through 1.7.1, the potassium to piperazine concentration was maintained at approximately 2:1. For Runs 1.8.1 to 1.17.2, 5 drums of condensate were removed to further concentrate the solvent system. The potassium concentration appeared to have slightly changed and may have been due to operations with an increased level in the liquid accumulator. In the final set of runs, an additional drum of condensate was removed and the liquid accumulator was operated with a higher liquid level.

A summary of the absorber gas rate, liquid rate, CO_2 gas concentration, and stream temperatures is given in Table 1-6. A total of 5 absorber temperature profiles were acquired using the infrared temperature gun. The infrared temperature gun measured the surface temperature of the absorber column, which also had a layer of white paint, whereas the RTD measurements consisted of probes inserted partially into the packing where it may contact gas, liquid or both. Both sets of results indicate that a large bulge occurred towards the top of the column and that at the spool piece, a large temperature gradient also exist. The complete raw data set for Campaign 1 is given in the appendix.

Table 1-5. Campaign 1 Absorber Analyses

Run ID	Date	Time	Titration				ICP		TOC		Ion Chromatograph		
			Ln Talk mol/kg	Lean PZ mol/kg	Lean K^+ mol/kg	Lean K^+ mol/kg	Lean V mmol/kg	Lean Fe mmol/kg	Lean PZ mol/kg	CO_2 Loading mol/kg	Ln Talk mol/kg	Lean PZ mol/kg	Lean K^+ mol/kg
1.1.1	6/16/04	15:30	4.51	1.22	2.06	2.00	18.7925	0.118	1.09	2.18	-	-	-
1.1.2	6/16/04	16:15	-	-	-	-	-	-	1.17	1.84	-	-	-
1.1.3	6/16/04	17:00	4.50	1.20	2.10	1.72	18.23	0.172	1.27	1.91	5.49	1.58	2.33
Added 3/4 Drum of K2CO3													
1.2.1	6/17/04	11:30	4.65	1.17	2.31	2.11	18.00	0.161	1.15	2.03	-	-	-
1.2.2	6/17/04	12:15	-	-	-	-	-	-	1.09	2.46	-	-	-
1.2.3	6/17/04	13:00	-	-	-	-	-	-	1.16	2.02	5.46	1.44	2.59
1.3.1	6/17/04	16:15	-	-	-	-	-	-	1.19	2.19	-	-	-
1.3.2	6/17/04	16:45	-	-	-	-	-	-	1.22	2.30	-	-	-
1.3.3	6/17/04	17:45	-	-	-	-	-	-	1.22	2.25	6.52	1.63	3.25
1.4.1	6/17/04	18:30	-	-	-	-	-	-	1.24	2.31	-	-	-
1.5.1	6/17/04	19:15	-	-	-	-	-	-	1.29	2.36	-	-	-
1.6.1	6/18/04	15:30	-	-	-	-	-	-	1.20	2.21	-	-	-
1.7.1	6/21/04	16:45	4.63	1.15	2.33	1.98	18.06	0.241	1.24	2.25	-	-	-
Removed Water													
1.8.1	6/22/04	17:45	5.66	1.40	2.87	1.87	18.55	0.172	1.41	2.63	-	-	-
1.8.2	6/22/04	18:30	-	-	-	-	-	-	1.48	2.66	-	-	-
1.9.1	6/22/04	19:30	-	-	-	-	-	-	1.46	2.63	6.49	1.63	3.23
1.9.2	6/22/04	20:15	-	-	-	-	-	-	1.44	2.67	-	-	-
1.10.1	6/22/04	21:15	-	-	-	-	-	-	1.49	2.76	-	-	-
1.10.2	6/22/04	22:00	-	-	-	-	-	-	1.44	2.70	-	-	-
1.11.1	6/23/04	8:15	-	-	-	-	-	-	1.47	2.75	6.53	1.64	3.25
1.11.2	6/23/04	9:00	-	-	-	-	-	-	1.46	2.84	-	-	-
1.12.1	6/23/04	14:30	-	-	-	-	-	-	1.44	2.93	-	-	-
1.12.2	6/23/04	15:15	-	-	-	-	-	-	1.28	3.37	-	-	-
1.13.1	6/23/04	17:30	-	-	-	-	-	-	1.36	2.94	-	-	-
1.14.1	6/23/04	18:15	-	-	-	-	-	-	1.41	3.07	6.64	1.66	3.31
1.15.1	6/24/04	9:00	-	-	-	-	-	-	1.42	3.05	-	-	-
1.15.2	6/24/04	9:30	-	-	-	-	-	-	1.49	3.08	-	-	-
1.16.1	6/24/04	10:30	-	-	-	-	-	-	1.48	3.09	-	-	-
1.16.2	6/24/04	11:00	-	-	-	-	-	-	1.48	3.09	-	-	-
1.17.1	6/24/04	12:15	-	-	-	-	-	-	1.42	3.12	-	-	-
1.17.2	6/24/04	12:30	5.84	1.44	2.96	2.42	21.97	0.593	1.48	3.15	-	-	-
Removed Water													
1.18.1	6/24/04	16:00	6.11	1.54	3.03	2.75	23.64	0.236	1.50	3.25	-	-	-
1.18.2	6/24/04	16:15	-	-	-	-	-	-	1.39	3.20	-	-	-
1.19.1	6/24/04	17:00	-	-	-	-	-	-	1.53	3.31	-	-	-
1.19.2	6/24/04	17:30	6.15	1.52	3.11	2.77	22.93	0.129	1.48	3.24	6.53	1.60	3.34

Table 1-6. Campaign 1 Absorber Results

Run#	Gas Rate Actual m^3/min	Liquid Rate L/min	L/G kg/kg	CO_2 In %	CO_2 Out %	CO_2 Removal %	Temp Gas In °C	Temp Gas Out °C	Temp Liq In °C	Temp Liq Out °C	Density Liq In kg/m^3	Density Liq Out kg/m^3	pH Liq In	DP Bot Bed kPa	DP Top Bed kPa
1.1.1	15.0	19.0	1.27	2.89	0.16	94.3	38.8	42.6	39.33	29.19	1145	1174	11.4	0.81	0.77
1.1.2	14.9	18.9	1.26	2.84	0.17	93.9	37.7	42.0	39.11	28.57	1146	1173	11.5	0.63	0.77
1.1.3	14.9	18.9	1.27	2.78	0.17	93.8	38.8	42.4	38.90	28.95	1147	1174	11.6	0.72	0.76
1.2.1	7.5	18.8	2.47	2.97	0.00	99.8	28.0	39.8	41.50	32.28	1163	1180	11.6	0.19	0.25
1.2.2	7.5	18.9	2.49	2.92	0.01	99.8	29.0	41.8	43.16	32.59	1163	1181	11.5	0.20	0.25
1.2.3	7.5	18.9	2.50	2.88	0.01	99.8	29.4	43.0	44.46	32.58	1162	1181	11.4	0.14	0.25
1.3.1	7.5	37.7	5.03	2.25	0.02	98.9	32.9	39.5	41.02	38.36	1165	1172	11.4	0.94	0.67
1.3.2	7.5	37.7	5.03	2.45	0.03	98.9	33.2	39.3	40.67	38.09	1165	1173	11.2	0.92	0.77
1.3.3	7.5	37.7	5.03	2.37	0.03	98.7	33.3	38.7	40.42	38.06	1166	1173	11.2	1.07	0.85
1.4.1	7.5	37.6	4.99	3.92	0.04	99.1	33.1	38.0	40.01	39.40	1166	1175	11.3	1.33	0.95
1.5.1	10.2	32.7	3.20	3.00	0.05	98.3	33.4	38.1	40.08	38.26	1166	1174	11.3	1.42	1.06
1.6.1	4.5	29.1	6.37	11.72	0.32	97.3	33.5	15.8	39.53	44.04	1165	1180	10.7	0.40	0.21
1.7.1	3.0	19.0	6.21	11.62	0.73	93.7	32.3	41.5	40.05	39.25	1163	1184	10.6	0.15	0.07
1.8.1	15.0	19.0	1.33	3.39	0.26	92.3	37.6	43.6	41.16	29.68	1207	1234	10.9	0.72	0.77
1.8.2	14.9	19.0	1.33	3.47	0.21	93.9	37.6	43.5	41.48	29.45	1207	1237	11.0	0.72	0.77
1.9.1	19.9	19.0	1.02	3.58	0.56	84.5	46.9	42.1	41.49	31.63	1206	1236	11.0	1.22	1.31
1.9.2	19.9	19.0	1.02	3.66	0.54	85.2	46.3	41.9	41.55	31.49	1207	1235	11.0	1.23	1.32
1.10.1	10.0	19.2	1.97	2.98	0.04	98.6	28.4	42.7	41.58	30.13	1208	1232	11.0	0.41	0.43
1.10.2	10.0	18.7	1.91	2.68	0.03	98.9	27.7	42.7	41.52	29.83	1208	1233	11.2	0.41	0.43
1.11.1	7.5	9.4	1.27	2.71	0.23	91.5	23.6	35.8	34.63	22.56	1212	1241	11.2	0.23	0.24
1.11.2	7.5	9.5	1.29	2.48	0.16	93.6	24.1	36.1	35.39	22.66	1211	1241	11.2	0.23	0.24
1.12.1	20.9	26.5	1.39	2.25	0.33	85.3	52.7	42.9	39.81	34.39	1211	1233	10.6	1.52	1.65
1.12.2	19.7	24.8	1.37	3.58	0.47	86.9	51.1	43.7	39.64	34.43	1211	1234	10.6	1.35	1.45
1.13.1	7.2	29.1	4.08	13.99	1.20	91.4	30.7	49.4	40.49	38.54	1211	1236	10.9	0.40	0.30
1.14.1	5.9	25.5	4.33	13.22	1.15	91.3	29.6	46.2	40.26	41.05	1212	1233	11.1	0.61	0.26
1.15.1	6.2	29.3	4.69	12.30	1.26	89.7	24.7	35.3	39.59	39.76	1216	1234	11.1	0.32	0.25
1.15.2	6.2	29.3	4.69	11.30	0.88	92.2	25.6	44.0	43.23	40.86	1214	1234	10.8	0.52	0.32
1.16.1	7.5	29.4	3.92	12.23	1.74	85.7	27.4	50.8	43.34	38.47	1212	1238	10.8	0.69	0.42
1.16.2	7.5	29.5	3.95	12.51	1.75	86.0	28.7	49.7	42.48	38.83	1213	1237	11.1	0.70	0.44
1.17.1	4.0	18.9	4.75	11.59	0.68	94.2	26.8	48.2	41.34	38.39	1214	1239	11.0	0.12	0.13
1.17.2	4.0	18.9	4.77	11.59	0.55	95.2	26.7	47.7	41.22	38.40	1214	1239	10.9	0.12	0.13
1.18.1	6.2	29.2	4.84	12.40	0.43	96.5	33.7	52.9	46.24	43.36	1229	1252	10.8	0.83	0.39
1.18.2	6.2	29.3	4.83	12.65	0.45	96.4	34.2	53.2	46.05	43.54	1228	1252	10.8	0.84	0.38
1.19.1	4.0	18.8	4.87	11.55	0.58	95.0	32.9	53.7	45.27	40.44	1229	1257	11.0	0.15	0.12
1.19.2	4.0	18.9	4.89	11.76	0.40	96.6	32.1	53.2	44.84	39.81	1228	1257	11.0	0.13	0.12

1.3.14 Campaign 1 Corrosion Evaluation

Corrosion coupons were purchased from Alabama Speciality Products Inc. Five different types of steel materials were tested: carbon steel (C1010), 304L stainless steel, 316L stainless steel, 317L stainless steel, and 2205 stainless steel (Duplex). All of the coupons are milled with a 120 grit finish and each coupon is stamped with a unique identification number. The corrosion coupons were mounted onto a 316L stainless steel 5-cm pipeline insertion rack with a 20-cm stem and three mounting holes. The coupons were mounted to the stem with 0.6-cm Teflon shoulder washers and 0.3-cm Teflon spacers were used in between each coupon. In all of the campaigns, the two sets of each material type were installed on two of the mounting holes. In addition, Z-core resin coupons manufactured by Smith Fibercast, which represented advance fiber reinforced plastic (FRP) material, was tested.

Corrosion coupons were inserted into a 5-cm pipe just downstream of the feed heater and left in the system over a 1 week period. Each coupon was weighed at the beginning and end of the week-long run and only visually inspected. Preliminary results show that all of the steel coupons remained relatively unchanged (Table 1-7). However, the FRP seemed to have absorbed some of the solvent, as the final weight seemed to be a little higher.

Table 1-7. Campaign 1 Corrosion Coupon Results

Sample ID	Initial Mass g	Final Mass g	Difference
C1010-1	15.6816	15.6824	-0.0008
C1010-2	15.8699	15.8705	-0.0006
304L-1	14.6760	14.6762	-0.0002
304L-2	14.7226	14.7232	-0.0006
316L-1	14.3783	14.3791	-0.0008
316L-2	14.3493	14.3496	-0.0003
317L-1	14.7838	14.7839	-0.0001
317L-2	14.7172	14.7179	-0.0007
2205-1	15.1899	15.1903	-0.0004
2205-2	15.3256	15.3267	-0.0011
FRP	10.4145	10.4408	-0.0263

1.3.15 Campaign 1 Summary

In Campaign 1, an existing extraction/distillation pilot plant was modified into an absorber/stripper system for CO_2 capture. New process equipment and instrumentation was added to the existing system. The carbon steel piping was replaced with 304 stainless steel. The pilot plant was operated for approximately 1 month, which included troubleshooting and one week of operation. The absorber contained Flexipac 1Y structured packing and the stripper contained 14 sieve trays at 0.46-m spacing. The pilot plant was operated with 5 molal potassium carbonate and 2.5 molal piperazine.

In Campaign 1, several problems arose that will need to be resolved in future campaigns. These issues include: (1) The loss of water from the solvent and low temperature points in the system resulted in the precipitation of piperazine and potassium compounds in the instrument lines and equipment. This created a number of problems during the operation plant and the pilot plant was shut down several times. (2) Foaming was observed in the absorber, which limited the operating range of liquid and gas flow

rates for pilot plant and required the addition of anti-foam. (3) The steam traps for the stripper feed preheater were undersized. As a result, the stripper feed was not adequately preheated and the stripper had an excessively high heat duty. (4) The liquid sampling method used in Campaign 1 may have resulted in the loss of CO_2 from flashing. (5) The absorber inlet gas was not representative of expected flue gas conditions. The temperature was too low and was not saturated with water at 40 °C. (6) Due to the loss of both pH meters, at times the pilot plant was blindly operated because there was significant delay with the liquid loading analyses. (7) The CO_2 loading analysis may have been compromised by the absorption of CO_2 into the diluted samples. The samples were analyzed using an autosampler and may have been exposed to the atmosphere for an extended period prior to analysis. (8) The DeltaV log sheet recorded the raw signal for the inlet and outlet Vaisala CO_2 gas analyzers and not the calibrated values.

1.4 CAMPAIGN TWO – ABSORBER/STRIPPER CHARACTERIZATION

The first objective of Campaign 2 was to obtain a more complete data set on absorber performance as a function of gas rate, liquid rate, CO_2 concentration, and CO_2 lean loading with FLEXIPAC® 1Y structured packing. Due to the problems encountered during Campaign 1, a portion of Campaign 2 was devoted to obtaining additional absorber data with FLEXIPAC® 1Y. The second objective was to obtain performance data for the stripper over a range of solvent rates, rich loadings, and stripper pressures with IMTP#40 random packing.

1.4.1 Campaign 2 Modifications

Before the commencement of Campaign 2, a number of issues were resolved. The two online Rosemount pH meters that failed were replaced. The original probes and transmitters were sent to Rosemount Analytical for examination, but it appeared that nothing was wrong. In the original setup, on one end the cable is hardwired to the transmitter and on the other end, the cable is connected to the pH probe via a quick-connect. Apparently, the pH probes and transmitters are not designed for outdoor use. It was suspected that the heavy rains had shorted the connection between the probe and transmitter, causing the pH meters to malfunction. Rosemount Analytical sent two new pH meters with one of the probes hardwired to the transmitter. Electrical tape was wrapped around the probe with the quick-connect cable in an attempt to prevent water intrusion.

At 12% CO_2, the 0–5% Horiba analyzer was over-ranged when taking measurements at the middle of the absorber. An existing Horiba PIR-2000 CO analyzer was converted by the manufacturer to a 0–20% CO_2 analyzer. The new analyzer was initially used to measure the absorber middle CO_2 gas concentration. However, due to the new blower configuration, the saturated inlet gas caused the Vaisala analyzer to malfunction at the beginning of the campaign. The absorber middle Horiba sampling system was then used to measure absorber inlet CO_2 gas concentration and no absorber middle gas samples were analyzed during Campaign 2.

At the conclusion of the first campaign, it was discovered that the polyethylene bag filter for the reboiler had completely dissolved. The filters were replaced with bags

made from cotton material. The polyethylene bag filter had previously been used in a C6/C7 system with no adverse effects at the approximately the same temperatures (~120 °C). Therefore, temperature should not have been an issue. However, it was discovered during the course of campaign 2 that the while the new bags were made from cotton, the stitching was still made of a synthetic fiber, which resulted in the bags to eventually fail. In the third and fourth campaign, filter bags made and stitched with cotton were used.

In the first campaign, the steam traps on the stripper feed heater were undersized and as a result the solvent was not adequately heated. New steam traps were installed on the stripper feed heater to rectify the problem. A larger orifice was installed for steam flow measurement to the reboiler. In the first campaign, the steam flow rates exceeded the measuring range of the orifice. The cooling water to the air cooler was blinded off to permit operation at higher gas temperatures. A bypass around the blower was constructed with PVC pipe. The bypass would allow a portion of the gas to be recycled and thus increase the temperature of the inlet absorber gas to reach 40 °C. A manually adjusted butterfly valve was used to regulate the gas flow rate through the blower recycle.

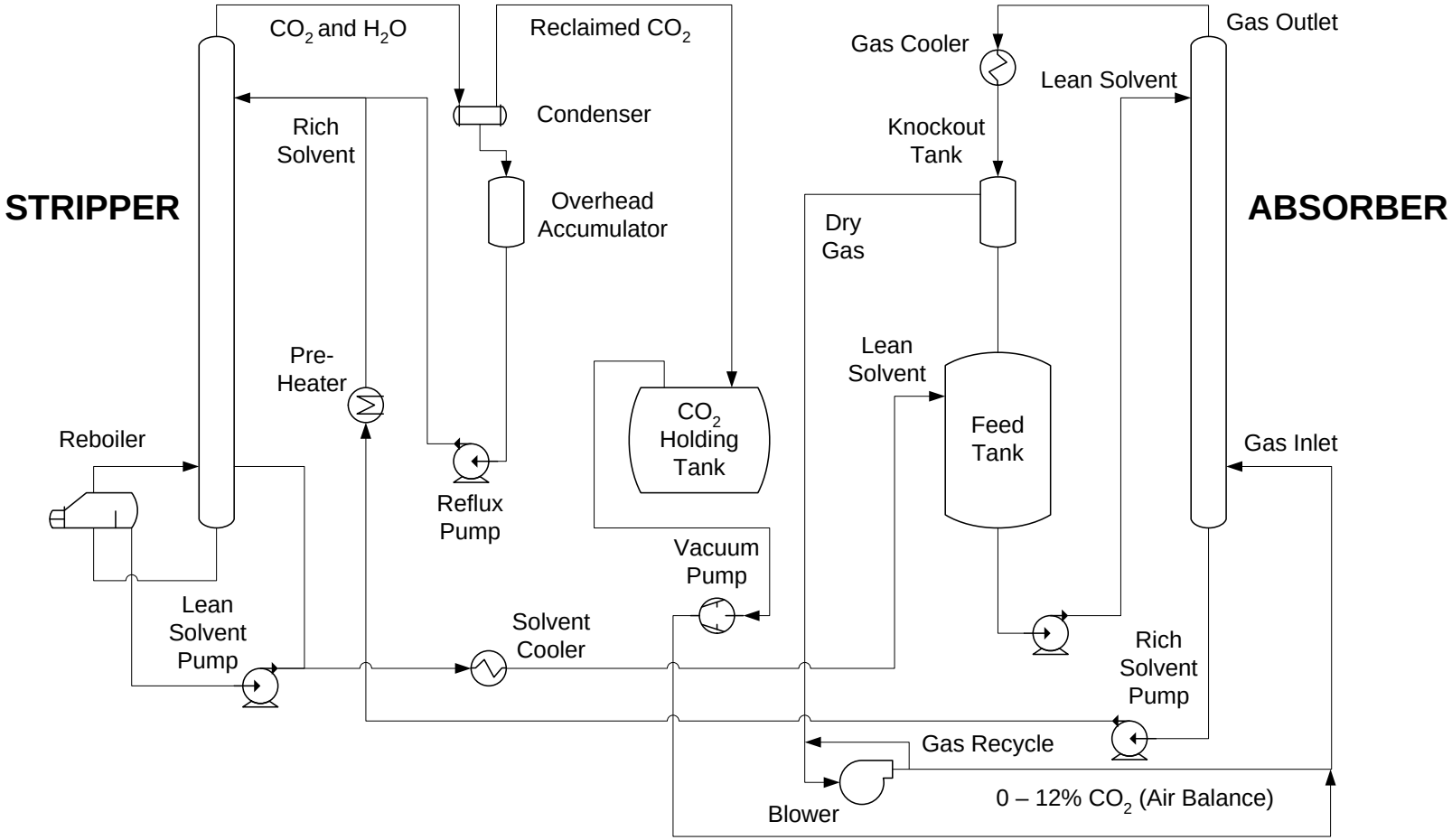

Figure 1-13. Process Flowsheet of Absorber/Stripper Pilot Plant for Campaign 2

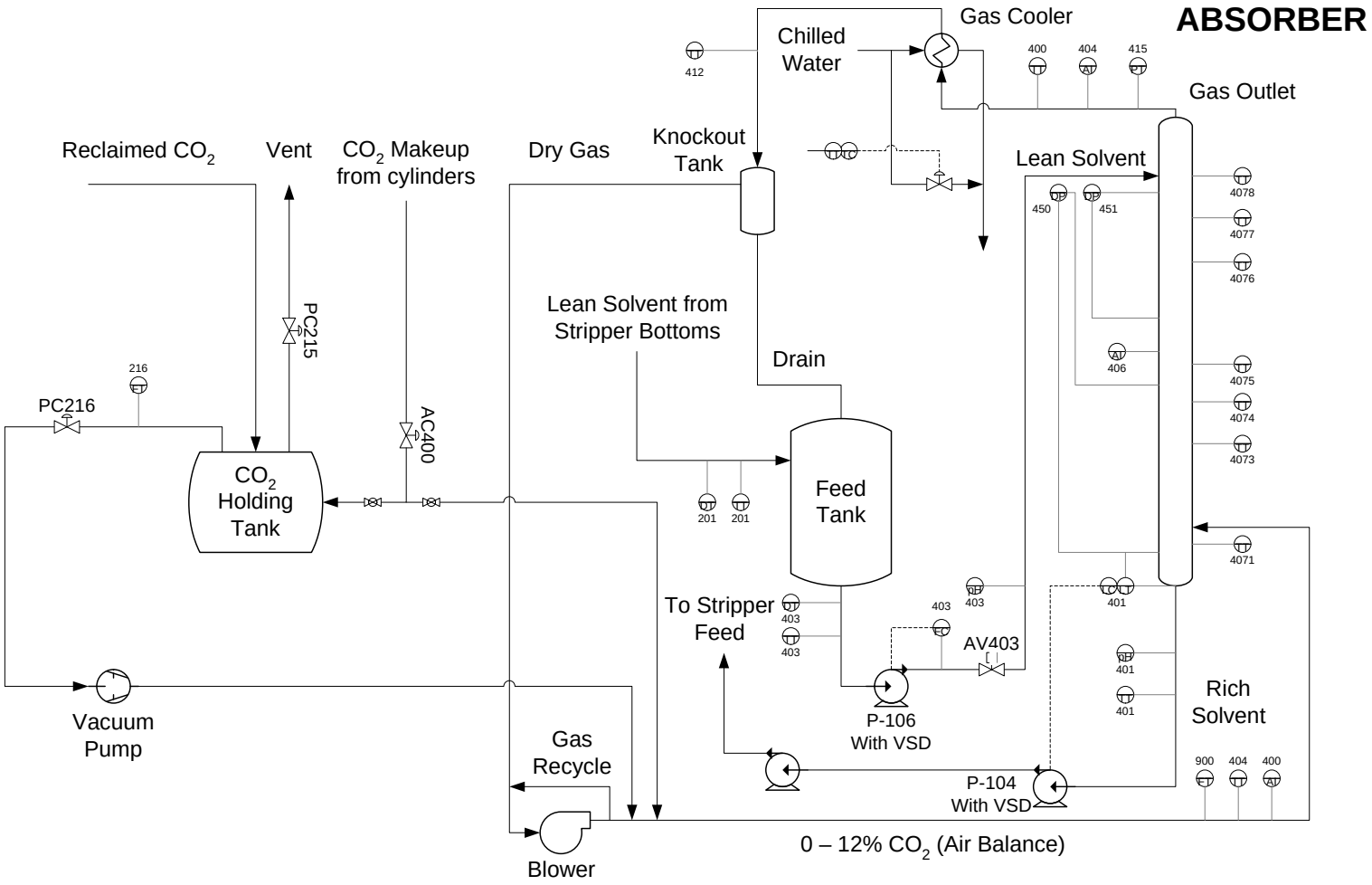

Figure 1-14. Process and Instrumentation Diagram of the Absorber for Campaign 2

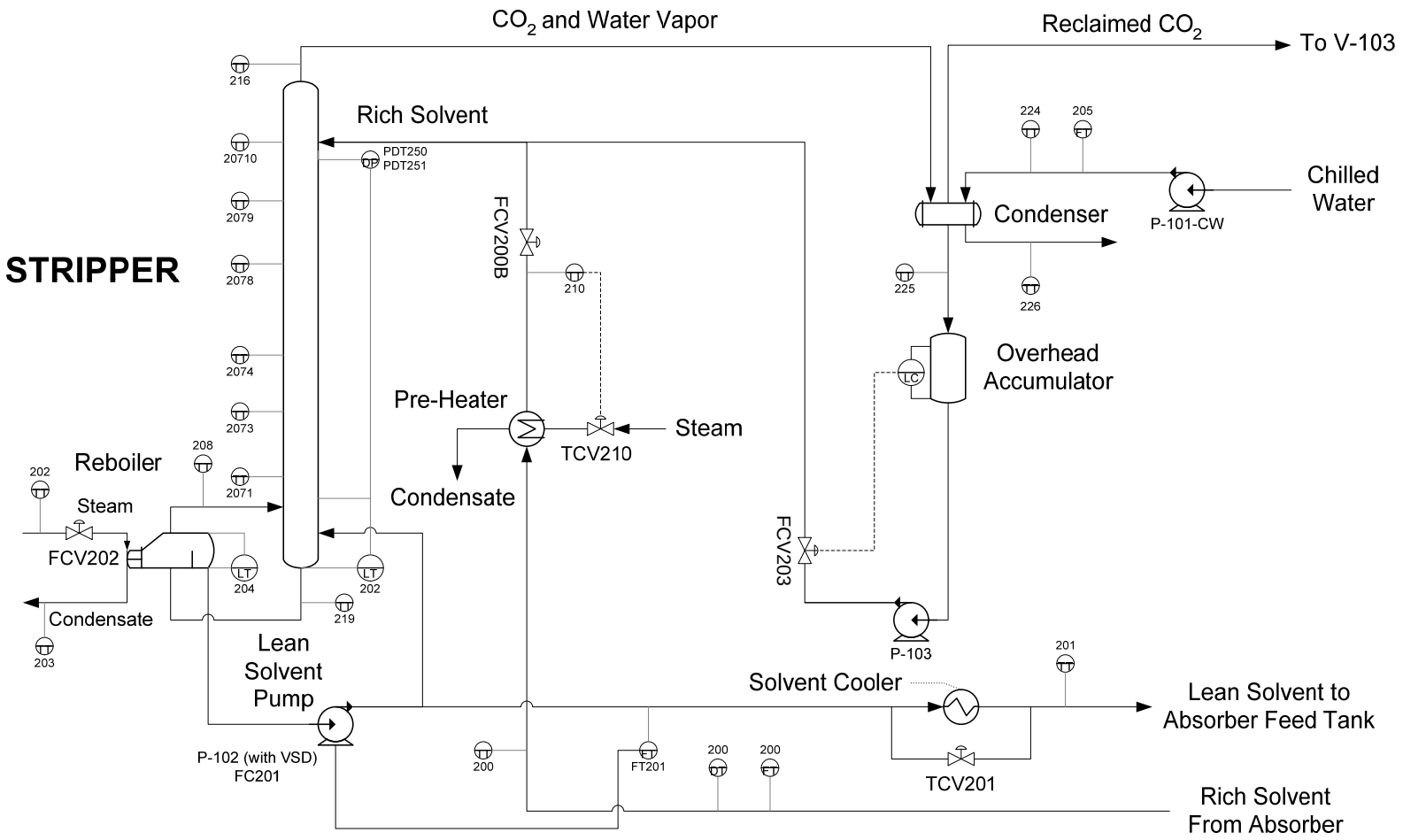

Figure 1-15. Process and Instrumentation Diagram of the Stripper for Campaign 2

1.4.2 Campaign 2 Liquid Sample Collection Method

In the first campaign, there were issues of material balance closure across the absorber column. It was believed that the CO_2 in the rich samples were flashing during the sample collection process. Therefore, sample bombs were constructed and used to take samples to eliminate this. The sample bombs were made from 1.3-cm OD stainless steel tubing and Swagelok® quick-connects and had a volume of about 10 mL. The stock o-rings in the quick-connects were replaced with EPDM o-rings.

A total of five liquid sample points were taken for Campaign 2: absorber lean, absorber middle, absorber rich, stripper middle, and stripper lean. Quick-connects and braided stainless steel hoses were attached to the pump discharge and suction of the pumps for the absorber lean, absorber rich, and stripper lean streams. The sample bomb was connected to the two ends of the sample hose and fluid was allowed to circulate for several minutes before the valves were shut and the sample bomb was disconnected. For the pump samples, the discharge valve was always shut first and then the suction side valve was closed. The sample bombs were colored coded to match the sample location.

For the absorber middle sample, fluid from the collector plate was allowed to flow through the sample bomb and discharge back into the absorber column for several minutes, before being disconnected. The stripper middle sample was taken from a bayonet collector, allowed to flow through the sample bomb and discharge into an eductor. Under vacuum operations, some of the stripper middle samples could not be withdrawn because the eductor did not provide enough suction.

The sample bombs were brought inside to the laboratory and attached to a sample extraction system. A syringe was used to extract the liquid sample from the sample bomb through a Teflon coated rubber septum. The sample was then injected into a 40-mL vial containing 30 mL of chilled de-ionized (DI) water. The sample was injected underneath the surface of the DI water. Therefore, the samples were all diluted to minimize any flashing and prevent precipitation. The mass of the injected sample was recorded and the sample bomb was allow drain and nitrogen was used to blow out any residual liquid in the sample extraction system. Two set of samples were taken for each operating condition. The standard operating procedure for collecting the liquid samples is listed in the appendix.

1.4.3 Campaign 2 Analytical Methods

In Campaign 2, the concentration of piperazine and potassium was initially determined by titration with 2N HCl and 2N NaOH using the method developed for Campaign 1. However, in Campaign 2, the titration method was conducted on samples that had been diluted by ratio of 3:1. When the results from the titration method for the two campaigns are compared, for a given liquid density and temperature, the results from the second campaign were consistently lower than the first campaign. It was assumed that the concentration of potassium and piperazine were correlated with density. This may have been due to a change in the indicator endpoint resulting from sample dilution. Also, it is possible that the when titrating the dilute solution with a concentrated acid, the endpoint may have been overshot. A method for analyzing piperazine and potassium using ion chromatography (IC) was later developed in Campaign 4 and used to verify the

correct the titration results. The IC results are given in the Campaign 4 Analytical Methods section of this chapter.

In Campaign 2, the Shimadzu 5050A TOC was used to determine the CO_2 loading in the solvent with the same method developed for Campaign 1. In addition, some of the diluted liquid samples from Campaign 2 were analyzed with the inorganic carbon (IC) analyzer located on the main UT campus to validate the TOC results. The results from the campus IC and from the Shimadzu total organic carbon (TOC) analyzer located at the Pickle Research Center (PRC) were plotted against online pH measurements. The results are shown in Figure 1-16. It was found that the campus loading numbers were systematically lower than that analyzed by the Shimadzu TOC.

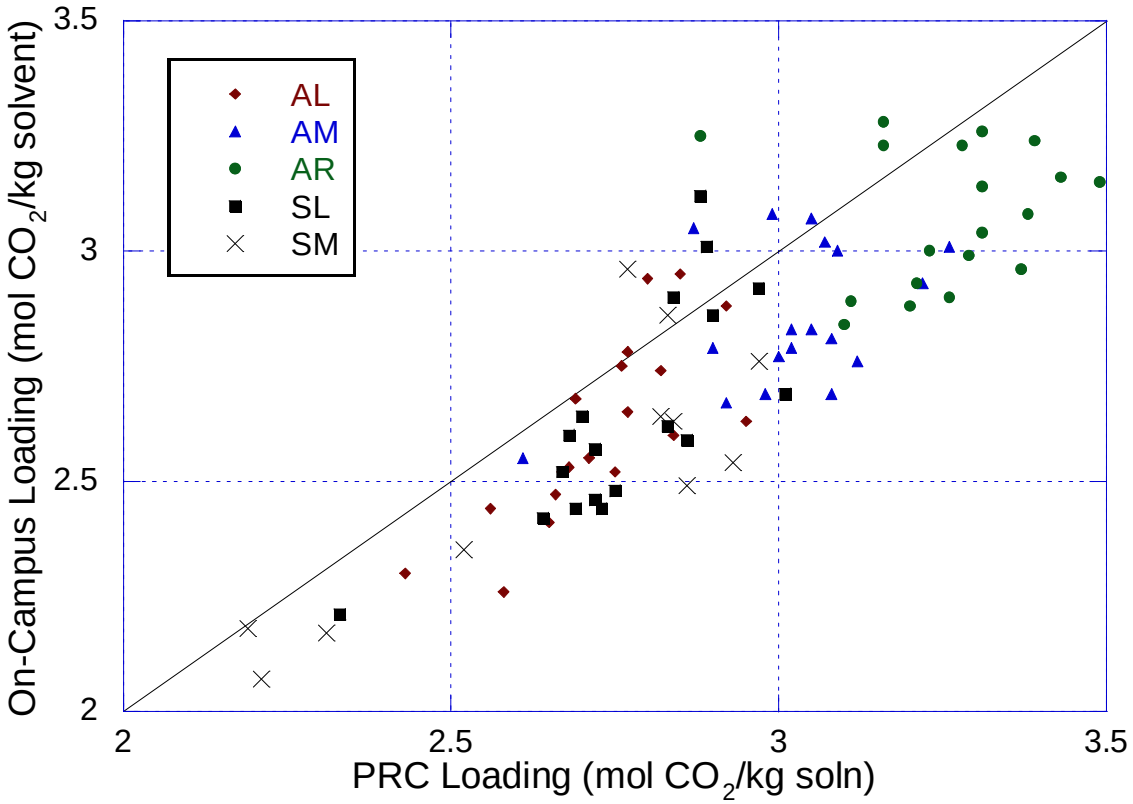

Figure 1-16. CO_2 Loading Results for PRC TOC analyzer and On-campus Inorganic Carbon Analyzer of Same Sample

In the process, it was discovered that the diluted sample solutions and the IC standard solutions absorbed CO_2 when left open to the atmosphere. The PRC IC standards are made up to a concentration of 1000 ppm of inorganic carbon using sodium carbonate and sodium bicarbonate. The on-campus IC standard is made up to a concentration of 7 molar (84 ppm) using sodium carbonate.

An experiment was conducted where the IC standard was parafilmed and the diluted samples were left open to the atmosphere and were analyzed over a period of five days (Figure 1-17). The results show that the diluted samples absorbed between 20 to 30 ppm of CO_2 from the atmosphere within a 17 hour period. In earlier analyses, the TOC was operated over a period of 12 hours. Therefore, if the samples were not parafilmed, a fairly large amount of CO_2 may have been absorbed. The results also show that the 100-ppm IC standard did not absorb any CO_2 over a period of 4 days when covered with parafilm. The slight change in concentration for the 100-ppm IC standard may have been due to analyzer drift. It was noticed that sometimes the Shimadzu carrier gas fluctuated over time, which gave slightly different results for a particular IC standard concentration. To account for analyzer drift in latter TOC analyses, IC standards were analyzed every 5–6 samples in the sample matrix.

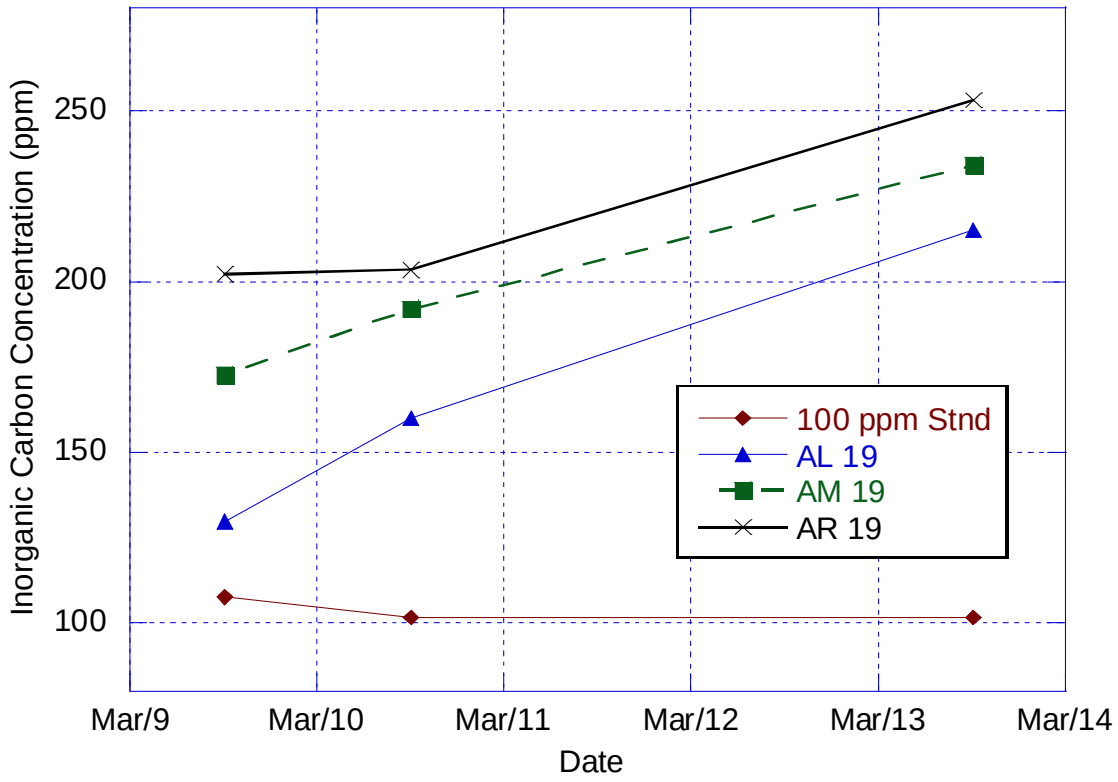

Figure 1-17. CO_2 Absorption in Diluted K^+/PZ Samples from Campaign 2

It was also observed that the 100 ppm IC standards consisting of sodium carbonate and bicarbonate will absorb up to 10 ppm of CO_2 when left open to the atmosphere overnight. Three sets of IC standards consisting of 100, 150, 200 ppm were made at PRC and analyzed by the on-campus IC. The values were found to be about 10–15% lower by the on-campus IC. The PRC standards were freshly prepared, while the on-campus standard that was used to calibrate the analyzer was not. Therefore, it is conceivable that the on-campus standard may have absorbed CO_2. In addition, the on-campus standard is made from Na_2CO_3, which readily absorbs water and CO_2 from the atmosphere. If the Na_2CO_3 was not properly heated or even heated before being used to make up the standard, this would also give erroneous results.

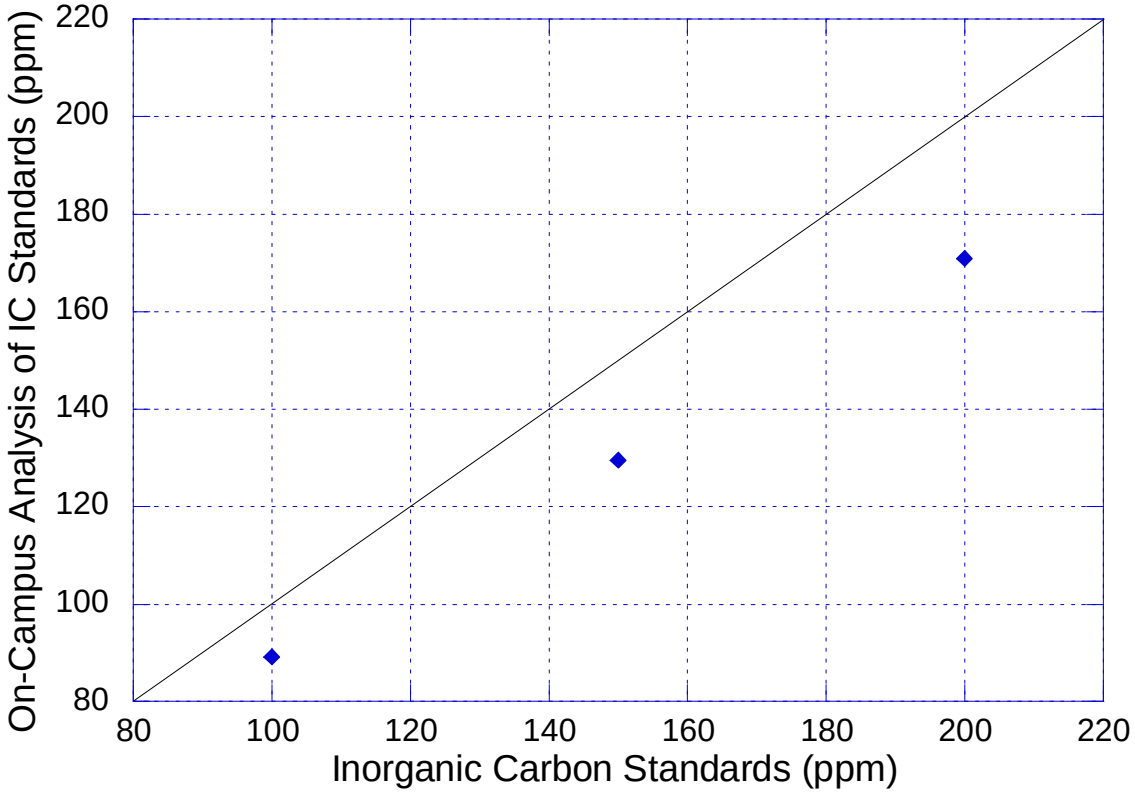

Figure 1-18. Analysis of 100, 150, 200 ppm Inorganic Carbon Standards by the On-campus Inorganics Carbon Analyzer

Finally, the sodium carbonate standard used for the main campus IC was measured by the Shimadzu and determined to be 96 ppm when the actual concentration should have been 84 ppm. This supports the observation that CO_2 is absorbed by the Na_2CO_3 standard. The on-campus standard is stored in a stopped glass flask at ambient temperature and not in the refrigerator. Overtime, it is possible that the standard may absorb CO_2 from the atmosphere.

Base on these results, the initial loading analysis was discarded and the absorber lean, middle, and rich samples were re-analyzed with the new and more rigorous method. In addition, the samples were diluted 40:1 with chilled DI water to minimize CO_2 losses.

100 ppm standards were made up daily from the 1000 ppm IC standard and were analyzed after every 6 samples. The 1000 ppm IC standard was stored in a capped bottle and kept in the refrigerator when not in use. The diluted liquid samples were transferred to the sample tubes and immediately covered with parafilm to minimize absorption of CO_2 from the atmosphere.

1.4.4 Campaign 2 Plant Operation

Pilot plant operation for Campaign 2 commenced at the end of October in 2004. The pilot plant was operated continuously for 10 days, 24 hours per day, except on weekends. A total of 40 runs and 23 operating condition were completed. Twenty-three runs were conducted at approximately a single solvent composition. The solvent from the first campaign was used in the second campaign. The solvent has been stored in steel drums in between the two campaigns.

The piperazine and potassium concentration were varied between 1.3 to 1.4 mol/kg soln and 2.8 to 2.9 mol/kg soln, respectively. The gas and liquid flow rates were varied from 1.2 to 2.2 kg/m^2-s and 2.7 to 11.9 kg/m^2-s, respectively. The L/G ratio was varied from 1.8 to 6.9 kg/kg. The inlet CO_2 concentrations were varied between 2.6 to 12.4 mole percent and the inlet gas temperatures were varied between 30 and 50 °C. The inlet temperature of the solvent to the absorber was maintained nominally at 40 °C. The stripper pressure was varied between 0.3 to 1.8 bar.

The absorber contained 6.1 m of Flexipac 1Y structured packing and the stripper contained 6.1 m of IMTP #40 random packing, divided into two 3.05 m beds of packing. A chimney tray and liquid redistributor was located in between each bed of packing. In

the stripper, two Koch 4C distributors were used as the distributor and redistributor for the top and bottom beds, respectively. The absorber contained a Koch 3C distributor at the top and a Montz II redistributor in the bottom bed. The CO_2 removal rate varied from 56.3 to 97.3 percent. No additional vanadium was added to the system. Base on preliminary analysis, the lean loading varied from 0.43 to 0.53 mol/total alkalinity. The lean density varied between 1221 to 1230 kg/m^3.

Table 1-8. Campaign 2 Absorber Operation

Parameter	Value
Inlet CO_2 (mol %)	2.6 – 12.6
PZ Concentration[1] (mol/kg)	1.3 – 1.4
K^+/PZ Ratio	2.0 – 2.3
Lean Loading[2] (mol CO_2/mol K+2PZ)	0.43 – 0.54
G (kg/m^2-s)	1.2 – 2.2
L/G (kg/kg)	1.7 – 7.1
$T_{GAS,IN}$ (°C)	29 – 64
T_{LEAN} (°C)	39 – 48

1. Concentration in mol/kg of solvent
2. TAlk = Total alkalinity (mol K+2 mol PZ)

Table 1-9. Campaign 2 Stripper Operation

Parameter	Value
□T Approach (°C)	31 – 81
Top Temperature (°C)	67 – 113
Bottom Temperature (°C)	74 – 143
Reboiler Heat Duty (kcal/mol CO_2)	107 – 223

In order to increase the inlet gas temperature, a bypass around the blower was constructed. A 15.2-cm PVC pipe run was added towards the beginning of the second campaign. As a result, water began to condense out downstream of the knockout pot and

accumulated in some of the lines, leaking out through the blower casing. Water was periodically drained from the lines and pumped back into the system.

The supersaturated conditions in the inlet gas eventually resulted in the failure of the inlet Vaisala CO_2 gas analyzer. The Horiba PIR-2000 analyzer was switched from analyzing the absorber middle and used to measure the inlet CO_2 gas concentration. However, there was some lag time associated with the Horiba extractive gas sampling system. As a result, it was difficult to control the system and took longer to reach steady state. No absorber middle gas samples were analyzed in Campaign 2.

Both of the online Rosemount pH meters were replaced prior to the commencement of the second campaign. The inlet pH meter was hardwired to the transmitter while the outlet pH meter still had the quick-disconnect cabling. Electrical tape was wrapped around the quick-connect in lieu of constructing a shelter. Unfortunately, the outlet online Rosemount pH meter failed just before the commencement of the second campaign, possibly due to the rain. The inlet loading was monitored by the online Rosemount pH meter and controlled by either the addition of makeup CO_2 or increasing the stream flow to the stripper reboiler.

Significant foaming was occasionally observed which limited the hydraulic rates. New anti-foam from GE was used in the second campaign, which the manufacturer claimed to be better suited for our solvent system. Antifoam was added periodically which eliminated the problem for 10–20 hours of operation. The foaming tendency appeared to increase with the higher carbon dioxide concentration, presence of significant temperature bulge and high gas rates.

1.4.5 Campaign 2 Results

A summary of the results for the liquid analyses of Campaign 2 is shown in Table 1-10. The acid-base titration method was used to determine the concentration of piperazine and potassium in the solvent. Later, before the strat of Campaign 4, the ion chromatography method was used to measure piperazine and potassium concentration. The two analyses appear to agree with each other. In Campaign 2, the titration analysis was performed with a 4:1 pre-diluted sample, while in Campaign 1, titrations were performed with undiluted piloted plant samples. It is possible that the dilution of the sample may have shifted the titration endpoint of methyl orange. CO_2 loading was measured using the Shimadzu TOC with the revised inorganic carbon analytical method. Piperazine analysis using organic carbon analysis was not performed in this campaign onward because of its unreliability. Table 1-11 is a summary of the absorber results from Campaign 2. The complete raw data set for Campaign 2 is given in the appendix. In campaign 2, no corrosion coupons were installed.

Table 1-10. Campaign 2 Absorber Analyses for 5m K^+/2.5m PZ

Run ID	Date	Time	Ion Chromatograph		Titration		CO_2 Loading		
			PZ Lean mol/kg	K^+ Lean mol/kg	PZ Lean mol/kg	K^+ Lean mol/kg	Lean mol/kg	Mid mol/kg	Rich mol/kg
2.1.1	10/26/04	10:35	1.24	2.90	1.29	2.97	2.65	2.96	3.14
2.1.2	10/26/04	11:00	-	-	-	-	2.47	-	3.24
2.2.1	10/26/04	14:45	-	-	-	-	2.45	3.22	3.21
2.3.1	10/27/04	0:15	-	-	-	-	2.60	3.16	3.43
2.4.1	10/27/04	2:30	-	-	-	-	2.65	3.06	3.29
2.5.1	10/27/04	3:30	-	-	-	-	2.65	2.90	3.21
2.6.1	10/27/04	6:00	-	-	-	-	2.61	2.98	3.24
2.7.1	10/27/04	7:00	1.32	3.08	1.38	3.01	3.00	2.93	3.28
2.8.1	10/27/04	12:00	-	-	-	-	2.58	2.99	3.13
2.8.2	10/27/04	13:00	1.25	2.91	1.28	2.87	2.67	3.00	3.30
2.9.1	10/28/04	4:15	1.21	2.77	1.32	2.72	2.52	2.96	3.22
2.9.2	10/28/04	5:15			-	-	2.50	3.08	3.28
2.10.1	10/28/04	13:40	1.33	3.09	1.41	2.97	2.84	3.06	3.39
2.10.2	10/28/04	14:55	-	-	-	-	2.65	3.06	3.28
2.11.1	10/28/04	16:35	-	-	-	-	2.94	3.26	3.41
2.11.2	10/28/04	17:15	-	-	-	-	2.89	3.05	3.48
2.12.1	10/28/04	19:15	-	-	-	-	2.83	3.26	3.57
2.12.2	10/28/04	20:15	-	-	-	-	2.73	3.16	3.55
2.13.1	10/29/04	5:45	-	-	-	-	2.50	2.95	3.25
2.13.2	10/29/04	6:45	1.26	2.95	1.32	2.86	2.78	2.91	3.08
2.14.1	11/2/04	20:32	-	-	1.30	2.82	-	-	-
2.14.2	11/2/04	21:45	-	-	-	-	2.94	3.33	3.39
2.15.1	11/3/04	0:30	1.24	2.90	-	-	2.84	3.01	3.24
2.16.1	11/3/04	1:30	-	-	-	-	2.82	3.14	3.27
2.17.1	11/3/04	5:15	-	-	-	-	2.73	2.97	3.12
2.17.2	11/3/04	6:15	-	-	1.35	2.74	2.70	3.00	3.15
2.18.1	11/3/04	11:30	-	-	1.36	2.79	2.82	2.95	3.10
2.18.2	11/3/04	12:30	-	-	-	-	2.82	3.20	3.16
2.19.1	11/3/04	15:45	-	-	-	-	2.90	2.99	3.40
2.19.2	11/3/04	16:45	-	-	-	-	2.93	3.01	3.21
2.20.1	11/4/04	6:00	-	-	-	-	2.66	3.02	3.13
2.20.2	11/4/04	7:30	-	-	-	-	2.74	3.16	3.43
2.21.1	11/4/04	10:15	-	-	-	-	2.94	2.71	3.53
2.21.2	11/4/04	11:15	1.39	3.23	1.43	3.06	2.90	3.12	3.40
2.22.1	11/4/04	13:30	1.30	3.03	1.36	2.88	2.78	3.02	3.29
2.22.2	11/4/04	15:15	-	-	-	-	2.77	3.07	3.35
2.23.1	11/4/04	21:15	-	-	-	-	2.68	3.22	3.43
2.23.2	11/4/04	23:00	-	-	-	-	2.66	3.00	3.21
2.24.1	11/5/04	3:45	-	-	-	-	2.65	3.08	3.29
2.24.2	11/5/04	4:45	1.24	2.92	1.35	2.77	2.43	2.90	3.11

Table 1-11. Campaign 2 Absorber Results for 5m K^+/2.5m PZ

Run#	Gas Rate Actual m^3/min	Liquid Rate L/min	CO_2 In mol%	CO_2 Out mol%	CO_2 Removal %	Temp Gas In °C	Temp Gas Out °C	Temp Liq In °C	Temp Liq Out °C	Density Liq In kg/m^3	Density Liq Out kg/m^3	pH Liq In	DP Bot Bed kPa	DP Top Bed kPa
2.1.1	17.0	30.2	11.1	2.1	81.2	49.1	49.2	40.2	47.4	1224	1242	11.2	0.79	0.86
2.1.2	17.0	30.3	11.0	2.4	78.5	49.4	48.8	40.3	47.2	1225	1240	11.1	0.81	0.87
2.2.1	17.0	30.1	12.3	5.4	56.3	54.4	50.8	41.2	50.5	1226	1240	11.0	0.80	0.87
2.3.1	12.8	34.0	11.5	4.0	64.7	46.2	44.6	40.7	44.7	1227	1240	10.7	0.57	0.63
2.4.1	12.7	41.5	12.0	3.7	69.5	45.6	40.9	40.6	44.6	1227	1239	10.6	0.83	0.76
2.5.1	12.7	41.4	10.7	2.7	74.3	46.7	40.7	40.6	44.6	1227	1239	10.6	0.88	0.81
2.6.1	12.7	47.2	10.4	1.9	81.5	47.2	38.6	41.2	45.9	1228	1237	10.6	1.02	0.83
2.7.1	12.7	47.4	11.1	2.2	80.0	48.2	39.5	41.3	46.4	1228	1238	10.6	1.03	0.86
2.8.1	17.0	49.4	11.7	4.0	65.7	50.8	45.8	41.4	46.6	1227	1238	10.6	1.45	1.60
2.8.2	17.0	49.2	11.4	3.8	67.1	53.2	46.2	41.6	47.8	1227	1237	10.6	1.48	1.62
2.9.1	9.9	32.4	11.3	3.5	68.9	36.2	41.1	40.6	41.8	1226	1241	10.6	1.32	0.26
2.9.2	9.9	32.3	11.3	3.4	70.2	37.4	42.2	40.8	42.3	1226	1241	10.6	1.34	0.25
2.10.1	9.9	43.7	11.9	1.9	84.3	47.2	38.6	41.2	48.0	1228	1238	10.6	1.98	1.02
2.10.2	9.9	43.5	12.0	2.0	83.6	48.2	38.9	41.3	48.2	1228	1238	10.6	2.01	1.06
2.11.1	9.9	43.4	11.5	1.8	84.4	51.2	39.3	41.4	48.4	1229	1238	10.6	2.11	1.20
2.11.2	9.9	43.6	11.7	1.9	83.5	51.5	39.6	41.4	48.6	1229	1238	10.6	2.11	1.20
2.12.1	9.9	45.6	11.7	0.6	94.8	59.8	37.4	41.0	48.4	1229	1239	10.6	2.38	7.05
2.12.2	9.9	45.3	11.4	0.3	97.3	47.9	37.4	41.0	48.0	1229	1239	10.7	2.36	8.26
2.13.1	9.9	37.9	11.6	2.7	76.7	33.5	39.3	40.7	45.0	1230	1242	10.6	0.77	0.86
2.13.2	9.9	37.9	12.0	3.0	74.6	32.0	37.6	40.3	44.1	1230	1243	10.6	0.77	0.86
2.14.1	9.9	18.9	4.9	0.8	84.1	29.3	38.2	43.5	30.7	1227	1246	10.4	0.25	0.28
2.14.2	9.9	19.0	4.7	0.9	81.0	28.2	36.8	42.5	30.1	1227	1245	10.4	0.26	0.28
2.15.1	9.9	22.9	5.4	0.7	86.4	29.9	36.6	41.9	34.6	1229	1242	10.4	0.28	0.29
2.16.1	9.9	22.3	5.3	0.6	88.1	29.5	36.1	42.0	34.5	1230	1244	10.4	0.28	0.30
2.17.1	12.7	20.8	4.4	0.5	88.4	33.0	35.6	38.8	31.5	1231	1245	10.5	0.43	0.47
2.17.2	12.7	20.8	4.3	1.1	74.6	31.7	34.9	39.0	30.0	1232	1248	10.5	0.44	0.47
2.18.1	12.7	30.5	4.0	0.5	87.8	35.7	39.0	44.8	37.2	1222	1233	10.3	0.45	0.48
2.18.2	12.7	29.9	3.9	0.4	88.6	36.6	39.2	44.8	37.6	1222	1233	10.3	0.45	0.49
2.19.1	12.7	37.8	3.9	0.3	92.5	37.4	40.5	47.0	40.5	1222	1231	10.2	0.54	0.52
2.19.2	12.7	37.8	3.9	0.3	91.7	39.7	41.8	47.8	42.3	1222	1230	10.2	0.55	0.56
2.20.1	14.2	77.4	16.2	2.0	87.7	47.1	36.3	40.1	48.0	1226	1233	10.6	1.46	1.08
2.20.2	14.2	77.1	16.0	1.8	88.5	49.7	36.3	40.1	48.3	1226	1233	10.6	1.53	1.15
2.21.1	14.2	83.4	16.1	1.2	92.6	58.4	35.8	40.1	48.3	1226	1232	10.6	1.91	1.42
2.21.2	14.2	83.3	16.4	1.4	91.3	64.3	38.1	40.9	50.7	1225	1231	10.5	1.92	1.44
2.22.1	14.2	83.0	17.9	2.5	86.2	49.5	39.3	41.8	51.2	1220	1227	10.5	1.70	1.19
2.22.2	14.2	83.3	17.4	1.8	89.4	49.1	38.7	41.1	50.9	1223	1229	10.5	1.72	1.19
2.23.1	14.2	56.8	17.2	4.5	73.9	42.0	41.5	39.9	47.9	1227	1237	10.7	0.89	0.95
2.23.2	14.2	56.5	16.3	4.0	75.6	41.0	39.8	39.8	47.3	1227	1237	10.7	0.92	0.96
2.24.1	14.2	57.0	16.9	3.4	79.8	41.7	41.5	39.7	47.6	1229	1240	10.8	1.00	1.07
2.24.2	14.2	56.5	17.4	3.8	78.4	41.5	42.0	39.6	47.5	1229	1240	10.8	1.02	1.10

1. Run 2.13 High Stripper Pressure Case
2. Run 2.14-2.19 Vacuum Stripping Cases

1.4.6 Campaign 2 Summary

In Campaign 2, several issues from Campaign 1 were resolved, which include: (1) Sample bombs were used for the liquid sampling, which minimized CO_2 losses from flashing. (2) The liquid sampling method was improved through the use of syringes and injection of samples into vials containing chilled DI water to minimize CO_2 losses and eliminate precipitation from cooling. (3) The liquid samples and standards for the CO_2 loading analysis were covered with parafilm to minimized CO_2 absorption. (4) The absorber inlet gas was heated the addition of a gas recycle. (5) The undersized steam traps for the stripper feed pre-heater was replaced.

In Campaign 2, there were several issues that needed to be resolved. These issues include: (1) The stripper feed still was not adequately pre-heated. (2) The absorber inlet gas was not saturated. (3) The absorber inlet gas temperature was not well controlled. (4) The Vaisala CO_2 gas analyzers were operated in a condensing environment which resulted in the failure of the absorber inlet analyzer and intermittent malfunction of the absorber outlet analyzer. (5) Foaming in the absorber was observed, which limited the matrix of run conditions. (6) The absorber outlet pH meter failed as a result water intrusion. (7) The water balance was not well maintained because the air cooler was not operated and water condensed in the gas lines and leak out through the blower. (8) Steady state operation of the pilot plant was difficult to the lag time associated with the extractive sampling method use with the Horiba CO_2 analyzer, which included the control of the steam flow to the reboiler, the CO_2 recycle flow rate, and the flow of CO_2 makeup. (9) The pilot plant was sometimes operated blindly because real-time analysis

of the absorber lean loading could not be provided. (10) The CO_2 material balance for the gas and liquid phase did not match up after the commencement of vacuum operation. (11) The DeltaV log sheet recorded the raw signal for the absorber outlet Vaisala CO_2 analyzer and not the calibrated value.

1.5 CAMPAIGN THREE – MEA BASELINE

The main objective of the MEA campaign was to establish a benchmark for comparison to the aqueous piperazine and potassium carbonate system in terms of performance and plant operation. The same FLEXIPAC® 1Y structured packing was used in the absorber and IMTP#40 was used in the stripper. Another objective was to evaluate and compare mass transfer rate data obtained by the pilot plant to bench-scale data from a wetted wall column for the two solvent systems.

1.5.1 Campaign 3 Modifications

Prior to the start of the third campaign, the additional modifications were made to the pilot plant correct the problems encountered in Campaign 2. At low gas rates, the annubar in the 20 cm PVC gas line gave erroneous results due to the low pressure drop and poor turndown characteristics. The 20.3 cm gas schedule 40 PVC line was replaced with 7.6 cm and 10.2 cm schedule 40 PVC gas lines. In the new setup, the gas could flow through either line or both and generate enough pressure drop to produce an accurate reading. Steam flow measurement for the solvent preheater was added. In addition, a Rosemount 3095MFA Mass Probar annubar was added to measure the gas flow rate of the CO_2 recycle stream leaving the overhead gas accumulator. The annubar has an accuracy of ±0.9 of the mass flow rate for gas and stream and a flow turndown of

8:1. The flowmeter was a way of verifying the gas and liquid material balance of the absorber and stripper when the system was at steady state. Unfortunately, the minimum Reynolds number for the flowmeter is 6000, which results in a minimum flow of approximately 63 ft^3/min at 293K and 1.013 bar. In Campaign 4, this flow requirement was satisfied under only one run condition. However, in the MEA campaign, it appeared that the flowmeter gave reasonable results above 30 scfm. Therefore, the results from the CO_2 recycle flowmeter were used only as a rough comparison.

Under vacuum conditions, the amount of CO_2 that could be stripped was limited by the diameter of the 2.5 cm gas line from the overhead condenser. This dictated the range of lean loadings and gas rates for the absorber and the range of stripper pressure for vacuum operation. To rectify this problem, a 5.1 cm gas line was added to the top of the overhead gas accumulator and connected to the overhead gas accumulator. In the new configuration, excess CO_2 from the condenser could exit the bottom of the condenser along with the water and flow to the overhead liquid accumulator. The liquid accumulator functioned as a separator, whereby the CO_2 gas could exit the top of the tank and flow into the overhead gas accumulator. A constant liquid level was maintained in the vessel, which prevented any gas from being returned with the liquid reflux. However, in Campaign 4, it appears that some of the condensed water became entrained with the CO_2 recycle stream and ended up in the gas accumulator. The overhead gas accumulator needed to be periodically drained of the water, which was then pumped back into the system.

In campaign 2, the solvent preheater still did not function properly. It was thought that the solvent was flashing after the control valve, which was just downstream of the heat exchangers, and created a something of vapor lock. In addition, the stripper did not have a two phase distributor, which may have helped with the two phase flow. To correct this problem, a spare pump was connected in series to the absorber outlet pump to increase the pressure of the solvent stream. The control valve was also relocated so that it was now just upstream of the stripper inlet nozzle.

A new extractive CO_2 sampling system was constructed for the additional Horiba analyzer. The sampling system consists of a water knockout, a sampling pump, a filter, a membrane filter and a rotameter. The gas flows from the sample point to a water knockout and then through the sample pump. Next the gas passes through a filter that removes any condensed water and then through a membrane filter that removes any residual moisture. The gas is then analyzed by the Horiba CO_2 analyzer. The gas flow rates are regulated by a rotameter located downstream of the Horiba analyzer. A large weather proof electrical cabinet was purchased and modified to fit two sampling pumps. A temperature controlled fan was added to help dissipate the build of heat inside the cabinet and to prevent the sampling pump from overheating or melting the diaphragm.

A new CO_2 makeup heater was constructed and installed. The previous heater was not sized for loading large amounts of CO_2 into the solution. As a result of being undersized, the heater began to leak due to the continuous stress resulting from differential thermal expansion. At high flow rates, the CO_2 was not adequately heated and the exchanger and makeup lines would freeze. The new double-pipe heat exchanger

was constructed out of 2.5 cm steel black pipe and 1.3 cm OD stainless steel tubing. The heater consisted of two 10 foot sections and was operated in parallel. Steam flow was on the shell side and the liquid CO_2 was on the tube side. In the new design, steam flow was directed in parallel to the heat exchangers and to the CO_2 regulator, whereas before, the steam flowed in series with the heat exchanger and regulator.

In the third campaign, the Gasmet DX-4000 FTIR from Temet Instruments was used for the analysis the absorber outlet gas stream. The FTIR has an accuracy of less than 2% of the measuring. The FTIR measured the concentration of CO_2 and water, MEA volatility, and ammonia accumulation for the MEA campaign. The FTIR was not connected to the DeltaV system because the Modbus hardware had not been purchased. Instead, the Calmet software that came with the FTIR was used to record the data. The results for the MEA campaign can be found in Dugas (2006).

1.5.2 Campaign 3 Summary

In Campaign 3, several issues from Campaign 1 were resolved, which include: (1) The control valve was moved just upstream of the inlet nozzle. (2) Two pumps were used in series to pressurize the stripper feed. (3) The liquid sampling and handling procedure developed in Campaign 2 were successfully implemented. (4) The results for CO_2 loading were corrected with standards placed periodically in between samples during the analysis. (5) Diluted liquid samples and standards were covered with parafilm to minimize CO_2 absorption

In Campaign 2, there were several issues that needed to be resolved. These issues include: (1) The stripper feed pre-heater was undersized. (2) The stripper feed was

flashing across the control valve at the top of the stripper, which resulted in poor mass transfer performance. (3) The absorber inlet and outlet conductivity meters were unreliable and both eventually failed. (4) The reboiler developed pin-hole sized leaks. (5) The absorber gas flow measurement did not zero properly.

1.6 CAMPAIGN FOUR – OPTIMIZED K^+/PZ PROCESS CONFIGURATION

The main objective of the last campaign was to obtain absorber and stripper data for the aqueous piperazine and potassium carbonate system with an optimized configuration. Based upon the learning experience from the three preceding campaigns, the optimized configuration included modifications such as a new plate and frame cross-exchanger, new high capacity FLEXIPAC® AQ Style 20 structured packing for the absorber and stripper, and a new heater for the absorber inlet gas. Data for the 5m K^+/2.5m PZ solvent was generated with the new packing and was compared to the FLEXIPAC® 1Y packing used in the previous campaigns.

The second objective was to test another K^+/PZ solvent composition. The first half of Campaign 3 was conducted with the original 5m K^+/2.5m PZ solvent while in the latter half 6.4m K^+/1.6m PZ solvent was used. The second solvent composition has a heat of absorption that is about 50% lower and a capacity that is approximately 0–10% higher than that of the 5mK^+/2.5mPZ. However, the CO_2 absorption rate is about 40% less than the 5mK^+/2.5mPZ solvent. Therefore, experiments with the second solvent composition should help establish the tradeoffs between fast CO_2 absorption rates, low heat of absorption and higher capacity solvents.

1.6.1 Bench-scale Experiments and Results

1.6.1.1 Potassium Carbonate and Piperazine Solubility

In order to determine the absolute concentrations of the second solvent, solubility experiments were conducted with 4 different compositions: 6m K^+/1.5m PZ, 6.4m K^+/1.6m PZ, 6.8m K^+/1.7m PZ, 7.2m K^+/1.8m PZ. The ratio of potassium to piperazine was maintained at 4. Experiments were conducted at 40, 50, and 60 °C and 4 different CO_2 loadings for each solution. Higher piperazine and potassium concentrations result in faster absorption rates and larger solution capacities, respectively. However, as the total concentration increases, the risk of salting out the potassium bicarbonate or precipitating piperazine also increases. The results are shown in Table 1-12.

At low CO_2 loadings, piperazine tended to form a separate layer from the potassium carbonate/bicarbonate solution. At rich CO_2 loadings, the potassium bicarbonate tended to salt out, precipitating as fine white crystals. The table shows that at 40 °C, only the 6.4m K^+/1.6m PZ solvent composition does not phase separate or form precipitates over the loading range that the pilot plant will be operated. Therefore, this particular solvent composition was selected for the fourth campaign.

Table 1-12. Potassium Carbonate/Piperazine Solubility Experiments

Composition	Temp (°C)	Loading (mol CO_2/K+2PZ)	Observation
6mK^+/1.5mPZ	40	0.33	2 Liquid Layer
		0.44	Fully Dissolved
		0.56	Fully Dissolved
		0.67	$KHCO_3$ Precipitate
6.4mK^+/1.6mPZ	40	0.40	Fully Dissolved
		0.47	Fully Dissolved
		0.53	Fully Dissolved
		0.60	Fully Dissolved
6.8mK^+/1.7mPZ	40	0.40	Fully Dissolved
		0.47	White Precipitate
		0.53	White Precipitate
		0.60	White Precipitate
6.8mK^+/1.7mPZ	50	0.40	Fully Dissolved
		0.47	White Precipitate
		0.53	White Precipitate
		0.60	White Precipitate
6.8mK^+/1.7mPZ	60	0.40	Fully Dissolved
		0.47	White Precipitate
		0.53	White Precipitate
		0.60	Fully Dissolved
7.2mK^+/1.8mPZ	40	0.33	2 Layers, Solid Top Layer
		0.42	White Precipitate
		0.50	White Precipitate
		0.58	White Precipitate

1.6.1.2 Density and pH Measurements

Previous density measurements of the piperazine promoted potassium carbonate solvent were limited to a temperature of 40 °C. It was desired to measure the density of the solvent over a temperature ranging from 40 to 60 °C. Hydrometers from Fisher Science were procured. A cylindrical water tank was constructed out of Plexiglas. A water bath was used to heat the water and circulate the warm water through the water tank. To make a density measurement, approximately 300 mL of solvent was poured into a graduated cylinder. The hydrometer was placed in the graduated cylinder, which was

then immersed in the heated water tank. A K-type thermocouple measure the temperature of the solvent and a magnetic stir bar was used to mix the solvent and maintain a uniform temperature throughout the cylinder. The stir bar was turned off when density measurements were recorded.

Density measurements were taken for the 5m K^+/ 2.5m PZ solvent and for the 6.4m K^+/ 1.6m PZ solvent at two different loadings. In addition, a density measurement was taken for the pilot plant solution. The results from the density measurements show that density decreases linearly with an increase in temperature (Figure 1-19). The figure also shows that density is not very sensitive CO_2 loading and piperazine concentration, which corroborates the density measurements made by Cullinane on a densitometer instrument.

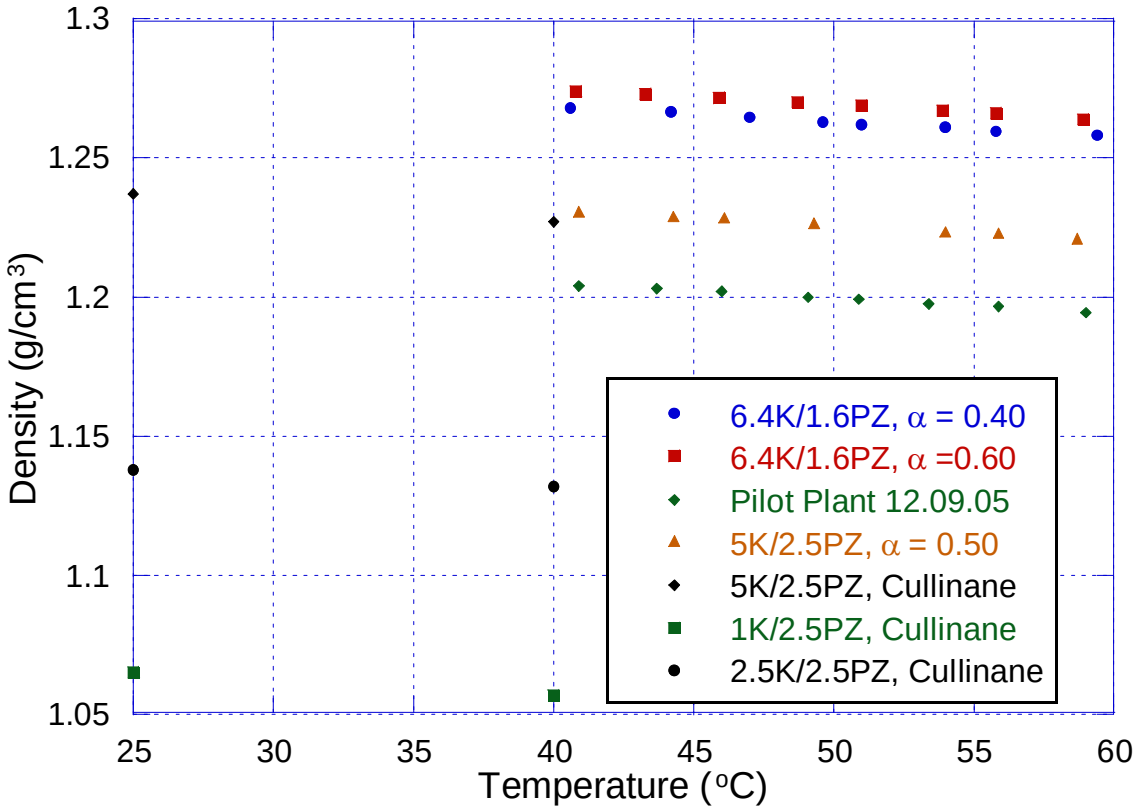

Figure 1-19. Bench-scale Measurements of Density for 5mK$^+$/2.5mPZ and 6.4mK+/1.6mPZ as a Function of Temperature

Bench-scale measurements of pH were made for the 6.4m K^+/ 1.6m PZ solvent at four different CO_2 loadings and over a temperature range from 40 to 60 °C. The pH measurements will be used in the pilot plant operations for controlling lean loading to the absorber. Measurements were made with a Cole Parmer pH meter. Figure 1-20 shows bench-scale measurements of pH dependence on CO_2 loading at different temperatures. The trends indicate that there is inconsistent variation of pH with temperature. However, pH does vary with CO_2 loading. The general slope of the bench-scale measurements can be used to determine online CO_2 loading values of the pilot plant once a pH and corresponding CO_2 loading value is established.

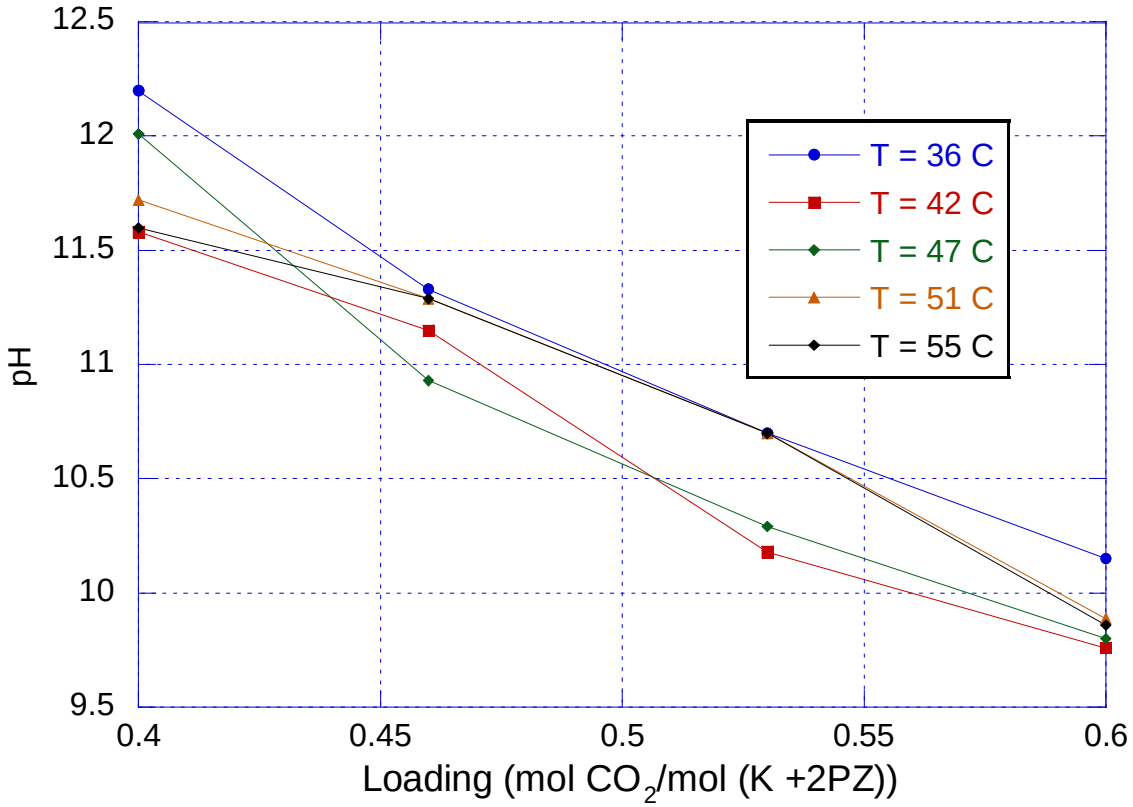

Figure 1-20. Bench-scale Measurements of pH for 6.4mK$^+$/1.6mPZ at 36 – 55 °C.

1.6.2 Campaign 4 Modifications

During the third campaign, even with the new modifications, the stripper feed stream was still pre-heated inadequately. In Campaign 4, a new plate and frame cross-exchanger was purchased from Alfa Laval. The Alfa Laval M6-FG exchanger was sized for a 10 °C approach and a pressure drop of 1.0 bar. The exchanger has a heat transfer area of 14.8 m^2, consists of 99 plates and is arranged for 5 pass flow. It is constructed of type 316 stainless steel and contains EPDM gaskets. The cost of the plate exchanger was approximately $5000.

Figure 1-21 illustrates the new absorber/stripper configuration of Campaign 4. The cross-exchanger takes the hot lean stream from the reboiler and uses it to preheat the cold rich stream from the outlet of the absorber. The existing feed preheater was used as a trim heater and was installed downstream of the cross-exchanger to simplify the amount of flow instrumentation and reduce costs. The process and instrumentation diagram for the absorber and stripper is shown Figures 1-22 and 1-23, respectively.

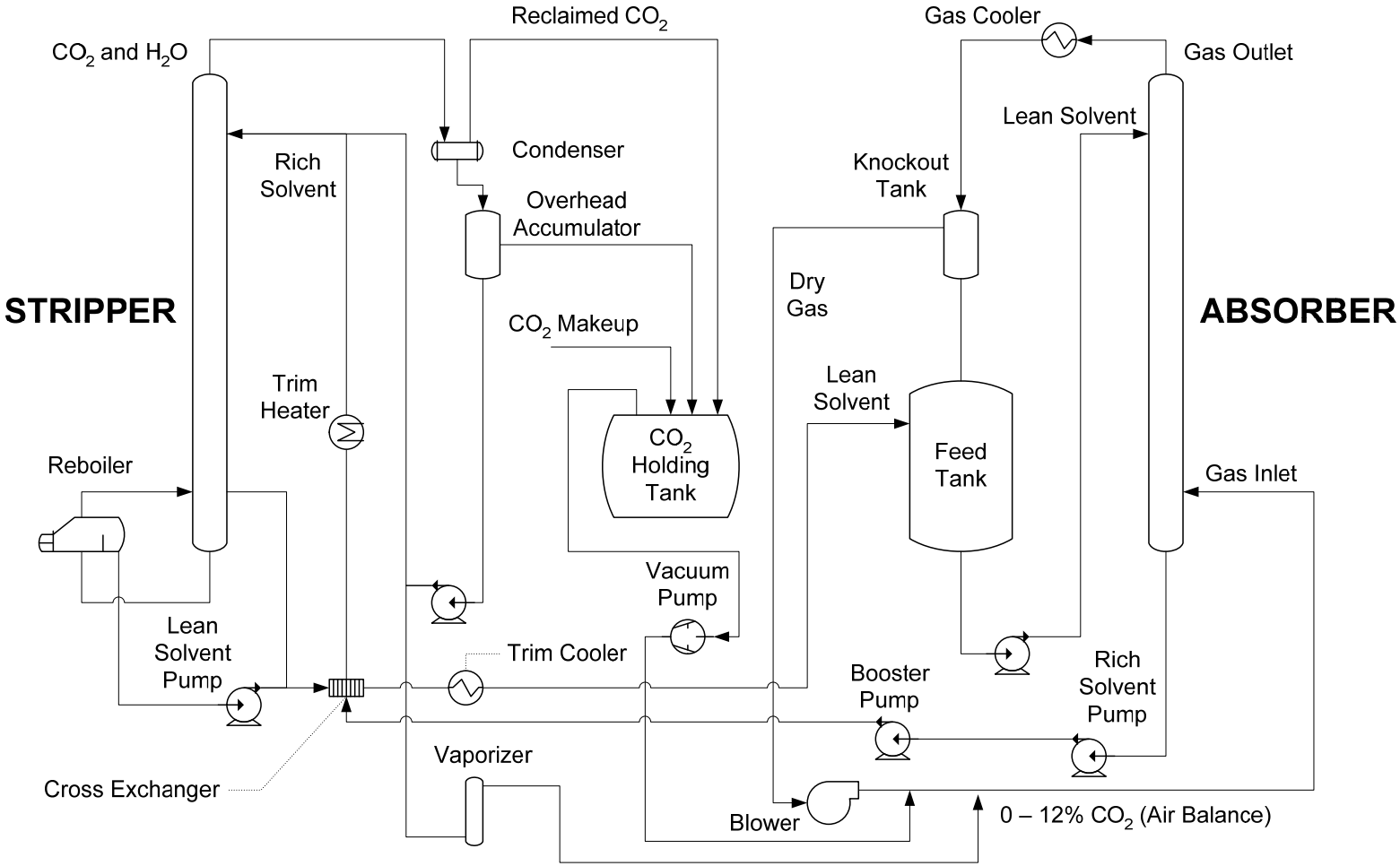

Figure 1-21. Absorber/Stripper Pilot Plant Configuration for Campaign 4

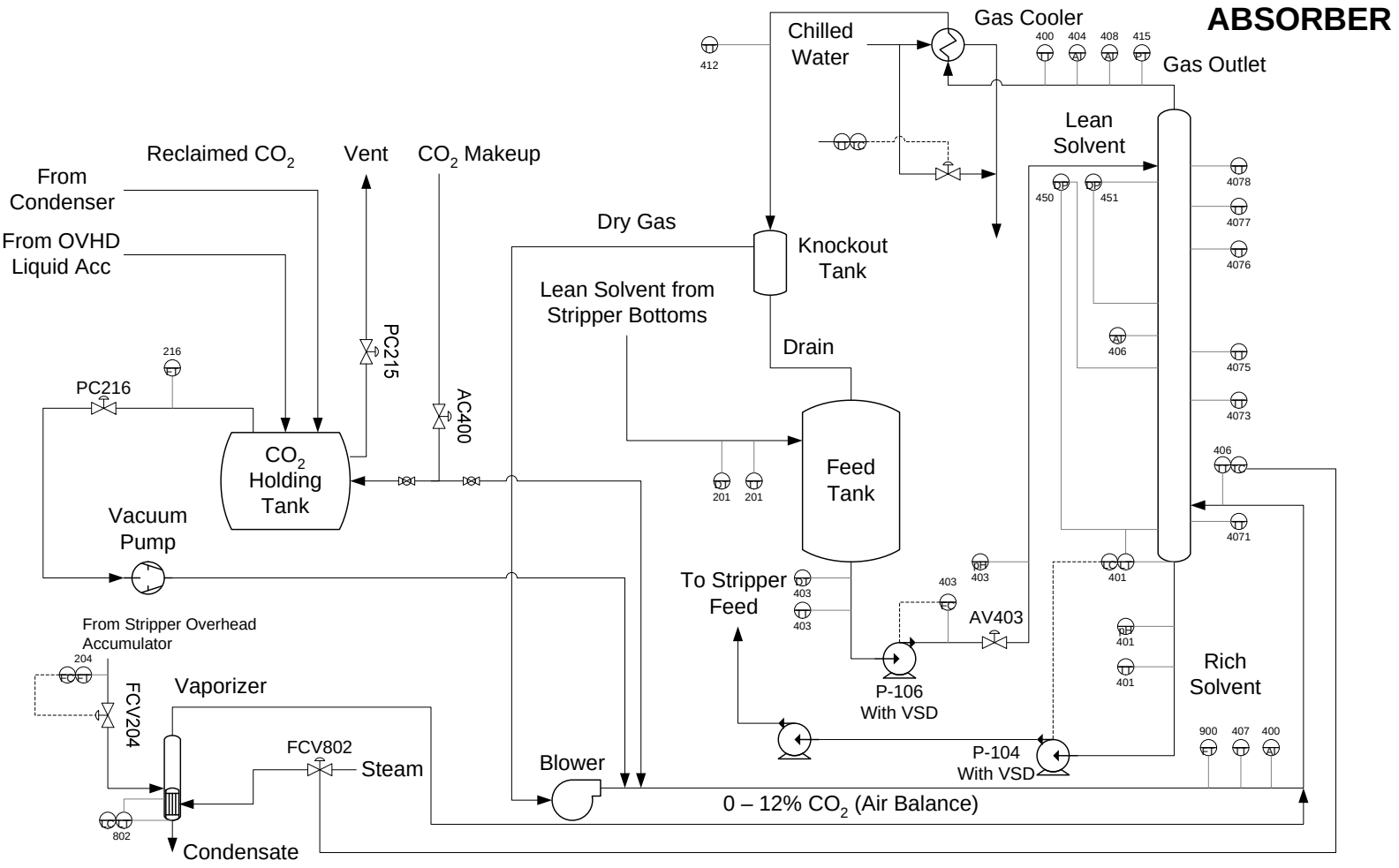

Figure 1-22. Process and Instrumentation Diagram of Absorber for Campaign 4

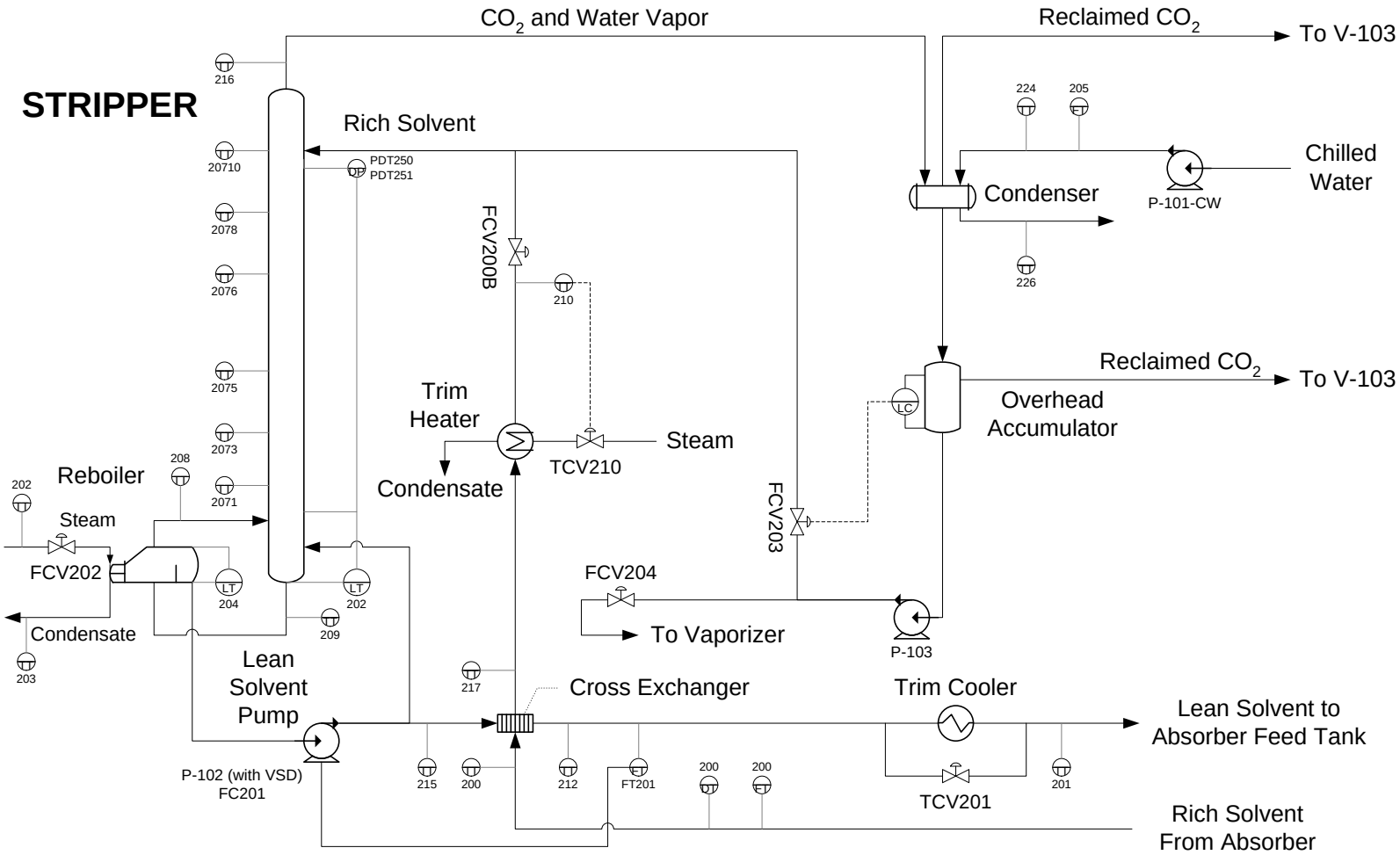

Figure 1-23. Process and Instrumentation Diagram of Stripper for Campaign 4

In the MEA campaign, the air cooler was operated to protect the Vaisala CO_2 probe and the blower recycle was used to preheat the gas. However, the absorber inlet gas was still not adequately preheated and not saturated with water, which was not representative of true plant operating conditions. To remedy this problem, an existing 10.2 cm reboiler was retrofitted and used to generate steam and heat the inlet gas. Distillate from the stripper condensate supplied the water for the reboiler. The level in the preheat reboiler was maintained by adjusting the steam flow to the 10.2 cm reboiler. Approximately 0.6 gpm of water was needed to saturate the inlet absorber gas to 20% water at a gas flow rate of 500 cfm. A 2.5 cm pipe was installed from the reboiler to the inlet gas line. The steam generated from the reboiler was injected into the inlet absorber gas downstream of the Vaisala CO_2 analyzers.

In the third campaign, the PVC pipe for the blower recycle was melted and partially destroyed due to the excessive that built up during the loading of the MEA solution. The pipe for the blower recycle was replaced with stainless steel pipe. In the fourth campaign, the remaining 20.3 cm PVC gas lines were replaced with 20.3 cm 304 L stainless steel pipe. In addition, the 7.6 and 10.3 cm schedule 40 PVC pipe for the gas flow rate was replaced with a single 10.3 cm schedule 10 stainless steel pipes. The blower recycle was not operated during Campaign 4.

In the fourth campaign, the Dietrich Standard Diamond II GCR-15 Annubar used in the 10.3 cm line from Campaign 3 was used to measure gas flow rate. The annubar was originally sized for schedule 40, but was used in the new 10.3 cm schedule 10. Corrections to the inner diameter were made in DeltaV. In addition, three Rosemount

differential pressure transmitters with different pressure ranges and a Rosemount RTD for temperature measurement were used. The flowmeter has an accuracy of ±1% of the actual value. Flow straighteners were installed upstream of the annubar to ensure the flow measurement was accurate. The flow meter was calibrated for air. In the interpretation of the data, density corrections were made to account for CO_2 and water.

The existing carbon steel reboiler for the stripper developed pinhole-sized leaks during the MEA campaign. Prior to the start of the fourth campaign, a new stainless steel kettle reboiler was installed and insulated. The new reboiler has the same design and specification of the carbon steel reboiler.

Figure 1-24. Stainless Reboiler and Stripper Column Sump with Calcium Silicate Insulation

An orifice plate was installed on the cooling water of the air cooler instead of a control valve to simplify plant operation. The cooling water knocked out most of the moisture from the absorber outlet gas stream to protect the downstream Vaisala CO_2 probe. The condensate from the air cooler and the knockout filter drained to the absorber feed tank as before.

To provide the capability of measuring multiple gas components, the Gasmet DX-4000 FTIR from the MEA campaign was retrofitted into the pilot plant. Two 30.5 m heated lines were procured from Environmental Supply Company, one for the absorber inlet and one for the outlet. The heated lines consist of 0.6 and 1.0 cm OD PFA lines. An additional sample pump and heater module for the FTIR was purchased from Air Quality Analytical, Inc. Gas samples were simultaneously drawn from the absorber inlet and outlet. The temperature of the heated line was maintained at approximately 180 °C. The gas analysis was alternated between the two sample-points via a three way valve located inside a heated box. A MODBUS card was used to connect the FTIR computer to the DeltaV process control system. The FTIR was used measure CO_2 and water concentration and piperazine volatility. In addition, two new Vaisala CO_2 probes with concentration ranges of 0 – 5% and 0 – 20% were purchased and used to replace the two existing Vaisala probes.

In an attempt to address the recurring foaming issues encountered during the first two campaigns, an activated carbon filter system was designed and installed. Two types of filters from Rosedale Products, Inc. were purchased: a 4-12 filter housing with a single pass carbon holding basket (Part No. 4-12-SP-304) and a 4-12 bag filter housing with

EPR gaskets. Both filters were made of type 304 stainless steel. The filter system was based on literature recommendations and was designed to filter 10–15% of the total lean solvent stream. The design would allow for the removal of enough degradation products without removing the anti-foam. The filter that contained activated carbon was installed downstream of the absorber lean Micro Motion® flowmeter. The second bag filter was installed downstream of the carbon filter to capture any fine charcoal particles.

Two types of activated carbon were available. Activated carbon from the filter manufacturer contained 10 x 50-mesh size activated carbon and was made of virgin coconut hulls. In addition, a lignite-based 8 x 30-mesh PETRODARCO activated carbon from NORIT was purchased. Four different filter bag materials (Nomex®, cotton, viscous rayon, and nylon) were tested because of material compatibility issues arising from the use of polyethylene in the previous campaigns. The filter materials were tested in warm solvent solutions and it was found that cotton performed the best based on visual inspections.

1.6.3 Campaign 4 Analytical Methods

1.6.3.1 CO_2 Analysis Analysis

The fourth campaign used the same liquid sample collection and preservation method developed in Campaign 2, which used sample bombs. However, the sample bombs were slightly modified through the use of clear PFA tubing instead of the stainless tubing originally used. This allowed the sample collector to visually verify whether the sample collection was successful. During the fourth campaign, the middle liquid samples

for the absorber and stripper both seem to be problematic at times. It was possible that the sample lines may have become partially blocked, which resulted in very low flows.

The liquid sample extraction procedure follow the standard methods developed over the course the last 3 campaigns. Ten milliliters of sample are withdrawn from the sample bombs with a syringe and injected into a vial containing 30 mL of chilled deionized water. For CO_2 loading analysis, the samples were further diluted by a factor of 40 and then analyzed on the Shimadzu 5050 Total Organic Carbon analyzer by utilizing its inorganic carbon analysis feature. 100ppm sodium carbonate/bicarbonate standards were placed every 6–7 samples to maintain quality control.

1.6.3.2 Piperazine and Potassium Analysis

1.6.3.2.1 Ion Chromatography Method Development and Analysis

A new IC column was purchased and installed in the ion chromatography analyzer. The new column was better suited for piperazine and amine analysis. A new method was developed for measuring piperazine and potassium on the IC. The method takes approximately 5 minutes and uses 6 mM and 55 mM monosulphonic acid (MSA) for the eluent. The standards contained both piperazine and potassium and a calibration curve was generated over the following range of concentrations: 0, 10, 20, 30, 40, and 50 ppm K^+/Pz. The ion chromatography samples for the fourth campaign were further diluted by a factor of 2000 from the pre-diluted 4:1 samples. The ion chromatography analyzer was calibrated with standards that contained both piperazine and potassium. Additional details regarding the new IC method for measuring K^+ and PZ can be found in the appendix.

Prior to the start of Campaign 4, selected K^+/PZ samples from the first and second campaign were analyzed with new IC method. The concentrated pilot plant solutions from Campaign 1 were diluted by a factor of 4000 and the prediluted pilot plant samples from campaign 2 were diluted by a factor of 1000. Tables 1-13 through 1-15 show the results of the sample analysis for the first two campaigns using the newly developed IC method. The results show that total alkalinity was not as well correlated to density measurements as previously assumed, which was based on Campaign 1 data. The total alkalinity results on the IC from Campaign 1 and Campaign 2 seem to show good agreement with the total alkalinity values obtained using the acid titration method used in those campaigns. The tables seem to show that there was some loss of potassium in between the transition from campaign 2 to the current campaign. The pilot plant samples were taken from the bottom of a large storage tank and therefore, may not have been a representative sample.

Table 1-13. Campaign 1 IC Results

Campaign 1 Data	K^+ gmol/kg	PZ gmol/kg	Talk gmol/kg	K^+/PZ	Density kg/m^3
C1 6/16 AL 17:00	2.3293	1.5802	5.4896	1.4741	1146.6
C1 6/17 AL 13:00	2.5907	1.4356	5.4619	1.8046	1162.4
C1 6/22 AL 17:45	3.2496	1.634	6.5177	1.9887	1206.1
C1 6/22 AL 19:30	3.2348	1.6258	6.4864	1.9897	1206.4
C1 6/23 AL 08:15	3.2509	1.6377	6.5263	1.9851	1212.6
C1 6/23 AL 18:10	3.3146	1.6624	6.6393	1.9939	1211.9
C1 6/24 AL 17:30	3.3365	1.5987	6.5339	2.0870	1228.1

1. Results are in mol/kg of solvent
2. TAlk = Total Alkalinity (mol CO_2/mol K+2PZ)

Table 1-14. Campaign 2 IC Results

Campaign 2 Data	K^+ gmol/kg	PZ gmol/kg	TAlk gmol/kg	K^+/PZ	Density kg/m^3
C2 AL8	2.8981	1.2421	5.3823	2.3332	1224.3
C2 AL11	3.0807	1.3216	5.724	2.331	1228.2
C2 AL13	2.908	1.2493	5.4066	2.3278	1227.0
C2 AL14	2.7736	1.205	5.1836	2.3018	1226.2
C2 AL16	3.085	1.327	5.739	2.3248	1228.4
C2 AL22	2.9487	1.2591	5.4669	2.3418	1230.4
C2 AL37	3.2303	1.3927	6.0158	2.3194	1224.4
C2 AL38	3.027	1.3038	5.6346	2.3218	1219.5
C2 AL43	2.9179	1.2404	5.3987	2.3523	1229.1
C2 AL 26	2.8967	1.2393	5.3753	2.3373	1228.5

1. Results are in mol/kg of solvent
2. TAlk = Total Alkalinity (mol CO_2/mol K+2PZ)

Table 1-15. IC Results of Pilot Plant Composition Prior to Campaign 4 Start-up on 12/09/05

K^+	PZ	Talk	K/PZ	Density
gmol/kg	gmol/kg	gmol/kg		kg/m3
3.0208	1.5888	6.1983	1.9013	1204

1. Results are in mol/kg of solvent
2. TAlk = Total Alkalinity (mol CO_2/mol K+2PZ)

The results from Campaign 2 of the titration and ion chromatograph are compared in Figure 1-25. The average difference between the ion chromatography and titration method for potassium, piperazine, and total alkalinity (K+2PZ) was 2.8%, -5.2% and -0.89%, respectively. It can be concluded that the measurement of total alkalinity can be reliably determined by both methods. However, the piperazine concentration was consistently higher for the titration method and since the potassium concentration was calculated as a difference between total alkalinity, it was consequently lower. This discrepancy is most likely due to errors with the perceived endpoint (-265 mV) in the titration method (-265 mV). Instead the determination of piperazine concentration should

have taken the difference between the two inflection points of NaOH titration. This technique is further detailed in the revised titration method section.

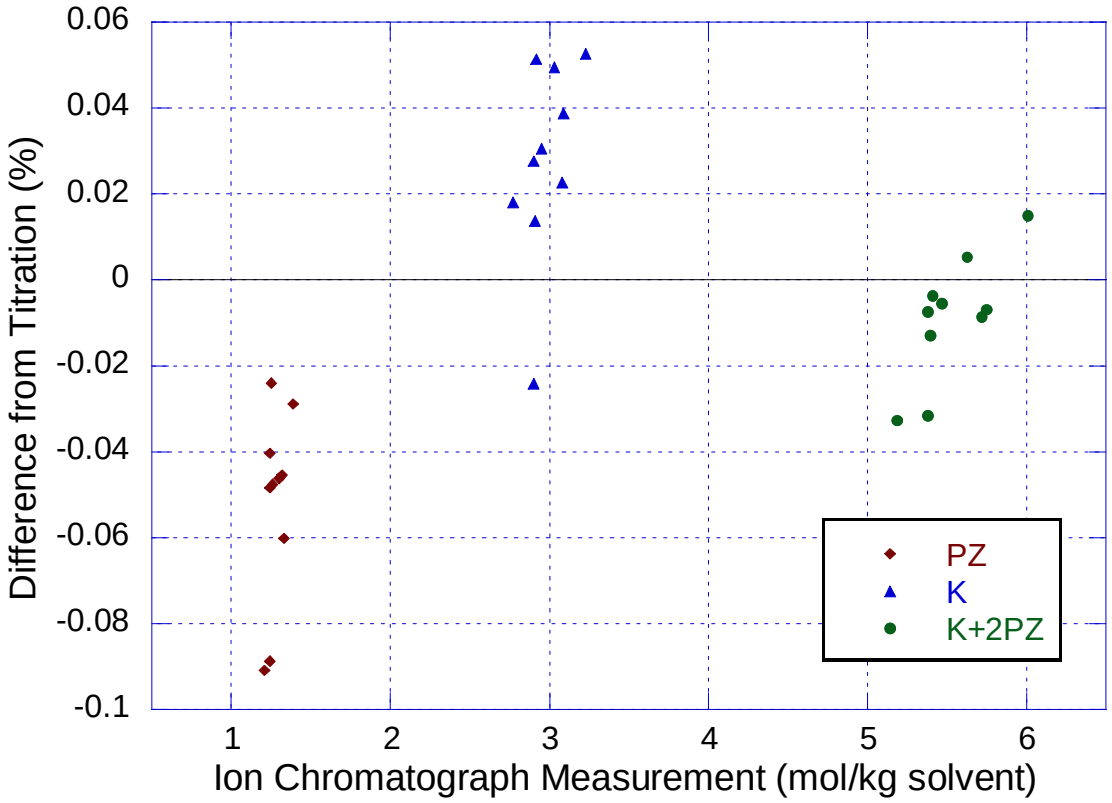

Figure 1-25. Comparison of Titration and Ion Chromatography Measurements of K^+ and PZ Concentration for Campaign 2

1.6.3.2.2 Revised Titration Method

In Campaign 4, the titration method that was used in Campaigns 1 and 2 was refined. However, it was only used during the campaign to perform a real-time check of the solution composition and was not used as the primary analysis of piperazine and potassium concentration. In the new titration method, due to the 3:1 dilution of liquid samples, the concentrations of both HCl and NaOH were changed to 0.2 N instead on 2 N. Also, the pH of the liquid sample was measured and recorded during the forward and

back titrations instead of relying on methyl orange as the color indicator and titration to 265 mV to obtain piperazine concentration. The inflection point of the forward acid titration curve measures the total alkalinity of the solution (Figure 1-26).

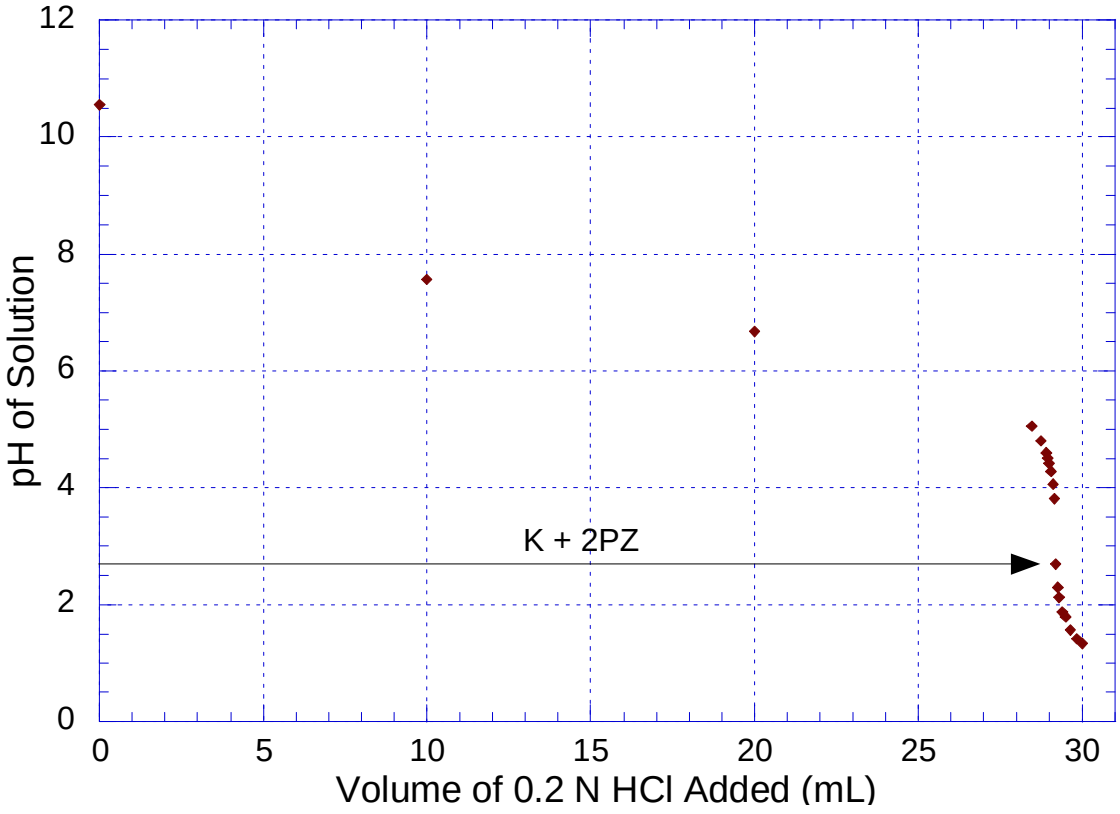

Figure 1-26. Forward Titration of 5mK$^+$/2.5mPZ solution with 0.2 N HCl to Determine the Total Alkalinity (mol K + 2 mol PZ)

The difference between the two inflection points for the back titration with 0.2 N NaOH gives the concentration of piperazine (Figure 1-27). The potassium concentration is determined by taking the difference between total alkalinity and two times the piperazine concentration. Two sets of titrations were performed on a known solution of 5mK$^+$/2.5mPZ solution to verify reproducibility (Table 1-16). Titrations were performed with 2 N HCl and 2 N NaOH with approximately of 10 grams of undiluted solution. The

results indicate that using the two endpoints for the back titration method yielded results that were 1.5% higher than that calculated. However, the difference in measurement of total alkalinity was less than 1% in one case and approximately 9% in the other. In the 9% error case, the burette containing acid needed to be refilled during the titration process. It is possible that during the refilling process, CO_2 may have been absorbed by the sample and required excess HCl.

Table 1-16. Validation of Reproducibility of Modified Titration Method Using Acid-Base Endpoints Determined from Direct pH Measurements

Sample ID	K+2PZ Expected	K+2PZ Measured	Diff %	PZ Expected	PZ Measured	Diff %
1	5.83	6.35	8.9	1.46	1.44	1.3
2	5.83	5.83	0.05	1.46	1.44	1.2

The original method for determining piperazine by back titrating to a reading of ~265 mV was not accurate because significant errors were introduced if the forward acid titration was overshot. Additional NaOH would need to be added to neutralize the excess acid and would result in an erroneous higher piperazine concentration and lower potassium concentration.

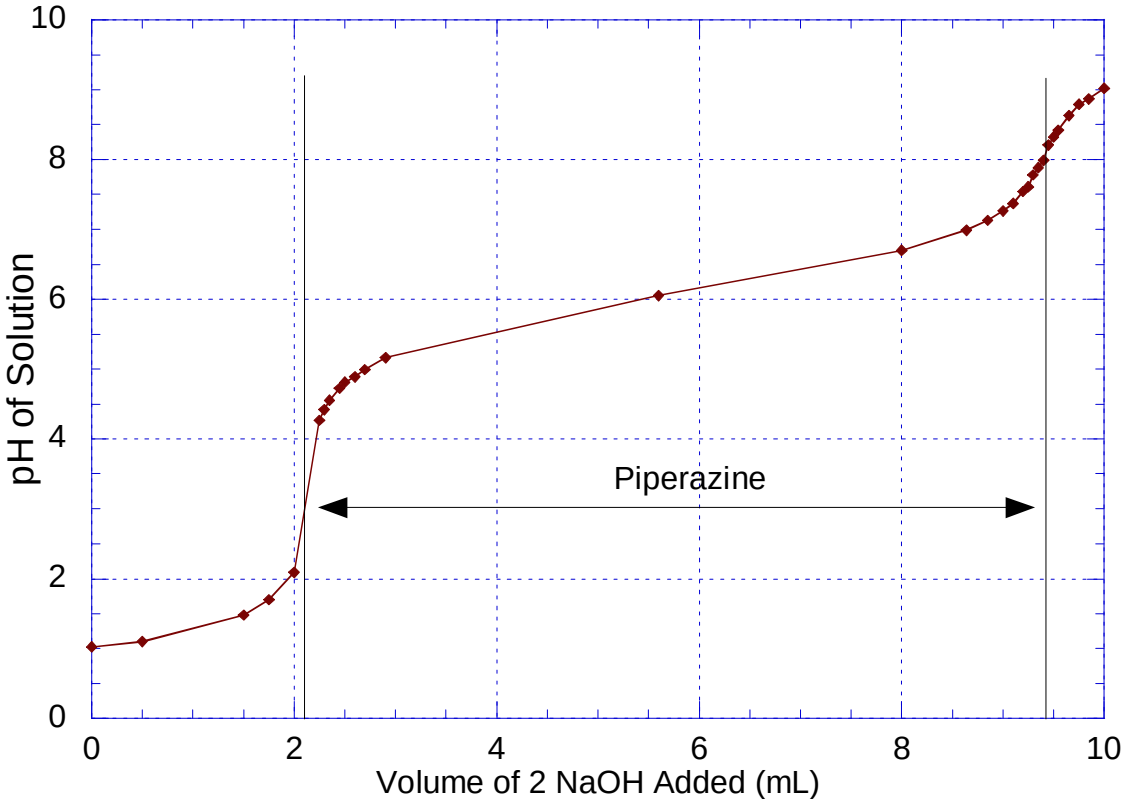

Figure 1-27. Back Titration of 5mK$^+$/2.5mPZ solution with 0.2 N NaOH to Determine the Piperazine Concentration

In addition, titration measurements were performed on absorber lean and absorber rich pilot plant solutions to verify that the endpoints from direct pH measurements and methyl orange technique matched. The results show that if both methods are performed properly, a difference of approximately 1% could be achieved (Table 1-17). Approximately 49 grams of water was added to 0.55 grams of sample prior to the start of each titration. The pH of the solution was recorded while the 0.2N HCl acid was added continuously. The titration curve for the absorber lean sample is shown in Figure 1-28.

Table 1-17. Validation of Methyl Orange Indicator with pH Measurement Based Titration Method Using 0.2 N HCl and Pilot Plant Samples Diluted 90:1

Sample ID	Date/Time	Total Alkalinity Methyl Orange	Total Alkalinity pH	Difference %
AL	01/09/06 13:30	5.51	5.55	-0.6
AR	01/09/06 13:30	5.37	5.42	-1.0

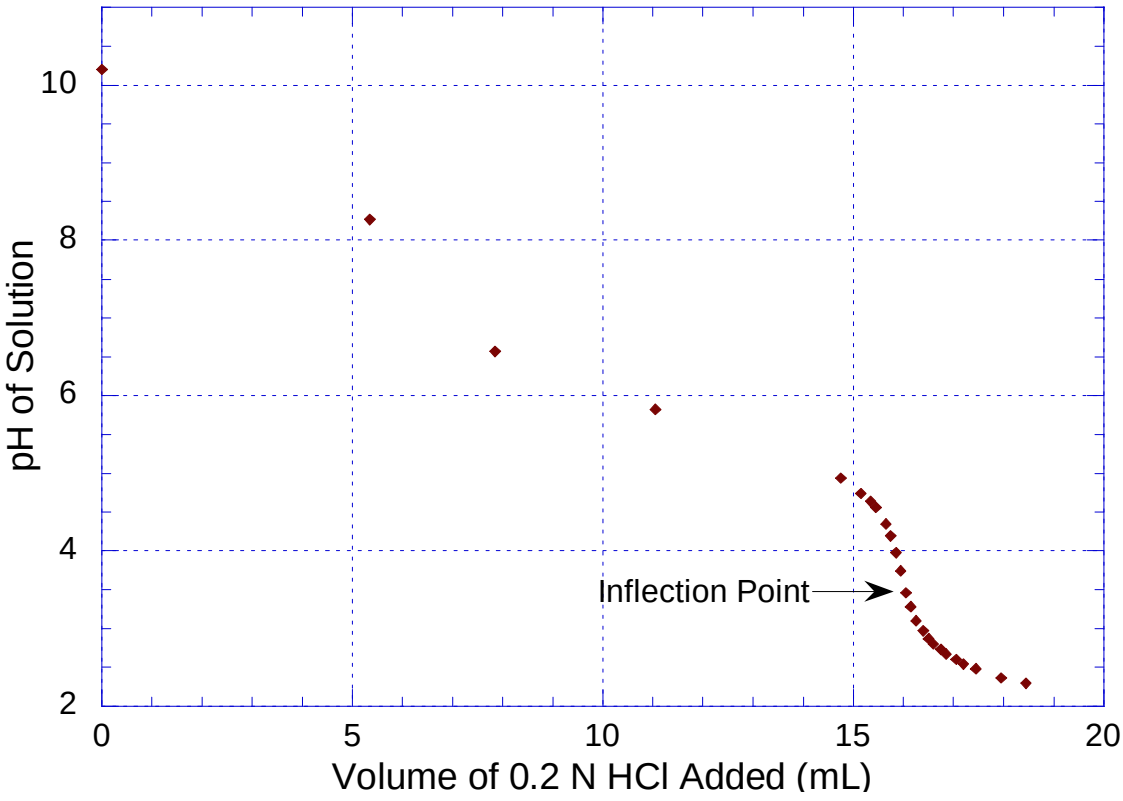

Figure 1-28. Titration of Absorber Lean Pilot Plant Sample (Taken 1/09/06 -13:30) with 0.2 N HCl to Determine Total Alkalinity (mol K+2 mol PZ)

In Campaign 4, the ion chromatograph was used as the primary analysis of piperazine and potassium concentration. A few titrations were performed to during the operation of the pilot plant for on-site verification of total alkalinity. The titration measurements were consistently lower than the results obtained by the post-campaign IC analysis (Table 1-18).

Table 1-18. Concentration of Piperazine and Potassium from Campaign 4 for the Titration and Ion Chromatograph Methods

Sample ID	Titration gmol/kg soln	Ion Chrom gmol/kg soln	Diff %
AL 97	5.55	6.12	10.4
AL 100	5.73	6.11	6.6
AL 103	5.66	6.00	6.2

While the IC and titration total alkalinity results of Campaign 2 matched relatively well, the titration and IC methods were slightly changed. The new titration method used a more dilute acid, which should actually make the method more accurate. Also, the Campaign 4 titrations were conducted using the pH end-point method, whereas the Campaign 2 method was titrated to the methyl orange endpoint, where a color change occurred.

However, this section has shown that results from the two endpoint methods have a difference of less than 2%. Also, in Campaign 4, the IC method was slightly modified from that used for the Campaign 2 sample analysis. The original IC method had a retention time of approximately 30–40 minutes. Due to the high volume of samples that were collected and to achieve a higher throughput, the method was modified to have a retention time of approximately 5–10 minutes. This may have slightly degraded the performance of the ion chromatograph analyzer. The performance of the column may also have degraded due to the build up of residual analytes. Also, for certain sets of analysis, the absorber lean sample analysis seemed to have substantial deviation from the absorber middle and absorber rich samples. Other concerns include degradation products of piperazine that may further complicate the interpretation of the IC results.

Overall, the IC method appeared to have an accuracy of approximately 10%. Therefore, it is concluded while the IC method may be more efficient at analyzing a large number of samples, the titration method maybe more accurate for piperazine and potassium determination.

1.6.3.3 Revised CO_2 Gas Concentration Analysis

Initially, there was some confusion regarding whether the gas cylinders were in mole or weight percent. The certificate of analysis for the CO_2 standards states that the cylinders are filled with CO_2 and air gravimetrically and the final concentration is verified via analysis by a gas chromatograph/thermal conductivity detector (TCD). In the earlier campaigns, it was assumed that the standards were in weight percent, which was why the 16.9% gas cylinder was ordered. Two of CO_2 cylinders were analyzed by another research group using gas chromatography. The GC analyzer was calibrated to measure mixtures of CO2, CH_4, and C4 and thus, slight discrepancies were expected. Analysis of the 12% and 16.9% CO_2 cylinders by the GC method resulted in CO_2 concentrations of 13.2 mol% and 18.3 mol%, respectively. Since, the analysis was closer to the mole percent values, it was concluded that the CO_2 standards were in mole percent and not weight percent.

1.6.4 Campaign 4 Plant Operation

The final pilot plant campaign using potassium carbonate and piperazine commenced at the beginning of January 2006 and was completed in early February. The pilot plant was operated for 12 days, 24 hours per day. A total of 59 runs and 33 operating condition were completed. Approximately 300 liquid samples were taken and

analyzed for CO_2 loading, piperazine and potassium concentration. The newly installed cross-exchanger reduced the approach temperature to less than 10°C.

The experiments were conducted with two different solvent compositions: 5m K^+/2.5m PZ and 6.4m K^+/1.6m PZ. The absorber and stripper were both packed with a new structured packing, FLEXIPAC® AQ Style 20, donated by Koch-Glitsch Inc. The new structured packing has a specific surface area of 213 m^2/m^3, which is approximately 50% less than the FLEXIPAC® 1Y packing used in the previous campaigns. FLEXIPAC® AQ Style 20 packing has a steeper corrugation angle (~50 degrees), whereas the Flexipac 1Y packing has a corrugation angle of 45 degrees. As a result, the new packing has less surface area, a lower liquid holdup, and will be less efficient. However, the packing will have a higher capacity and allow operation at higher gas rates with reduced pressure drop.

The absorber and stripper column each contained 6.1 m of FLEXIPAC® AQ structured packing, which was divided into two 3.05 m beds. In between the top and bottom bed of packing there was a chimney tray and an orifice riser redistributor. In the stripper, a Montz II distributor was used in the upper bed and a Koch collector plate with an inverted screen and a 4C redistributor was used for the bottom bed. The absorber contained a Koch 3C distributor at the top and a chimney tray and Montz II redistributor for the bottom bed.

In this campaign, the air cooler was in full operation and was used to protect the Vaisala CO_2 analyzers that were downstream. The newly installed cross-exchanger performed as designed and the trim heater and cooler were not used during the campaign.

A summary of the absorber and stripper operations is shown in Tables 1-19 and 1-20, respectively.

Table 1-19. Campaign 4 Absorber Operation

Parameter	5m K^+/2.5m PZ	6.4m K^+/1.6m PZ
Inlet CO_2 (mol %)	8.0 – 17.6	14.3 – 18.0
PZ Concentration[1] (mol/kg)	1.4 – 1.5	1.0 – 1.2
K^+/PZ Ratio	2.1 – 2.3	3.9 – 4.0
Lean Loading[2] (mol CO_2/TAlk)	0.39 – 0.45	0.45 – 0.51
G (kg/m^2-s)	1.2 – 2.0	1.2 – 2.0
L/G (kg/kg)	3.9 – 10.8	8.3 – 14.5
$T_{GAS,IN}$ (°C)	40	40 – 41
T_{LEAN} (°C)	40 – 46	39 – 46

1. Concentration in mol/kg of solvent
2. TAlk = Total alkalinity (mol K+2 mol PZ)

Table 1-20. Campaign 4 Stripper Operation

Parameter	5m K^+/2.5m PZ	6.4m K^+/1.6m PZ
□T Approach (°C)	6.9 – 8.9	3.7 – 6.4
Top Temperature (°C)	103 – 115	71.5 – 94
Bottom Temperature (°C)	117 – 118	77 – 97
Reboiler Heat Duty (kcal/mol CO_2)	85 – 290	90 – 180
NTU per pass (5 pass PFE)	1.5 – 2.1	1.5 – 1.9
$C_{P,COLD}/C_{P,HOT}$	1.04 – 1.08	1.05 – 1.11

In campaign 4, foaming was also observed. However, this time foaming was observed in the stripper instead of the absorber as in the first 2 campaigns. The magnitude of the temperature bulge was not as significant in the absorber for the 6.4m K^+/1.6m PZ solvent due to the slower absorption rate. The installation of the cross-exchanger resulted in a higher temperature profile across the stripper. It is possible that the foaming may have had some sort of temperature dependence. Approximately 750 mL of DOW Corning DSP and DOW Corning Q2-3183A anti-foam was added throughout the duration of the campaign. Both antifoams are silicon-based and were previously used

in the MEA campaign. However, the Q2-3183A antifoam appeared to be more effective than the DSP antifoam for the piperazine and potassium carbonate solvent. The antifoam was typically added into the absorber feed tank or into the suction side of the absorber rich pump (P-104).

Table 1-21. Campaign 4 Antifoam Addition Date, Location, and Type

Date	Time	Volume (mL)	Antifoam	Location
01/10/06	11:06	50	Q2-3183A	P-104
01/12/06	10:10	100	DSP	P-104
01/12/06	10:40	100	DSP	Feed tank
01/12/06	12:45	100	DSP	Feed tank
01/12/06	14:30	100	Q2-3183A	Feed tank
01/19/06	11:00	100	Q2-3183A	Feed tank
01/19/06	17:30	100	Q2-3183A	Feed tank
01/19/06	20:00	25	Q2-3183A	Feed tank
01/20/06	00:15	25	Q2-3183A	Feed tank
01/20/06	03:11	25	Q2-3183A	Feed tank
01/20/06	03:45	25	Q2-3183A	Feed tank

A carbon filter was installed in this campaign to remove the degradation products that may have been a source of the foaming issues encountered in the first 2 campaigns. However, it was uncertain whether the carbon filter performed its intended function. The orifice plate that was installed in series with the carbon filter was improperly sized and steps were not taken to address this issue. The flow rate through the carbon filter was not measurable on the rotameter and hence, did not meet the design flow rate of 10-20% of the total liquid flow through the system.

Due to the lack of temperature control on the inlet absorber gas, a steam injector was installed. Steam was generated in the 10.2 cm reboiler using the distillate from the stripper and injected into the inlet gas to maintain a constant temperature of 40 °C. The

steam generator worked well for most of the campaign. However, in the middle of the campaign, the generator plugged up due to the accumulation of solids from the distillate. Apparently the distillate contained small amounts of potassium carbonate and piperazine. Since the reboiler was never bled, solids accumulated over time and eventually impeded steam production. The 10.2-cm reboiler was bled, washed, and restarted. The reboiler operated without additional problems after the initial shutdown.

There were some solubility issues during the second half of the campaign after the composition was changed. The experiments with the 6.4m K^+/1.6m PZ solvent were designed to operate at the solubility limits of the solvent. As a result, any loss of water inventory in the system would cause solids to precipitate out. During the course of plant operation, water was continually lost and at first could not be found. It was later discovered that water had begun to accumulate in the overhead CO_2 gas accumulator. Therefore, water had to be periodically pumped from the gas accumulator and back into the solvent stream, which resulted in some density fluctuations.

Before the start of this campaign, the pH meters were repaired and the transmitters were shielded from possible water intrusion with a makeshift cover. Both pH meters did not fail as in the previous campaigns and performed quite well. Continuous online measurements were taken at the lean and rich end of the absorber. However, there were issues with maintaining a constant lean loading. It was concluded that having an additional pH meter upstream of the absorber feed tank would have facilitated this because it would give the operator direct feedback on the lean loading going into the feed tank. Then, adjustments to the heat duty could be made immediately

instead of waiting for the residence time of the feed tank and finding out that the loading was incorrect or had drifted.

At the end of Campaign 4, an air-water test was conducted on the absorber to determine the effective wetted area of the Flexipac AQ Style 20 structured packing. Several water rinses was performed on the system to remove any residual solvent. The experiments were conducted by absorbing atmospheric CO_2 into 0.1 N NaOH solution. However, the CO_2 absorption rate appeared to be too high. This may have been an indication that there was residual piperazine and potassium carbonate in the NaOH solution, which helped to enhance the absorption rate. The results were not used for the determination the effective interfacial area in the mass transfer calculations. Instead, effective area measurements from the PVC air-water column were used.

1.6.5 Campaign 4 Results

In the fourth campaign, a comprehensive analysis of the liquid samples was undertaken. CO_2 loading was measure for the five sample points using the Shimadzu TOC with the updated protocol. In addition, piperazine and potassium was analyzed using the ion chromatography method developed at the start of this campaign. The results of the absorber liquid analyses for the 5m K^+/2.5m PZ and 6.4m K^+/1.6m PZ solution are shown below. In addition, the results for the gas rate, liquid rate, CO_2 gas concentration, density, pH, temperature, and pressure drop are shown in the table below.

Table 1-22. Campaign 4 Absorber Analyses for 5m K^+/2.5m PZ

Run ID	Date	Time	Piperazine			Potassium			CO_2 Loading		
			Lean mol/kg	Mid mol/kg	Rich mol/kg	Lean mol/kg	Mid mol/kg	Rich mol/kg	Lean mol/kg	Mid mol/kg	Rich mol/kg
4.1	01/10/06	15:30	1.43	1.54	1.43	3.04	3.24	3.02	2.55	2.80	2.88
4.2.1	01/10/06	21:04	1.49	1.46	1.48	3.15	2.97	3.13	2.56	2.90	3.28
4.2.2	01/10/06	22:08	1.49	1.45	1.47	3.16	3.06	3.12	2.50	2.64	3.40
4.3.1	01/11/06	12:00	1.47	1.53	1.41	3.10	3.12	2.97	2.68	3.19	3.19
4.3.2	01/11/06	13:01	1.49	1.66	1.48	3.15	3.34	3.11	2.68	3.45	3.32
4.4.1	01/11/06	15:59	1.50	-	1.43	3.15	-	3.04	2.66	-	3.30
4.4.2	01/11/06	17:28	1.67	1.57	2.01	3.48	3.31	4.23	2.99	3.23	4.25
4.5.1	01/11/06	21:19	1.49	1.43	1.48	3.14	3.01	3.09	2.66	3.02	3.30
4.5.2	01/11/06	22:20	1.50	1.66	1.46	3.15	3.53	3.08	2.70	3.57	3.36
4.6.1	01/12/06	6:28	1.45	1.44	1.39	3.05	3.02	2.93	2.42	2.97	3.13
4.6.2	01/12/06	7:35	1.46	1.44	1.40	3.08	3.03	2.95	2.43	3.06	3.15
4.7.1	01/12/06	14:04	1.47	1.39	1.40	3.12	2.93	2.97	2.34	2.62	2.91
4.7.2	01/12/06	15:00	1.45	1.37	1.41	3.09	2.88	2.99	2.33	2.56	2.89
4.8	01/12/06	17:06	1.42	1.39	1.38	2.96	2.91	2.90	2.26	2.65	2.84
4.9.1	01/12/06	18:03	1.44	1.35	1.38	3.06	2.85	2.93	2.27	2.82	2.97
4.9.2	01/12/06	18:31	1.43	1.36	1.43	3.05	2.89	3.02	2.28	2.80	2.96
4.10.1	01/12/06	22:31	1.43	1.39	1.39	3.04	2.92	2.93	2.63	2.89	2.90
4.10.2	01/12/06	23:31	1.40	1.36	1.42	2.95	2.83	2.96	2.58	2.90	3.09
4.11.1	01/13/06	2:07	1.59	1.38	1.40	3.54	2.85	2.94	2.60	2.93	3.11
4.11.2	01/13/06	3:03	1.45	1.36	1.39	3.05	2.83	2.91	2.58	2.97	3.13
4.12.1	01/13/06	5:12	1.47	1.39	1.40	3.10	2.87	2.94	2.58	2.96	3.06
4.12.2	01/13/06	5:59	1.46	1.39	1.39	3.09	2.91	2.91	2.62	2.96	3.10
4.13.1	01/18/06	17:00	1.30	1.41	1.47	2.94	2.96	3.06	2.38	2.89	2.76
4.13.2	01/18/06	17:45	1.51	1.35	1.39	3.38	2.83	2.88	2.49	2.73	2.88
4.14.1	01/19/06	10:27	1.53	1.36	1.37	3.47	2.83	2.86	2.56	2.71	2.88
4.14.2	01/19/06	12:20	1.33	1.34	1.40	2.99	2.83	2.93	2.51	2.78	2.88
4.15.1	01/19/06	13:56	1.39	1.38	1.36	3.14	2.90	2.86	2.56	2.82	2.95
4.15.2	01/19/06	15:10	1.39	1.36	1.43	3.13	2.85	3.04	2.56	2.80	2.95
4.16.1	01/19/06	19:35	1.78	1.64	1.42	4.06	3.54	2.93	3.09	2.83	3.41
4.16.2	01/19/06	21:03	1.60	1.36	1.50	3.34	2.83	3.16	2.87	2.76	3.08
4.17.1	01/20/06	4:13	1.40	1.37	1.43	3.19	2.86	3.03	2.36	2.71	2.89
4.17.2	01/20/06	5:13	1.38	1.39	1.41	3.10	2.74	2.96	2.38	2.72	2.93
4.18	01/20/06	13:30	1.39	1.59	1.51	3.15	3.35	3.18	2.48	3.05	3.09
4.19	01/20/06	14:34	1.48	1.55	1.54	3.34	3.26	3.27	2.68	2.95	3.24

1. Piperazine and potassium measured using ion chromatography method developed by this work
2. CO_2 loading analysis done with Shimadzu TOC
3. Concentration in units of mol/kg of solvent

Table 1-23. Campaign 4 Absorber Results for 5m K^+/2.5m PZ

Run#	Gas Rate Actual m^3/min	Liq Rate L/min	CO_2 In mol%	CO_2 Out mol%	FTIR CO_2 mol%	CO_2 Removal %	Temp Gas In °C	Temp Gas Out °C	Temp Liq In °C	Temp Liq Out °C	Density Liq In kg/m^3	Density Liq Out kg/m^3	pH Liq In	pH Liq Out	DP Bot Bed kPa	DP Top Bed kPa
4.1	14.2	53.0	7.98	0.59	0.83	92.1	39.9	42.4	39.9	48.6	1226	1232	11.0	9.6	0.58	0.58
4.2.1	11.3	47.2	16.28	4.08	-	74.8	39.9	45.8	38.9	48.1	1230	1242	11.1	9.3	0.50	0.43
4.2.2	11.3	47.3	17.19	5.00	4.91	70.8	40.1	46.1	39.0	47.8	1231	1244	11.1	9.3	0.50	0.43
4.3.1	8.5	49.2	15.49	2.60	15.16	82.8	40.6	38.1	42.1	50.0	1232	1238	10.7	9.3	0.37	0.25
4.3.2	8.5	49.2	16.04	2.81	15.70	82.2	40.6	38.7	42.5	50.2	1232	1239	10.7	9.3	0.37	0.25
4.4.1	11.3	54.9	16.95	5.22	5.24	69.1	40.0	41.8	43.6	50.3	1232	1240	10.7	9.3	0.51	0.39
4.4.2	11.3	55.2	17.09	5.49	16.64	67.8	40.0	42.4	43.9	50.2	1232	1240	10.7	9.2	0.52	0.41
4.5.1	14.2	54.9	16.59	6.89	16.44	58.6	40.1	45.7	42.0	47.0	1233	1243	10.7	9.3	0.65	0.62
4.5.2	14.2	55.0	17.55	6.89	9.03	60.8	40.0	43.6	41.4	46.2	1234	1244	10.7	9.3	0.66	0.62
4.6.1	8.5	45.4	16.63	2.35	2.25	85.5	40.1	46.7	46.7	50.9	1217	1230	10.9	9.2	0.42	0.29
4.6.2	8.5	45.0	16.43	2.03	2.03	87.4	39.9	40.4	43.6	50.9	1219	1229	10.9	9.2	0.42	0.27
4.7.1	11.3	55.1	13.17	1.33	1.42	89.6	40.0	44.9	45.2	50.7	1218	1229	10.9	9.4	0.43	0.35
4.7.2	11.3	54.8	12.77	1.01	12.63	91.8	40.1	43.4	45.0	50.6	1218	1228	10.9	9.4	0.40	0.32
4.8	14.2	55.1	10.75	1.89	10.60	82.2	39.9	47.2	43.3	47.3	1215	1227	10.9	9.5	0.53	0.54
4.9.1	14.2	54.7	16.38	5.89	16.29	64.2	40.0	50.9	43.2	47.4	1216	1231	10.9	9.3	0.54	0.57
4.9.2	14.2	55.0	16.03	5.70	16.13	64.6	40.0	51.0	43.2	47.3	1216	1232	10.9	9.3	0.54	0.58
4.10.1	8.5	49.2	17.56	4.95	5.12	71.5	40.0	39.8	44.3	50.9	1219	1227	10.5	9.1	0.32	0.21
4.10.2	8.5	49.2	17.62	5.09	5.26	70.8	40.0	38.6	41.7	51.3	1221	1227	10.5	9.1	0.33	0.20
4.11.1	11.3	54.7	14.93	5.13	15.06	65.4	40.1	36.3	41.6	48.8	1221	1227	10.5	9.2	0.46	0.37
4.11.2	11.3	54.9	15.08	5.42	14.89	63.8	40.0	35.6	41.2	48.4	1222	1228	10.5	9.2	0.48	0.38
4.12.1	14.2	55.0	11.23	4.76	4.79	57.5	40.1	38.1	39.8	46.3	1223	1228	10.6	9.4	0.65	0.61
4.12.2	14.2	54.9	12.64	5.89	5.70	53.5	40.1	38.6	39.9	46.2	1223	1229	10.5	9.3	0.65	0.62
4.13.1	14.2	109.8	17.11	5.21	17.23	69.6	40.0	38.4	41.5	47.9	1218	1222	10.3	9.3	0.83	0.73
4.13.2	14.2	110.0	16.28	4.43	16.42	72.8	39.9	39.9	43.0	49.5	1217	1221	10.3	9.3	0.88	0.77
4.14.1	11.3	113.7	17.16	2.94	2.70	82.7	40.1	37.8	42.8	48.1	1219	1222	10.3	9.4	0.77	0.71
4.14.2	11.3	113.6	15.88	2.19	15.97	86.0	39.9	38.1	42.8	47.8	1219	1222	10.3	9.4	0.68	0.59
4.15.1	8.5	88.9	16.49	1.91	1.83	88.1	40.0	35.5	39.5	45.2	1221	1224	10.3	9.5	0.44	0.35
4.15.2	8.5	89.2	16.76	2.17	2.23	86.7	40.0	35.6	39.6	45.4	1221	1224	10.3	9.4	0.45	0.34
4.16.1	14.2	94.4	16.44	6.28	5.78	61.9	40.0	38.2	41.4	48.4	1219	1223	10.5	9.3	0.76	0.60
4.16.2	14.2	94.6	13.24	3.82	3.49	71.0	40.1	37.4	41.3	47.7	1218	1222	10.5	9.4	0.72	0.58
4.17.1	14.2	94.7	16.62	4.89	4.86	70.6	40.0	37.2	40.1	49.5	1217	1222	10.7	9.4	0.73	0.54
4.17.2	14.1	94.7	17.04	4.27	17.32	74.9	40.1	37.9	40.6	50.9	1217	1222	10.7	9.4	0.65	0.47
4.18	14.2	75.8	13.94	1.91	1.91	86.1	40.5	37.3	40.0	51.2	1223	1228	10.9	9.5	0.48	0.33
4.19	14.2	75.5	13.04	1.34	1.39	89.5	40.4	38.2	40.3	52.1	1224	1228	10.9	9.5	0.48	0.32

1. CO_2 OUT with no value means analyzer was over-ranged with 5.96 reading
2.FTIR CO_2 shown was includes water, while CO_2 In and Out has less than 2% water

Table 1-24. Campaign 4 Absorber Analyses for 6.4m K^+/1.6m PZ

Run ID	Date	Time	Piperazine			Potassium			CO_2 Loading		
			Lean mol/kg	Mid mol/kg	Rich mol/kg	Lean mol/kg	Mid mol/kg	Rich mol/kg	Lean mol/kg	Mid mol/kg	Rich mol/kg
4.20.1	01/23/06	18:40	0.96	0.99	1.00	3.79	3.64	3.72	2.97	3.10	3.18
4.20.2	01/23/06	21:40	0.99	0.98	0.95	4.04	3.71	3.88	2.94	3.09	3.15
4.21.1	01/24/06	7:38	0.99	0.98	0.99	3.64	3.57	3.59	2.83	2.95	3.02
4.21.2.	01/24/06	9:00	1.00	1.00	0.98	3.67	3.65	3.56	2.87	2.99	3.07
4.22.1	01/24/06	11:30	-	0.98	1.01	-	3.57	3.68	3.01	3.11	3.23
4.22.2	01/24/06	12:35	1.21	1.02	0.85	4.78	3.71	2.76	3.11	3.31	3.02
4.23	01/24/06	19:33	1.18	0.97	1.13	4.74	3.53	3.61	3.17	3.15	3.29
4.24	01/24/06	21:34	1.07	1.06	1.06	4.25	3.92	3.84	3.04	3.40	3.41
4.25	01/25/06	4:58	1.02	1.00	1.04	4.01	3.58	3.65	2.80	3.01	3.08
4.26.1	01/25/06	15:00	1.01	1.01	0.96	3.97	3.65	3.52	2.76	2.91	3.09
4.26.2	01/25/06	16:00	0.99	1.00	0.99	3.90	3.62	3.64	2.78	2.92	3.10
4.27.1	01/25/06	21:00	1.00	1.01	0.99	3.94	3.65	3.64	2.78	3.00	3.22
4.27.2	01/25/06	22:04	1.05	0.99	1.00	4.14	3.58	3.70	2.80	2.99	3.17
4.28.1	01/26/06	0:58	1.00	0.97	0.96	3.92	3.49	3.45	2.73	3.01	3.14
4.28.2	01/26/06	2:00	0.99	0.98	0.99	3.90	3.50	3.66	2.75	2.96	3.13
4.29.1	01/26/06	5:32	1.02	0.99	0.99	3.98	3.56	3.59	2.73	2.99	3.15
4.29.2	01/26/06	6:32	1.03	0.95	1.09	4.06	3.43	3.73	2.75	3.01	3.15
4.30.1	01/26/06	10:00	1.18	0.99	1.02	4.61	3.58	3.77	2.64	2.92	3.11
4.30.2	01/26/06	11:00	1.00	1.04	0.99	3.91	3.72	3.62	2.67	2.94	3.15
4.31.1	01/26/06	15:00	1.05	0.99	0.96	4.14	3.57	3.53	2.85	3.01	3.16
4.31.2	01/26/06	16:00	1.07	1.00	0.99	4.17	3.60	3.70	2.94	3.00	3.18
4.32.1	01/26/06	19:00	1.01	0.99	1.02	3.98	3.54	3.71	2.78	3.03	3.24
4.32.2	01/26/06	20:00	1.02	1.12	1.08	3.81	4.01	3.88	2.78	3.29	3.53
4.33.1	01/27/06	0:30	1.00	0.98	0.98	3.92	3.49	3.29	2.73	3.06	2.99
4.33.2	01/27/06	1:30	1.01	0.98	0.96	3.76	3.51	3.09	2.73	3.06	2.78

1. Piperazine and potassium measured using ion chromatography method developed by this work
2. **CO_2 loading analysis done with Shimadzu TOC**

Table 1-25. Campaign 4 Absorber Results for 6.4m K^+/1.6m PZ

Run#	Gas Rate Actual m^3/min	Liquid Rate L/min	CO_2 In mol%	CO_2 Out mol%	FTIR CO_2 mol%	CO_2 Removal %	Temp Gas In °C	Temp Gas Out °C	Temp Liq In °C	Temp Liq Out °C	Density Liq In kg/m^3	Density Liq Out kg/m^3	pH Liq In	pH Liq Out	DP Bot Bed kPa	DP Top Bed kPa
4.20.1	8.5	87.0	15.72	4.98	-	68.0	41.1	34.1	38.8	43.7	1278	1275	10.3	9.7	0.33	0.36
4.20.2	8.5	87.1	15.73	5.26	-	66.5	41.1	34.4	38.6	43.5	1276	1275	10.3	9.7	0.37	1.51
4.21.1	8.5	98.2	14.32	3.23	-	77.1	41.1	33.3	39.0	43.1	1264	1262	10.4	9.8	0.38	0.27
4.21.2.	8.5	98.6	16.15	4.19	-	73.8	41.1	35.2	40.5	44.9	1267	1265	10.3	9.6	0.37	0.26
4.22.1	8.5	56.7	17.60	-	8.78	50.1	41.2	33.8	36.8	43.5	1273	1271	10.3	9.5	0.13	0.12
4.22.2	8.5	56.8	18.02	-	8.88	50.7	41.7	34.3	36.7	43.7	1274	1272	10.3	9.5	0.13	0.11
4.23	8.5	56.8	17.64	-	7.60	56.9	41.7	34.5	37.8	45.3	1276	1273	10.5	9.5	0.19	0.17
4.24	8.5	56.9	17.03	7.31	7.13	58.2	41.7	34.2	37.5	44.9	1276	1273	10.5	9.5	0.21	0.21
4.25	8.5	64.4	16.17	5.41	16.28	66.3	41.7	33.0	39.5	44.5	1267	1266	10.6	9.6	0.25	0.18
4.26.1	8.5	79.3	16.64	3.58	3.63	78.2	38.7	36.8	38.3	44.5	1265	1265	10.5	9.7	0.25	0.14
4.26.2	8.5	79.5	17.24	4.11	4.18	75.9	40.0	37.4	38.7	45.3	1266	1265	10.5	9.7	0.26	0.15
4.27.1	8.5	68.2	16.69	5.18	5.19	68.7	40.0	36.6	40.0	46.2	1266	1266	10.5	9.6	0.28	0.18
4.27.2	8.5	68.2	16.01	4.80	4.91	69.7	40.0	35.8	39.3	45.4	1268	1267	10.5	9.6	0.28	0.19
4.28.1	8.5	56.8	16.48	6.24	16.39	61.8	40.1	35.1	38.9	45.5	1264	1264	10.6	9.5	0.25	0.18
4.28.2	8.5	56.8	14.76	5.04	15.16	65.5	40.0	34.2	38.4	44.5	1265	1264	10.6	9.6	0.26	0.18
4.29.1	8.5	56.8	15.17	4.27	15.68	71.6	40.0	35.3	39.4	46.1	1268	1267	10.7	9.6	0.25	0.18
4.29.2	8.5	56.8	16.20	4.96	16.34	69.1	39.9	35.6	39.5	46.4	1270	1269	10.7	9.6	0.26	0.18
4.30.1	8.5	68.1	15.53	3.12	3.16	79.6	40.0	35.7	41.0	46.5	1265	1265	10.7	9.6	0.26	0.17
4.30.2	8.5	68.3	16.92	4.01	17.31	76.0	39.9	34.9	40.4	46.2	1267	1267	10.7	9.7	0.29	0.19
4.31.1	14.2	79.5	16.56	-	8.86	46.5	39.9	38.4	41.6	47.0	1263	1263	10.6	9.5	0.62	0.54
4.31.2	14.2	79.4	16.37	-	8.68	47.0	40.2	38.4	41.6	46.9	1265	1265	10.6	9.6	0.62	0.54
4.32.1	14.2	68.0	17.29	-	9.92	42.6	39.9	40.9	43.5	47.9	1266	1267	10.5	9.4	0.64	0.56
4.32.2	14.2	68.1	16.57	-	9.44	43.0	39.9	41.1	43.7	48.0	1266	1267	10.5	9.4	0.66	0.57
4.33.1	14.2	56.8	17.24	-	10.28	40.4	39.8	44.8	45.6	45.3	1260	1265	10.5	9.4	0.61	0.60
4.33.2	14.2	56.7	16.88	-	10.14	39.9	40.1	43.6	45.1	45.4	1261	1265	10.5	9.4	0.61	0.59

1. CO_2 OUT with no value means analyzer was over-ranged with 5.96 reading
2.FTIR CO_2 shown was includes water, while CO_2 In and Out has less than 2% water

In campaign 4, corrosion coupons were inserted downstream of the trim heater. The coupons were weighed prior to installation at the beginning of the campaign and reweighed after removal approximately 8 weeks later. The coupons were scrubbed and cleaned of accumulation prior to being reweighed. The results do not show a consistent trend (Table 1-26). For the same material some coupons exhibit somewhat significant losses (316L-5 and 2205-6), while other coupons showed an increase in weight. It was possible that the weighing scale was not performing properly. Based on the mixed results, it was concluded that there was no appreciable corrosion during Campaign 4.

Table 1-26. Campaign 4 Corrosion Coupon Results

Sample ID	Initial Mass g	Final Mass g	Difference Initial-Final
C1010-5	15.8236	15.8235	0.0001
C1010-6	16.0942	16.0966	-0.0024
304L-5	14.6822	14.6820	0.0002
304L-6	14.6066	14.6087	-0.0021
316L-5	14.3729	14.3693	0.0036
316L-6	14.3915	14.3986	-0.0071
317L-5	14.8248	14.8253	-0.0005
317L-6	14.8699	14.8716	-0.0017
2205-5	15.3240	15.3243	-0.0003
2205-6	15.3818	15.3773	0.0045
FRP	11.3150	11.4238	-0.1088

1.6.6 Campaign 4 Summary

Several issues from the previous campaigns that were resolved include: (1) An approach temperature of 10 °C for the stripper feed was finally achieved through a plate and frame exchanger that was procured. (2) The absorber inlet gas was saturated and consistently maintained at 40 °C by steam injection. (3) The Vaisala CO_2 analyzers were operated in an non-condensing gas stream. (4) The tubing of the sample bombs were

replaced with PFA fluoroplastic tubing for sample verification. (5) A higher capacity pump for the stripper lean stream was installed. (6) A slipstream carbon filter was installed to remove degradation products and reduce foaming.

In Campaign 4, some unresolved problems include: (1) The DeltaV log sheet recorded the raw signal for the absorber outlet Vaisala CO_2 analyzer and not the calibrated value. (2) The probe of the Vaisala CO_2 analyzer had an odd-size diameter. Sometimes, the pressure of the absorber outlet was under vacuum and there may have been a possible leak through fitting. (3) The CO_2 recycle flowmeter was over-sized for pressurized stripper operation. (4) The temperature and pressure from the recycle flowmeter were not recorded. (5) There was not enough flow through the carbon filter because the orifice plate on the main liquid line was too large. (6) In the fourth campaign, foaming was observed in the stripper, instead of the absorber.

1.7 RECOMMENDATIONS FOR FUTURE PILOT PLANT STUDIES

1.7.1 Pilot Plant Operation

The proper operation of the pilot plant requires real-time analysis for the process control and steady state operation. The in-situ measurement by the Vaisala CO_2 gas analyzers allowed the operator to adjust the steam rate to the reboiler control the flow of CO_2 recycle and makeup to quickly reach steady state and control of CO_2 concentration in the gas stream. However, real-time liquid analysis is critical for the determining the steam rate to the reboiler and is also useful to the operator for determining the whether the lean loading conditions has been attained. It would be useful to develop a more robust real-time measurement of loading. In addition, measurements of loading should

be taken both upstream and downstream of the absorber feed tank. The upstream measurement will provide the operator with real-time feedback and maintain a constant lean loading, which will dampen composition variation in the feed tank. In addition, the system will reach steady state more quickly.

1.7.2 Water Balance

Maintaining the water balance in the solvent system is critical for the operation of the pilot plant. Throughout the three piperazine and potassium carbonate campaigns, the loss of water from the system resulted in solubility issues, which resulted in process instrument error, plugged filters and instrument lines, and several major plant shutdowns. The water hold-up from the overhead liquid accumulator should be minimized or water should be added to the system to account for this loss in water.

Also, to accommodate high gas flows at vacuum operation in the stripper, a portion of the gas was routed through the liquid accumulator because the diameter of overhead gas line from the condenser was too small. This resulted in significant carryover of water into the overhead gas accumulator where the CO_2 is stored. It is recommended that the diameter of the gas line from the condenser be enlarged and to not use the dual flow path for the gas.

The loss of water also affects the measurement of pH in the solution. In the K^+/PZ an attempt was made to correlate pH with lean loading in order to control and maintain process conditions and the when the desired run condition was achieved. However, variations in water balance affected the precision of the pH measurements and could not reliably be used to control the steam flow to the reboiler of the stripper.

Maintaining a constant water balance will enable the use of real time loading measurements and help with process control.

1.7.3 Process Instrumentation

Temperature measurements are an important indicator of mass transfer performance and are useful when the data is for modeling and computer simulation applications. For the absorber column, it would be useful to add a gas temperature measurement at or near the outlet nozzle of the absorber. It would also be useful to have a temperature measurement at the absorber liquid inlet nozzle. For the stripper column, a temperature measurement at the liquid inlet nozzle after the stripper feed and reflux has been mixed would useful.

The addition of a flowmeter for the cooling water to the solvent cooler would provide valuable heat capacity information of the process solvent. In the current configuration, the temperatures of the cooling water and process stream are measured and the flow of the process solvent is measured. The heat capacity of the process fluid can be calculated if the flow rate of the cooling water is known.

1.7.4 Foaming

Foaming was observed in all of the K^+/PZ campaigns. In the first two campaigns, foaming was observed in the absorber and in Campaign 4, foaming was observed in the stripper. The higher temperatures approaches that were attained with the new cross-exchanger resulted in flashing across the control valve at the top of the stripper. The flashing feed may have caused the foaming and also resulted in poor mass transfer

performance in the stripper. It is recommended that a two-phase distributor installed in the stripper for future service.

Since the pilot plant is routinely used run experiments with organic liquids, there is typically some residue left in the system. A slip-stream carbon filter was installed in the fourth to filter out residual organic compounds and piperazine degradation products to reduce foaming. However, during the operation of the pilot plant there was essentially no flow through the carbon filter unit. It is recommended that a new orifice plate be installed to force some flow through the carbon filter.

During the operation of the pilot plant, anti-foam was periodically added to the system to eliminate foaming. It was found that the DOW Corning Q2-3183A anti-foam worked well for the piperazine and potassium carbonate system. According to the vendor, anti-foam is typically designed for once-through processes. In the pilot plant, the liquid is continuously recycled and over-time the anti-foam loses its efficacy. Therefore, it is recommended that anti-foam be continuously added through a metering or peristaltic pump.

1.7.5 Material Balance

In all of four of the pilot plant campaigns, the CO_2 material balance for the absorber could not be consistently closed. Some of the related issues such as better liquid sampling and analytical techniques have been resolved over the course of the four campaigns. Verification of critical measurements can be used as a tool to validate the data set and pinpoint problems.

The closure of the material balance depends on precise absorber inlet and outlet measurements of the (1) gas and liquid mass flow rates, (2) CO_2 concentration in the gas, and (3) the loading of CO_2 in the liquid. In future experiments it is recommended that the material balance across the absorber be established prior to the start of the campaign. In the analysis of the data, it was found that the precision of the liquid phase measurements were critical to the material balance. A 10% shift in the gas material balance was equivalent to a 2% shift in the liquid phase.

Several procedures are recommended to validate the accuracy and consistency of the critical measurements, which include: (1) Re-zero and run the three Micro Motion® flowmeters for the absorber lean, absorber rich, and stripper lean in series to make sure the density, flowrates, and temperature readings are consistent. The flow check should be performed with both water and the process solvent (2) Run a flow check of the Micro Motion® flowmeters with the bucket and stopwatch method to validate flow and to compare density measurements with another method such a hydrometer. The actual process solvent should be used. (3) A second measurement of gas flow should be added at the absorber outlet to validate inlet gas flow measurements. (4) The liquid sampling and analytical method for CO_2 loading and solvent composition should be thoroughly developed and validated in the laboratory prior to the start of the campaign. (5) The calibration of the CO_2 gas analyzers should be validated both in the laboratory and in the field. (6) Gas phase water measurements are also critical in determining the gas flow measurements and CO_2 gas concentration. It is recommended that the FTIR be used for the gas phase measurement of CO_2 and H_2O.

1.7.6 Gas Analysis

During the pilot plant campaigns, the CO_2 gas analyzers were re-calibrated approximately once a week. Significant drift was observed in the Horiba over the course of the 4 campaigns and the outlet Vaisala analyzer appeared to exhibit some drift. Therefore, it is recommended that 2 point calibration checks be conducted once every 24 hours and that the analyzers be recalibrated once every 3 days.

In Campaign 4, the CO_2 concentration measured by the FTIR and the Vaisala analyzers unexpectedly matched. The inlet and outlet FTIR measurements were performed at 40 °C and were assumed to be saturated with water. The inlet and outlet Vaisala measurements were conducted between 20 to 27 °C and between 10 to 15 °C, respectively. It was assumed that the Vaisala measure wet CO_2. Therefore, under different water concentrations, the wet CO_2 concentrations were not expected to be the same. Therefore, it is recommended that further testing be done to compare the CO_2 gas measurements of the Vaisala and FTIR at dry and wet conditions, different temperature ranges, and various degrees of water saturation. The pressure effects, in particular vacuum should also be investigated for the Vaisala CO_2 analyzers.

1.7.7 Material Compatibility

Material compatibility is important for safety and long-term operation of a pilot and industrial scale plants. During the operation of the pilot plants, it was found that the Viton® seals were not compatible with the piperazine and potassium carbonate solvent. The pump seals eventually developed failed and were replaced with EPDM seals, which appeared to be compatible. The o-rings in the sample bombs were also replaced with

EPDM. However, the filters contained Viton® o-rings, which seemed to swell in the presence of the K^+/PZ solvent. It was also found that the cotton filters were compatible with the K^+/PZ where as other materials such as polyethylene and polypropylene appeared to dissolve over time. The bag filter for the stripper completely dissolved in the high temperature solvent. In addition, it was found that while the vendors used cotton material, the polyethylene or polypropylene threads were used to manufacture the bags, which also resulted in failure of the filter bag. Cotton bag filters with cotton threading should be specified.

1.7.8 Data Acquisition

In all of the campaigns, the raw signal for the CO_2 gas concentration was recorded instead of the calibrated value. Also, in DeltaV, once the coefficients for the calibration curve have been entered, the new coefficients need to be manually uploaded into the system. In the course of the calibration procedure, this step may have been inadvertently left out. If the updated values are not uploaded, the values from the previous calibration are used. Depending on the amount of analyzer drift, there may be a significant error. Therefore, whenever new instrumentation is added, it should be verified that the calibrated signal is being logged. If may also be helpful to record both the raw and calibrated signals of critical measurements such as CO_2 gas concentration for use as a backup data set.

Chapter 2: Analysis of Pilot Plant Data

In this section, an analysis of the pilot plant data for Campaigns 1, 2, and 4 was performed. Real time process measurements of the gas and liquid flow rates, temperatures, densities, CO_2 gas concentration, and CO_2 gas recycle were examined. Evaluation of the liquid analysis for potassium and piperazine concentration and CO_2 loading was also undertaken. A material balance for the rate of CO_2 removal in the absorber and stripper was obtained. Mass transfer performance between the Flexipac 1Y and Flexipac AQ Style 20 structured packing and the $5mK^+/2.5mPZ$ and $6.4mK^+/1.6mPZ$ solvents were evaluated and compared to bench-scale measurements made in the wetted wall column.. The location and magnitude of the temperature bulge in the absorber was identified for each run and was quantified by integrating the area under the temperature profile. In addition, the general trends for pressure drop, pH, loading, capacity, stripper heat duty, and cross-exchanger performance are presented.

2.1 Real Time Process Measurements

The process measurements are continuously logged in real-time by the DeltaV process control system. Typically, the data recorded by DeltaV is downloaded into an Excel spreadsheet at one minute intervals at the end of each 24 hour shift. The real time

measurements of gas and liquid flow rates, liquid density, temperature and CO_2 concentration are analyzed in this section.

The volumetric flow rate of the absorber inlet gas is shown in Figure 2-1. The plot shows the actual measured gas flow rate from 11:00 to 13:00 on 1/24/06 for Campaign 4. During this period, the pilot plant was assumed to be at steady state and liquid samples were taken at 11:30 and 12:30. The plot shows there is slight variation in the measured gas rate but it appears to remain relatively constant. The standard deviation for the gas flow rate was 0.03 m^3/min over the 2 hour period. A summary of the average and standard deviation for the real-time measurement analysis are shown in Table 2-1.

Table 2-1. Average and Standard Deviation of Real time Process Measurements of Gas Flow Rate, Liquid Flow Rate, and Liquid Density for Campaign 4, 1/24/06, 11:00-13:00

Parameter	Unit	Location	AVE	STD DEV	SD/AVE %
Gas Vol Flow	m^3/min	Absorber Inlet	8.49	0.03	0.30
Gas Mole Flow	gmol/min	Absorber Inlet	349.23	2.06	0.59
Liq Vol Flow	L/min	Absorber Lean	56.78	0.58	1.02
Liq Vol Flow	L/min	Absorber Rich	58.67	0.48	0.82
Liq Vol Flow	L/min	Stripper Lean	56.72	2.24	3.95
Liq Density	kg/m^3	Absorber Lean	1273.38	0.36	0.03
Liq Density	kg/m^3	Absorber Rich	1271.41	0.43	0.03
Liq Density	kg/m^3	Stripper Lean	1271.27	0.61	0.05
Liq Mass Flow	kg/min	Absorber Lean	72.31	0.74	1.02
Liq Mass Flow	kg/min	Absorber Rich	74.60	0.61	0.82
Liq Mass Flow	kg/min	Stripper Lean	72.11	2.83	3.93

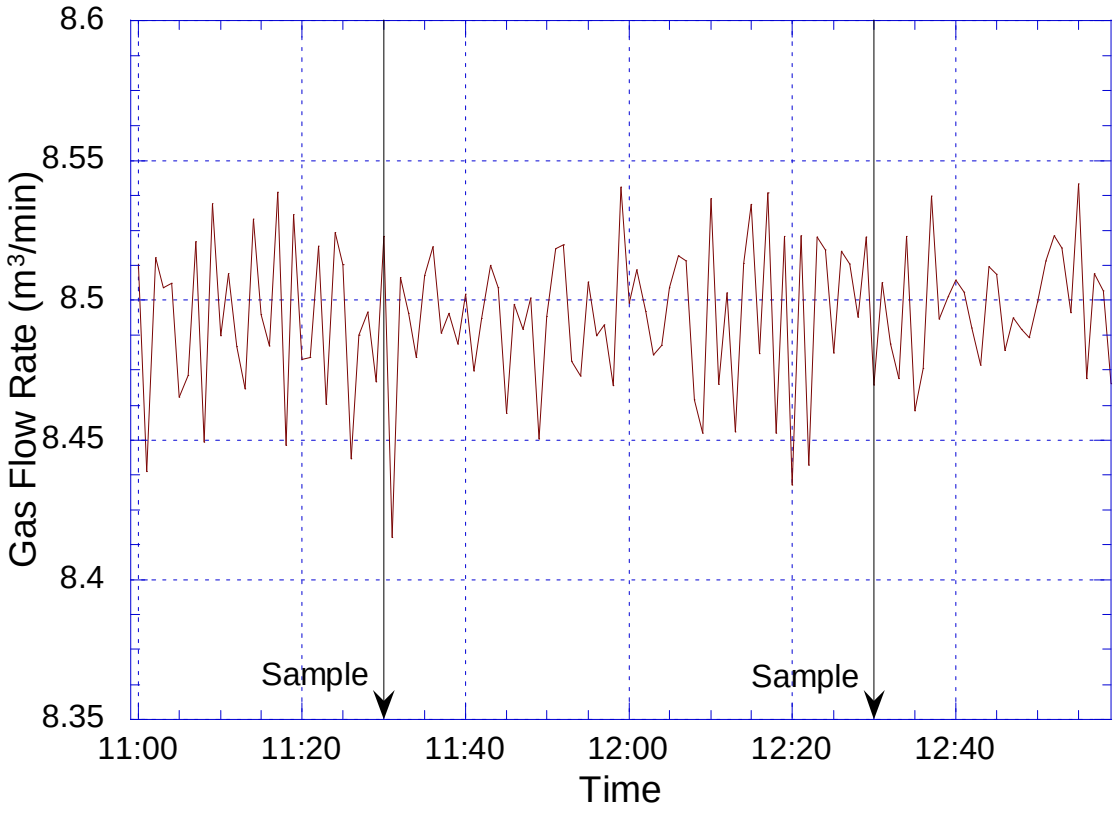

Figure 2-1. Real-time Volumetric Flow Rate of Absorber Inlet Gas for Campaign 4 (6.4mK$^+$/1.6mPZ, 1/24/06, 11:00 - 13:00)

A plot of the molar gas flow rate, which accounts for pressure and temperature, for the same data is shown in Figure 2-2. The plot shows that the molar gas flow rate is gradually decreasing over time. The decrease in flow is a result of the rise in gas temperature. The gas pressure remained constant during this time interval. This figure suggests that maintaining a constant mole flow of gas rather than volumetric flow may be better. The standard deviation of the molar gas flow rate was ±0.6%. It was concluded that the real-time gas flow measurement was within reasonable error.

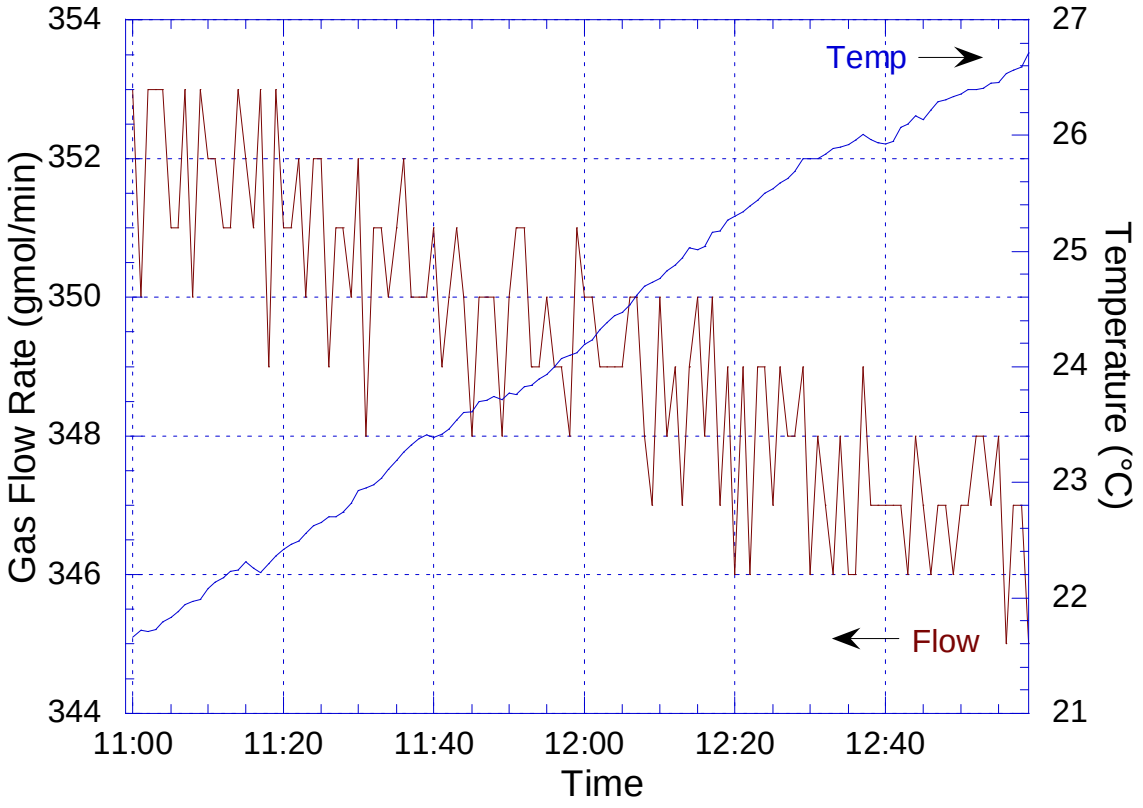

Figure 2-2. Real-time Molar Flow Rate of Absorber Inlet Gas for Campaign 4 (6.4mK$^+$/1.6mPZ, 1/24/06, 11:00 - 13:00)

The volumetric flow rate and density for the absorber lean, absorber rich and stripper lean streams as measured by the Micro Motion® flowmeters over the same time period are shown in Figure 2-3. The figure shows that the liquid flow rates oscillate over time. The flow rate for the stripper lean exhibits the highest degree of oscillation and the highest standard deviation among the three flows rates. The standard deviation for absorber lean, absorber rich, and stripper lean flow rates were 1.0, 0.8, and 4.0%, respectively. The density measurements also demonstrate a similar trend. The absorber lean and rich densities follow a smooth line and trend well with each other, whereas the density of the stripper lean tends to oscillate. The figure seems to indicate that a filter

was used to smooth out the density measurements for the absorber lean and absorber rich, whereas the stripper lean density measurement did not have a filter. When a measurement is filtered, a running average over a period of 20 seconds is recorded instead of the instantaneous signal. The standard deviation of the absorber lean, absorber rich, and stripper lean densities were 0.03, 0.03, and 0.05%, respectively. The figure also seems to indicate that the density of the stripper lean matched the absorber rich instead of the absorber lean, which is unexpected. The stripper lean density was adjusted to match the absorber lean measurements in the Data Reconciliation section of this chapter.

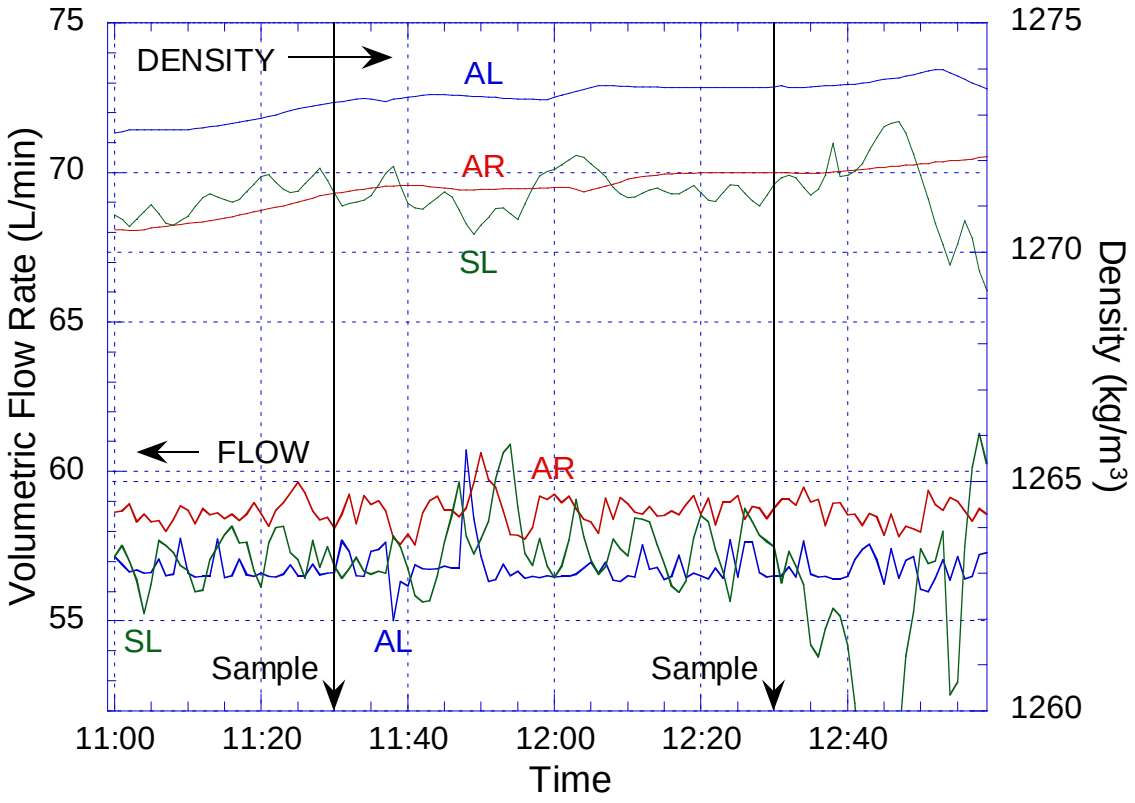

Figure 2-3. Real-time Liquid Flow Rate and Density Measurements of Absorber Lean (AL), Absorber Rich (AR), and Stripper Lean (SL) for Campaign 4 (6.4mK$^+$/1.6mPZ, 1/24/06 11:00 - 13:00)

The mass flow rates of the three liquid streams were obtained by multiplying the volumetric flow rate with the density (Figure 2-4). The mass flow rates exhibit the cycling trend observed for the volumetric flow rates. The absorber rich solution also has a consistently higher mass flow because of the absorption of CO_2. The figure also shows that after each liquid sample is taken, the stripper lean experiences a major upset and may take 20-30 minutes for it to recover from the disturbance.

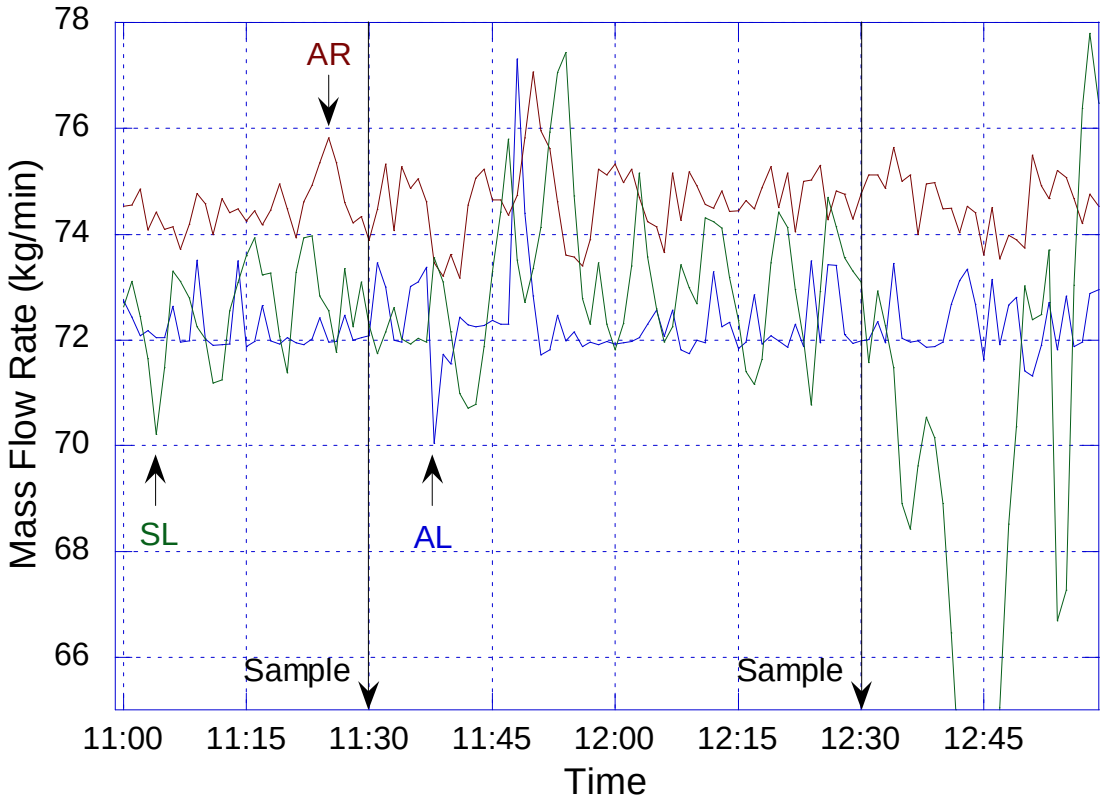

Figure 2-4. Real-time Mass Flow Rate Measurements of Absorber Lean (AL), Absorber Rich (AR), and Stripper Lean (SL) for Campaign 4 (6.4mK$^+$/1.6mPZ, 1/24/06, 11:00 - 13:00)

The temperature of the absorber lean, absorber rich, and stripper lean streams were measured by the Micro Motion® flowmeters (Figure 2-5). The measurements show that the absorber rich temperature is consistently higher than the absorber lean

temperature by approximately 7.5 °C and that the absorber lean and absorber rich temperatures trend well each other. The figure also shows that the stripper lean temperature oscillates excessively just like the density and flow measurements. Finally, the stripper lean temperature did not match the absorber lean temperature in the first 30 minutes of the time interval.

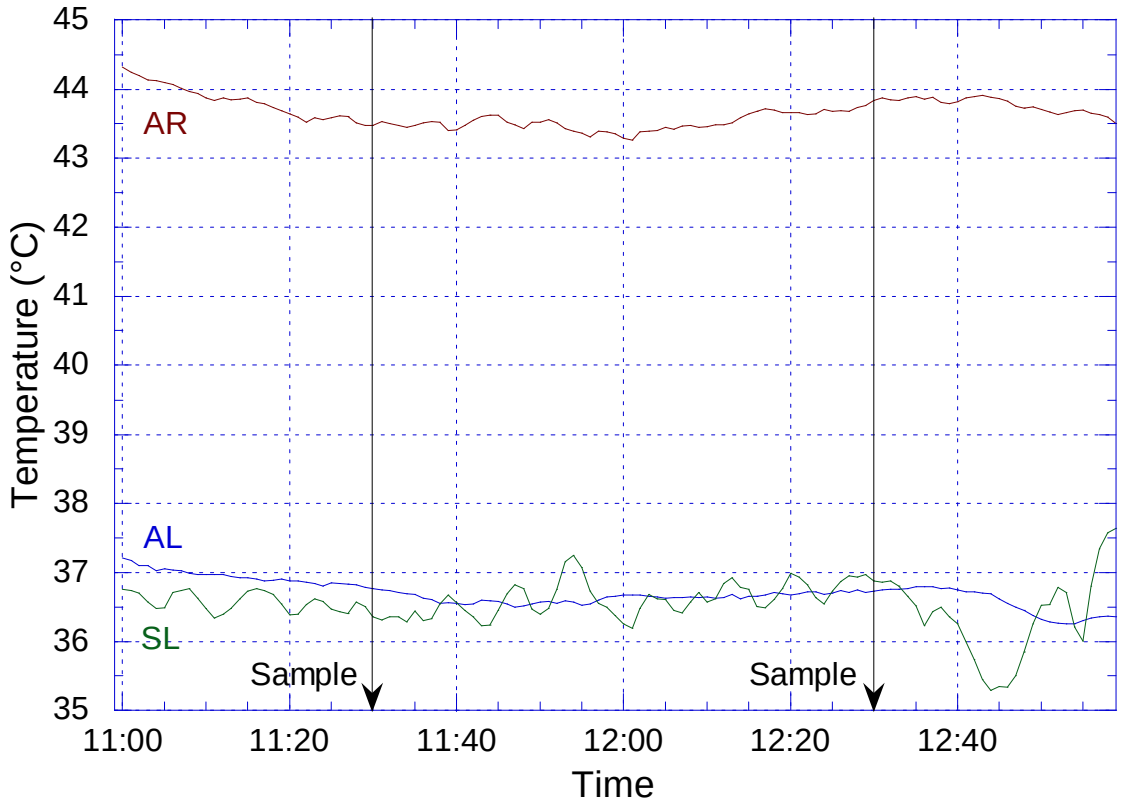

Figure 2-5. Real-time Temperature Measurements of Absorber Lean (AL), Absorber Rich (AR), and Stripper Lean (SL) for Campaign 4 (6.4mK$^+$/1.6mPZ, 1/24/06, 11:00 - 13:00)

The stripper lean Micro Motion® measures the liquid flow from the stripper reboiler. The level in the reboiler is maintained by the stripper bottoms pump (P-102) through a variable speed drive (VSD). Due to the inherent design of the kettle reboiler, the volume of liquid is spread out over a large area. Slight changes to the reboiler level

results in a large displacement of liquid volume. As a result, maintaining a constant level in the reboiler was difficult to do. Also, the stripper bottoms pump was controlled in CASCADE mode base on the level of the reboiler. In CASCADE mode, the level of the reboiler is manually set by the operator and the VSD of the pump is varied to maintain the specified reboiler level. Therefore, the liquid flow to the stripper lean flowmeter would have constantly oscillated due to changes of the pump VSD. In addition, upstream of the Micro Motion® flowmeter, there is a control valve which regulates the amount of stripper lean liquid that is bypassed around the solvent cooler. The two liquid streams are recombined just upstream of the flowmeter. This may have also contributed to the fluctuations in temperature and flow measurements. The oscillating temperatures may have also contributed to the fluctuating density readings. Based on the above analysis, it was found that both the absorber lean and absorber rich flow rates had a standard error of ±1%, while the stripper lean had a standard error of ±4%.

The real time measurements of CO_2 concentration for the inlet, middle, and outlet of the absorber for Campaign on 1/20/06 from 3:00 to 5:30 AM are shown in Figure 2-6. The inlet and outlet CO_2 concentration was measured with the in-situ Vaisala analyzers; the middle concentration was measured with the Horiba analyzer. The figure also shows the concentration of carbon dioxide and water measured by the FTIR analyzer at the inlet and outlet of the absorber. The FTIR and Horiba analyzers utilize an extractive sampling system and the measurements for the two instruments were shifted by several minutes to account for the residence time in the sampling system.

The Horiba measures dry CO_2 gas concentration and the FTIR measures wet CO_2 gas concentration. Experiments that were performed seemed to indicate the Vaisala analyzer measured wet CO_2 gas concentration and this was assumed. The figure shows that all of the measured CO_2 gas concentrations trend relatively well each other. The slight oscillation in CO_2 concentration over time was concluded to be reflective of real-time changes in the concentration and not associated with instrument noise or sampling error since all four measurements demonstrated the same peaks and valleys at the same time.

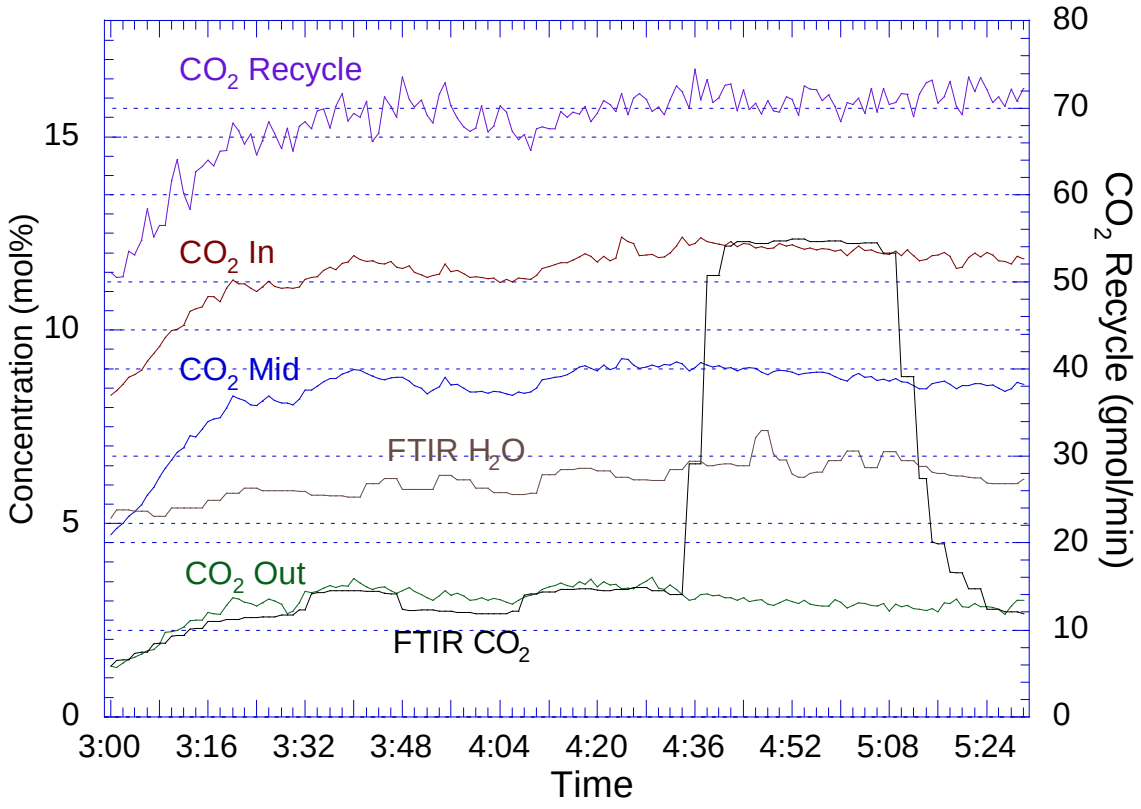

Figure 2-6. Real-time Measurements of CO_2 and H_2O Gas Concentrations in the Absorber and CO_2 Recycle from the Stripper for Campaign 4 (5mK^+/2.5mPZ, 1/20/06, 3:00 – 5:30)

The FTIR CO_2 concentrations matched the inlet and outlet Vaisala measurements. This was unexpected since the water content for the two analyzers were assumed to be different. The oscillation of the outlet FTIR water concentration appeared to trend with the outlet CO_2 concentration, whereas the inlet H_2O concentration did not follow trend of the inlet CO_2 concentration. The FTIR sample point is located 0.6 meters downstream of the steam injection point and the steam may not have completely mixed with the gas, which resulted in erratic measurements.

Finally, the plot shows that the CO_2 recycle stream from the stripper trends well with the measurements of CO_2 concentration. However, the CO_2 recycle measurements appeared to oscillate excessively. Over the time interval from 4:20 to 5:30 AM, the standard deviation of the CO_2 recycle measurement was ±1.8%. The CO_2 recycle stream was measured with an annubar that was originally designed for vacuum operation and was oversized for pressure operation. It was concluded that the real-time CO_2 gas measurements were reliable, but the discrepancy between the FTIR and Vaisala measurements should be addressed in future experiments. Also, the outlet FTIR water measurement and CO_2 recycle stream under high flow conditions were determined to be reliable.

2.2 LIQUID DENSITY, FLOW RATE AND TEMPERATURE

For each run condition, the real-time process measurements were averaged over the period ten minutes before and after the sample point. In this section, the averaged values of the liquid density, flow rate, and temperatures for Campaign 4 were analyzed. It was assumed that the data for the previous campaigns followed the same trends.

Figure 2-7 compares the densities measured by the Micro Motion® flowmeters for the absorber lean, absorber rich, and stripper lean streams as a parity plot. The figure shows that relative to the absorber lean, for the 5mK$^+$/2.5mPZ and 6.4mK$^+$/1.6mPZ solvents, the stripper lean was on average 0.33% and 0.13% lower, respectively and the absorber rich stream was on average 0.6% higher and 0.04% lower, respectively. The plot also shows that the 5mK$^+$/2.5mPZ density data appeared to show more variation than the 6.4mK$^+$/1.6mPZ data. Part of this discrepancy may have been due to the difference in temperature relative to the absorber lean stream.

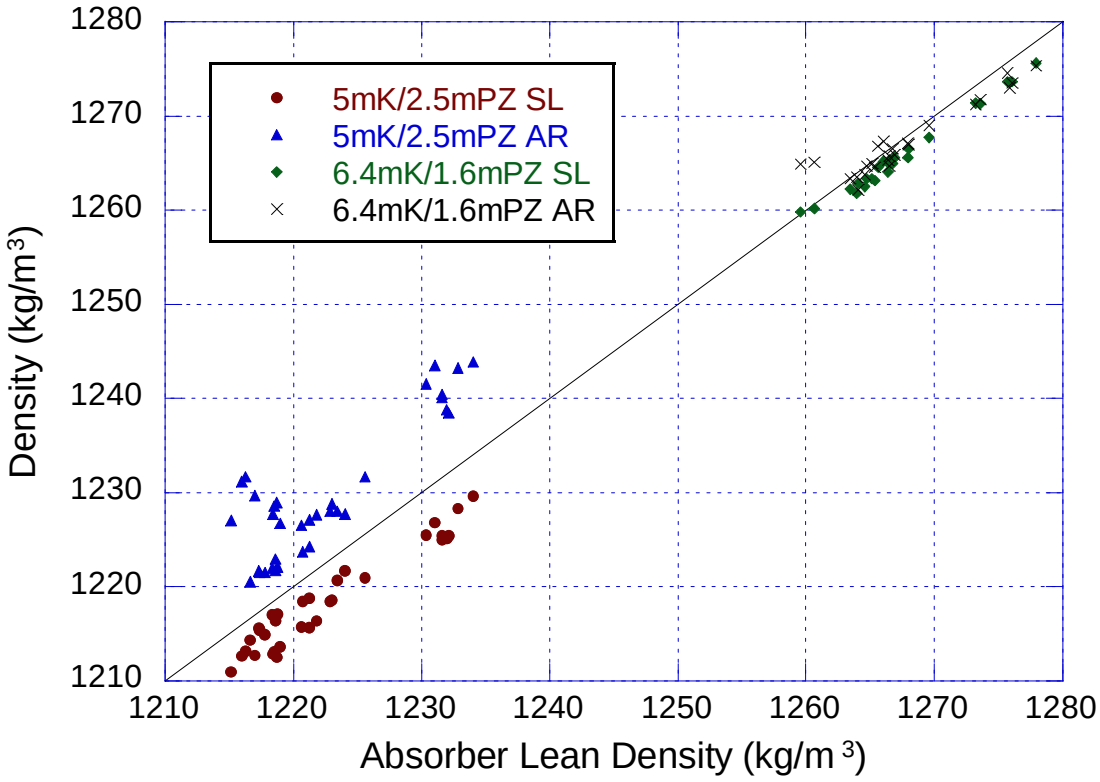

Figure 2-7. Measured Density of Absorber Lean (AL), Absorber Rich (AR), and Stripper Lean (SL) by Micro Motion® Flowmeters of 5mK$^+$/2.5mPZ and 6.4mK$^+$/1.6mPZ for Campaign 4

Figure 2-8 is a plot of the temperature difference for the absorber rich and stripper lean streams relative to the absorber lean stream. The figure shows that for the 5mK$^+$/2.5mPZ solvent, the majority of the stripper lean temperatures were 1 to 2°C higher than that absorber lean and the difference in temperature for the 6.4mK$^+$/1.6mPZ stripper lean and absorber lean streams were on average less than a 1°C. The absorber rich temperatures for the 5mK$^+$/2.5mPZ and 6.4mK$^+$/1.6mPZ solvents were typically 4 to 12 °C and 4 to 8 °C higher than the absorber lean streams, respectively. There relative difference in temperature between the absorber lean and rich streams appeared to decrease with increasing absorber lean temperatures. Another interpretation of this is that the liquid outlet temperature remained relatively constant and was to some degree independent of the inlet liquid stream temperature.

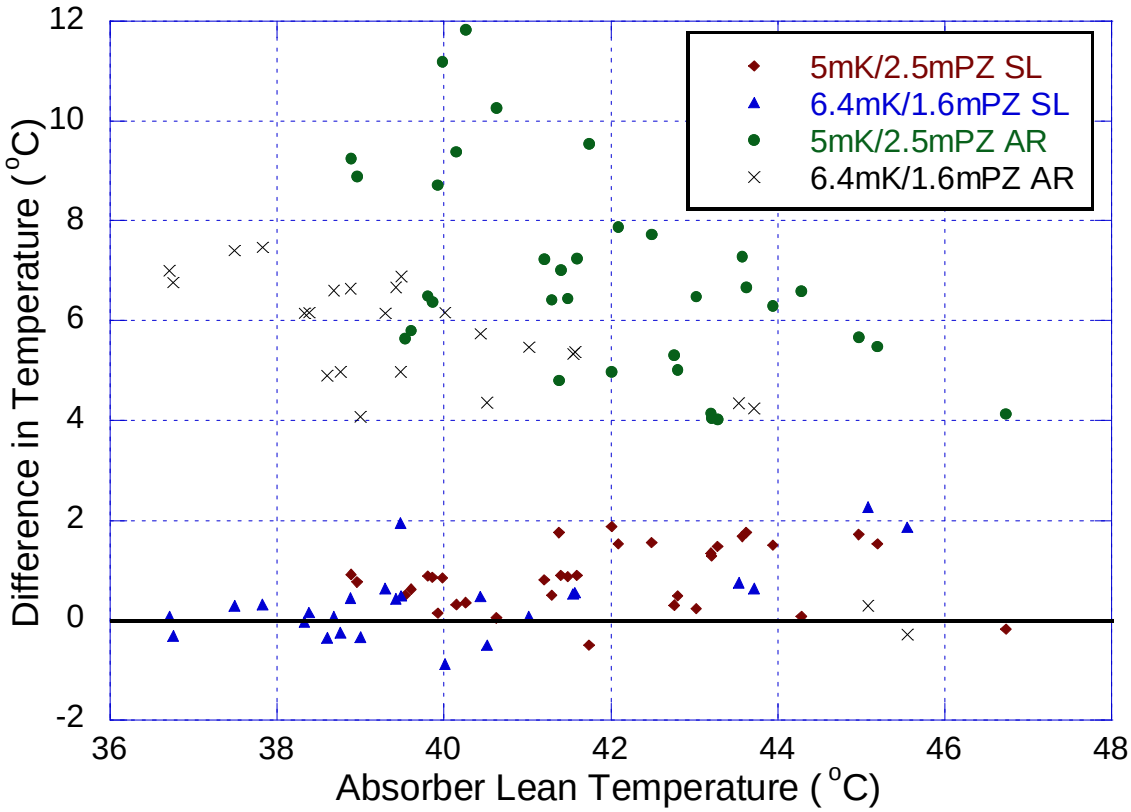

Figure 2-8. Temperatures of Absorber Lean (AL), Stripper Lean (SL), and Absorber Rich (AR) for 5mK^+/2.5mPZ and 6.4mK^+/1.6mPZ of Campaign 4

The absorber inlet and outlet temperatures were measured by the Micro Motion® flowmeters and Rosemount pH meters at each respective location. Figure 2-9 shows that the temperature measurement by the pH probe for the absorber lean stream were on average consistently lower than that measured by the flowmeter. The absorber lean pH probe is approximately 4 to 5 meters downstream of the flowmeter and thus one would expect the temperature to be slightly lower. However, temperature differences of 5 to 7 °C were observed for the absorber lean pH meter and flowmeter, which seemed unreasonable. The absorber rich pH meter is located a few meters below the absorber sump and the absorber rich flowmeter is located approximately 37 meters downstream of the pH meter. The absorber rich liquid passes through a pump in between the pH probe measurement and the flowmeter measurement. The pump may slightly increase the temperature of the absorber rich stream and this is reflected in the slightly higher temperatures measured by flowmeter. In both solvent compositions, the flowmeter temperatures are no more than 1 °C higher than the pH probe temperatures. It was concluded that the temperatures measured by absorber inlet and outlet Micro Motion® flowmeters and absorber rich pH meter were reliable, while the absorber lean pH meter temperatures were not.

Data analysis of the absorber utilized the absorber lean Micro Motion® flowmeter and absorber rich pH probe temperature measurements as the absorber inlet and outlet temperatures, respectively. However, it should be noted that the liquid temperature

entering the absorber may be slightly cooler than the measured temperature because the temperature is measured approximately 22 meters upstream of the inlet nozzle.

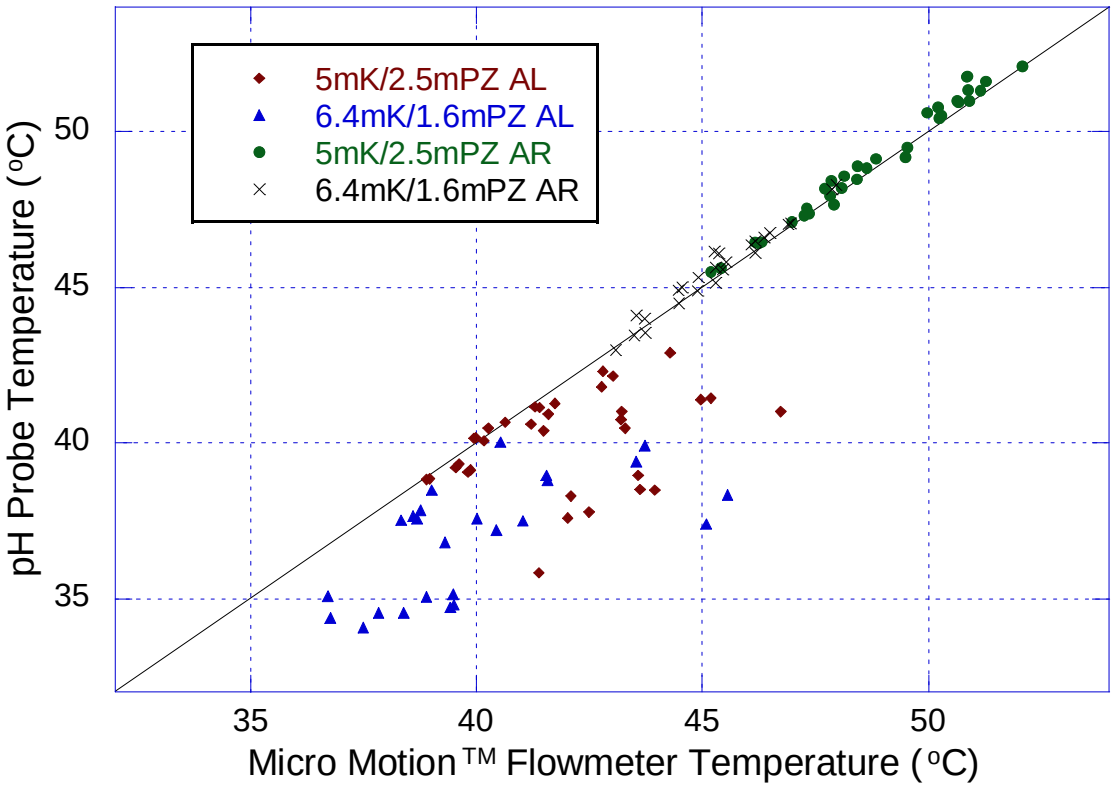

Figure 2-9. Temperature Comparison of Micro Motion® Flowmeters and Rosemount pH Meters for the Absorber Inlet and Outlet of Campaign 4

The Micro Motion® Coriolis flowmeters measure mass flow, density, and temperature, which are then used to calculate the volumetric flow rate. The volumetric flow rate of the absorber lean, absorber rich, and stripper lean streams for Campaign 4 are compared in Figure 2-10. The volumetric flow rates of the stripper lean for the 5mK^+/2.5mPZ and 6.4mK^+/1.6mPZ solvents were on average, 0.9% lower and 0.3% higher than the absorber lean stream, respectively. The volumetric flow rates of the

absorber rich for the 5mK$^+$/2.5mPZ and 6.4mK$^+$/1.6mPZ solvents were on average, 2.4% and 3.3% higher than the absorber lean stream, respectively.

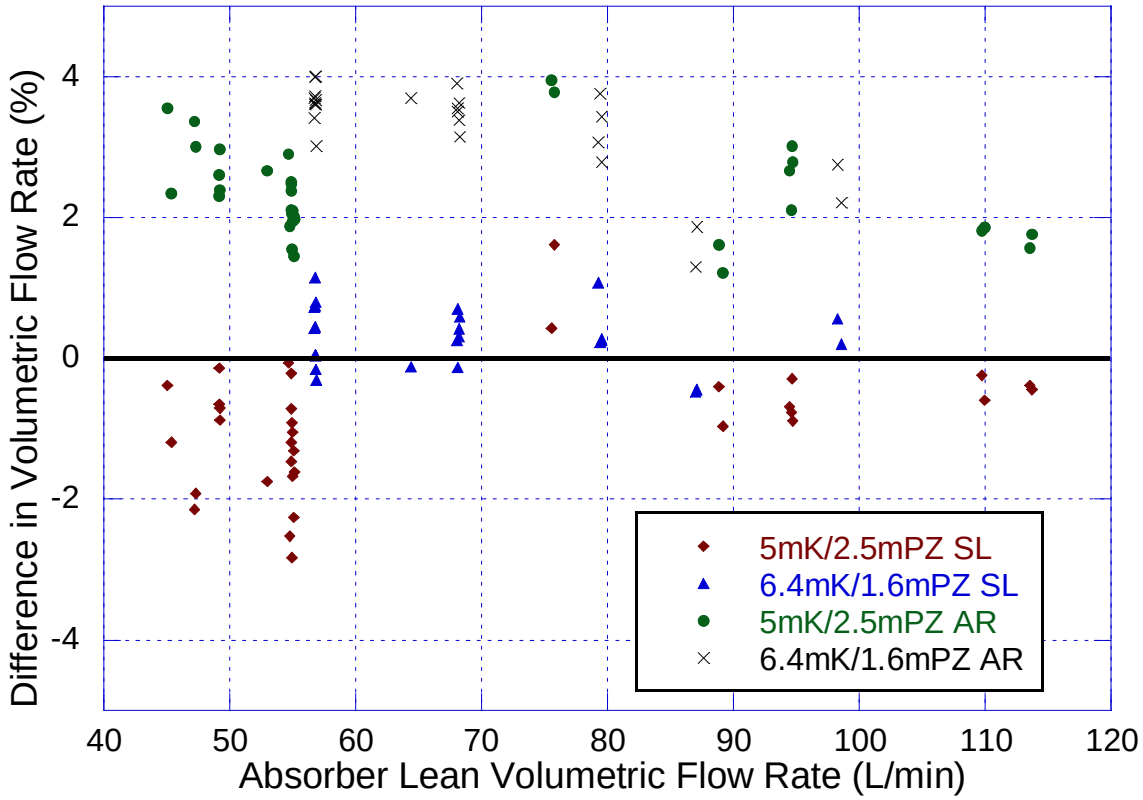

Figure 2-10. Volumetric Flow Rate Comparison of Absorber Lean (AL), Stripper Lean (SL), and Absorber Rich (AR) of 5mK$^+$/2.5mPZ and 6.4mK$^+$/1.6mPZ for Campaign 4

Figure 2-11 illustrates the difference in mass flow rate between the absorber lean, absorber rich, and stripper lean stream of Campaign 4. The mass flow rates of the stripper lean for the 5mK$^+$/2.5mPZ and 6.4mK$^+$/1.6mPZ solvents were on average, 1.2% lower and 0.2% higher than the absorber lean stream, respectively. The mass flow rates of the absorber rich for the 5mK$^+$/2.5mPZ and 6.4mK$^+$/1.6mPZ solvents were on average, 3.0% and 3.3% higher than the absorber lean streams, respectively.

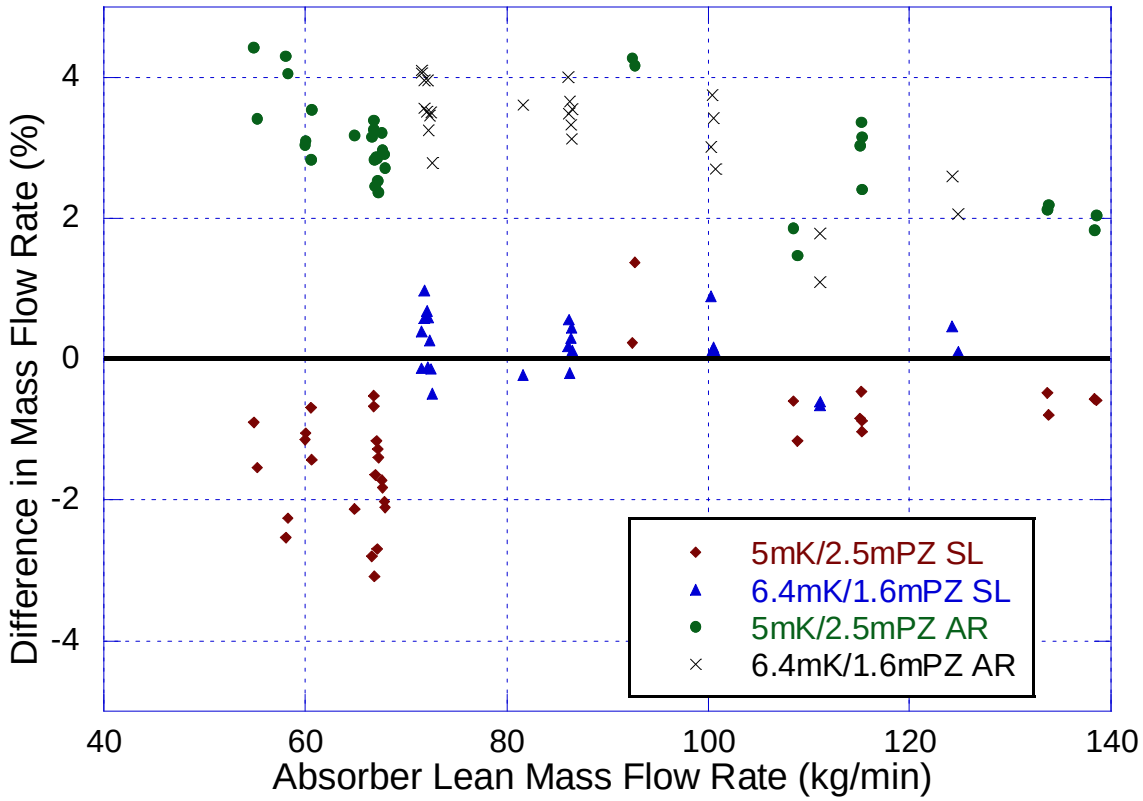

Figure 2-11. Mass Flow Rate of Absorber Lean (AL), Stripper Lean (SL), and Absorber Rich (AR) for 5mK$^+$/2.5mPZ and 6.4mK$^+$/1.6mPZ of Campaign 4

The slightly higher absorber rich mass flow rate was attributed to the absorption of CO_2, possible absorption of water from the gas. It was concluded that the discrepancy between the absorber lean and stripper lean mass flow rates was attributed to fluctuations in liquid flow due to reboiler level control issues and to possible error with the stripper lean density measurement. The figure also shows that about 40% of the 5mK$^+$/2.5mPZ runs were operated at 67 kg/min, with additional points at 55, 60, 90, 109, 115, 134 kg/min. For 6.4mK$^+$/1.6mPZ solvent, approximately 40% of the runs were conducted at 72 kg/min, with additional points at 82, 86, 100, 111, and 125 kg/min.

2.3 LIQUID POTASSIUM AND PIPERAZINE CONCENTRATION

For Campaign 4, the concentration of potassium and piperazine was analyzed using ion chromatography method developed in this work. The method is detailed in the previous chapter under Campaign 4 Analytical Methods. The concentration of both species were analyzed for all of the samples that were taken, which included the absorber lean, absorber rich, absorber middle, stripper lean, and stripper middle samples. The results of the piperazine and potassium analysis for the $5mK^+/2.5mPZ$ solvent are shown in Figure 2-12.

The plot shows that the concentration of both piperazine and potassium for the stripper middle samples were consistently lower than the other four sample locations by approximately 10%. A similar trend was also observed for the $6.4mK^+/1.6mPZ$ solvent, where the stripper middle samples were 8.5% lower (Figure 2-13). In the stripper, reflux is continuously added as water to the solvent feed and it is possible that the solvent was being diluted. However, at the same time there is water loss from the solvent in the form of steam generation, which would concentrate the solvent. At steady state, the evaporated water should be equivalent to amount of reflux that is being returned. The ion chromatograph analysis of the stripper middle was conducted contiguously. Therefore, it is possible that the calibration of analyzer for that set of runs was systemically offset by 10%. The plot also shows that the piperazine concentration for several of the absorber lean points was systematically lower. A more detailed analysis is presented later in this section.

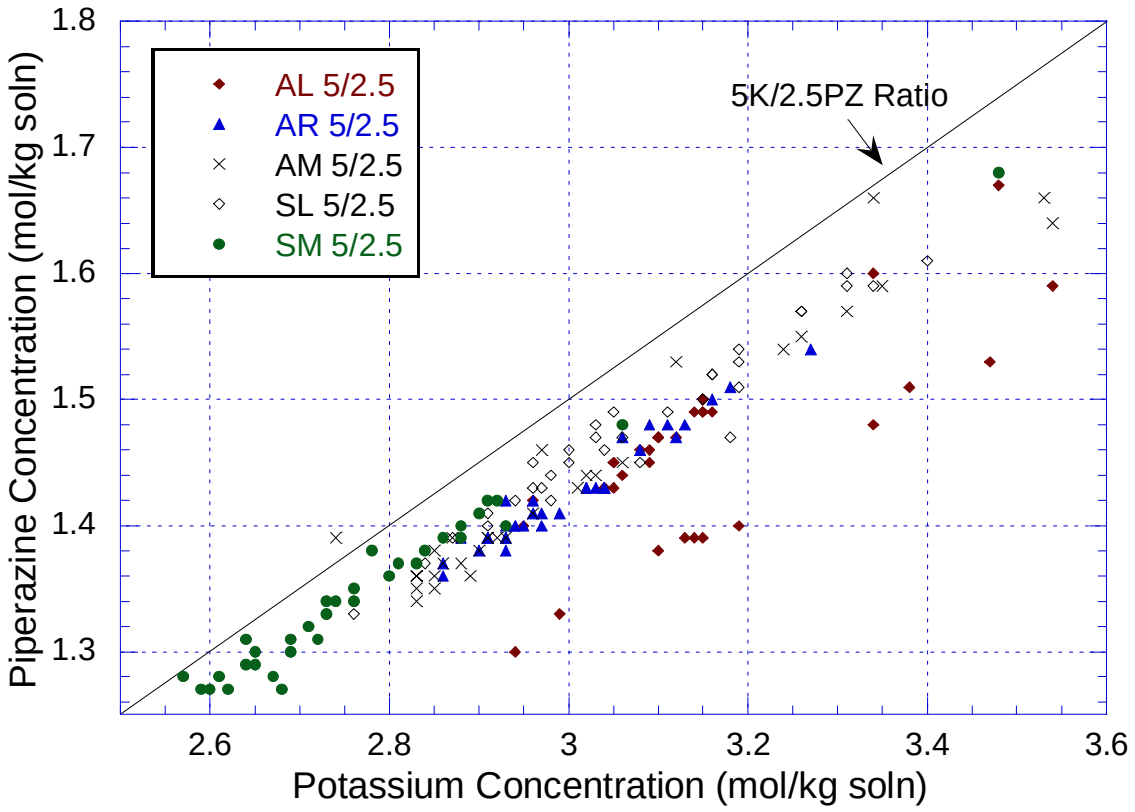

Figure 2-12. Potassium and Piperazine Measurements from Ion Chromatography for 5mK^+/2.5mPZ of Campaign 5 for Absorber Lean (AL), Rich (AR), Middle (AM), and Stripper Lean (SL) and Middle (SM)

A similar plot for the 6.4mK^+/1.6mPZ solvent shows that the potassium concentration for the absorber lean points was consistently higher than the other sample points.

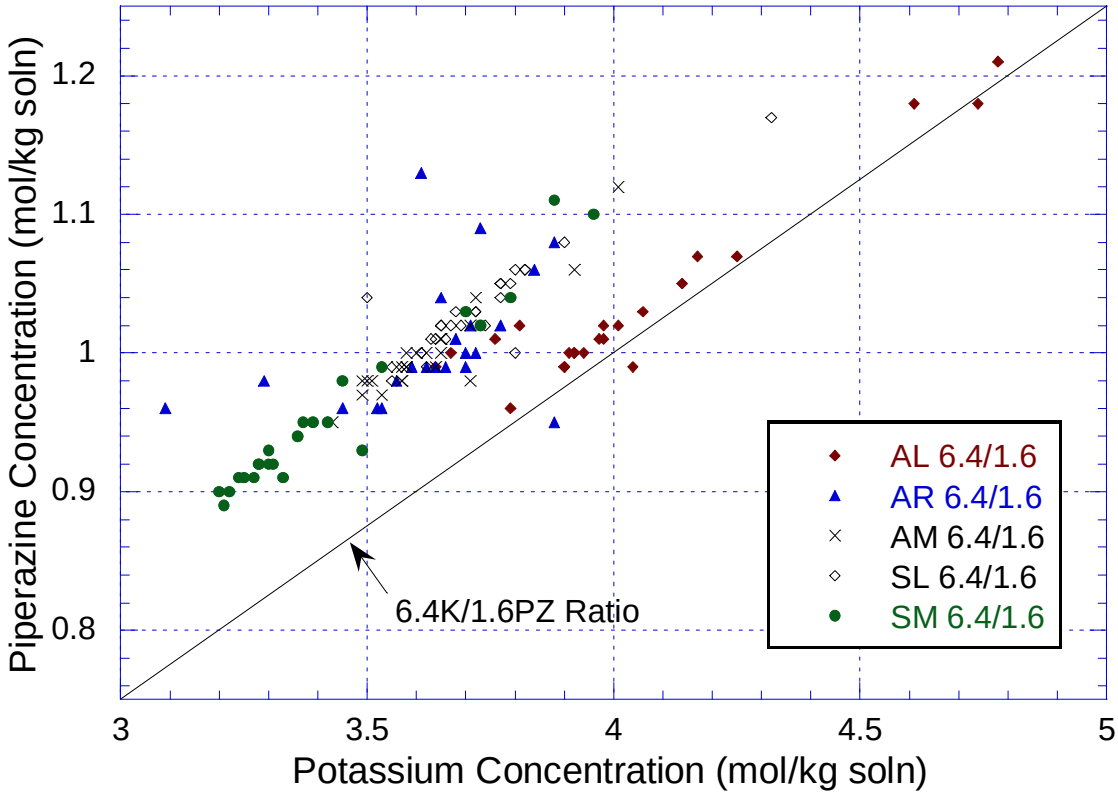

Figure 2-13. Potassium and Piperazine Measurements from Ion Chromatography for 6.4mK^+/1.6mPZ of Campaign 5 for Absorber Lean (AL), Rich (AR), Middle (AM), and Stripper Lean (SL) and Middle (SM)

2.3.1 Potassium and Piperazine Concentration Adjustments

A parity plot of the potassium concentrations for the absorber lean, absorber rich and stripper lean streams of Campaign 4 as measured by ion chromatography is shown in Figure 2-14. The plot shows that the potassium concentration of the 5mK^+/2.5mPZ absorber lean and stripper lean streams match up relatively well. However, the absorber rich potassium analysis seems to be consistently lower than the absorber lean stream. It is possible that the absorber rich stream was slightly diluted by the addition of water from the steam injection of the gas pre-heater or the absorption of water from the gas due to condensation. Another possibility is analytical error during the calibration or analysis of

the solution on the ion chromatograph. A similar trend was also observed for the piperazine analysis of the 5mK^+/2.5mPZ absorber rich solution. The plot was used to help identify outliers of the potassium analysis for the 5mK^+/2.5mPZ solutions.

The 6.4mK^+/1.6mPZ points seemed to indicate that the potassium concentration of the absorber lean was consistently higher than the absorber rich and stripper lean. The absorber rich and stripper lean potassium values were consistent with each other. The analysis of the piperazine data for the 6.4mK^+/1.6mPZ solutions did not demonstrate this trend. Therefore, a correction factor of 0.924 was applied to the measured potassium concentrations of the 6.4mK^+/1.6mPZ absorber lean data. The factor was obtained using MS Excel Solver function and setting the target of the average K/PZ mol ratio for the absorber lean equal to 3.61. Figure 2-15 shows the adjusted potassium concentration of the absorber lean points for the 6.4mK^+/1.6mPZ solution. The figure was used to help identify outliers for the potassium analysis of the 6.4mK^+/1.6mPZ solution.

The 5mK^+/2.5mPZ and 6.4mK^+/1.6mPZ solutions were both analyzed using standards containing piperazine and potassium carbonate at a K^+/PZ ratio of 2:1, which may have resulted in the possible discrepancies in the IC analysis of the 6.4mK^+/1.6mPZ samples. However, analysis of the 6.4mK^+/1.6mPZ absorber rich and stripper lean for potassium and piperazine appear to be consistent with each other and do not support this hypothesis. It was concluded that the IC method developed for the analysis of potassium and piperazine could be applied to the analysis of the 6.4mK^+/1.6mPZ samples.

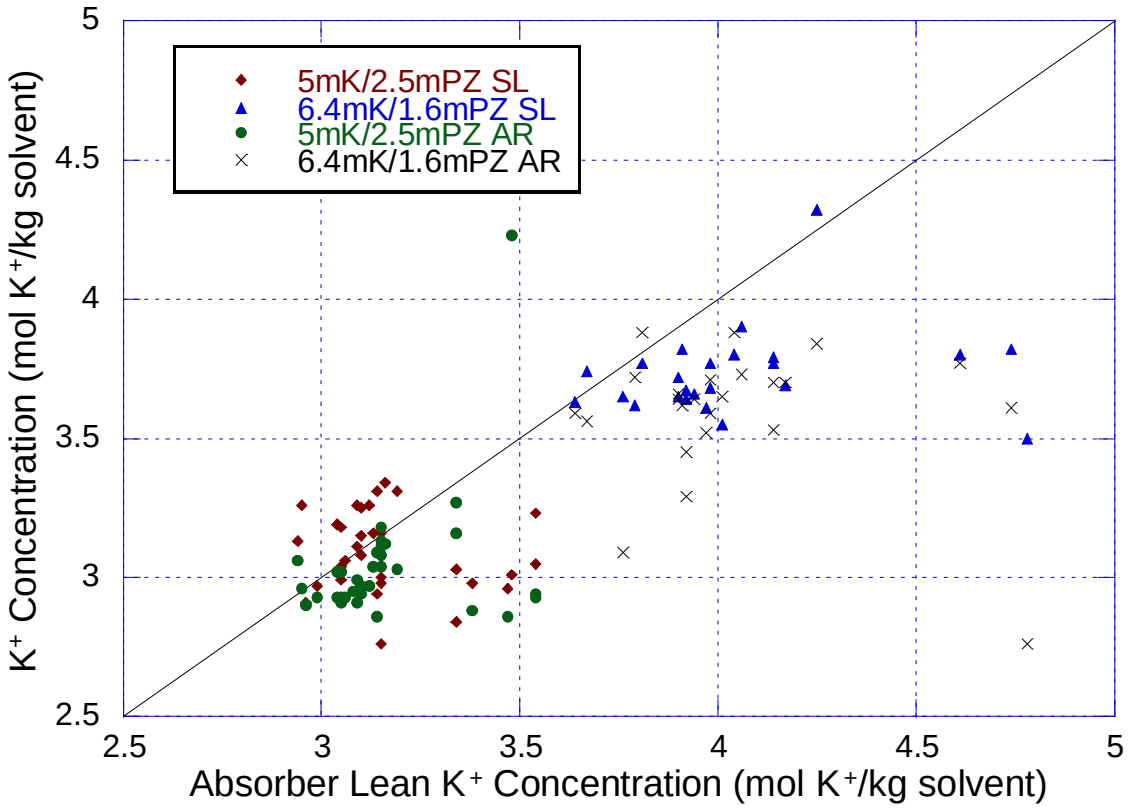

Figure 2-14. Potassium Concentration Comparison of Absorber Lean (AL), Absorber Rich (AR), and Stripper Lean (SL) for Campaign 4

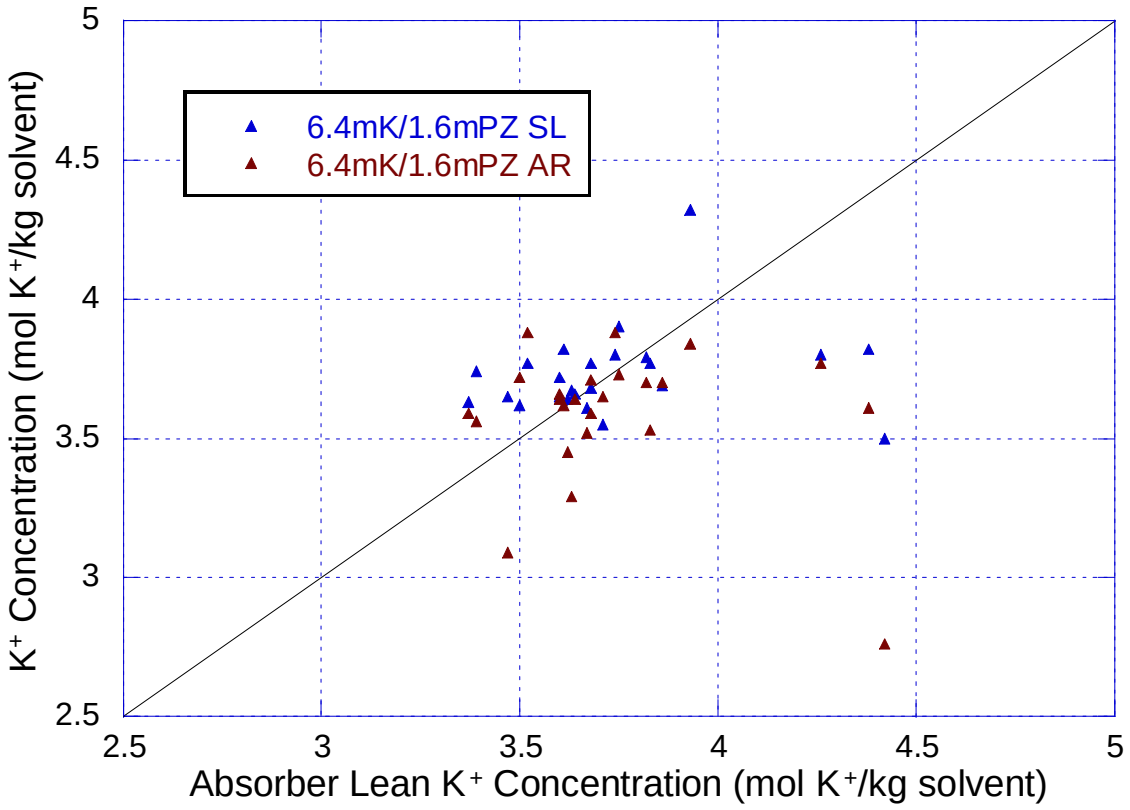

Figure 2-15. Corrected Absorber Lean Potassium Concentrations for 6.4mK$^+$/1.6mPZ of Campaign 4

The piperazine analyses from the ion chromatograph of the absorber lean, absorber rich and stripper lean solutions for Campaign 4 are shown in Figure 2-16. The piperazine analysis for the 5mK$^+$/2.5mPZ solution shows that the absorber rich values are on average slightly lower than the absorber lean, while the stripper lean values were slightly higher than the absorber lean values. However, since the differences were relatively minor, corrections were not applied to the measured values. The piperazine values for the 6.4mK$^+$/1.6mPZ samples appeared to be consistent with each other and no corrections were made. The plot was used to eliminate outliers for the piperazine analysis.

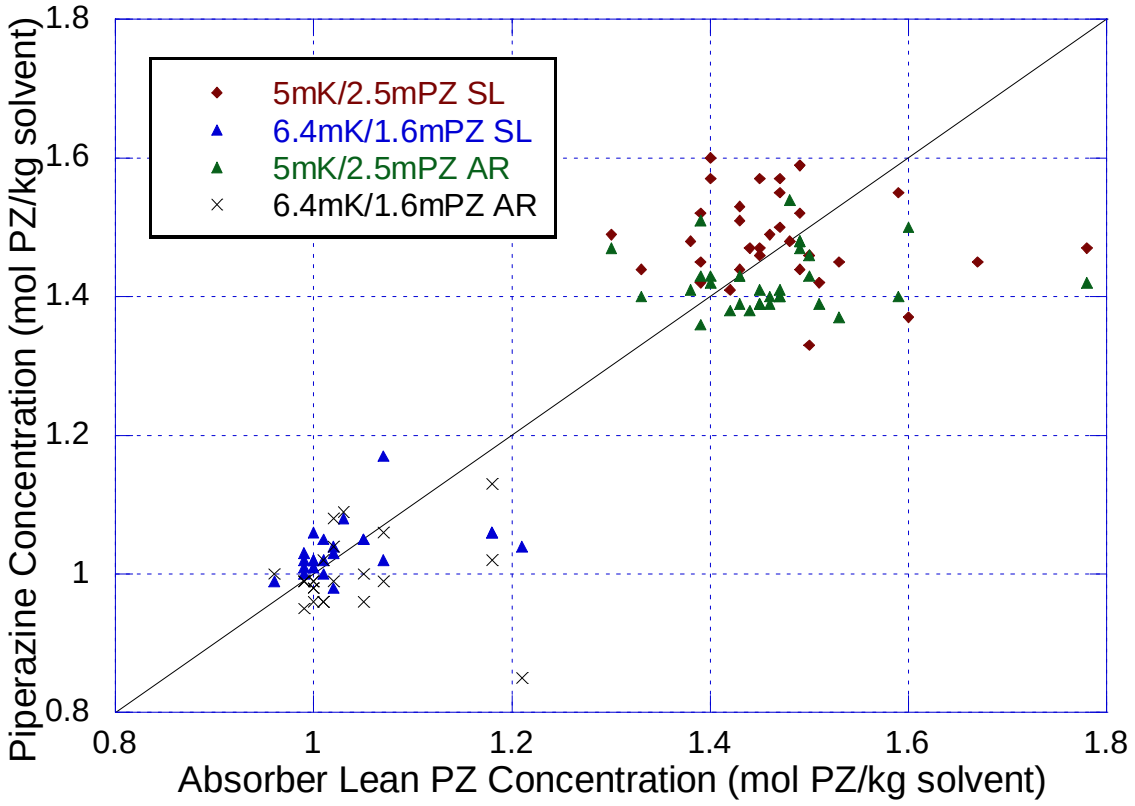

Figure 2-16. Piperazine Concentration of Absorber Lean (AL), Absorber Rich (AR), and Stripper Lean (SL) for Campaign 4

While the absolute values of the piperazine and potassium values may change from sample to sample due to changes in solvent density, the ratio of K^+ to PZ should remain the same. An analysis of the 5mK^+/2.5mPZ solution shows that a portion of the absorber lean K^+/PZ was 2.25 instead of 2.1. Closer examination of the piperazine and potassium data indicated the piperazine concentration for 25% of the data set was 6% lower than the stripper lean and absorber rich piperazine concentration. The piperazine concentrations for those points were corrected by a factor of 1.068 to give a K^+/PZ ratio of 2.11

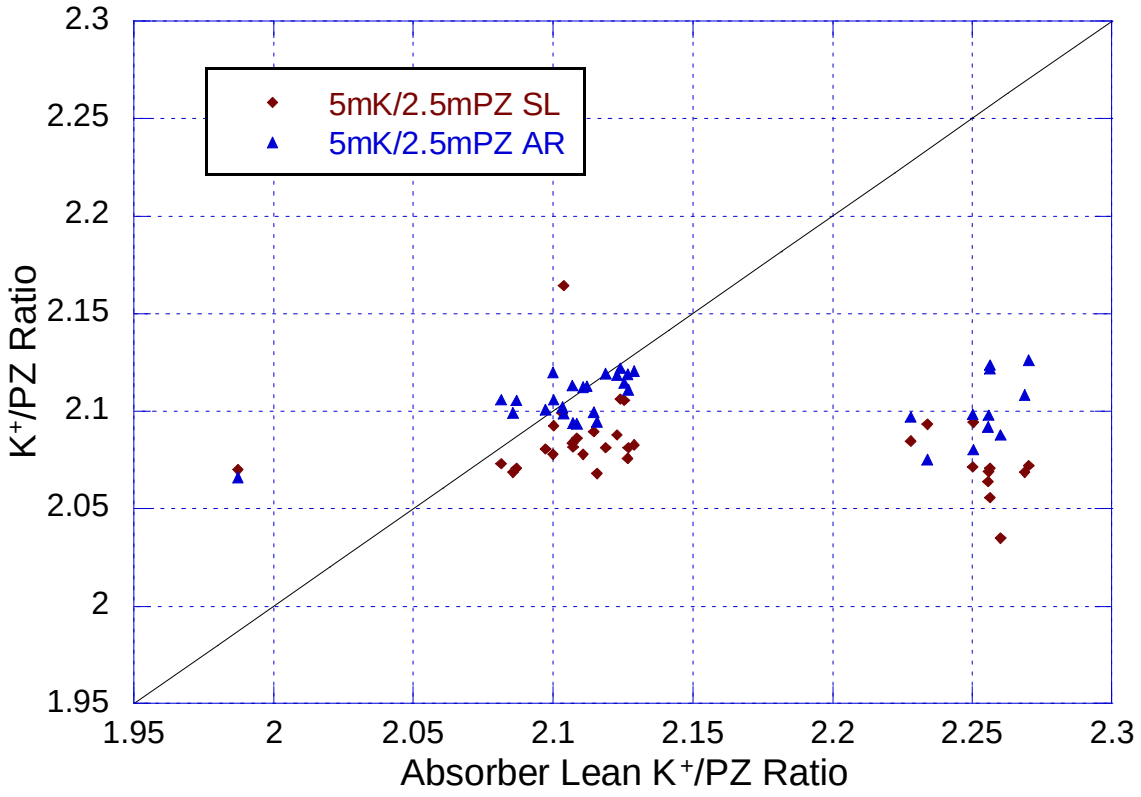

Figure 2-17. K^+/PZ Ratio Comparison Absorber Lean (AL), Absorber Rich (AR) and Stripper Lean (SL) for 5mK^+/2.5mPZ of Campaign 4

A similar analysis for the 6.4mK^+/1.6mPZ samples shows that the average K^+/PZ ratio for the three solvent streams was approximately 3.6 instead of 4 (Figure 2-18). The stripper leans samples matched relatively well with the absorber lean while the absorber rich points were just slightly higher than absorber lean (Figure 2-18). The figure also indicates that some of absorber lean points did not match the absorber rich and stripper lean. Also, some of the absorber rich points appeared to be consistently lower than the absorber lean. The outlying points were identified for data analysis.

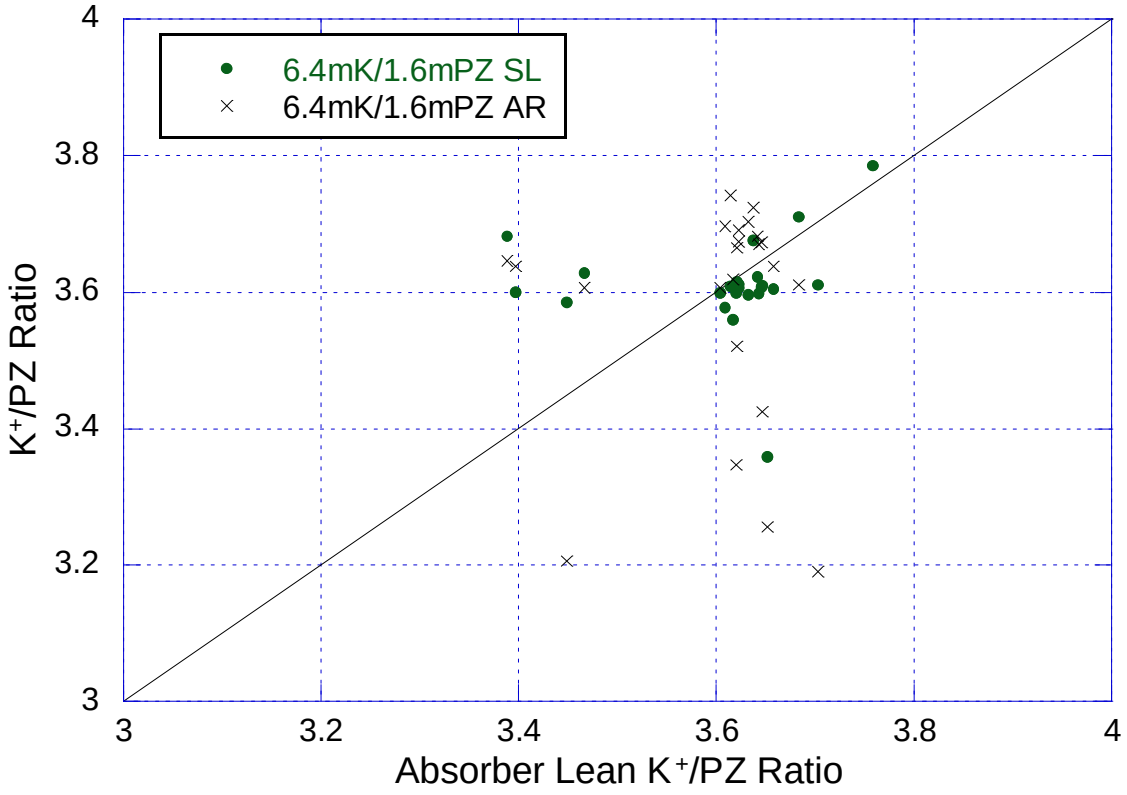

Figure 2-18. K^+/PZ Ratio Comparison Absorber Lean (AL), Absorber Rich (AR) and Stripper Lean (SL) for 6.4mK^+/1.6mPZ of Campaign 4

The total alkalinity (mol K^+ + 2 mol PZ) of the absorber lean, absorber rich, and stripper lean sample was calculated from the piperazine and potassium analysis. Figure 2-19 shows that the total alkalinity of the absorber rich was consistently lower than the absorber lean stream for the 5mK^+/2.5mPZ solvent, while the stripper lean points were on average slightly higher than the absorber lean points.

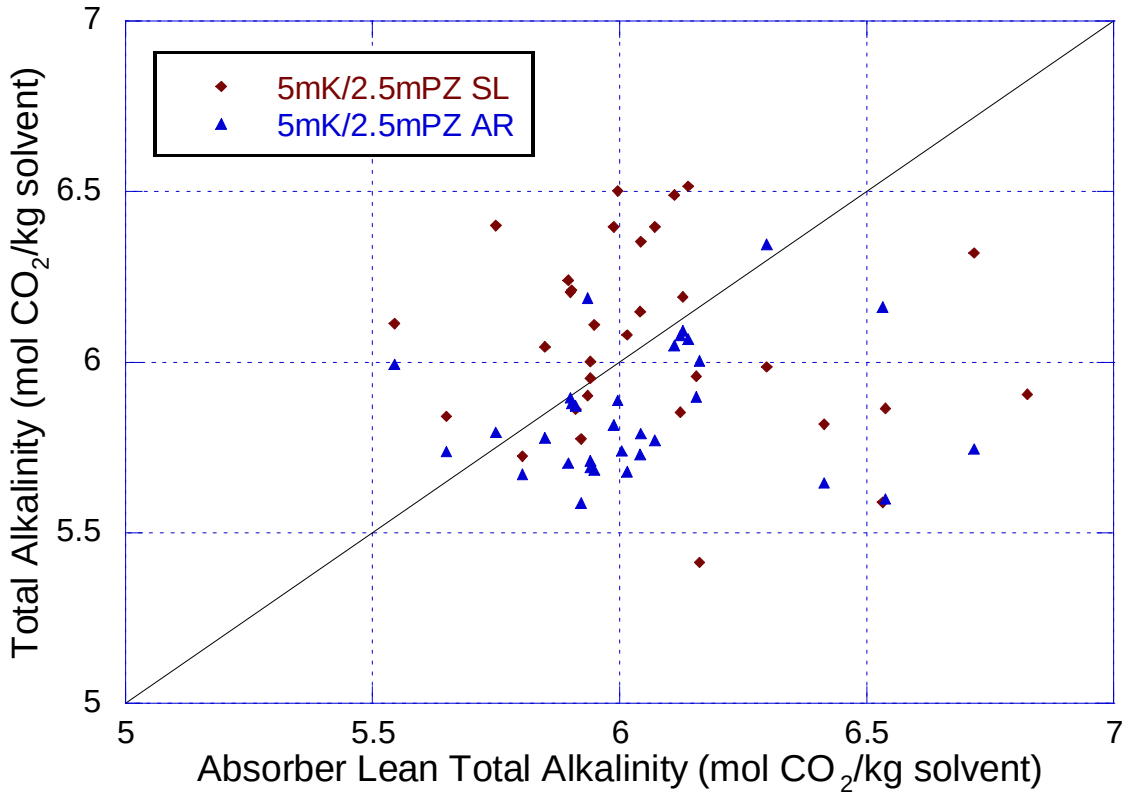

Figure 2-19. Total Alkalinity of Absorber Lean (AL), Absorber Rich (AR) and Stripper Lean (SL) for 5mK$^+$/2.5mPZ of Campaign 4

The total alkalinity was calculated for the 6.4mK$^+$/1.6mPZ absorber lean, absorber rich, and stripper lean samples (Figure 2-20). The stripper lean values appeared to be slightly higher than the absorber lean, while differences with absorber rich values were evenly distributed. Based on the data analysis performed, it was concluded that the ion chromatography analysis for piperazine and potassium concentration developed and used in this work produced results that were ±10%. It was also found that the titration method used in the initial analysis of piperazine and potassium produced results that were consistently lower than the ion chromatography method.

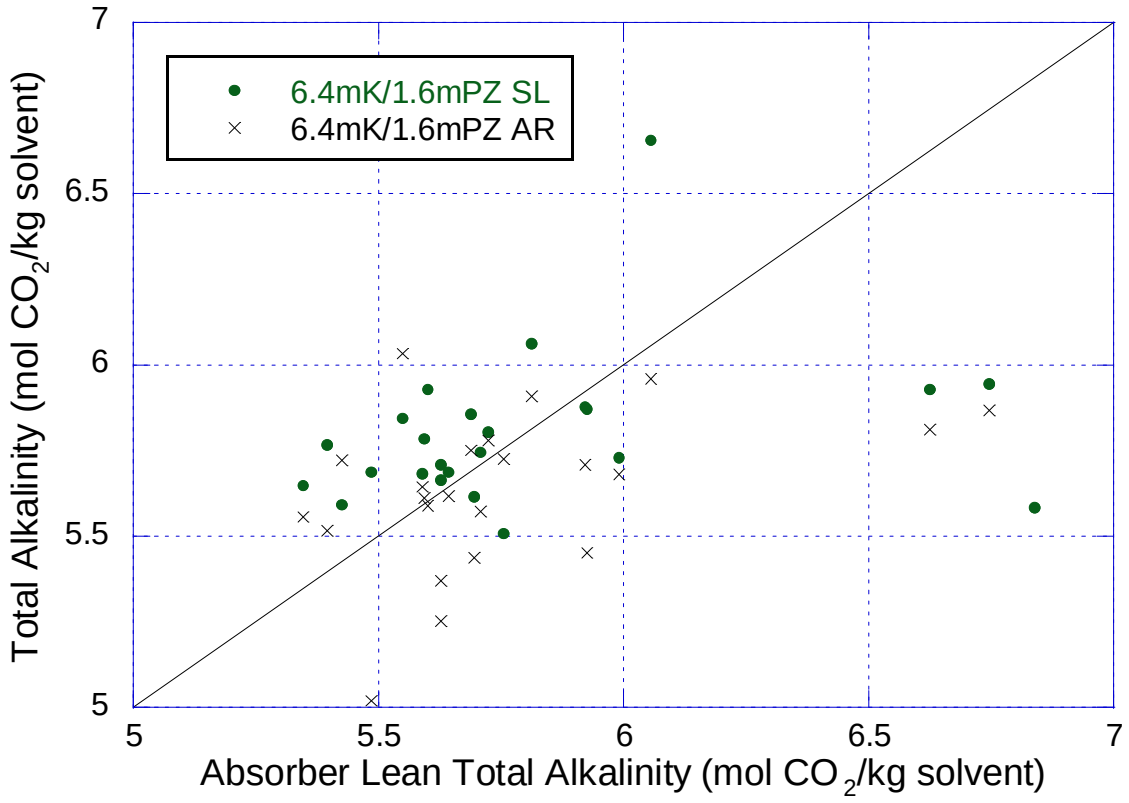

Figure 2-20. Total Alkalinity of Absorber Lean (AL), Absorber Rich (AR) and Stripper Lean (SL) for 6.4mK$^+$/1.6mPZ of Campaign 4

2.4 CO_2 LOADING

An analysis of the CO_2 loading for the absorber lean and stripper lean for Campaign 2 is shown in Figure 2-21. The loading for the two samples should match if the system is at steady state. The parity plot shows that there is some discrepancy between the absorber lean and stripper lean loading data. The absolute average deviation for the CO_2 loading of the two streams was 11.3%. This discrepancy may be related to some of the analytical issues and possible inconsistencies that were encountered during the loading analysis. It is also possible that the pilot plant was not at steady state and the

composition of the stripper lean was different from the absorber lean composition. Since the error appears to be randomly distributed, it is difficult to determine the exact cause.

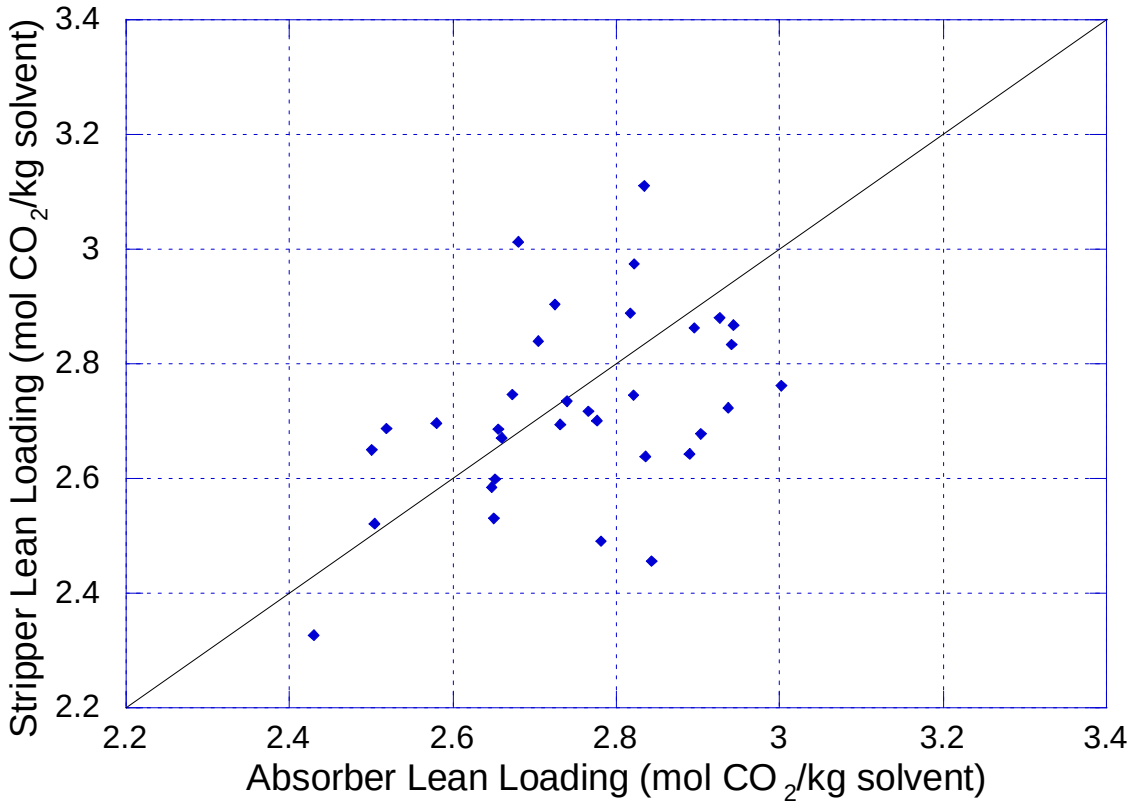

Figure 2-21. Absorber Lean and Stripper Lean CO_2 Loading for 5mK^+/2.5mPZ of Campaign 2

Figure 2-22 is a parity plot of CO_2 loading for the absorber lean and stripper lean of Campaign 4. The figure shows that the loading analysis was relatively reliable because the absorber lean and stripper lean loading matched relatively well. The absolute average deviation for the 5mK^+/2.5mPZ and 6.4mK^+/1.6mPZ solvents was 2.7% and 2.2%, respectively. The plot was used to eliminate outlying absorber lean and stripper lean loading points. The points that had deviations greater than 5% were flagged and/or eliminated.

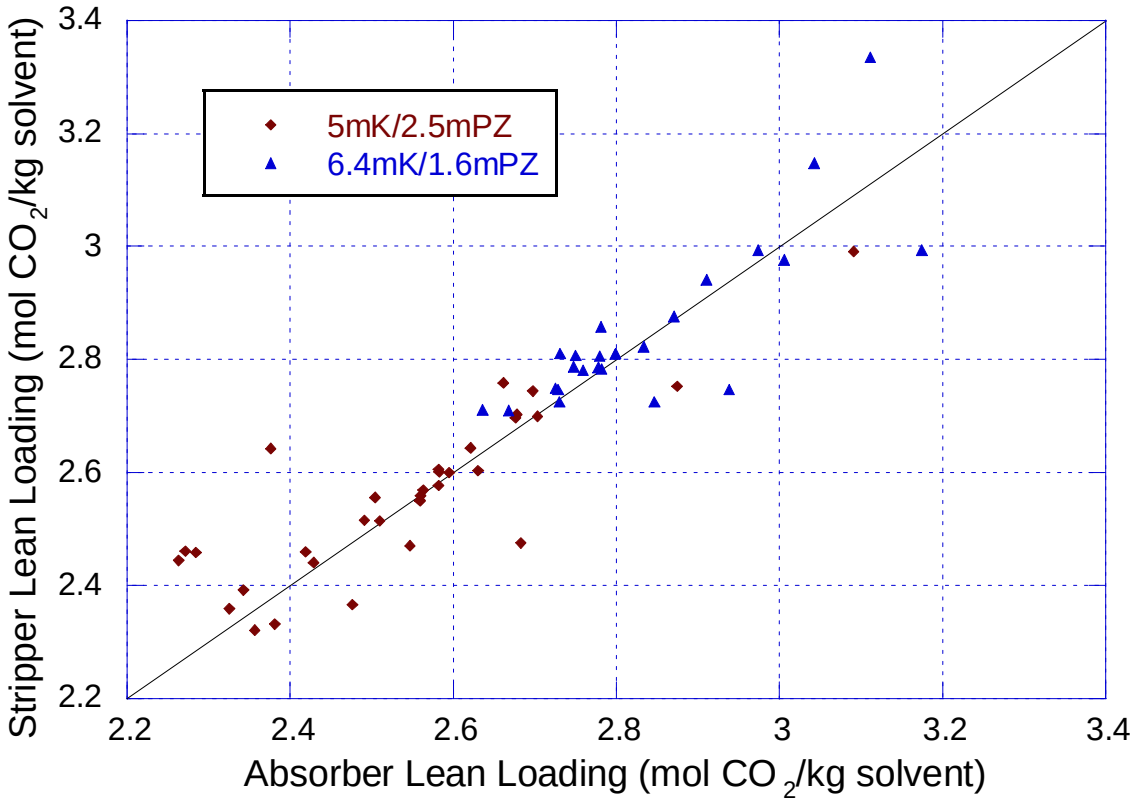

Figure 2-22. Absorber Lean and Stripper Lean Loading for 5mK$^+$/2.5mPZ and 6.4mK$^+$/1.6mPZ of Campaign 4

The capacity of a solvent is defined as the amount of CO_2 that is absorbed per unit mass of solvent. The capacity for the experimental runs was calculated by taking the difference in CO_2 loading between the absorber rich and absorber lean stream. A plot of the absorber lean and absorber rich loading for Campaign 4 shows that the 5mK$^+$/2.5mPZ solvent operated with a greater capacity than the 6.4mK$^+$/1.6mPZ solvent (Figure 2-23). The figure also shows that the range of lean loading for the two solvents was completely different. The 5mK$^+$/2.5mPZ solvent was operated at a lower range of lean loading, 2.3 to 2.7 mol CO_2/kg soln, while the 6.4mK$^+$/1.6mPZ solvent was operated from 2.6 to 3.2 mol CO_2/kg soln.

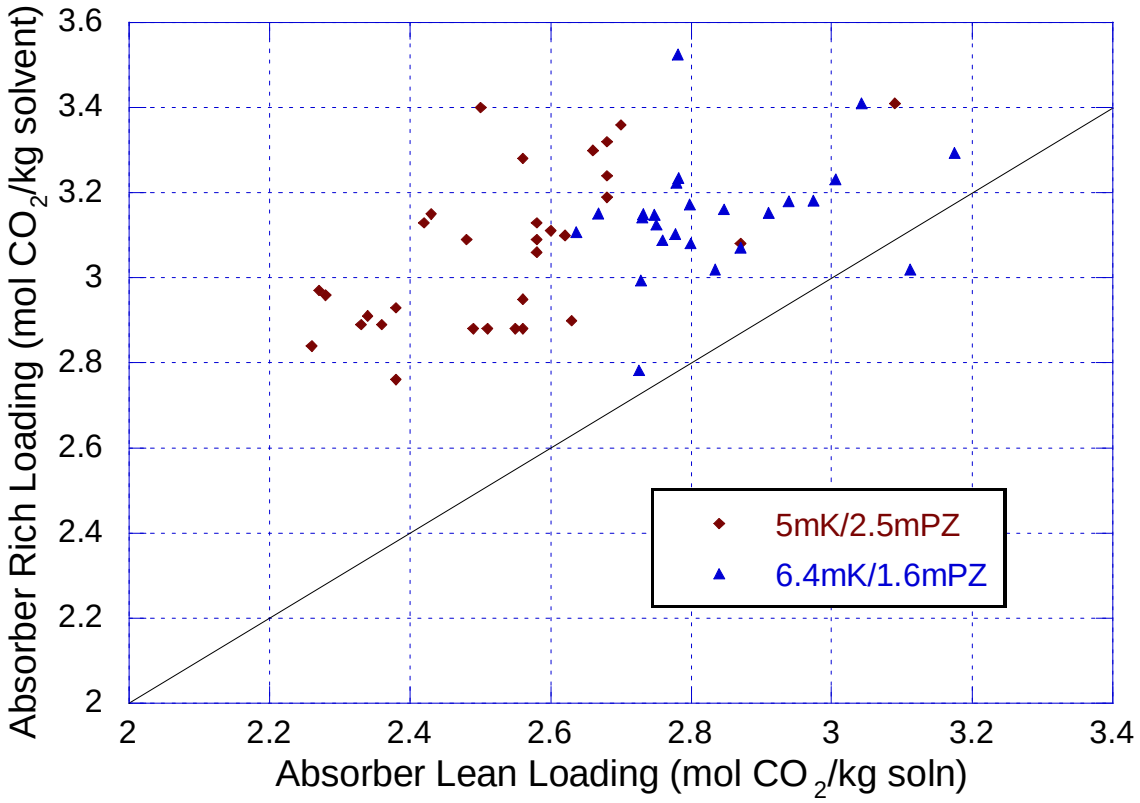

Figure 2-23. Absorber Lean and Absorber Rich Loading Comparison for 5mK$^+$/2.5mPZ and 6.4mK$^+$/1.6mPZ of Campaign 4

Direct correlations of solvent loading to absolute pH values are difficult to measure and often unreliable due to limitations and differences among pH meters. However, indirect measurement of CO_2 loading through pH provides the operator real-time feedback of process conditions and simplifies operation of the plant. The difference between the measured pH values for the absorber lean and absorber rich was plotted against the difference in CO_2 loading of the absorber lean and rich streams, or capacity, of the solvent (Figure 2-24). The figure shows that the liquid capacity for the 5mK$^+$/2.5mPZ solvent correlated well with the □pH, whereas there was some scatter with the 6.4mK$^+$/1.6mPZ data. Temperature corrections for the solvent and pH probe

were not applied. The automatic temperature compensation function for the pH meter had been disabled. The figure also shows that the 5mK$^+$/2.5mPZ solvent has a capacity that ranges from approximately 0.35 to 0.74 mol CO_2/kg soln, while the 6.4mK$^+$/1.6mPZ solvent has a capacity that ranges from 0.20 to 0.45 mol CO_2/kg soln. It was assumed that the measured pH values were more reliable than the CO_2 loading analysis. Therefore, the figure shows that the some of the loading measurements for 6.4mK$^+$/1.6mPZ solvent contained significant error. The plot can be used to determine the correct value of the erroneous loading measurements. By taking the difference in pH and knowing at least one of the loading points are accurate, the incorrect loading measurement can be calculated from the capacity plot. This method was not used in the analysis of the pilot plant data.

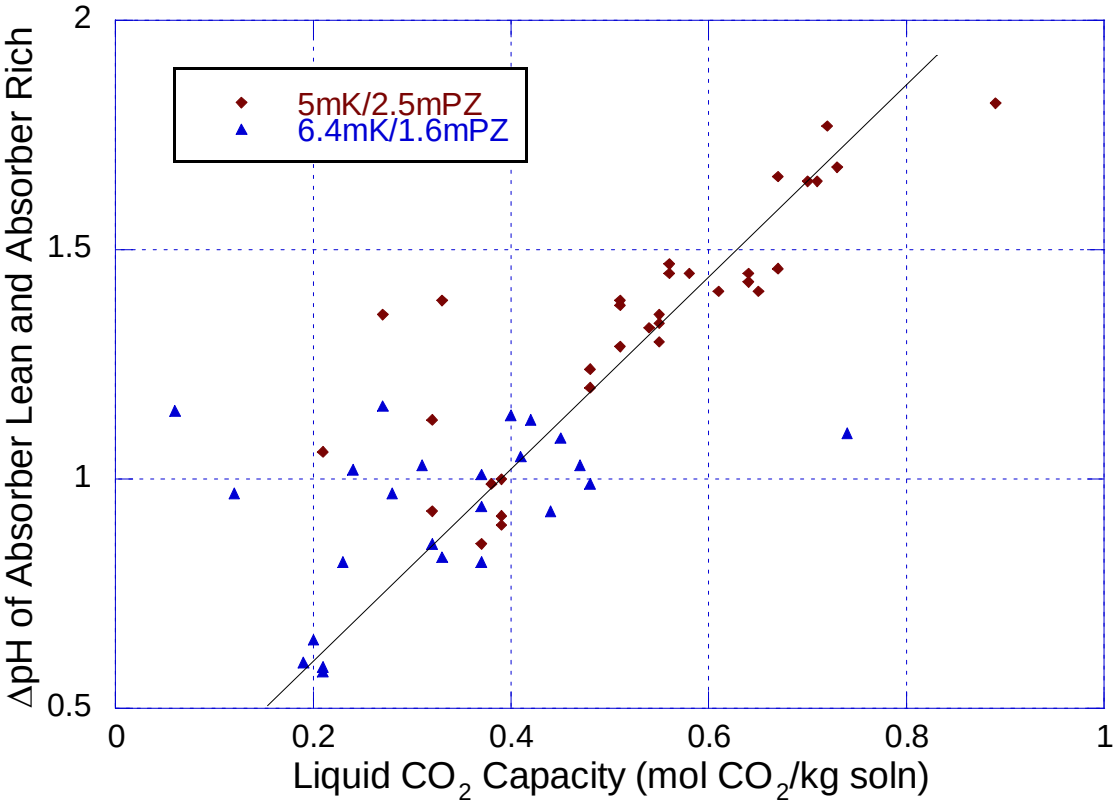

Figure 2-24. Liquid CO_2 Capacity and pH Difference Between Absorber Lean and Rich for 5mK^+/2.5mPZ and 6.4mK^+/1.6mPZ of Campaign 4

The pH and loading measurements obtained in Campaign 4 are shown in Figure 2-25. The plot shows that the pH decreases with an increase in CO_2 loading of the solution. The figure shows that there is quite a bit of scatter with the pH and loading measurements. Correlation of absolute pH measurements with CO_2 loading were difficult to obtain because the water content was constantly changing. Also, due to the high ionic strength of the solvent, the pH measurements were not reliable. In addition, the pH meters could only be calibrated at the beginning of each campaign. Instrument drift or pH probe degradation over time will affect absolute pH measurement. Finally, the accuracy of the loading measurements will contribute to some of the error.

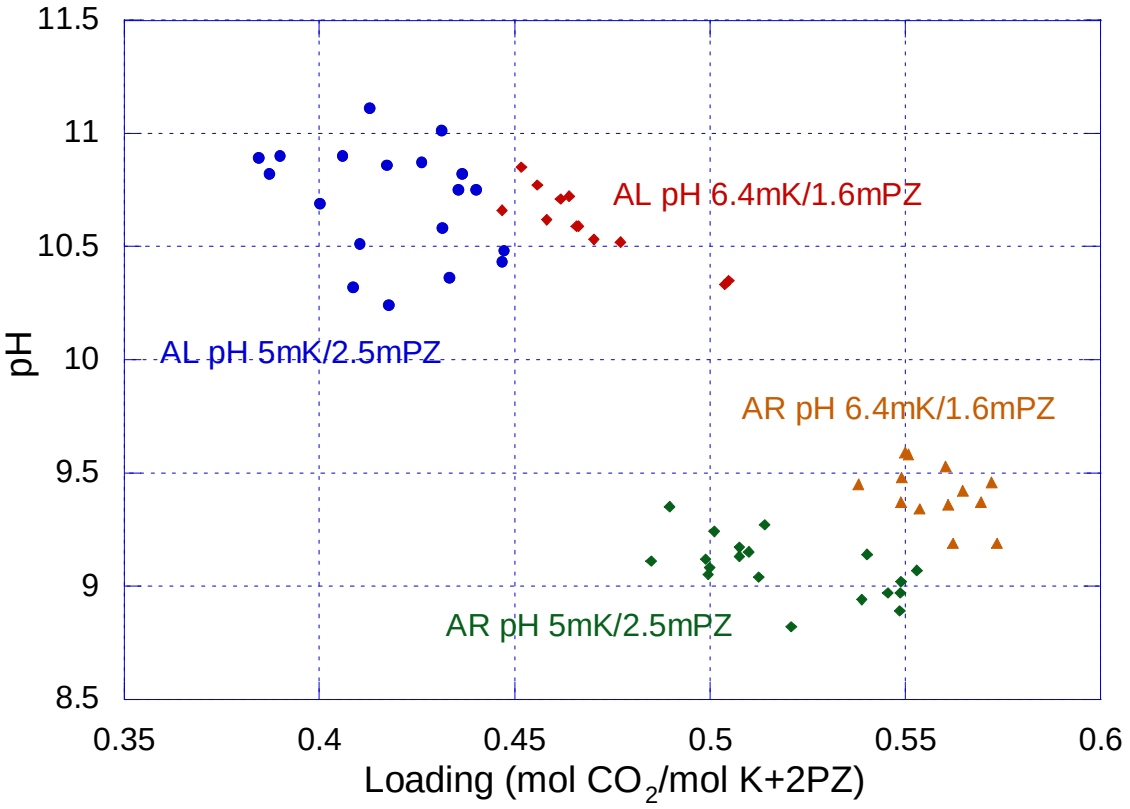

Figure 2-25. Loading and pH Measurements for Absorber Lean (AL) and Absorber Rich (AR) of Campaign 4

2.5 GAS FLOW RATE

In the first two campaigns, the gas flow was measured with a Dietrich Standard AN-75 annubar and Ashcroft pressure transmitters in a 20.3 cm diameter PVC pipe. There were some issues with the Ashcroft transmitters and they were eventually replaced with Rosemount 3051 pressure transmitters. The replacement date of the pressure transmitters is unclear, but may have occurred during Campaign 2. The gas flow rate was verified using a pitot tube traverse in February 2004, before the start of Campaign 1 and was determined to be relatively accurate.

In Campaign 3, the 20.3 cm diameter gas line was replaced with smaller diameter gas lines, 7.6 cm and 10.2 cm schedule 40 PVC pipe and new annubars were installed in each of the gas lines. During the operation of Campaign 3, there were some issues with the gas rate measurement. When the gas flow was shut off, the transmitter still displayed a relatively large flow rate. The gas flow was manually zeroed in DeltaV to correct the offset.

In Campaign 4, the two PVC gas lines were replaced with a single 10.2 cm diameter Schedule 10 stainless steel pipe and the annubar used in the previous campaign was reinstalled. A correction factor for the new inner diameter was applied in DeltaV. The gas flow rate was not re-evaluated after the modifications made in Campaign 3 and 4. However, packing tests performed after Campaign 3 and 4 have demonstrated

comparable pressure drop values as reported by the vendors. Analysis of the real-time gas flow indicates that the measurements are consistent.

The gas flows for all of the annubars were calibrated for pure air. However, during the operation of the CO_2 capture pilot plant, the composition of the gas contained between 3 to 18% CO_2 and from 2 to 10% H_2O. Therefore, the molecular weight of the air stream was corrected to reflect the difference in composition. The correction term was applied as the square root of the ratio of the two molecular weights of the gases. The correction term reduced the measured gas rate by approximately 3–5%.

2.6 CO_2 GAS CALIBRATION STANDARDS

In the second campaign, it was erroneously concluded that the CO_2 calibration gas cylinders were based on a weight percent instead of volume percent. If it was assumed that the gases were weight percent, the material balance for the gas phase seemed to match the liquid phase. When the sales representative of the gas provider was initially consulted, we were informed that the cylinders were filled gravimetrically and it was assumed that the percentages were weight based. Therefore, in MEA campaign, a gas cylinder for 17% was purchased and used to calibrate the CO_2 analyzers. It was assumed that the 17% was in weight percent, which was equivalent to 12 mole percent.

However, after the completion of the Campaign 4, the material balance did not close when a weight based assumption was made. Further investigation into the matter and additional contacts with the manufacturer indicated that the concentrations were indeed volume percent and not mass percent. To further corroborate this, some of the cylinders were tested.

The CO_2 calibration gas verification experiments were conducted on a gas chromatograph (GC) analyzer from the Freeman research group at the UT Pickle Research Center. The GC is normally calibrated using methane and carbon dioxide and therefore it was recognized that the results may slightly be off. The experiment was conducted by one of the members of the research group and the standard operating procedure was followed. The 12% and 16.9% CO_2 gas cylinders were tested. First, gas from the CO_2 cylinder was flowed to a mass flow controller and the volumetric flow was measured using a soap bubble flow meter. Next, the CO_2 gas was diluted with helium and the total gas flow was measured using the soap bubble flow meter. The gas mixture was then sent to the GC for analysis.

The results for the 12% and 16.9% were 13.2 mol% and 18.3 mol%, respectively. If a mass concentration was assumed for the gas cylinders, the concentrations would have been 8.3 mol% and 11.8 mol%. Since the results were much closer to the mole percent value, it was concluded that the cylinders were such. However, the correction of the CO_2 concentration implies that perhaps the gas rate, liquid rate or liquid loading analysis were incorrect or incorrectly used for the material balance of the first 2 campaigns.

2.7 CO_2 GAS ANALYZER CALIBRATION

The Vaisala and Horiba analyzers are calibrated on a dry basis with Primary Standards for 1%, 4%, 4.9%, 12%, and 16.9 mol% CO_2 purchased from Praxair, Inc. The Vaisala analyzers are located in situ and provide real time CO_2 gas measurements, while the Horiba uses an extractive sampling system. Although calibrations are performed on a dry basis, online Vaisala measurements of CO_2 are taken under wet, sometimes even

condensing conditions. The gas stream for the Horiba analyzer, on the other hand, is conditioned and the water is removed prior to analysis.

An analysis of the method, procedure, and results for the calibration of the CO_2 analyzers was performed and a few errors were discovered. In Campaign 1 and 2, linear calibration curves were used whereas in Campaign 3 and 4, a second order polynomial was used to fit the calibration curve. Once the calibration curves are created, the parameters are inputted into the DeltaV process control system and need to be uploaded into DeltaV in order for the changes to take effect. If the new parameters are not uploaded, DeltaV continues to use the original calibration parameters.

A review of the logged CO_2 gas concentration data found that the calibration parameters for Campaign 2 were not properly updated. A comparison of the process screen printouts and logged data showed that the calibration curve parameters for the outlet CO_2 concentration had not been uploaded and updated after the 11/02/04 calibration. The printout indicated that the 10/27/04 calibration parameters were being used for the CO_2 outlet. In addition, it is possible that the inlet calibration curve had also not been updated, which may be significant since the slope of the calibration curve for the Horiba had changed from 1.24 to 1.42. The material balance for Campaign 2 did not close after the pilot plant was reconfigured for vacuum operation, which also corresponded to when the analyzer was recalibrated on 11/02/04.

In addition, it was later discovered that the raw signals for the CO_2 concentration were being logged by DeltaV instead of the calibrated values. The error was discovered at the conclusion of all four pilot plant campaigns by comparing the online process

screens that were printed to the logged data. In Campaign 1, was also discovered that the raw signals for the inlet and outlet CO_2 were logged instead of the calibrated values. In Campaign 2 and 4, the raw outlet CO_2 concentration was again logged, while the corrected inlet CO_2 concentration was logged. The raw outlet CO_2 concentration for Campaign 3 was also likely logged, but this was not verified. The erroneous inlet and outlet CO_2 concentrations for Campaign 1, 2 and 4 were updated using the log sheet for the CO_2 calibration curves.

The calibration date and parameters for the CO_2 analyzer calibration curves for Campaign 1, 2, 3, and 4 are listed in Tables 2-2, 2-3, 2-4, and 2-5, respectively. The calibration curves for Campaign 3 and 4 have been refitted to a linear equation instead of a polynomial to facilitate comparison. Three to four calibration points were used to generate the calibration equations, which all had R^2 values greater than 0.999.

Table 2-2. Campaign 1 CO_2 Gas Analyzer Calibration Date and Equations

Date	Time	CO_2 In Vaisala 0-20%	CO_2 Mid Horiba 0-5%	CO_2 Out Vaisala 0-1%
6/15/04		y = 1.0359x + 0.0045	-	-
6/18/04	9:37	y = 1.0234x + 0.0219	y = 0.3087x - 1.193	y = 1.1001x - 0.0154
6/23/04	9:00	y = 1.0555x - 0.0166	y = 0.4278x - 1.7112	y = 1.0373x - 0.0373
6/24/04	7:30	y = 1.0355x + 0.0085	y = 0.4479x - 1.7237	y = 1.0808x - 0.0203

Table 2-3. Campaign 2 CO_2 Gas Analyzer Calibration Date and Equations

Date	Time	CO_2 In Horiba 0-20%	CO_2 Out Vaisala 0-5%
10/24/04		-	y = 1.1534x - 0.0528
10/25/04	16:59	y = 1.2631x - 4.8906	-
10/26/04		y = 1.2342x - 4.7243	-
10/27/04		y = 1.2383x - 4.8413	y = 1.1529x - 0.0305
11/02/04		y = 1.4169x - 5.4974	y = 1.1008x - 0.0562

Table 2-4. Campaign 3 CO_2 Gas Analyzer Calibration Date and Equations

Date	Time	CO_2 In Vaisala 0-20%	CO_2 Mid Horiba 0-20%	CO_2 Out Vaisala 0-5%
2/25/05	15:00	y = 0.9927x - 0.0318	y = 1.5533x - 6.2009	-
2/28/05	-	-	-	y = 1.1079x - 0.0744
3/08/05	17:35	-	y = 1.5675x - 5.7953	-
3/14/05	-	-	-	y = 1.1179x - 0.0508
3/17/05	-	y = 0.9731x - 0.0265	y = 1.5583x - 5.7671	y = 1.1049x - 0.0650
4/05/05	-	y = 0.9731x + 0.0114	y = 1.6127x - 5.9312	y = 1.1988x - 0.0580
4/14/05	-	y = 0.9221x + 0.0531	y = 1.5916x - 5.9856	y = 1.1980x - 0.0752

Table 2-5. Campaign 4 CO_2 Gas Analyzer Calibration Date and Equations

Date	Time	CO_2 In Vaisala 0-20%	CO_2 Mid Horiba 0-20%	CO_2 Out Vaisala 0-5%
11/07/05	12:29	y = 0.9473x - 0.0004	y = 1.5856x - 6.3451	y = 1.2264x - 0.1223
1/10/06	7:55	y = 0.9560x - 0.1172	y = 1.6613x - 6.5822	y = 1.1508x - 0.1399
1/18/06	13:18	y = 0.9443x - 0.0863	y = 1.7545x - 6.7772	y = 1.2164x - 0.1403
FTIR		CO_2 In	-	CO_2 Out
1/10/06	7:55	y = 1.0885x - 2E-05	-	Same

The tables show that the slope of the calibration curve for the 0-5% Horiba analyzer increased by 30% from the 6/18/04 to 6/23/04 calibration, but remaining relatively constant in the calibration the following day. The high concentration Horiba analyzer (0-20%) steadily increased with each campaign, changing from 1.23 to 1.75. In

Campaign 2, the slope changed by approximately 15% for the 11/02/04 calibration. In Campaign 3, the slope for the Horiba remained relatively constant and fluctuated between 1.5 and 1.6. In Campaign 4, the slope increased from 1.66 to 1.75, an increase of 5.4%. Also, the Horiba produces a 4–20mA signal, which should give an offset of 4. The tables show that the calibration curve intercept increased from 4.7 to 6.8 over the course of the three campaigns.

In Campaign 1, the slope of the inlet 0-20% Vaisala CO_2 analyzer remained relatively constant, fluctuating between 1.02 and 1.06. In Campaign 2, the inlet 0–20% Vaisala CO_2 analyzer failed at the beginning of the experiments due to excessive moisture in the gas. A new 0–20% Vaisala probe was purchased and installed for Campaign 3. The inlet 0-20% Vaisala CO_2 analyzer was calibrated a total of four times during Campaign 3. At the start of the campaign, the slope the calibration curve was 0.99 and eventually drifted down to 0.92. Prior to the start of Campaign 4, another 0 – 20% Vaisala probe was purchased. The new probe was installed and the old probe was retained as the backup in event of another probe failure. In Campaign 4, the inlet Vaisala analyzer was calibrated twice and remained relatively stable. The slope for the calibration equations varied between 0.96 and 0.94 and intercept varied from 0.11 to 0.09.

The outlet 0-5% Vaisala CO_2 analyzer also appeared to remain relatively stable. In Campaign 1, the slope of the calibration curve ranged from 1.04 to 1.10 (~5% difference). In Campaign 2, the slope of the calibration curve also varied by 5%, changing from 1.15 to 1.10. In Campaign 3, the slope of the calibration changed from 1.11 to 1.20, a difference of 10%. In Campaign 4, a new 0–5% Vaisala probe was

installed, but the existing transmitter was retained. The slope of the calibration curve was 1.15 at the beginning of the campaign had slightly drifted to 1.22 when the analyzer was recalibrated at the start of the 6.4mK^+/1.6mPZ solvent composition change.

In Campaign 4, the FTIR was calibrated at the start of the campaign (1/10/06) with the same CO_2 gas standards used for the Horiba and Vaisala following the same standard procedure. A calibration curve was generated and the parameters were entered into the DeltaV system. The slope of the calibration curve was determined to be 1.09. On 1/23/06, the baseline for the FTIR was re-zeroed. There is some concern regarding the results of the FTIR calibration. First, the FTIR had previously been calibrated in the laboratory and according some sources, did not need to be recalibrated once transported into the field. If this is true, this indicates that either the 3 gas cylinders used to calibrate the FTIR were all off by 9% or there was a leak in the sample gas line.

During the analysis of the CO_2 gas concentration, it was found that the response for FTIR and Horiba lagged slightly behind that of the Vaisala analyzers, due to extractive sampling methods used by both analyzers. At each sample point, the data points 10 minutes before and after were averaged. The amount of time that the FTIR and Horiba data was shifted was evaluated on a case by case basis. The trend lines for all of the CO_2 gas concentrations were plotted and visually matched up. The logged values for the FTIR were shifted by 4 minutes for the data taken on the 10, 11, 12, 18, and 19th. The data taken on the 11th was shifted by 5 minutes. The data for remaining dates were shifted by 8 minutes. The Horiba data was shifted by 3 minutes for 1/12 and by 1 minute for 1/18 and 1/19. The remaining points were shifted by 2 minutes. In some cases, some

of the FTIR points were deleted from the average because it occurred during the period when the location of the FITR analysis was switched from inlet to outlet or vice versa.

Some possible sources of error for the CO_2 analyzers include differences in the flow rate between the calibration and the flow rate once the analyzers are placed into service. If the sample gas rate is different than the calibration flow rate, there may be slight discrepancies with the measured CO_2 concentration. In addition, it is possible that there may have been slight leaks in the sample gas lines. The Horiba sampling system consists of an initial water knockout, a sample pump, another water knockout and a membrane for further drying. During the operation of the pilot plant, the initial knockout continuously condensed out water from the system and may have contained a residual solvent that may skew the results by absorbing CO_2. In addition, a portion of the sample gas is diverted through the second water knockout and the residual gas is sent to the Horiba analyzer for analysis. A rotameter on the outlet of the Horiba analyzer was used to control the sample gas flow rate. Depending on the conditions in the absorber, there appeared to be some variation in sampling gas rate as the rotameter on the outlet of the Horiba needed to be adjusted periodically and this may have contributed to some discrepancies in the analysis.

2.8 CO_2 GAS CONCENTRATION

Figure 2-26 shows that the inlet CO_2 gas concentration measured by the FTIR and Vaisala analyzers matched relatively well. The absolute average deviation for the $5mK^+/2.5mPZ$ and $6.4mK^+/1.6mPZ$ solvents was 1.2% and 1.7%, respectively. However, both gas concentrations were measured on a wet basis and were expected to be different

because the water content for the two locations should have been different. Wet and dry CO_2 calibration experiments performed on the Vaisala CO_2 analyzers indicated that the sensors were responsive to water vapor pressure. A gas mixture of CO_2 and air was preheated and humidified prior to analysis by the Vaisala. The results showed that increases in water vapor resulted in a proportionate decrease in reading for CO_2 concentration. However, the water vapor concentration was adjusted by increasing the temperature and the changes may have partially been a result of the effect of temperature on the Vaisala analyzers.

The inlet Vaisala analyzer is located upstream of the steam injection and was assumed to be at the annubar temperature, which varied between 16 to 27°C, which results in a saturated water concentration ranging from 1.8 to 3.5 mol%. The FTIR, on the other hand, was analyzed at gas temperature that was approximately 40°C, which results in a saturated water concentration of 7.3 mol%.

One possible interpretation of the unexpected discrepancy is that while the steam injection may have heated the gas to 40°C, the gas may not have been fully saturated. This resulted in water concentrations comparable to the conditions at the Vaisala analyzer. It was also observed that the Vaisala probes were wet and had condensing water. A thin paper-like membrane is used in the Vaisala probes to prevent water from contacting the working parts of the probe. However, the membrane is not mechanically sealed and there is a possibility of water leakage. The Vaisala probes are designed to work in non-condensing environments. In Campaign 2, the inlet Vaisala CO_2 analyzer failed mostly likely because condensing water had penetrated the membrane. It was concluded that the

selection of the in situ Vaisala analyzers was useful for real time feedback for use in process control, but not suitable for accurate measurements of CO_2 in a pilot plant environment. Finally, the liquid used for the steam injection is taken as distillate from the stripper condenser and may have contained residual amounts of piperazine and may have depressed the vapor pressure of water.

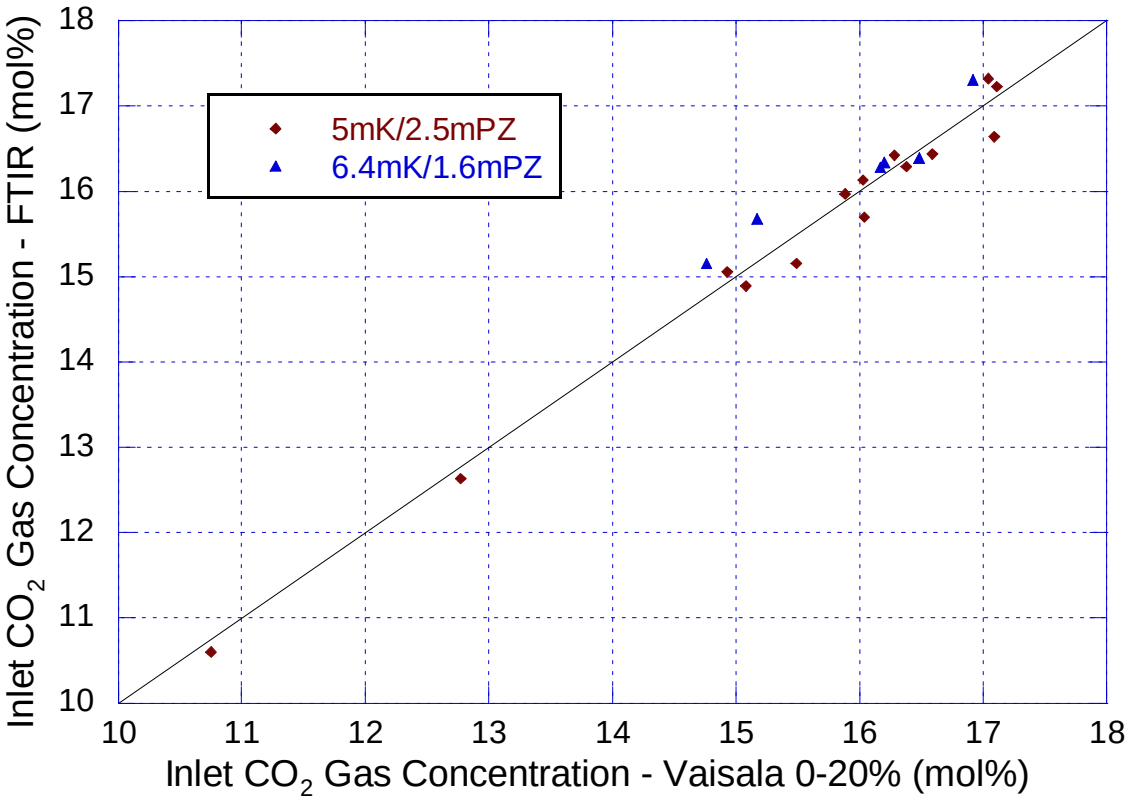

Figure 2-26. Campaign 4 Inlet CO_2 Gas Concentration of Vaisala 0-20% and FTIR (Wet Basis) for 5mK^+/2.5mPZ and 6.4mK^+/1.6mPZ

The outlet CO_2 gas concentration (wet basis) measured by the FTIR and Vaisala analyzers also matched relatively well (Figure 2-27). The absolute average deviation for the 5mK^+/2.5mPZ and 6.4mK^+/1.6mPZ solvents was 5.7% and 1.3%, respectively. The two measurements of CO_2 were expected to be different because of the water content and

gas temperature. The FTIR withdraws the gas sample directly from the head section at the top of the absorber, whereas the Vaisala analyzer, which is located downstream of the FTIR, analyzes gas that has passed through the air cooler, a water knockout and is at a temperature of 10 to 16°C. However, the equilibrium vapor pressure of water exiting the absorber will be lower than that of pure water because of the presence of potassium carbonate and piperazine.

Also, the outlet Vaisala analyzer was operated under a slight vacuum (-0.4 – 1.5 kPag) and it was possible that there may have been a slight leak. The diameter of the Vaisala probe was a non-standard metric size and was inserted in the gas pipe using a Swagelok fitting with Teflon ferrules. While the seal around the outside of the probe may have been sufficient, it is unknown whether the probe itself was gas tight. There is a cable that connects the probe to the transmitter and the seal between the probe and cable was probably not designed to be gas tight. Therefore, depending operating conditions and vacuum pressure a slight leak may have been possible.

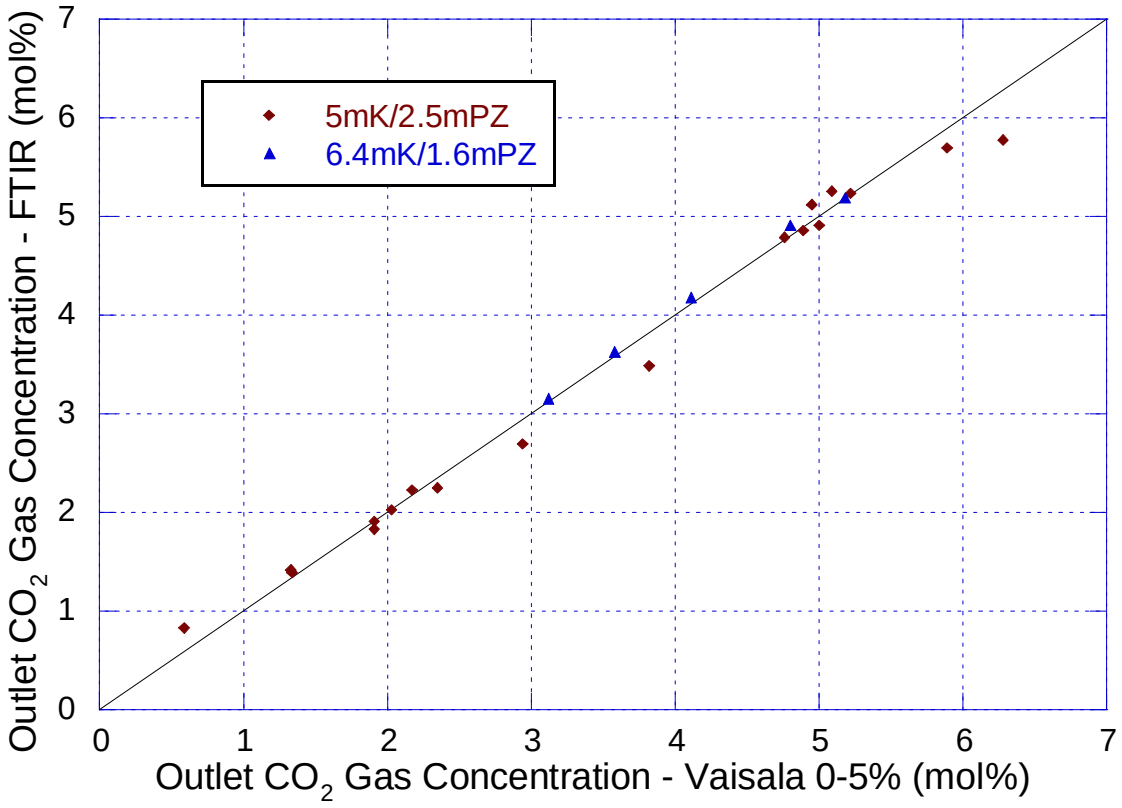

Figure 2-27. Campaign 4 Outlet CO_2 Gas Concentration of Vaisala 0-20% and FTIR (Wet Basis) for 5mK^+/2.5mPZ and 6.4mK^+/1.6mPZ

2.9 H_2O Gas Concentration

The concentration of water in the gas is important for determining the concentration of CO_2 in the gas. The absorber inlet and outlet water concentration was measured with the FTIR and was used as way to verify assumptions made regarding water content in the gas. The saturated vapor pressure of water calculated at the measured inlet and outlet gas temperatures and plotted against the values obtained by the FTIR (Figure 2-28).

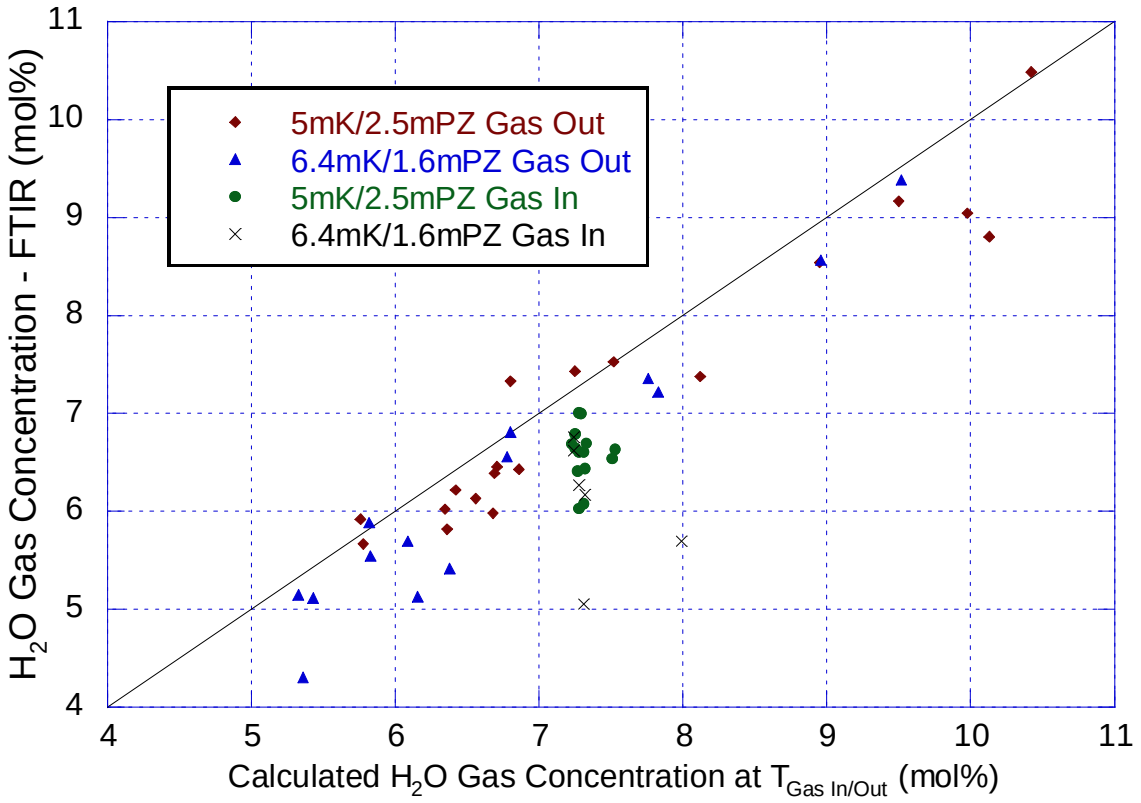

Figure 2-28. Gas Phase H_2O Concentration Measured by FTIR and Calculated Values Assuming Saturation at Measured Inlet and Outlet Gas Temperatures for 5mK^+/2.5mPZ and 6.4mK^+/1.6mPZ of Campaign 4

The calculated vapor pressure of water assumed that the solvent was pure water and may not be valid for the outlet gas because the solvent contained piperazine and potassium carbonate. Therefore, the vapor pressure of water for the outlet gas should be slightly depressed. The absolute average deviation of the measured outlet water concentration was 5.5% and 7.9% lower than the calculated values for the 5mK^+/2.5mPZ and 6.4mK^+/1.6mPZ solvent, respectively. The absolute average deviation of the measured inlet water concentration was 10% and 17.4% lower than the calculated values, for the 5mK^+/2.5mPZ and 6.4mK^+/1.6mPZ solvent, respectively. The variation of the measured values is most likely due to the close proximity of the FTIR inlet sample port to

the steam injection point. The gas was not well mixed at the sample point and resulted in erratic water measurements. In addition, the depressed values may be due to the presence of residual solvent in the distillate. This was confirmed when the absorber gas preheater had to be shut down to remove solvent residue that had accumulated over time on the reboiler tubes.

The vapor pressure of water over the 5mK^+/2.5mPZ solvent was calculated with the Hilliard Aspen Plus® VLE model using a flash calculation from 25 – 60°C. Figure 2-29 shows that the vapor pressure values predicted by Aspen Plus® are approximately 14 – 14.5% lower than that predicted by the DIPPR equation over pure water. The points predicted by the VLE model were fitted to a second order polynomial is given by:

$$P_{H_2O\ AspenPlus} = 8.8518 \times \left(T(^\circ C)\right)^2 - 348.12 \times \left(T(^\circ C)\right) + 6016.7 \quad (2.1)$$

The values given the outlet FTIR would most likely correspond to the values predicted by the Aspen Plus® VLE model, but the FTIR values were not as low as that predicted by the simulation. However, the FTIR sample was taken approximately 7 meters upstream of the outlet gas temperature measurement, which may have been at a higher temperature. Thus, a higher water vapor pressure would be expected. Also, the measured pressure at the top of the absorber column may not have corresponded to the value at the FTIR sample location and will slightly affect the mole percent reading of the FTIR. Finally, the values of the water vapor pressure predicted by the Aspen Plus® model may not be completely accurate.

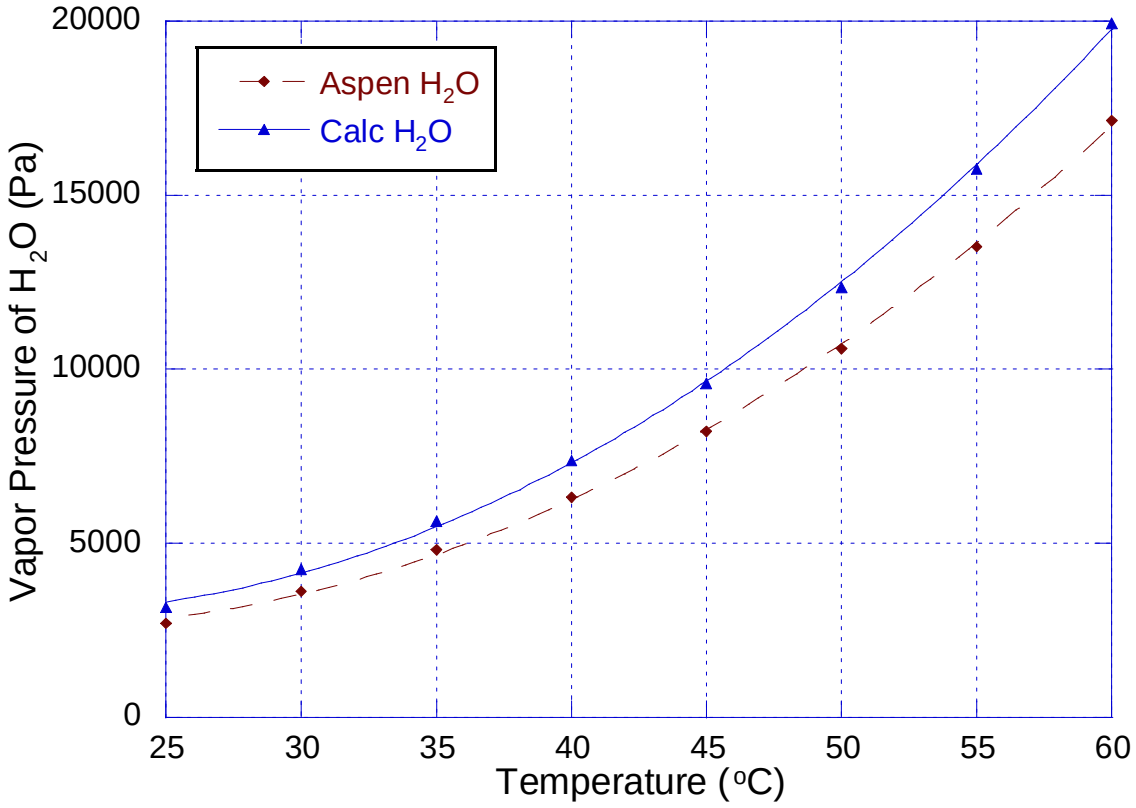

Figure 2-29. Predicted Vapor Pressure of Water Using Hilliard Aspen Plus® VLE Model and Calculated Vapor Pressure Over Pure Water

2.10 DATA RECONCILIATION

2.10.1 Stripper Lean Density

The density of the stripper lean measurements for Campaign 4 was adjusted to match the absorber lean measurements. Based on bench-scale density measurements made in Campaign 4, the dependence of temperature of the solvent was correlated and found have an average slope of -0.000542±0.0000095. The measured absorber lean and stripper lean densities were corrected to 40 °C and correlated based on a parity plot. For $5mK^+/2.5mPZ$ solvent, the density was corrected by the following equation:

$$\rho_{CORR,SL} = 1.0343 \cdot \rho_{SL,5K/2.5PZ} - 0.0401 \qquad (2.2)$$

For the 6.4mK$^+$/1.6mPZ solvent, the density was corrected by the following equation:

$$\rho_{CORR,SL} = 1.0419 \cdot \rho_{SL,6.4K/1.6PZ} - 0.0515 \tag{2.3}$$

where ρ has units of g/cm^3. The corrected density measurements are enumerated by the following table:

Table 2-6. Campaign 4 Corrected Stripper Lean Density Measurements for 5mK$^+$/2.5mPZ and 6.4mK$^+$/1.6mPZ

Run#	SL Density Original kg/m^3	SL Density Corrected kg/m^3
4.1	1221	1223
4.2.1	1226	1228
4.2.2	1227	1229
4.3.1	1225	1227
4.3.2	1225	1227
4.4.1	1225	1227
4.4.2	1225	1227
4.5.1	1228	1230
4.5.2	1230	1232
4.6.1	1212	1214
4.6.2	1213	1214
4.7.1	1213	1215
4.7.2	1213	1214
4.8	1211	1212
4.9.1	1213	1214
4.9.2	1213	1215
4.10.1	1212	1214
4.10.2	1215	1217
4.11.1	1216	1217
4.11.2	1216	1218
4.12.1	1218	1220
4.12.2	1219	1220
4.13.1	1215	1217
4.13.2	1215	1216
4.14.1	1217	1219
4.14.2	1216	1218
4.15.1	1218	1220
4.15.2	1219	1220
4.16.1	1217	1218
4.16.2	1217	1219
4.17.1	1216	1217
4.17.2	1215	1217
4.18	1221	1223
4.19	1221	1222

Run#	SL Density Original kg/m^3	SL Density Corrected kg/m^3
4.20.1	1276	1278
4.20.2	1274	1276
4.21.1	1263	1264
4.21.2.	1265	1267
4.22.1	1271	1273
4.22.2	1272	1274
4.23	1274	1276
4.24	1271	1272
4.25	1265	1267
4.26.1	1263	1264
4.26.2	1264	1265
4.27.1	1265	1266
4.27.2	1266	1267
4.28.1	1262	1263
4.28.2	1263	1264
4.29.1	1266	1268
4.29.2	1268	1269
4.30.1	1263	1265
4.30.2	1265	1267
4.31.1	1262	1263
4.31.2	1263	1265
4.32.1	1265	1266
4.32.2	1265	1267
4.33.1	1260	1261
4.33.2	1260	1262

2.11 MATERIAL BALANCE

A material balance for carbon dioxide was performed across the absorber. The rate of carbon dioxide removal was determined for the gas phase by taking the difference between the inlet and outlet CO_2 gas flow. The CO_2 gas flow was determined from the measurements of CO_2 gas concentration, the gas flow rate measured by the annubar, and the calculated water content. The annubar was originally calibrated for air and a density correction was applied to the account for CO_2 and H_2O. The liquid phase CO_2 mass balance was obtained by taking the difference between the inlet and outlet CO_2 liquid flow. The molar flow rate of CO_2 in the liquid was calculated from the measured loading and the flow rate and density measured by the Micro Motion® flowmeters for each stream. No adjustments were made to the raw data for the CO_2 material balance calculations.

2.11.1 Campaign 1

The material balance for Campaign 1 indicates that gas side removal of CO_2 was on average approximately 14% higher than the liquid phase (Figure 2-30). In the first campaign, the measurements from the Vaisala analyzer were used for the inlet and outlet CO_2 concentration. The outlet water concentration was assumed to be saturated at the outlet gas temperature and the inlet water concentration was assumed to be saturated at the gas temperature measured downstream of the air cooler. In Campaign 1, samples were taken with Erlenmeyer flasks and it was likely that CO_2 was lost due to flashing. In addition, the analytical method for CO_2 loading was not fully developed at the time, which may have contributed to addition errors on the liquid side. However, the error appeared to be systematic, which indicates that the gas or liquid rate or CO_2 gas

concentration may be offset. The liquid phase measurements are critical to the CO_2 material balance. If the absorber rich CO_2 loading is increased by 2.5%, the offset is eliminated. For gas–side adjustments, the total gas rate would need to be decreased by 12% to correct the offset.

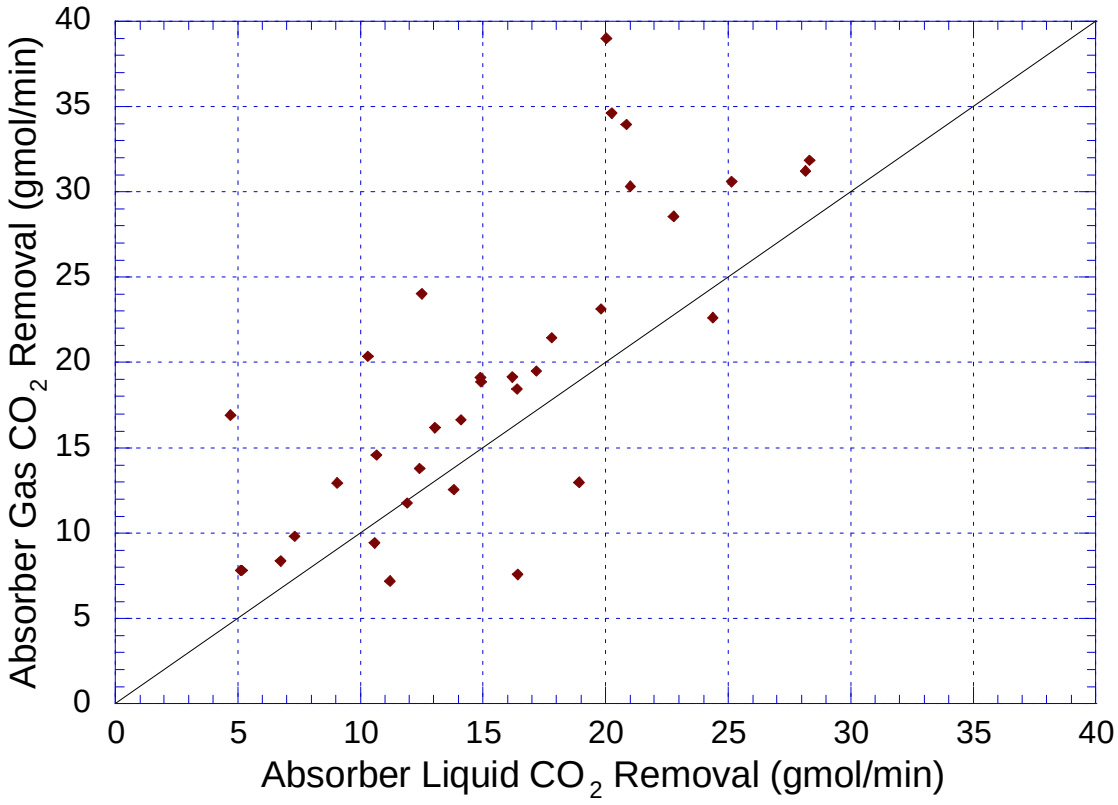

Figure 2-30. Campaign 1 CO_2 Material Balance on Absorber Liquid and Absorber Gas (5mK$^+$/2.5mPZ, Flexipac 1Y)

2.11.2 Campaign 2

The material balance for Campaign 2 is shown in Figure 2-31. In Campaign 2, the inlet and outlet gas was assumed to be saturated at the measured inlet and outlet gas temperatures. During this campaign, the air cooler was not operated and the inlet gas was recycled around the blower in order to increase the inlet gas temperature. Due to the

saturated conditions, the inlet Vaisala analyzer failed and was replaced with the Horiba analyzers. In the second campaign, the stripper was first operated at a pressure of 1.8 bar and one run at 3.4 bar was conducted. The plant was then shut down and reconfigured to operate the stripper in under vacuum. The pilot plant was then shut down again and reconfigured to operate at a stripper pressure of 1.8 bar.

The figure shows that the material balance for the gas and liquid matched relatively well prior to vacuum operation, which is represented by PSTR1 = 1.8 bar and PSTR = 3.4 bar. However, the results for vacuum operation indicated that the gas phase material was consistently higher than the liquid side by approximately 45%. Even after the pilot plant was reconfigured back to pressurized stripping, the material balance was somewhat scattered (PSTR2 = 1.8 bar). During the second set of high pressure runs, the absorber was operated with an inlet CO_2 concentration of 17% because it had initially been assumed that the CO_2 gas calibration standards were in mass percent.

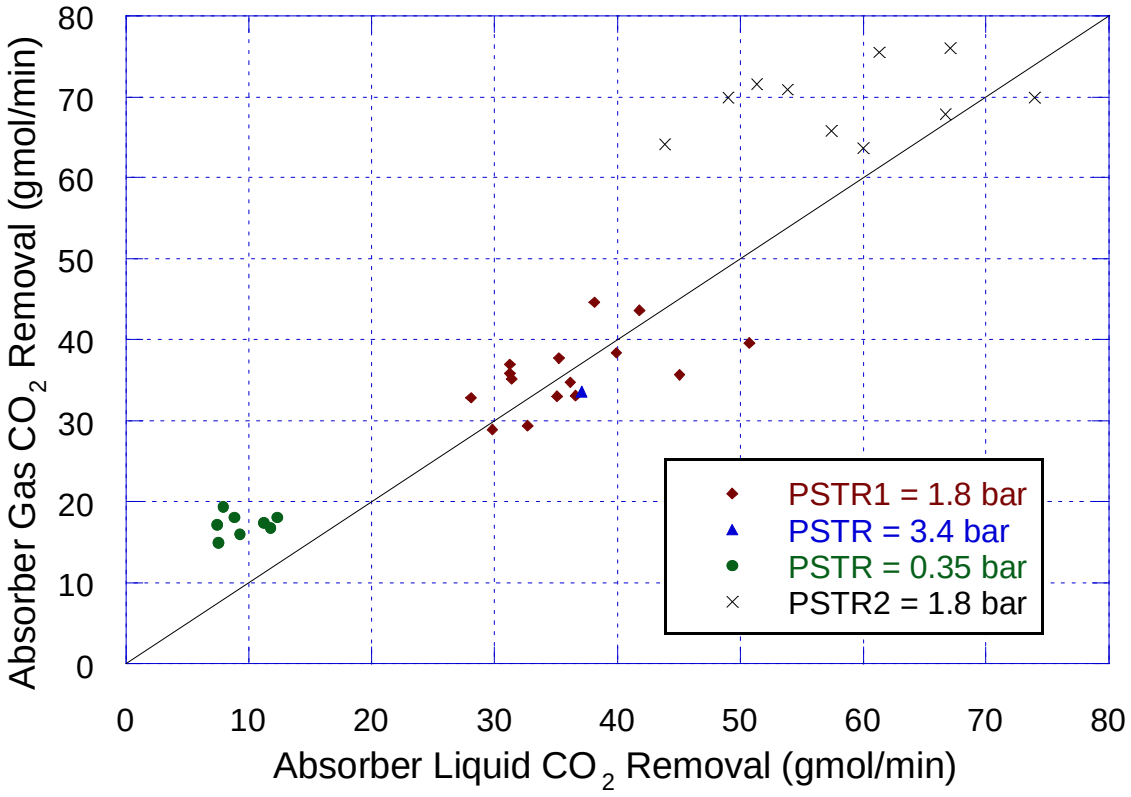

Figure 2-31. Campaign 2 CO_2 Material Balance on Absorber Liquid and Absorber Gas (5mK^+/2.5mPZ, Flexipac 1Y)

When the pilot plant was configured to vacuum stripping, all of the CO_2 gas analyzers were calibrated on 11/02/04. In the recalibration, the slope of the inlet Horiba analyzer had increased from 1.24 to 1.42. It is possible that the new calibration was performed incorrectly. However, examination of the Horiba calibration curves from Campaign 2, 3, and 4 shows that the slope gradually increased in each campaign. The slope of the outlet Vaisala CO_2 analyzer did not change much, therefore, it was concluded that the CO_2 analyzers were calibrated properly. In the second campaign, sample bombs were used take samples. In the improved loading analysis, samples were covered with parafilm and IC standards were analyzed every 6 to 10 samples to correct for analyzer

drift. Corrections based on the standards to the loading analysis varied between 5 to 10 percent. The liquid sampling and analytical method for liquid CO_2 loading remained consistent throughout the campaign. The IC standards were made on a routine basis and the TOC analyzer used for the loading analysis was calibrated at the beginning of each analytical run. Dilutions to the samples were made on a mass basis.

2.11.3 Campaign 4

A material balance was performed for the absorber gas and absorber liquid for $5mK^+/2.5mPZ$ and $6.4mK^+/1.6mPZ$ solvents of Campaign 4 (Figure 2-32). The material balance for the $5mK^{+/}2.5mPZ$ runs seemed to have a systematic offset. If the absorber gas flow is adjusted by downward by 10% or the absorber rich CO_2 loading is increased by 2%, the systematic offset is eliminated.

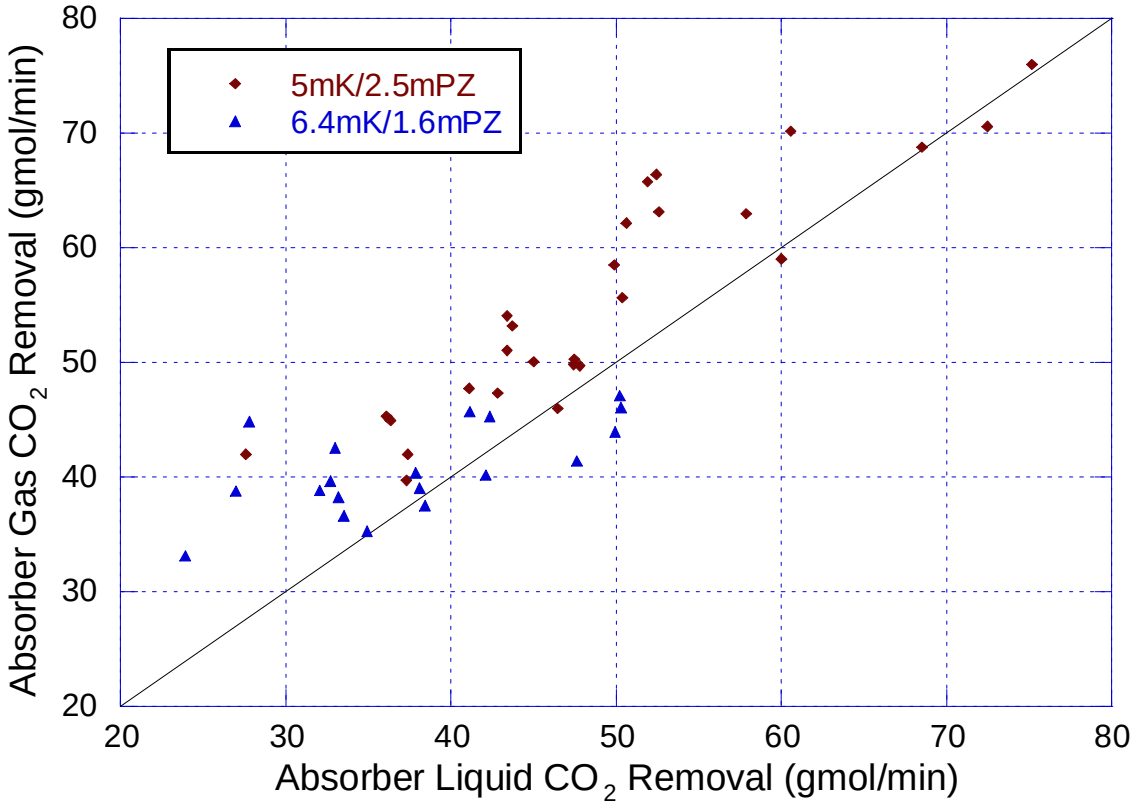

Figure 2-32. Campaign 4 CO_2 Material Balance on Absorber Liquid and Absorber Gas for 5mK^+/2.5mPZ and 6.4mK^+/1.6mPZ (Flexipac AQ Style 20)

In the fourth campaign, the flow rate of CO_2 gas from the overhead gas accumulator was measured with an annubar. At steady state, the flow of the CO_2 recycle stream should match the CO_2 removal rate in the absorber. The material balance for the absorber gas and CO_2 recycle is shown in Figure 2-33. The material balance assumed the flow was pure CO_2 from the recycle stream. The CO_2 recycle and absorber gas CO_2 of the 6.4mK^+/1.6mPZ data match relatively well. While the 5mK^+/2.5mPZ data for the CO_2 recycle appeared to be reproducible, it was not accurate because the CO_2 recycle annubar was originally specified for vacuum operation. The runs with 6.4mK^+/1.6mPZ were conducted under vacuum and a sufficiently high superficial gas velocity was achieved. The CO_2 recycle annubar outputs the flow measurement in terms of standard cubic feet per minute (SCFM). Since the pressure, pressure drop and temperature at the annubar were not logged, the flow measurement could not be verified at the two stripper conditions.

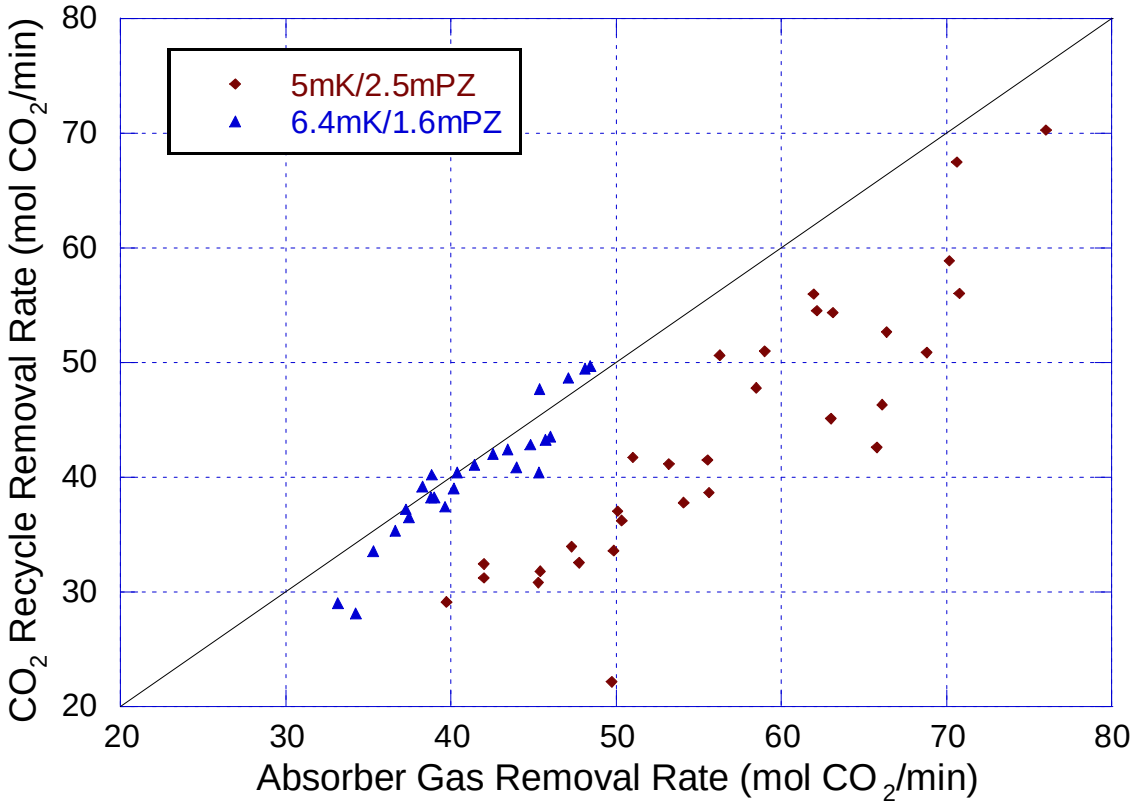

Figure 2-33. Absorber Gas and CO_2 Recycle Material Balance for 5mK^+/2.5mPZ and 6.4mK^+/1.6mPZ of Campaign 4 Assuming Pure CO_2

However, during the operation of the pilot plant, approximately 150 liters of water was discovered in the overhead gas accumulator where the CO_2 gas was stored and 38 liters of water had to be periodically pumped out each day. If the CO_2 recycle stream is assumed to be saturated with water at the condensate temperature, the CO_2 recycle the material balance for the recycle and absorber gas does not work as well. However, since the water content in CO_2 recycle could not be verified, this effect was ignored.

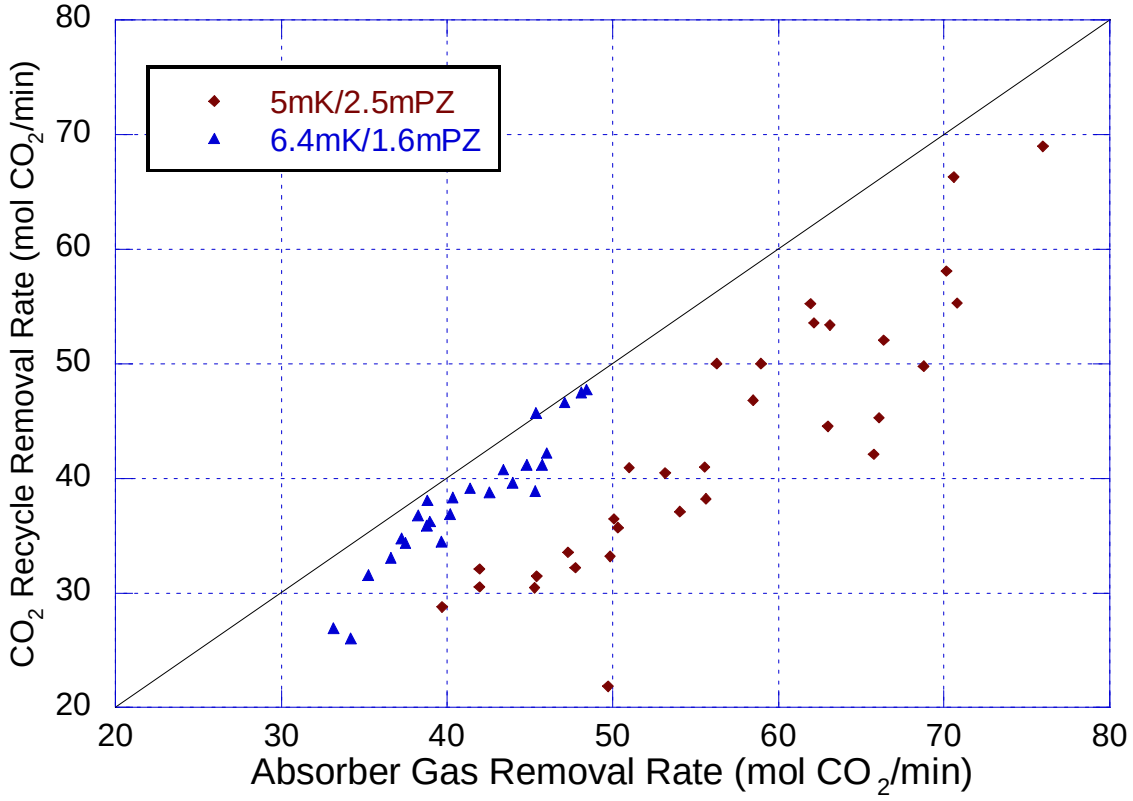

Figure 2-34. CO_2 Recycle and Absorber Gas Material Balance for $5mK^+/2.5mPZ$ and $6.4mK^+/1.6mPZ$ of Campaign 4 Assuming Pure CO_2

Since the material balance for the CO_2 recycle seemed to match the absorber gas flow measurements, it was concluded that there was a systematic error with the liquid-side CO_2 material balance. This is consistent with the fact that a two percent adjustment of the liquid loading measurement or liquid mass flow rate would have accounted for the discrepancy between the absorber gas and liquid CO_2 material balance. It should be noted that in some instances, the liquid loading measurements were adjusted by up to 10% based on the analysis of the 100 ppm IC standards used to correct for analyzer drift. Also, an error of 1–2% in the liquid mass flow rate is entirely possible, while an error of 10% in the gas flow measurement is less likely.

2.12 ABSORBER MASS TRANSFER PERFORMANCE

The mass transfer performance of the absorber for Campaigns 1, 2 and 4 was evaluated using the CO_2 material balance obtained in the previous section. The overall gas phase mass transfer coefficient (K_G) was calculated using the following equation:

$$K_G = \frac{N_{CO_2}}{a_{eff} \cdot V_p \cdot \Delta P_{CO_2,lm}} \tag{2.4}$$

where K_G is the overall gas phase mass transfer coefficient with units of gmol/Pa-cm^2-s, N_{CO_2} is the number moles of CO_2 that are absorbed with units of (gmol/min), a_{eff} is the effective interfacial area with units of cm^2/cm^3, and V_p is the volume of packing in units of cm^3. The log mean driving force, $\Delta P_{CO_2,lm}$, has units of Pa and is given by the following equation:

$$\Delta P_{CO_2,lm} = \frac{(P_{CO_2,in} - P^*_{CO_2,in}) - (P_{CO_2,out} - P^*_{CO_2,out})}{\ln\left(\frac{P_{CO_2,in} - P^*_{CO_2,in}}{P_{CO_2,out} - P^*_{CO_2,out}}\right)} \tag{2.5}$$

where $P_{CO_2,in/out}$ is the partial pressure of CO_2 at the inlet and outlet of the absorber and $P^*_{CO_2,in/out}$ is the partial of pressure of CO_2 in equilibrium with the liquid composition at the inlet and outlet of the absorber.

2.12.1 Equilibrium CO_2 Partial Pressure

Recent measurements of amine volatility by Hilliard have shown that the VLE data obtained by Cullinane may not be correct. The Hilliard experimental results indicate that the equilibrium partial pressure of CO_2 was offset by a factor of 10 percent in CO_2

loading or 20 °C in temperature (Figure 2-35). To obtain the correct partial pressure of CO_2, the measured CO_2 loading would need to be multiplied by a factor of 0.9. In this work, it was assumed that the rate data obtained by Cullinane was consistent with the given partial pressures of CO_2, but not with the CO_2 loading.

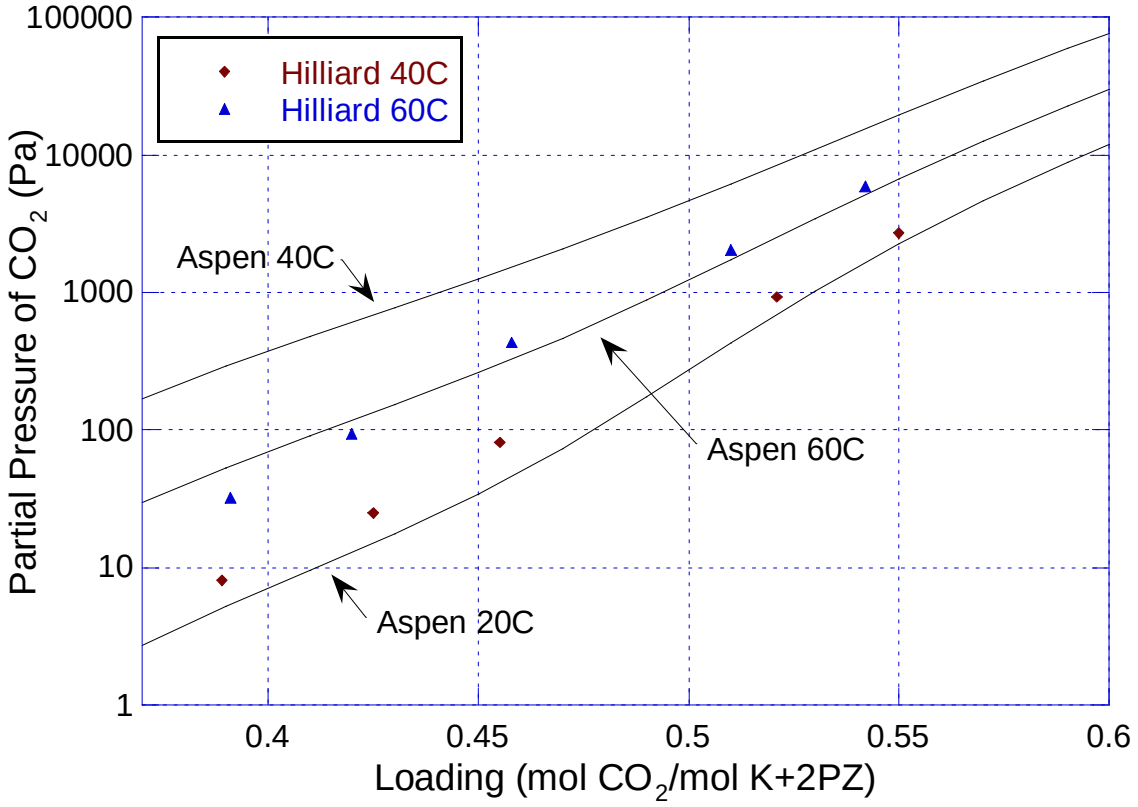

Figure 2-35. Updated Bench-scale Vapor-Liquid Equilibrium Data Measured by Hilliard for 5mK^+/2.5mPZ and Aspen Plus® Model Based on Cullinane Data

For the pilot plant mass transfer calculations, the equilibrium partial pressure of CO_2 was obtained through a flash calculation using the Hilliard K^+/PZ VLE model developed in Aspen Plus®. Since the model was developed based on the Cullinane VLE data, the predicted results were also incorrect. For the Aspen Plus® flash calculation, the molar flow rate per hour was for carbon dioxide, potassium carbonate, piperazine, and

water were entered. The molar flow rate of K_2CO_3, PZ, and H_2O were entered as 2.5, 2.5, and 55.5 mol/hr. To calculate the molar flow rate of CO_2, the concentration of water was calculated using the measurements of CO_2 loading, K^+ and PZ concentration from the liquid analysis. The CO_2 concentration was converted to molality by dividing through by the water concentration and multiplied by 0.9 to account for the VLE error. Since, K_2CO_3 contains one mole of CO_2, the concentration of CO_2 was then adjusted by subtracting the measured concentration of potassium divided by two. The equation that was used to calculate the Aspen Plus® input for the flow rate of CO_2 is given below:

$$CO_{2,Aspen} = \frac{[CO_2]\cdot 0.90}{[H_2O]} - \frac{[K_2CO_3]}{2} \tag{2.6}$$

where $CO_{2,Aspen}$ is the CO_2 flow rate with units of mol/hr, $[CO_2]$ is the concentration of the CO_2 in units of mol/kg soln, $[H_2O]$ is the concentration of water in units of kg H_2O/kg soln, and $[K_2CO_3]$ is the concentration of K_2CO_3 in units of mol/kg H_2O.

The concentration of potassium and piperazine measured by ion chromatography indicated that there was slight difference between the expected concentrations and the actual solution composition. For the flash calculation, the average potassium and piperazine concentration for each campaign composition was used. In Campaign 1, four different solution compositions were used and the concentrations were adjusted accordingly. The difference in solution composition will affect the calculation of the equilibrium partial pressure of CO_2. For example, the IC analysis showed that for Campaign 4, the concentration of potassium was actually 5.9 molal and not 6.4 molal as originally planned. According a flash calculation, for a given loading, the partial pressure

of CO_2 for 5.9mK^+/1.6mPZ may be 50-100 % higher than the 6.4mK^+/1.6mPZ (Figure 2-36). The K_g calculation used the 5.9mK^+/1.6mPZ solvent formulation.

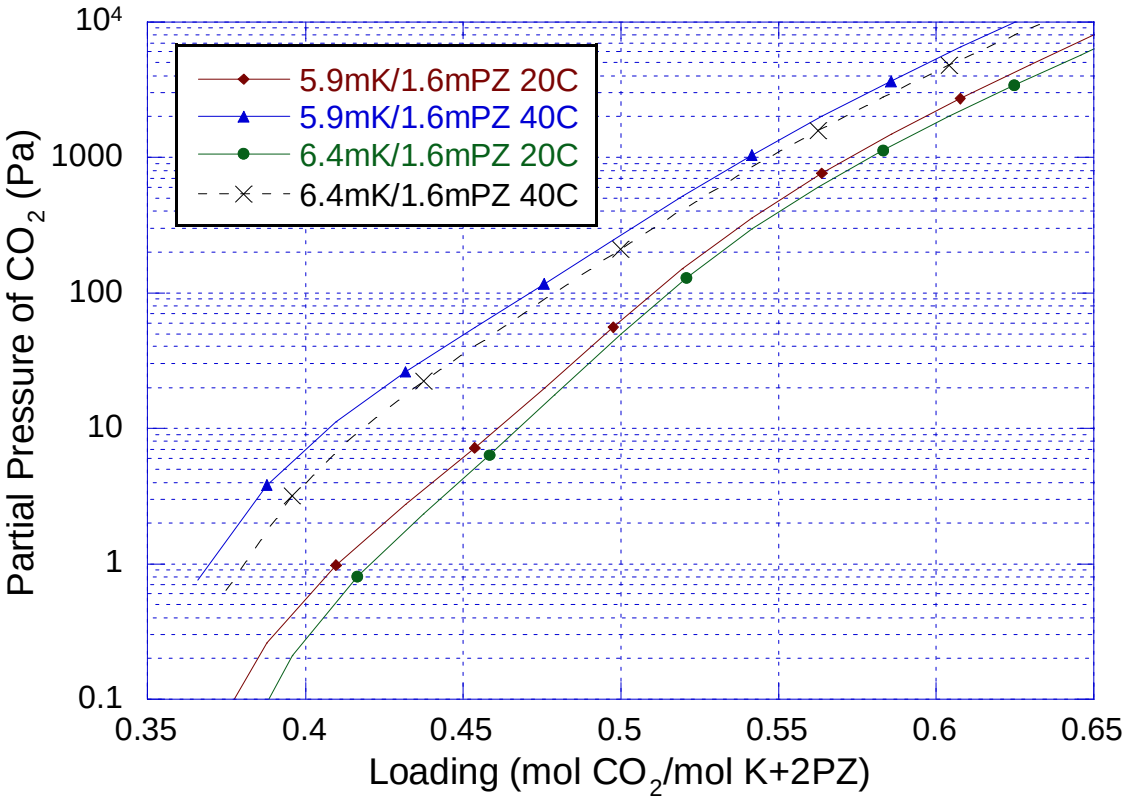

Figure 2-36. Vapor-Liquid Equilibrium Data for 5.9mK^+/1.6mPZ and 6.4mK^+/1.6mPZ at 20 and 40°C Generated from Aspen Plus® Model

The following tables list the values that we calculated and entered into Aspen Plus® flash calculation to determine the partial pressure of CO_2 in equilibrium with the bulk solution. The equilibrium pressure was calculated at using the absorber lean solution composition at the top of the column and the absorber rich solution composition at the bottom of the column.

Table 2-7. Campaign 1 Aspen Plus® Input for P_{CO2}* Calculation (5mK^+/2.5mPZ)

Run#	H_2O	K_2CO_3	PZ	K/PZ	H_2O	Temp Top	Aspen CO_2 Top	Temp Bot	Aspen CO_2 Bot
	kg/kg soln	mol/hr	mol/hr		mol/hr	°C	mol/hr	°C	mol/hr
1.1.1	0.70	1.67	2.26	1.48	55.5	39.33	0.953	29.19	1.255
1.1.2	0.70	1.67	2.26	1.48	55.5	39.11	0.434	28.57	1.232
1.1.3	0.70	1.67	2.26	1.48	55.5	38.90	0.524	28.95	1.298
1.2.1	0.70	1.86	2.06	1.81	55.5	41.50	0.468	32.28	0.888
1.2.2	0.70	1.86	2.06	1.81	55.5	43.16	1.105	32.59	1.053
1.2.3	0.70	1.86	2.06	1.81	55.5	44.46	0.448	32.58	1.094
1.3.1	0.70	1.86	2.06	1.81	55.5	41.02	0.647	38.36	0.976
1.3.2	0.70	1.86	2.06	1.81	55.5	40.67	0.767	38.09	0.910
1.3.3	0.70	1.86	2.06	1.81	55.5	40.42	0.715	38.06	1.192
1.4.1	0.70	1.86	2.06	1.81	55.5	40.01	0.783	39.40	1.173
1.5.1	0.70	1.86	2.06	1.81	55.5	40.08	0.836	38.26	1.073
1.6.1	0.70	1.86	2.06	1.81	55.5	39.53	0.673	44.04	1.268
1.7.1	0.70	1.86	2.06	1.81	55.5	40.05	0.712	39.25	1.374
1.8.1	0.63	2.57	2.58	1.99	55.5	41.16	0.789	29.68	1.894
1.8.2	0.63	2.57	2.58	1.99	55.5	41.48	0.826	29.45	1.421
1.9.1	0.63	2.57	2.58	1.99	55.5	41.49	0.786	31.63	1.947
1.9.2	0.63	2.57	2.58	1.99	55.5	41.55	0.825	31.49	1.538
1.10.1	0.63	2.57	2.58	1.99	55.5	41.58	0.935	30.13	1.464
1.10.2	0.63	2.57	2.58	1.99	55.5	41.52	0.870	29.83	1.569
1.11.1	0.63	2.57	2.58	1.99	55.5	34.63	0.910	22.56	1.759
1.11.2	0.63	2.57	2.58	1.99	55.5	35.39	0.963	22.66	1.542
1.12.1	0.63	2.57	2.58	1.99	55.5	39.81	1.004	34.39	1.465
1.12.2	0.63	2.57	2.58	1.99	55.5	39.64	0.468	34.43	1.567
1.13.1	0.63	2.57	2.58	1.99	55.5	40.49	1.373	38.54	2.051
1.14.1	0.63	2.57	2.58	1.99	55.5	40.26	1.536	41.05	2.346
1.15.1	0.63	2.57	2.58	1.99	55.5	39.59	1.511	39.76	2.193
1.15.2	0.63	2.57	2.58	1.99	55.5	43.23	1.552	40.86	2.288
1.16.1	0.63	2.57	2.58	1.99	55.5	43.34	1.567	38.47	2.309
1.16.2	0.63	2.57	2.58	1.99	55.5	42.48	1.567	38.83	2.317
1.17.1	0.63	2.57	2.58	1.99	55.5	41.34	1.603	38.39	2.282
1.17.2	0.63	2.57	2.58	1.99	55.5	41.22	1.644	38.40	2.357
1.18.1	0.60	2.79	2.67	2.09	55.5	46.24	1.774	43.36	2.799
1.18.2	0.60	2.79	2.67	2.09	55.5	46.05	1.691	43.54	2.765
1.19.1	0.60	2.79	2.67	2.09	55.5	45.27	1.865	40.44	2.787
1.19.2	0.60	2.79	2.67	2.09	55.5	44.84	1.766	39.81	2.704

Table 2-8. Campaign 2 Aspen Plus® Input for P_{CO2}* Calculation (5mK^+/2.5mPZ)

Run#	H_2O	K_2CO_3	PZ	K/PZ	H_2O	Temp Top	Aspen CO_2 Top	Temp Bot	Aspen CO_2 Bot
	kg/kg soln	mol/hr	mol/hr		mol/hr	°C	mol/hr	°C	mol/hr
2.1.1	0.65	2.29	1.96	2.33	55.5	40.20	1.383	47.44	2.066
2.1.2	0.65	2.29	1.96	2.33	55.5	40.27	1.133	47.16	2.201
2.2.1	0.65	2.29	1.96	2.33	55.5	41.21	1.113	50.51	2.166
2.3.1	0.65	2.29	1.96	2.33	55.5	40.73	1.310	44.74	2.466
2.4.1	0.65	2.29	1.96	2.33	55.5	40.60	1.381	44.59	2.277
2.5.1	0.65	2.29	1.96	2.33	55.5	40.55	1.378	44.61	2.154
2.6.1	0.65	2.29	1.96	2.33	55.5	41.20	1.330	45.93	2.203
2.7.1	0.65	2.29	1.96	2.33	55.5	41.27	1.872	46.41	2.254
2.8.1	0.65	2.29	1.96	2.33	55.5	41.36	1.287	46.64	2.055
2.8.2	0.65	2.29	1.96	2.33	55.5	41.59	1.416	47.77	2.279
2.9.1	0.65	2.29	1.96	2.33	55.5	40.56	1.203	41.84	2.167
2.9.2	0.65	2.29	1.96	2.33	55.5	40.79	1.182	42.34	2.254
2.10.1	0.65	2.29	1.96	2.33	55.5	41.20	1.652	48.00	2.405
2.10.2	0.65	2.29	1.96	2.33	55.5	41.30	1.387	48.19	2.252
2.11.1	0.65	2.29	1.96	2.33	55.5	41.39	1.791	48.45	2.431
2.11.2	0.65	2.29	1.96	2.33	55.5	41.42	1.716	48.56	2.536
2.12.1	0.65	2.29	1.96	2.33	55.5	41.05	1.640	48.38	2.665
2.12.2	0.65	2.29	1.96	2.33	55.5	40.97	1.497	47.97	2.633
2.13.1	0.65	2.29	1.96	2.33	55.5	40.68	1.178	44.97	2.213
2.13.2	0.65	2.29	1.96	2.33	55.5	40.31	1.566	44.12	1.983
2.14.1	0.65	2.29	1.96	2.33	55.5	43.47	-2.285	30.74	-2.285
2.14.2	0.65	2.29	1.96	2.33	55.5	42.52	1.787	30.08	2.402
2.15.1	0.65	2.29	1.96	2.33	55.5	41.90	1.641	34.57	2.195
2.16.1	0.65	2.29	1.96	2.33	55.5	41.98	1.621	34.47	2.242
2.16.2	0.65	2.29	1.96	2.33	55.5	38.78	1.488	31.50	2.040
2.17.1	0.65	2.29	1.96	2.33	55.5	38.99	1.460	29.96	2.081
2.18.1	0.65	2.29	1.96	2.33	55.5	44.79	1.623	37.17	2.014
2.18.2	0.65	2.29	1.96	2.33	55.5	44.81	1.616	37.56	2.090
2.19.1	0.65	2.29	1.96	2.33	55.5	46.99	1.725	40.51	2.428
2.19.2	0.65	2.29	1.96	2.33	55.5	47.82	1.768	42.35	2.159
2.20.1	0.65	2.29	1.96	2.33	55.5	40.11	1.393	47.96	2.051
2.20.2	0.65	2.29	1.96	2.33	55.5	40.08	1.508	48.27	2.471
2.21.1	0.65	2.29	1.96	2.33	55.5	40.10	1.782	48.30	2.600
2.21.2	0.65	2.29	1.96	2.33	55.5	40.86	1.735	50.70	2.428
2.22.1	0.65	2.29	1.96	2.33	55.5	41.77	1.559	51.19	2.273
2.22.2	0.65	2.29	1.96	2.33	55.5	41.08	1.544	50.94	2.348
2.23.1	0.65	2.29	1.96	2.33	55.5	39.86	1.426	47.95	2.464
2.23.2	0.65	2.29	1.96	2.33	55.5	39.82	1.398	47.27	2.160
2.24.1	0.65	2.29	1.96	2.33	55.5	39.68	1.384	47.57	2.270
2.24.2	0.65	2.29	1.96	2.33	55.5	39.65	1.080	47.49	2.021

Table 2-9. Campaign 4 Aspen Plus® Input for P_{CO2}* Calculation (5mK^+/2.5mPZ)

Run#	H_2O Top kg/kg soln	H_2O Bot kg/kg soln	K_2CO_3 mol/hr	PZ mol/hr	K/PZ	H_2O mol/hr	Temp Top °C	Aspen CO_2 Top mol/hr	Temp Bot °C	Aspen CO_2 Bot mol/hr
4.1	0.65	0.63	2.44	2.32	2.10	55.5	39.93	1.194	48.83	1.710
4.2.1	0.64	0.61	2.44	2.32	2.10	55.5	38.89	1.150	48.56	2.288
4.2.2	0.64	0.60	2.44	2.32	2.10	55.5	38.96	1.055	48.42	2.486
4.3.1	0.63	0.62	2.44	2.32	2.10	55.5	42.09	1.360	50.59	2.224
4.3.2	0.63	0.60	2.44	2.32	2.10	55.5	42.49	1.324	50.78	2.379
4.4.1	0.63	0.61	2.44	2.32	2.10	55.5	43.62	1.299	50.52	2.371
4.4.2	0.63	0.47	2.44	2.32	2.10	55.5	43.94	1.364	50.43	3.605
4.5.1	0.63	0.61	2.44	2.32	2.10	55.5	42.01	1.305	47.08	2.347
4.5.2	0.63	0.61	2.44	2.32	2.10	55.5	41.38	1.354	46.46	2.460
4.6.1	0.65	0.63	2.44	2.32	2.10	55.5	46.73	1.006	51.77	2.146
4.6.2	0.65	0.63	2.44	2.32	2.10	55.5	43.57	0.996	51.75	2.181
4.7.1	0.65	0.64	2.44	2.32	2.10	55.5	45.19	0.844	50.95	1.780
4.7.2	0.65	0.63	2.44	2.32	2.10	55.5	44.97	0.843	50.99	1.740
4.8	0.66	0.64	2.44	2.32	2.10	55.5	43.28	0.839	47.54	1.721
4.9.1	0.66	0.64	2.44	2.32	2.10	55.5	43.20	0.781	47.36	1.898
4.9.2	0.66	0.63	2.44	2.32	2.10	55.5	43.21	0.811	47.30	1.830
4.10.1	0.64	0.64	2.44	2.32	2.10	55.5	44.28	1.322	51.32	1.794
4.10.2	0.65	0.63	2.44	2.32	2.10	55.5	41.74	1.305	51.61	2.070
4.11.1	0.64	0.63	2.44	2.32	2.10	55.5	41.59	1.210	49.13	2.110
4.11.2	0.64	0.63	2.44	2.32	2.10	55.5	41.20	1.245	48.89	2.167
4.12.1	0.64	0.63	2.44	2.32	2.10	55.5	39.81	1.214	46.45	2.046
4.12.2	0.64	0.63	2.44	2.32	2.10	55.5	39.86	1.275	46.41	2.117
4.13.1	0.66	0.63	2.44	2.32	2.10	55.5	41.48	1.017	47.65	1.504
4.13.2	0.65	0.64	2.44	2.32	2.10	55.5	43.02	1.146	49.17	1.801
4.14.1	0.64	0.64	2.44	2.32	2.10	55.5	42.76	1.196	48.19	1.804
4.14.2	0.65	0.64	2.44	2.32	2.10	55.5	42.80	1.171	47.93	1.757
4.15.1	0.64	0.64	2.44	2.32	2.10	55.5	39.54	1.159	45.48	1.909
4.15.2	0.64	0.63	2.44	2.32	2.10	55.5	39.61	1.160	45.61	1.812
4.16.1	0.61	0.61	2.44	2.32	2.10	55.5	41.40	1.480	48.46	2.620
4.16.2	0.64	0.61	2.44	2.32	2.10	55.5	41.29	1.283	48.15	1.954
4.17.1	0.64	0.63	2.44	2.32	2.10	55.5	40.15	0.821	49.49	1.723
4.17.2	0.65	0.63	2.44	2.32	2.10	55.5	40.63	0.918	50.98	1.833
4.18	0.64	0.61	2.44	2.32	2.10	55.5	39.98	1.018	51.31	1.950
4.19	0.62	0.60	2.44	2.32	2.10	55.5	40.26	1.212	52.11	2.141

Table 2-10. Campaign 4 Aspen Plus® Input for P_{CO2}* Calculation (6.4mK^+/1.6mPZ)

Run#	H_2O Top kg/kg soln	H_2O Bot kg/kg soln	K_2CO_3 mol/hr	PZ mol/hr	K/PZ	H_2O mol/hr	Temp Top °C	Aspen CO_2 Top mol/hr	Temp Bot °C	Aspen CO_2 Bot mol/hr
4.20.1	0.65	0.63	2.90	1.61	3.60	55.5	38.76	1.426	43.53	1.595
4.20.2	0.64	0.63	2.90	1.61	3.60	55.5	38.60	1.217	43.45	1.432
4.21.1	0.66	0.64	2.90	1.61	3.60	55.5	39.00	1.318	42.98	1.440
4.21.2.	0.65	0.64	2.90	1.61	3.60	55.5	40.52	1.354	44.89	1.532
4.22.1	-	0.63	2.90	1.61	3.60	55.5	36.76	-	44.09	1.706
4.22.2	0.59	0.69	2.90	1.61	3.60	55.5	36.71	1.008	43.98	1.951
4.23	0.59	0.62	2.90	1.61	3.60	55.5	37.83	1.136	45.64	1.881
4.24	0.62	0.61	2.90	1.61	3.60	55.5	37.49	1.250	45.31	1.891
4.25	0.64	0.63	2.90	1.61	3.60	55.5	39.48	1.033	44.90	1.497
4.26.1	0.65	0.64	2.90	1.61	3.60	55.5	38.33	1.001	44.47	1.584
4.26.2	0.65	0.64	2.90	1.61	3.60	55.5	38.68	1.072	45.14	1.529
4.27.1	0.65	0.63	2.90	1.61	3.60	55.5	40.01	1.047	46.10	1.717
4.27.2	0.64	0.63	2.90	1.61	3.60	55.5	39.30	0.953	45.57	1.598
4.28.1	0.65	0.64	2.90	1.61	3.60	55.5	38.88	0.994	45.80	1.708
4.28.2	0.65	0.63	2.90	1.61	3.60	55.5	38.39	1.031	45.00	1.546
4.29.1	0.65	0.64	2.90	1.61	3.60	55.5	39.42	0.957	46.36	1.636
4.29.2	0.64	0.62	2.90	1.61	3.60	55.5	39.49	0.926	46.60	1.557
4.30.1	0.62	0.63	2.90	1.61	3.60	55.5	41.02	0.391	46.75	1.449
4.30.2	0.66	0.63	2.90	1.61	3.60	55.5	40.44	0.910	46.50	1.616
4.31.1	0.63	0.64	2.90	1.61	3.60	55.5	41.57	1.022	47.06	1.688
4.31.2	0.63	0.63	2.90	1.61	3.60	55.5	41.55	1.141	47.02	1.604
4.32.1	0.65	0.62	2.90	1.61	3.60	55.5	43.53	1.027	48.14	1.690
4.32.2	0.65	0.60	2.90	1.61	3.60	55.5	43.72	1.139	48.28	2.052
4.33.1	0.65	0.66	2.90	1.61	3.60	55.5	45.55	0.987	46.16	1.604
4.33.2	0.66	0.67	2.90	1.61	3.60	55.5	45.08	1.090	46.08	1.425

2.12.2 Effective Interfacial Area of Packing

In the first two campaigns, Flexipac 1Y structured packing (a_{sp} = 410 m^2/m^3) was used in the absorber and in the final campaign, Flexipac AQ Style 20 structured packing (a_{sp} = 213 m^2/m^3) was used. Effective area measurements for Flexipac 1Y were conducted by absorbing CO_2 from ambient air into a solution of 0.1 N KOH with 6.1 m of packing in the absorber column. For Flexipac AQ Style 20, air-water tests were conducted with 0.1 NaOH with 3.05 m of packing in the PVC air-water column. The effective area measurements were correlated solely as a function of the superficial liquid rate. A plot of the data points used for the correlation is shown.

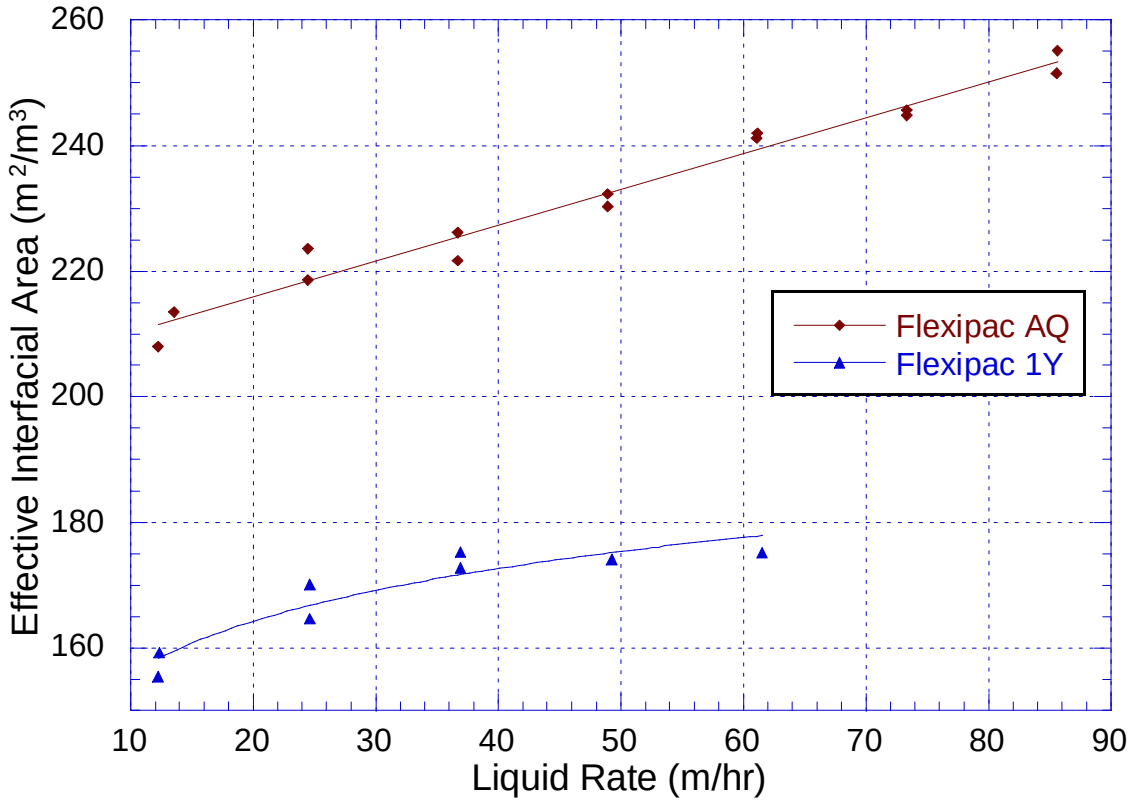

Figure 2-37. Correlation of Effective Interfacial Area for Flexipac 1Y and Flexipac AQ Style 20 from Air-Water Experiments

The effective area (m^2/m^3) for Flexipac 1Y was correlated to the following equation:

$$a_{eff,Flexipac1Y} = 12.142 \cdot (\ln L) + 127.87 \tag{2.7}$$

And the effective area for Flexipac AQ Style 20 was correlated to the following equation:

$$a_{eff,FlexipacAQ} = 0.569 \cdot (L) + 204.57 \tag{2.8}$$

where, L is the superficial liquid velocity with units of m/hr. The correlations for the effective area do not account for differences in density, surface tension, and viscosity of

the potassium carbonate and piperazine solvent, which may be dramatically different than of the 0.1 N hydroxide solutions. Preliminary results from the Separations Research Program at the University of Texas at Austin have shown that the interfacial area may increase by 1–1.5 times if the surface tension is reduced by a one-half.

The figure shows that the interfacial area measurement of the Flexipac AQ packing is approximately 30% higher than Flexipac 1Y, which is unexpected. The Flexipac AQ structured packing half the specific area and a steeper corrugation angle and should therefore have less effective interfacial area. The discrepancy may be due to the differences in solution composition (KOH vs. NaOH) and from the test apparatus (6 meter steel absorber column vs. 3 meter PVC air-water column).

2.12.3 K_g Mass Transfer Coefficient

The results of the K_g calculation for Campaigns 1, 2, and 4 are tabulated in Tables 2-11, 2-12, 2-13, and 2-14. Since the gas-side CO_2 removal rate provided more consistent results, these values were used as N_{CO2}. Since the gas side CO_2 removal rates were consistently higher than the liquid side by approximately 10%, the K_g results should be interpreted with this in mind. An average equilibrium partial pressure of CO_2 was calculated for each K_g based on an arithmetic average of the inlet and outlet equilibrium CO_2 partial pressure. Finally pinch point locations were identified as occurring in the bottom or top of the absorber column. The pinches were identified when value of the equilibrium partial pressure of CO_2 divided by the bulk CO_2 partial pressure approached one. Outliers were also identified in the table based on the graphical plots of K_g.

Table 2-11. Campaign 1 Results for K_G Calculation

Run#	N_{CO2} gmol/min	Liq Rate m/hr	Eff Intf Area m^2/m^3	P_{CO2} Top Pa	P_{CO2}* Top Pa	P_{CO2} Bot Pa	P_{CO2}* Bot Pa	LMCD Pa	Kgx10^{10} gmol/ Pa-cm^2-s	P_{CO2}* Ave Pa	Comments
1.1.1	14.89	7.84	152.9	178	32	2826	30	897	2.08	31	-
1.1.2	14.63	7.90	153.0	188	1	2783	26	954	1.92	14	-
1.1.3	14.23	7.85	152.9	187	3	2720	34	934	1.91	18	-
1.2.1	8.63	7.84	152.9	5	2	2950	11	418	2.58	7	-
1.2.2	8.46	7.83	152.9	6	76	2901	22	-	-	-	Outlier
1.2.3	8.30	7.83	152.9	7	3	2855	25	444	2.34	14	-
1.3.1	6.34	15.78	161.4	26	8	2223	30	451	1.67	19	-
1.3.2	6.89	15.79	161.4	29	16	2420	23	458	1.78	19	-
1.3.3	6.66	15.76	161.4	32	12	2346	62	477	1.65	37	-
1.4.1	11.04	15.77	161.4	39	16	3883	67	739	1.77	41	-
1.5.1	11.42	14.59	160.4	56	21	2979	43	655	2.08	32	-
1.6.1	18.86	12.29	158.3	330	8	11346	139	3064	0.74	74	Outlier
1.7.1	12.12	7.97	153.1	793	11	11426	124	3939	0.38	67	Outlier
1.8.1	17.16	7.86	152.9	285	6	3333	59	1217	1.77	33	-
1.8.2	17.90	7.91	153.0	230	7	3410	16	1165	1.92	11	-
1.9.1	20.36	7.92	153.0	599	6	3407	85	1584	1.61	45	-
1.9.2	21.16	7.93	153.0	582	7	3495	28	1609	1.65	17	-
1.10.1	11.39	8.02	153.1	47	12	2974	19	657	2.16	16	Top Pinch
1.10.2	10.35	7.80	152.8	32	9	2683	25	555	2.33	17	Top Pinch
1.11.1	7.36	3.90	144.4	245	5	2713	18	1016	0.96	11	Outlier
1.11.2	6.88	3.97	144.6	168	7	2482	10	846	1.08	8	Outlier
1.12.1	12.84	11.04	157.0	359	13	2080	31	957	1.64	22	-
1.12.2	19.90	10.37	156.3	508	0	3329	41	1488	1.64	21	-
1.13.1	34.31	12.26	158.3	1346	46	13878	221	5255	0.79	133	-
1.14.1	26.90	10.98	157.0	1274	69	13139	637	4828	0.68	353	-
1.15.1	26.69	12.41	158.4	1338	61	12312	366	4772	0.68	213	-
1.15.2	25.14	12.42	158.5	957	96	11315	528	3927	0.77	312	-
1.16.1	29.86	12.33	158.4	1978	101	12261	461	5398	0.67	281	-
1.16.2	30.44	12.32	158.4	1968	93	12512	487	5461	0.68	290	-
1.17.1	16.63	8.03	153.2	756	92	11529	422	3708	0.56	257	-
1.17.2	16.80	8.02	153.1	617	100	11527	532	3426	0.61	316	-
1.18.1	27.49	12.31	158.3	498	169	12224	2060	2868	1.16	1114	Top Pinch
1.18.2	28.04	12.28	158.3	521	136	12463	1876	3078	1.10	1006	Top Pinch
1.19.1	16.22	7.90	153.0	668	192	11341	1639	3061	0.66	915	Top Pinch
1.19.2	16.84	7.92	153.0	460	146	11572	1204	2873	0.73	675	Top Pinch

1. LMCD = Log Mean Concentration Difference
2. $P_{CO2,AVE}$* = Average of Inlet and Outlet P_{CO2}*. Plotted against K_g Results.

Table 2-12. Campaign 2 Results for K_G Calculatio

Run#	N_{CO2} gmol/min	Liq Rate m/hr	Eff Intf Area m^2/m^3	P_{CO2} Top Pa	P_{CO2}* Top Pa	P_{CO2} Bot Pa	P_{CO2}* Bot Pa	LMCD Pa	Kgx10^{10} gmol/ Pa-cm^2-s	P_{CO2}* Ave Pa	Comments
2.1.1	52.74	12.73	158.8	2261	105	11523	1844	5010	1.27	975	-
2.1.2	50.28	12.73	158.8	2582	47	11410	2949	4917	1.23	1498	-
2.2.1	37.00	12.74	158.8	6109	48	12810	3153	7720	0.58	1600	-
2.3.1	33.09	14.28	160.2	4445	87	11889	6654	4783	0.83	3370	-
2.4.1	37.70	17.45	162.6	3969	108	12460	3363	6110	0.73	1735	-
2.5.1	35.77	17.43	162.6	2962	106	11133	2143	5349	0.79	1125	-
2.6.1	38.39	19.92	164.2	2051	97	10888	2769	4328	1.03	1433	-
2.7.1	39.83	19.96	164.2	2379	603	11616	3423	4196	1.11	2013	-
2.8.1	44.61	20.87	164.8	4388	86	12292	1688	6986	0.74	887	-
2.8.2	43.60	20.79	164.7	4118	132	12013	4035	5753	0.88	2084	-
2.9.1	28.92	13.62	159.6	3702	61	11577	1909	6172	0.56	985	-
2.9.2	29.35	13.57	159.5	3579	58	11627	2724	5802	0.61	1391	-
2.10.1	35.12	18.36	163.2	1934	275	12390	6365	3385	1.22	3320	-
2.10.2	34.77	18.33	163.2	2029	117	12493	3751	4493	0.91	1934	-
2.11.1	32.87	18.30	163.2	1840	454	11963	7128	2760	1.40	3791	-
2.11.2	32.98	18.38	163.2	1997	349	12189	10246	1791	2.16	5298	-
2.12.1	35.61	19.21	163.8	557	261	12590	15545	-	-	7903	Outlier
2.12.2	39.58	19.16	163.7	240	162	12179	13732	-	-	6947	Outlier
2.13.1	33.57	15.96	161.5	2813	57	11876	2719	5331	0.75	1388	-
2.13.2	34.28	15.88	161.4	3186	192	12349	1106	6235	0.65	649	-
2.14.1	15.93	7.76	152.7	784	-	4980	-	-	-	-	Outlier
2.14.2	14.87	7.78	152.8	910	487	4801	2438	1128	1.65	1463	-
2.15.1	18.03	9.43	155.1	738	281	5510	1378	1669	1.33	830	-
2.16.1	18.05	9.30	154.9	626	265	5395	1655	1446	1.54	960	-
2.16.2	19.35	8.54	153.9	513	129	4566	592	1536	1.57	361	-
2.17.1	16.01	8.55	153.9	1148	120	4461	638	2128	0.93	379	-
2.18.1	17.13	12.57	158.6	467	334	4107	782	991	2.08	558	-
2.18.2	16.74	12.47	158.5	419	327	3994	1087	815	2.48	707	-
2.19.1	17.58	15.69	161.3	251	551	4027	4672	-	-	2612	Top Pinch
2.19.2	17.42	15.70	161.3	285	674	4084	1909	-	-	1292	Top Pinch
2.20.1	71.52	32.70	170.2	2141	107	17111	1805	6576	1.22	956	-
2.20.2	69.91	32.66	170.2	1978	155	16931	8103	4440	1.77	4129	-
2.21.1	67.80	35.20	171.1	1259	398	17075	12519	2218	3.42	6458	Outlier
2.21.2	63.62	35.30	171.1	1528	357	17485	7917	3998	1.78	4137	-
2.22.1	75.52	35.18	171.1	2609	212	18737	4759	6568	1.29	2486	-
2.22.2	75.95	35.28	171.1	1928	190	18160	6091	5330	1.59	3141	-
2.23.1	65.79	24.00	166.5	4861	117	17873	7784	7084	1.07	3950	-
2.23.2	64.16	23.90	166.4	4286	106	16938	2560	8254	0.89	1333	-
2.24.1	69.88	24.01	166.5	3686	100	17604	3865	7558	1.06	1983	-
2.24.2	70.91	23.96	166.4	4080	37	18160	1575	8886	0.92	806	-

1. LMCD = Log Mean Concentration Difference
2. $P_{CO2,AVE}$* = Average of Inlet and Outlet P_{CO2}*. Plotted against K_g Results.

Table 2-13. Campaign 4 - 5mK^+/2.5mPZ Results for K_G Calculation

Run#	N_{CO2} gmol/min	Liq Rate m/hr	Eff Intf Area m^2/m^3	P_{CO2} Top Pa	P_{CO2}* Top Pa	P_{CO2} Bot Pa	P_{CO2}* Bot Pa	LMCD Pa	Kgx10^{10} gmol/ Pa-cm^2-s	P_{CO2}* Ave Pa	Comment
4.1	41.98	22.51	217.4	641	35	8404	329	2884	1.28	182	-
4.2.1	58.48	20.13	216.0	4184	27	16830	1688	8498	0.61	858	-
4.2.2	58.99	20.15	216.0	5110	20	17761	3174	9020	0.58	1597	-
4.3.1	44.92	20.87	216.5	2712	71	16151	1587	6983	0.57	829	-
4.3.2	45.97	20.96	216.5	2919	66	16773	2604	7061	0.57	1335	-
4.4.1	55.62	23.32	217.8	5327	68	17789	2495	9400	0.52	1282	-
4.4.2	55.54	23.37	217.9	5601	85	17848	97798	-	-	-	Outlier
4.5.1	0.00	23.27	217.8	6949	60	17215	1849	10567	-	955	Outlier
4.5.2	65.77	23.32	217.8	6947	65	18182	2581	10654	0.54	1323	-
4.6.1	50.09	19.26	215.5	2453	36	17219	1365	7144	0.62	701	-
4.6.2	50.32	19.24	215.5	2119	25	17016	1509	6699	0.67	767	-
4.7.1	54.09	23.34	217.9	1398	16	13792	468	5270	0.90	242	-
4.7.2	53.19	23.30	217.8	1074	16	13432	422	4763	0.98	219	-
4.8	51.03	23.27	217.8	1948	13	11291	304	5213	0.86	159	-
4.9.1	63.13	23.18	217.8	5958	10	17138	485	10398	0.53	247	-
4.9.2	62.14	23.23	217.8	5766	11	16761	401	10150	0.54	206	-
4.10.1	45.41	20.89	216.5	5107	78	18170	500	10060	0.40	289	-
4.10.2	45.30	20.90	216.5	5246	58	18224	1085	10000	0.40	572	-
4.11.1	47.75	23.27	217.8	5253	43	15431	1020	9043	0.46	531	-
4.11.2	47.32	23.31	217.8	5549	46	15563	1186	9240	0.45	616	-
4.12.1	39.71	23.29	217.8	4816	37	11605	691	7429	0.47	364	-
4.12.2	41.97	23.28	217.8	5942	44	13064	853	8675	0.42	449	-
4.13.1	70.78	46.46	231.0	5267	22	17976	173	10275	0.57	98	-
4.13.2	70.17	46.56	231.1	4474	41	17063	430	9226	0.63	235	-
4.14.1	66.38	48.12	232.0	3015	46	17895	401	8189	0.67	224	-
4.14.2	63.00	48.02	231.9	2263	43	16637	347	7060	0.74	195	-
4.15.1	49.73	37.59	226.0	2007	30	17319	431	6952	0.61	230	-
4.15.2	49.84	37.64	226.0	2270	30	17607	332	7360	0.57	181	-
4.16.1	61.95	40.14	227.4	6333	93	17113	4944	8877	-	-	Outlier
4.16.2	56.27	40.11	227.4	3883	52	13761	604	7558	0.63	328	-
4.17.1	70.61	40.29	227.5	4956	9	17249	359	9726	0.61	184	-
4.17.2	76.00	40.31	227.5	4352	14	17672	539	9315	0.69	276	-
4.18	68.79	32.39	223.0	1982	19	14632	758	6090	0.97	389	-
4.19	66.08	32.32	223.0	1403	38	13749	1375	4994	-	-	Outlier

1. LMCD = Log Mean Concentration Difference
2. $P_{CO2,AVE}$* = Average of Inlet and Outlet P_{CO2}*. Plotted against K_g Results.

Table 2-14. Campaign 4 – 6.4mK$^+$/1.6mPZ Results for K_G Calculation

Run#	N_{CO2} gmol/min	Liq Rate m/hr	Eff Intf Area m^2/m^3	P_{CO2} Top Pa	P_{CO2}* Top Pa	P_{CO2} Bot Pa	P_{CO2}* Bot Pa	LMCD Pa	Kgx10^{10} gmol/ Pa-cm^2-s	P_{CO2}* Ave Pa	Pinch
4.20.1	38.78	36.72	225.5	5134	121	16308	319	9463	0.35	220	-
4.20.2	38.27	36.89	225.6	5324	54	16373	177	9732	0.33	116	-
4.21.1	39.65	41.79	228.4	3349	82	14795	176	7576	0.44	129	-
4.21.2.	42.55	41.80	228.4	4325	106	16782	279	9006	0.40	193	-
4.22.1	33.15	24.20	218.3	8969	20	18340	492	12891	-	-	Outlier
4.22.2	34.22	24.26	218.4	9081	20	18870	1142	12914	-	-	Outlier
4.23	37.26	24.27	218.4	7769	37	18308	984	11890	0.27	511	-
4.24	36.63	24.24	218.4	7278	56	17652	1001	11288	0.28	528	-
4.25	38.84	27.51	220.2	5577	29	16768	247	10056	0.34	138	-
4.26.1	45.33	33.77	223.8	3718	23	17484	327	8767	0.44	175	-
4.26.2	45.73	33.84	223.8	4259	31	18147	281	9462	0.41	156	-
4.27.1	41.40	29.10	221.1	5338	32	17325	576	9954	0.36	304	-
4.27.2	40.18	29.13	221.2	4958	21	16608	369	9492	0.37	195	-
4.28.1	37.48	24.31	218.4	6429	24	17052	549	10669	0.31	286	-
4.28.2	35.27	24.27	218.4	5206	26	15248	296	9218	0.33	161	-
4.29.1	38.99	24.28	218.4	4412	21	15714	442	8729	0.39	232	-
4.29.2	40.37	24.32	218.4	5121	19	16777	342	9689	0.36	180	-
4.30.1	43.96	29.08	221.1	3244	1	16062	238	7938	0.48	119	-
4.30.2	46.03	29.09	221.1	4148	20	17511	416	9125	0.44	218	-
4.31.1	48.43	33.94	223.9	9008	34	17232	552	12432	0.33	293	-
4.31.2	48.10	33.94	223.9	8822	53	17095	413	12304	0.33	233	-
4.32.1	47.11	29.10	221.1	10050	41	17931	593	13339	0.31	317	-
4.32.2	45.38	29.08	221.1	9563	64	17180	1967	12133	-	-	Outlier
4.33.1	44.82	24.28	218.4	10402	43	17826	391	13592	0.29	217	-
4.33.2	43.42	24.24	218.4	10257	60	17435	209	13406	-	-	Outlier

1. LMCD = Log Mean Concentration Difference
2. $P_{CO2,AVE}$* = Average of Inlet and Outlet P_{CO2}*. Plotted against K_g Results.

Figure 2-38 shows the K_g results for the absorber of Campaign 1. In the first campaign, the four slightly different compositions of the K$^+$/PZ solvent were used. The four different compositions are differentiated as Run 1, Run 2-7, Run 8-17, and Run 18-19. The figure shows that the first three sets of solvent compositions gave comparable results for an equilibrium CO_2 partial pressure that ranged from 6 to 1000 Pa. The averaged results for each set of runs are also plotted. However, the results for the last run were much higher and not consistent with the other three sets. In Run 18-19, water was removed in order to further concentrate the solvent, so the absorption rate was expected to higher. In addition, the calculated results seemed to indicate that there was a pinch at

the top of the absorber. The figure also shows that the Kg results match the wetted wall column results at 40 °C. This is somewhat unexpected since temperature bulges that ranged from 50 to 70 °C were observed. It is possible that there was some gas film resistance, which would reduce the mass transfer rate. Also, the temperature bulges, may have resulted in a mid-column pinch.

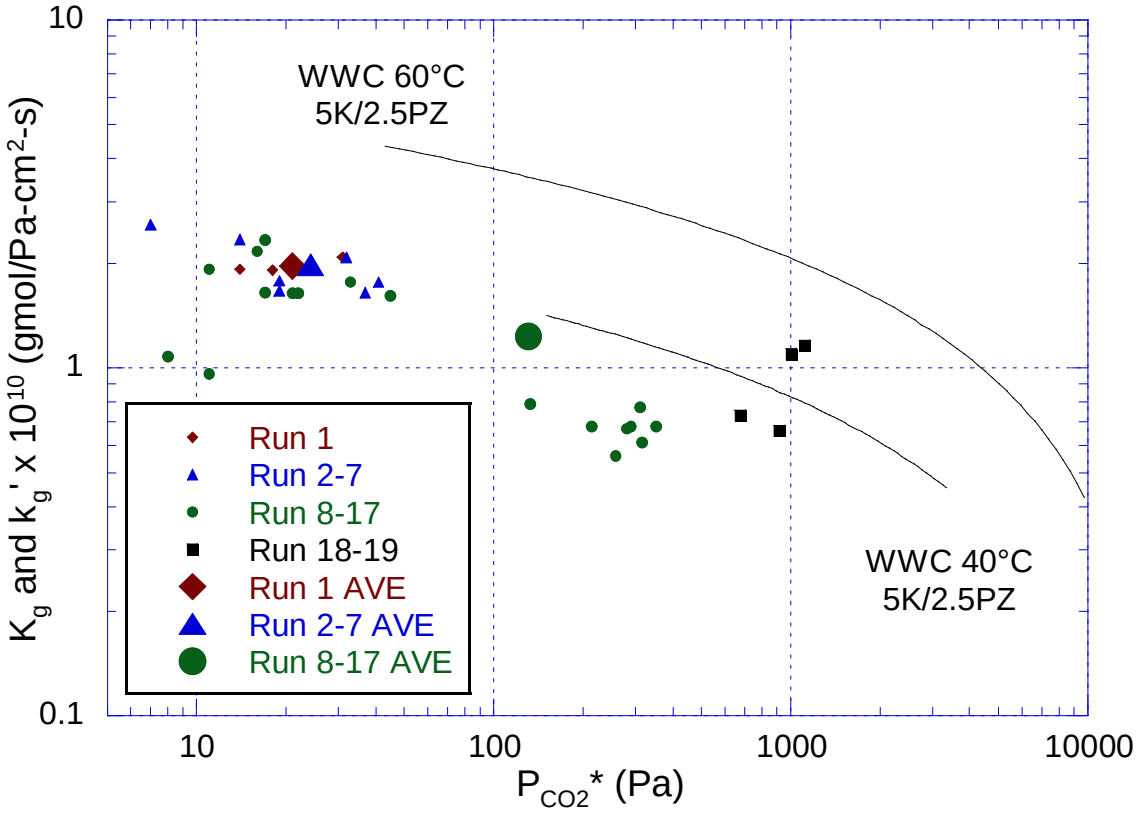

Figure 2-38. Absorber K_g Results for Campaign 1 (Flexipac 1Y Structured Packing), Wetted Wall Column Results (k_g') for 5mK^+/2.5mPZ at 40 and 60 °C

In the second campaign, the absorber was operated over an equilibrium partial pressure that ranged from 200 to 3000 Pa (Figure 2-39). The absorber was operated at three different inlet CO_2 gas concentrations: 5, 12, and 17 mole percent CO_2. The average K_g results for the three run conditions were all slightly higher than the 40 °C

wetted wall column results and seemed to be consistent with the results obtained for in Campaign 1. However, the 17% CO_2 points were slightly higher than the 5 and 12% points.

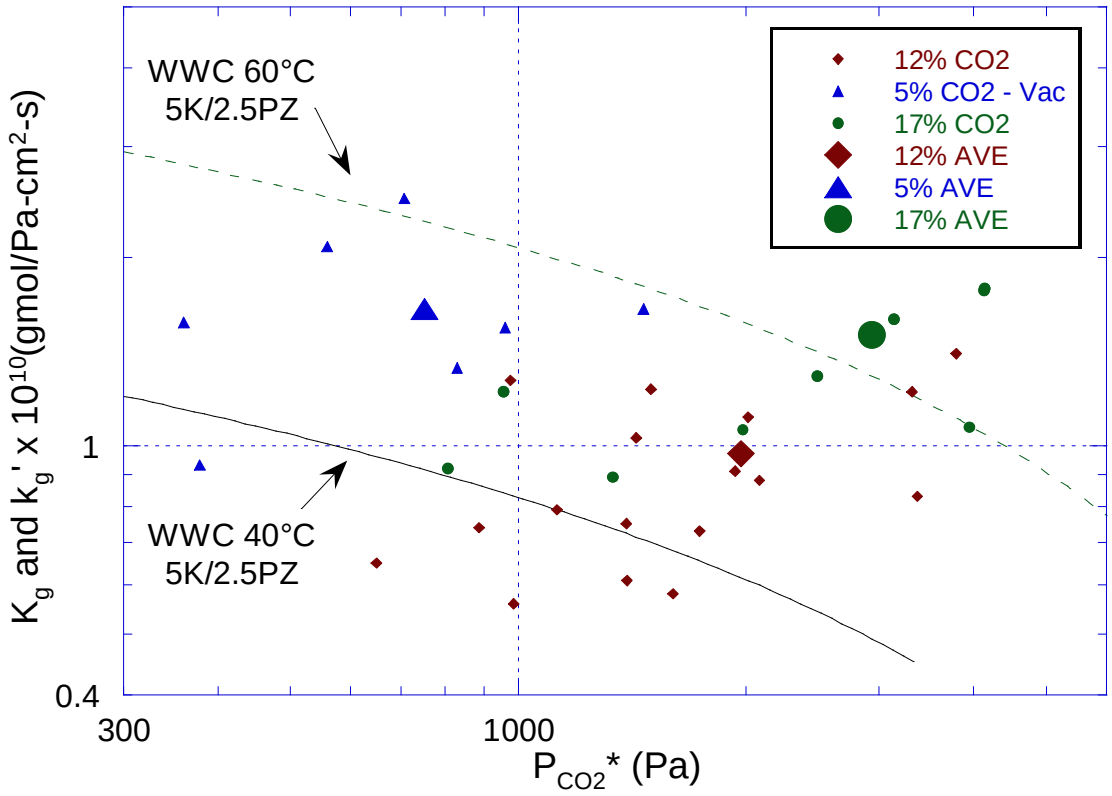

Figure 2-39. Absorber K_g Results for Campaign 2 (Flexipac 1Y Structured Packing), Wetted Wall Column Results (k_g') for 5mK^+/2.5mPZ at 40 and 60 °C

Figure 2-40 shows that in Campaign 4, the 5mK^+/2.5mPZ solvent had an absorption rate that is approximately twice that of the 6.4mK^+/1.6mPZ solvent. The figure also shows that both solvents had slower absorption rates than the wetted wall column at 40 °C. In addition, the k_g' for the 6.4mK^+/1.6mPZ solvent at 40 °C was calculated from the FORTRAN model developed by Cullinane (2005). The FORTRAN model assumes k_l = 0.0004 m/s and k_g = 5.0 x 10^{-9} kmol/Pa-m^2-s. The plot shows that

the normalized flux of FORTRAN model for 6.4mK^+/1.6mPZ matched the wetted wall column data for the 5mK^+/2.5mPZ solvent, which is not expected.

In the fourth campaign, Flexipac AQ Style 20 structured packing was used, whereas in the first and second campaigns, Flexipac 1Y was used. The results show that the mass transfer performance was worse with the new packing. The new packing is designed to have a lower liquid holdup, which may reduce the mass transfer performance. Also, the effect of bridging between the channels in the packing will be more prevalent with the Flexipac 1Y because it is a high surface area packing and the channels are narrower. Although the net effect of bridging is to decrease available interfacial area, it may result in an increase in liquid holdup and provide better mass transfer performance for this system.

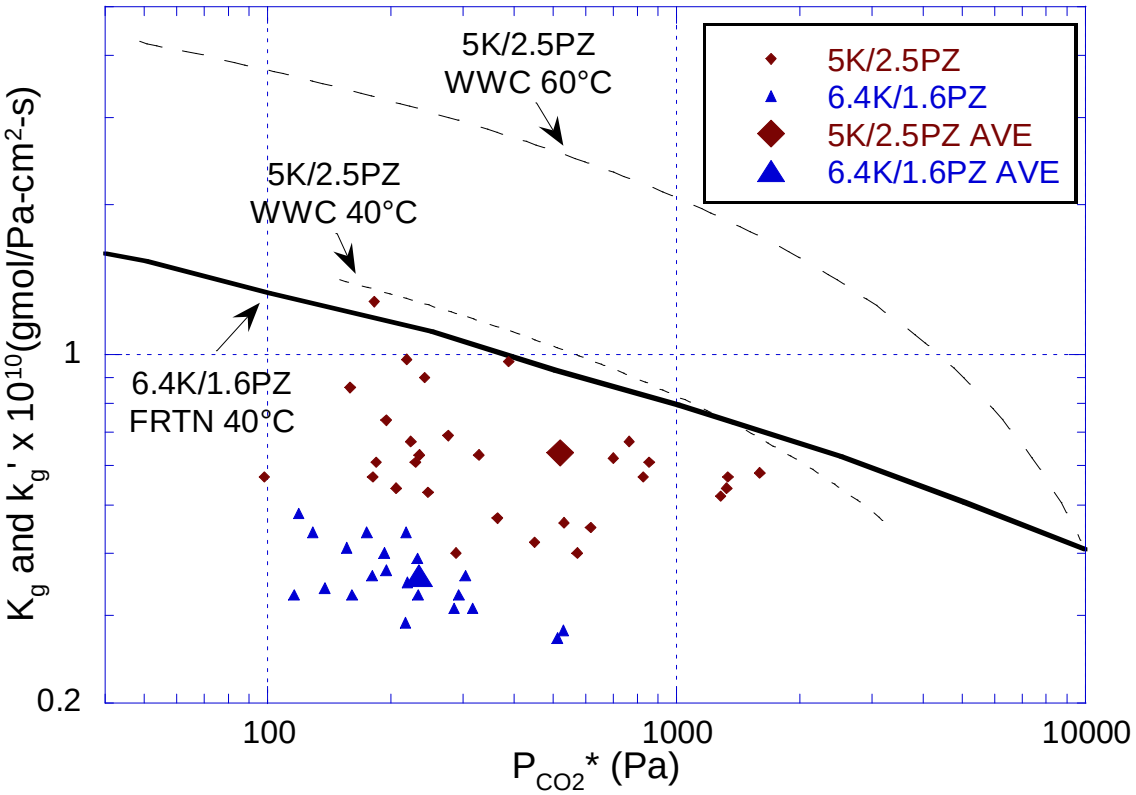

Figure 2-40. Absorber K_g Results for Campaign 4 (5mK^+/2.5mPZ and 6.4mK^+/1.6mPZ, Flexipac AQ Style 20 Structured Packing) and Wetted Wall Column Results (k_g') for 5mK^+/2.5mPZ at 40 and 60 °C, 6.4mK^+/1.6mPZ FORTRAN Model Results at 40 °C

Finally, the results for all three potassium carbonate and piperazine campaign are compared to the 7 m MEA results from Campaign 3 (Dugas, 2006). The MEA mass transfer coefficient that was calculated assuming 17% inlet CO_2 concentration was used for the comparison. In the third campaign, Flexipac 1Y structured packing in the absorber. Figure 2-41 shows that for the same packing, the 5mK+/2.5mPZ solvent was approximately 1.5 times faster than 7 m MEA. The results also seem to show that comparable mass transfer performance was achieved with MEA when the Flexipac AQ packing was used with the 5mK^+/2.5mPZ solvent.

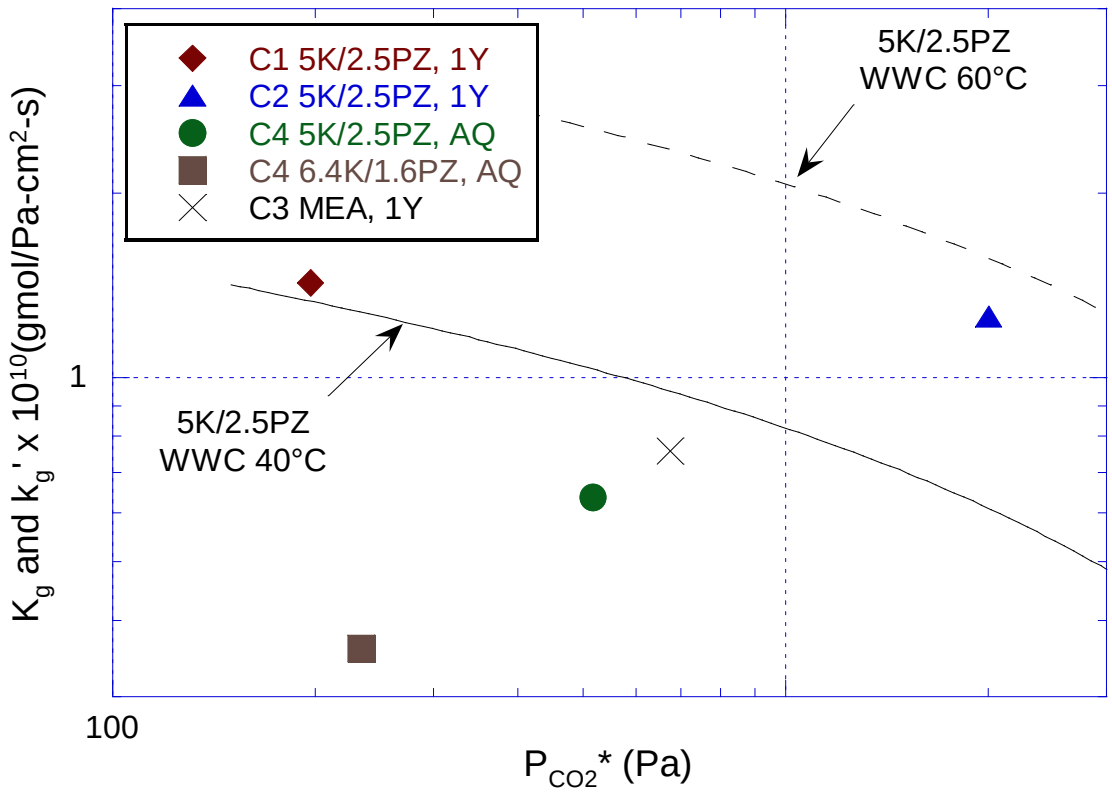

Figure 2-41. Comparison of K_g Results for 5mK+/2.5mPZ, 6.4mK+/1.6mPZ, 7mMEA, and k_g' of Wetted Wall Column (Cullinane, 2005)

Based on the K_g analysis, it was found that the 5mK^+/2.5mPZ solvent had an absorption rate 1.5 times faster than 7 m MEA and 2 times faster than 6.4mK^+/1.6mPZ. Also, the Flexipac 1Y structured packing performed 1.8 times better than the Flexipac AQ Style 20 structured packing, even after accounting for the measured values of wetted area. Finally, the K_g results for the 5mK^+/2.5mPZ solvent matched the performance of the wetted wall column at 40 °C.

2.13 ABSORBER TEMPERATURE PROFILE

The absorption of CO_2 into piperazine promoted potassium carbonate is an exothermic reaction. One of the advantages of the K^+/PZ solvent is that the heat of absorption is tunable with a composition change. The heat of absorption can be varied from 10 to 20 kcal/mol of CO_2 absorbed. The heat that is produced results in an increase in temperatures of the liquid and gas and the transfer of water between the two phases. At the location in the absorber column where the bulk of the CO_2 is absorbed, the temperature profile of the absorber will reach a maximum and produce a temperature bulge. At a high liquid to gas (L/G) ratio, the temperature bulge will be observed towards the bottom of the column and at low L/G ratios, the temperature bulge will be located at the top of the column.

The increase in temperature typically increases the kinetics of the absorption of CO_2, but at the same will affect the vapor-liquid equilibrium. At high temperatures, the partial pressure of CO_2 in equilibrium with the liquid may begin to approach to the partial

pressure of CO_2 in the bulk gas. The lack of a driving force results in a "pinch", where additional CO_2 is not absorbed by the solvent. As a result, the mass transfer performance of the column is reduced. In the operation of a plant, pinch points are typically avoided in order to maximize the available mass transfer area of the column.

2.13.1 Temperature Sensor Location

The temperature profile of the absorber was characterized with RTDs installed along the length of the column. The RTD sensors are inserted several centimeters into the packing and contact a mixture of gas and liquid. It is almost impossible to surmise whether the temperature of the gas or liquid is being measured. The location of the temperature sensors in absorber are shown in Figure 2-42. The reference point is given as the bottom of the lower bed of packing. The absorber is divided into two beds of packing, each with a height of 3.05 meters. The two beds of packing are separated by a 1.67 meter section that contains a spool piece where the collector plate and redistributor are located.

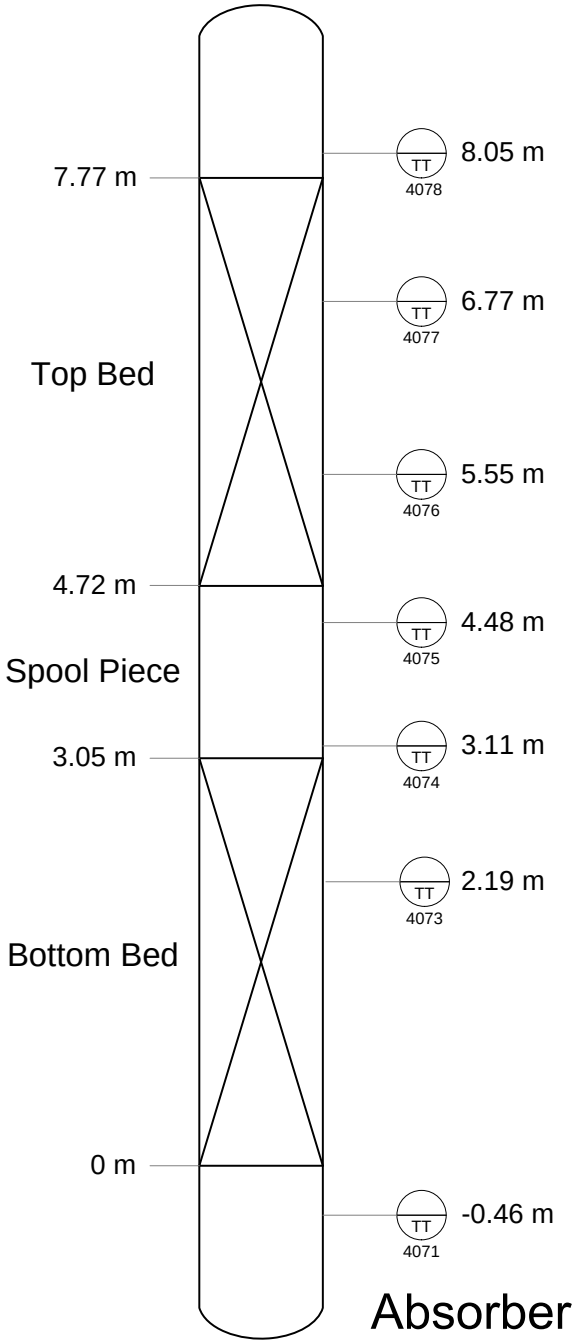

Figure 2-42. Location of Temperature Sensors in Absorber Column

In Campaign 1, the following temperature sensors were used: TT4071, TT7073, TT4076, and TT4078. However, temperature sensor TT4076 was located 6.31 m above

the reference point. In the first campaign, the surface temperature of the absorber column was measured with an infrared (IR) temperature sensor to estimate the amount of heat loss from the uninsulated absorber column. The IR measurements were made every 0.15 meters along the length of each packed bed.

2.13.2 Infrared and RTD Measurements

Figure 2-43 illustrates the IR and RTD measurements made on 6/24/04 at 10:45 AM. The gas and liquid flow rates were 8.5 m^3/min and 19.5 L/min, respectively. The inlet CO2 concentration was approximately 12% and the lean loading was 0.53 mol CO_2/mol K+2PZ. The figure shows that there is approximately a 2–3 °C difference between the two measurements (TT4073 and TT4076). It can be concluded that the resulting temperature difference is a result of heat loss. A simple heat loss calculation was performed for the just the surface area containing the packing and assuming the thermal conductivity of steel was 43.3 W/m-K and that there was a temperature difference of 2 °C between the inside and outside of the column across the entire length of the column. The heat loss for 6.1 m of the column was estimated to be 51.4 kW.

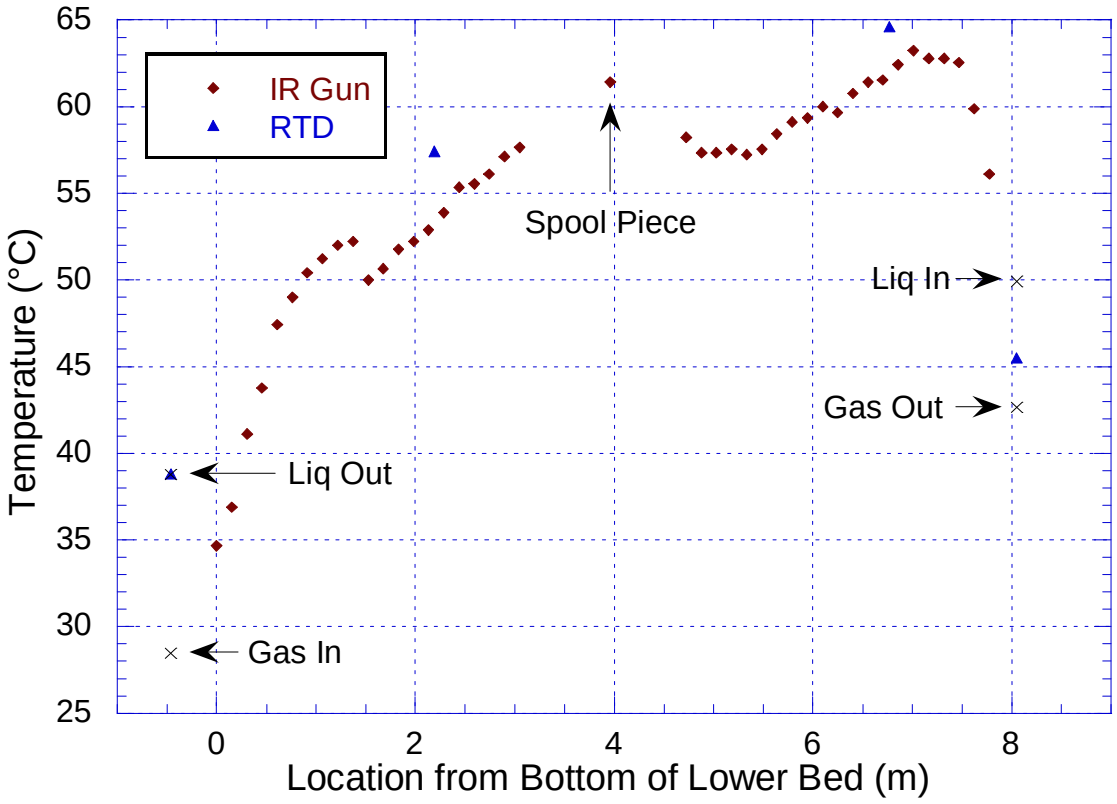

Figure 2-43. Absorber Temperature Profile for Run Performed on 6/24/04 at 10:45 AM (G = 8.5 m^3/min, L = 29.5 L/min, CO_2 In = 12%, Lean Ldg = 0.53 mol/Talk)

The figure also shows that there is a drop in temperature of ~2.5 °C at 1.4 meters. The dip in temperature is most likely a result of heat loss from the two support fixtures of the absorber column, which are located in the immediate vicinity. The support fixtures behave as two large fins, conducting and dissipating heat from the absorber column.

An IR temperature measurement taken at middle of the spool piece was 3.8 °C higher than the surrounding measurements made above and below. The higher temperature would seem to indicate that CO_2 is being absorbed in the collector plate or redistributor. However, this not expected to happen. Future studies should examine this phenomenon in more detail.

Finally, the inlet and outlet temperatures for the gas and liquid are shown. The liquid inlet temperature is about 5 °C higher than topmost RTD temperature (TT4078), while the outlet gas temperature is approximately 3 °C lower. Temperature sensor TT4078 is located directly above the distributor and does not contact any liquid and therefore, TT4078 should be a good indicator of outlet gas temperature. The outlet gas sensor is located approximately 8 meters downstream of the absorber and is expected to be lower than TT4078 because of heat loss. However, during some runs, the temperature measurement of TT4078 was actually lower than that measured at the gas outlet. It is possible that the probe was not inserted far enough into the column or evaporative cooling from condensation may have skewed the temperature measurement. At the bottom of the column, temperature sensor TT4071 is located 6.3 cm below the inlet gas nozzle and should have intermittent contact with liquid falling down through the packing. In this case, the inlet gas measurement was lower than TT4071 while the outlet liquid temperature matched the RTD measurement. However, it should be noted that the outlet liquid passes through a pump, a filter and approximately 38 meters of piping before the temperature is measured.

The absorber liquid outlet has two temperature measurements. The outlet pH meter is located 0.9 meters from the absorber outlet and the absorber rich Micro Motion® is located approximately 38 meters downstream of the absorber outlet. The absorber lean Micro Motion® is located 22 meters upstream of the absorber inlet nozzle. The lean pH temperature measurement is located approximately 5 meters downstream of the Micro Motion®.

2.13.3 Temperature Bulge

The location and magnitude of the temperature bulge is dependent upon several factors such as liquid flow rate, liquid to gas flow rate ratio (L/G), inlet CO_2 gas concentration, solvent composition, mass transfer area, and inlet gas and liquid temperatures. An analysis of the temperature bulge was carried out for the three potassium carbonate and piperazine campaigns.

Figure 2-44 shows that the location of the temperature bulge depends on the liquid to gas flow rate ratio (L/G). At low L/G ratios, the temperature bulge will typically be located near the top of the column. As the L/G ratio increases, the temperature bulge will begin to move down the column and at some point cease to exist. At a high L/G ratio, the bulk of the enthalpy is carried out of the column by the high liquid flow rate.

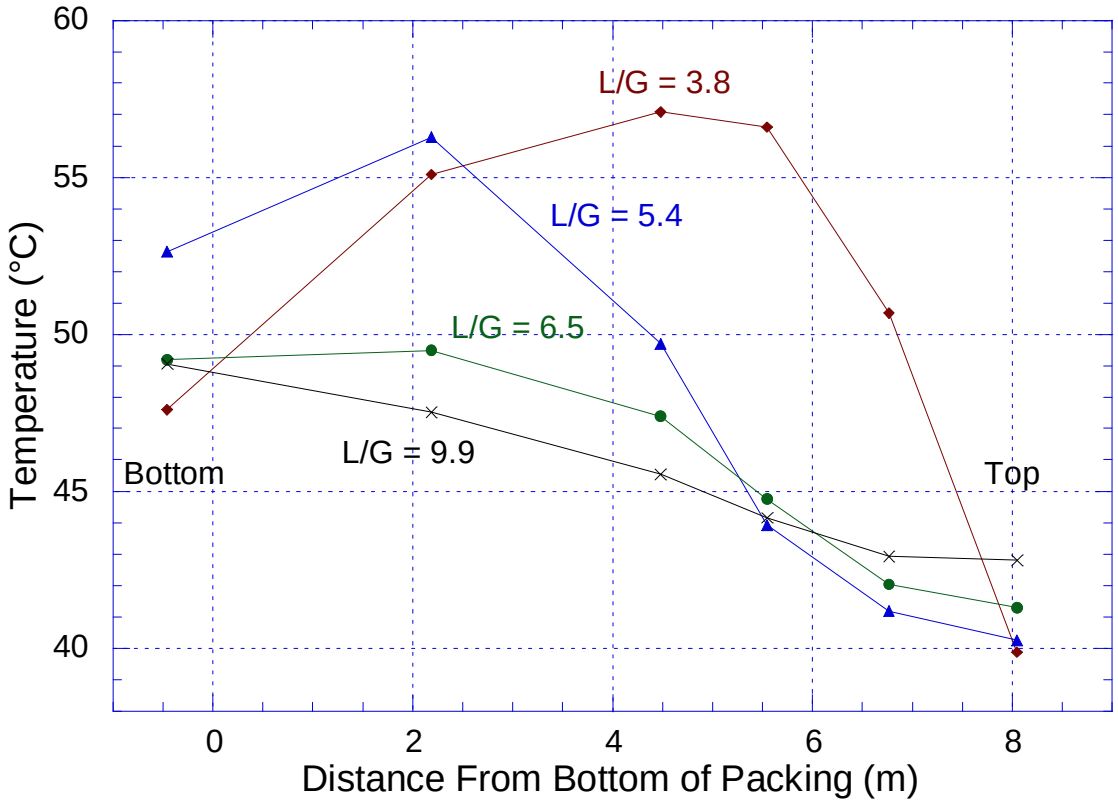

Figure 2-44. Temperature Bulge Location and Magnitude in Absorber (Campaign 4, 5mK$^+$/2.5mPZ, CO_2 In = 17 mol%, L = 93–139 kg/min)

The location of the temperature bulge (T_{max}) was determined based on the RTD measurements. The true maximum temperature and corresponding location could not be determined since it was not possible to have temperature measurements every 5 cm along the entire length of the column. Figure 2-45 shows that as the L/G ratio increases, the location of T_{max} will move from the top of the column to the bottom, which was also shown in the previous figure. The plot also shows that at lower inlet CO_2 gas concentrations, the temperature bulge will begin to shift down the column at lower L/G ratios. The T_{max} location of the 3-5% inlet CO_2 runs begin to shift at a L/G = 2, while the transition point for the 12% runs occur at L/G = 3.5 and the 17% runs occur at L/G = 4.5

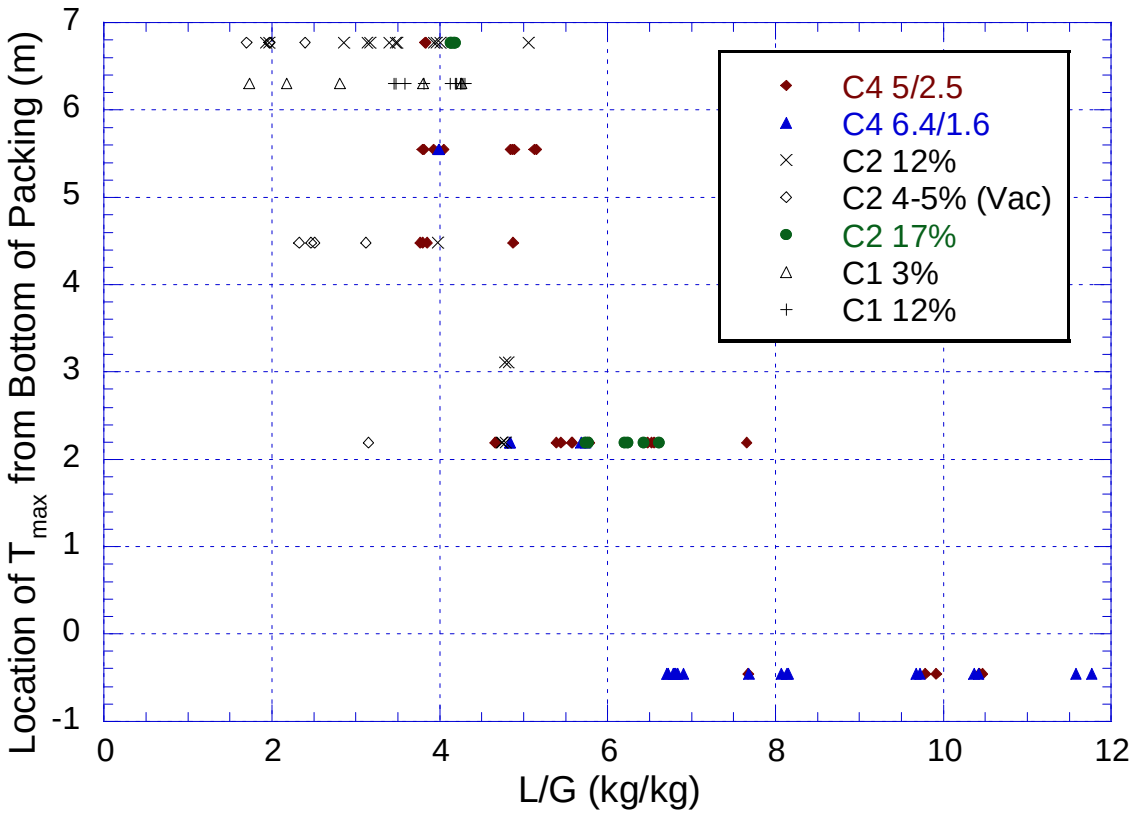

Figure 2-45. Location of Temperature Bulge as a Function of Liquid to Gas Ratio and inlet CO_2 Gas Concentration for Campaigns 1, 2, and 4

A plot of the T_{max} measurements and L/G ratio illustrates the magnitude of the temperatures that were attained in the three campaigns (Figure 2-46). The figure shows that the maximum temperatures were achieved at an L/G ratio of 4 to 5 kg/kg. The 12% CO_2 data from Campaign 2 also suggests that the temperature bulge passes through a maximum at L/G = 3.5.

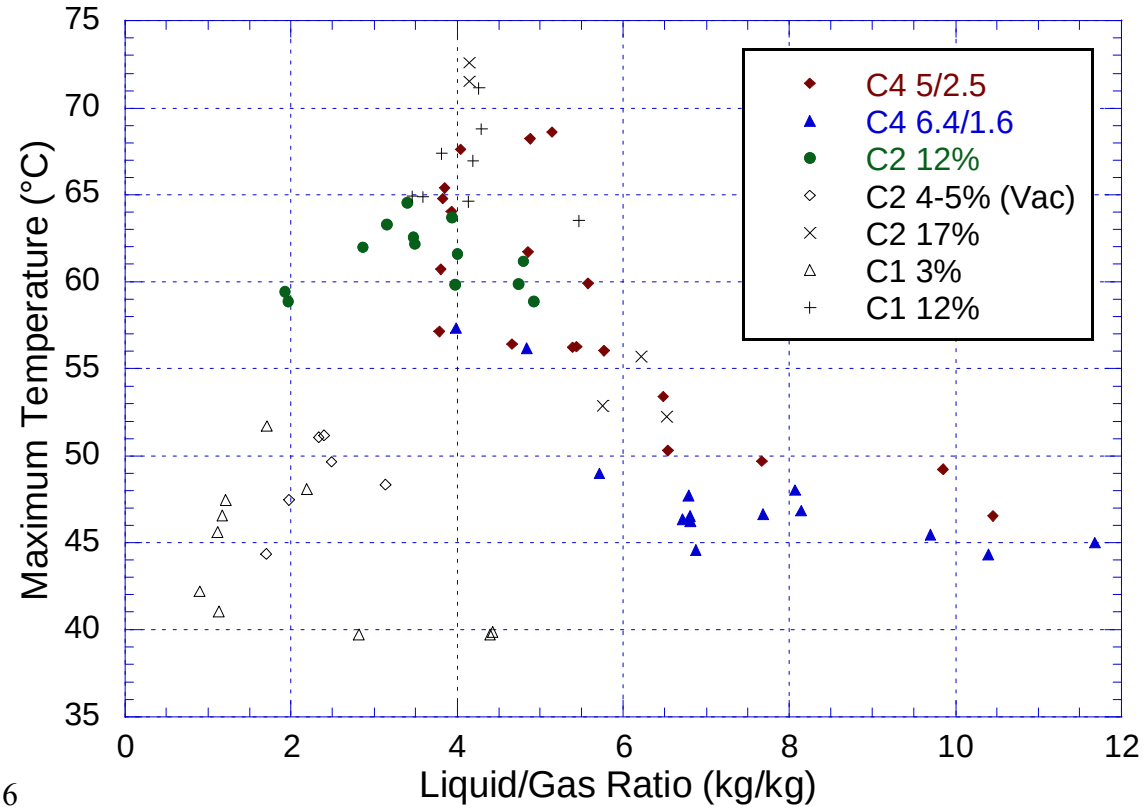

6

Figure 2-46. Magnitude of Temperature Bulge as a Function of Liquid to Gas Ratio and inlet CO_2 Gas Concentration for Campaigns 1, 2, and

The average temperature of the absorber column was calculated by integrating the area under the temperature profile curve and dividing by the height of the column. There

were some issues with the TT4078 temperature measurements located at the top of the absorber (8.05 meters). For the analysis, the highest of the following three temperatures were used as the top temperature: gas out, liquid in or TT4078. At the bottom of the absorber, where TT4071 was located (-0.46 m), the higher of the following two temperatures was used: liquid out or TT4071.

In Campaign 1, only four RTD temperature measurements were available, whereas in Campaign 2 and 4, there were 7 and 6 RTD measurements, respectively. Therefore, the integrated temperature profiles of Campaign 1 should not be directly compared to those obtained in the other two campaigns because the profile was not characterized as well. Finally, the temperature profile was integrated from the -0.46 m to 8.05 m on the x-axis. The lowest temperature in the profile was used as the reference point for the y-axis as a way of normalizing the difference between top and bottom temperatures, which varied with each of the runs and were typically the lowest temperatures in the temperature profile.

Table 2-15. Campaign 1 Temperature Profile Analysis

Run#	L/G	L	Temp 8.05 m	Temp 6.31 m	Temp 2.19 m	Temp -0.46 m	T_{max}	T_{max} Loc	T_{ave}	CO_2 Rem Gas-side
	kg/kg	kg/min	°C	°C	°C	°C	°C	m	°C	gmol/min
1.1.1	1.11	21.7	42.6	45.8	39.9	29.2	45.8	6.31	40.6	16.92
1.1.2	1.11	21.7	42.0	45.5	39.5	28.6	45.5	6.31	40.1	16.63
1.1.3	1.12	21.7	42.4	45.6	39.6	29.0	45.6	6.31	40.3	16.17
1.2.1	2.18	21.9	41.5	46.8	46.6	32.9	46.8	6.31	44.0	9.81
1.2.2	2.19	21.9	43.2	48.6	47.3	33.1	48.6	6.31	45.1	9.61
1.2.3	2.20	22.0	44.5	48.8	47.5	33.0	48.8	6.31	45.4	9.44
1.3.1	4.43	43.9	41.0	39.9	37.8	38.4	39.9	6.31	38.9	7.20
1.3.2	4.43	44.0	40.7	40.0	37.7	38.1	40.0	6.31	38.9	7.83
1.3.3	4.43	43.9	40.4	39.7	37.4	38.1	39.7	6.31	38.6	7.57
1.4.1	4.40	43.9	40.0	39.7	37.5	39.4	39.7	6.31	38.8	12.54
1.5.1	2.81	38.1	40.1	39.7	37.3	38.3	39.7	6.31	38.6	12.97
1.6.1	5.60	33.9	39.5	48.2	48.0	44.0	48.2	6.31	46.6	21.43
1.7.1	5.46	22.1	41.5	63.5	51.4	39.2	63.5	6.31	52.7	13.78
1.8.1	1.17	23.0	43.6	46.8	40.9	29.7	46.8	6.31	41.5	19.50
1.8.2	1.17	22.9	43.5	46.3	40.6	29.4	46.3	6.31	41.1	20.34
1.9.1	0.90	22.9	42.1	42.3	36.7	31.6	42.3	6.31	38.4	23.13
1.9.2	0.89	22.9	41.9	42.1	36.8	31.5	42.1	6.31	38.3	24.05
1.10.1	1.73	23.2	42.7	51.6	48.0	30.1	51.6	6.31	45.9	12.95
1.10.2	1.68	22.5	42.7	51.8	48.1	29.8	51.8	6.31	46.0	11.76
1.11.1	1.12	11.4	35.8	40.7	33.9	22.6	40.7	6.31	34.7	8.36
1.11.2	1.13	11.5	36.1	41.4	34.3	22.7	41.4	6.31	35.1	7.82
1.12.1	1.22	32.1	42.9	47.2	41.8	34.4	47.2	6.31	42.6	14.59
1.12.2	1.20	30.0	43.7	47.7	41.7	34.4	47.7	6.31	42.8	22.61
1.13.1	3.59	35.3	49.4	64.9	54.8	38.5	64.9	6.31	55.2	38.98
1.14.1	3.81	30.9	46.2	67.4	57.7	41.0	67.4	6.31	57.3	30.57
1.15.1	4.13	35.6	39.6	61.5	53.0	39.8	61.5	6.31	52.5	30.33
1.15.2	4.13	35.6	44.0	67.7	59.0	40.9	67.7	6.31	57.7	28.57
1.16.1	3.45	35.7	50.8	65.2	57.2	38.5	65.2	6.31	56.4	33.93
1.16.2	3.48	35.8	49.7	64.6	57.4	38.8	64.6	6.31	56.2	34.60
1.17.1	4.18	22.9	48.2	66.8	56.7	38.4	66.8	6.31	56.5	18.89
1.17.2	4.20	22.9	47.7	67.2	57.1	38.4	67.2	6.31	56.7	19.09
1.18.1	4.26	35.9	52.9	71.0	63.5	44.6	71.0	6.31	62.0	31.23
1.18.2	4.25	35.9	53.2	71.3	63.5	46.7	71.3	6.31	62.5	31.86
1.19.1	4.28	23.1	53.7	68.3	59.0	40.4	68.3	6.31	58.8	18.43
1.19.2	4.30	23.2	53.2	69.3	59.0	39.8	69.3	6.31	58.9	19.14

Table 2-16. Campaign 2 Temperature Profile Analysis

Run#	L/G	L	Temp 8.05 m	Temp 6.77 m	Temp 5.55 m	Temp 4.48 m	Temp 3.11 m	Temp 2.19 m	Temp -0.46 m	T_{max}	T_{max} Loc	T_{ave}	CO_2 Rem Gas-side
	kg/kg	kg/min	°C	°C	°C	°C		°C	°C	°C	m	°C	gmol/min
2.1.1	1.93	36.9	49.2	59.7	53.2	52.7	48.3	48.5	49.1	59.7	6.77	51.5	52.74
2.1.2	1.93	37.0	48.8	59.1	52.8	52.4	48.1	48.1	48.8	59.1	6.77	51.1	50.28
2.2.1	1.97	37.0	50.8	58.9	53.1	53.5	49.8	50.0	51.8	58.9	6.77	52.5	37.00
2.3.1	2.86	41.7	44.6	62.0	56.7	57.2	52.3	51.4	45.5	62.0	6.77	53.2	33.09
2.4.1	3.48	51.0	40.9	62.5	58.3	59.2	54.1	54.3	45.4	62.5	6.77	54.3	37.70
2.5.1	3.49	50.8	40.7	62.2	58.4	59.4	54.5	54.5	45.8	62.2	6.77	54.4	35.77
2.6.1	3.98	58.0	41.2	59.3	59.1	59.8	56.6	58.0	47.5	59.8	4.48	55.5	38.39
2.7.1	4.01	58.2	41.3	61.6	60.0	61.0	57.5	58.5	47.7	61.6	6.77	56.4	39.83
2.8.1	3.14	60.6	45.8	63.2	59.1	59.1	57.6	54.7	48.0	63.2	6.77	55.9	44.61
2.8.2	3.17	60.4	46.2	63.4	59.4	59.4	58.1	55.6	48.9	63.4	6.77	56.4	43.60
2.9.1	3.40	39.7	41.1	64.2	58.7	57.3	55.5	53.7	42.7	64.2	6.77	54.0	28.92
2.9.2	3.40	39.6	42.2	64.8	59.1	57.5	55.9	54.0	43.0	64.8	6.77	54.4	29.35
2.10.1	4.74	53.6	41.2	52.2	58.8	58.7	59.1	59.8	48.9	59.8	2.19	55.2	35.12
2.10.2	4.75	53.5	41.3	52.6	59.2	59.0	59.3	59.9	49.7	59.9	2.19	55.5	34.77
2.11.1	4.78	53.3	41.4	55.0	60.6	60.8	61.0	60.7	49.4	61.0	3.11	56.7	32.87
2.11.2	4.82	53.6	41.4	56.0	61.0	61.1	61.4	60.9	50.5	61.4	3.11	57.2	32.98
2.12.1	5.06	56.0	41.0	59.7	59.2	57.3	57.2	57.3	50.5	59.7	6.77	55.6	35.61
2.12.2	4.79	55.7	41.0	52.4	57.0	56.6	56.9	58.1	48.7	58.1	2.19	54.0	39.58
2.13.1	3.96	46.7	40.7	65.0	61.4	62.1	61.5	59.0	45.0	65.0	6.77	57.4	33.57
2.13.2	3.93	46.6	40.3	62.5	59.9	61.0	60.1	57.9	44.1	62.5	6.77	56.1	34.28
2.14.1	1.97	23.2	43.5	48.0	44.1	43.7	36.6	39.7	34.1	48.0	6.77	41.1	15.93
2.14.2	1.98	23.3	42.5	46.9	43.4	43.3	36.2	39.5	33.3	46.9	6.77	40.5	14.87
2.15.1	2.40	28.1	41.9	51.2	49.5	50.6	44.6	46.3	37.0	51.2	6.77	46.1	18.03
2.16.1	2.33	27.4	42.0	50.9	49.8	51.0	45.1	46.7	36.9	51.0	4.48	46.3	18.05
2.16.2	1.70	25.6	38.8	44.8	40.8	41.3	35.6	36.9	34.0	44.8	6.77	38.7	19.35
2.17.1	1.70	25.6	39.0	43.9	40.1	40.7	34.9	36.6	33.0	43.9	6.77	38.1	16.01
2.18.1	2.51	37.3	44.8	45.9	47.5	49.6	43.7	46.7	40.5	49.6	4.48	45.6	17.13
2.18.2	2.47	36.6	44.8	45.7	47.5	49.7	43.9	47.1	40.9	49.7	4.48	45.7	16.74
2.19.1	3.12	46.1	47.0	44.2	44.3	46.9	41.2	46.6	43.6	46.9	4.48	44.8	17.58
2.19.2	3.15	46.2	47.8	46.3	46.5	49.2	44.4	49.8	44.9	49.8	2.19	47.1	17.42
2.20.1	5.73	94.8	40.1	42.5	46.7	51.7	49.3	52.9	49.7	52.9	2.19	48.4	71.52
2.20.2	5.77	94.5	40.1	42.2	45.8	51.4	48.9	52.8	50.1	52.8	2.19	48.2	69.91
2.21.1	6.43	102.2	40.1	40.7	43.4	48.9	47.1	50.8	50.1	50.8	2.19	46.6	67.80
2.21.2	6.61	102.0	40.9	42.3	45.6	51.1	49.9	53.7	52.0	53.7	2.19	48.8	63.62
2.22.1	6.20	101.2	41.8	44.4	49.0	54.0	53.0	56.3	52.4	56.3	2.19	51.1	75.52
2.22.2	6.24	101.9	41.1	42.9	47.2	52.5	51.6	55.1	52.1	55.1	2.19	49.9	75.95
2.23.1	4.17	69.7	41.5	72.1	67.5	67.6	64.7	63.2	49.0	72.1	6.77	62.1	65.79
2.23.2	4.14	69.3	39.8	71.0	67.1	67.4	64.6	62.9	48.6	71.0	6.77	61.6	64.16
2.24.1	4.18	70.0	41.5	72.6	67.6	68.1	65.2	63.8	49.1	72.6	6.77	62.4	69.88
2.24.2	4.13	69.5	42.0	72.5	67.6	68.0	65.0	63.6	49.0	72.5	6.77	62.4	70.91

Table 2-17. Campaign 4 – 5mK^+/2.5mPZ Temperature Profile Analysis

Run#	L/G	L	Temp 8.05 m	Temp 6.77 m	Temp 5.55 m	Temp 4.48 m	Temp 2.19 m	Temp -0.46 m	T_{max}	T_{max} Loc	T_{ave}	CO_2 Rem Gas-side
	kg/kg	kg/min	°C	°C	°C	°C	°C	°C	°C	m	°C	gmol/min
4.1	3.85	64.9	42.4	57.1	64.9	65.4	62.1	49.4	65.4	4.48	58.9	42.0
4.2.1	4.05	58.1	45.8	64.8	67.9	64.9	61.3	49.3	67.9	5.55	60.4	58.5
4.2.2	4.05	58.3	46.1	64.9	67.3	64.3	60.5	49.3	67.3	5.55	60.0	59.0
4.3.1	5.75	60.6	42.1	44.3	50.5	52.2	55.7	50.9	55.7	2.19	50.9	44.9
4.3.2	5.79	60.6	42.5	44.8	51.3	52.9	56.3	51.2	56.3	2.19	51.5	46.0
4.4.1	4.87	67.6	43.6	52.7	60.5	61.0	60.9	50.7	61.0	4.48	56.8	55.6
4.4.2	4.84	67.9	43.9	54.1	62.4	62.4	61.5	50.8	62.4	5.55	57.7	55.5
4.5.1	3.81	67.7	45.7	58.4	61.5	59.6	56.7	48.1	61.5	5.55	56.0	-
4.5.2	3.79	67.9	43.6	56.9	59.9	58.1	55.4	47.8	59.9	5.55	54.7	65.8
4.6.1	5.15	55.2	46.7	66.8	69.7	68.4	64.7	52.3	69.7	5.55	63.1	50.1
4.6.2	5.13	54.9	43.6	58.4	67.5	67.3	64.7	51.9	67.5	5.55	61.1	50.3
4.7.1	4.86	67.1	45.2	62.2	68.4	67.5	64.7	51.1	68.4	5.55	61.8	54.1
4.7.2	4.89	66.8	45.0	59.9	68.0	67.8	65.3	51.2	68.0	5.55	61.6	53.2
4.8	3.93	66.9	47.2	62.1	64.1	62.2	58.0	48.2	64.1	5.55	57.9	51.0
4.9.1	3.82	66.6	50.9	65.0	64.2	61.2	57.0	48.0	65.0	6.77	58.1	63.1
4.9.2	3.84	66.8	51.0	64.6	64.0	61.0	56.8	47.9	64.6	6.77	57.9	62.1
4.10.1	5.58	60.0	44.3	49.9	56.7	58.6	60.2	51.3	60.2	2.19	55.3	45.4
4.10.2	5.57	60.0	41.7	46.8	53.4	57.5	59.6	51.0	59.6	2.19	53.8	45.3
4.11.1	4.66	66.8	41.6	46.1	52.2	54.4	56.8	49.6	56.8	2.19	51.9	47.7
4.11.2	4.67	67.1	41.2	45.4	51.3	53.5	56.0	49.4	56.0	2.19	51.2	47.3
4.12.1	3.79	67.2	39.8	49.5	56.3	57.2	55.5	47.6	57.2	4.48	52.6	39.7
4.12.2	3.77	67.2	39.9	50.7	56.6	57.1	55.1	47.6	57.1	4.48	52.7	42.0
4.13.1	7.68	133.7	41.5	42.6	44.8	46.6	48.5	48.8	48.8	-0.46	46.3	70.8
4.13.2	7.66	133.8	43.0	44.1	46.3	48.5	50.5	50.2	50.5	2.19	48.0	70.2
4.14.1	9.79	138.6	42.8	43.1	44.7	46.2	48.1	49.3	49.3	-0.46	46.3	66.4
4.14.2	9.92	138.4	42.8	42.9	44.2	45.6	47.5	49.1	49.1	-0.46	45.9	63.0
4.15.1	10.43	108.5	39.5	39.7	41.0	42.2	44.0	46.5	46.5	-0.46	42.7	49.7
4.15.2	10.47	108.9	39.6	39.8	41.2	42.5	44.1	46.6	46.6	-0.46	42.8	49.8
4.16.1	6.53	115.1	41.4	42.9	46.4	49.2	51.1	49.8	51.1	2.19	48.0	61.9
4.16.2	6.56	115.3	41.3	42.0	44.7	47.4	49.5	49.2	49.5	2.19	46.7	56.3
4.17.1	6.48	115.3	40.1	41.5	45.9	49.9	52.8	51.0	52.8	2.19	48.4	70.6
4.17.2	6.48	115.2	40.6	42.0	46.4	50.8	54.0	51.9	54.0	2.19	49.2	76.0
4.18	5.39	92.7	40.0	41.1	44.5	50.4	56.2	52.2	56.2	2.19	49.4	68.8
4.19	5.44	92.5	40.3	41.2	43.9	49.7	56.3	52.6	56.3	2.19	49.3	66.1

Table 2-18. Campaign 4 – 6.4mK$^+$/1.6mPZ Temperature Profile Analysis

Run#	L/G	L	Temp 8.05 m	Temp 6.77 m	Temp 5.55 m	Temp 4.48 m	Temp 2.19 m	Temp -0.46 m	T_{max}	T_{max} Loc	T_{ave}	CO_2 Rem Gas-side
	kg/kg	kg/min	°C	°C	°C	°C	°C	°C	°C	m	°C	gmol/min
4.20.1	10.43	111.1	38.8	37.7	37.5	40.9	41.4	44.4	44.4	-0.46	40.5	38.8
4.20.2	10.36	111.1	38.6	37.2	38.2	39.8	41.1	44.3	44.3	-0.46	40.2	38.3
4.21.1	11.58	124.2	39.0	38.8	39.2	40.4	41.5	44.3	44.3	-0.46	40.8	39.7
4.21.2.	11.77	124.8	40.5	40.5	41.1	42.4	43.6	45.7	45.7	-0.46	42.7	42.6
4.22.1	6.84	72.2	36.8	37.5	37.6	40.5	41.0	44.5	44.5	-0.46	40.1	33.1
4.22.2	6.91	72.3	36.7	37.6	37.8	40.4	41.0	44.6	44.6	-0.46	40.2	34.2
4.23	6.80	72.5	37.8	39.0	40.2	42.2	43.3	46.5	46.5	-0.46	42.1	37.3
4.24	6.81	72.6	37.5	38.6	40.0	41.6	42.9	46.2	46.2	-0.46	41.7	36.6
4.25	7.69	81.6	39.5	39.8	40.3	42.5	43.5	46.7	46.7	-0.46	42.5	38.8
4.26.1	9.67	100.3	38.3	38.9	39.9	41.6	43.1	45.1	45.1	-0.46	41.7	45.3
4.26.2	9.72	100.7	38.7	39.3	40.6	42.3	43.8	45.8	45.8	-0.46	42.3	45.7
4.27.1	8.14	86.4	40.0	40.9	42.7	44.4	45.8	47.2	47.2	-0.46	44.2	41.4
4.27.2	8.15	86.5	39.3	39.9	41.6	43.4	44.8	46.5	46.5	-0.46	43.2	40.2
4.28.1	6.71	71.8	38.9	40.0	41.9	43.8	45.3	46.8	46.8	-0.46	43.5	37.5
4.28.2	6.72	71.8	38.4	39.0	40.5	42.5	43.8	45.9	45.9	-0.46	42.3	35.3
4.29.1	6.79	72.1	39.4	40.3	42.2	44.4	46.0	47.5	47.5	-0.46	44.1	39.0
4.29.2	6.79	72.2	39.5	40.6	42.7	45.0	46.8	47.9	47.9	-0.46	44.6	40.4
4.30.1	8.07	86.2	41.0	41.2	42.4	44.7	46.2	48.2	48.2	-0.46	44.6	44.0
4.30.2	8.07	86.5	40.4	40.6	42.5	44.5	45.9	47.9	47.9	-0.46	44.3	46.0
4.31.1	5.69	100.5	41.6	42.5	45.4	47.5	49.1	48.7	49.1	2.19	46.7	48.4
4.31.2	5.74	100.4	41.6	42.4	45.1	47.2	48.8	48.7	48.8	2.19	46.5	48.1
4.32.1	4.83	86.1	43.5	45.6	50.7	53.9	55.8	49.9	55.8	2.19	51.4	47.1
4.32.2	4.85	86.2	43.7	45.9	51.3	55.1	56.6	49.9	56.6	2.19	52.0	45.4
4.33.1	3.99	71.6	45.6	54.3	57.8	56.6	53.7	48.1	57.8	5.55	53.4	44.8
4.33.2	3.99	71.5	45.1	52.6	56.9	56.0	53.7	48.2	56.9	5.55	52.9	43.4

The average temperature of the absorber was found to correlate relatively well with the maximum temperature measured in the absorber column (Figure 2-47). The average absorber temperature increased as the maximum temperature increased. The figure also shows the distribution of the integrated temperature profiles among the three campaigns. The plot shows that the highest temperature was achieved with 5mK+/2.5mPZ solvent with the Flexipac 1Y packing and at inlet CO_2 gas concentrations of 12 and 17%.

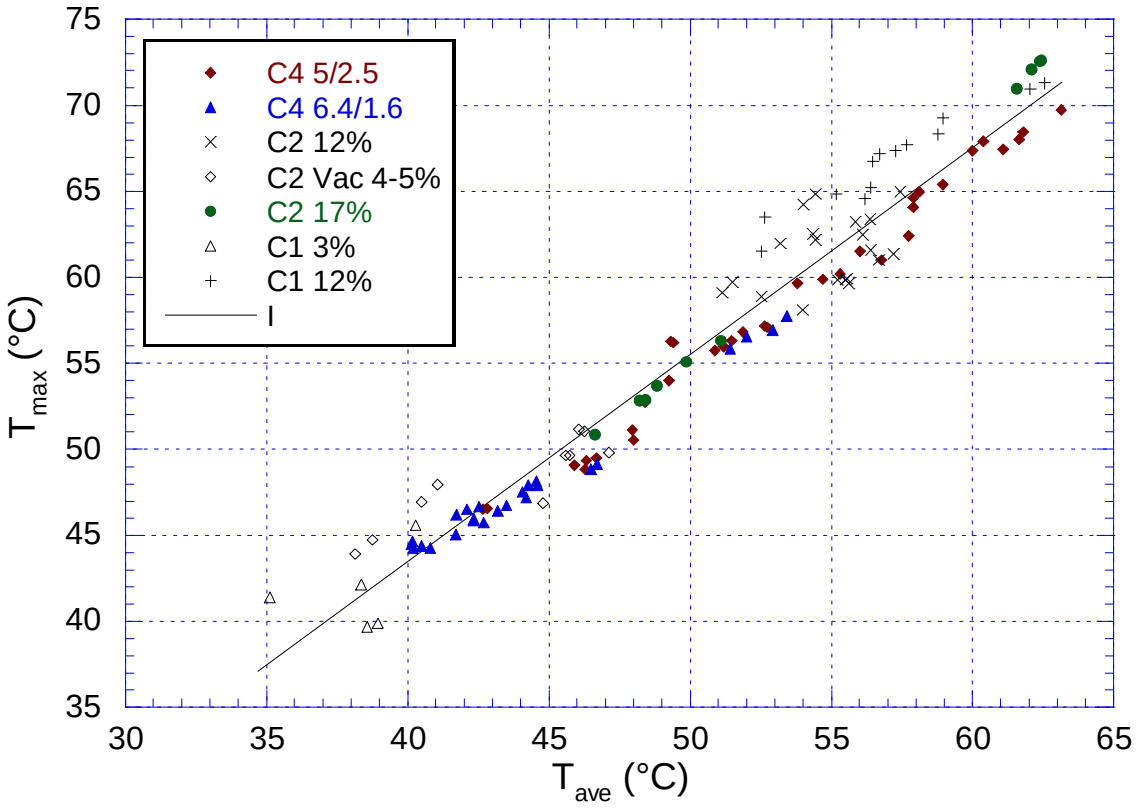

Figure 2-47. Integrated Area of Absorber Temperature Profile and Maximum Temperature Measurements in the Absorber

2.14 PRESSURE DROP

The Flexipac AQ Style 20 structure packing has a corrugation angle of approximately 50 degrees. This results in lower liquid holdup, lower pressure drop, and a higher capacity. The Flexipac 1Y packing has a corrugation angle of 45 degrees, narrower channels, and a higher pressure drop.

Figure 2-48 shows the pressure drop data obtained for all three K^+/PZ campaigns. The pressure drop was calculated taking the square root of the total pressure drop across the absorber column and normalizing by the inlet superficial gas velocity. The total pressure drop was calculated as the sum of the pressure drop for the top (PDT 451) and bottom (PDT 450) packing bed. The figure shows that the Flexipac 1Y packing used in Campaigns 1 and 2 had a higher pressure drop normalized by gas velocity than the

Flexipac AQ structured packing used in Campaign 4. The total pressure drop across the column in Campaigns 1 and 2 were comparable, but the gas rate was typically higher in Campaign 2. The average superficial gas velocity for Campaigns 1 and 2 were 1.06 and 1.43 m/s, respectively.

An analysis of the Campaign 1 pressure drop data, found that when the ratio for the pressure drop of the bottom bed to top bed exceeded one, the points fell inside the circled region of the figure, where the ratio ranged from 1.1 to 2.2. The majority of the remaining points were had bottom to top bed ratios of approximately 0.95. The pressure drop for the low gas flow rate points in Campaign 2 was similar to the high bottom to top bed ratio values of Campaign 1. However in Campaign 2, the threshold for bottom to top bed ratio was 1.4. The low gas rate points of Campaign 2 that felled in the circled region had a bottom to top bed ratio that ranged from 1.8–5.3. It is possible that for some of these points, the bottom bed of the absorber column was foaming. For other points of Campaign 2, the ratio of the pressure drop for the bottom and top bed ranged from 0.9 to 1.4.

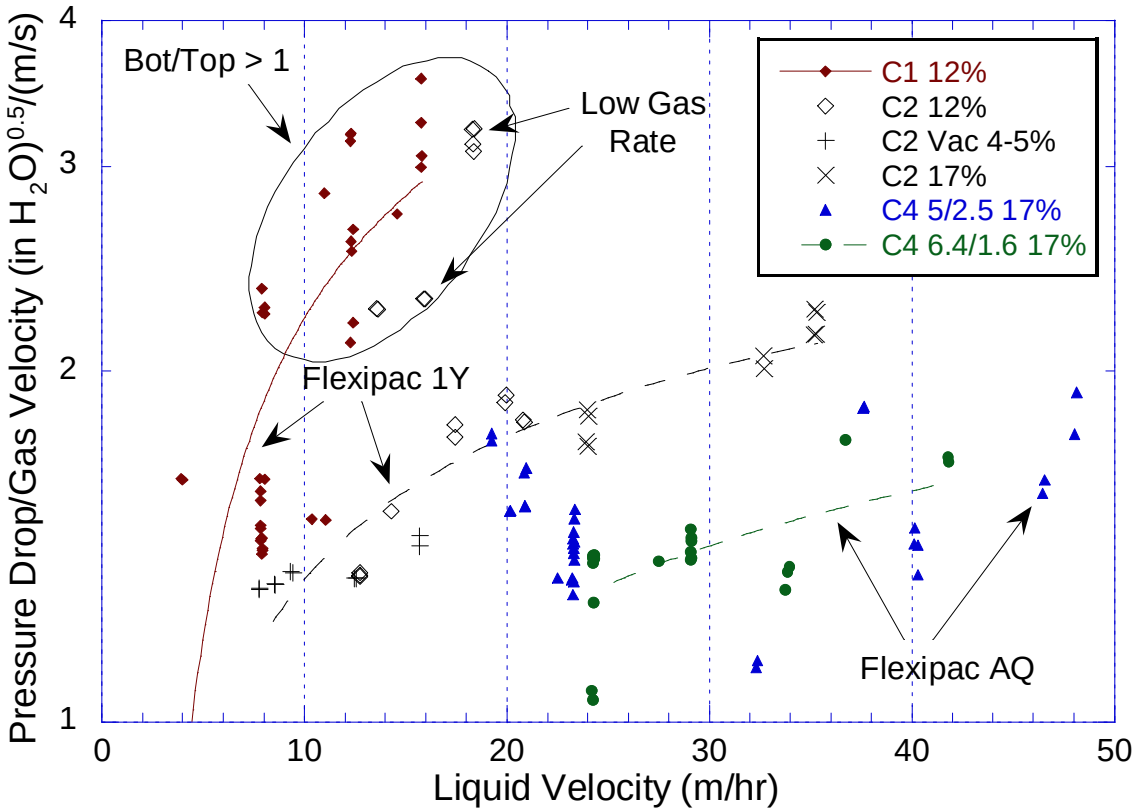

Figure 2-48. Pressure Drop Data of Flexipac 1Y and Flexipac AQ Style 20 for Campaigns 1,2, and 4 (5mK$^+$/2.5mPZ and 6.4mK$^+$/1.6mPZ Solvent)

Figure 2-49 is a plot of the Flexipac AQ Style 20 data for the 5mK$^+$/2.5mPZ and 6.4mK$^+$/1.6mPZ solvent compositions. For a given liquid rate and a gas rate of 0.95 m/s, the figures shows that the 6.4mK$^+$/1.6mPZ solvent has a lower total pressure drop than the 5mK$^+$/2.5mPZ. At a gas rate of 1.59 m/s both solvents had comparable pressure drop measurements. This is most likely due to temperature bulge effect. When the temperature bulge is large, the density of the gas is much lower and will increase the pressure drop. The 6.4mK$^+$/1.6mPZ has a slower CO_2 absorption rate and does not generate much of temperature bulge at low gas rates (high L/G), which results in a lower pressure drop. At high gas rates (low L/G), the figure suggests that the hydrodynamics of

the gas and liquid outweigh the effects of the temperature bulge since the temperature bulge for the 6.4mK$^+$/1.6mPZ solvent were lower than the 5mK$^+$/2.5mPZ solvent.

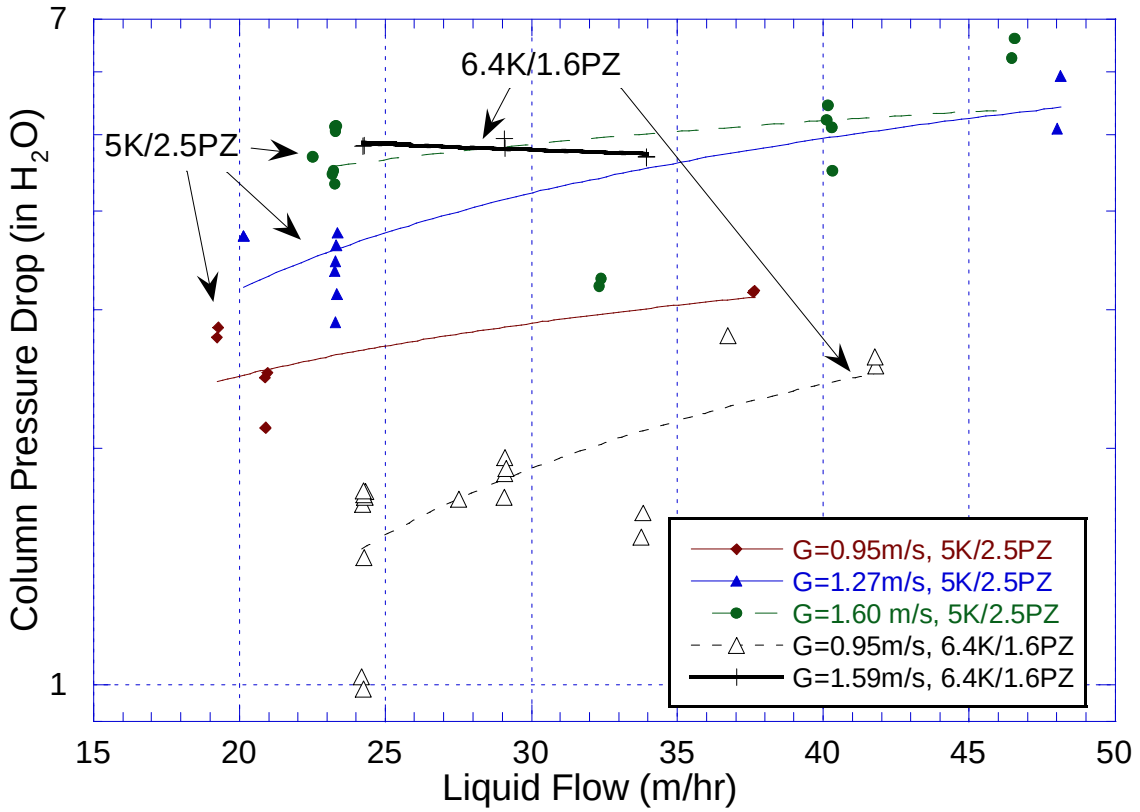

Figure 2-49. Pressure Drop of Flexipac AQ Style 20 for Campaign 4 as a Function of Solvent Composition (5mK$^+$/2.5mPZ and 6.4mK$^+$/1.6mPZ)

2.15 STRIPPER HEAT DUTY

In the first two campaigns, the stripper feed was not pre-heated adequately. Therefore, the heat duty obtained for the Campaigns 1 and 2 were not representative. In Campaign 4, a plate and frame cross-exchanger was installed which reduced the approach temperature relative to the reboiler to 5-10 °C. However, due to the high temperature, the stripper feed to the distributor was severely flashing. It was estimated that the feed entering the distributor was approximately 90–95% gas. In future pilot plant campaigns,

a two-phase distributor should be used, which should improve the mass transfer performance in the stripper.

The reboiler heat duty for Campaign 4 is shown in Figure 2-50. The heat duty was calculated based on the steam rate to the reboiler and does not account for heat loss from the stripper. A detailed analysis of stripper performance for the fourth campaign is presented in Oyenekan (2007). The plot shows that reboiler heat duty increases with CO_2 removal efficiency for the $5mK^+/2.5mPZ$ and $6.4mK^+/1.6mPZ$ solvent compositions. However, it appears that the $5mK^+/2.5mPZ$ solvent has a lower heat duty for a given CO_2 removal efficiency. This was unexpected since the $6.4mK^+/1.6mPZ$ solvent has a lower heat of absorption than $5mK^+/2.5mPZ$ solvent.

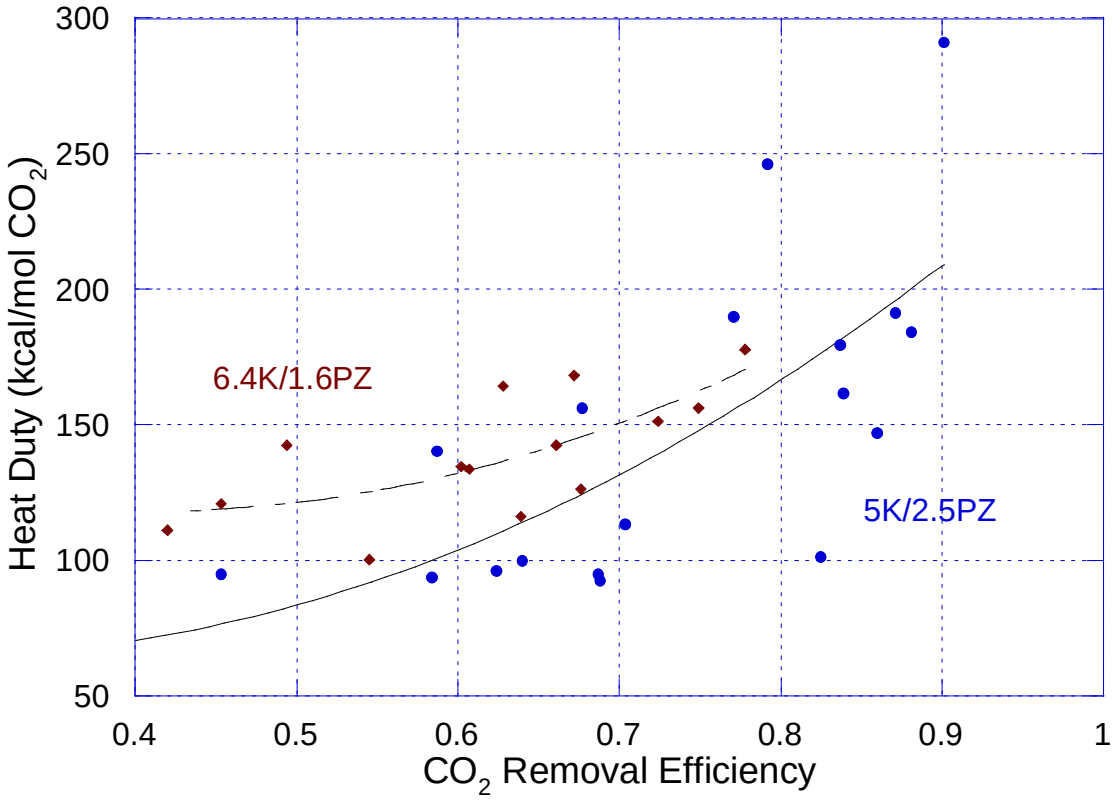

Figure 2-50. Campaign 4 Stripper Performance for 5mK^+/2.5mPZ and 6.4mK^+/1.6mPZ

2.16 CROSS EXCHANGER PERFORMANCE

The number of transfer units (NTU) per pass for the Alfa Laval M6-FG plate and frame cross-exchanger was calculated and plotted against the solvent flow rate. The cross-exchanger has a heat transfer area of 14.8 m^2, consists of 99 plates and is arranged for 5 pass flow. Figure 2-51 shows that the NTUs per pass are inversely related to the liquid flow rate. The approach temperatures of the 5m K^+/2.5m PZ and the 6.4m K^+/1.6m PZ solvent ranged from 6.9 to 8.9°C and 3.4 to 6.4°C, respectively. The approach temperature was lower for the 6.4m K^+/1.6m PZ because it was operated under vacuum and the stripper temperature profile was much lower. As a result, the NTU dependence is slightly different than the 5m K^+/2.5m PZ solvent.

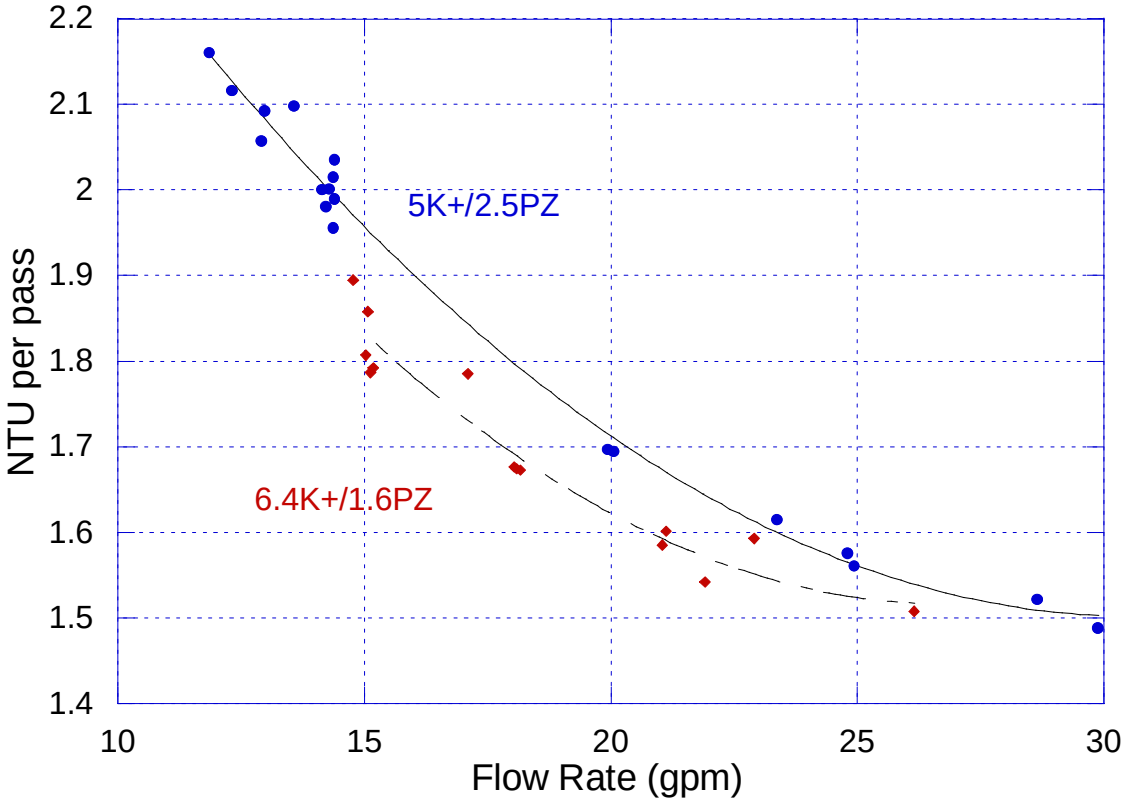

Figure 2-51. Number of Transfer Units for Alfa Laval M6-FG Plate and Frame Cross-Exchanger (Area = 14.8 m^2, 99 Plates, 5 Pass Flow)

2.17 CONCLUSIONS

The real-time process measurements were reasonably accurate, with the exception of the temperature measurement for the absorber inlet pH meter. The stripper lean mass flowmeter needs to be examined to determine the cause of the oscillating density, temperature, and volumetric flow measurements. The liquid flow measurements demonstrated some oscillation, which had a standard deviation between 1 and 4%.

The effective interfacial area of Flexipac 1Y was 30% less than Flexipac AQ Style 20, while the specific dry area of Flexipac 1Y was approximately twice that of the Flexipac AQ packing. Better mass transfer performance was observed with Flexipac 1Y

packing, which may due to higher liquid holdup from the inherent design of the packing and from bridging. The K_g for Flexipac 1Y was approximately two times higher than that of Flexipac AQ over the same partial pressure range. The K_g of the $5mK^+/2.5mPZ$ solvent was approximately three times higher than the $6.4mK^+/1.6mPZ$ solvent. The capacity of the $5mK^+/2.5mPZ$ solvent was also about 50% higher than the $6.4mK^+/1.6mPZ$. For Flexipac 1Y, the K_g for the $5mK^+/2.5mPZ$ solvent was approximately two times higher than the 7 molal MEA.

Heat loss from the uninsulated absorber column may be significant. The temperature bulge was quantified by integrating the area under the absorber temperature profile and was correlated with the maximum measured temperature. The location of the temperature bulge moves from the top of the column to bottom as the L/G ratio is increased.

The pressure drop normalized by the gas rate was approximately 1.5–2 times higher in the Flexipac 1Y than in Flexipac AQ Style 20, which had steeper corrugation angle. Lower pressure drop was observed with $6.4mK^+/1.6mPZ$ at the lower gas rate because of a low magnitude temperature bulge. However, at high gas rates, the pressure bulge will be dictated only by hydraulics.

In future campaigns, it is recommended that the concentration of water in the liquid samples be analyzed. This would greatly help to interpret and validate the liquid analysis for potassium, piperazine and carbon dioxide concentration. It is also recommended that quality control and quality assurance for the liquid sampling and liquid analysis of CO_2 loading be verified and validated.

References

Aseyev, G. G., *Electrolytes. Transport Phenomena. Methods for Calculation of Multicomponent Solutions and Experimental Data on Viscosities and Diffusion Coefficients*. Begell House Inc. : New York, 1998; p 549.

Aseyev, G. G.; Zaytsev, I. D., *Volumetric Properties of Electrolyte Solutions - Estimation Methods and Experimental Data*. Begell House Inc.: New York, 1996; p 1572.

Aspen Technology Inc. *Aspen Plus Help File*, Cambridge, Massachusetts, 2006.

Aspiron, N., Surface Tension Models for Aqueous Blends. *Ind. Eng. Chem. Res.* **2005,** 44, 7270-7278.

Aspiron, N., Nonequilibrium Rate-Based Simulation of Reaction Systems: Simulation Model, Heat Transfer, and Influence of Film Discretization. *Ind. Eng. Chem. Res.* **2006,** 45, 2054-2069.

Billet, R.; Schultes, M., Predicting mass transfer in packed columns. *Chem. Eng. Technol.* **1993,** 16, (1), 1-9.

Bishnoi, S.; Rochelle, G. T., Absorption of Carbon Dioxide in Aqueous Piperazine/Methyldiethanolamine. *AIChE J.* **2002,** 48, 2788-2799.

Bosch, H.; Versteeg, G. F.; Van Swaaij, W. P. M., Gas-Liquid Mass Transfer with Parallel Reversible Reactions-II. Absorption of CO_2 into Amine-Promoted Carbonate Solutions. *Chem. Eng. Sci.* **1989,** 44, (11), 2735-2743.

Bravo, J. L.; Fair, J. R., Generalized correlation for mass transfer in packed distillation columns. *Ind. Eng. Chem. Proc. Des. Dev.* **1982,** 21, (1), 162-170.

Bravo, J. L.; Rocha, J. A.; Fair, J. R., Mass transfer in gauze packings. *Hyd. Proc.* **1985,** 64, (1), 91-95.

Caplow, M., Kinetics of Carbamates Formation and Breakdown. *J. Am. Chem. Soc.* **1968,** 90, 6795-6803.

Chen, C.-C., Email from Aspen Tech Regarding HPZCOO IONMOB Adjustments. In 2006.

Chen, C. C.; Britt, H. I.; Boston, J. F.; Clarke, W. M., Thermodynamic Property Evaluation in Computer-Based Flowsheet Simulation for Aqueous Electrolyte

Systems. *AIChE Symposium Series, Tutorial Lectures in Electrochemical Eng. and Tech. II, no. 229* **1983,** 79, 126.

Chilton, T. H.; Colburn, A. P., Mass Transfer (Absorption) Coefficients Prediction from Data on Heat Transfer and Fluid Friction. *Ind. Eng. Chem.* **1934,** 26, (11), 1183-1187.

CO2Net Capturing and Storing Carbon Dioxide: Technical Lessons Learned September 2004. www.co2net.com/infocentre/reports/technical_lessons_learned_final_report.pdf

Criss, C. M.; Cobble, J. W., The thermodynamic properties of high-temperature aqueous solutions. V. The calculation of ionic heat capacities up to 200 Deg. Entropies and heat capacities above 200 Deg. *J. Am. Chem. Soc.* **1964,** 86, (24), 5390-3.

Cullinane, J. T. Carbon Dioxide Absorption in Aqueous Mixtures of Potassium Carbonate and Piperazine. M.S. Thesis, The University of Texas as Austin, Austin, 2002.

Cullinane, J. T. Thermodynamics and Kinetics of Aqueous Piperazine with Potassium Carbonate for Carbon Dioxide Absorption. Ph.D. Dissertation, The University of Texas at Austin, Austin, 2005.

Danckwerts, P. V., The Reaction of Carbon Dioxide with Ethanolamines. *Chem. Eng. Sci.* **1979,** 34, 443-446.

deMontigny, D.; Aboudheir, A.; Tontiwachwuthikul, P.; Chakma, A., Modelling the Performance of a CO_2 Absorber Containing Structured Packing. *Ind. Eng. Chem. Res.* **2006,** 45, (8), 2594-2600.

Design Institute for Physical Properties (DIPPR), *Project 801 - Database of Physical and Thermodynamic Properties of Pure Chemicals*. American Institute of Chemical Engineers: New York, 2006.

Ducroux, R.; Jean-Bapiste, P. *Technologies, Methods, and Modelling for CO_2 Capture*, 7th International Greenhouse Gas Control Technologies, Vancouver, Canada, 2004.

Dugas, R. Pilot Plant Study of Carbon Dioxide Capture by Aqueous Monoethanolamine. M.S. Thesis, The University of Texas at Austin, Austin, 2006.

Escobillana, G. P.; Saez, J. A.; Perez-Correa, J. R.; Neuburg, H. J.; Kershenbaum, L. S., Behavior of Absorption/Stripping Columns for the CO_2-MEA System; Modeling and Experiments. *Can. J. Chem. Eng.* **1991,** 69, 969-977.

Freguia, S. Modeling of CO_2 Removal from Flue Gases with Monoethanolamine. M.S. Thesis, The University of Texas at Austin, Austin, 2002.

Furukawa, S. K.; Bartoo, R. K. Improved Benfield Process for Ammonia Plants. http://www.uop.com/gasprocessing/TechPapers/ImprovedBenfield.pdf (1/28),

Gabrielsen, J.; Michelsen, M. L.; Stenby, E. H.; Kontogeorgis, G. M., Modeling of CO_2 Absorber using an AMP Solution. *AIChE J.* **2006,** 52, (10), 3443-3451.

Hee-Moon, E.; Jun-Han, K.; Kyoung-Ryong, J.; Young-Mo, A. *CO2 Recovery Pilot Plant*, 7th International Conference on Greenhouse Gas Control Technologies, Vancouver, Canada, 2004.

Hilliard, M. *CO_2 Capture by Absorption with Potassium Carbonate - First Quarterly Report*; U.S. Dept. of Energy: 2003.

Hilliard, M. Thermodynamics of Aqueous Piperazine, Potassium Carbonate, Carbon Dioxide Characterized by Electrolyte NRTL Model within Aspen Plus. M.S. Thesis, The University of Texas at Austin, Austin, 2005.

Horvath, A. L., *Handbook of Aqueous Electrolyte Solutions*. Ellis Horwood, Ltd: Chichester, 1985.

Idem, R.; Wilson, M.; Tontiwachwuthikul, P.; Chakma, A.; Veawab, A.; Aroonwilas, A.; Gelowitz, D., Pilot Plant Studies of the CO_2 Capture Performance of Aqueous MEA and Mixed MEA/MDEA Solvents at the University of Regina CO_2 Capture Technology Development Plant and the Boundary Dam CO_2 Capture Demonstration Plant. *Ind. Eng. Chem. Res.* **2006,** 45, (8), 2414-2420.

Iijama, M.; Ishida, K.; Takashina, T.; Tanaka, H.; Hirata, T.; Yonekawa, T. *Carbon Dioxide Capture Technology for Coal Fired Boiler*, 7th International Conference on Greenhouse Gas Control Technologies Vancouver, Canada, 2004.

IPCC, *Special Report on Carbon Dioxide Capture and Storage. Prepared by Working Group III of the Intergovernmental Panel on Climate Change*. Cambridge University Press: Cambridge, 2005; p 442.

Kenig, E. Y.; Schneider, R.; Gorak, A., Reactive Absorption: Optimal Process Design Via Optimal Modeling. *Chem. Eng. Sci.* **2001,** 56, 343-350.

King, C. J., *Separation Processes*. 2nd ed.; McGraw-Hill Book Company: New York, 1980.

Knudsen, J. N.; Vilhelmsen, P.-J.; Biede, O.; Jensen, J. N. *CASTOR 1 t/h CO2 Absorption Pilot Plant at the Elsam Kraft A/S Esberg Power Plant - First Year Operation Experience*, 8th International Conference on Greenhouse Gas Control Technologies, Trondheim, Norway, 2006.

Kohl, A. L.; Neilsen, R. B., *Gas Purification*. 5th ed.; Gulf Publishing Co.: Houston, 1997.

Krishna, R.; Standart, G. L., A Multicomponent Film Model Incorporating an Exact Matrix Method of Solution to the Maxwell-Stefan Equations. *AIChE J.* **1976,** 22, 383-389.

Kucka, L.; Muller, I.; Kenig, E. Y.; Gorak, A., On the Modeling and Simulation of Sour Gas Absorption by Aqueous Amine Solutions. *Chem. Eng. Sci.* **2003,** 58, 3571-3578.

Lewis, J. C.; Seibert, A. F.; Fair, J. R., Effective Mass Transfer Areas in Packed Absorbers. In *AIChE 2006 Annual Meeting*, San Francisco, CA, 2006.

Littel, R. J. Selective Carbonyl Sulfide Removal in Acid Gas Treating Processes. Ph.D. Dissertation, Twente University, 1991.

Littel, R. J.; Van Swaaij, W. P. M.; Versteeg, G. F., Kinetics of Carbon Dioxide with Tertiary Amines in Aqueous Solution. *AIChE J.* **1990,** 36, (11), 1633-1640.

Littel, R. J.; Versteeg, G. F.; Van Swaaij, W. P. M., Kinetics of CO_2 with Primary and Secondary Amines in Aqueous Solutions. I. Zwitterion Deprotonation Kinetics of DEA and DIPA in Aqueous Blends of Alkanolamines. *Chem. Eng. Sci.* **1992a,** 47, 2027-2035.

Littel, R. J.; Versteeg, G. F.; Van Swaaij, W. P. M., Kinetics of CO2 with Primary and Secondary Amines in Aqueous Solutions. II. Influence of Temperature on Zwitterion Formation and Deprotonation Rates. *Chem. Eng. Sci.* **1992b,** 47, 2037-2045.

Marland, G.; Boden, T. A.; Andres, R. J. *Global, Regional, and National CO2 Emissions. In Trends: A Compendium of Data on Global Change*; Carbon Dioxide Information Analysis Center, Oak Ridge National Laboratory, U.S. Department of Energy: Oak Ridge, Tenn., U.S.A., May 30, 2006.

Ohishi, T.; Iwasaki, S.; Tanaka, H.; Hirata, T.; Iijama, M.; Ishida, K.; Yonekawa, T. *Long Term Testing of the Capture of CO2 from a Coal-fired Boiler*, 8th International Conference on Greenhouse Gas Control Technologies, Trondheim, Norway, 2006.

Onda, K.; Takeuchi, H.; Okumoto, Y., Mass Transfer Coefficients between Gas and Liquid Phases in Packed Columns. *J. Chem. Eng. Japan* **1968,** 1, 56-62.

Oyenekan, B. Modeling of Strippers for CO_2 Capture by Aqueous Amines. Ph.D. Dissertation, The University of Texas at Austin, Austin, 2007.

Pacheco, M. A. Mass Transfer, Kinetics, and Rate-based Modeling of Reactive Absorption. Ph.D. Dissertation, The University of Texas at Austin, Austin, 1998.

Pacheco, M. A.; Rochelle, G. T., Rate-Based Modeling of Reactive Absorption of CO_2 and H_2S into Aqueous Methyldiethanolamine. *Ind. Eng. Chem. Fundam.* **1998,** 37, 4107-4117.

Pandya, J. D., Adiabatic Gas Absorption and Stripping with Chemical Reaction in Packed Towers. *Chem. Eng. Commun.* **1983,** 19, 343-361.

Peng, J. J., Email from Aspen Tech Regarding Liquid Holdup Specification in RateSep. In 2007.

Pintola, T.; Tontiwachwuthikul, P.; Meisen, A., A Simulation of Pilot Plant and Industrial CO_2-MEA Absorbers. *Gas Sep. Purif.* **1993,** 7, 47-52.

Pohorecki, R. M., Wladyslaw. , Kinetics of Reaction Between Carbon Dioxide and Hydroxyl Ions in Aqueous Electrolyte Solutions. . *Chem. Eng. Sci.* **1988,** 43, (7), 1677-1684.

Reid, R. C.; Prausnitz, J. M.; Poling, B. E., *The Properties of Gases and Liquids*. 4th ed.; McGraw-Hill: New York, 1987.

Rizzuti, L.; Augugliaro, V.; Cascio, G. L., The influence of the liquid viscosity on the effective interfacial area in packed columns. *Chem. Eng. Sci.* **1981,** 36, (6), 973-978.

Rocha, J. A.; Bravo, J. L.; Fair, J. R., Distillation Columns Containing Structured Packings: A Comprehensive Model for Their Performance. 1. Hydraulic Models. *Ind. Eng. Chem. Res.* **1993,** 32, 641-651.

Rocha, J. A.; Bravo, J. L.; Fair, J. R., Distillation Columns Containing Structured Packings: A Comprehensive Model for Their Performance. 2. Mass Transfer Model. *Ind. Eng. Chem. Res.* **1996,** 35, 1660-1667.

Sartori, G.; Savage, D. W., Sterically Hindered Amines for CO_2 Removal from Gases. *Ind. Eng. Chem. Fundam.* **1983,** 22, 239-249.

Saxena, M. N.; Flintoff, W., Engineering and Economics of CO_2 Removal and Sequestration. *Hyd. Proc.* **2006**, (December), 57-64.

Say, G. R.; Heinzelmann, F. J.; Iyengar, J. N.; Savage, D. W.; Bisio, A.; Sartori, G., A New, Hindered Amine Concept for Simultaneous Removal of CO_2 and H_2S from Gases. *Chem. Eng. Prog.* **1984,** 80, (10), 72-77.

Stichlmair, J.; Bravo, J. L.; Fair, J. R., General Model for Prediction of Pressure Drop and Capacity of Countercurrent Gas/Liquid Packed Columns. *Gas Sep. Purif.* **1989,** 3, 19-28.

Tontiwachwuthikul, P.; Meisen, A.; Lim, C. J., CO_2 Absorption by NaOH, Monoethanolamine and 2-Amino-2-Methyl-1-Propanol Solutions in a Packed Column. *Chem. Eng. Sci.* **1992,** 47, (2), 381-390.

Treybal, R. E., Adiabatic Gas Absorption and Stripping in Packed Towers. *Ind. Eng. Chem.* **1969,** 61, (7), 36-41.

Tseng, P. C.; Ho, W. S.; Savage, D. W., Carbon Dioxide Absorption into Promoted Carbonate Solutions. *AIChE J.* **1988,** 34, (6), 922-931.

Tseng, P. C.; Ho, W. S.; Savage, D. W., Carbon Dioxide Absorption into Promoted Carbonate Solutions. *AIChE. J.* **1998,** 34, (6), 922-931.

U.S. EPA *Inventory of U.S. Greenhouse Gas Emissions and Sinks: 1990-2004*; EPA 430R06002; Washington D.C., April 15, 2006, 2006.

Wang, G. Q.; Yuan, X. G.; Yu, K. T., Review of Mass-Transfer Correlations for Packed Columns. *Ind. Eng. Chem. Res.* **2005,** 44, (23), 8715-8729.

Wilke, C. R.; Chang, P., Correlation of Diffusion Coefficients in Dilute Solutions. *AIChE J.* **1955,** 2, 264-270.

Wilson, I. Gas-Liquid Contact Area of Random and Structured Packing. M.S. Thesis, The University of Texas at Austin, Austin, 2004.

Wilson, M.; Tontiwachwuthikul, P.; Chakma, A.; Idem, R.; Veawab, A.; Aroonwilas, A.; Gelowitz, D.; Henni, A.; Mahinpey, N. *The International Test Centre for Carbon Dioxide Capture (ITC)*, 7th International Conference on Greenhouse Gas Control Technologies, Vancouver, Canada, 2004a.

Wilson, M.; Tontiwachwuthikul, P.; Chakma, A.; Idem, R.; Veawab, A.; Aroonwilas, A.; Gelowitz, D.; Stobbs, R. *Evaluation of the CO2 Capture Performance of the University of Regina CO2 Technology Development Plant and the Boundary Dam*

CO2 Demonstration Plant, 7th International Conference on Greenhouse Gas Control Technologies, Vancouver, Canada, 2004b.

Xiao, J.; Li, C.-W.; Li, M.-H., Kinetics of Absorption of Carbon Dioxide into Aqueous Solutions of 2-Amino-2-Methyl-1-Propanol + Monoethanolamine. *Chem. Eng. Sci.* **2000,** 55, 161-175.

Yagi, Y.; Mimura, T.; Ishida, K.; Yoshiyama, R.; Kamijo, T.; Yonekawa, T. *Improvements of Carbon Dioxide Capture Technology from Flue Gas*, 7th International Conference on Greenhouse Gas Control Technologies, Vancouver, Canada, 2005.